DOE-ER-0313/69
ORNL/SPR-2021/1910

Distribution
Categories
UC-423, -424

FUSION MATERIALS
SEMIANNUAL PROGRESS REPORT
FOR THE PERIOD ENDING

December 31, 2020

Prepared for
DOE Office of Fusion Energy Sciences
(AT 60 20 10 0)

DATE PUBLISHED: March 2021

Prepared by
OAK RIDGE NATIONAL LABORATORY
Oak Ridge, Tennessee 37831
Managed by
UT-Battelle, LLC
For the
U.S. DEPARTMENT OF ENERGY

FOREWORD

This is the sixty-ninth in a series of semiannual technical progress reports on fusion materials science activity supported by the Fusion Energy Sciences Program of the U.S. Department of Energy. It covers the period ending December 31, 2020. This report focuses on research addressing the effects on materials properties and performance of exposure to the neutronic, thermal and chemical environments anticipated in the chambers of fusion experiments and energy systems. This research is a major element of the national effort to establish the materials knowledge base for an economically and environmentally attractive fusion energy source. Research activities on issues related to the interaction of materials with plasmas are reported separately.

The results reported are the products of a national effort involving a number of national laboratories and universities. A large fraction of this work, particularly in relation to fission reactor irradiations, is carried out collaboratively with partners in Japan, Russia, and the European Union. The purpose of this series of reports is to provide a working technical record for the use of program participants, and to provide a means of communicating the efforts of fusion materials scientists to the broader fusion community, both nationally and worldwide.

This report has been compiled by Stephanie Melton, Oak Ridge National Laboratory. Her efforts, and the efforts of the many persons who made technical contributions, are gratefully acknowledged.

Daniel Clark
Research Division
Office of Fusion Energy Sciences

TABLE OF CONTENTS

1 FERRITIC/MARTENSITIC STEEL DEVELOPMENT

1.1 MICROHARDNESS MEASUREMENT UPDATES FOR SELECTED SSJ3 SPECIMENS IN JP28&29, F8B1, F8B2, F13B5, AND RB19J—X. Chen, J. Reed, J.W. Geringer, Y. Katoh (Oak Ridge National Laboratory), T. Nozawa, H. Tanigawa (QST) **1**

1.2 RESPONSE OF CANDIDATE FUSION BLANKET MATERIALS TO DUAL AND TRIPLE ION IRRADIATION TO UNDERSTAND THE SYNERGIES BETWEEN H, He and RADIATION DAMAGE—Logan N. Clowers, Zhijie Jiao, Gary S. Was (University of Michigan) **2**

1.3 CREEP/TOUGHNESS PROPERTY EVALUATION OF MODIFIED 3Cr BAINITIC STEELS—Y. Yamamoto (Oak Ridge National Laboratory) **9**

1.4 THE EVOLUTION OF ALPHA-PRIME (α') PRECIPITATES IN HIGH PURITY Fe-(10-18)Cr ALLOYS AFTER THERMAL AGING AND ION IRRADIATIONS—Y. Zhao, S.J. Zinkle, P. Zhu (University of Tennessee), A. Bhattacharya (Oak Ridge National Laboratory), J. Henry (CEA) **12**

1.5 ADVANCED CHARACTERIZATION OF RAFM STEEL MICROSTRUCTURES—C. M. Parish (ORNL) **20**

1.6 GLOBAL THERMAL CREEP MODELS DERIVED FROM A COMPREHENSIVE MULTIPLE HEAT DATABASE ON 9Cr TEMPERED MARTENSITIC STEELS—M.E. Alam, T. Yamamoto, G.R. Odette (University of California Santa Barbara) **24**

1.7 A MICROSTRUCTURALLY BASED MODEL FOR POST INCUBATION VOID SWELLING IN DUAL ION BEAM IRRADIATED TEMPERED MARTENSITIC STEELS—Takuya Yamamoto, G. Robert Odette (University of California Santa Barbara), Kenta Yoshida (Tohoku University), Kiyohiro Yabuuchi (Kyoto University) **38**

1.8 TENSILE PROPERTIES OF EUROFER97 STEEL VARIANTS IRRADIATED TO TARGET 2.5 DPA, 300°C IN THE EUROFUSION PROGRAM—A. Bhattacharya, X. Chen, J. Reed, T. Graening, J.W. Geringer, Y. Katoh (Oak Ridge National Laboratory), M. Rieth (KIT) **48**

2 ODS AND NANOCOMPOSITED ALLOY DEVELOPMENT

2.1 EFFECT OF CARBON CONTENT ON CARBIDE-VERSION CASTABLE NANOSTRUCTURED ALLOYS—L. Tan, W. Zhong, Y. Yang (Oak Ridge National Laboratory) **53**

2.2 STEM STUDY OF HELIUM-IMPLANTED NANOSTRUCTURED FERRITIC ALLOYS—Yan-Ru Lin, Steven John Zinkle (University of Tennessee), David T. Hoelzer, Lizhen Tan (Oak Ridge National Laboratory) **56**

TABLE OF CONTENTS

2.3 **X-RAY DIFFRACTION STUDY OF NANOSTRUCTURED FERRITIC ALLOYS AND REDUCED ACTIVATION FERRITIC MARTENSITIC STEELS**—D.J. Sprouster, L.L. Snead (Stony Brook University), A. Bhattacharya, Y. Katoh (Oak Ridge National Laboratory), S. Levine, S. Zinkle (University of Tennessee) **59**

2.4 **DEVELOPMENT OF ODS Fe-10Cr ALLOYS**—D.T. Hoelzer, C.P. Massey (Oak Ridge National Laboratory) **67**

2.5 **NEUTRON IRRADIATION INDUCED HARDENING IN RAFM AND ODS STEELS**—A. Bhattacharya, J. Reed, X. Chen, J.W. Geringer, Y. Katoh (Oak Ridge National Laboratory), T. Nozawa, H. Tanigawa (QST) **78**

2.6 **APPLICATION OF PRINCIPAL COMPONENT ANALYSIS TO VISUALIZE NANO-OXIDES AND PRECIPITATES IN NEUTRON-IRRADIATED AND HELIUM INJECTED PM2000**—Dalong Zhang, Danny J. Edwards, Matthew J. Olszta, Alan Schemer-Kohrn, Karen Kruska, Wahyu Setyawan (Pacific Northwest National Laboratory), T. Yamamoto, Y. Wu, G.R. Odette (University of California Santa Barbara) **83**

2.7 **A NEW CRACK HEALING MECHANISM IN AN ANNEALED 14YWT NANOSTRUCTURED FERRITIC ALLOY—**M.E. Alam, S. Pal, N. J. Cunningham, G. R. Odette (University of California Santa Barbara) **90**

3 **CERAMIC COMPOSITE STRUCTURAL MATERIAL DEVELOPMENT**

3.1 **ADDITIVE MANUFACTURING OF SILICON CARBIDE FOR NUCLEAR FUSION APPLICATIONS**—Takaaki Koyanagi, Kurt Terrani, Yutai Katoh (Oak Ridge National Laboratory), Shay Harrison (Free Form Fibers), Jian Liu (PolarOnyx, Inc.) **105**

4 **PLASMA-FACING AND HIGH HEAT FLUX MATERIALS AND COMPONENT TESTING**

4.1 **INCORPORATING CRYSTALLOGRAPHIC ORIENTATION INTO THE STUDY OF TUNGSTEN HEAVY ALLOY BOUNDARIES**—James V. Haag IV, Mitsu Murayama (Virginia Tech), Danny Edwards, Jing Wang, Wahyu Setyawan (Pacific Northwest National Laboratory) **106**

4.2 **TEM STUDY OF Ni^+ AND He^+ ION IRRADIATED DUCTILE-PHASE TOUGHENED TUNGSTEN**—Weilin Jiang, Dalong Zhang, Alan Schemer-Kohrn, Bethany Matthews, Wahyu Setyawan (Pacific Northwest National Laboratory) **112**

4.3 **MICROSTRUCTURE-MECHANICAL PROPERTY CORRELATION IN DUCTILE PHASE TOUGHENED W-NiFe HEAVY ALLOY**—Jing Wang, David Collins, Nicole R. Overman, Ramprashad Prabhakaran, Ziqing Zhai, Wahyu Setyawan, Charles H. Henager (Pacific Northwest National Laboratory) **117**

4.4 **MATERIALS FOR THE US-JAPAN FRONTIER IRRADIATIONS—**L. M. Garrison, J. R. Echols, N. C. Reid, Y. Katoh (Oak Ridge National Laboratory) **132**

TABLE OF CONTENTS

4.5 **ELECTRICAL CONDUCTIVITY EVALUATION OF NEUTRON IRRADIATED TUNGSTEN MATERIALS FROM THE PHENIX CAMPAIGN—**J. R. Echols, L. M. Garrison (Oak Ridge National Laboratory) **137**

4.6 **FABRICATION OF ULTRA HIGH TEMPERATURE CERAMICS THROUGH DIRECT CURRENT SINTERING—**B. Cheng, D.J. Sprouster, J. R. Trelewicz, L.L. Snead (Stony Brook University) **141**

4.7 **MULTIMODAL MICROSTRUCTURAL CHARACTERIZATION AND THERMAL STABILITY OF SOLUTE-STABILIZED NANOSTRUCTURED TUNGSTEN ALLOYS—**N. Olynik, D.J. Sprouster, J.R. Trelewicz (Stony Brook University), C.M. Parish (Oak Ridge National Laboratory) **144**

5.0 **ADVANCED MANUFACTURING**

5.1 **DEVELOPMENT OF NOVEL STEELS WITH NANOPRECIPITATE DISPERSIONS VIA ADDITIVE MANUFACTURING FOR HELIUM EFFECTS STUDIES**—Weicheng Zhong, Ying Yang, Lizhen Tan (Oak Ridge National Laboratory), Niyanth Sridharan (Lincoln Electric), Dieter Isheim (Northwestern University), T.M. Kelsy Green, Kevin G. Field (University of Michigan) **150**

5.2 **SYNCHROTRON ANALYSIS OF WIRE ARC ADDITIVE MANUFACTURED G-91 STEEL—**I.K. Robin, S. J. Zinkle (University of Tennessee), D.J. Sprouster, L.L. Snead (Stony Brook University) **154**

5.3 **ODS FeCrAl PRODUCTION USING ADDITIVE MANUFACTURING WITH IN SITU OXIDATION**—Ty Austin, Steven J. Zinkle (University of Tennessee), Niyanth Sridharan (Lincoln Electric) **163**

5.4 **CHEMICAL VAPOR INFILTRATION OF BINDER JETTED TUNGSTEN**—J. R. Echols, L. M. Garrison, Y. Katoh (Oak Ridge National Laboratory) **170**

5.5 **AM PRODUCTION OF TUNGSTEN FOR DIVERTOR COMPONENTS**—Betsy Ellis, Christopher Ledford, Lauren Garrison, Michael Kirka, Yutai Kato, Ryan Dehoff (Oak Ridge National Laboratory) **173**

6.0 **EFFECTS OF RADIATION**

6.1 **DYNAMIC OBSERVATION OF DUAL-BEAM IRRADIATED IRON AND Fe-10Cr AT 435°C**—Yan-Ru Lin, Steven John Zinkle (University of Tennessee), Wei-Ying Chen, Meimei Li (Argonne National Laboratory) **177**

6.2 **TEMPERATURE-DEPENDENT CAVITY SWELLING IN DUAL-ION IRRADIATED IRON AND IRON-CHROMIUM FERRITIC ALLOYS**—Yan-Ru Lin, Steven John Zinkle (University of Tennessee), Arunodaya Bhattacharya (Oak Ridge National Laboratory) **178**

6.3 **POST-IRRADIATION EVALUATION OF FRACTURE TOUGHNESS PROPERTIES OF F82H-Mod3 IRRADIATED IN THE RABBIT CAPSULE F13A5**—X. Chen, R. Swain, J. Reed, A. Campbell, J.W. Geringer, Y. Katoh (Oak Ridge National Laboratory), T. Nozawa, H. Tanigawa (QST) **180**

TABLE OF CONTENTS

6.4 **AN ELECTRON MICROSCOPE STUDY OF HEAVY ION IRRADIATED ULTRA-HIGH PURITY Fe AND Fe-Cr ALLOYS AT 350℃**—Yao Li, Steven John Zinkle (University of Tennessee), Arunodaya Bhattacharya (Oak Ridge National Lab) **186**

6.5 **DEVELOPMENT OF OPEN-SOURCE, HIGH-FIDELITY APT DATA ANALYSIS ALGORITHMS FOR CHARACTERIZING NUCLEAR STRUCTURAL MATERIALS—**Samara Levine, Steven Zinkle (University of Tennessee), Arunodaya Bhattacharya (Oak Ridge National Laboratory), Cristelle Pareige (University of Rouen) **199**

7.0 **PLASMA MATERIALS INTERACTIONS**

7.1 **ENHANCED THERMAL STABILITY OF HELIUM-IMPLANTED SURFACE GRAINS IN WARM-ROLLED TUNGSTEN—**Cuncai Fan, Yutai Katoh, Xunxiang Hu (Oak Ridge National Laboratory) **202**

7.2 **DAMAGE-MECHANISM INTERACTIONS AT THE PLASMA-MATERIALS INTERFACE—**C. M. Parish, D. G. Morrall (Oak Ridge National Laboratory) **204**

7.3 **EFFECTS OF NITROGEN ON TUNGSTEN SURFACES INVESTIGATED WITH LOW ENERGY ION SCATTERING—**C. S. Wong, J. A. Whaley, R. D. Kolasinski (Sandia National Laboratories) **206**

8.0 **FUSION CORROSION AND COMPATIBILITY SCIENCE**

8.1 **LIQUID METAL COMPATIBILITY OF SiC AND FeCrAl IN FLOWING Pb-Li—**B. A. Pint, J. Jun, M. Romedenne (Oak Ridge National Laboratory) **212**

9.0 **MODELING AND COMPUTATIONAL STUDY**

9.1 **AB INITIO MODELING OF He-SOLUTE INTERACTION IN ALPHA-IRON**—Huibin Ke, Wahyu Setyawan (Pacific Northwest National Laboratory) **218**

9.2 **CALCULATION OF DEPTH DEPENDENT ACTIVATION ENERGY BARRIERS OF TRAP MUTATION REACTIONS IN W(111) SURFACE**—Giridhar Nandipati, Kenneth J. Roche, Richard J. Kurtz, Wahyu Setyawan (Pacific Northwest National Laboratory), Karl D. Hammond (University of Missouri), Dimitrios Maroudas (University of Massachusetts), Brian D. Wirth (University of Tennessee) **219**

9.3 **INVESTIGATION OF THE MICROSTRUCTURAL EFFECTS ON THE MECHANICAL BEHAVIOR AND DAMAGE DEVELOPMENT IN DUCTILE-PHASE TOUGHENED TUNGSTEN COMPOSITES**—Ba Nghiep Nguyen, Jing Wang, Charles H. Henager Jr., Lay Paw, Wahyu Setyawan (Pacific Northwest National Laboratory) **224**

9.4 **VIRTUAL CRYSTAL APPROXIMATION CALCULATION OF LATTICE MISMATCH IN INTERPHASE BOUNDARIES IN W-NiFe ALLOYS**—W. Setyawan (Pacific Northwest National Laboratory) **235**

TABLE OF CONTENTS

9.5 **ANALYSIS OF DISLOCATION LOOP IMPINGEMENT PROBABILITIES IN IRRADIATED MATERIALS**—Peter Doyle, Steven Zinkle (University of Tennessee) **239**

10 **IRRADIATION & TESTING METHODS, EXPERIMENTS AND SCHEDULES**

10.1 **IRRADIATION TEMPERATURE ESTIMATION OF EUROFUSION 2.5 DPA PHASE- I IRRADIATIONS FOR SS-J3 SAMPLES USING SiC THERMOMETRY**—A. Bhattacharya, J.W. Geringer, Y. Katoh (Oak Ridge National Laboratory), M. Rieth (KIT) **245**

10.2 **HFIR IRRADIATION EXPERIMENTS**—C. On, J. W. Geringer, J. L. McDuffee (Oak Ridge National Laboratory) **253**

10.3 **MINIATURE MECHANICAL TEST DEVELOPMENT FOR TUNGSTEN-BASED MATERIALS**—L. M. Garrison, N. C. Reid, M. N. Gussev (Oak Ridge National Laboratory), J. P. Allain (Pennsylvania State University) **256**

10.4 **AN UPDATE ON THE FRACTURE TOUGHNESS OF THE PNNL AS-SINTERED AND HOT-ROLLED W-NiFe HEAVY TUNGSTEN ALLOY: EFFECTS OF ALLOY STRENGTH, SPECIMEN ORIENTATION AND PRE-CRACK VERSUS NOTCH DEFECT GEOMETRY**—M.E. Alam, G.R. Odette (University of California Santa Barbara), J. Wang, C.H. Henager, W. Setyawan (Pacific Northwest National Laboratory) **257**

10.5 **IRRADIATION OF QST F82H TENSILE AND BEND BAR SPECIMENS IN HFIR**—N. Russell, C. On, X. Chen, J. Geringer (Oak Ridge National Laboratory) **266**

1. FERRITIC/MARTENSITIC STEEL DEVELOPMENT

1.1 MICROHARDNESS MEASUREMENT UPDATES FOR SELECTED SSJ3 SPECIMENS IN JP28&29, F8B1, F8B2, F13B5, AND RB19J—X. Chen, J. Reed, J.W. Geringer, Y. Katoh (Oak Ridge National Laboratory), T. Nozawa, H. Tanigawa (QST)

The extended abstract presents updates of hot cell microhardness measurements on selected SSJ3 tensile specimens in JP28&29, F8B1, F8B2, F13B5, and RB19J

Vickers microhardness measurements were performed on selected SSJ3 tensile specimens in JP28&29, F8B1, F8B2, F13B5, and RB19J. The hardness tester used was Mitutoyo HV-120B located in cell #4 of the irradiated materials examination and testing facility at Oak Ridge National Laboratory. All tested were performed with 1 kg force and 15 sec dwell time. The measurement results are summarized in Table 1.

Table 1. Summary of microhardness measurement results for selected SSJ3 tensile specimens in JP28&29, F8B1, F8B2, F13B5, and RB19J

Capsule ID	Specimen ID	Hardness measurements (HV)											Avg. HV	Std. Dev. HV
		1	2	3	4	5	6	7	8	9	10	11		
JP28&29	065	359	386.8	401.4	412.9	399.5	395.8	385.9	381.5	394.9	366.3	-	388.4	16.3
	H64	339.1	335.5	329.8	328.4	316.9	313	345.1	346.6	343.6	334.1	342.8	334.1	11.2
	H65	351.9	334.1	321.6	334.8	341.4	330.5	349.6	328.4	342.1	318.2	337.3	335.4	10.6
F8B1	5Y0	429.1	428.1	411	422.9	445.2	426	441.9	445.2	425	-	-	430.5	11.5
	5Y1	417.9	428.1	424	423.3	428.1	428.1	433.1	436.5	438.6	440.8	-	429.9	7.3
	5Y2	398.6	416.9	428.1	417.9	424	420.9	398.6	414.9	408.1	426	-	415.4	10.6
	5Z2	410	432.3	403.3	422.9	407.1	407.1	420.9	422.9	407.1	427	-	416.1	10.2
	5Z3	417.9	408.1	415.9	415.9	425	412.9	417.9	427	422.9	-	-	418.2	6.0
	TH0	435.4	458.6	435.4	459.8	398.6	462.1	390.3	393.1	453	-	-	431.8	30.0
	TH2	352.7	323.6	388.5	405.2	390.3	367.1	395.8	356.6	380.6	350.4	-	371.1	25.4
	TH3	373.7	362.2	343.6	332	384.1	337.7	372.1	378	345.8	366.3	-	359.6	18.4
	TH0T	427	459.8	359	367.1	402.4	371.2	385.9	390.3	372.1	378.9	-	391.4	31.0
F8B2	FG0	383.2	401.4	424	413.9	436.5	425	398.6	441.9	438.6	-	-	418.1	20.3
	FG1	404.2	357.4	374.6	369.6	400.5	402.4	362.2	374.6	352.7	362.2	-	376.0	19.5
	FG2	387.7	353.5	376.3	417.9	418.9	369.6	398.6	392.2	382.3	-	-	388.6	21.4
	FG3	381.5	372.9	439.7	353.5	349.6	412.9	355	362.2	383.2	350.4	-	376.1	29.8
	FG4	394	390.3	367.1	402.4	363.8	412.9	385	378	403.3	394	-	389.1	15.8
	IW0	381.5	379.7	367.1	360.6	374.6	376.3	396.7	374.6	381.5	382.3	-	377.5	9.7
	IW1	384.1	372.9	367.1	367.1	394	385	389.4	402.4	367.9	382.3	-	381.2	12.2
	IW2	381.5	387.7	370.4	372.9	378.9	363.8	393.1	372.9	382.3	326.4	-	373.0	18.5
	IW3	400.5	365.4	390.3	374.6	383.2	379.7	385.9	369.6	398.6	372.9	-	382.1	11.9
	IW4	407.1	383.2	388.5	372.9	398.6	378.9	393.1	406.2	359	371.2	-	385.9	15.8
F13B5	HW0	447.4	394	474.8	425	434.4	378	355	470.4	440.8	388.5	-	420.8	40.3
	HW3	437.6	389.4	490.1	480.1	381.5	335.5	386.8	392.2	404.2	430.2	-	412.8	47.3
	HW4	404.2	394.9	401.4	379.7	359	405.2	394.9	395.8	392.2	414.9	-	394.2	15.5
	HW5	434.4	437.6	462.1	353.5	391.3	413.9	390.3	392.2	405.2	398.6	-	407.9	30.6
	XKT1	361.4	366.3	372.9	352.7	351.9	364.6	334.1	345.1	367.9	-	-	357.4	12.5
	XKT2	323.6	366.3	379.7	360.6	359	392.2	416.9	332.7	372.9	375.4	-	367.9	27.0
	XMT1	357.4	383.2	370.4	348.1	348.9	376.3	356.6	314.3	320.9	402.4	-	357.9	27.0
	XMT2	378.9	355.8	346.6	363.8	373.7	353.5	372.1	358.2	358.2	338.4	-	359.9	12.6
RB19J	OV6E	242.3	247.6	244.5	251.3	249	258.5	-	-	-	-	-	248.9	5.7
	OV6F	268	263.4	253.2	254.6	253.2	257.5	264.4	252.7	250.9	259.4	-	257.7	5.8
	OV6G	252.7	259.4	257	258.5	259	258	-	-	-	-	-	257.4	2.5

1.2 RESPONSE OF CANDIDATE FUSION BLANKET MATERIALS TO DUAL AND TRIPLE ION IRRADIATION TO UNDERSTAND THE SYNERGIES BETWEEN H, He and RADIATION DAMAGE—Logan N. Clowers, Zhijie Jiao, Gary S. Was (University of Michigan)

OBJECTIVE

The objective of this project is to understand the synergy between transmutation gasses H and He on cavity evolution in ferritic-martensitic fusion blanket materials.

SUMMARY

Three ferritic/martensitic alloys; F82H, Fe8Cr2W and CNA3 were studied for the effect of H and He on swelling. Single ion beam (Fe^{2+}), dual ion beam (Fe^{2+}+He^{2+}), and triple ion beam (Fe^{2+}+He^{2+}+H^{+}) irradiations were conducted at 500°C to a damage level of 50 dpa and dual and triple beam irradiation experiments were conducted at 450°C to 50 dpa. Cavity distribution and swelling were comparable in dual ion beam and triple ion beam irradiated F82H at 500°C, indicating that the role of hydrogen in swelling in triple beam irradiated F82H appeared to be insignificant compared to the role of helium. Swelling in Fe8Cr2W and CNA3 at 500°C was approximately 3-4X greater than that at 450°C. In F82H, the average cavity size and swelling were minimally larger at 500°C than at 450°C. The significant role of hydrogen in swelling has yet to be confirmed. Future efforts will focus on separate effects experiments to understand the role of hydrogen in cavity swelling.

PROGRESS AND STATUS

Experiments

Ion irradiation

Three reduced activation ferritic/martensitic (RAFM) steels; F82H (IEA heat from the National Institutes of Quantum and Radiological Science and Technology in Japan), CNA3 (from ORNL) and Fe8Cr2W (made at Ames laboratory) were used in this project. The nominal compositions of the three alloys are given in Table 1. Ion irradiations were conducted at the Michigan Ion Beam Laboratory (MIBL) using the 3 MV Pelletron accelerator to provide a defocused beam of 5 MeV Fe^{2+} for irradiation damage, the 1.7 MV Tandetron to provide a raster-scanned beam of 2 MeV He^{2+} to be passed through a ~3 μm thick Al degrader foil for helium implantation, and the implanter to provide a raster-scanned beam of 400 keV H^{+} through a second ~2.3 μm Al degrader foil for hydrogen implantation. Samples were irradiated in the multi-beam chamber (Figure 1a). Three types of ion irradiation; single ion beam (Fe^{2+}), dual ion beam (Fe^{2+}+He^{2+}), and triple ion beam (Fe^{2+}+He^{2+}+H^{+}) were conducted at 500°C to a damage level of 50 dpa. In addition, dual and triple beam irradiation experiments were conducted at 450°C to 50 dpa. The damage profiles from self-ions and the concentration profiles of injected H/He calculated using a custom MATLAB script along with SRIM-2013 are shown in Figure 1b. The appm/dpa ratios for helium and hydrogen are 40 appm/dpa and 10 appm/dpa, respectively, at the depth of analysis (400-800nm from the surface). A narrower band of 500-700nm was used to minimize dpa variation in cavity data. Helium reached 2000 appm and hydrogen reached 500 appm in the region of interest (500-700nm) at the end of 50 dpa irradiation at a damage rate of ~$1x10^{-3}$ dpa/s.

Table 1. Nominal composition of each alloy of interest (wt%)

Alloy	Fe	Cr	W	C	V	Ta	Ni	Mn	Mo	Si	Other
F82H	Bal	7.71	1.95	0.09	0.16	0.02	0.02	0.16	0.003	0.11	-
CNA3	Bal	8.6	1.3	0.10	0.10	0.10	-	1.00	-	0.15	0.15Ti
Fe8Cr2W	Bal	8.47	2.02	0.06	-	-	-	-	-	0.02	

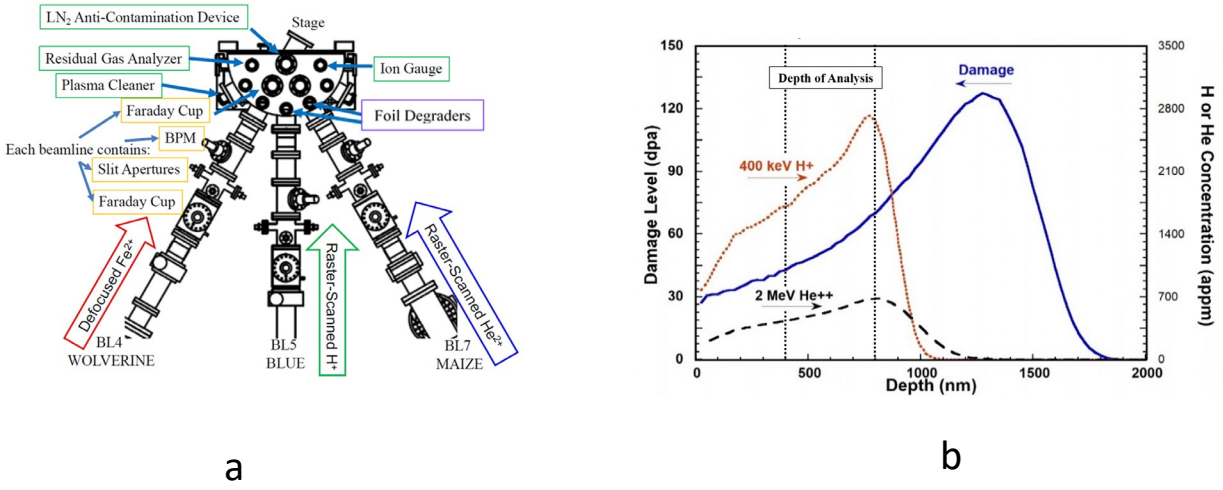

Figure 1. (a) Diagram of the multi-beam chamber at MIBL; (b) SRIM depth profiles of damage and H/He gas injection.

Cavity microstructure characterization

Transmission electron microscopy (TEM) samples were prepared using standard FIB lift-out methods in a TFS Nova 200 or a Helios 650 Nanolab SEM/FIBs at the Michigan Center for Materials Characterization (MC^2). Cavities greater than 5 nm were characterized using High-angle annular dark-field imaging - scanning transmission electron microscopy (HAADF-STEM) while cavities less than 5 nm were characterized using the bright field (BF) TEM technique with a defocus depth of 1 µm in the TFS Talos TEM/STEM microscope. Typically, 500 cavities were characterized in the region of interest (500-700nm) per alloy and irradiation condition. The foil thicknesses were measured to be in the range 40-70 nm via electron energy loss spectroscopy (EELS) conducted on a JEOL 2100F transmission electron microscope or the Talos at MC^2. Errors in cavity size, density and swelling were estimated to be 10%, 10% and 30%, respectively.

RESULTS

Comparison of cavities in single beam, dual beam and triple beam irradiated F82H at 500°C

A TEM-BF image of single beam irradiated F82H at 500°C to 50 dpa is shown in Figure 2. Some cavities were observed in the first ~300nm probably due to the oversaturation of vacancies near the surface which promoted nucleation and growth. However, no resolvable cavities were detected in the region of interest (500-700nm between the dashed lines). The dual and triple ion irradiated samples, on the other hand, exhibited substantial densities of cavities as shown in both HAADF and BF images in Figure 3a. This indicates that gas implantation is necessary for cavity

nucleation in F82H. The size distributions of cavities in dual beam and triple beam irradiated F82H are qualitatively similar (Figure 3b). It was observed that the triple beam irradiated case exhibited both a higher density of small (<2nm) bubbles as well as a higher density of larger (>20nm) sized cavities from the size distribution plot, perhaps hinting at a (subtle) role of injected hydrogen on the nucleation of small bubbles as well as the stable growth of cavities to larger sizes. A summary of the cavity characterization data for these irradiations is given in Table 2 and the comparison of size, density of cavities>5nm and total swelling is shown in Figure 3c. The average cavity size and the total swelling are slightly larger in the triple beam irradiated sample, but the difference between the two is within the error bars. The role of hydrogen in swelling at 500°C in triple beam irradiated F82H appears to be insignificant compared to the role of helium in dual beam irradiated sample. The total swelling between dual and triple ion irradiated F82H in these conditions were 0.72% and 0.93% respectively. The dual ion irradiation swelling appears to be larger than those reported in the literature [1,2] (0.04 at 510°C and 0.08% at 470°C) but the triple ion irradiation swelling is within the reported range (0.15% at 510°C and 3.2% at 470°C). It is noteworthy though the helium/dpa level in these references is 18 appm/dpa, or nearly twice as large as that used in this project. A planned dual ion beam irradiation experiment with $Fe^{2+}$and H^{+} will help to clarify the role of hydrogen at this temperature.

Table 2. Summary of cavity characterization result in dual beam and triple beam irradiated F82H at 500°C to 50 dpa

	Dual ion beam					Triple ion beam				
	Cavity<5nm		Cavity>5nm			Cavity <5nm		Cavity >5nm		
	Avg. Dia. (nm)	Number Density (10^{21} m^{-3})	Avg. Dia. (nm)	Number Density (10^{21} m^{-3})	Swelling (%)	Avg. Dia. (nm)	Number Density (10^{21} m^{-3})	Avg. Dia. (nm)	Number Density (10^{21} m^{-3})	Swelling (%)
F82H	2.0	53.5	12.1	4.0	0.72	1.5	77.6	13.8	3.4	0.95

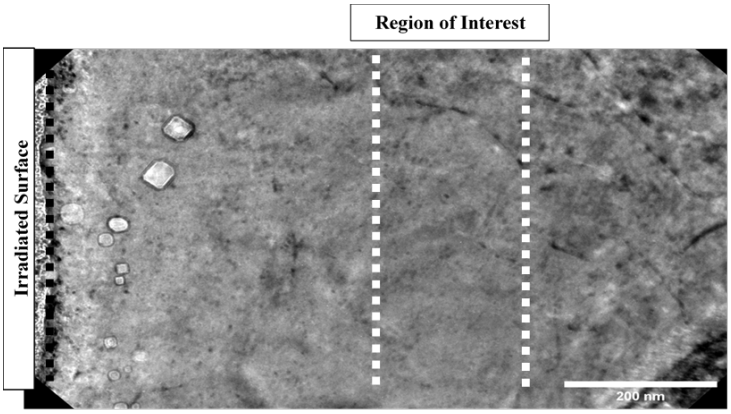

Figure 2. TEM-BF image of single beam irradiated F82H at 500°C to 50 dpa showing absence of cavities in the region of interest (between dashed lines).

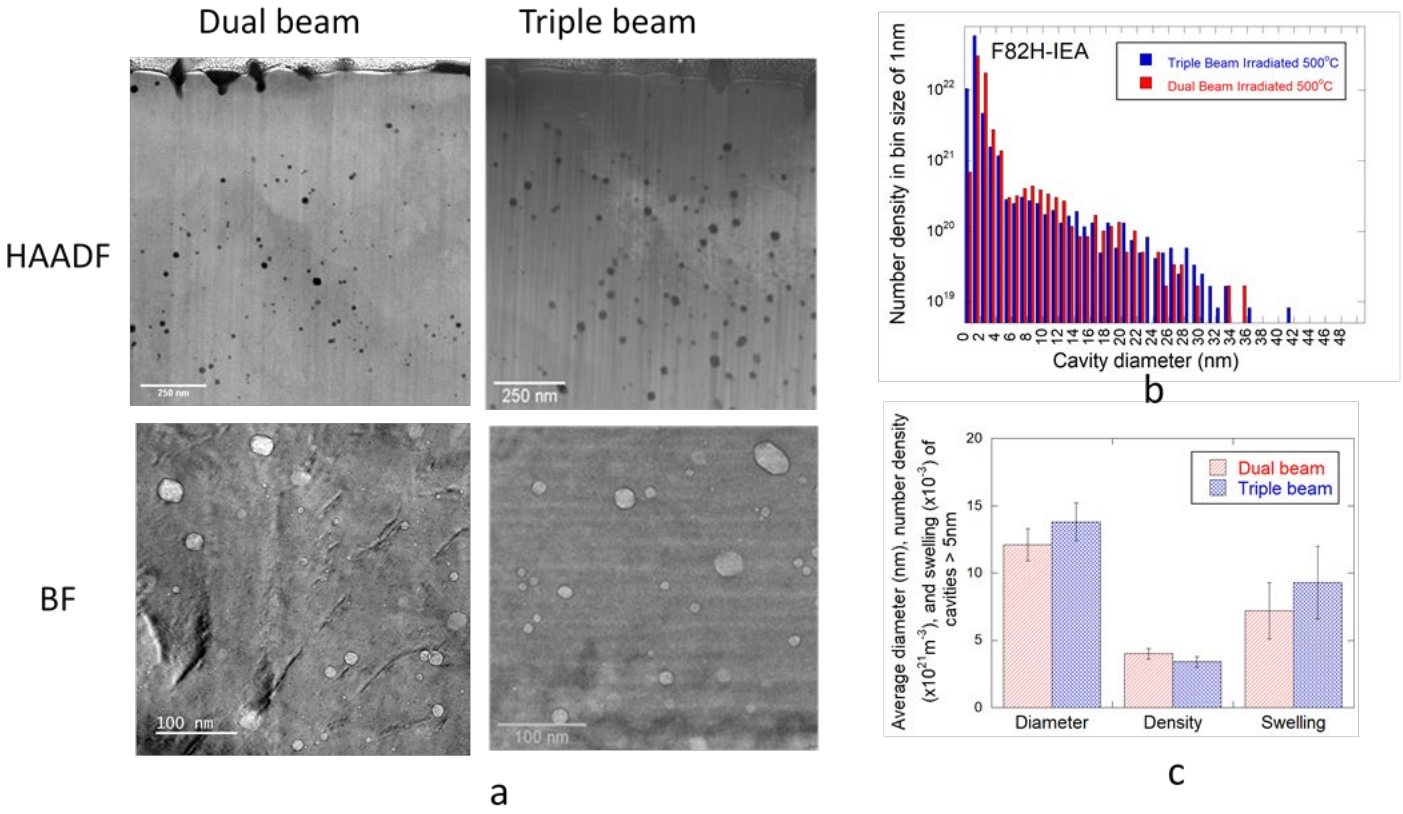

Figure 3. (a) STEM-HAADF and TEM-BF images of cavities and comparison of (b) size distribution and (c) average size, number density and swelling of cavities in dual beam and triple beam irradiated F82H at 500°C to 50 dpa.

Temperature effect on swelling in triple beam irradiated F82H, Fe8Cr2W and CNA3

In addition to irradiations at 500°C, cavities were characterized in triple ion beam irradiated F82H, Fe8Cr2W and CNA3 at 450°C to 50 dpa. The results are given in Table 3 for both irradiation temperatures. Comparison of cavities at 450°C and 500°C in F82H, Fe8Cr2W and CNA3 are shown in Figures 4-6, respectively. Comparisons of average cavity diameter, number density and swelling among the three alloys at 450°C and 500°C are shown in Figure 7a-7c, respectively. In general, the average cavity size and swelling are larger at 500°C with minimal difference in F82H (swelling: 0.85% at 450°C and 0.93% at 500°C). The effect of temperature on swelling in Fe8Cr2W and CNA3 is greater with increase of 3-4X at 500°C over that at 450°C. Swelling in F82H at 500°C (0.93%) is the smallest among the three alloys (2.12% in Fe8Cr2W and 1.57% in CNA3), perhaps due to the higher number density (7.8x 10^{22} m^{-3}) of small cavities (<5nm) or bubbles observed in this alloy. Suppression of swelling due to over-nucleation of small bubbles has been demonstrated in the literature [3]. However, suppression of swelling in CNA3 due to the added nanosized precipitates was expected but not observed in the triple ion beam irradiation experiments at either 450°C or 500°C.

Table 3. Summary of cavity characterization results in triple beam irradiated Fe8Cr2W, CNA3 and F82H at 450°C and 500°C to 50 dpa

	450°C					500°C				
	Cavity <5nm		Cavity >5nm			Cavity <5nm		Cavity >5nm		
	Avg. Dia. (nm)	Number Density (10^{21} m^{-3})	Avg. Dia. (nm)	Number Density (10^{21} m^{-3})	Swelling (%)	Avg. Dia. (nm)	Number Density (10^{21} m^{-3})	Avg. Dia. (nm)	Number Density (10^{21} m^{-3})	Swelling (%)
Fe8Cr2W	2.0	37.0	9.8	5.7	0.48	2.6	16.9	14.4	5.8	2.14
CNA3	2.3	46.2	10.5	4.2	0.56	2.1	46.3	19.5	2.1	1.60
F82H	1.8	51.3	11.8	6.4	0.88	1.5	77.6	13.8	3.4	0.95

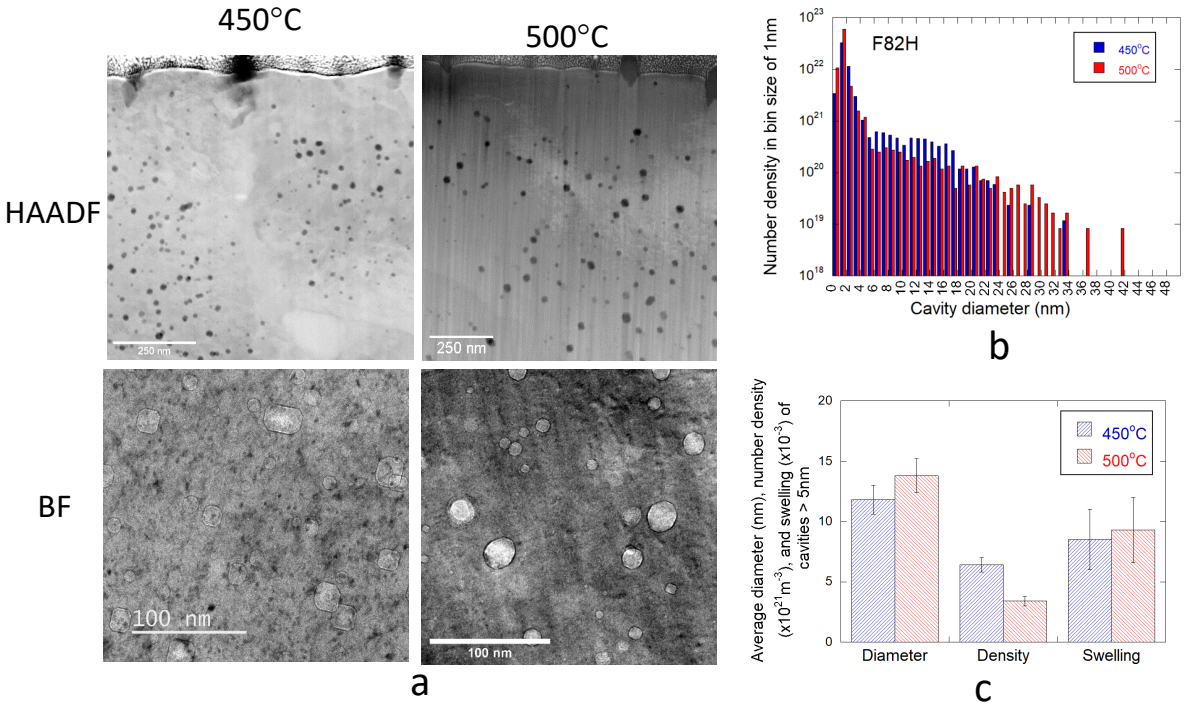

Figure 4. (a) STEM-HAADF and TEM-BF images of cavities and comparison of (b) size distribution and (c) average size, number density and swelling of cavities in triple beam irradiated F82H at 450°C and 500°C to 50 dpa.

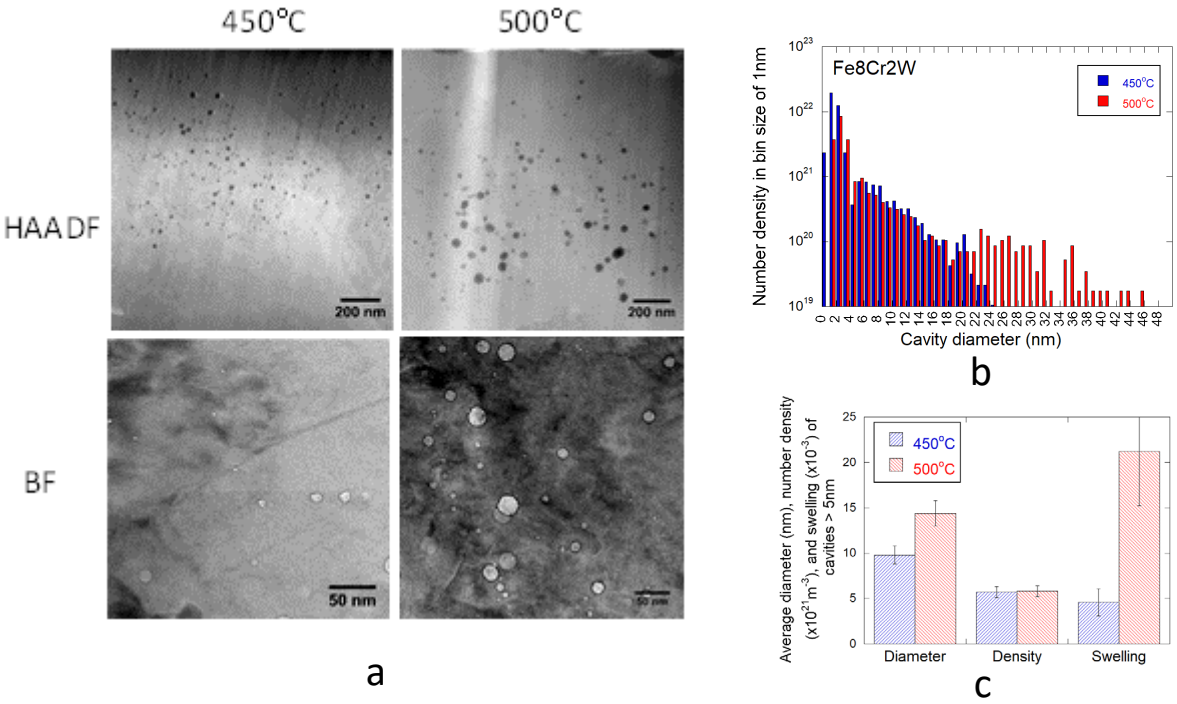

Figure 5. (a) STEM-HAADF and TEM-BF images of cavities and comparison of (b) size distribution and (c) average size, number density and swelling of cavities in triple beam irradiated Fe8Cr2W at 450°C and 500°C to 50 dpa.

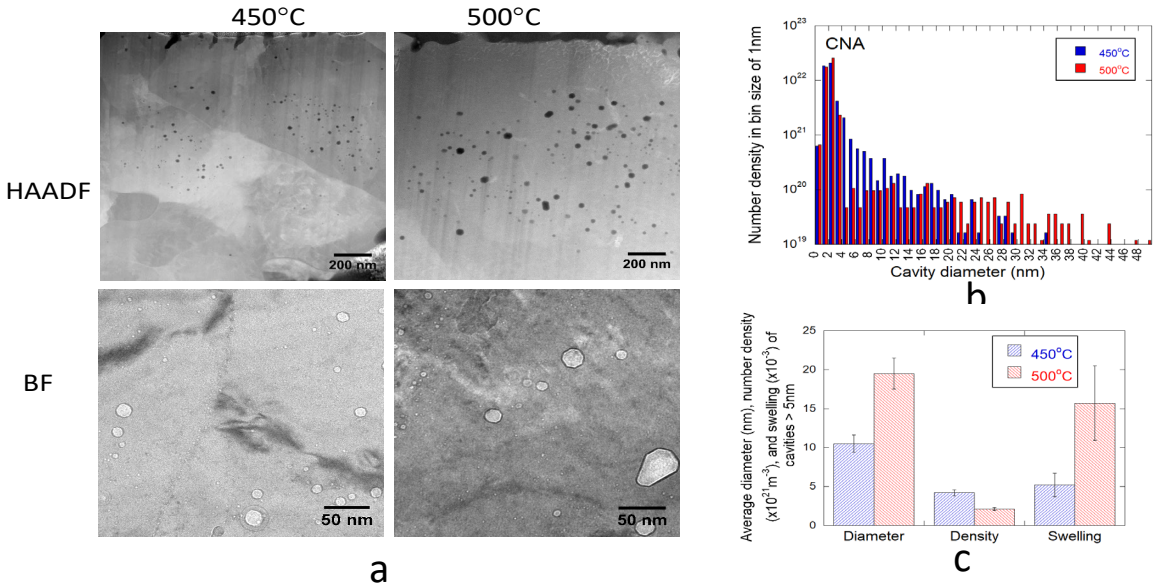

Figure 6. (a) STEM-HAADF and TEM-BF images of cavities and comparison of (b) size distribution and (c) average size, number density and swelling of cavities in triple beam irradiated CNA3 at 450°C and 500°C to 50 dpa.

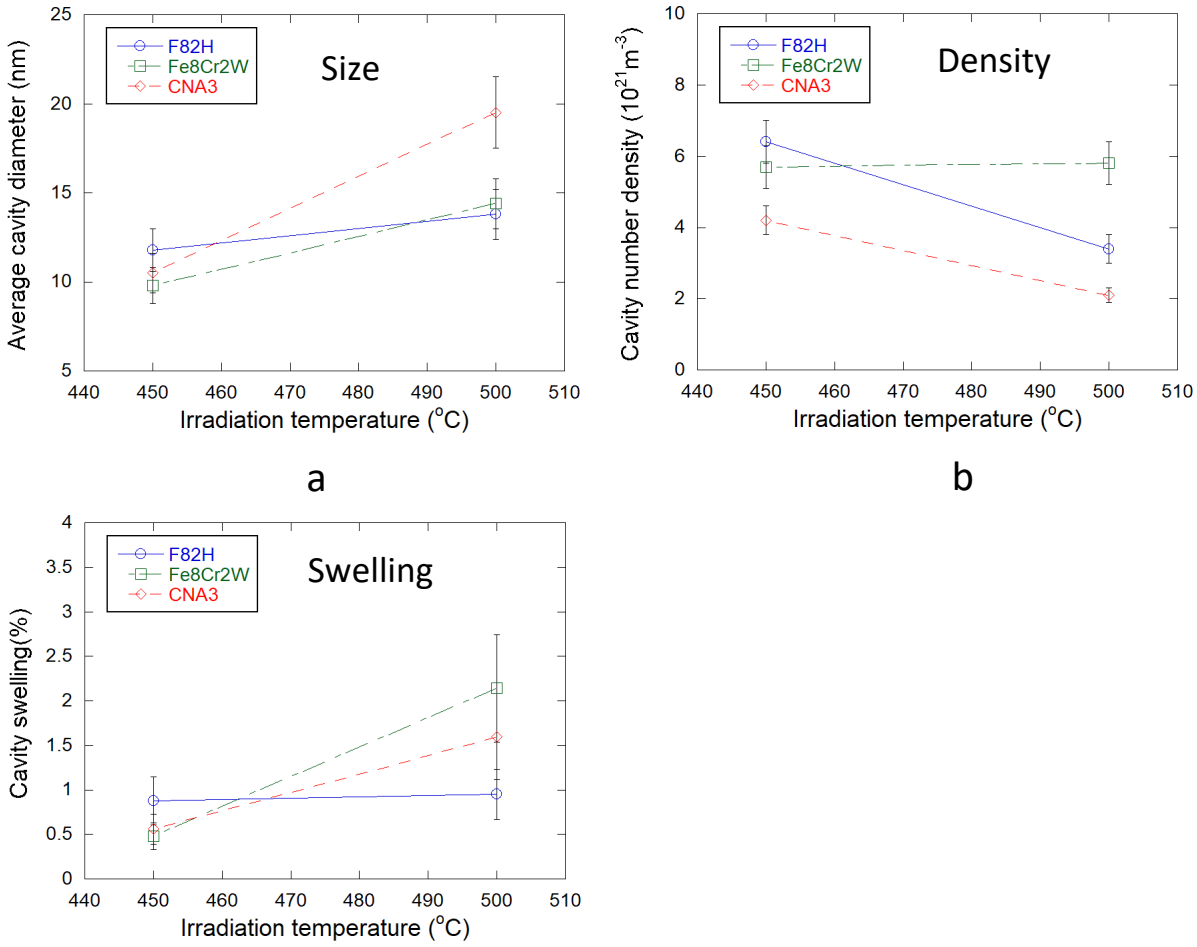

Figure 7. Comparison of size (a), number density (b) of cavities > 5nm and total cavity swelling (c) among alloys F82H, Fe8Cr2W and CNA3 at 450°C and 500°C.

FUTURE PLANS

Further experiments are planned that include dual ion irradiation (Fe^{2+} + H^{+}) at 500°C and additional temperatures and H/He concentrations. Irradiation experiments are also being designed to isolate the role of hydrogen. The future characterization will help understand the role of hydrogen in cavity swelling. Thus far, the significant role of hydrogen in swelling has not been confirmed.

References

[1] E. Wakai *et al.*, "Effect of triple ion beams in ferritic/martensitic steel on swelling behavior," *J. Nucl. Mater.*, vol. 307–311, no. 1 SUPPL., pp. 278–282, 2002, doi: 10.1016/S0022-3115(02)01076-0.

[2] E. Wakai *et al.*, "Swelling behavior of F82H steel irradiated by triple/dual ion beams" J. Nucl. Mater., 318 (2003) 267-273.

[3] Monterrosa, A.M., Jiao, Z., Was, G.S. "The influence of helium on cavity evolution in ion-irradiated T91" , J. Nucl. Mater., 509 (2018)707-721

1.3 CREEP/TOUGHNESS PROPERTY EVALUATION OF MODIFIED 3Cr BAINITIC STEELS—Y. Yamamoto (Oak Ridge National Laboratory)

OBJECTIVE

This work aims to develop new bainitic steels, based on 3Cr-3WVTa steels originally developed at ORNL. The goal is to obtain mechanical properties of both base metal and weldments superior to those of existing commercial bainitic steels or ferritic-martensitic (F-M) steels, together with no requirement for post-weld heat treatment (PWHT). The target applications are high-temperature structural components in fusion reactors such as helium cooled vacuum vessels operating up to 450°C and blanket support structures up to 550°C. Improvements of creep performance and room-temperature toughness are targeted via optimization of alloy composition and thermo-mechanical treatment.

SUMMARY

Evaluation of creep-rupture performance and Charpy impact toughness of newly proposed 3Cr-3WVTa base bainitic steel, containing high Mn and low C contents (ID: MLC02T), have been conducted. Although the base metal creep-rupture strength was lower than that of original 3C-3WVTa steel, the cross-weld creep performance of MLC02T was almost comparable to the base metal with the weld strength reduction factor (WSRF) of 0.9-1.0 at 500/550°C. Since the WSRF of the original 3Cr-3WVTa steel is 0.6 at 550°C, MLC02T showed a strong advantage in the cross-weld creep performance. It was found that the RT impact toughness of MLC02T decreased by tempering at 680-720°C, resulting in the ductile-brittle transition temperature (DBTT) raised above RT after tempering. The optimization of as-normalized microstructure has been initiated to maximize the balanced properties of MLC02T in untempered condition.

PROGRESS AND STATUS

A new heat of modified 3Cr-3WVTa base steel was proposed and prepared. The heat (ID: MLC02T) contains higher Mn and lower C than the original 3Cr-3WVTa steel, which is expected to maintain high hardenability and reduce the as-normalized hardness, targeting a reduced property inhomogeneity across the weldment in as-welded (no PWHT) condition. The nominal compositions of the original and newly modified steels are summarized in Table 1. A vacuum-induction-melted ingot of MLC02T was homogenized at 1200°C, hot-rolled and annealed at 1100°C, and then air-cooled to RT (normalization). The rolled plate was tempered at 700°C for 1h, followed by air-cooling to RT (tempering). A gas tungsten arc weld (GTAW) with a filler metal wire made of original 3Cr-3WVTa steel was applied to the tempered plates to prepare the cross-weld specimens. For Charpy impact toughness tests, the additional materials with three different conditions were prepared; as-normalized, tempered at 680°C for 1h, and tempered at 720°C for 1h. A half-size Charpy specimen was used in the present study.

Table 1. Nominal and analyzed compositions of the steels

Name	Alloy composition, wt.%	*A1,°C	*A3,°C	Remarks
Original	3Cr-3W-0.2V-0.16Si-0.4Mn-0.1Ta-0.1C	790.6	899.7	Reference
MLC02T	3Cr-3W-0.2V-0.16Si-2.0Mn-0.1Ta-0.05C	737.7	854.9	New heat

*calculated by JMatPro v.9

Figure 1 illustrates the creep-rupture test results of MLC02T base and cross-weld specimens tested at 500 and 550°C. The results of original 3C-3WVTa steel were also plotted for comparison. At 500°C, MLC02T base and cross-weld creep-rupture test results were mostly overlapped to each other, indicating that the WSRF is nearly 1 and the weldment did not cause the reduction of creep-rupture lives. The results at 550°C

indicated that the base metal creep-rupture strength was ~30% lower than the original 3Cr-3WVTa steel in the range of stress studied. On the other hand, the cross-weld creep-rupture test of MLC02T at 550°C (only one test was completed to date, though) showed the creep-rupture strength comparable to (or slightly better than that of original 3Cr-3WVTa steel weldment. The WSRF of MLC02T is ~0.9 at 550°C, which is significantly higher than that of original 3Cr-3WVTa steel, ~0.6, indicating that MLC02T is expected to show less creep strength variation across the weldments than the original 3Cr-3WVTa steel. Larson-Miller Parameter (LMP) plot in Figure 1b also showed the same trends that MLC02T weldment would exhibit the creep-rupture performance similar to that of the base metal in the wide stress range from ~300MPa to 500MPa, which are quite different characteristics from the original 3Cr-3WVTa steel showing a significant gap between the base and cross-weld creep-rupture properties.

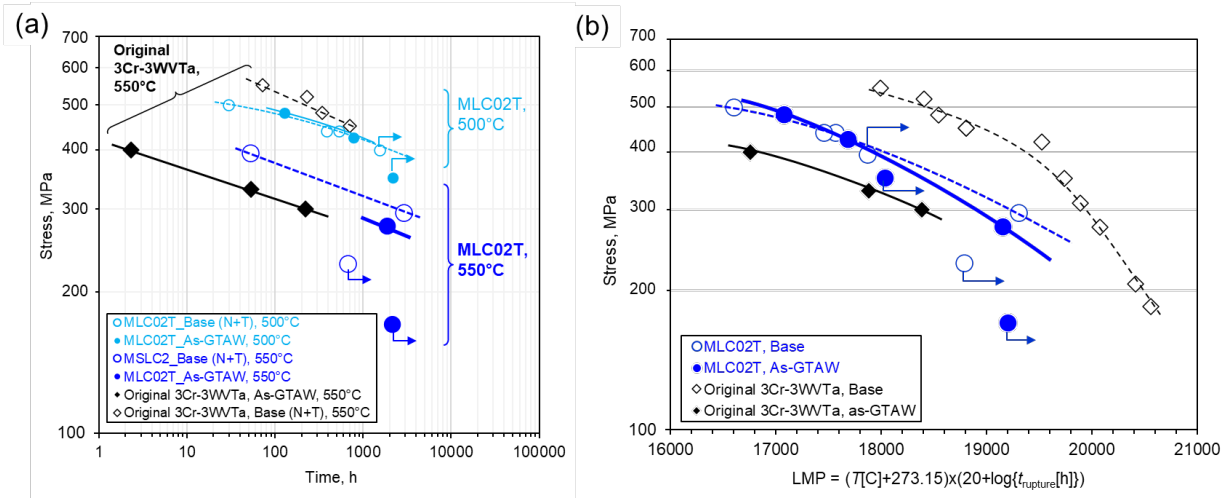

Figure 1. Creep-rupture test results of MLC02T base and cross-weld specimens tested at 500 and 550°C, together with those of original 3Cr-3WVTa steel [1]; (a) creep-rupture lives and (b) LMP plotted as function of stress.

The effect of heat treatment (as-normalized, tempered at 680, 700, and 720°C) on Charpy impact toughness of MLC02T was also evaluated. Figure 2 represents the Charpy absorbed energy of MLC02T as a function of test temperature (Figure 2a). The DBTT and the upper shelf energy (USE) obtained from the temperature dependences are shown in Figure 2b. The as-normalized sample showed the DBTT below RT, whereas that of the samples tempered at 680 and 700°C raised above RT (31 and 41°C, respectively). Tempering at 720°C lowered the DBTT to 14°C which was still higher than that of the as-normalized sample. The shift of DBTT cannot be explained from a simple mechanism (e.g. temper-embrittlement through impurity segregation) since the USE also increased with increasing tempering temperature. However, it is obvious that the as-normalized condition is much preferable for MLC02T to the tempered condition from toughness viewpoint.

The present MLC02T sample used for the property evaluation was prepared by hot-rolling and normalization at 1100°C, followed by tempering at 700°C for 1h. As shown in Figure 3a, the as-normalized microstructure consisted of fully bainitic ferritic structure with relatively coarse prior austenite grain size (PAGS) of ~188 μm (measured by a mean-intercept method). Since coarse PAGS is known to negatively impact room-temperature toughness and tensile ductility, the PAG refinement is considered to be one of the effective microstructure controls to expect the property improvement of MLC02T. It was found that a hot-rolling and normalization conducted at 1050°C resulted in less than a half of PAGS (~69 μm, Figure 3b) compared to that at 1100°C. The optimization of the as-normalized microstructure is currently in progress, targeting to evaluate the effect of PAGS on mechanical properties, in order to maximize the balanced properties of MLC02T in untempered condition.

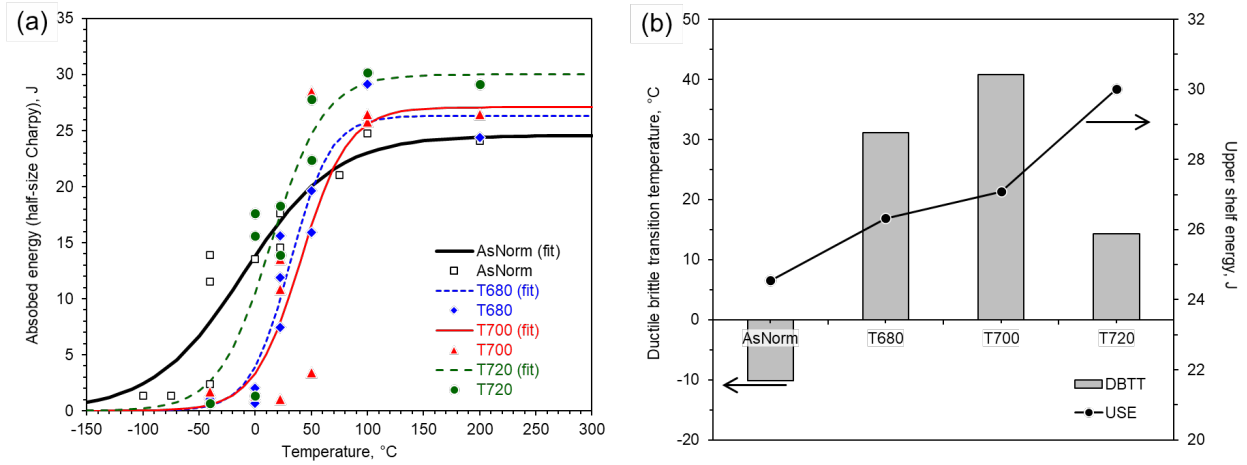

Figure 2. Vickers hardness of normalized-and-tempered original 3Cr-3WVTa and MLC02T plotted as a function of tempering temperature.

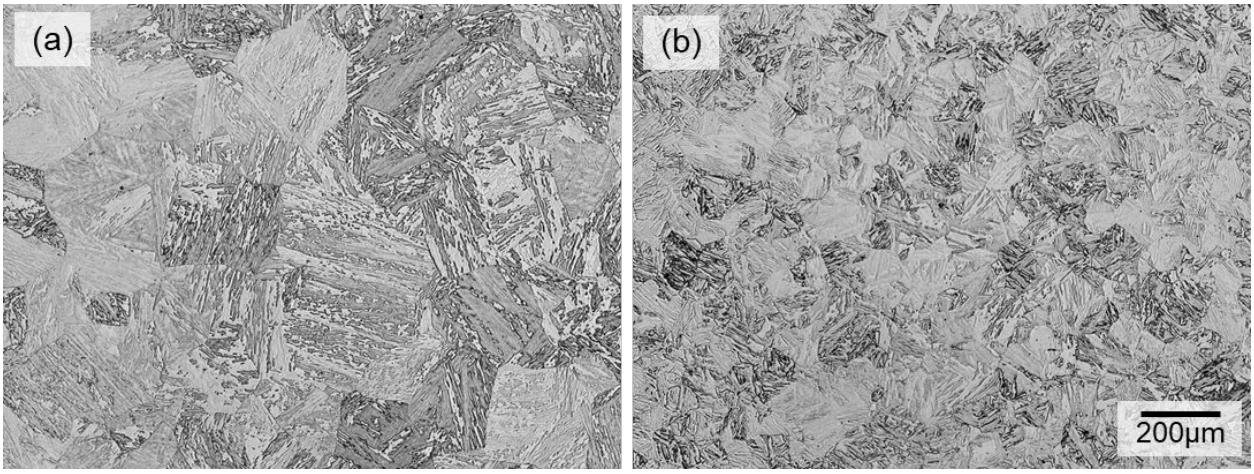

Figure 3. Optical micrographs of MLC02T after applying thermomechanical treatment (hot-rolling) and normalization at (a) 1100°C, and (b) 1050°C.

FUTURE PLANS

Property evaluation of MLC02T with optimized microstructure (fine PAGS, untempered) are to be conducted, mainly focusing on short-term creep-rupture tests for both the base and the cross-weld specimens, as well as room-temperature Charpy impact toughness tests. Once the performance benefits are confirmed, the evaluation of the long-term creep property and the DBTT measurement are to be conducted.

References

[1] R.L. Klueh et al., Int. J. Pressure Vessels and Piping, 84 (2007) 29-36.

1.4 THE EVOLUTION OF ALPHA-PRIME (α') PRECIPITATES IN HIGH PURITY Fe-(10-18)Cr ALLOYS AFTER THERMAL AGING AND ION IRRADIATIONS—Y. Zhao, S.J. Zinkle, P. Zhu (University of Tennessee), A. Bhattacharya (Oak Ridge National Laboratory), J. Henry (CEA)

OBJECTIVE

The first objective of this work is to study the effect of ion irradiation conditions including dose rate and temperature on the stability of Cr-enriched α' precipitates. Because the distribution of α' clusters are influenced by both radiation enhanced diffusion (controlled by both temperature and dose rate) and ballistic dissolution (mainly controlled by dose rate), a systematic and careful study could provide insight on the stability of α' precipitates under this complicated environment, which could be potentially useful for understanding any precipitation systems. Our second objective focuses on how the bulk Cr content will influence the formation of α' phase. Ferritic-martensitic (FM) steels which could potentially be used as structural materials for fusion reactors covers a relative wide range of Cr content (<20%). Our study on the effect of bulk Cr content on α' precipitation provides experimental data that is useful for selecting the optimum Cr content based on operating temperature and embrittlement considerations.

SUMMARY

Ultra-high purity Fe-Cr alloys with 10-18 wt.% Cr were irradiated with 8 MeV Fe ions to a midrange (~1 um) dose of 0.37 displacements per atom (dpa) between 300-450 °C at 10^{-3}, 10^{-4} and 10^{-5} dpa/s. Following irradiation, atom probe tomography (APT) was employed to characterize the number density, radius, volume fraction and Cr concentration of the Cr-rich clusters. Homogeneously distributed α' precipitates were revealed in Fe18Cr after ion irradiation at most conditions except for the 300 °C at 10^{-3} dpa/s. The effect of bulk Cr content was studied by irradiating Fe(10-18%)Cr alloys at the fixed irradiation condition of 350 °C, 10^{-4} dpa/s and 3.7 dpa. The α' precipitates were found in Fe(12-18%)Cr specimens, but not in the Fe10%Cr alloy. Thermal aging on Fe18Cr was conducted at 475 °C for either 100, 300 or 900 hours. The α' precipitates were observed to nucleate and grow during the aging process based on APT characterizations. These specimens will be used for mechanical testing or further ion irradiation studies.

PROGRESS AND STATUS

As noted in a prior report [1], high purity Fe-Cr alloys with 0-25 wt. % Cr were received from CEA, France (EUROfusion collaboration) and TEM - shaped specimens were prepared and irradiated with 8 MeV Fe ions at the Michigan ion beam laboratory (MIBL). All the ion irradiations including 9 conditions as shown in Table 1 have been completed. In this reporting period, we mainly focused on continuing the characterization of α' precipitation with APT, which has been completed for Fe18Cr and partially completed for other specimens with lower Cr contents. During the APT characterization, significant anomalies were discovered in the Integrated Visualization and Analysis Software (IVAS) provided by the APT vendor in terms of size, density and cluster compositions.

Here, we report our progress on the development of a concentration-based cluster searching algorithm using Python codes, which we found to give more realistic results than the maximum separation method inherent to IVAS software.

Table 1. The conditions for irradiations performed in this study. × means the conducted experiments

Final dose (dpa)	0.37			3.7	
Temperature (°C)	300	350	450	350	450
10^{-3} dpa/s	×	×	×		
10^{-4} dpa/s	×	×	×	×	×
10^{-5} dpa/s			×		

EXPERIMENTAL PROCEDURES

The specimens' chemical compositions, sample preparation procedures, and details related to ion irradiation experiments can be found in the prior report [1]. All irradiations were performed using 8 MeV Fe ions and the APT analyses were performed in the midrange region (depth of ~1 μm) in order to minimize potential artifacts from the implanted ions and surface sink effects. A portion of the as-received (AR) Fe18%Cr specimens were thermally aged at 475 °C to 100, 300 and 900 hours in a tube furnace. The specimens were sealed in quartz tubes under high purity nitrogen gas atmosphere prior to the long-time annealing.

After ion irradiations, the precipitates in the samples were characterized by the Local Electrode Atom Probe (LEAP) 4000X HR model APT located at the Center for Nanophase Materials Sciences (CNMS), Oak Ridge National Laboratory (ORNL). The samples for APT analysis were prepared by focused ion beam (FIB). All the datasets were collected in voltage mode for the sake of higher spatial resolution. Cr-enriched α' precipitates were identified and quantified through a solute concentration-based cluster analysis algorithm written with Python codes. The specialties of this newly developed method are the solute concentration filtering, background clusters subtraction, cluster size-dependent erosion distances and the ability to separate connected clusters. Details regarding this Python code will be documented in a separate publication.

PRELIMINARY RESULTS

Fe18%Cr after ion irradiation to a wide range of conditions

Figure 1 shows the distribution of cluster atoms filtered by the Python codes for the samples irradiated to 0.37 dpa. A large number of clusters were identified in most irradiation conditions, including 300 °C at 10^{-5} and 10^{-4} dpa/s. At 300 °C and 10^{-3} dpa/s, only 1 cluster was found in the presented volume. This status may correspond to the critical irradiation condition for α' formation as described in [2], in which the continuous formation and dissolution of α' by ballistic mixing was observed and no precipitates could be stabilized. The clusters formed at 450 °C have a relatively spherical shape while the shapes of the precipitates formed at the lower temperatures are more irregular. The formation of α' precipitates under these conditions indicates that cluster formation process from radiation enhanced diffusion is dominant compared to ballistic dissolution processes.

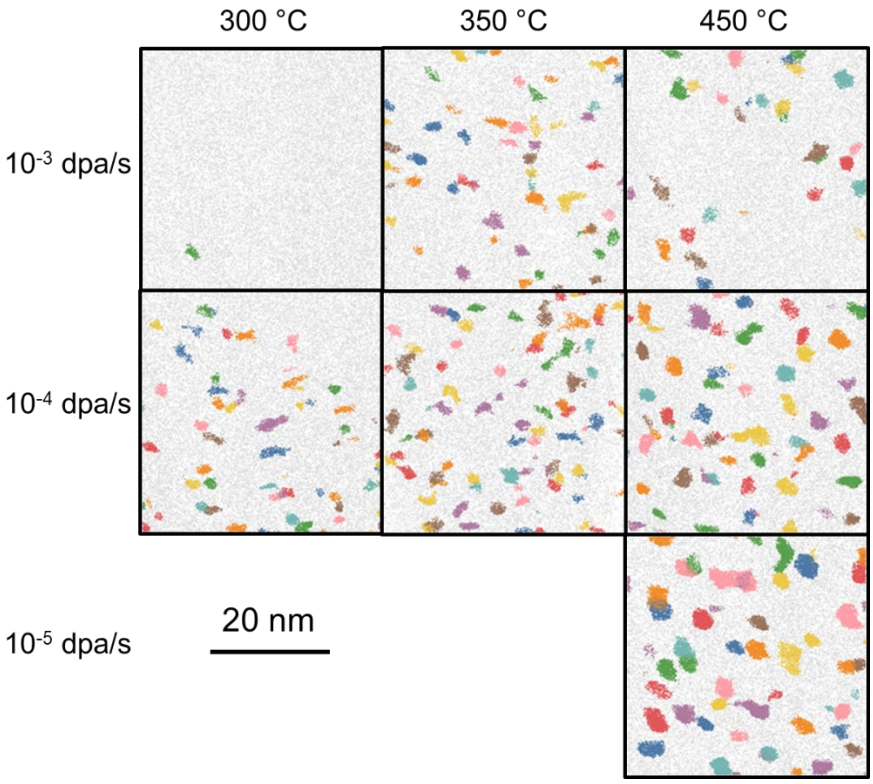

Figure 1. Cluster atom maps for Fe18Cr irradiated to 0.37 dpa in a sampled volume of 40×40×10 nm3. Clusters are indexed with different colors. All elements including both Fe and Cr atoms are shown.

The evolutions of radius, number density and volume fraction of Cr-enriched clusters with irradiation conditions are plotted in Figure 2. The cluster radii were~1-2 nm in all cases, which is consistent with the results in literature [3-5]. The general trend is that the cluster size increases with increasing temperature or decreasing dose rate. Within the range of investigated parameters, increasing the temperature from 300 to 450 °C had a much larger effect on cluster size than decreasing the dose rate from 10^{-3} to 10^{-5} dpa/s. As for the evolution of the cluster number density, it reaches the highest point at 350 °C for both investigated dose rates. This trend agrees with the one obtained from the number density of iso-concentration interfaces using IVAS, although the latter method incorrectly provided smaller number density values for each condition due to the presence of interconnected clusters which cannot be separated in the IVAS algorithm. The peak at 350 °C might be related to the competition between coarsening (dominant at 450 °C) and the dissolution by damage cascades (dominant at 300 °C). Increasing the dose rate decreased the number density at all temperatures, which is most significant at 300 °C. It must be pointed out that for the clusters formed after irradiation at 300 °C and 10^{-3} dpa/s, their positions were closely related to low index crystallographic poles. Although the main poles along <110> or <200> directions were removed before the cluster analysis, the large regions in the vicinity of them are influenced by this artifact and showed nonhomogeneous Cr enrichment. The same cluster search method was applied on the datasets for the as-received Fe18Cr specimen, and the similar artifact of Cr-enriched regions were revealed around the poles. The number density and radius of these features in the as-received sample were $(2.9\pm0.6)\times10^{23}/m^3$ and 0.94±0.4 nm respectively, which are similar to the ones detected after irradiation at 300 °C and 10^{-3} dpa/s. Based on these results, we think it is more reasonable to claim that the detected features originate from APT artifacts. Therefore, the critical irradiation condition for the α' precipitates to dissolve is 300 °C and 10^{-3} dpa/s. For all other irradiation conditions, these APT artifact features are expected to have smaller

influence on the cluster quantifications due to the large amount of observed cluster formation and, thus, less Cr atoms are available for nonhomogeneous segregation. Great care must be taken to analyze the APT results, so that such artifacts are not erroneously identified as real precipitates. The negligible volume fraction of α' phase after irradiation at 300 °C and 10^{-3} dpa/s also supports its absence. For other conditions, the trend of volume fraction change, combined with the radius and number density, agrees with a classical nucleation and Ostwald ripening of precipitates, the kinetics of which decrease with lower temperatures or higher dose rates. The highest volume fraction (~ 7.6%) occurred after irradiation at 450 °C and 10^{-5} dpa/s for ~10 hours, with a value close to the saturated volume fraction (~ 6.9%) for the same Fe18Cr thermally aged at 500 °C for 2008 hours reported in [6]. The small discrepancy might be attributed to the temperature difference of 50 °C or the more dilute clusters formed after ion irradiation.

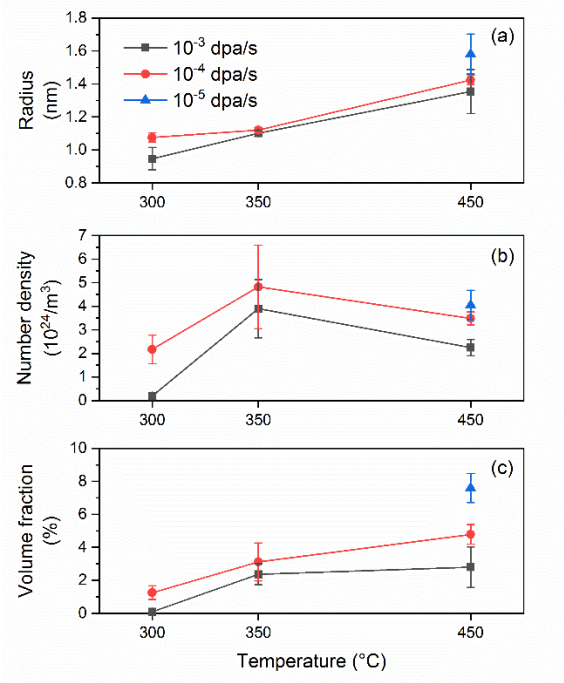

Figure 2. The evolution for the (a) radius, (b) number density and (c) volume fraction of α' precipitates irradiated to low fluence at different temperatures and dose rates.

Solute cluster evolution in Fe(10-18%)Cr after ion irradiation at 350 °C

Figure 3 shows the results for FeCr alloys with Cr content of 10-18% after ion irradiation at 350 °C, 10^{-4} dpa/s to 3.7 dpa. The α' precipitates with very high density were observed in specimens with Cr content ≥ 12%, while no precipitates were detected in Fe10%Cr. It must be pointed out this is the first time that α' precipitates have ever been reported in Fe12%Cr after heavy ion irradiation.

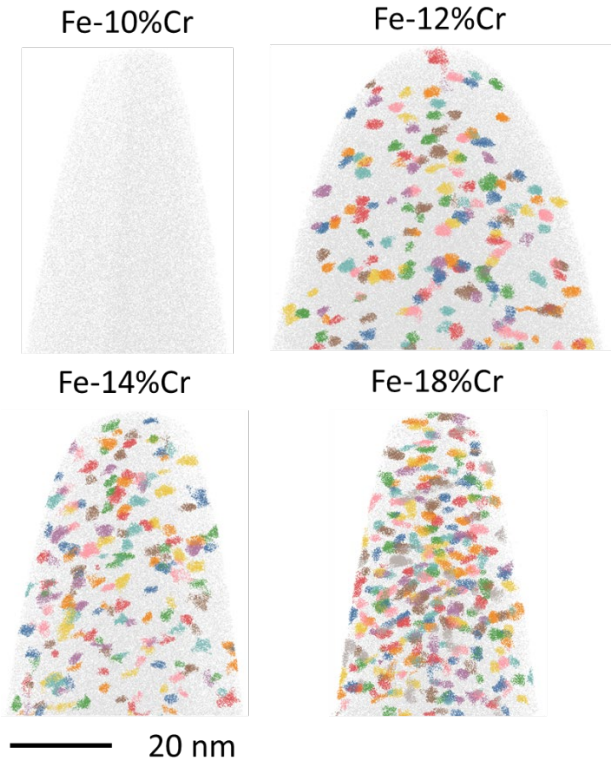

Figure 3. APT reconstruction for Fe(10-18%)Cr irradiated at 350 °C and 10-4 dpa/s to 3.7 dpa. The specimen compositions are presented above each reconstruction. All the particles indexed by different colors are α' precipitates.

The evolution of the cluster radii, number density and volume fraction with bulk Cr content are plotted in Figure 4. The average radii are around 1.2-1.5 nm for all three specimens. The smallest radii were detected at Fe14%Cr, which is questionable and might be related to the uncertainty with depth measurement, or some inhomogeneity in ion irradiation dose/dose rates because they were placed on the different locations of the irradiation holder. The number density and volume fraction of precipitates increase with bulk Cr content, which agrees with the higher nucleation rates for alloys with larger solute supersaturations.

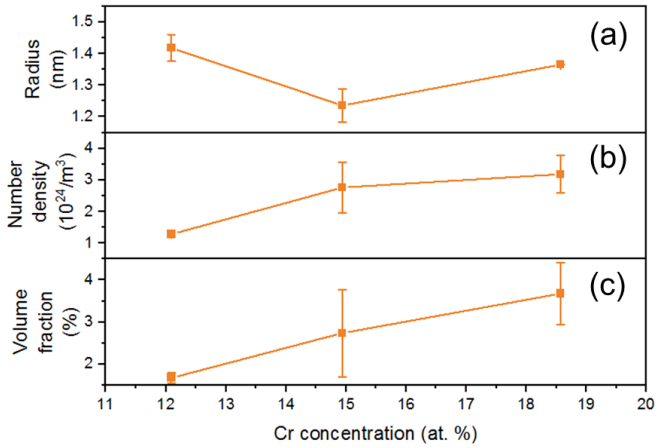

Figure 4. The evolution for the (a) radius, (b) number density and (c) volume fraction of α' precipitates in Fe(12-18%)Cr irradiated at 350 °C, 10-4 dpa/s to 3.7 dpa.

Fe18%Cr after thermal aging

The formation of α' precipitates was observed in Fe18%Cr after thermal aging at 475 °C for 100, 300 and 900 hours. The APT reconstructions are presented in Figure 5. The parameters of the α' precipitates are listed in Table 2. Only very small precipitates could be detected after aging for 100 hours. As the aging time increases, growth and coarsening occurred. The Cr concentration in clusters increased gradually towards its equilibrium content of ~80-90%, while the bulk Cr concentration decreased down to ~13% with increasing aging time.

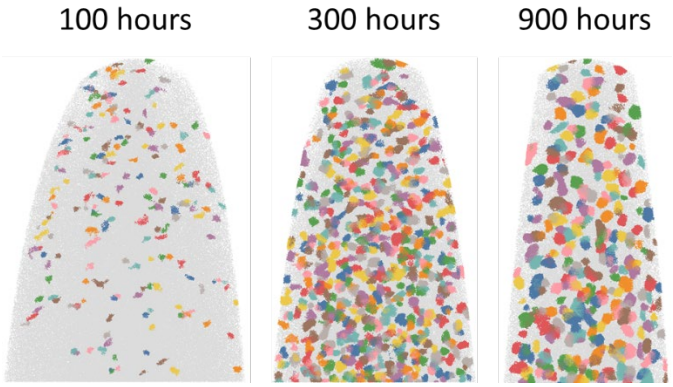

Figure 5. APT reconstruction for Fe18%Cr thermally aged at 475 °C for 100, 300 and 900 hours. The aging times are presented above each reconstruction. All the particles indexed by different colors are α' precipitates.

Table 2. The properties of α' precipitates in Fe18%Cr after thermally aged at 475 °C for 100, 300 and 900 hours

Materials	Density ($10^{24}/m^3$)	Radius (nm)	Cr in clusters (at. %)	Cr in matrix (at. %)	Volume fraction (%)
Fe18Cr AR	-	-	-	19.21	-
Fe18Cr 100h	0.71±0.01	1.06±0.01	40.10±5.41	18.84±0.35	0.39±0.06
Fe18Cr 300h	3.34±0.04	1.56±0.01	64.78±2.20	15.25±0.30	6.01±0.14
Fe18Cr 900h	2.41±0.07	1.89±0.02	79.67±3.71	13.39±0.37	7.99±0.07

CONCLUSIONS

1. In Fe18%Cr, α' precipitates were found to be absent after irradiation at 300 °C and 10^{-3} dpa/s to 0.37 dpa, while they were observed to form and coarsen after irradiation at higher temperatures or lower dose rates. The evolution of α' precipitates generally agrees with the classical Ostwald ripening mechanism.
2. Precipitate stability increases with decreasing dose rate. Among the investigated dose rates, 10^{-5} dpa/s is most effective for Cr clustering compared to 10^{-4} and 10^{-3} dpa/s. The Cr clustering kinetics decrease monotonically with lower temperature because radiation enhanced diffusion is largely reduced.
3. At 350 °C and 10^{-4} dpa/s, α' precipitates are observed in Fe(12-18%)Cr, but not in Fe10%Cr. This is attributed to Fe10Cr being in the single-phase region of the phase diagram at 350 °C, although further modeling of ballistic dissolution effects is needed for confirmation.
4. The α' precipitates were observed to nucleate and grow after thermal aging at 475 °C up to 900 hours.

FUTURE WORK

1. APT characterization will be performed on Fe(10-14%)Cr after irradiation at condtions listed in Table 1 to look for the critical temperature/dose rate for α' precipitation.
2. 2 ion irradiated samples with either strong or weak tendency to form α' precipitates will be selected for full range mapping of alpha prime precipitates.
3. TEM characterization of the dislocation loops at different depths will be performed, so their potential influence on radiation enhanced diffusion coefficient can be calculated.

REFERENCES

[1] Zhao Yajie et al. "A study on the stability of Alpha-prime (α') precipitates in high purity Fe-18Cr alloys after ion irradiation" Fusion materials semiannual progress report for the period ending Dec. 31, 2019, DOE/ER-0313/67, p. 33.

[2] J.-H. Ke, E.R. Reese, E.A. Marquis, G.R. Odette, D. Morgan, Flux effects in precipitation under irradiation – Simulation of Fe-Cr alloys, Acta Mater. 164 (2019) 586-601.

[3] O. Tissot, C. Pareige, E. Meslin, B. Décamps, J. Henry, Influence of injected interstitials on α′ precipitation in Fe–Cr alloys under self-ion irradiation, Materials Research Letters 5(2) (2016) 117-123.

[4] O. Tissot, C. Pareige, E. Meslin, B. Decamps, J. Henry, Kinetics of α′ precipitation in an electron-irradiated Fe15Cr alloy, Scr. Mater. 122 (2016) 31-35.

[5] M. Bachhav, G. Robert Odette, E.A. Marquis, α′ precipitation in neutron-irradiated Fe–Cr alloys, Scr. Mater. 74 (2014) 48-51.

[6] O. Tissot, C. Pareige, M.H. Mathon, M. Roussel, E. Meslin, B. Décamps, J. Henry, Comparison between SANS and APT measurements in a thermally aged Fe-19 at.%Cr alloy, Mater. Charact. 151 (2019) 332-341.

1.5 ADVANCED CHARACTERIZATION OF RAFM STEEL MICROSTRUCTURES—C. M. Parish (ORNL)

OBJECTIVE

The overarching objective of this work is to develop new, state-of-the-art characterization techniques for application to the expected future needs of the Fusion Materials program.

SUMMARY

In this reporting period, first results were obtained on large-area, high-throughput X-ray spectrum imaging (XSI) of nanoprecipitates from an AM FM (additively manufactured ferritic/martensitic) steel. The large size of the data required the development of new algorithms and optimization of computer codes. Samples were provided via collaboration with A. Bhattacharya, L. Tan, and the ORNL Manufacturing Demonstration Facility.

PROGRESS AND STATUS

Prior work in the ORNL Fusion Materials program has used the *carbon extraction replica* method to make scanning transmission electron microscopy (STEM) specimens. In the carbon extraction replica method, the hard precipitates (i.e., carbides, carbonitrides, etc.) from a steel are embedded in a thin, electron-transparent film of amorphous carbon and that film, with the embedded carbides, is analyzed. This technique has two major advantages. First, large areas (potentially square millimeters) are obtained; with FIB samples, specimens are a few square microns, at most. Second, the precipitates are not embedded in the FM matrix, so their cation content can be measured without confounding effects from the matrix.

Newly obtained at ORNL is a software package (Thermo Scientific "MAPS") that allows for automated acquisition of multiple XSIs from a specimen, using the Talos F200X STEM in the LAMDA laboratory. This allows very large datasets to be obtained without human supervision. In this example, a 10×10 grid of XSIs was obtained, where each XSI was 1024×1024 pixels in space and 4096 channels in spectral space. This allows, potentially, thousands or millions of carbides to be analyzed in a single experiment, opening new vistas of statistics. The goal is to compare pre- and post-irradiation populations in FM steels, but to do so, we first are developing data pipelines based upon machine learning to perform automated and unbiased analyses of the datasets.

Figure 1 shows the 10×10 tileset of HAADF (high angle annular dark field) images; large numbers of carbides (bright) are seen on the carbon-film background (dark).

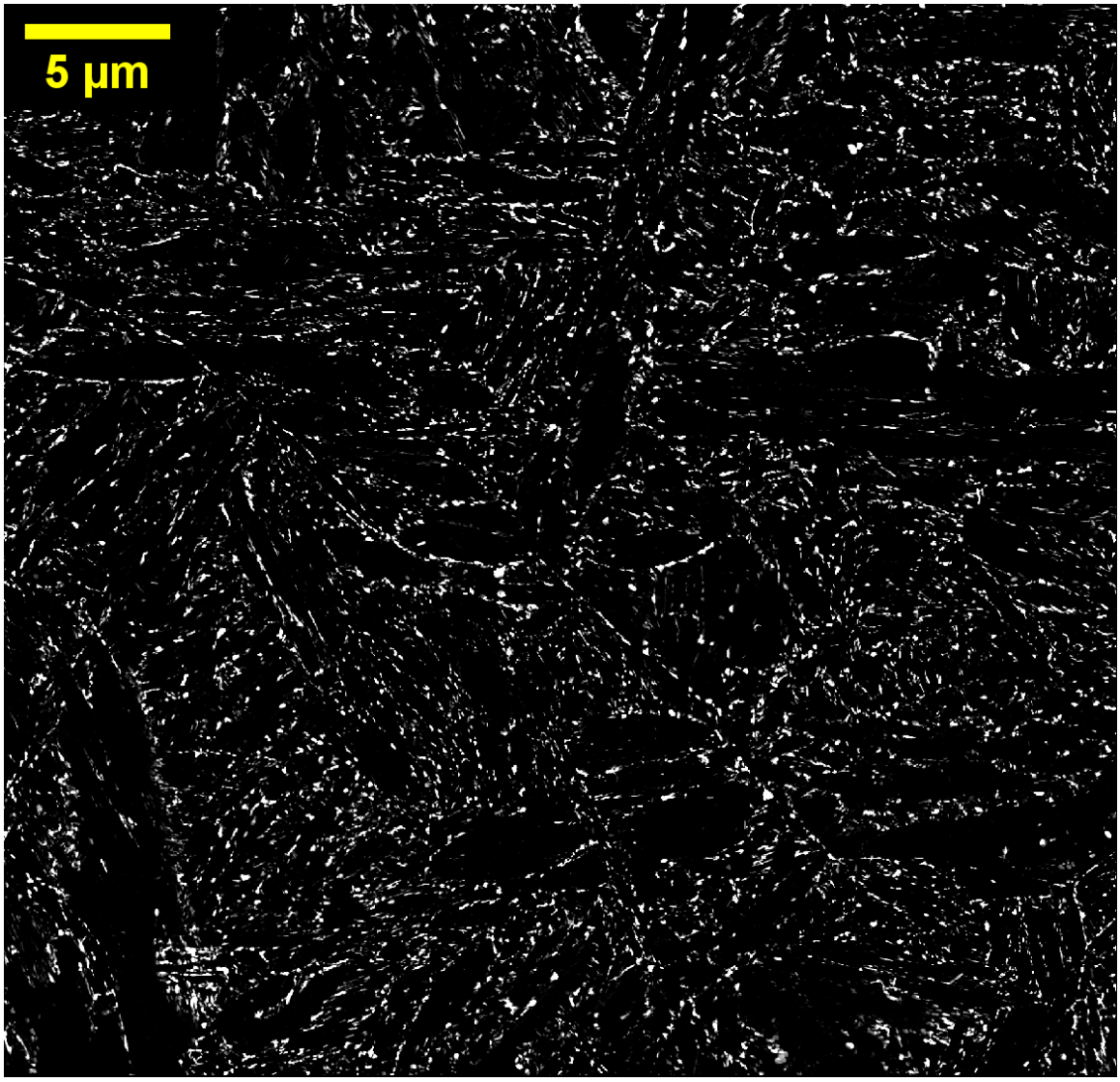

Figure 1. HAADF montage of the 10×10 STEM tiles. The effective size, with overlap at the edges of panels, is roughly 7100×7100 pixels (50 megapixels).

An important point to keep in mind is that (10×10×1024×1024×4096) is ≈4.3×10^{11} data elements. At 4 bytes per data element, this would be roughly 1.6 TB of data, and analysis of a dense 1.6 TB dataset is obviously intractable without high performance computing resources. However, the XSI data can be handled in computationally- and memory efficient fashions. First, XSI data is very sparse; even with a high-efficiency X-ray detector, such as the ORNL Talos microscope, the 10×10×1024×1024×4096 data hypercube is well over 99% sparse. Storage using sparse datatypes allows for very efficient memory and CPU usage. Second, the X-rays of interest (C, V, Cr, W, etc.) only occupy the first ≈1500 channels, reducing the 4096-order spectral space to ≈1500. Last, data that is too sparse is not amenable to data mining, as correlations will not be observed, so the data is further reduced in size by binning adjacent pixels and channels. Highly efficient sparse-binning algorithms are available in the literature and are implemented.

Once the data from all 100 of the tiles in the montage are loaded, sparsified, binned, and stored with proper metadata tagging, all using newly developed algorithms, it's possible to perform data mining using standard methods. For this work, Poisson-pre-scaled sparse singular value decomposition, de-scaling, re-

orthogonalization, VARIMAX rotation, and finally blind-source separation methods are used to find the underlying chemical contributions and make materials science interpretations. In this example specimen, three chemical contributions were found: the carbon support film, Fe-Cr-W carbides (presumably $M_{23}C_6$), and V-rich carbides (presumably VX); this contributing spectral endmembers are given in Figure 2.

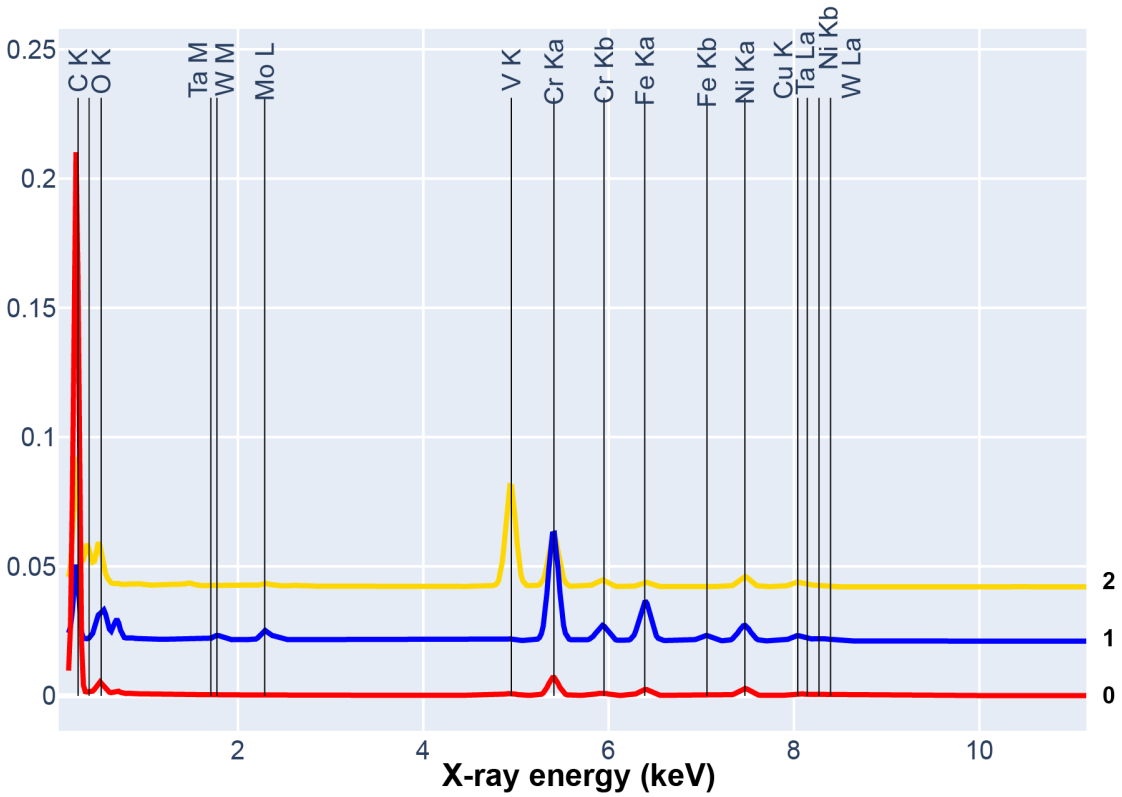

Figure 2. The three derived spectral endmembers from the carbide dataset, indicating the carbon film (#0), the $M_{23}C_6$ (#1), and the VX (#2).

The spatial distributions of the three components are given in Figure 3. The carbon film (#0), unsurprisingly, is uniformly around the area of interest. (Three "dim" tiles, marked with arrows, are due to a software bug with the commercial acquisition software, and we are in communication with the vendor to find a fix.) The $M_{23}C_6$ particles, #1, are spread around and appear to decorate what had been lath boundaries prior to the etching away of the matrix to create the carbon extraction replica. The VX precipitates, #2, are more scattered than the $M_{23}C_6$. As a result of the high density of data that results from the new method, the full level of detail is invisible at the scale of the first tiles in Figure 3, so an expended sub-region (denoted by the boxes in abundances #1-#2) with false-colored overlays of the two carbide populations is also given, showing that there are both isolated particles of the two populations and regions where the two different types are in intimate contact.

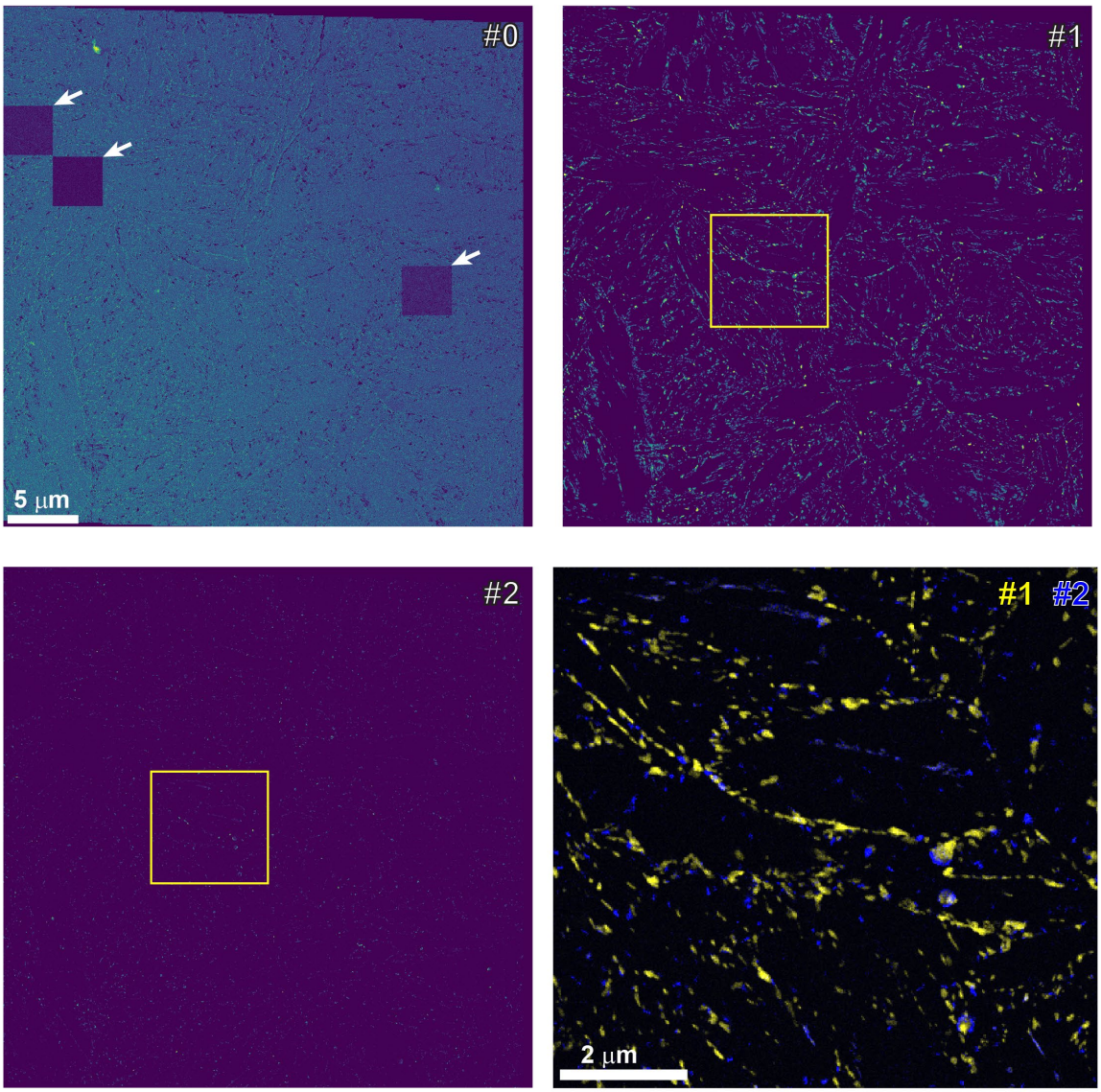

Figure 3. Abundance maps of the three spectral endmembers in Figure 2. #0: carbon support film; #1: $M_{23}C_6$-type; #2: VX-type. Arrows in #0 denote tiles that had fewer counts; a software bug report is in to the TEM vendor. The final panel shows a false color overlay of the M23C6 (yellow) and VX (blue) precipitates from the boxed area.

ONGOING WORK

Developments on the software to allow more detailed analysis are underway, and further datasets will be acquired. It is hoped to obtain much larger datasets and, if necessary, move to high-performance computing nodes, rather than desktop computing, if the datasets are large enough. Also underway is to implement automated particle counting machine vision algorithms to quantify the precipitates' sizes, shapes, and areal densities.

1.6 GLOBAL THERMAL CREEP MODELS DERIVED FROM A COMPREHENSIVE MULTIPLE HEAT DATABASE ON 9Cr TEMPERED MARTENSITIC STEELS—M.E. Alam, T. Yamamoto, G.R. Odette (University of California Santa Barbara)

OBJECTIVE

The main objective of this study is to explore the recently developed primary creep models to the extended database at their primary creep regime for assessing the dimensional stability of reduced activation tempered martensitic steels used in large fusion structures.

SUMMARY

In our previous study, we have developed three primary creep models that include: 1) the Larson-Miller parameter (LMP); 2) the applied stress (σ) normalized to the temperature (T) dependent 0.2% tensile yield stress, [$\sigma/\sigma_y(T)$]; and 3) a threshold stress that scales with σ_y, (σ-Cσ_y) [1]. These models were calibrated to a database reported by Reith et al. [2] for 8 heats of Eurofer97 for 0.2 to 2% primary strains at 450 to 550ºC with reasonably well predicted primary creep stress of ≈ 12 MPa standard deviation (SD). In this study, we have extended the database by adding more heats of 9Cr TMS (total 17 heats), and explored two more models similar to normalized and threshold stress models by applying ultimate tensile stress (σ_u) instead of σ_y. It has been seen that the normalized [$\sigma/\sigma_u(T)$] model predicts the best creep stress with ≈11 MPa SD, ≈ 0 MPa mean error (ME) and 1:1 M-P (measured vs predicted) lines at 0 MPa interception for a larger dataset with creep time, t_x>10h, T = 375 to 550ºC and strains (ε_x) from 0.2 to 2%. These models were further applied individually to 5% strains, initiation of tertiary creep, strains to rupture, rupture time and minimum creep rates with very satisfactory outcomes.

PROGRESS AND STATUS

Introduction

Creep testing of structural alloys and design of metallic structures are often limited to the consideration of secondary, or minimum creep rates (ε'_m), based on a simple Norton's power law model. However, the accumulation of strain during the primary creep cannot be neglected, especially for the large structures, like fusion first wall and blankets energy conversion systems, which must maintain precise dimensional tolerances. Primary creep is also important for long time service environments manifesting cyclic stresses and temperatures; this is even true for much more benign environments, like pressure boundaries in fossil energy systems [3,4]. A number of empirical models treating primary creep strains (ε_x, where x is the primary creep strain) have been proposed [4–10], with their advantages and limitations. Details introduction can be found in previous report [1].

In our previous study [1], we have developed three new primary creep models, namely: 1) a Larson-Miller Parameter (LMP) based model; 2) a normalized stress model; and, (3) a threshold stress model. In the latter two cases, the normalization and threshold stresses are related to quasi-static tensile properties. These models were calibrated to a database reported by Reith et al. [2] for 8 heats of Eurofer97 for ε_x = 0.2 to 2% at T = 450 to 550ºC. In this study, we have explored two more models similar to the normalized and threshold stress models by applying ultimate tensile stress (σ_u) instead of 0.2% yield stress, i.e. [$\sigma/\sigma_u(T)$]; and [σ-C$\sigma_u(T)$]. These models have been applied to extended database by adding more heats (now 17) of 9Cr TMS that includes 8 heats from Rieth's Eurofer97 (9Cr-1W) [2], 4 heats from NIMS 9Cr-1Mo-V-Nb (Gr91 of T91/P91) [11], 4 heats from NIMS 9Cr-0.5Mo-1.8W-V-Nb (Gr92 of T92/P92) [12], and one heat from Holmstrom's 9Cr-1Mo-V-N (Gr91) [13]. Details chemical compositions and heat treatment procedures can be found in their respective references [2,11–13], whereas nominal compositions are tabulated in Table 1, and general heat treatment procedures are shortly discussed in previous report [1].

Table 1. Nominal compositions (wt.%) of Eurofer97 [2] and Gr 91/92 steels [11–13] used in this study

Comp	C	Cr	Mo	V	Nb	Mn	Ni	Si	W	Ta	Cu	N	S	Ti
Eu97	0.09 - 0.12	8.1-9.5	-	0.15-0.25	-	0.2-0.6	0.005	-	1-1.2	0.05 - 0.09	-	0.03	-	0.01
NIMS -Gr.91	0.09 - 0.1	8.5 - 8.7	0.9 - 0.96	0.21	0.076	0.35-0.45	0.04 - 0.28	0.24 - 0.38	-	-	0.012 - 0.032	0.042 - 0.058	0.001	-
NIMS-Gr.92	0.092 - 0.11	8.91-9.5	0.36 - 0.44	0.16-0.2	-	0.41 - 0.44	0.13 - 0.27	0.1-0.29	1.68-1.85	-	-	0.039 - 0.046	0.0003 - 0.0037	0.003
Holms -Gr.91	0.12	8.32	1.02	0.235	0.084	0.41	0.1	0.24	-	-	0.05	0.041	0.001	0.002

The mentioned references [2,11–13] cover a wide range of σ and T for primary strain and other creep properties. The new models developed here are for primary creep strains (ε_x) from x = 0.2 to 2% at T = 375 to 550ºC (whenever available) and σ from 160 to 420 MPa (depending on the T). Note, the database does not include the full creep curves, so the σ, T, ε_x and t_x data were used for least square fitting (LSF) optimization of the models. The primary least square fit parameter is the predicted minus measured standard deviation (SD) of σ. For the baseline models, the results show that all five models predict σ differently, with SD varies from 16 up to 40 MPa for the entire database and the fixed values of C_{LM} = 30 and Q = 300 kJ/mole, since these choices are physically motivated and/or are consistent with other sources of information. The main fitting was to parameterize functions that allowed application of the model over the entire range of ε_x. However, the LSF values for other parameters resulted in systematic bias in some variable residual trends. The secondary best-fit criteria are discussed below. In short, constrained models for t_x >10h and unconstrained Larson-Miller constant (C_{LM}) or activation energy (Q) have also been developed that resulted much better SD ranged from 11 to 21 MPa for T = 375 to 550ºC, with much lower systematic residual biases. The further optimization minimized bias, while reducing the SD and ME to ≤ 8 MPa and 0.1 MPa, respectively for all five models for the Eurofer97 dataset of t_x >10h, ε_x = 0.2 to 2% and T = 450 to 500ºC. These models are intended to provide design engineers a convenient tool to predict the stress (σ) for primary creep at ε_x at specified t and T. These models were further applied individually to 5% strains, initiation of tertiary creep, strains to rupture, rupture time and minimum creep rates.

Creep in 9Cr TMS: Basic characteristics and primary creep mechanisms

Basic characteristics and primary creep mechanisms for Grade 91 type 9Cr TMS has been discussed in previous report [1] and are not repeated here.

Primary creep models for 375 to 550°C

The tensile properties (σ_y and σ_u) used in this study are plotted in Figure 1 [2,11–13]. Here we focus on T between 375 and 550°C marking the likely limit of standard Grade 91/92 type steels for extended irradiation service. Any untested tensile properties for a temperature of available creep data has been chosen by interpolation between the two adjacent values. It can be seen from the graph that both the σ_y and σ_u have relatively wide spectrum of data range for any tested temperatures. At first, we have developed models for all database for primary strains (ε_x) 0.2 to 2%, temperature (T) = 375 to 550ºC and time to primary strains (t_x) from 0.2 to ≈ 80,000h, with fixed C_{LM} for LMP and Q = 300 kJ/mol for all 17 heats of 9Cr TMS, that we dubbed as baseline models. It was found that the residual biases are relatively high in many cases, even though the global average is reasonable. Therefore, in our second attempt, we have considered t_x that are only >10h, and relaxed the constrained from C_{LM} or Q, for respective models, while T and heats are same as of baseline models. The logic behind these boundary conditions is that the shorter time below 10h is

irrelevant and unconstrained C_{LM} is not unusual, though that is generally ≤ 30 for 9Cr steel. We call these as unconstrained model. We further applied these models to more restricted dataset, say only for 8 heats of Eurofer97 at T= 450-500ºC, t_x> 10h with unconstrained C_{LM} or Q, and we name them 'confined database' models.

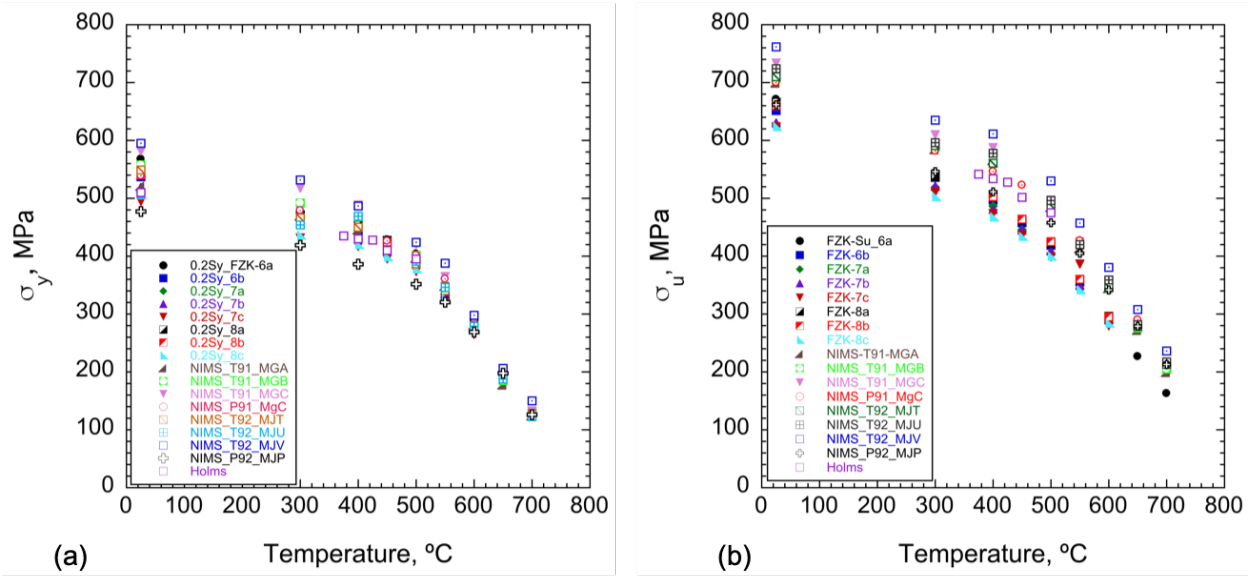

Figure 1. a) $\sigma_y(T)$; and, b) $\sigma_u(T)$ of 17 heats of 9Cr TMS [2,11–13] used in this study.

Primary Creep Models for 0.2 to 2% Strains from 375 to 550°C

(1) Larson-Miller parameter (LMP) model

The Larson-Miller parameter (LMP) is one of the most commonly used creep data correlation and extrapolation procedures, for using short time laboratory test results to estimate longer in service life rupture times and various ε. The procedure plots the t-T dependent LMP parameter versus the σ, as σ = f(LMP). The LMP for various t and T is given by

$$LMP = T(C_{LM} + \log t_x) \quad (1)$$

C_{LM} is the Larson-Miller constant with different values for various alloys and alloy conditions [4,10,14]. LMP plots are also applied to correlating minimum creep rate (ε'_m) data in terms of $1/\varepsilon'_m$. Here we have adopted the same LMP procedure to estimate the primary creep σ as a function of t_x and T, where t_x is the time to reach ε_x. As shown in Figure 2a the primary creep data can be approximately represented by a simple linear fit:

$$\sigma(\varepsilon_x, T) = M_0(\varepsilon_x) + M_1(\varepsilon_x, LMP) \quad (2)$$

The fit parameters $M_0(\varepsilon_x)$ and $M_1(\varepsilon_x)$ are used to predict the σ needed to reach various ε_x as a function of the corresponding t_x and T. Specifically, M_0 and M_1 are the LMP = 0 intercepts and slopes of σ vs. LMP fitted line, respectively. Figure 2a shows σ versus LMP (t in h) for C_{LM} = 30 for ε_x from 0.2 to 2% for the Rieth's Eurofer97 heats. However, many of the primary creep data overlaps when considering all 17 heats of 9Cr TMS (not shown here) [2,11–13].

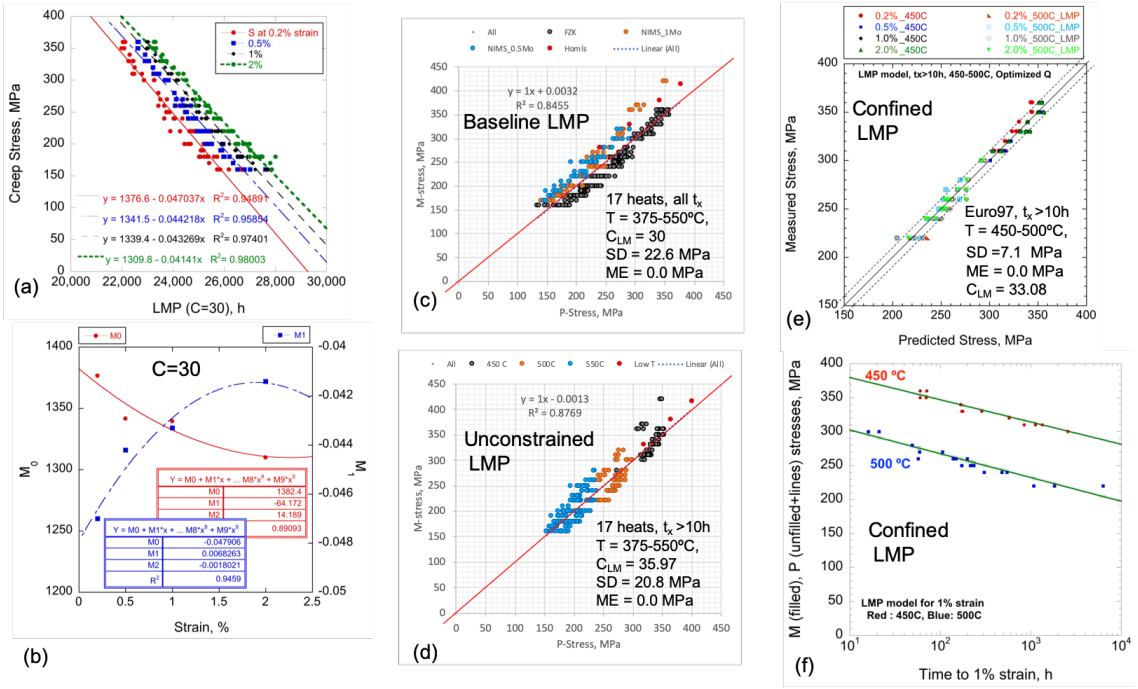

Figure 2. a) the measured σ versus the LMP for various ε_x and fit lines, and b) LSF for M_0 and M_1 as a function of ε_x, respectively, for Eurofer97 dataset. Fig. c-e) shows M versus P σ for the LMP model for c) all t_x, d) t_x >10h for all 17 heats at T = 375 - 550ºC, and e) t_x>10h, T= 450 and 500ºC for only Eurofer97 heats whereas f) shows M (points) and P (lines) σ for $t_{1\%}$ for 'confined dataset' of Eurofer97 heats.

Note a slightly better fit over the entire range of σ - LMP data is provided by a second order polynomial; however, the linear fit is also adequate, while third order polynomial fit further improves for the model. Figure 2b shows the M_0 and M_1, as a function of ε_x, fitted for the Eureofer97 data with a second order polynomial for C_{LM} = 30 from Figure 2a, where σ is

$$\sigma = (C_{00} + C_{01}\varepsilon + C_{02}\,\varepsilon^2) + (C_{10} + C_{11}\varepsilon + C_{12}\,\varepsilon^2)\,\mathrm{LMP} \qquad (3)$$

The Excel equation solver was used to determine the LSF C_{ij} parameters. The fits minimized the standard deviation (SD) between measured (M) and predicted (P) σ:

$$SD = \sqrt{[\sum(P - M)^2 / N]} \qquad (4)$$

N is the number of data points. A secondary fitting requirement is that the P-M data are well centered on a 1:1 line with a SD, σ versus LMP intercept mean error (ME) that are all small, where the ME = $[\Sigma(M - P)]/N$. Figure 2c plots the corresponding measured (M) versus predicted (P) σ_a, yielding a SD ≈ 22.6 MPa, a ME = 0.0 MPa, a fit line slope of 1 and ≈ 0 MPa intercept for all 17 heats of 9Cr TMS steels for stains from 0.2 to 2%, t_x = 0.2 to 80000 h, and T = 375 to 550ºC. Although the LMP model, on average, gives reasonably good overall global fit considering huge range of scattered data set from different heats and alloy variants, the residual systematic biases are still considerably high for the base model. The unconstrained LMP model slightly improves the SD from 22.6 to 20.8 MPa, while ME, slope and intercept are 0, 1:1 and 0, respectively. However, SD improvement is negligible considering unusually high C_{LM} (≈ 46), therefore, the unconstrained LMP model is not a huge success for these scattered datasets. However, we have further restricted the database only for Eurofer97 heats for t_x>10h, T = 450 and 500ºC with relaxed C_{LM}, that resulted a very impressive SD ≈ 7 MPa with residual biases less than 10 MPa and reasonable C_{LM} ≈ 33 (see Figure 2e). Figure 2f shows the M and P stresses for times to 1% strain, t(ε_x) = 1%, for the 'confined database' model. The corresponding LMP model parameters are summarized in Table 2.

Table 2. Least square fit (LSF) parameters and SD for primary LMP creep model

Fit Parameters	Baseline LMP model (17 heats, t_x= all, C_{LM}= fixed, T= 375-550ºC)	Unconstrained model (17 heats, t_x>10h, C_{LM} = free, T = 375-550ºC)	Confined database model (Eurofer97, t_x>10h, C_{LM}= free, T = 450-500ºC)
C_{00}	1310.22	1388.55	1506.4
C_{01}	- 0.001024	-0031154	-0.001
C_{02}	- 40	-26.949	-8.31
C_{10}	-0.044574	-0.03	-0.048331
C_{11}	0.004855	0.0022378	0.00382
C_{12}	0	0	-0.000793
C_{LM}	30	45.97	33.14
Slope	1	1	1
Intercept (MPa)	0.0	0	0
R^2	0.8455	0.8769	0.973
SD (MPa)	22.6	20.8	7.1
ME (MPa)	0.0	-0.004	0.01

(2) Tensile σ_y or σ_u Normalized Stress Model

The most common approach to fitting data at higher σ and lower T, in the dislocation creep (climb-glide) regime, is the use of the simple Norton power law model as:

$$\varepsilon' = A\sigma^n \exp(-Q/RT) \quad (5)$$

While the parameters *A*, the stress exponent *n* and the activation energy *Q* are often assumed to be constant, they actually depend on the combination of σ and T; and fitted values tend to be non-physical, for example with high values of Q and n. Q and n also tend to be highly covariant [10]. Some improvement in the model parameterization is possible by using ratio σ to the shear modulus (G) as a normalized dimensionless σ/G.

The Norton model is usually used for t_r and ε_m (minimum creep) data correlations. Here we normalized σ, by dividing it by tensile strength properties. The potential advantages of this approach include achieving a more physical parameterization for n and Q, and exploiting the relation to microstructures and their general, static and creep, strengthening contributions. Further, once calibrated, such models could be applied to some range of alloy conditions, encompassing different strengths, albeit with some fine tuning. Wilshire et al [10] proposed dividing σ by the ultimate tensile stress, σ_u:

$$\varepsilon' = A^* (\sigma/\sigma_u)^n \exp(-Q/RT) \quad (6)$$

He further modified the Equation (6) for σ/σ_u over the entire stress range from σ/σ_u = 1 to 0, where $\varepsilon' \rightarrow \infty$ *and* $t_f \rightarrow 0$ *as* $\sigma/\sigma_u \rightarrow 1$, *and where* $\varepsilon' \rightarrow 0$ *and* $t_f \rightarrow \infty$ *as* $\sigma/\sigma_u \rightarrow 0$, as:

$$\sigma/\sigma_u = \exp\{-k[t_x \exp(-Q/RT)]^n\} \quad (7)$$

The k and n are fit parameters, and t_x is the time to reach for strain ε_x.

In our previous report [1], we applied a modified Equation 7 to four primary ε_x at the three different T for all eight heats of Eurofer97. Since the primary ε_x are low, we have used σ_y rather than σ_u for the normalization. Details fitting procedures can be found in [1]. The normalized σ/σ_y model predicts relatively better creep stress for the Eurofer97 heats with SD 11.7 and ME ≈ - 0.1 MPa (see [1]). However, for the extended database, say for 17 heats from all different Mo containing or Mo-free -W-added alloys, the normalized σ/σ_y baseline model inferiorly predicts the creep stress with SD ≈ 40 MPa and ME ≈ - 26 MPa (see Table 3 and Figure 3a). The residual biases even go higher up to 90 MPa. Figure 3b and c show the temperature compensated primary creep time for 1% strain for normalized σ/σ_y and σ/σ_u, respectively. It can be clearly seen that, even for a particular strain (1% in this case), the normalized σ/σ_y defers significantly for different alloys, whereas normalized σ/σ_u relatively falls in a single fit line. At high temperature, the σ_y value might not be representable as they highly depend on strain rate. The σ_y is a resistance against instantaneous failure rather than time depended properties like creep. Therefore, for our extended dataset, we have applied the normalized σ/σ_u model following the same procedures as described in report [1], only by replacing σ_y with σ_u. Now, the predicted stress for all primary creep strains (0.2 to 2%) for normalized σ/σ_u model is:

$$\sigma(\varepsilon_x, T) = \sigma_y \{(C_{10} + C_{11}\,\varepsilon + C_{12}\,\varepsilon^2) + (C_{10} + C_{11}\,\varepsilon + C_{12}\,\varepsilon^2)\, ln[t_x\, exp(-Q/RT)]\} \quad (8)$$

Here, C_{ij}'s are again the intercept and slope fit parameters and Q is the effective activation energy.

Table 3. LSF parameters and SD for normalized σ/σ_y and σ/σ_u primary creep models

Fit Parameters	Baseline σ/σ_y model (17 heats, t_x= all, Q = fixed, T= 375-550ºC)	Baseline σ/σ_u model (17 heats, t_x= all, Q = fixed, T= 375-550ºC)	Constrained σ/σ_u model (17 heats, t_x= >10h, Q = free, T= 375-550ºC)	Confined database σ/σ_u (Eu97, t_x= >10h, Q = free, T= 450-550ºC),
C_{00}	-1.0345	-1.0345	-1.07813	-1.053
C_{01}	25.905	25.905	24	0.00001
C_{02}	-0.1	-0.1	-0.1	-0.3193
C_{10}	-0.036447	-0.036447	-0.030149	-0.03195
C_{11}	-0.036	-0.036	-0.0024	-0.45
C_{12}	24.04	24.04	13.81	12.94
Q (kJ/mol)	300	300	363	339
Slope	1	1	1	1
Intercept (MPa)	-0.67	0	-0.06	0
R^2	0.9041	0.9124	0.9649	0.9663
SD (MPa)	40.4	16.0	11.1	7.9
ME (MPa)	-26.2	-2.6	-0.05	0.01

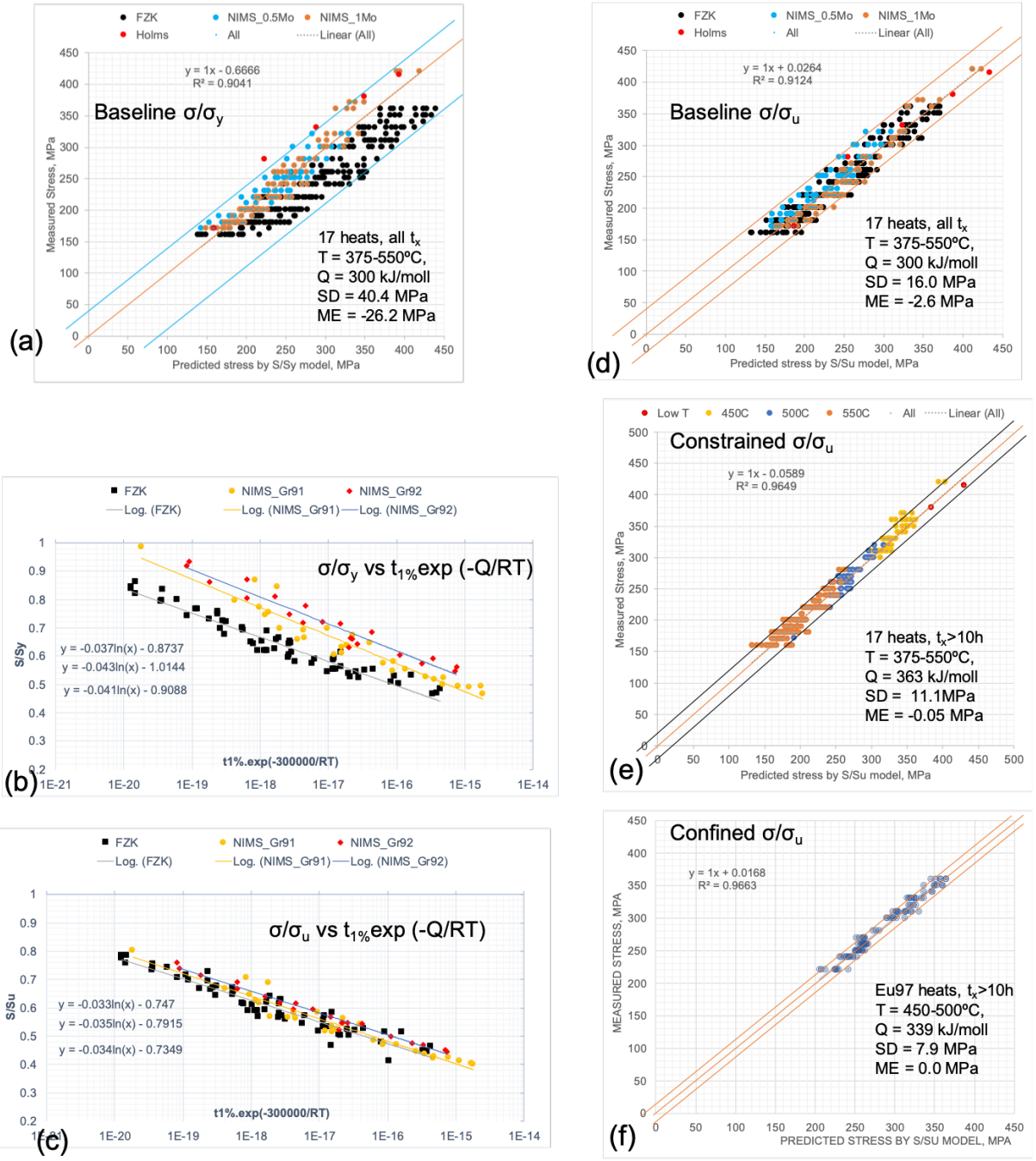

Figure 3. a) P versus M σ for the baseline σ/σ_y model, b-c) temperature-compensated t_x versus σ/σ_y and σ/σ_u, respectively, for 1% strains, and d) P versus M σ for the baseline σ/σ_u model for all 17 heats. Figure e-f shows P versus M σ for the e) constrained σ/σ_u model for all heats, and f) only for Eurofer97 heats.

Compare to the baseline σ/σ_y model, the σ/σ_u model predicts creep stress excellently well with a SD = 16.0 MPa, ME = -2.6 MPa, a slope = 1 and intercepts at 0 MPa for the same Q = 300 kJ/mol (see Figure 3d and Table 3). The prediction is further improved when the creep time (t_x) is constrained to >10h and Q is unconstrained to 363 kJ/mol, which is slightly high but reasonable, that yields a SD = 11.1, a ME = 0, and an intercept = 0 for 1:1 line for the normalized σ/σ_u constrained model of all 17 heats (see Table 3 and

Figure 3e). For the Eurofer97 heats with t_x>10h and Q= 339 kJ/mol, the SD is only 7.9 MPa with 0 MPa ME and intercept for the M vs. P 1:1 line while the residual bias is within 10 MPa (see Figure 3f). All the normalized stress model parameters are summarized in Table 3.

(3) Threshold stress model

In many engineering alloys creep occurs under the reduced threshold stress (σ–σ_t), such that $\varepsilon' \infty (\sigma-\sigma_t)^n$, where σ_t often viewed as a threshold stress [10,15]. A variety of models exist for dispersion-strengthened alloys, which relate σ_t to a fraction of the particle strengthening in static tensile tests [16]. A model that treats σ_t as a function of strain is expected to be especially pertinent to primary creep. In our previous study [1], we have defined threshold stress as $C(\varepsilon)\sigma_y(T)$, where C is the function of primary strains as $C = C_0\varepsilon^{C_1}$ and C_0 and C_1 are fit parameters for Rieth's eurofer97 heats [2]. Details procedures of fitting parameters and SD and ME of measured versus predicted creep stresses on Eurofer97 heats can be found in [1]. In short for the baseline $\sigma - C\sigma_y$ model and for Eurofer97 heats, the SD, ME and intercept is 10.4, 0 and 0 MPa, respectively for a 1:1 M:P line. The M vs. P SD increases to 22.0 MPa while ME and intercept is ≈ 0 MPa for the extended database for 17 heats (see Table 4, and Figure 4a). Therefore, in this study, we have applied the baseline $\sigma - C\sigma_u$ model for all alloys and heats by simply replacing replaced σ_y by σ_u for the similar reasons as described in normalized model section. Thus, the new equation is

$$\varepsilon' = A\,(\sigma - C\sigma_u)^n \exp(-Q/RT) \quad (9)$$

The corresponding required applied creep stress is

$$\sigma = \{\varepsilon' \exp(Q/RT)/A\}^{1/n} + C\sigma_u \quad (10)$$

Table 4. LSF parameters and SD for the threshold σ–$C\sigma_y$ and σ–$C\sigma_u$ primary creep models

Fit Parameters	Baseline σ–$C\sigma_y$ model (17 heats, t_x= all, Q = fixed, T= 375-550ºC)	Baseline σ–$C\sigma_u$ model (17 heats, t_x= all, Q = fixed, T= 375-550ºC)	Constrained σ–$C\sigma_u$ model (17 heats, t_x= >10h, Q = free, T= 375-550ºC)	Confined database σ–$C\sigma_u$ (Eu97, t_x= >10h, Q = free, T= 450-550ºC),
C_1	0.69	0.8067	0.568	0.54328801
C_2	0.116	0.194	0.1058	0.1187
n	6.564	6.981	7.800	9.846
A	0.18	0.009	98	0.325933255
Q (kJ/mol)	300	300	380.46	412
Slope	1	1	1	1
Intercept (MPa)	0.02	-0.04	-0.09	0
R^2	0.8537	0.9096	0.9307	0.9728
SD (MPa)	22.01	17.3	15.6	7.1
ME (MPa)	0.02	- 0.04	-0.1	- 0.01

The baseline $\sigma - C\sigma_u$ model improves the SD to 17.3 MPa with ≈ 0 MPa ME and intercept for all 17 heats and strain times. Though the global SD is reasonable and improves over $\sigma - C\sigma_y$ model, however, residual biases still remains relatively high from - 80 to +40 MPa (see Figure 4b). Constrained t_x to >10h and

unconstrained Q ≈ 380 kJ/mol improves SD to 15.6 MPa and residual biases to within 30 MPa (excluding few far-off points, see Fig. 4c). The Threshold σ - $C\sigma_u$ model works best for individual alloys, say for Eurofer97 heats, with a constrained dataset for t_x> 10h, T = 450 and 500ºC and unconstrained Q to 412 kJ/mol with a SD ≈ 7.1 MPa, ≈ 0 MPa ME and intercept for 1:1 M vs. P line (see Figure 4d). The SD slightly increases with reducing Q, per say Q ≈ 300 kJ/mol, the SD ≈ 8.7 MPa. The LSF parameters are A, n, C_0 and C_1 are also summarized in Table 4.

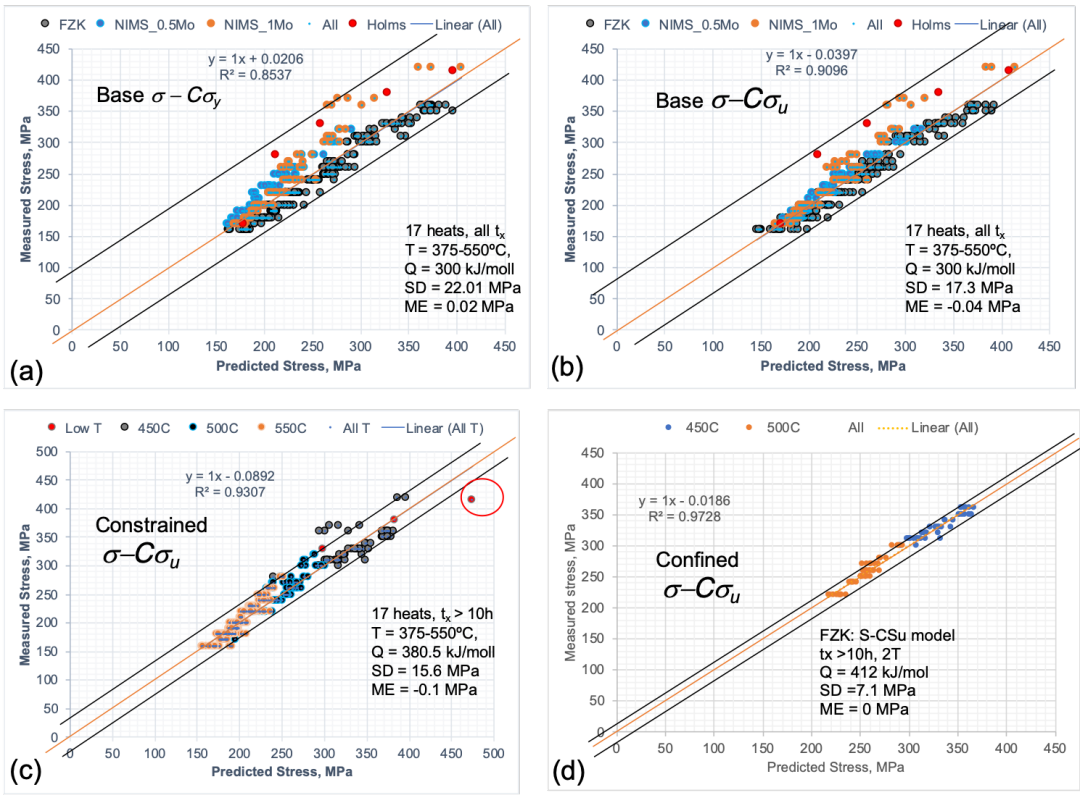

Figure 4. P versus M σ for the: a) baseline σ–$C\sigma_y$ model, b) baseline σ–$C\sigma_u$ model, c) constrained σ–$C\sigma_u$ model for all 17 heats, while d) for confined database σ–$C\sigma_u$ model for Eurofer97 heats only.

We have also applied these models to many combinations of these heats with different set up. Some of them are summarized in Table 5. It can be seen that the W added and Mo-free to less reduced activation TMS (i.e. Eurofer97 and NIMS Gr.92) together relatively well predicts the creep stress, especially for the normalized σ/σ_u and threshold $\sigma - C\sigma_u$ models for t_x>10h and T= 450 - 550ºC with a SD ≈ 11 MPa. Details LSF parameters are available upon request.

Table 5. SD, ME and C or Q values for constrained models (t_x>10h) for different heats

Models	Eu97 T= 450-500ºC SD/ME (MPa) C or Q (kJ/mol)	Eu97 T = 450-550ºC SD/ME (MPa) C or Q (kJ/mol)	Eu97 + Gr92 T = 450-550ºC SD/ME (MPa) C or Q (kJ/mol)	All Heats T = 375-550ºC SD/ME (MPa) C or Q (kJ/mol)	All Heats T = 450-550ºC SD/ME (MPa) C or Q (kJ/mol)
LMP	7.1/0.0 C = 33	9.3/0.0 C = 40	18/0.0 C = 40.10	20.8/0.0 C = 45.97	20.9/0.0 C = 45.87
σ/σ_y	8.5/0.1 Q = 393.2	11.3/ 0.1 350	19.3/0.0 310	20.6/0.0 424	20.7/-0.1 400
σ/σ_u	7.9/0.0 Q = 339	11.1/0.0 320	10.9/0.05 321	11.1/-0.1 363	11.1/ -0.1 369
$\sigma - C\sigma_y$	7.3/ 0.0 Q = 440	7.5/0.1 427	16.0/0.1 351	21.7/ -0.02 300	20.5/ 0.1 470
$\sigma - C\sigma_u$	7.1 / 0.0 Q = 412	11.1/0.1 276	11.1/ -0.1 331	15.6/ -0.1 380.46	15.5/0.0 350

Primary Creep Curve Prediction

The primary creep models can be used to approximately convert discrete data points to continuous creep curves as ε_x (t_x). Note, Rieth's or other mentioned reports do not include any creep curves. These models can also be used to predict ε'_x (t_x) and ε'_x (ε_x), for instance, the threshold stress model has been used to predict the primary creep curves ε_x (t_x), ε'_x (t_x) and ε'_x (ε_x) at 450 and 500ºC, see Figure 5. Note, here the model is optimized for t_x, rather than σ for Rieth's Eurofer97 heats [2].

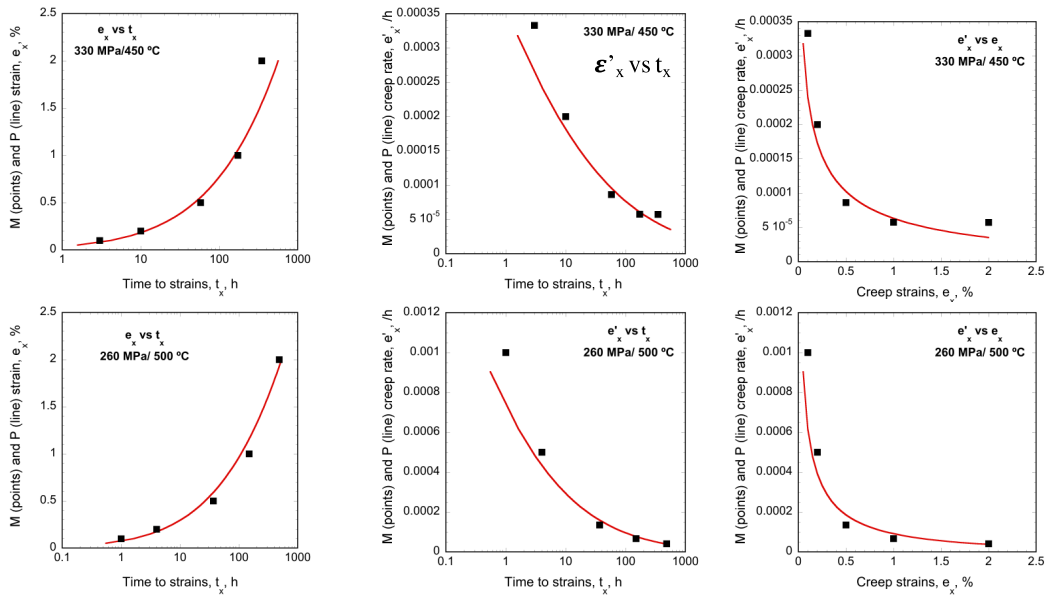

Figure 5. Predicted vs measured primary creep models, ε'_x (t_x) and ε'_x (ε_x) at 450 (top row) and 500ºC (bottom row), respectively.

Models for Higher Strains

For 5% strain

The same primary creep models are also used to predict σ for 5% strains. Only Eurofer97 and NIMS Gr 92 have 5% strain data. Here, C_{LM} = 30 for LMP model, Q = 300kJ/mol for other 4 models, and T = 450 to 550ºC was used. We have first used these models for Eurofer97 dataset, which shows very good fittings for all models with the SD ranged from 6 to 8 MPa for a 1:1 M vs P and 0 MPa intercept line (see Figure 6a-e). Adding NIMS Gr.92 data with Eurofer97 increases the SD up to ≈ 22 MPa, expect for the normalized σ/σ_u (SD ≈ 10.4 MPa, see Figure 6f) and σ-$C\sigma_u$ models (SD ≈ 12 MPa).

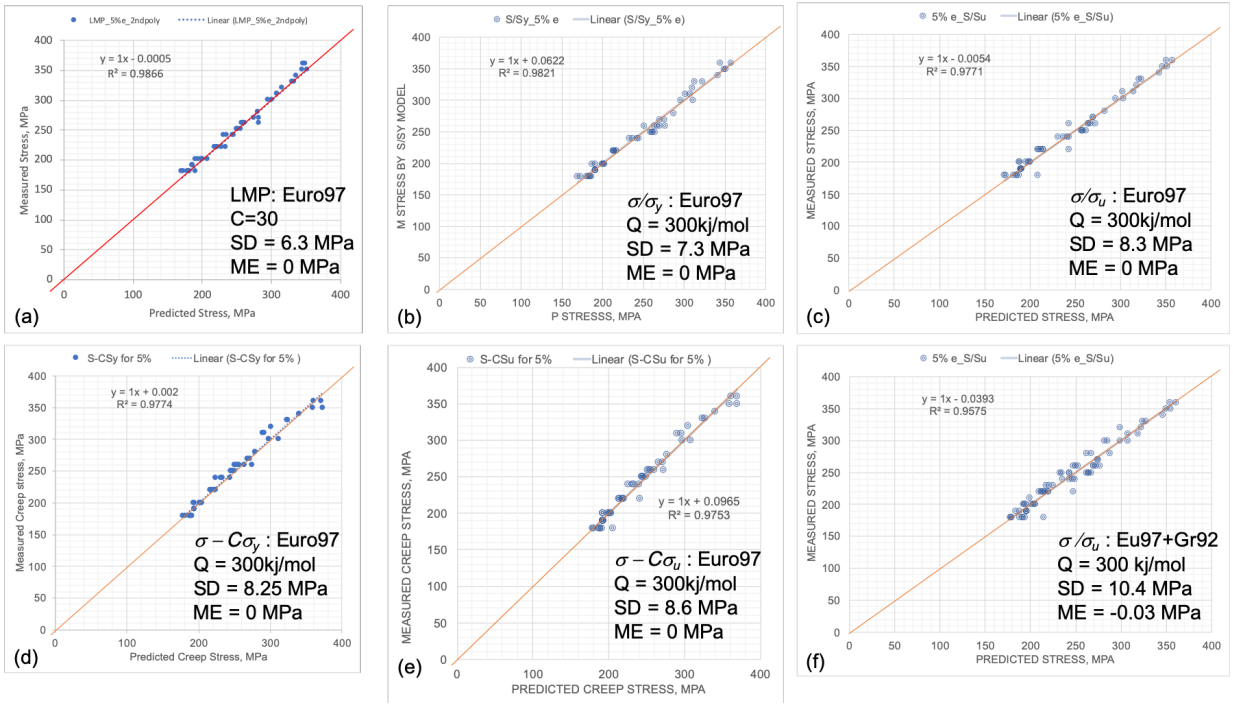

Figure 6. P versus M σ for 5% strains: a) LMP, b) σ/σ_y, c) σ/σ_u, d) σ-$C\sigma_y$, and e) σ-$C\sigma_u$ models for Eurofer97 heats, while f) shows fittings for Eurofer97 + NIMS Gr92 datasets using σ/σ_u baseline model.

For Strains to Rupture

Again, these models are implied to predict σ for the strains to rupture dataset. Except the Holms Gr91 heat, all other 16 heats have rupture strains. While LMP and normalized σ/σ_y, and σ/σ_u models predicts σ with reasonable SD for the Eurofer97dataset, both the threshold models seem unable to predict stress for strains to rupture, t_r (see Figure 7a-e). Only the σ/σ_u model predicts reasonably well for all dataset with an SD ≈ 11.3 MPa (see Figure 7f), while other models predict M vs P SD from 23 (for LMP) up to 40 MPa (for threshold models). Here, for all cases, C_{LM} = 30 or Q = 300kJ/mol has been used for a 1:1 M vs P line with ≈ 0 MPa intercept and ≈ 0 MPa ME. Details fit parameters are not provided here but available upon request.

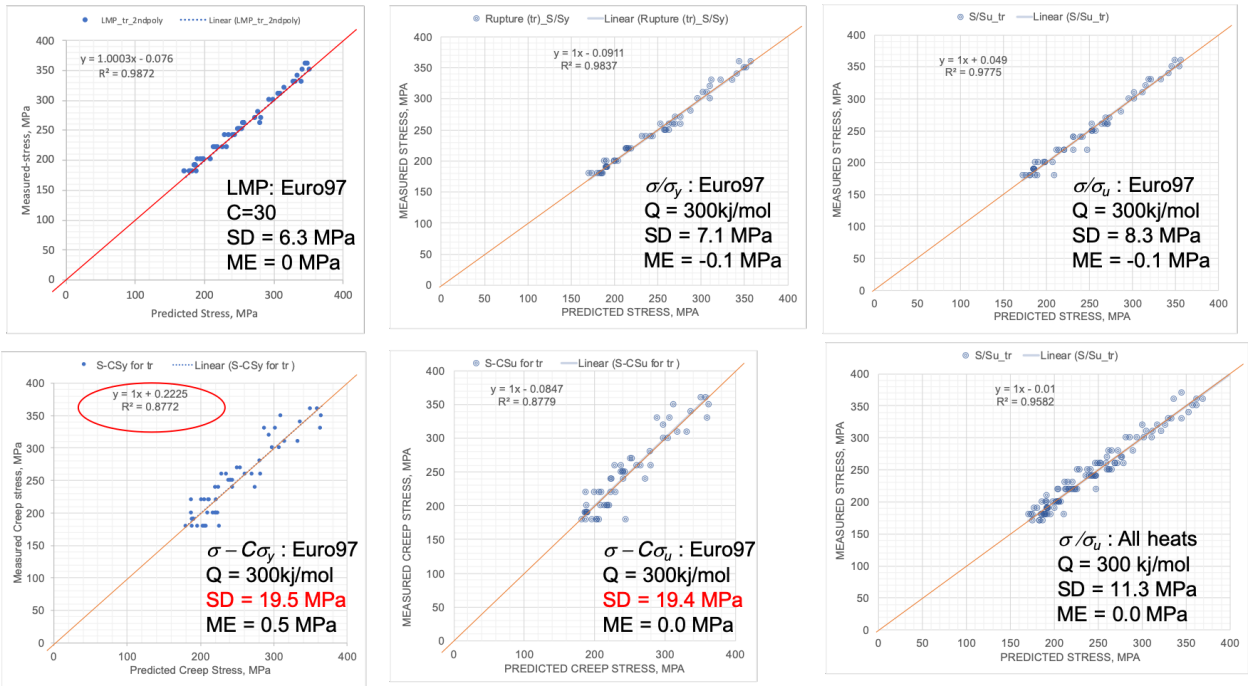

Figure 7. P versus M σ for rupture strains: a) LMP, b) σ/σ_y, c) σ/σ_u, d) σ-Cσ_y, and e) σ-Cσ_u models for Eurofer97 heats, while f) shows fittings for Eurofer97 + NIMS Gr 91 and Gr92 heats using σ/σ_u model.

Models for Initiation of Tertiary Creep, Times to Rupture and Minimum Creep Rate

We have used LMP model to predict time to initiate tertiary creep and time to rupture in h. Only NIMS Gr.91 and Gr92 have recorded tertiary creep initiation time while all the alloys, except Holms one heat, have recorded rupture times. We have also used C_{LM} = 30 in all cases, and T up to 550ºC, whenever available. Here the SD is calculated in log scale by $10^{[\sqrt{\{\Sigma \log(P/M)2\}/N}]}$, where variance is $\{\log (P/M)\}^2$, and N is the number of counts. Figure 8a shows the M vs P time (h) to tertiary initiation creep for a 1:1 line, with a very good SD ≈ 35.2 h (log-based). Same LMP model was also applied to rupture time which predicts excellently with even lower SD ≈ 23h and R^2 = 0.9964 for a 1:1 fit line (see Figure 8b). First, t_r vs LMPs (for C_{LM} = 30) are plotted for different T's, and then predicted tertiary or rupture time is calculated by:

$$t_t \text{ or } t_r = M_0 \exp\{(C_1 + C_2 T)LMP\} \qquad 11$$

where C's are estimated from the fit curves as shown in Figure 8c.

Minimum creep rate (MCR) is modeled by normalized σ/σ_y or σ/σ_u models. First, T compensated MCR is plotted against σ/σ_y for 3T's, which shows similar trends (Figure 8d), and the MCR is calculated by

$$\boldsymbol{\varepsilon}'_{min} = A(\sigma/\sigma_y)^n \exp(-Q/RT) \qquad 12$$

Note, for the σ/σ_u model, the σ_y has been replaced by σ_u. Figure 8e and plots the M vs P MCR with a 1/1 slope, inferred reasonably good fit between P and M rates with a SD ≈ 0.56 /s in log-scale. In contrast, two different data trends are found for the σ/σ_u model with higher SD of ≈ 0.655/s (log-based). In all cases, Q = 300 kJ/mol has been used. Details fit parameters are summarized in Table 6.

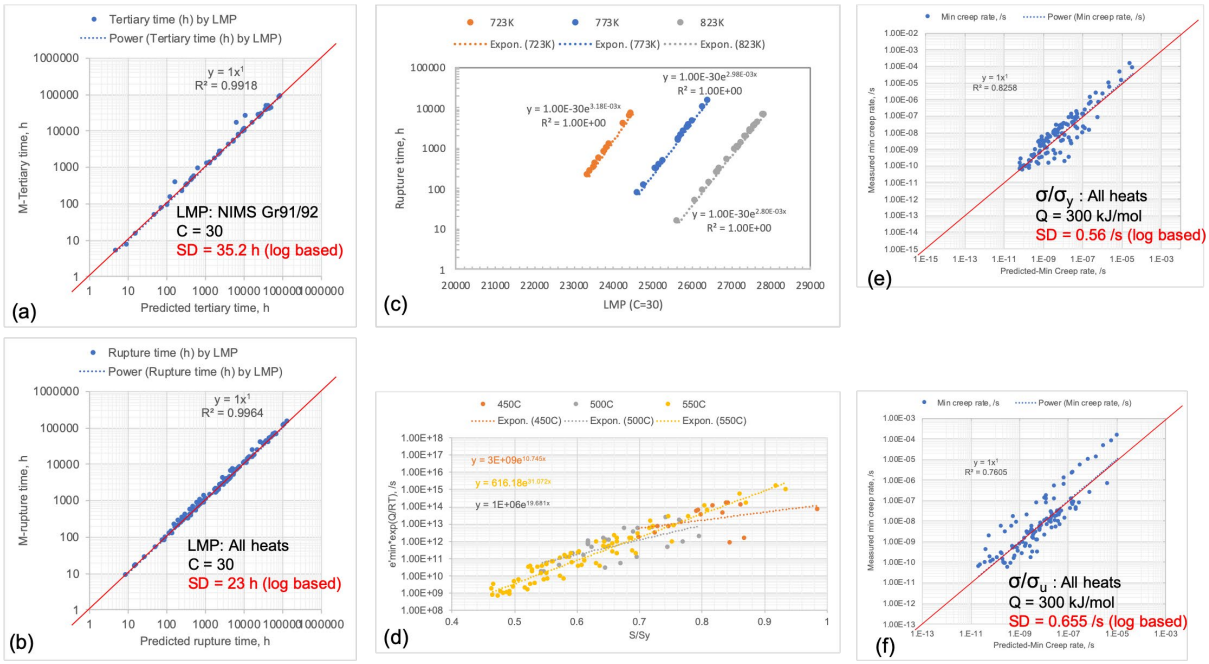

Figure 8. M vs P time for a) tertiary creep initiation time, and b) rupture strain time, respectively, using LMP model, c) approach for LMP model. Figure d) shows ε'_{min} exp(Q/RT) vs σ/σ_y, and e-f) M vs P minimum creep rate (MCR) using normalized e) σ/σ_y and f) σ/σ_u model.

Table 6. LSF parameters for time to tertiary creep and MCR models

Fit Parameters	LMP model for tertiary creep time (h) NIMS Gr91+Gr92 T= 450-550ºC	LMP model for rupture strain time (h) NIMS Gr91+Gr92 T= 450-550ºC	σ/σ_y model for MRC (/s) 16 heats, T= 450-550ºC	σ/σ_u model for MRC (/s) 16 heats, T= 450-550ºC
M_0	6.862×10^{-32}	1.6042×10^{-30}		
C_1	0.005854	0.005854		
C_2	-3.6115×10^{-06}	-3.7345×10^{-06}		
C_{LM}	30	30		
C_{00}	6.564	6.981	1.5205×10^{15}	3.044E+16
C_{01}	0.18	0.009	0.03845	0.4
C_{10}			18.958	20.348
C_{11}			0.011	0.011
Q (kJ/mol)			300	300
Slope	1	1	1	1
R^2	0.9918	0.9964	0.8258	0.7605
SD (log)	35.2 h	23 h	0.56 /s	0.655 /s

CONCLUSIONS

The σ/σ_u model shows the best overall primary, 5% (tertiary region) and strain to rupture creep predictions when the data are versatile from 17 different heats for 9Cr TMS steel. Models were also used to construct primary creep curves, and minimum creep rates.

ACKNOWLEDGEMENTS

We acknowledge the support provided by U.S. Department of Energy through the Office of Fusion Energy Sciences (8-442520-22419-3).

REFERENCES

[1] M.E. Alam, T. Yamamoto, G.R. Odette, Primary Creep Models for 9CrW Tempered Martensitic Steels: Effects on the High Temperature Dimensional Stability of Fusion Structures, Fusion React. Mater. Progr. Semiannu. Prog. Rep. DOE0313/68 (2020) 41–54.

[2] M. Rieth, M. Schirra, A. Falkenstein, P. Graf, S. Heger, H. Kempe, R. Lindau, H. Zimmermann, EUROFER 97. Tensile, charpy, creep and structural tests, in: (No. FZKA--6911). Forschungszentrum Karlsruhe GmbH Technik und Umwelt (Germany). Inst. fuer Materialforschung., 2003.

[3] L. Esposito, N. Bonora, A primary creep model for Class M materials, Mater. Sci. Eng. A. 528 (2011) 5496–5501.

[4] S.J. Williams, M.R. Bache, B. Wilshire, 25 year perspective: Recent developments in analysis of high temperature creep and creep fracture behaviour, Mater. Sci. Technol. 26 (2010) 1332–1337.

[5] F. Ren, X. Tang, Study on creep behavior of Grade 91 heat-resistant steel using theta projection method, AIP Conf. Proc. 1890 (2017) 040003.

[6] L. Zhang, H. Xu, Q. Ma, Z. Wang, Low-temperature creep behavior of commercially pure titanium TA2, Rare Met. Mater. Eng. 37 (2008) 2114–2117.

[7] J. Peng, C.Y. Zhou, Q. Dai, X.H. He, The temperature and stress dependent primary creep of CP-Ti at low and intermediate temperature, Mater. Sci. Eng. A. 611 (2014) 123–135.

[8] J. Koike, K. Maruyama, Study of primary creep in Ti-6-22-22S alloys, Mater. Sci. Eng. A. 263 (1999) 155–159.

[9] S. Gollapudi, D.V.V. Satyanarayana, C. Phaniraj, T.K. Nandy, Transient creep in titanium alloys: Effect of stress, temperature and trace element concentration, Mater. Sci. Eng. A. 556 (2012) 510–518.

[10] B. Wilshire, P.J. Scharning, A new methodology for analysis of creep and creep fracture data for 9-12% chromium steels, Int. Mater. Rev. 53 (2008) 91–104.

[11] NIMS-D1, NIMS Creep Datasheet: Atlas of creep deformation property, Vol. D-1, Creep deformation properties of 9Cr1MoVNb steel for boiler and heat exchangers, 2007.

[12] NIMS-48B, NIMS creep data sheet: No. 48B Data sheet on the elevated temperature properties of 9Cr-0.5Mo-1.8W-V-Nb steel tubes and pipes for power boilers and high temperature service, 2018.

[13] S. Holmström, Defining a negligible creep temperature curve for Gr. 91 steel, Int. J. Press. Vessel. Pip. 146 (2016) 198–202.

[14] T. Shrestha, M. Basirat, I. Charit, G.P. Potirniche, K.K. Rink, Creep rupture behavior of Grade 91 steel, Mater. Sci. Eng. A. 565 (2013) 382–391.

[15] K.R. Williams, B. Wilshire, On the stress- and temperature-dependenceof creep of nimonic 80A, Met. Sci. J. 7 (1973) 176–179.

[16] J. Rösler, E. Arzt, A new model-based creep equation for dispersion strengthened materials, Acta Metall. Mater. 38 (1990) 671–683.

1.7 A MICROSTRUCTURALLY BASED MODEL FOR POST INCUBATION VOID SWELLING IN DUAL ION BEAM IRRADIATED TEMPERED MARTENSITIC STEELS—Takuya Yamamoto, G. Robert Odette (University of California Santa Barbara), Kenta Yoshida (Tohoku University), Kiyohiro Yabuuchi (Kyoto University)

OBJECTIVE

The objective of this research is to characterize and correlate dislocation and cavity microstructures with post incubation void swelling rates in dual ion beam irradiated tempered martensitic steels (TMS).

SUMMARY

Conventional TEM and scanning TEM (STEM) microstructures in F82H steel irradiated and He implanted in a dual ion-beam irradiation (DII), nominally up to 82 dpa and 3700 appm He, have been characterized. The cavity microstructures were imaged by through-focus series bright field TEM, as well as by high angular annual dark field STEM, while dislocations were characterized using weak-beam dark field STEM. The total dislocation density in the analyzed area is ≈ 2.5 x 10^{15} m^{-2}, along sink densities of 1.6 x 10^{15} (m^{-2}) for both bubbles and voids predict a swelling rate of ≈ 0.073%/dpa, which is in good agreement with the database trends. The key result of this study is that post incubation void swelling rates in DII TMS are consistent with simple defect partitioning between dislocation, bubble and void sinks. In the framework of this very simplified model, dislocations have a small bias for self-interstitial atoms (SIA) of B_d ≈ 1%. It appears that defect recombination effects in the high dpa rate DII, in the range used in this study (< ≈ 3x10^{-3} dpa/s), are not large, at least at 500°C. This is hugely important since it indicates that ion irradiations can reasonably emulate post incubation neutron swelling, again at sufficiently high temperature.

BACKGROUND

Predicting and mitigating the effects of a combination of large levels of transmutant He and displacement damage (dpa), produced by high energy neutrons, on the dimensional stability and mechanical properties of structural materials is one of the key challenges in the development of fusion energy [1]. The fundamental overriding questions about He-dpa synergisms include: a) What are the basic interacting mechanisms controlling He and defect transport, fate and consequences, and how are they influenced by the starting microstructure and irradiation variables (dpa rate, He/dpa ratio, temperature and applied stress); and, b) how can the detrimental effects of He-dpa synergisms be mitigated and managed by proper microstructural design? In order to answer the questions, we have been analyzing TEM cavity microstructures in dual ion-beam irradiated F82H steels. The cavity evolution, or more specifically void nucleation and growth swelling rates, are strongly influenced by the balance of sink strengths (k) and sink biases (B) for self-interstitial atoms (SIA) and vacancies. In the post incubation swelling regime, when injected interstitial and vacancy emission effects can be neglected, and assuming dislocations are the major biased sink, the swelling rate $f_v' = \Delta f_v/\Delta dpa$, is mediated by the balance of the dislocation (k_d), bubble (k_b), void (k_v) sink strengths and the dislocation SIA bias (B_d). Based on nominal sink strengths of $k_{dv} = \rho_d$, $k_{di} = \rho(1+ B_d)$, $k_b = 4\pi N_b r_b$ and $k_v = 4\pi N_v r_v$, we compare the predicted f_v' to experimentally observed values. Here, ρ is the dislocation density, N is the bubble/void number density and the r are the corresponding average cavity radii. The comparison is based on characterization of the dislocation and cavity microstructures in the same probed volume. To the best of our knowledge this is the first time this has been done in an irradiated TMS.

PROGRESS AND STATUS

Experimental Procedure

We have been developing microstructure database for tempered martensitic steels (TMS) under dual ion-beam irradiation (DII) in DuET facility located at the Institute of Advanced Energy, Kyoto University in Japan. Here, Fe^{3+} and He^{+} ions are accelerated to 6.4MeV and 1MeV, respectively [2]. Table 1 summarizes nominal He and dpa conditions at a reference 600 nm and at the peak He 1050 nm depth, along with the alloys in the current database. Here, TEM and STEM observations have been carried out for the IEA heat of F82H in the most recent (DI16A+19A) 500°C irradiation condition, nominally up to 82 dpa and 3700 appm He.

The DII specimen was in the form of 0.5 mm thick ≈ 1 x 20 mm rectangular coupons mechanically- and electro-polished prior to irradiation. TEM foil samples were FIBed in Helios FIB-SEM G4, Thermo Fisher Scientific, followed by gentle milling by Ar ions at energies down to 300 eV. Through-focus series cavity images were observed using a JEOL JEM-2100. Plus, TEM and STEM bright field (BF), weak beam (WB) and high angle annular darkfield (HAADF) images were obtained in a spherical aberration corrected STEM JOEL ARM 200F; both are located in Oarai International Research Center of Tohoku University. The observable area of the foil was wedge shaped after Ga/Ar ion milling, with measured thickness distribution that were derived from HAADF intensity profiles. For a given crystal orientation, HAADF intensity, I, to an incident electron beam intensity, I_o, ratio I/I_o for a sample with thickness, t, is expressed as [3]:

$$\frac{I}{I_o} = \frac{K}{I_o}(1 - e^{-Ft})e^{-\mu t} \qquad (1)$$

Here, F is the fraction of electrons scattered per unit thickness and μ is the linear attenuation coefficient of electrons in the material. For an iron foil Yuan reports HAADF intensity profile of a dimensionally confirmed wedge-shaped sample, as shown in Figure 1 [3]. Both F and μ depend on the elemental density of the material while K can encompass other factors such as the crystallographic orientation and extended defects. Thus, we derived F and μ based on the reported I(t) profile refitted to get a better representation for the actual thickness range. Here, K is fitted to the observed HAADF intensity profiles.

Table 1. The nominal dpa-He conditions of DII experiments

Exp ID	T (°C)	Nominal Condition (@550-650nm)				Peak He (@1000-1100nm)			Alloys
		dpa	(appm) He	He/dpa	dpa/s	dpa	(appm) He	He/dpa	
DI10B1	500	26	1210	47	5.0×10^{-4}	45	2100	47	F82H mod.3, MA957
DI10B2	500	9.9	457	46	5.2×10^{-4}	17	795	46	F82H mod.3, MA957
DI10B3	500	10	480	47	5.1×10^{-4}	18	840	47	F82H mod.3, MA957
DI13A	500	26	390	15	5.1×10^{-4}	44	670	15	mod.3, IEA (AT,20,80), MA957
DI13B1	500	30	848	29	1.5×10^{-3}	51	1467	29	F82H mod.3, F82H IEA (AT)
DI13B2	500	27	730	27	1.6×10^{-3}	46	1262	27	F82H IEA (20%CW or 80%CW)
DI13B1+2	500	57	1578	28	1.5×10^{-3}	97	2729	28	MA957
DI14A1	500	30	1200	47	1.3×10^{-3}	45	2100	47	F82H mod.3, F82H IEA (AT)
DI14A2	500	30	1200	47	1.3×10^{-3}	45	2100	47	F82H IEA (20%CW or 80%CW)
DI14A1+2	500	52	2400	47	1.3×10^{-3}	90	4200	47	MA957
DI14B	500	45	1290	28	8×10^{-4}	79	2230	28	F82H mod.3, F82H IEA (AT)
DI15A1	500	51	1360	27	8.6×10^{-4}	88	2350	27	F82H mod.3, IEA (AT,20,80)
DI16A	500	51.5	2327	45	6.5×10^{-4}	89.2	4024	45	F82H mod.3, IEA (AT,20,80)
DI16A+19A	500	81.5	3748	45	6.27×10^{-4}	141.7	6397	45	F82H mod.3, IEA (AT,20,80)

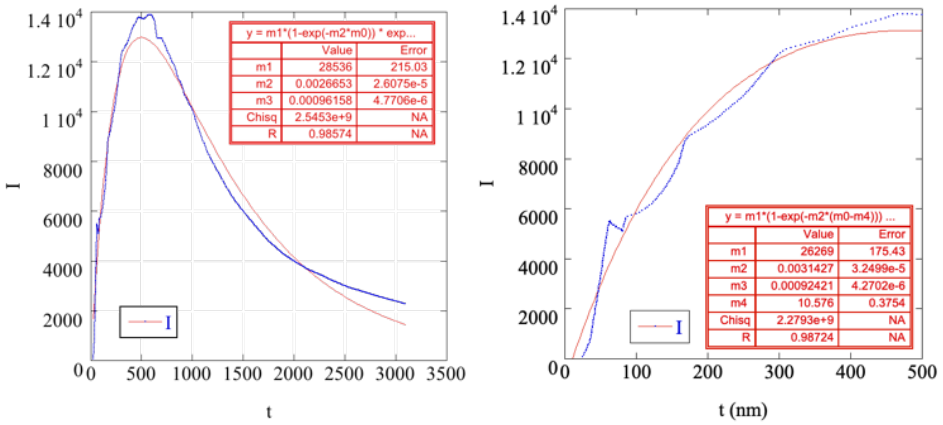

Figure 1. A refit of HAADF intensity profile of a wedge-shaped Fe sample of known thickness profile reported by Yuan [3].

RESULTS

TEM/STEM characterization of the coupled cavity and dislocation microstructure of DII F82H

Figure 2 shows STEM and TEM images of DII F82H. Figures 2a to 2c are a set of BF, HAADF and, WB (g = [110], (g,5g)) STEM images observed at a location where the nominal irradiation condition is estimated to be 53 dpa and 710 appm He (at irradiation depth from 100 to 200 nm). Figure 1d shows the traces of dislocations (green lines) and cavities (red lines) observed in Figure 2b and Figure 2c, respectively. The traces were used to calculate dislocation densities, and cavity sizes and number densities, for the location dependent sample thickness, as described in the next section. Figure 2e shows TEM under-focus image at another location in the sample, where the nominal irradiation condition changes from 53 dpa and 710 appm He (from 100 to 200 nm) to 63 dpa and 3200 appm He (from 300 to 400 nm).

Figure 3a and 3b show STEM HAADF images in nearby locations at two different magnifications. The inserts show the corresponding HAADF intensity variation profiles along the light blue line in the image, as a function of the distance from the specimen wedge edge. The calibration thickness vs. distance profiles for a wedge without cavities shown in Figure 3c which yields fitted K ≈ 2.1 x 10^7 and ≈ 2.9x10^6 for the 600k and 200k times magnifications, respectively. It is notable that the thickness profiles in the overlapping ranges for the two magnifications are in good agreement. The actual measured profiles, along the line over the cavities in the image on the left, are shown by the red dots in the Figures 3d-g. The simulated profile, with the cavities removed, are shown by the gray dots. The thin black line interpolates between the end of the cavitated region. The dimensions of the dip in the profiles, where they cross cavity locations, are consistent with both the fitted K and the corresponding cavity size measured in x-y plane. Figures 3e-g show a few cases where multiple cavities overlap in z-direction, as illustrated by the 2 to 4 solid line profiles at the bottom of the plot, which indicate the individual overlapping cavity contributions to the dip in the intensity profile. Only one cavity in Figure 3f, appears to be truncated by the wedge surface. A smaller K would allow for a fully embedded cavity in Figure 3f, but it would be inconsistent with the other cases, where the dips would be too large for the observed cavity sizes.

Dislocation and cavity quantification in the observed areas

The weak beam dark field imaging revealed a dislocation density of $\rho \approx 2.5 \times 10^{15}$ m^{-2} for the 52 dpa-710 appm He condition. This ρ is relatively high, but not unreasonable, considering base dislocation density of 6×10^{14} m^{-2} [4] and the dislocation density added as loops ranging ≈ 0.5 to 1 x 10^{15} m^{-2} in He-rich irradiations such as Spallation proton irradiation (SPI) and in-situ He injection (ISHI) studies [5,6]. The corresponding

cavity number densities (N), diameters (d) and volume fractions (f) were determined, based on the HAADF STEM profiles and through focus, bright field TEM as shown in Figure 4. The cavity f is ≈ 2.2% for the STEM and ≈ 1.5% for TEM imaging, respectively. The f for the other 2 conditions ranged from 0.75 to 1.55%. These are in reasonable agreement in our overall DII database [7]. Figure 5 shows the cavity size distribution in the STEM and TEM or the 52 dpa-710 appm He condition. The bubble portion of the distribution, presumed to be at d < ≈ 4 nm, is enhanced in STEM imaging, while void portions (f_v) differ by only ≈ 0.3%, as shown in Figure 4. A likely reason for this difference is that the wedge was too thick for the relatively low beam intensity in the TEM through focus technique to detect small bubbles. Figure 6 shows the corresponding TEM size distribution for all 3 conditions characterized. The cavity statistic for bubbles (d < 4 nm) and voids (d≥ 4 nm) are summarized in Table 2.

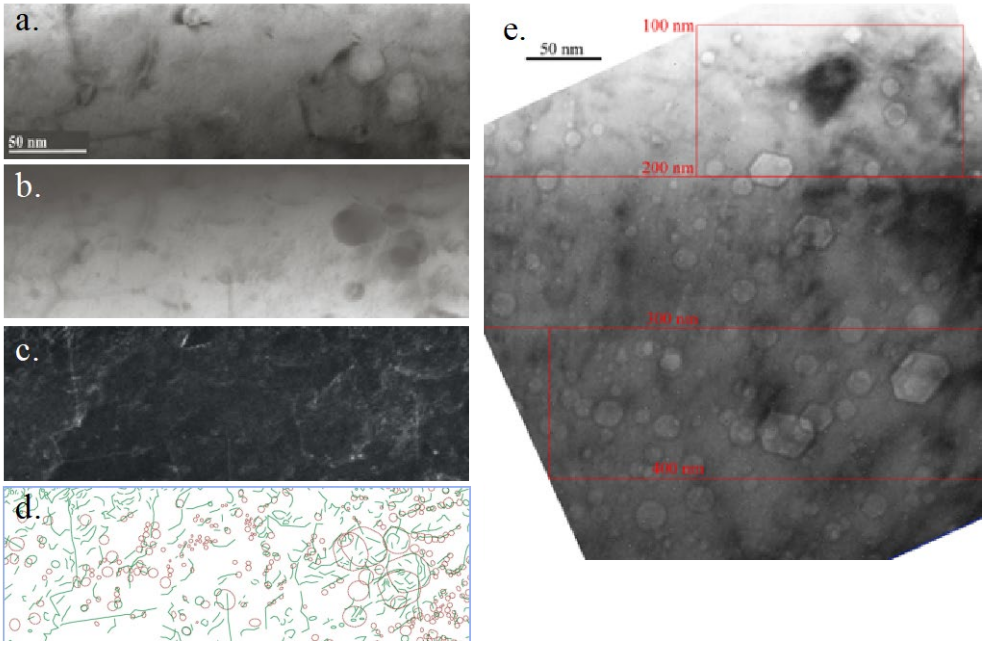

Figure 2. a) BF; b) HAADF; and, c) WB STEM images and d) dislocations (green solid lines) and cavities (red dotted lines) schematics in F82H IEA irradiated to average 53 dpa and 710 appm He; and e) TEM under-focus image of the same specimen from ≈ 53 dpa (710 appm He) to ≈ 63 dpa (3200 appm He) locations.

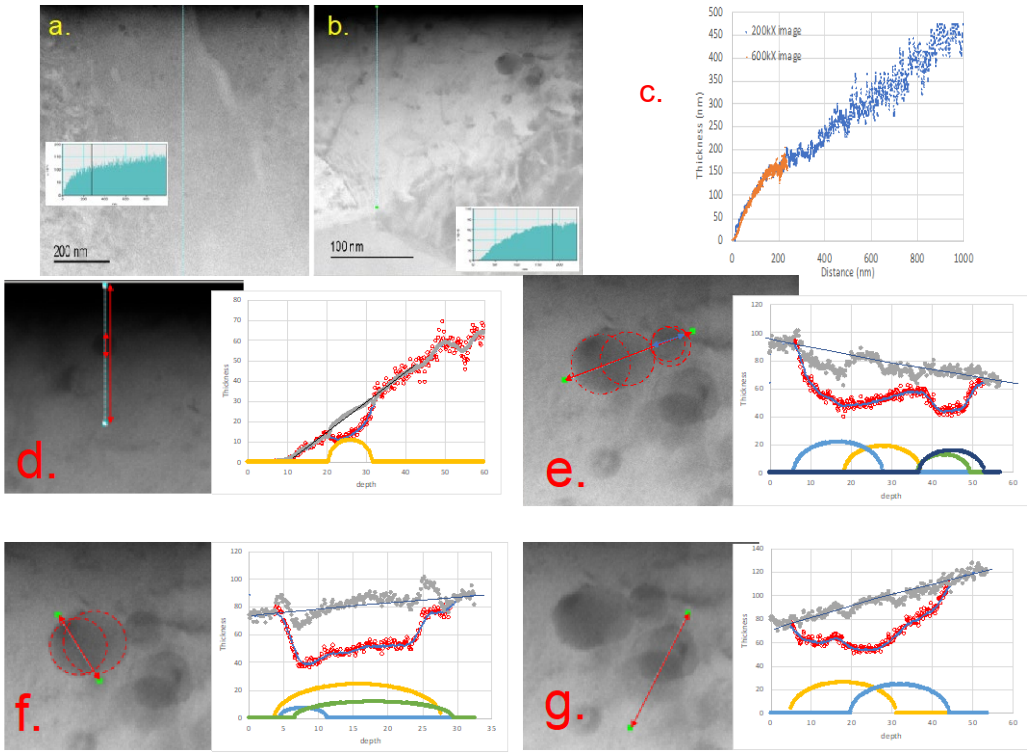

Figure 3. STEM HAADF images with an intensity profile for the indicated light-blue line for at the magnifications of a) 200k; and b) 600k times; c) calibrated thickness – distance profiles of the samples; d) to g) plots on the right showing measured (red dots) and average (blue line) thickness profiles across various cavities (shown in the image on the left) as well as that with the simulated profiles (gray dots) after removing the dips corresponding observed single or multiple cavities, whose depth profiles are shown by solid lines at the bottom.

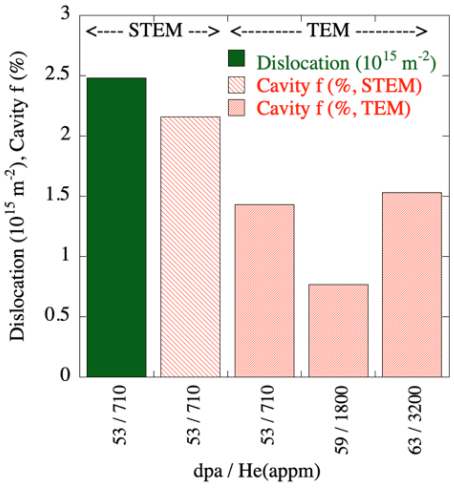

Figure 4. Summary of dislocation density and cavity volume fraction in F82H irradiated to 53~63 dpa with 710~3200 appm He.

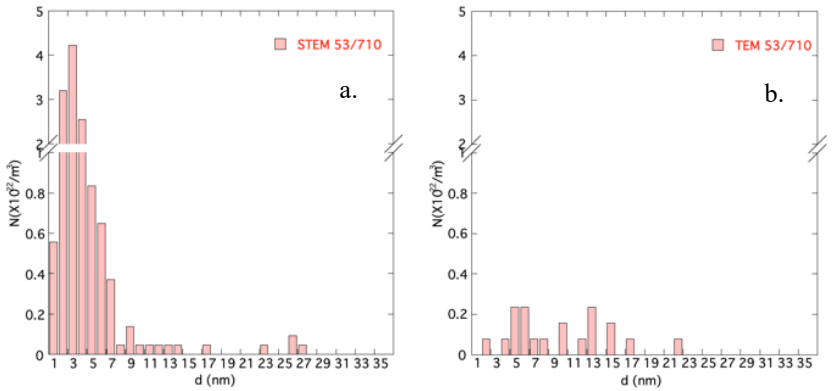

Figure 5. Size distribution of cavities in a) STEM and b) TEM for the dpa and He (appm) conditions shown at the top right corner.

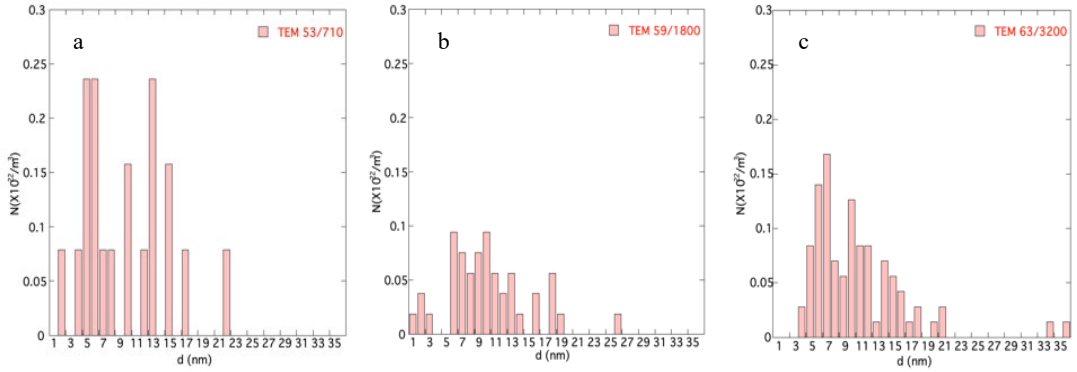

Figure 6. The size distributions of cavities in TEM for the dpa and He (appm) conditions shown at the top right corner.

Table 2. Average size (<d>) and number density (N) of bubbles and voids

dpa	He (appm)	Cavity (d < 4 nm)		Cavity (d > 4 nm)		TEM/STEM
		<d> (nm)	N (x10^{22}/m^3)	<d> (nm)	N (x10^{22}/m^3)	
53	710	2.7	9.4	7.0	3.6	STEM
53	710	2.4	0.079	10.1	1.5	TEM
59	1800	2.2	0.075	11.1	0.70	TEM
63	3200	-	0	10.6	1.1	TEM

ANALYSIS AND DISCUSSION

Post incubation swelling rate (f_v') sink balance analysis

Based on the STEM results, the swelling rate per dpa, f_v' (%/dpa), for the observed microstructures can be estimated [1],

$$f_v' \approx C\eta B_d k_d k_v/[(k_d + k_v + k_b)(k_d(1 + B_d) + k_v + k_b)] \quad (2)$$

The C is a factor to adjust the swelling, to account for factors such as reductions due to excess SIA from injected Fe^{3+} ions (injected interstitials, II) as well as by point defect recombination at the high dose rate; $\eta \approx 0.3$ is the fraction of point defects surviving cascade recombination; B_d is dislocation sink bias for SIA and k_j (j = d,b,v) are sink densities of dislocations, bubbles and voids. Table 3 shows the sink densities based on the measured r, N and d. For a nominal value of $Z_d = 0.015$, the predicted swelling rate $f_v' \approx 0.073\%/dpa$. We can compare this to the general post incubation swelling trends observed in the DII database [7]. The post incubation dpa is dpa' = dpa - dpa_i, where dpa_i is the He/dpa dependent incubation dose for the onset of swelling [7]. As shown in Figure 7a, general post-incubation f_v(dpa') trend (the red solid line) has an average slope, $f_v' \approx 0.07$, up to ≈ 30 dpa', for a range of He/dpa. This is in excellent agreement with the sink strength-based prediction assuming C ≈ 1. Figure 7b shows post-incubation swelling trend for a wide range of TMS and irradiation conditions, including neutrons (the FFTF and BOR60 reactors), single ion, in-situ He injection in HFIR (ISHI) as well as DII [7]. The swelling rate derivative of the f_v(dpa') curve shown in Figure 7c, shows a lower average swelling rate of 0.045 ± 0.010%/dpa, over the dpa' range of 10 to 70 dpa. However, this f_v' estimate is highly sensitive to the dpa_i, which are fairly uncertain. Thus, overall f_v' data are reasonably consistent with the simple sink partitioning model.

Table 3. Sink densities and predicted swelling rate, f_v' (%/dpa), for the observed microstructure

Property	Values
B_d	0.015
k_d	2.5 x 10^{15} (m^{-2})
k_b	1.6 x 10^{15} (m^{-2})
k_v	1.6 x 10^{15} (m^{-2})
f_v'	0.073 (%/dpa)

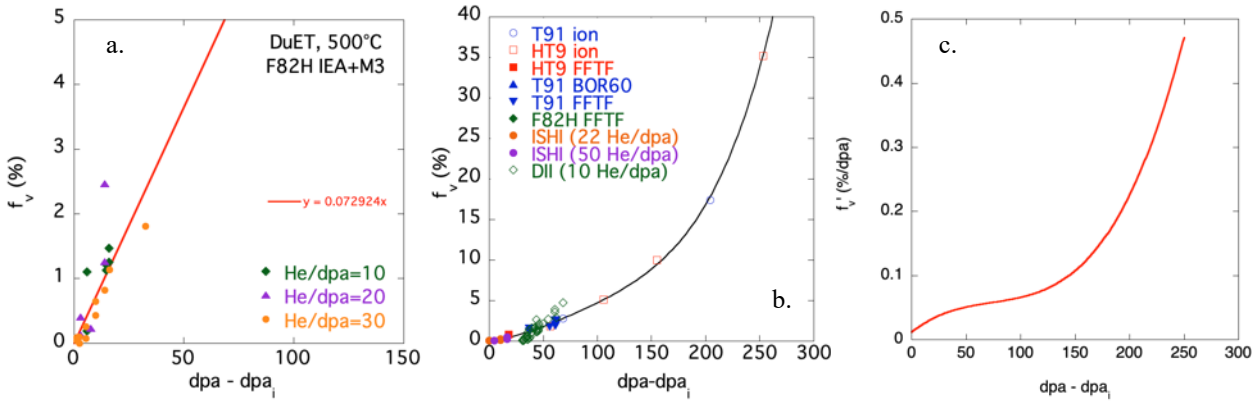

Figure 7. a) post incubation swelling trends in DII F82H IEA and Mod.3 heats at relatively lower He/dpa rates (≈ 10 to ≈ 30) in out DII database with overall fitting line; b) collection of TMS swelling data from neutron, single ion, dual ion and in situ He injection irradiation experiments, on a common post-incubation dpa scale; c) the derivative of fitted curve in Figure 7b giving swelling rate (f_v') as a function of dpa.

The f_v' model was extended to the whole DII database, with slightly more conservative assumption of k_d = 2 x 10^{15} m^{-2}, C = 1 and B_d = 0.009, while otherwise using measured values of k_b and k_v. Figure 8a and b show all the f_v data for 25 ≤ He/dpa < 35 and 35 ≤ He/dpa < 55, respectively, in the database. Two distinct groups with high and low f_v' were observed, as shown by red circles and blue diamonds, respectively. As previously reported, this variation in swelling is likely due to the effects of injected ion interstitials (II) and the effects of the local microstructure [7-11]. The observed areas in the high f_v' cases are protected by the effect of extended features, such as a grain boundary or arrays of large carbides, in restricting the back flow of II [7]. Thus, the high swelling rate data in Figure 7a are considered to be the actual f_v'.

A post incubation swelling rate analyses for the high and low f_v' groups are shown in Figures 8c and 8d, respectively. The incubation dpa_i was determined by linearly extending the f_v vs. dpa trend back to $f_v = 0$ in both groups. Unfortunately, the estimated dpa_i are subject to significant uncertainties. The resulting swelling rate, $f_v' = \Delta f_v/\Delta dpa$ (or $\Delta dpa'$) in %/dpa are the data points in the figures, which can be compared to the prediction of Equation 2 as a function of the ratios k_b/k_v (measured) and k_v/k_d (partially measured with k_v), here for a specified $B_d = 0.009$. The k_v/k_d range from 0.14 to 1.7. The f_v' data are in good agreement with the model predictions, with a peak f_v' of ≈ 0.075 (peak prediction) and 0.1%/dpa (peak data), respectively. The predictions are in better agreement with the average measured f_v'. These results are also consistent with the swelling rate based on the measured values of k_v/k_d and ρ, shown above. The low swelling group has a correspondingly lower peak predicted f_v' of ≈ 0.016%/dpa versus a measured peak value of ≈ 0.03%/dpa. The predictions are in better agreement with the average f_v'. Thus, here the C for the II effects is ≈ 0.21.

While we have assumed the high and low f_v data sets are due to the absence or presence of II, there may be other reasons associated with effects like recombination at high dpa rates. In this case, II would be expected to vary strongly with the sampling depth. Table 3 shows the range and averages of the dpa rate, sampling depth and total sink density for the high and low f_v' data sets. The ranges overlap and do not show distinct f_v' differences between high and low swelling rate cases. However, the average dpa rate is slightly higher and sampling depth is slightly shallower for the higher swelling group. The total sink densities do not show any particular effect. These results suggest that the f_v' differences are not directly related to the dpa rate. As noted previously, the high swelling cases are in some cases associated with features that block the back flow of II. A smaller effect of II is also associated with a shallower depth. This needs further confirmation, but is very important since it means that DII result in post incubation f_v' that are similar to those expected for much lower neutron dpa rate conditions, at least at 500°C.

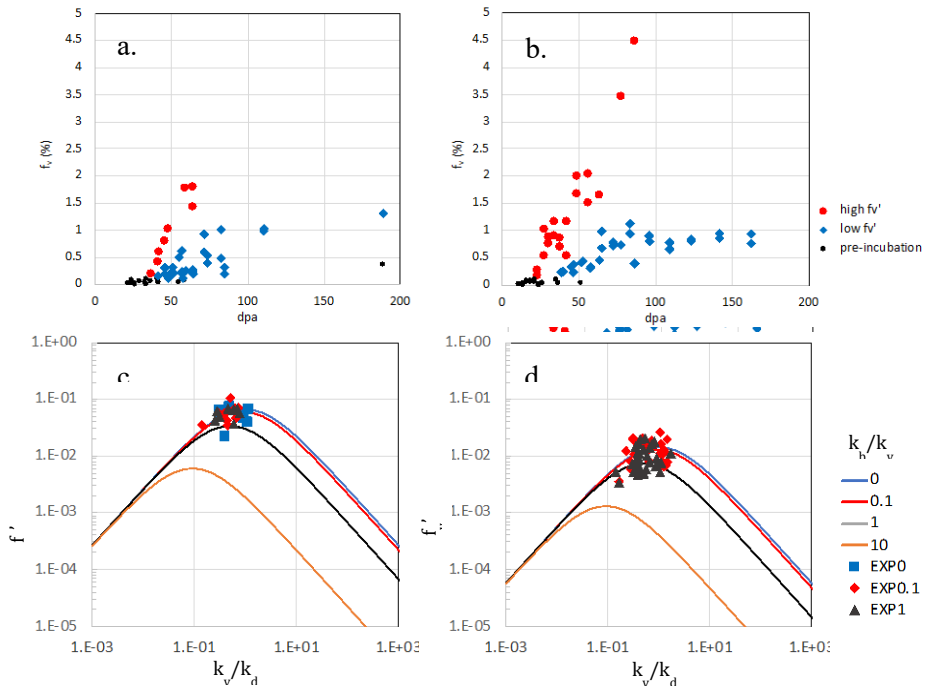

Figure 8. Swelling f_v versus dpa for a) 25 ≤ He/dpa < 35 and b) 35 ≤ He/dpa < 55 showing groups of high (red circle) and low (blue diamond) swelling rates; estimated swelling rate $f_v' = f_v / (dpa - dpa_i)$ versus sink density ratios k_v/k_d for various k_b/k_v groups, compared with Eq. (2) predictions, for c) high and d) low swelling rate groups, using C = 1 and 0.21, respectively, for $k_d = 2x10^{15}/m^2$ and $B_d = 0.009$.

Table 3. dose rate, sample depth and total sink density for high versus low swelling rate data sets

figure	f_v'	He/dpa	dose rate (dpa/s)			depth (nm)			Total Sink k_t ($x10^{15}$ m^{-2})		
			Min.	Max.	Avg.	Min.	Max.	Avg.	Min.	Max.	Avg.
8a	High	30 ± 5	$4.5x10^{-4}$	$3.2x10^{-3}$	$1.7x10^{-3}$	0.25	1.2	0.78	2.9	4.5	3.6
	Low	30 ± 5	$7.3x10^{-4}$	$2.8x10^{-3}$	$1.2x10^{-3}$	0.5	1.25	0.87	2.4	6.7	3.4
8b	High	45 ± 10	$4.9x10^{-4}$	$2.7x\ 10^{-3}$	$1.6x10^{-3}$	0.3	1.1	0.70	2.3	4.4	3.3
	Low	45 ± 10	$4.9x10^{-4}$	$1.3x10^{-3}$	$8.6x10^{-4}$	0.3	1.15	0.82	2.4	5.6	4.1

SUMMARY AND FUTURE RESEARCH

The key result of this study is that post incubation void swelling rates in DII TMS are consistent with simple defect partitioning between dislocation, bubble and void sinks. In the framework of this very simplified model, dislocations have a small bias for SIA of $B_d \approx 1\%$. It appears that defect recombination effects in the high dpa rate DII, in the range used in this study ($< \approx 3x10^{-3}$ dpa/s), are not large, at least at 500°C. This is hugely important since it indicates that ion irradiations can reasonably emulate post incubation neutron swelling, again at sufficiently high temperature. The TEM results suggest that the total dislocation line density increases under irradiation, with contributions both from loops and network evolution. Due to this along with the development of void sinks, the observed swelling rates are near the predicted maximum values with a good balance of void and dislocation sinks ($k_v \approx k_d$). However, a significant population of bubbles reduces the peak f_v', likely up to factors of order 2 or more. This hypothesis is consistent with the increase in f_v' observed at high ion irradiation dpa [7], where bubbles are not present, or transition into voids. Limitations in this highly over simplified analysis and model include is that they: a) apply to temperatures around 500°C and relatively high He/dpa ratios; b) involve assumptions that are not fully verified and may not fully account for important physics, like cavity bias for SIA [13]; c) do not deal with the critical issues of the incubation dose for swelling (dpa_i); and, d) are based on limited observations of dislocation structures and their evolution.

Near future work will focus on resolving these issues and refining the model. In particular, we will continue to develop our multiscale-multiphysics master model of He transport, fate and consequences. In part to inform simpler and more focused models and analysis like those presented in this report.

ACKNOWLEDGEMENTS

The dual ion-beam irradiations were conducted under the support of the "Joint Research Program on Zero-Emission Energy Research, Institute of Advanced Energy, Kyoto University (ZE31A29). The work performed at UCSB was supported by the U. S. Department of Energy, Office of Fusion Energy Sciences, under contract DE-FG03-94ER54275. TEM and STEM work were carried out in support of International Research Center for Nuclear Materials Science, Tohoku University (Oarai, Japan).

REFERENCES

[1] Y. Dai, G.R. Odette, T. Yamamoto, *The Effects of helium on irradiated structural alloys, in Comprehensive Nuclear Materials, R.J.M. Konings and R.E. Stoller Eds. (2020) Elsevier.*

[2] T. Yamamoto, Y. Wu, G.R. Odette, K. Yabuuchi, S. Kondo, A. Kimura, "A Dual Ion Irradiation Study of Helium-DPA Interactions on Cavity Evolution in Tempered Martensitic Steels and Nanostructured Ferritic Alloys," J. Nucl. Mater. 449 (2014) 190.

[3] Biao Yuan, "Direct Measurement of Thicknesses, Volumes or Compositions of nanomaterials by Quantitative Atomic Number Contrast in High Angle Annular Dark Field Scanning Transmission Electron Microscopy" Ph. D thesis at University of Central Florida (2012)

[4] T. Yamamoto, G. R. Odette, Y. Wu, "Constitutive, Damage and Plasticity Laws for Candidate Fusion Alloys," DOE/ER-0313/51 (2012) 78.

[5] T. Zhang, C. Vieh, K. Wang, Y. Dai, *J. Nucl. Mater.,* 450 (2014) 48.

[6] H. J. Jung, D. J. Edwards, R. J. Kurtz, G. R. Odette, Y. Wu, T. Yamamoto, DOE/ER-0313/58 (2015) 48-54.
[7] T. Yamamoto, G.R. Odette, “A Fusion Relevant Engineering Void Swelling Model For 9cr Tempered Martensitic Steels,” DOE/ER-0313/67 (2020) 21.
[8] M.B. Toloczko, F.A. Garner, J. Nucl. Mater. 233-237 (1996) 289.
[9] Lin Shao, C.-C. Wei, J. Gigax, A. Aitkaliyeva, D. Chen, B.H. Sencer, F.A. Garner, J. Nucl. Mater. 453 (2014) 176.
[10] M.P. Short, D.R. Gaston, M. Jin, L. Shao, F.A. Garner, J. Nucl. Mater. 471 (2016) 200.
[11] J.G. Gigax, T. Chen, Hyosim Kim, J.Wang, L.M. Price, E. Aydogan, S.A. Maloy, D.K. Schreiber, M.B. Toloczko, F.A. Garner, Lin Shao, J. Nucl. Mater. 482 (2016) 257.
[12] C. Sun, F.A. Garner, L. Shao, X. Zhang, S.A. Maloy, Nuc. Inst. Methods Phys. Res. B 409 (2017) 322.
[13] A.A. Kohnert, M.A. Cusentino, B.D. Wirth, J. Nucl. Mater. 499 (2018) 460.

1.8 TENSILE PROPERTIES OF EUROFER97 STEEL VARIANTS IRRADIATED TO TARGET 2.5 DPA, 300°C IN THE EUROFUSION PROGRAM—A. Bhattacharya, X. Chen, J. Reed, T. Graening, J.W. Geringer, Y. Katoh (Oak Ridge National Laboratory), M. Rieth (KIT)

OBJECTIVE

Ten Eurofer97 steel variants (designated as H, I, J, K, L, M, N, O, P and reference E) were irradiated in HFIR for EUROfusion targeting 2.5 dpa, 300 °C. Tensile testing in the hot cells were performed at room temperature and 300 °C to screen the irradiation induced mechanical property degradation in terms of the effect of different processing routes and chemistry on the alloy behavior.

SUMMARY

Uniaxial tensile tests were completed on the ten Eurofer97 variants in the EUROfusion Phase-I irradiations, targeting 2.5 dpa, 300 °C. The testing, performed at room temperature and 300 °C, revealed irradiation induced hardening of all the alloys. This was reflected in the increase in the yield stress (YS) and ultimate tensile stress (UTS) of the materials. Hardening was accompanied with reduction in uniform and total elongations of all the alloys. The expected behavior of lower ductility for testing at 300 °C was consistent between all the alloys, that is attributed to dynamic strain ageing (DSA). Reduction in area (RA) was also estimated, using scanning electron microscopy (SEM) fractography which revealed lower necking in all the irradiated alloys, with >20% reduced necking observed in some alloy variants. The reference Eurofer97 alloy showed necking reduction much lower than 10% with absolute RA value of >75% for the irradiated alloy as compared to ~80-83% RA in the unirradiated state.

PROGRESS AND STATUS

The manufacturing/processing conditions and varying chemistries of the ten Eurofer97 alloy variants are provided in Table 1 and Table 2 respectively. After HFIR irradiations, uniaxial tensile tests were performed on these alloys at room temperature and irradiation temperature of 300 °C on the irradiated SS-J3 tensile specimens per the ASTM E8 Standard Test Methods for Tension Testing of Metallic Materials, using a strain rate of 10^{-3} s^{-1} ($5x10^{-3}$ mm/s extension rate). The specimens were shoulder loaded for testing using an Instron 3367 tensile machine equipped with a 5kN load cell and connected with an Instron Bluehill3 analysis software. This tensile machine is equipped with an Oxy-Gon tungsten mesh furnace capable of reaching 1200 °C. All the tests were performed at vacuum levels of ~$5x10^{-6}$ torr or better. The elongation was measured by machine stroke. Using machine stroke obviously introduces uncertainties in the elongation behavior in the elastic regime due to machine compliance, but it does not affect the plastic regime or the calculated strength values. Because the elongation is provided by machine stroke, the strain rate is the extension rate and not the cross-head speed as is taken in cases with an extensometer. One specimen each was tensile tested at both room temperature and irradiation temperature. Here, one must note that the intention is comparing the irradiated tensile properties with the unirradiated room temperature properties that were estimated in a fracture mechanics lab (i.e. outside the hot-cell facility using an MTS servo-hydraulic frame with a 22.2-kN load cell), but keeping same testing parameters (reported in Ref. [1]). For irradiation temperature tests, the temperature was measured using two thermocouples welded onto the fixture. The temperature ramp-up time from room temperature to 300 °C is typically between ~25-30 minutes. The tests were performed only when the temperature stabilized to the set-point of 300±5 °C. During the data analysis, efforts were devoted to remove the machine slack in the experimentally observed stress-strain curves.

Table 1. Summary of different Eurofer-97 steel variants. AQ: air quenched, WQ: water quenched, LT: low temperature application, HT: high temperature application.

M-Code	Material type	Heat	Condition	Provider
E	EUROFER97/2	993391	980°C/0.5h + AQ + 760°C + AC (second batch)	KIT
H	EUROFER-LT	J362A	1000°C/0.5h + WQ + 820°C + AC	KIT
I	EUROFER-LT	J363A	1000°C/0.5h + WQ + 820°C + AC	KIT
P	EUROFER-LT	J361A	1000°C/0.5h + WQ + 820°C + AC	KIT
L	EUROFER97/2	994578	1150°C/0.5h + AQ + 700°C + AC	CEA
J	EUROFER-LT	I196C	TMT:1250°C/1h and then rolling to a final rolling temperature of 850°C in 6 rolling steps with a reduction of 20-30% for each rolling pass, then AC. Q&T: 880°C/0.5h+WQ+750°C/2h+AC	SCK.CEN
K	EUROFER-HT	I427A	TMT:1250°C/1h and then rolling to a final rolling temperature of 850°C in 6 rolling steps with a reduction of 20-30% for each rolling pass, then AC. Q&T: 1050°C/15min + WQ + 675°C/1.5h + AC	SCK.CEN
M	EUROFER97/2	993391	1020°C/0.5h + AQ + 1020°C/0.5h + AQ +760°C/1.5h + AC (double austenitization)	ENEA
O	EUROFER-LT	VM2991	TMT: 1080°C/1h, cooling to 650°C and rolling, reduction 40% (from 30 mm to 18mm) Tempering: 760°C/1h + AC	ENEA
N	EUROFER-LT	VM2897	920°C/1.5h + AQ + 920°C/1.5h + AQ + 760°C/1h + AC (double austenitization)	ENEA

Table 2. Chemical compositions of different Eurofer-97 steel variants as provided by KIT. Values in wt.%.

Element	P	H	I	E, M	L	J	K	O	N
Cr	8.7	8.7	8.73	8.83	9.14	9	7.84	8.8	9.04
C	0.105	0.0583	0.11	0.107	0.106	0.107	0.017	0.06	0.092
Mn	0.021	0.0223	0.0189	0.527	0.54	0.39	<0.03	0.5	0.11
V	0.2	0.353	0.351	0.2	0.2	0.22	0.2212	0.3	<0.05
N	0.0445	0.0465	0.0422	0.019	0.038	0.022	0.022	0.07	0.0024
W	1.14	1.07	1.08	1.081	1.11	1.1	0.99	0.97	0.99
Ta	0.093	0.1	0.0918	0.117	0.12	0.11	0.1265	0.05	0.092
Si	0.032	0.0362	0.0363	0.0352	0.025	<0.04	<0.04	0.15	0.037
S	0.0015	0.0014	0.0011	0.0009	0.0037	0.0011	0.0011	0.003	0.001
B	<0.0005	<0.0005	<0.0005	<0.0005	0.0011	<0.0005	<0.0005	<0.001	<0.001
Ti	<0.0001	<0.0001	<0.0001	<0.0001	0.001	<0.0001	<0.0001	<0.01	<0.01
O	0.0036	0.0022	0.0052	0.0043	<0.001	0.007	0.0043	0.006	<0.004
Nb	<0.0004	<0.0004	<0.0004	<0.0004	0.004	<0.0004	<0.0004	<0.01	<0.01
Mo	0.0012	0.0009	0.0009	0.0009	0.002			<0.01	<0.01
Ni	0.0057	0.004	0.0036	0.0034	0.01			<0.02	<0.02
Cu	0.0075	0.0077	0.0072	0.007	0.003			<0.01	<0.01
Al	0.0016	0.0017	0.0014	0.0012	0.002			<0.01	<0.01
Co	0.0021	0.0017	0.0017	0.0017	0.003			<0.01	<0.01
As,Zr,Sn,Sb					<0.007			<0.005	<0.005
P					0.0015			<0.006	<0.005

A comparison of absolute values of YS/UTS and percentage elongation for tests performed on unirradiated and irradiated samples are plotted in Figure 1. In addition, the percentage change in the YS/UTS and the associated reduction of elongation values are plotted in Figure 2. It is evident from these figures that all the steels hardened after the irradiation reflected by an increase in the YS and UTS. This was accompanied with reduction in uniform elongation (UE) and total elongation (TE). The increase in YS varied between differing steels, ranging from as low as ~13% to values greater than 60 %. Highest increase in room temperature YS was shown by the P series steel, nearly 66%. The harder L series steel showed the least increase in YS, at ~13.4%. The reference E series steel showed ~65% increase in the room temperature YS. Most of the steels showed lower tensile ductility for tests conducted at 300 °C as compared to tests at RT in both unirradiated and irradiated conditions, which is to be expected from 9% Cr FM steels due to dynamic strain ageing (DSA) [2].

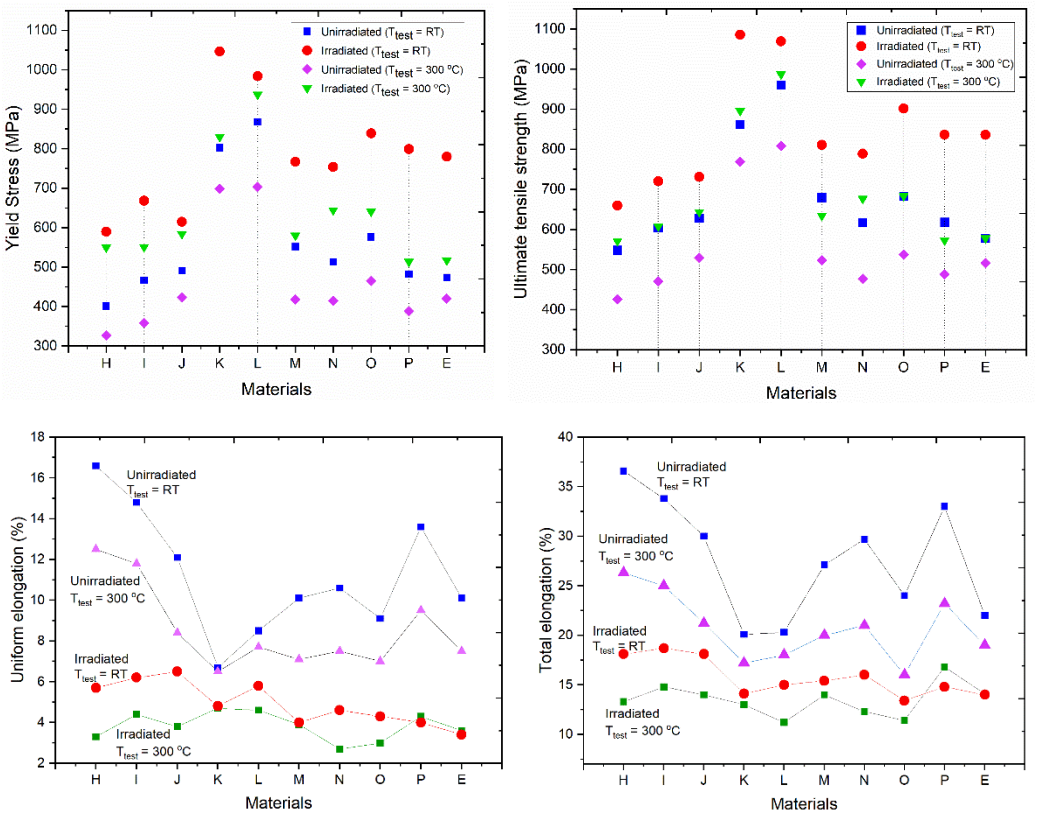

Figure 1. A comparison of the uniform and total elongations of the ten steels in unirradiated and irradiated conditions.

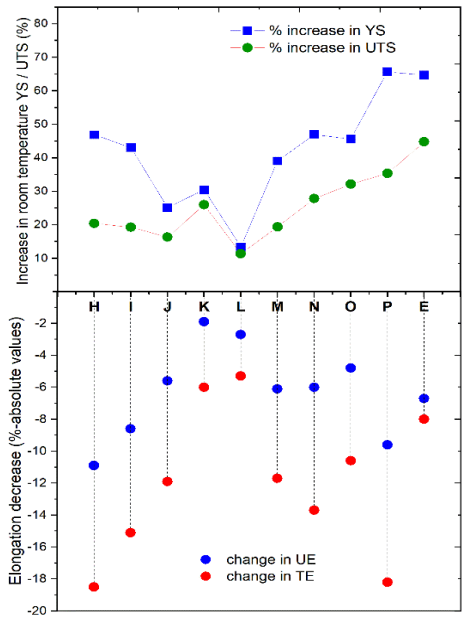

Figure 2. Percentage change in the strength values of the ten steels and the reduction of the elongation obtained after comparing unirradiated and irradiated results (in absolute values).

Reduction in area (RA), which represents the extent of necking, was calculated using SEM imaging on the fracture surface after the room temperature tensile tests. Figure 3 compares RA for the ten steels in unirradiated and irradiated conditions. In the unirradiated state, the steels showed RA in the range of >75-85%. After neutron irradiations, all the steels showed significant reduction in necking as evidenced by a decrease in RA. The percentage change in RA after the irradiation is plotted in Figure 4. From both these figures, it is evident that RA reduced significantly for the harder L series steel with more than 25% reduction from the unirradiated values. Least change in RA was measured for the reference E series steel. Except L series steel, the RA of the other variants after irradiation ranged between ~65-75%.

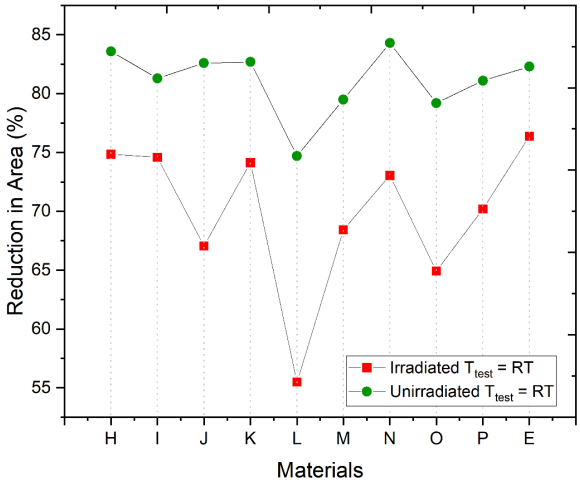

Figure 3. A comparison of RA for the ten steels in unirradiated and irradiated form, tensile tested at the room temperature.

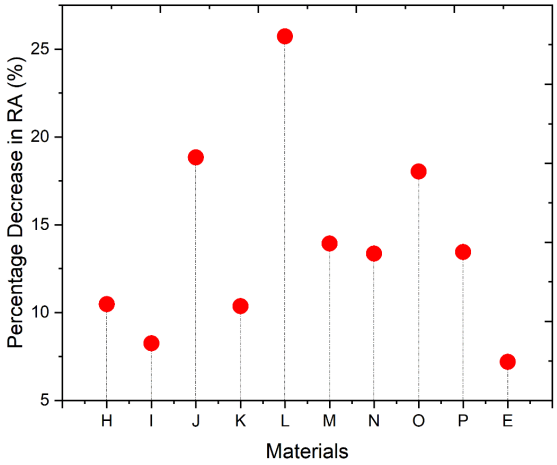

Figure 4. Percentage loss in RA from the unirradiated state when tensile tested at room temperature.

References

[1] Bhattacharya et al., Mechanical properties and microstructure characterization of unirradiated Eurofer-97 steel variants for the EUROfusion project, ORNL/SPR-2018/882, (2018).

[2] Vanaja et. al, Influence of strain rate and temperature on tensile properties and flow behavior of a reduced activation ferritic-martensitic steel, J. Nucl. Mater. 424 (2012) 116-122.

2. ODS AND NANOCOMPOSITED ALLOY DEVELOPMENT

2.1 EFFECT OF CARBON CONTENT ON CARBIDE-VERSION CASTABLE NANOSTRUCTURED ALLOYS—L. Tan, W. Zhong, Y. Yang (Oak Ridge National Laboratory)

OBJECTIVE

The preliminary systematic performance comparison showed the advantages of carbide-CNAs (Castable Nanostructured Alloys) over carbonitride-CNAs. To further improve carbide-CNAs, one direction is to refine the alloying composition. Carbon is a critical element in the alloy to stabilize the austenite phase over a larger temperature range and to determine the amount of carbides formed. This work focuses on understanding the effects of carbon content on carbide-CNAs.

SUMMARY

Because of the high coarsening rate of Cr-rich $M_{23}C_6$, minimizing the $M_{23}C_6$ amount while maintaining a high density of MC (M=Ti/Ta/W/etc.) is hypothesized to provide better mechanical properties to ferritic-martensitic steels, including CNAs. Two heats of CNAs, called CNA8 and CNA9, were designed and fabricated to test the hypothesis. CNA8 has a maximized MC amount with reduced $M_{23}C_6$ amount (half of Eurofer97/F82H). In contrast, CNA9, with a lower carbon content, has a comparable amount of MC but nearly two orders of magnitude lower content of $M_{23}C_6$ compared to CNA8. Tensile tests indicate that comparable strength of the two alloys but larger elongation of CNA8 at higher temperatures. Charpy impact testing results tend to have slightly higher or comparable upper-self energy (USE) with higher ductile-brittle transition temperature (DBTT) for the low-C CNA9 compared to CNA8. Microstructural characterization results explain the mechanical testing results.

PROGRESS AND STATUS

Introduction

Following the previously designed carbide-CNAs with a base composition of Fe-9Cr-1W, CNA8 was designed to have a maximum mole fraction of MC at the tempering temperature 750°C without forming this precipitate phase in δ-ferrite. Figure 1 shows the calculated temperature-dependent phase mole fractions with the solid lines denoting the phases in CNA8. Other than MC, the $M_{23}C_6$ amount is ~50% reduced in CNA8 compared with that in Eurofer97/F82H. With CNA8 as a reference, the carbon content is further reduced in CNA9, denoted with dashed lines for the phases in Figure 1. The reduced carbon intends to keep the MC amount in CNA9 (~0.45 mole%) comparable to that in CNA8 (~0.48 mole%), but significantly lower $M_{23}C_6$ amount in CNA9 (<0.1 mole%) than in CNA8 (~1.05 mole%). The reduced carbon also decreased the austenite temperature range in CNA9.

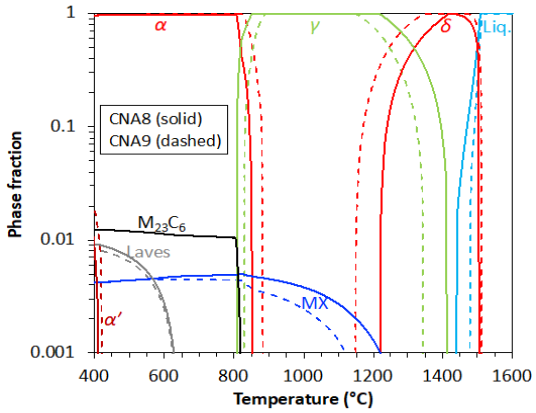

Figure 1. Calculated temperature-dependent phase mole fraction in alloys CNA8 and CNA9.

Experimental Procedure

Laboratory heats of CNA8 and CNA9 were arc melted into large buttons and then drop cast into 25.4 × 25.4 × 152 mm. The CNA8 heat was annealed at 1150°C for 1 h and hot-rolled into a 6.3-mm thick plate. The plate was finally normalized at 1150°C for 15 min with water quenching and tempered at 750°C for 30 min with air cooling. The processing and heat treatment of the CNA9 heat was about the same as the CNA8 heat, except for the use of 1100°C in CNA9 for the high temperature heat treatment. Tensile (type SS-3 specimens) and Charpy V-notch impact (half-size specimens in the T-L orientation) tests were conducted for the two alloys. Electron backscatter diffraction (EBSD) and transmission electron microscopy (TEM) were used to characterize the grain structures and precipitates, respectively.

Results

Figure 2a shows the temperature-dependent yield strength (YS), ultimate tensile strength (UTS), uniform plastic elongation (UPE), and total plastic elongation (TPE) of alloys CNA8 and CNA9. The tensile tests indicate generally comparable strength of the two alloys but larger UPE and TPE of CNA8 at higher temperatures. Figure 2b shows the temperature-dependent absorbed impact energies of CNA8 and CNA9. CNA8 has a DBTT ~40°C lower than CNA9 while CNA8 has a USE ~5 J lower than CNA9.

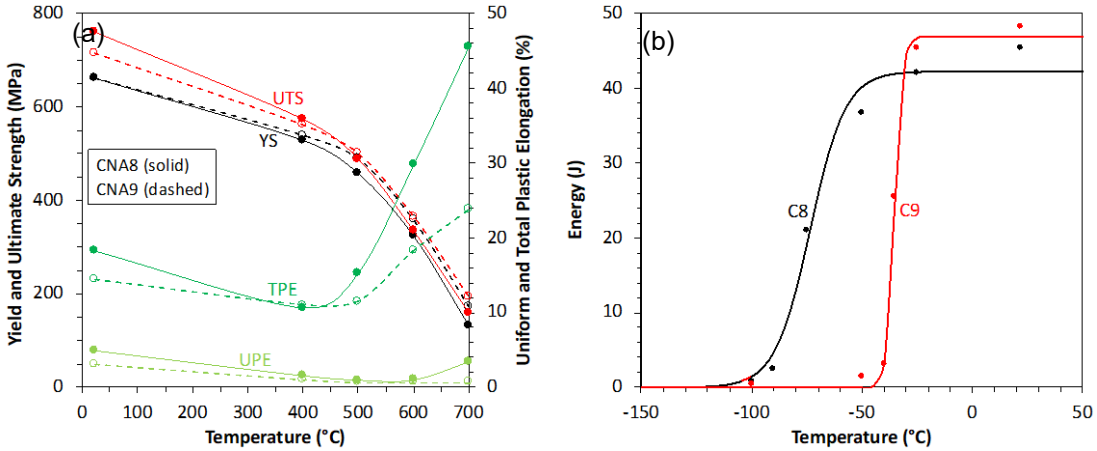

Figure 2. Temperature-dependent (a) yield and ultimate strength and uniform and total plastic elongation and (b) Charpy impact absorbed energies of CNA8 (C8) and CNA9 (C9).

The TEM characterization indicated that CNA8 contains both MC and $M_{23}C_6$ while CNA9 only has MC, which is consistent with the alloy design. EBSD inverse pole figure (IPF) of CNA8 and CNA9, as shown in Figure 3, exhibits fine grain structures of CNA8 but coarse grain structures of CNA9. It directly supports the Charpy impact testing results that finer grain structures favor lower DBTT. Consistent with the previous analytical result, the lower carbon content of CNA9 favored its higher USE.

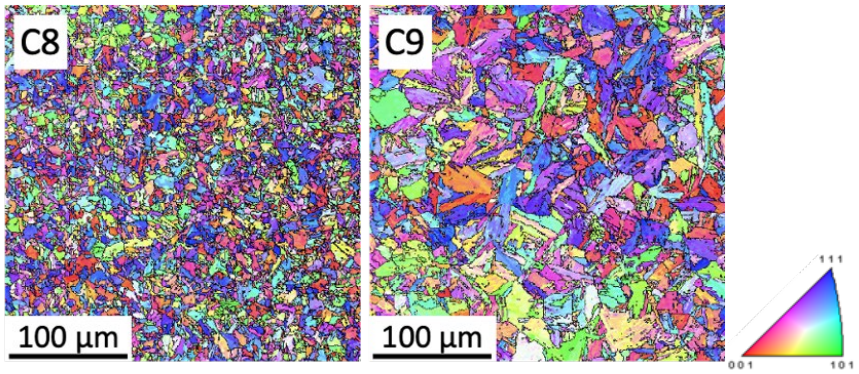

Figure 3. EBSD IPF of alloys C8 and C9.

2.2 STEM STUDY OF HELIUM-IMPLANTED NANOSTRUCTURED FERRITIC ALLOYS—Yan-Ru Lin, Steven John Zinkle (University of Tennessee), David T. Hoelzer, Lizhen Tan (Oak Ridge National Laboratory)

OBJECTIVE

The objective of this task is to study the He trapping ability (binding energy) of two types of nanoparticles (Y-Ti-O and MX type precipitates) in advanced nanostructured ferritic alloys. High-resolution scanning transmission electron microscopy (HR-STEM) imaging techniques were performed to identify the nanoparticle structure and the attached bubbles.

SUMMARY

He bubbles in nanostructured ferritic alloys (CNA3 and 14YWT) after He implantation (to ~8000 appm at 700 °C) were examined by scanning transmission electron microscopy. The Y-Ti-O nanoparticles in 14YWT exhibited a one-to-one relationship for bubble attachment to the Y-Ti-O, while a coarse TiN particle attached ~5 bubbles. Bubbles were also attached to V-C nanoparticles in CNA3 and were observed at the grain boundary. In our HR-STEM images, no significant difference in the atomic structure of the bubble and nanocluster projected regime was observed. This may due to the overlap of matrix atoms above and below the nanocluster that may impact the contrast in the STEM images.

PROGRESS AND STATUS

Nano-scale dispersoids, that are stable under prolonged high temperature neutron service, can sequester large amounts of helium into small bubbles based on the concept of high sink strength. CNA3 and 14YWT are two promising nanostructured alloys with high density of nano-scale dispersoids. In Figure 1, a series of high-resolution high-angle annular dark-field (HAADF) images of helium-implanted (to ~8000 appm at 700 °C) CNA3 and 14YWT were taken at the junction of the bubble (B) and nanoparticle (P), or bubble and grain boundary (Figure 1d). The images were viewed along low index zone axes (<001>, <011>, and <111>) of the Fe-Cr matrix. HAADF scattering signal from a single column of atoms is strongly dependent on the atomic number and the number of atoms in a single atom column [1, 2]. Hence, the bubbles are shown as black contrast in HAADF images due to the absence of atoms. However, for the fine Y-Ti-O and VC clusters with diameter < 5 nm (Figures 1a and 1b), the atomic structure under TEM as well as their fast Fourier transform (FFT) images taken at the B and P regions remains the same as the matrix ferritic structure. The cavities and nanoparticles with a diameter of less than ~10 nm are embedded in the matrix structure. Considering a sample thickness of ~80 nm, seven-eighth of the atoms in an atomic column would be associated with the Fe or Cr matrix atoms lying above or below the nanocluster. Therefore, an overlap of atoms may occur and impact the contrast in the STEM images. For the coarse TiN particles with diameter > 10 nm (Figure 1c), a possible NaCl atomic structure was observed, which agrees with a previous report that indicated Ti(N,C,O) precipitates in 14YWT may have a NaCl structure [3]. However, the distinct structure was observed in the bubble (B) region, but not the particle (P) region. Speculation is made that the overlap of particles and cavities, which subtracts the number of matrix atoms, could aid the imaging of the atomic structure of particles. In addition, Figure 1d shows a few bubbles attached to a grain boundary. The atomic structure on the left (L) and right (R) regions are obviously different. In order to minimize the matrix atom distribution, a thinner TEM sample or conducting heat treatment to coarsen the bubbles or nanoparticles (as reported by Stan et al. [4]) may be beneficial to improve the visualization of the atomic structure of the nanoparticles.

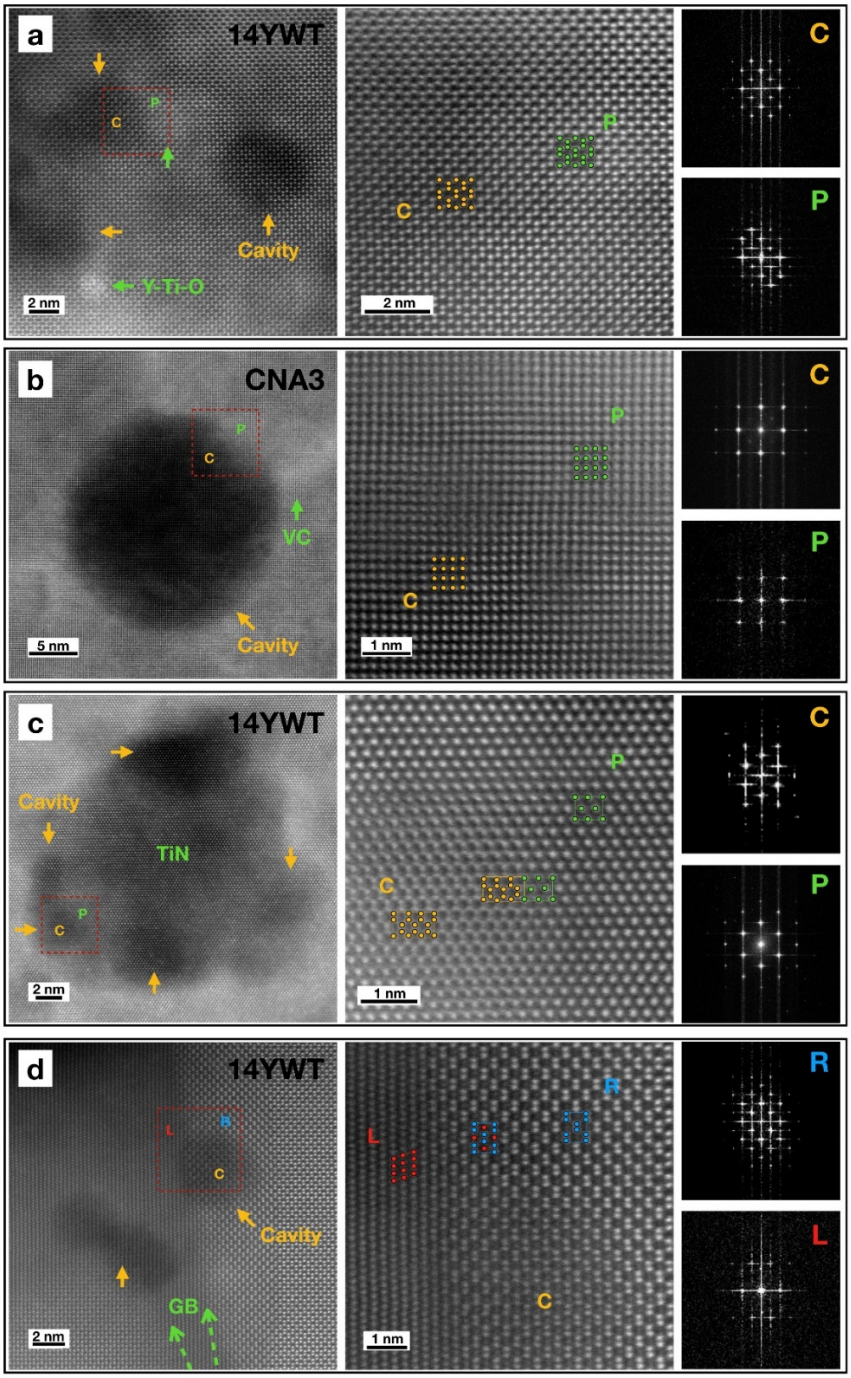

Figure 1. High resolution STEM-HAADF images of nanoparticles or grain boundary attached with helium bubble. (a) Y-Ti-O, viewed along the <001> Fe-Cr matrix zone axis; (b) V-C, viewed along the <011> Fe-Cr matrix zone axis; (c) Ti-N, viewed along the <111> Fe-Cr zone axis; and (d) grain boundary, viewed along the <133>(L)/<001>(R) Fe-Cr matrix zone axis. The corresponding FFT patterns of the labeled area are on the right of each figures. (B: He bubble, P: nanoparticle, L: left-grain, R: right-grain).

FUTURE PLANS

Detailed study on the correlation between nanoparticle density and cavity density (and spatial correlation) will be completed to understand the He management phenomena in nanostructured alloys. Small Angle Neutron Scattering (SANS) technique is a candidate option to obtain the overall particle density, interprecipitate distance and, average particle size.

References

[1] Y.-R. Lin, L.-G. Chen, C.-Y. Hsieh, A. Hu, S.-C. Lo, F.-R. Chen, J.-J. Kai, Atomic structure of nano voids in irradiated 3C-SiC, Journal of Nuclear Materials 498 (2018) 71-75.
[2] S. Van Aert, K.J. Batenburg, M.D. Rossell, R. Erni, G. Van Tendeloo, Three-dimensional atomic imaging of crystalline nanoparticles, Nature 470(7334) (2011) 374-377.
[3] P.D. Edmondson, C.M. Parish, Q. Li, M.K. Miller, Thermal stability of nanoscale helium bubbles in a 14YWT nanostructured ferritic alloy, Journal of Nuclear Materials 445(1) (2014) 84-90.
[4] T. Stan, Y. Wu, J. Ciston, T. Yamamoto, G.R. Odette, Characterization of polyhedral nano-oxides and helium bubbles in an annealed nanostructured ferritic alloy, Acta Materialia 183 (2020) 484-492.

2.3 X-RAY DIFFRACTION STUDY OF NANOSTRUCTURED FERRITIC ALLOYS AND REDUCED ACTIVATION FERRITIC MARTENSITIC STEELS—D.J. Sprouster, L.L. Snead (Stony Brook University), A. Bhattacharya, Y. Katoh (Oak Ridge National Laboratory), S. Levine, S. Zinkle (University of Tennessee)

OBJECTIVE

In this report, we show the utility of high-energy x-ray diffraction to identify and capture minor phases in advanced nanostructured ferritic alloys and reduced activation ferritic martensitic alloys. XRD is appreciably sensitive to the different nm-scale precipitates, and quantitative atomic structure can be extracted for both the BCC host and minor precipitate populations. These results highlight that synchrotron-based XRD could be utilized to examine irradiated alloys, to track and quantify changes in the nm-scale populations introduced to give the host improved mechanical and radiation resistance.

SUMMARY

Strategies to improve the radiation performance of structural materials for fusion energy applications have led to the realization of engineered microstructures [1]. Current strategies for designing alloys for fusion energy applications include intentionally engineering high non-cavity sink strengths via incorporating precipitates within the BCC host matrix. Two classes of such materials include (i) Nanostructured Ferritic Alloys (NFA) [2], and (ii) Reduced Activation Ferritic Martensitic (RAFM) alloys [3]. Both NFA and RAFM microstructures are heterogeneous with several nanometer-sized precipitate phases purposely introduced through the fabrication process. Quantification of the different nm-scale precipitates and BCC host matrix with processing is needed to optimize material builds and develop microstructural insights that can be compared to thermodynamic modelling. In NFA alloys the nm-scale precipitates are typically TiO, Y-Ti-O, or Y-Al-O. In RAFM alloys, the nanoprecipitates are commonly $M_{23}C_6$ and MX nitrides/carbonitrides. In this work, we employ high energy x-ray diffraction to both identify and quantify the minor phases in a series of NFA and RAFM steels. Rietveld and modified Rietveld methods were employed to quantify the different atomic and microstructural properties of the BCC host and nm-scale precipitates.

PROGRESS AND STATUS

Experimental Procedure

The XRD measurements were performed at the National Synchrotron Light Source-II (NSLS-II) using the high-energy X-rays available at the X-ray Powder Diffraction beamline (XPD) [4]. All measurements were performed in transmission mode with an amorphous Silicon-based flat panel detector (Perken-Elmer) mounted orthogonal to and centered on the beam path. The sample-to-detector distances and tilts of the detector relative to the beam were refined using a LaB_6 powder standard (NIST standard reference material 660c). The wavelength of the incident X-rays was 0.1917 Å (66.676 keV). The sample-to-detector distance was calculated to be 1387.81 mm. 300 individual patterns with detector exposures of 0.2s were collected for each specimen. All raw two-dimensional patterns were background corrected by subtracting the dark current image and the air scattering and Kapton background within IgorPro (Wavemetrics). Noticeable artefact regions of the detector (like the beam stop, dead pixels) were masked. The corrected and masked two-dimensional detector images were then radially integrated to obtain one-dimensional powder diffraction patterns. The list of specimens measured is given in Table 1.

Phase identification was performed using Match3! (Crystal Impact, Bonn, Germany). The background subtracted XRD patterns were Rietveld or modified Rietveld refined (to include texture) with the MAUD software package. The peak profiles were modeled by a modified pseudo-Voigt function. The instrument contribution to the broadening of the measured profiles was quantified by fitting the LaB_6 NIST powder standard measured in a capillary, with a known coherent grain size and negligible micro strain contribution. The Gaussian and Lorentzian-based broadening parameters were subsequently fixed during the analysis

of the alloys under investigation to quantify the microstructure (coherent grain size and micro strain components). The phase fraction, lattice parameter, micro strain (MS) and coherent grain size (CGS) components were allowed to vary for the different crystal phases present. The micro strain components for the TiO and Y-Ti-O, Al-Y-O, MX and $M_{23}C_6$ phases were not included in the refinements. Therefore, the refined coherent grain size parameters of are lower limits. The phase fractions from the modified-Rietveld refinements are also approximate, as they allow peak intensities of the BCC Fe host to arbitrarily refine (similar to Le-Bail refinements).

Results

The XRD patterns for the 14YWT, 12YWT, MA957 and PM2000 specimens are shown in Figure 1 (a). The minor phases identified for the 12YWT, 14YWT and MA957 specimens are shown in Figure 1 (b). The phases with distinct reflections include BCC Fe host (strongest peaks) and TiO phase (structure $Fm\bar{3}m$). An additional diffuse component, presumably from the Y-Ti-O nanoparticles is also observable in the background corrected MA957, 12YWT and 14YWT specimens. Small peaks are observable in the MA957 and 14YWT specimens, consistent with the larger $Y_2Ti_2O_7$ (structure $Fd\bar{3}m$) particles. Additional peaks are observable and may potentially be attributable to carbides or small oxides. The PM2000 specimens show strong single-crystal diffraction spots in the 2D detector images as shown in Figure 2 (a), due to the large BCC Fe matrix grains. Additional powder rings in the 2D patterns were also observed in both PM2000_1 and PM2000_2. Figure 2 (a) shows a representative two-dimensional XRD pattern for a PM2000 specimen, and Figure 2 (b) shows the modified Rietveld refinement. The rings and peaks in the XRD patterns were indexed as YAP (Pnma, $YAlO_3$) and could be refined using a modified Rietveld refinement. The structure and size of the YAP precipitates from the XRD analysis are given in Table 2. In addition to the BCC host and YAP phase, a broad diffuse background, potentially from an XRD-amorphous and/or amorphous component is observable in the XRD patterns for PM2000 (confirmation from TEM is being explored). Further identification, with known chemistries or precipitate phases from microscopy could be performed as a next step. The refined matrix and TiO phase from Rietveld refinements are given in Table 2.

Table 1. Measured NFA specimens and phases identified from the XRD analysis

Specimen	Comments
12YWT	BCC Fe, TiO, nano$Y_2Ti_2O_7$
12YWT_2	BCC Fe, TiO, nano $Y_2Ti_2O_7$
14YWT	BCC Fe, TiO, nano $Y_2Ti_2O_7$, Carbide/oxide
MA957	BCC Fe, TiO, $Y_2Ti_2O_7$
PM2000_1	BCC Fe, YAP, **amorphous/disordered phase**
PM2000_2	BCC Fe, YAP, **amorphous/disordered phase**

Table 2. Quantitative XRD analysis for NFA specimens

Specimen	Phase	a	±	CGS	±	MS	±	wt%	±
12YWT	BCC Fe	2.85571	0.00006	253.7	5.2	0.82	0.01	99.1	0.4
	TiO	4.21198	0.00355	44.8	25.0			0.9	0.2
12YWT_2	BCC Fe	2.85698	0.00007	240.8	2.8	1.02	0.01	98.3	0.4
	TiO	4.24900	0.00964	44.8	25.0			1.7	0.9
14YWT	BCC Fe	2.87179	0.00028	178.5	14.2	1.20	0.06		
MA957	BCC Fe	2.85505	0.00004	425.4	11.2	0.57	0.01	95.8	0.4
	TiO	4.20589	0.00377	34.5	1.7			3.5	1.0
	$Y_2Ti_2O_7$	10.14080	0.10400	3.5				0.6	0.3
PM2000_1	BCC Fe	2.86519	0.00011	>900nm		3.25	0.02		
a	YAP	5.27074	0.00216	45.3	3.0				
b		7.30893	0.0029						
c		5.14321	0.0021						
PM2000_2	BCC Fe	2.86253	0.00006	>900nm		3.27	0.02		
a	YAP	5.26888	0.00373	49.5	7.5				
b		7.31892	0.00492						
c		5.14055	0.00367						

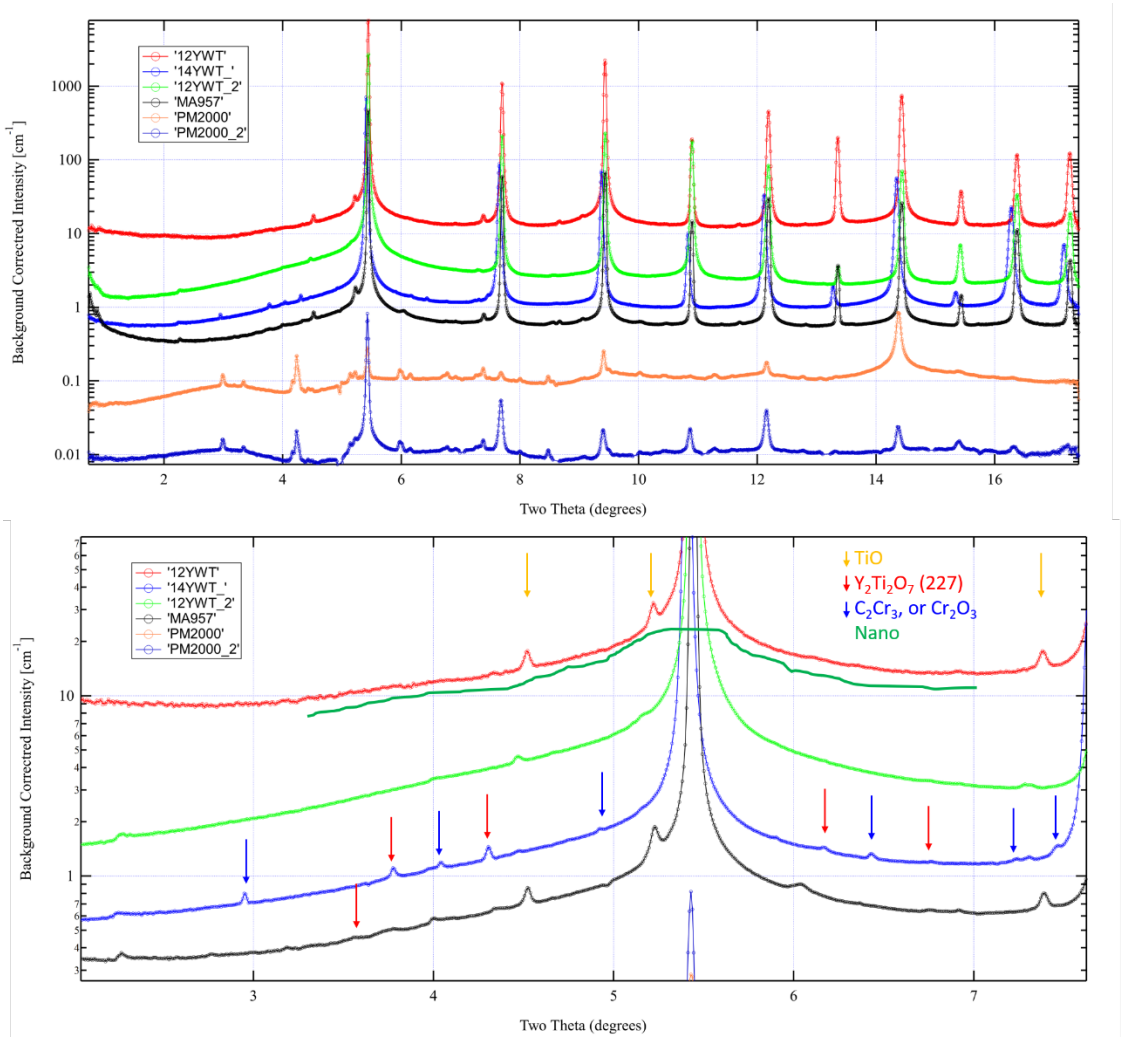

Figure 1. (a) XRD patterns for NFA alloys. (b) minor Y-Ti-O phases identified for the 12YWT, 14YWT and MA957 specimens.

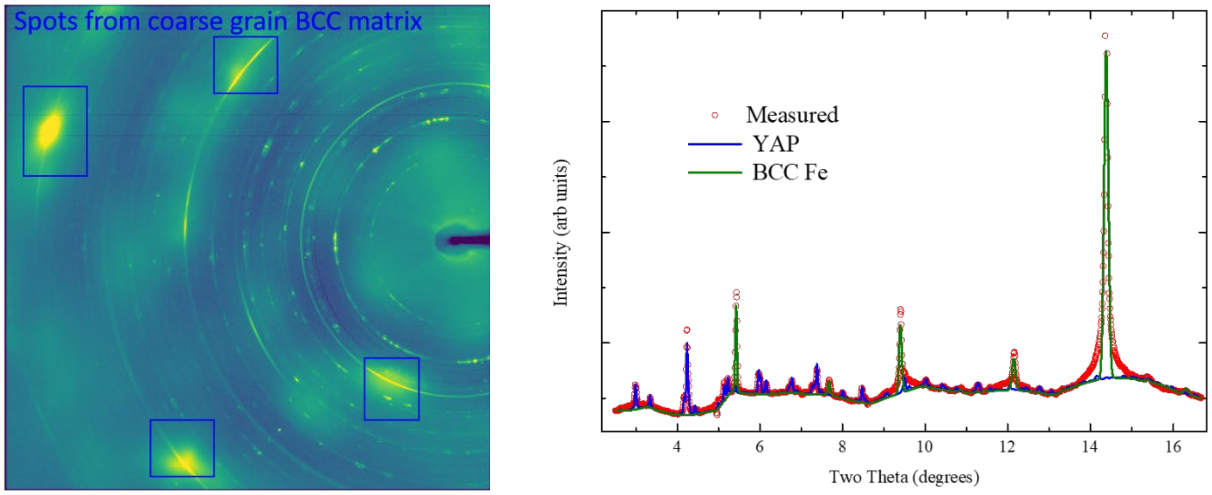

Figure 2. (a) Two dimensional XRD pattern for PM2000 showing coarse BCC matrix grains that result in intense spots on image. Minor phases are powder-like and display Debye-ring patterns. (b) Modified Rietveld refinement of PM2000. The Fe and YAP phases were included in refinement.

Results for RAFM alloys

The XRD patterns for the RAFM specimens are shown in Figure 3 (a). Figure 3 (b) shows a zoomed view of the low two-theta region to highlight the minor phases. The phases identified in the RAFM samples include MX (MN and MC), $M_{23}C_6$ and FCC Fe. All specimens contained $M_{23}C_6$ carbides. The different phases identified for the series are listed in Table 3. The MX (MC or MN) phases appear to be different in the different specimens (presumably due to different alloy contents). The MC and MN phases have peak locations and heights similar to the TaC and VN phases, respectively. The first pass at the quantitative analysis for the different specimens is given in Table 3. The analysis resulted in residual weights (RWPs) less than 10 %. This analysis could be improved to include some of the minor MN/MC phases to further reduce the RWPs. The microstructure including lattice parameters, coherent grain size and micro strain appear to be sample dependent. The micro strain parameter is directly attributable to two-dimensional defects (such as dislocations), and the coherent grain size is the amount of defect free material (and is thus usually smaller than the grain size from SEM). The lattice parameters appear to show variations among the different specimens and is potentially related to the processing/alloy chemistry and residual strain.

Table 3. Samples and phases identified from the XRD analysis for the RAFM materials studied here

F82H	BCC Fe, MC, $M_{23}C_6$
I427A	BCC Fe, minor MN/MX (VC or VN), $M_{23}C_6$
M119	BCC Fe, MC (TaC-like), $M_{23}C_6$
P109	BCC Fe, MN/MX (VC or VN), $M_{23}C_6$
I107	BCC Fe, MN/MX (VC or VN), $M_{23}C_6$
N115	BCC Fe, MC (TaC-like), $M_{23}C_6$
O115	BCC Fe, MN/MX (VC or VN) $M_{23}C_6$
L110	BCC Fe, FCC Fe, MC (TaC-like), $M_{23}C_6$
H108	BCC Fe, MN/MX (VC or VN), $M_{23}C_6$
J106	BCC Fe, FCC Fe, (minor) MC (TaC or VN-like), $M_{23}C_6$

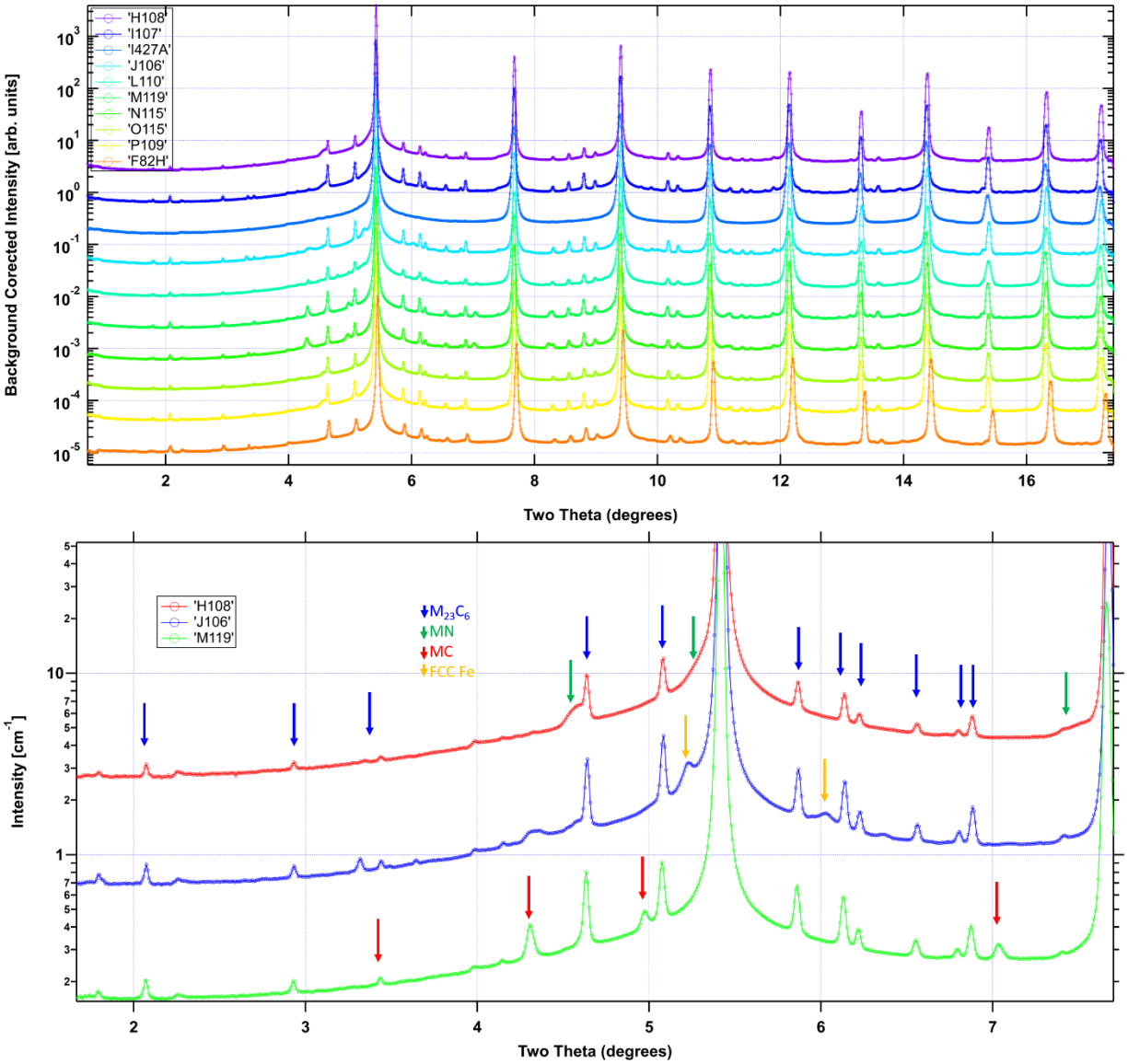

Figure 3. (a) XRD patterns for all RAFM steels. (b) highlighted region around the BCC (110) peak with phases identified for three specimens that show different combinations of FCC Fe, MN and MC phases.

Table 4. Rietveld refinement for the RAFM specimens. Some phases were not refined due to their very small fraction. CGS = Coherent grain size, MS = micro strain.

Specimen	Phase	a	±	CGS	±	MS	±	Wt	±
		Å		nm		10^{-3}		(%)	
M119	BCC Fe	2.86827	0.00001	481	14	0.41	0.02	98.60	0.20
	$M_{23}C_6$	10.60385	0.00126	120	21			1.30	0.10
	MX	4.41643	0.00293	37	7			0.10	0.01
N115	BCC Fe	2.86638	0.00001	486	6	0.34	0.01	98.70	0.20
	$M_{23}C_6$	10.59548	0.00164	122	1			1.10	0.10
	MX	4.42706	0.00273	38	0			0.09	0.02
L110	BCC Fe	2.86594	0.00002	247	1	1.33	0.01	95.20	0.20
	$M_{23}C_6$	10.60058	0.00241	153	0			4.70	0.40
	MX	4.40399	0.06549	41	23			0.10	0.10
J106	BCC Fe	2.86456	0.00001	532	8	0.33	0.01	97.10	0.40
	$M_{23}C_6$	10.59003	0.00105	163	4			1.30	0.10
	MX	4.19239	0.01900	4	3			1.00	0.40
	FCC Fe	3.64398	0.00289	0	0			0.60	0.10
I427A	BCC Fe	2.86880	0.00002	417	18	1.30	0.01	100.00	-
I107	BCC Fe	2.86690	0.00001	503	10	0.08	0.09	98.20	0.30
	$M_{23}C_6$	10.59683	0.00141	169	13			1.20	0.10
	MX	4.20078	0.01856	8	1			0.60	0.20
H108	BCC Fe	2.86517	0.00002	574	31	0.25	0.04	98.90	0.40
	$M_{23}C_6$	10.59286	0.00338	134	20			0.60	0.10
	MX	4.15636	0.01061	19	0			0.50	0.10
O115	BCC Fe	2.86608	0.00001	541	10	0.55	0.01	99.20	0.20
	$M_{23}C_6$	10.59243	0.00165	110	0			0.80	0.10
P109	BCC Fe	2.86733	0.00002	623	17	0.30	0.01	98.40	0.30
	$M_{23}C_6$	10.60094	0.00200	118	38			1.20	0.10
	MX	4.17817	0.01355	17	6			0.40	0.10
F82H	BCC Fe	2.85286	0.00001	757	25	0.75	0.01	98.90	0.20
	$M_{23}C_6$	10.55400	0.00110	84	0			1.10	0.10
	MX	-	-	-	-			0.10	0.10

CONCLUSIONS

The high energy XRD measurements were sensitive to the different minor nm-scale precipitates present in the base NFA and RAFM alloys. The phase identification and quantification were complete for all specimens, forming an initial database for understanding the effects of neutron irradiation on the stability and phase evolution (a potential upcoming characterization campaign). The Rietveld and XRD modified analysis yields quantitative atomic information for both the BCC host and precipitate phases. Next steps include benchmarking the phase identification with those predicted from TEM or Thermo-Calc simulations.

ACKNOWLEDGEMENTS

These experiments and analysis were supported by the DOE Office of Fusion Energy Sciences under contract DE-SC0018322 with the Research Foundation for the State University of New York at Stony Brook. This research used The X-ray Powder Diffraction beamline of the National Synchrotron Light Source II, a U.S. Department of Energy (DOE) Office of Science User Facility operated for the DOE Office of Science by Brookhaven National Laboratory under Contract No. DE-SC0012704.

REFERENCES

[1] S.J. Zinkle, L.L. Snead, Designing Radiation Resistance in Materials for Fusion Energy, Annu Rev Mater Res 44 (2014) 241-267.

[2] G.R. Odette, M.J. Alinger, B.D. Wirth, Recent developments in irradiation-resistant steels, Annual Review of Materials Research 38 (2008) 471-503.

[3] L. Tan, L.L. Snead, Y. Katoh, Development of new generation reduced activation ferritic-martensitic steels for advanced fusion reactors, J Nucl Mater 478 (2016) 42-49.

[4] D.J. Sprouster, R. Weidner, S.K. Ghose, E. Dooryhee, T.J. Novakowski, T. Stan, P. Wells, N. Almirall, G.R. Odette, L.E. Ecker, Infrastructure development for radioactive materials at the NSLS-II, Nucl Instrum Meth A 880 (2018) 40-45.

2.4 DEVELOPMENT OF ODS Fe-10Cr ALLOYS—D.T. Hoelzer, C.P. Massey (Oak Ridge National Laboratory)

OBJECTIVE

Two oxide dispersion strengthened (ODS) Fe-10Cr alloys were developed for fusion reactor applications requiring high-temperature strength and toughness properties and microstructural stability during exposure to energetic neutrons and transmutated He concentrations. The effect of W on the microstructure and mechanical properties was investigated by adding 1%W to one ODS Fe-10Cr alloy and no addition of W to the other ODS Fe-10Cr alloy. The objective of this study is to select one of the ODS Fe-10Cr alloys for further development based on the microstructure and mechanical properties.

SUMMARY

Two ODS Fe-10Cr alloys, one with 1%W (wt. %) and the other with no W, were developed to investigate if 1%W had any benefit on the microstructure and mechanical properties. In this study, scanning electron microscopy (SEM) and transmission electron microscopy (TEM) combined with energy filtered transmission electron microscopy (EFTEM) revealed both alloys contained ultra-small grains and oxide particle dispersions consisting of high number densities (4.5 - 5.0 × 10^{23} m^{-3}) and nano-sizes (2.2 - 2.3 nm). Although these results were not conclusive on the beneficial effect of 1%W, the tensile and creep properties determined that further alloy development will only occur with the 1%W containing ODS Fe-10Cr alloy.

PROGRESS AND STATUS

Introduction

The next generation advanced ODS Fe-Cr ferritic alloy being developed for the Fusion Materials Program contains 10%Cr with addition of reduced activation solutes of W, Ti and V. Compared to the advanced oxide dispersion strengthened (ODS) 14YWT ferritic alloy that was developed in the early 2000s, which contained 14%Cr and had a fully ferritic (α-bcc) matrix that was stable to the melting point of ~1510ºC, the lower 10%Cr level will allow the use of thermal mechanical treatments (TMT) for partial transformation of the bcc-ferritic (α) matrix to a low fraction of dispersed fcc-austenite (γ) grains at elevated temperatures. This concept is similar to that used in development of ODS 9%Cr alloys, except that the C level in ODS 9%Cr alloys is typically high in order to promote formation of martensite from the austenite grains during cooling. The goal for developing the Fe-10Cr alloy is to maintain low C and N levels for hindering the transformation of the austenite grains to martensite during cooling. Instead, the TMT studies conducted in the future will explore the effects of time, temperature and deformation on the size and distribution of the austenite grains and cooling rates that will promote the retention of the austenite grains at room temperature. If successful, studies will then be conducted to determine the effect of retained austenite grains on the mechanical properties of the advanced ODS Fe-10Cr alloy.

Experimental Procedure

Alloy Production

Two powders were produced by Ar gas atomization by ATI Powder Metals with nominal compositions of Fe-10Cr-1W-0.3Ti-0.2V and Fe-10Cr-0.3Ti-0.2V (all values in weight percent). The only difference between the two compositions was that 1%W was added to Fe-10Cr-1W-0.3Ti-0.2V and no W was added to Fe-10Cr-0.3Ti-0.2V. The atomized powders were mixed with 0.3%Y_2O_3 and ball milled in the high kinetic energy CM08 Simoloyer (Zoz GmbH, Germany) for 40 h in an Ar gas atmosphere. Mild steel cans were filled with ~1.3 kg of ball milled Fe-10Cr-1W-0.3Ti-0.2V-0.3Y_2O_3 (M4) powder and 1 kg of the Fe-10Cr-0.3Ti-0.2V-0.3Y_2O_3 (M5) powder followed by degassing in vacuum at 300ºC for 24 hours and sealing. The

sealed cans were heated to 850ºC for 1 h followed by extrusion through a rectangular shaped die (2.5-inch-wide and 1.25-inch-high) into bars.

Chemical analysis was performed on the extruded samples of M4 and M5 by DIRATS and the results are shown in Table 1. The quantitative analysis consisted of inductively couples optical emission spectroscopy (ICP-OES) for Fe, Cr, Ti, W, V and Y, combustive analysis for C and inert gas fusion for N. The results confirmed that the W level in M4 was much higher than that in M5 and while the Cr, Ti, V and Y levels were similar between M4 and M5. The ball milling conditions that were used resulted in relatively low C and N levels. Unfortunately, the chemical analysis conducted by DIRATS did not determine the O levels in M4 and M5.

Table 1. Composition of M4 and M5 determined by chemical analysis

Alloy	Fe	Cr	W	Ti	V	Y	C	N
M4	Bal.	9.70	0.97	0.15	0.18	0.23	0.031	0.018
M5	Bal.	9.57	0.08	0.18	0.17	0.22	0.027	0.018

Microstructure Characterization

The microstructure characterization of M4 and M5 was conducted using scanning electron microscopy (SEM), transmission electron microscopy (TEM), and energy filtered transmission electron microscopy (EFTEM). Metallographic samples for SEM analysis were prepared from the longitudinal transverse (L-T) plane, where L was parallel and T was normal to the extrusion direction. The samples were ground to a smooth surface followed by a final polishing step using colloidal silica. The polished specimens were examined in the Hitachi S-4800 FEG (Field Emission Gun) SEM equipped with a YAG backscattered electron detector. For detailed analysis of the nano-size oxide dispersions, a specimen was lifted out from the polished region of the metallographic samples and thinned by Focused Ion Beam (FIB) milling using the Hitachi NB5000 FIB-SEM. The FIB specimens of M4 and M5 were examined using the JEOL JEM 2100F Scanning/TEM instrument equipped with a Gatan Image Filter (GIF) for EFTEM analysis. This instrument in operated in the Low Activation Materials Development and Analysis (LAMDA) Laboratory.

Mechanical Properties Characterization

The mechanical properties of M4 and M5 involved tensile and creep tests. Both tests were conducted using flat sheet SS-3 specimens with gage dimension of 7.6 mm length × 5 mm width × 0.75 mm thickness. The tensile tests were conducted in air using an Instron screw driven tensile machine over temperatures ranging from 22ºC to 800ºC with a strain rate of 1×10^{-3} s^{-1}. The creep properties were assessed using the strain rate jump tensile (SRJ) method on an Instron 5900R screw driven tensile machine with convection heating. In the SRJ tests, the start of the test is at the lowest attainable strain rate of the tensile machine and the corresponding stress is measured. The stress increases with strain until it saturates and does not change with increasing strain. The strain rate is increased by one order of magnitude and the stress changes in response until it saturates and this procedure is then repeated until the final strain rate is reached that leads to specimen failure. The SRJ tests were conducted in air at 550ºC, 600ºC, 700ºC and 800ºC.

Results

Alloy Production

Figure 1 shows the extruded bars of M4 and M5. The ODS section of the extruded bars was located by cutting off the nose and tail sections. Each extruded bar was ~7 inches long with rectangular dimensions of 2.5 inches wide and 1.25 inches thick. The enclosed ODS section was ~2 inches wide and 1 inch thick. Figure 1 also shows the designated orientations for the extruded bars, where L-T is normal to the extrusion (L) and transverse (T) directions, T-S is normal to the transverse and thickness (S) directions and L-S is normal to the extrusion and thickness directions.

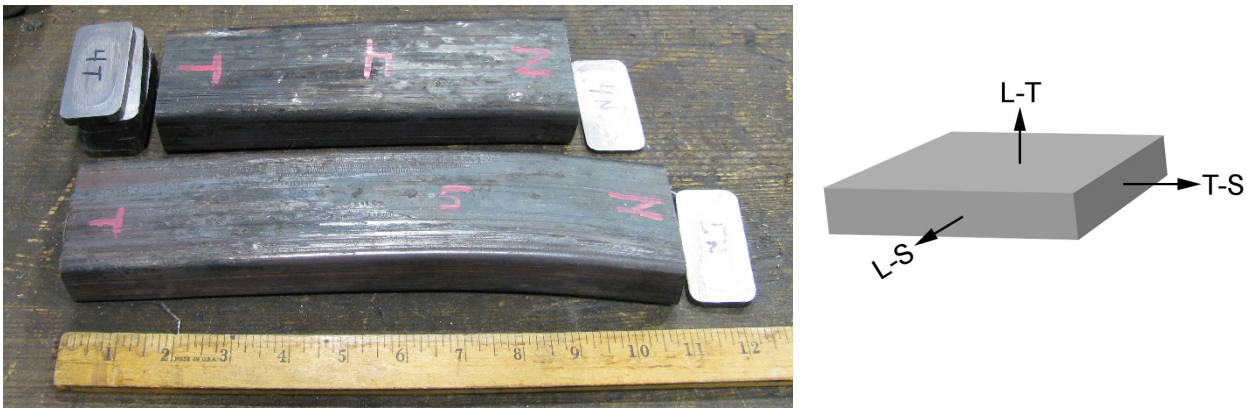

Figure 1. Digital images showing the extruded bars of M4 containing 1%W and M5 that is W-free.

Microstructure Characterization

Figures 2 and 3 show SEM backscattered electron (BSE) micrographs of the extruded M4 and M5. The microstructures of M4 and M5 observed in the L-T orientation are shown in Figure 2. The grains in the L-T orientation reveal the anisotropy caused by extrusion. The results indicated that M4 showed a greater amount of grain size inhomogeneity than M5. Figure 3 shows the microstructure of M4 and M5 in the T-S orientation. The grains in the T-S orientation appear isotropic in shape and the grain size is similar for M4 and M5. The higher magnification of the microstructures shown in Figure 3 revealed very few particles indicating that the size of the oxide and carbide particles was less than the resolution of the BSE micrograph, which is ~13 nm.

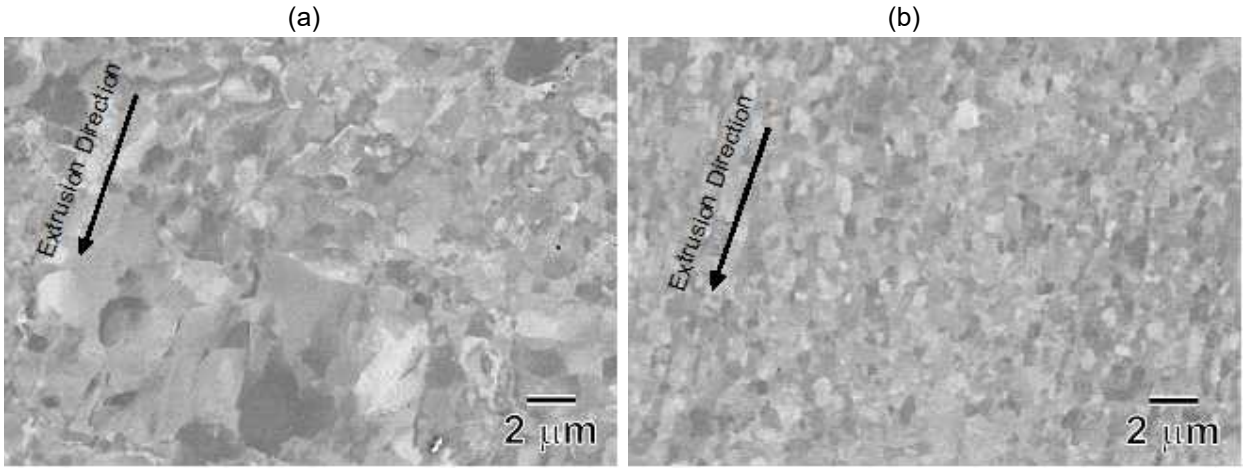

Figure 2. The grain structure observed by BSE in the L-T orientation of (a) M4 containing 1%W and (b) M5 that is W-free. Note: the arrow inserts show the extrusion direction.

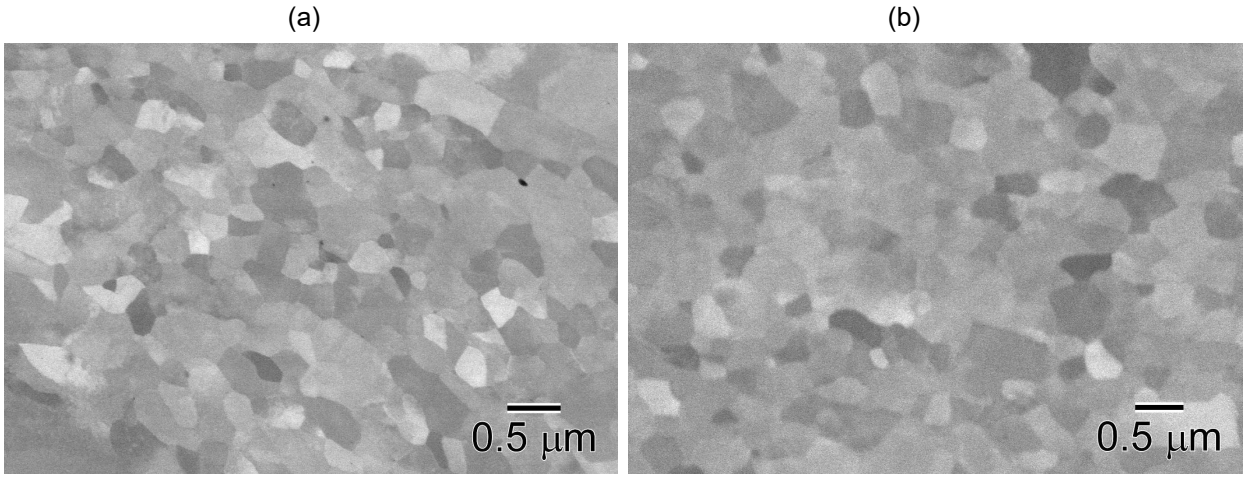

Figure 3. The grain structure observed by BSE in the T-S orientation of (a) M4 containing 1%W and (b) M5 that is W-free. Extrusion direction in the image is out of the page.

The grain size of M4 and M5 was determined by the mean lineal intercept ($\overline{\lambda}$) method using a line of calibrated length. The grain aspect ratio (GAR) due to extrusion was determined from the L-T orientation by measuring the grain size for the extrusion (E) and transverse (T) directions at 90º to each other. Since the grains are not distorted by extrusion in the T-S orientation, the grain size was determined from randomly oriented placement of the calibrated line length on the BSE micrographs. Table 2 shows the results of the grain size analysis of M4 and M5. The results indicated that the GAR of both ODS alloys was smaller than 1.5 (E/T ratio) and the grain sizes in the T-S orientation were very similar between M4 and M5.

Table 2. The grain size of M4 and M5 in the LT and TS orientations and the measured GAR

Alloy	LT Orientation			TS Orientation
	Extrusion (μm)	Transverse (μm)	GAR (E/T)	Random (μm)
M4	0.904 ± 0.056	0.654 ± 0.065	1.381	0.528 ± 0.041
M5	0.757 ± 0.039	0.525 ± 0.028	1.440	0.548 ± 0.031

Bright-field TEM micrographs revealing the ultra-small grains of M4 containing 1%W and M5 that is W free are shown in Figure 4. The grains are elongated along the extrusion axis with grain aspect ratios of <2 in length-to-width, which corresponds with the GAR values shown in Table 2. Very few coarse size particles were observed in the microstructures of M4 and M5 based on diffraction contrast imaging in the TEM.

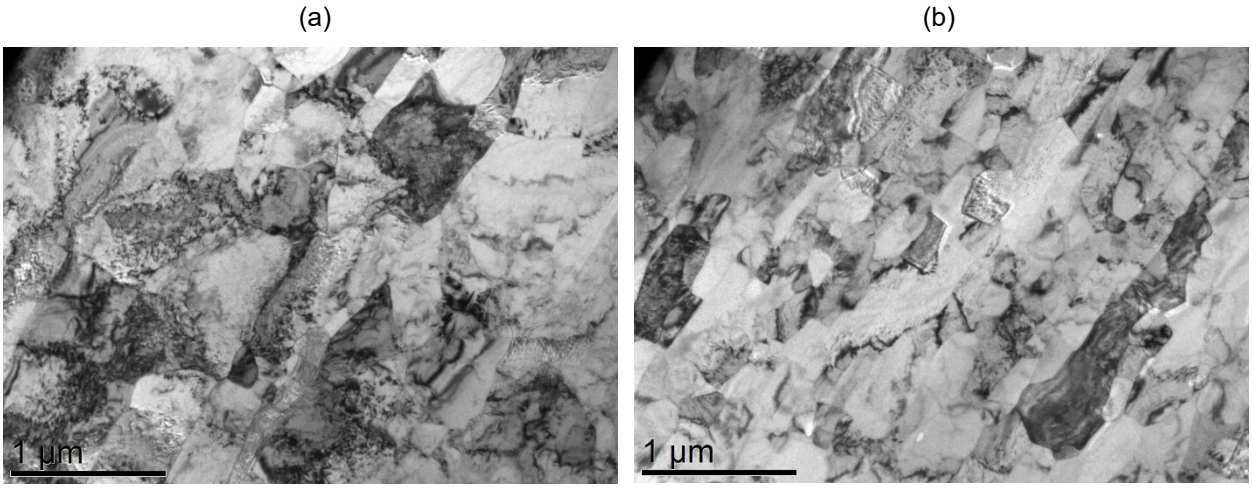

Figure 4. Bright-field TEM micrographs showing the ultra-small grains present in (a) M4 containing 1%W and (b) M5 that is W-free.

Figure 5 shows results obtained from EFTEM analysis of the Y-Ti-oxide particles present in M4 and M5. Fe-M jump ratio maps successfully resolved the nano-size of the Y-Ti-oxide particles in M4 containing 1%W (Figure 5a) and M5 that is W-free (Figure 5b). The dark contrast of the oxide particles in the Fe-M jump ratio map is due to local depletion of Fe from the Y-Ti-oxide composition. The corresponding Ti-M jump ratio maps of the Y-Ti-oxide particles for M4 (Figure 5c) and M5 (Figure 5d) are noisier than the Fe-M jump ratio maps. The bright contrast of oxide particles in the Ti-M jump ratio map is due to enrichment in Ti which is consistent with the Y-Ti-oxide composition.

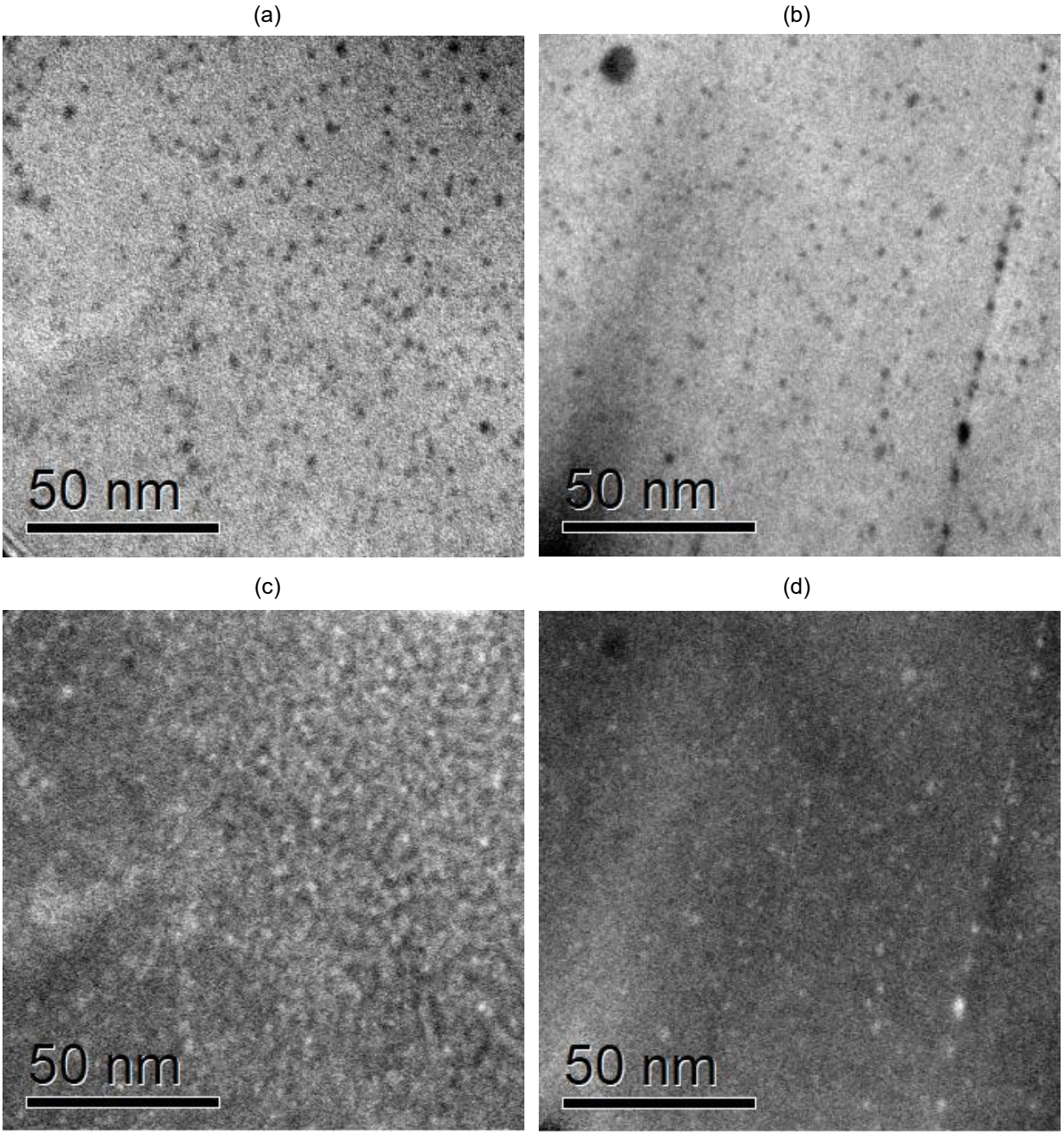

Figure 5. EFTEM jump ratio maps showing the dispersion of nano-size oxide particles present in M4 containing 1%W (a) and (c) and M5 that is W-free (b) and (d). Figures (a) and (b) are Fe-M jump ratio maps and figures (c) and (d) are Ti-M jump ratio maps.

The average size and number density of Y-Ti-O particles present in M4 and M5 were quantified using Image J software. The EFTEM Fe-M jump ratio maps shown in Figure 5 and the t/λ thickness maps shown in Figure 6 were used for the Image J analysis. The thickness maps are from the same area of that the EFTEM

Fe-jump ratio maps were obtained from. The t/λ map is obtained from the unfiltered and zero loss images with the following equation:

$$\ln\left(\frac{unfiltered\ image}{zero\ loss\ image}\right)$$

where t is thickness and λ is the inelastic electron scattering mean from path, which for Fe is ~140 nm. The results showed that the thicknesses of M4 and M5 were 32 (+/- 7.3) nm and 25.5 (+/- 3.9) nm, respectively. These values indicated that the thickness of the M5 specimen (Figure 6b) was more uniform than that of the M4 specimen (Figure 6a).

The number density of the Y-Ti-O particles was obtained by counting the number of particles in a region of interest (ROI) in the Fe-M jump ratio maps of M4 and M5. The thickness and the areal dimensions of the ROI were determined, and the number density was calculated by dividing the number of particles counted in the ROI by the dimensions of the ROI. Image J was used for analyzing the size and the size distribution of the Y-Ti-O particles in M4 and M5. The procedure involved calibrating the scale of the tiff image from the Fe-M jump ratio map and processing the area using the FFT Passband filter at 20%. The threshold setting of the FFT processed tiff image was adjusted and the particles in the image were set to black contrast surrounded by white matrix. An outline of the area of each Y-Ti-O particle was obtained by the Image J software and tabulated. The size was obtained from the equation for area of a circle, or $A = \pi r^2$. Table 3 shows the values for average size and number density of Y-Ti-O particles in M4 and M5.

(a) (b)

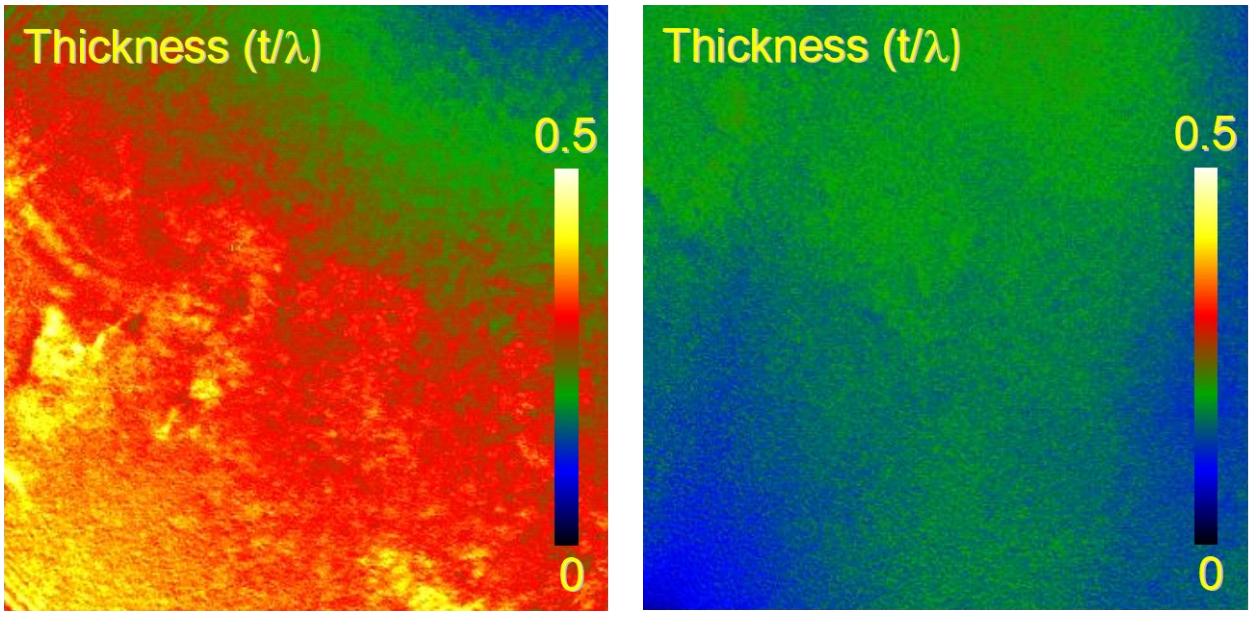

Figure 6. Thickness maps of the areas shown in the EFTEM Fe-M jump ratio maps in Figure 5 for (a) M4 containing 1%W and (b) M5 that is W-free.

Table 3. The average size and number density of the Y-Ti-oxides measured in M4 and M5

Temperature	Diameter (nm)	Number Density (10^{23} m^{-3})
M4 (1%W)	2.29 +/- 0.83	4.50 +/- 0.84
M5 (no W)	2.17 +/- 0.74	5.00 +/- 0.63

The size distribution of the Y-Ti-O particles was obtained from the Image J data on particle size for M4 and M5. Figure 7 shows the size distribution of the oxide particle arranged by starting with the smallest size to the largest size. These plots show that the size of most Y-Ti-O particles followed a linear relationship. Some of the larger oxide particles in the size distributions were from oxides that formed on grain boundaries where the diffusion rates of the Y, Ti, and O solutes are enhanced compared to bulk diffusion rates.

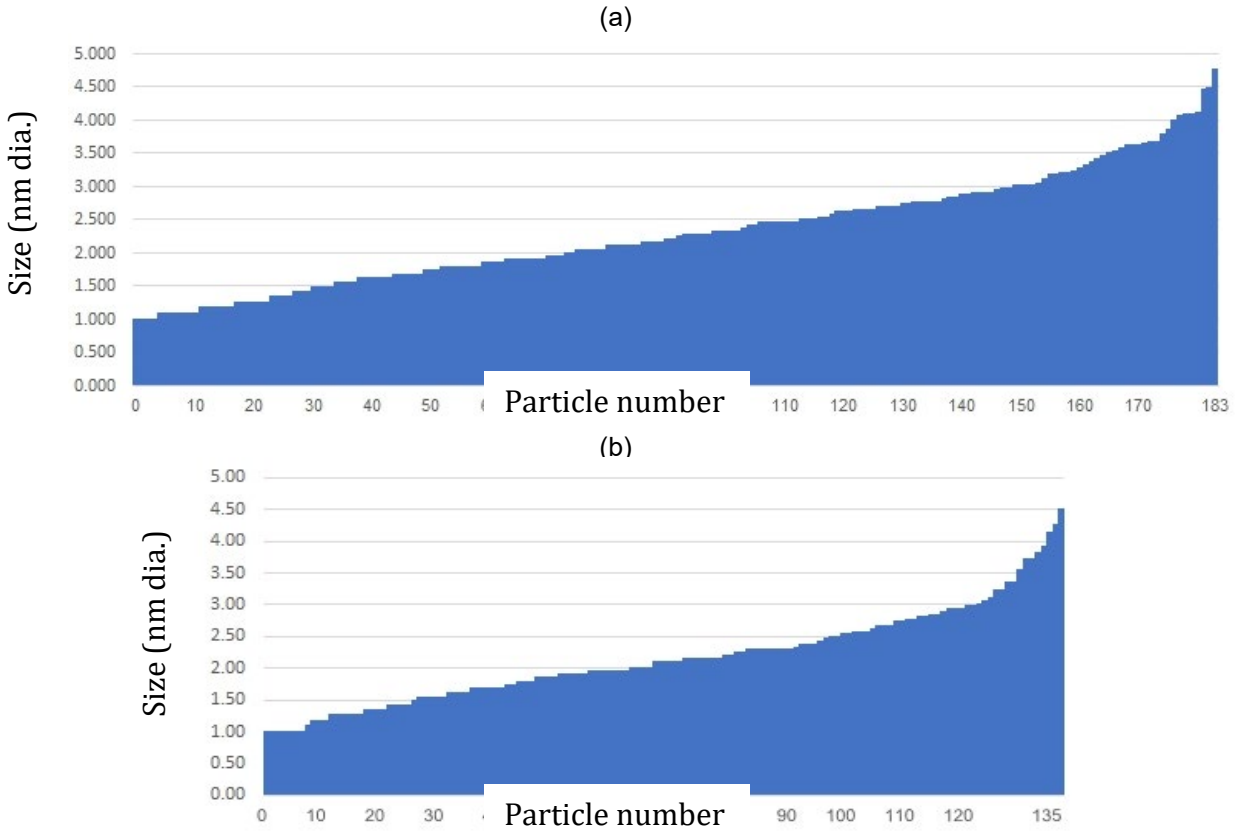

Figure 7. The size distribution of the oxide particle dispersions obtained from Image J analysis of (a) M4 containing 1%W and (b) M5 that is W-free. The x-axis shows the number associated with each analyzed oxide particle arranged in size from the smallest (left) to largest (right).

Mechanical Properties Characterization

The stress-strain curves for M4 and M5 obtained from the tensile tests from room temperature (22ºC) to 800ºC are shown in Figure 8. Both alloys possessed high strengths up to 800ºC. Below 400ºC, M5 (Figure 8b) exhibited higher yield and ultimate tensile strengths, but lower uniform elongation compared to M4 (Figure 8a). The stress-strain curves of M4 and M5 show differences in the plastic flow behavior below 400ºC. The flow stress for M4 increases after the yield stress to the ultimate tensile stress with measurable

uniform elongation. For M5, the flow stress rapidly approaches the ultimate tensile stress after yielding with very little uniform elongation followed by concomitant drop in stress with increasing strain to failure. The reason for this behavior in plastic flow stress for M5 is not clear and warrants further study. It is also not clear if the 1%W in M4 resulted in the better plastic flow stress behavior below 400ºC. Above 400ºC, M4 exhibited slightly higher strengths than M4 while M5 showed much higher total elongations, especially between 400ºC and 700ºC compared to M4. These results appear to show that the 1%W addition to M4 alloy has a substantial effect on the tensile properties and the plastic deformation behavior compared to M5. The tabulated values of yield stress, ultimate tensile strength and uniform and total elongations are shown in Table 4.

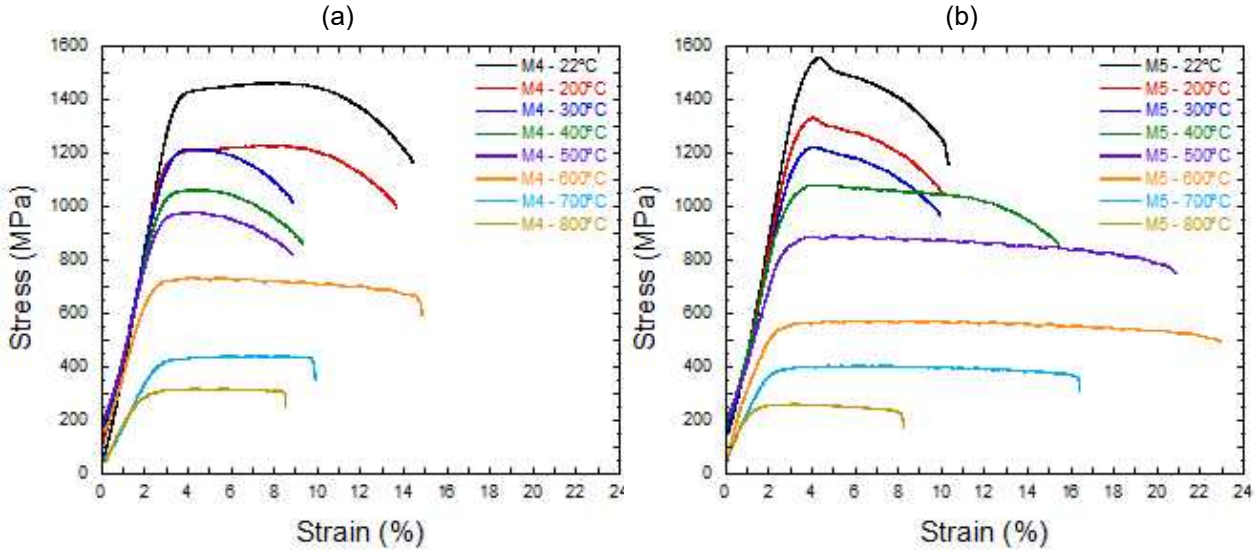

Figure 8. Stress-strain curves of the ODS Fe-10Cr M4 and M5 alloys from 22 to 800ºC.

Table 4. Tensile properties of the ODS Fe-10Cr M4 and M5 alloys

Test Temp.	M4				M5			
	Strength		Elongation		Strength		Elongation	
(ºC)	σ_{ys}	σ_{uts}	E_u	E_t	σ_{ys}	σ_{uts}	E_u	E_t
22	1379	1462	5.42	11.99	1458	1563	1.01	7.60
200	1165	1227	5.44	11.61	1260	1340	0.81	7.75
300	1158	1215	1.43	6.63	1158	1226	0.88	7.75
400	1014	1062	1.79	7.42	993	1083	1.13	13.48
500	926	978	1.96	7.01	838	887	2.18	18.92
600	674	732	1.82	13.46	528	570	6.05	21.44
700	403	441	6.10	7.42	372	403	5.20	14.85
800	286	318	3.51	7.16	238	260	1.90	7.82

The creep properties of M4 and M5 were assessed using the strain rate jump tensile (SRJ) test at high temperatures. The SRJ tests were conducted with SS-3 tensile specimens that were fabricated from the as-extruded bars. An Instron 5900R screw driven tensile machine with convection heating in air was used for the SRJ tests. The SRJ test begins at the lowest strain rate based on the crosshead speed of the tensile machine while measuring stress. The stress increases with strain until it saturates and does not change with increasing strain. This value of stress is correlated with the strain rate. The strain rate is increased and the stress changes in response until it saturates and this procedure is then repeated until the final strain

rate is reached that leads to specimen failure. The SRJ tests for M4 and M5 were conducted at 550ºC, 600ºC, 700ºC and 800ºC.

The data obtained from the SRJ tests at each temperature is plotted as log strain rate verses log stress with linear line fits. The slope of the lines corresponds to the stress exponent (n), which is:

$$n = \left(\frac{\log \dot{\sigma}}{\log \dot{\varepsilon}} \right)$$

Figure 9 shows the plot of log $\dot{\varepsilon}$ (s^{-1}) versus log $\dot{\sigma}$ (MPa) that was obtained from the SRJ tests on M4 and M5 at each temperature. The SRJ data obtained on MA957 is shown in Figure 9 for comparison with M4 and M5 [1]. The results showed that the creep properties of M4 (1%W) were superior to that of M5 (0%W) at 550ºC, 600ºC and 700ºC. M4 showed better creep properties at 800ºC but the specimen failed before reaching the final strain rate. However, the creep properties of M4 and M5 were better than MA957 at comparable temperatures. The calculated stress exponent from the linear line fits of the data shown in Figure 9 are listed in Table 5 for M4, M5 and MA957. The stress exponents for M4 (1%W) and M5 (0%W) are slightly higher than for MA957 but are consistent with the threshold stress creep mechanism that is characteristic of oxide dispersion strengthened alloys.

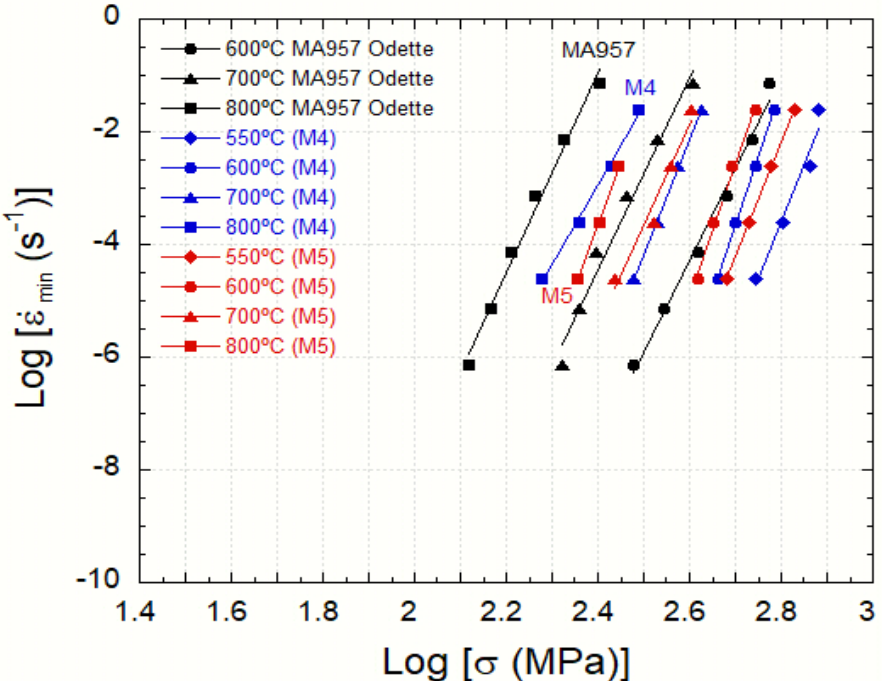

Figure 9. Comparison of creep properties obtained from SRJ tests for M4, M5 and MA957 [1] at elevated temperatures.

Table 5. Values of stress exponent calculated from SRJ tests for M4, M5 and MA957 at elevated temperatures

Temperature	MA957	M4	M5
550ºC	-	20.4	20.4
600ºC	16.3	24.1	23.5
700ºC	16.9	20.3	18.0
800ºC	17.6	14.2	22.1

CONCLUSION

The objective of this study was to investigate the microstructure and mechanical properties of two ODS Fe-10Cr alloys to determine if there was any benefit to the addition of 1%W in the base composition. Therefore, one ODS Fe-10Cr (M4) was produced with 1%W addition while the other (M5) was produced with no W addition. The SEM results showed that both ODS Fe-10Cr alloys possessed similar microstructures consisting of ultra-small (<0.5 μm) grains with low grain aspect ratios. The TEM and EFTEM results showed no significant differences in the size and number density of the Y-Ti-O particles between M4 and M5. These microstructure results revealed that the 1%W contained in M4 had no effect on the nucleation and growth of the Y-Ti-O particles or grain structure. The tensile properties showed that the 1%W addition in M4 improved the balance between strength and ductility from room temperature to 800ºC compared to the W free M5. The results of the strain rate jump tests indicated that high temperature creep properties of M4 containing 1%W was superior to that of M5 with no addition of W. The results of the mechanical properties support the selection of M4 containing 1%W for further development for structural applications in fusion reactors.

FUTURE PLANS

A larger heat of M4 will be produced for studying the effects of thermal mechanical treatments (TMT) on the transformation kinetics and volume fraction of the face centered cubic iron phase from the body centered cubic iron phase that occurs above the ~910ºC transition temperature. The purpose of the TMT study is to improve the strength, ductility, creep and fracture toughness properties of M4 without degrading the ultra-fine grain structure and the dispersion of a high number density of nano-size Y-Ti-oxide particles that provide the high point defect sink strength required for radiation tolerance.

Reference

[1.] G.R. Odette and T. Yamamoto, NERI Final Report 05-074 (2009).

2.5 NEUTRON IRRADIATION INDUCED HARDENING IN RAFM AND ODS STEELS—A. Bhattacharya, J. Reed, X. Chen, J.W. Geringer, Y. Katoh (Oak Ridge National Laboratory), T. Nozawa, H. Tanigawa (QST)

OBJECTIVE

Neutron irradiated RAFM steels and nanostructured ODS alloys were hardness tested from various irradiation campaigns: JP26, JP27, JP28, JP29, RB15J, F8B1 and F13B5. The RAFM steel studied was F82H-IEA heat and ODS steels were 12YWT, MA957 and PM2000. The irradiations were performed in the HFIR on SS-J3 tensile samples, with doses ranging between ~3.5 to > 60 dpa at target irradiation temperatures of 300, 400 and 500 °C. This report details the dose and temperature dependent hardening behavior of the studied materials.

SUMMARY

Vickers microhardness indentation tests were completed on: (i) 9% Cr base F82H-IEA heat steel, (ii) 14% Cr base MA957, (iii) 12% Cr base 12YWT and (iv) 18% Cr-5.5%Al base PM2000 after irradiation in the HFIR to understand the low temperature hardening/embrittlement (LTHE) behavior. Hardening in F82H increased with neutron doses. With an initial sharp increase in the hardening at low doses, microhardness seemed to continually increase with doses up to ~50 dpa. At 80 dpa, a reduction in the average hardness was observed which could be attributed to fluctuations in the irradiation temperature. Surprisingly, all the ODS steels showed profuse hardening for irradiation temperatures as high as 500 °C when irradiated at relatively low doses ~4.5 – 13 dpa. This is vastly different from the behavior of RAFM steels which do not typically show much hardness changes for T_{irr}>350 °C [1]. The unexpected hardening behavior of the ODS alloys suggests different underlying irradiation damage mechanisms compared to RAFM steels might be operating which require a fundamental analysis.

PROGRESS AND STATUS

F82H-IEA heat and ODS alloys MA957, 12YWT and PM2000 were neutron irradiated at ORNL in various irradiation campaigns to map the dose-temperature dependent irradiation behavior of these materials. Here, irradiated hardness of these alloys was tested using Vickers microhardness tests to understand their susceptibility to LTHE. The tests were conducted on the head/grip sections of SS-J3 flat tensile samples, with 1 kg load, 15 s dwell time. Table 1 summarizes the result of the tests specifically performed for F82H-IEA heat samples irradiated over a variety of doses at 300 °C target irradiation temperature. The results also include tests on ^{54}Fe doped F82H for the purpose of studying He effect. Table 2 summarizes the hardness test results on the three studied ODS alloys irradiated at target 300, 400 and 500 °C.

Table 1. Vickers microhardness test results from F82H-IEA heat steel neutron irradiated in the HFIR. Values from each tested indentation are reported.

Campaign	Target dose (dpa)	Target T_{irr} (°C)	Material	Sample IDS	Vickers Hardness (HV) , ×9.8 MPa (value of each tested indent)					
RB15J	~3.5	300	F82H-IEA	OX1	287.4	284.1	309.1	290.3	307.2	X
					291.5	291.5	289.2	304.7	296.2	X
				OX2	293.2	290.9	290.3	290.3	284.1	X
					296.2	290.9	288.6	286.9	299.2	X
F13B5	28	300	F82H-IEA	OT2	389.4	395.8	407.1	372.1	382.3	X
					383.2	391.3	377.2	371.2	361.4	X
				OT3	394	383.2	412	390.3	363.8	X
					386.8	351.2	398.6	394	426	X
				OT4	375.4	363	362.2	355.8	376.3	X
					350.4	383.2	354.3	394.9	404.2	X
				OT5	385	354.3	490.1	408.1	360.6	X
					373.7	385.9	412.9	437.6	410	X
F8B1	28	300	F82H-IEA	OWAm	462.1	446.3	458.6	455.2	434.4	X
					451.8	435.4	454.1	487.5	440.8	X
				OWAn	415.9	428.1	381.5	378.9	393.1	X
					461	435.4	481.3	465.6	433.3	X
				OWAp	410	448.5	409	426	413.9	X
					422.9	402.4	402.4	483.8	461	X
F8B2	50	300	F82H-IEA	OXM	376.3	397.7	370.4	408.1	371.2	X
					345.1	356.6	406.2	337.7	389.4	X
				OXN	389.4	412.9	350.4	372.1	382.3	X
					403.3	396.7	366.3	370.4	412	X
JP29	~80	300	F82H-IEA	O64	347.3	401.4	367.1	350.4	363.8	X
					348.9	342.8	397.7	356.6	314.9	X
				O65	359	386.8	401.4	412.9	399.5	X
					395.8	385.9	381.5	394.9	366.3	X
JP28	~80	300	^{54}Fe-F82H	S60	359	393.1	380.6	385	360.6	363.8
					358.2	374.6	369.6	350.4	386.8	X
				S61 Grip	402.4	414.9	410	408.1	382.3	421.9
					428.1	411	432.3	400.5	404.2	X
				S61 Gauge	409	405.2	408.1	418.9	407.1	X

Table 2. Vickers microhardness of ODS alloys neutron irradiated in the HFIR. Values from each tested indentation are reported. ZP = 12 YWT Fe-12Cr-0.4Ti-3W-0.25Y2O3 : Kobelco ODS, ZQ = Inco MA957, ZR = Plansee PM2000.

Campaign	Target dose (dpa)	Target T_{irr} (°C)	Material	Sample IDS	Vickers Hardness (HV) , x9.8 MPa (value of each tested indent)				
JP26	~4.5	300	12YWT	ZP01	500.4	493.9	468	481.3	485
					459.8	471.6	482.5	459.8	482.5
			MA957	ZQ01	394.9	404.2	403.3	412	407.1
					402.4	399.5	411	415.9	419.9
			PM2000	ZR01	411	411	402.4	403.3	410
					398.6	416.9	409	407.1	407.1
JP26	~5.5	400	12YWT	ZP10	463.3	507	481.3	464.4	490.1
					505.7	481.3	458.6	474	475.2
			MA957	ZQ10	386.8	392.2	395.8	425	438.6
					427	453	445.2	457.5	415.9
			PM2000	ZR10	363	355	402.4	406.2	341.4
					421.9	404.2	409	400.5	405.2
JP26	~8.7	500	12YWT	ZP21	451.8	412.9	422.9	438.6	455.2
					487.5	487.5	463.3	444.1	450.7
			MA957	ZQ21	381.5	379.7	370.4	382.3	384.1
					380.6	380.6	380.6	376.3	381.5
			PM2000	ZR21	383.2	387.7	381.5	330.5	381.5
					398.6	407.1	403.3	401.4	394.9
JP27	~13	300	12YWT	ZP30	465.6	488.8	486.3	481.3	500.4
					499.1	511	493.9	480.1	485
			MA957	ZQ30	419.9	421.9	420.9	413.9	424
					430.2	424	419.9	424	417.9
JP27	~23.3	400	12YWT	ZP40	482.5	476.4	507	486.3	480.1
					478.8	474	478.8	488.8	496.5
			MA957	ZQ41	457.5	463.3	455.2	446.3	436.5
					456.4	434.4	448.5	436.5	443

Comparing dose and temperature dependent hardening in F82H-IEA and ODS alloys

Vickers microhardness of F82H-IEA steel irradiated at 300 °C, as a function of the neutron dose is plotted in Figure 1. Further, the unirradiated and irradiated hardness of the three studied ODS alloys are also plotted for comparison. It is evident that hardness in F82H seems to continually increase. There is a slight decrease in hardness detected for the highest neutron dose. But this anomaly requires analysis of the irradiation temperature and net accumulated dose to arrive at a conclusion. MA957 and 12YWT, which were significantly harder in the unirradiated state, also experienced hardness gain. From ~4.5 to 13 dpa at 300 °C, the hardness in these two alloys did not significantly increase. PM2000, which was the softest steel among the studied materials, showed the highest hardness gain when irradiated at 300 °C.

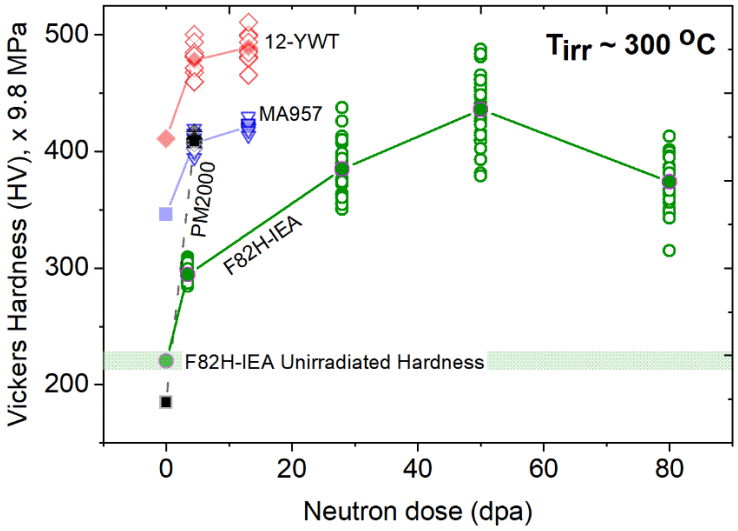

Figure 1. Dose dependent Vickers microhardness of F82H-IEA heat, MA957, 12YWT and PM2000 after 300 °C HFIR neutron irradiations.

Figure 2 presents the irradiation temperature dependent Vickers microhardness evolution of the HFIR irradiated ODS alloys. From these results, hardening is evident in all the three studied ODS alloys at all the irradiation temperatures. What is surprising is that the average hardness does not recover significantly when these alloys were irradiated at 400 and 500 °C. This is striking because RAFM steels typically do not show significant LTHE for T_{irr}> ~330-350 °C [1]. The hardening trends between the three ODS alloys were qualitatively similar despite having vastly different chemistries and microstructure. Currently, the lower temperature limit imposed due to LTHE phenomenon on RAFM steels in fusion environments is set at ~350 °C [1]. If ODS steels show significant hardening, as revealed by the present results, it is likely that the lower temperature limit for ODS steels for fusion in-vessel structures may have to be raised significantly. The 12YWT alloy, which is the least concentrated in terms of Cr, showed the lowest hardness gain among the studied ODS alloys. This is expected because lower Cr level implies lower fraction of embrittling Cr rich α' phase formation in this alloy.

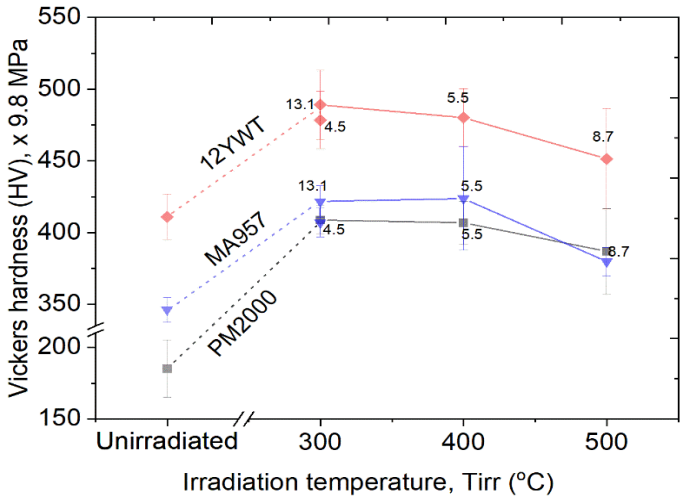

Figure 2. Temperature dependent Vickers microhardness of MA957, 12YWT and PM2000 alloys after HFIR neutron irradiations. The neutron doses are annotated in the figure.

FUTURE PLANS

Tensile tests and advanced microstructure characterization using STEM and APT are planned on F82H-IEA steel and the ODS alloys to develop the structure property relationship.

References

[1] E. Gaganidze and J. Aktaa. Assessment of neutron irradiation effects on RAFM steels. Fus. Eng. Des (88) 2013 (118-128).

[2] S.J. Zinkle et al. Development of next generation tempered and ODS reduced activation ferritic/martensitic steels for fusion energy applications. Nucl. Fusion (57) 2017 092005.

2.6 APPLICATION OF PRINCIPAL COMPONENT ANALYSIS TO VISUALIZE NANO-OXIDES AND PRECIPITATES IN NEUTRON-IRRADIATED AND HELIUM INJECTED PM2000—Dalong Zhang, Danny J. Edwards, Matthew J. Olszta, Alan Schemer-Kohrn, Karen Kruska, Wahyu Setyawan (Pacific Northwest National Laboratory), T. Yamamoto, Y. Wu, G.R. Odette (University of California Santa Barbara)

OBJECTIVE

The objective of this work is to apply commercially available principal component analysis (PCA) algorithm to provide better visualization of nano-sized features, particularly Y-Al-O nano-oxides embedded in the Fe-matrix in in situ helium injected (ISHI) PM2000 sample irradiated at 400 °C. Correlative PCA method combined with direct imaging and conventional element mapping is a robust and promising approach to gain a holistic view of all compositional features detectable by microscopy.

SUMMARY

Neutron-irradiated PM2000 alloy at 400 °C was milled and thinned by standard FIB procedure for TEM specimen preparation. High-current aberration-corrected transmission electron microscope (TEM) combined with high counting rate energy dispersive spectroscopy (EDS) detector was able to capture the Cr-enriched precipitates with sizes 20-50 nm through conventional element mapping in scanning TEM (STEM) mode. However, the smaller Y-Al-O nano-oxides embedded in the Fe-matrix cannot be reliably visualized by element mapping, even though they were clearly present based on STEM bright field (BF) as well as Z-contrast high angle annular dark field (HAADF) imaging. Fortunately, the state-of-the-art Pathfinder EDS analysis software (Thermo Fisher Scientific) includes the COMPASS program designed for unbiased PCA analysis on multivariate spectral images. Preliminary results showed that COMPASS was able to capture features corresponding to nano-oxides and Cr-enriched precipitates alike, which has been challenging for conventional STEM-EDS element mapping routine.

PROGRESS AND STATUS

Introduction

Modern-day TEM equipped with high current field emission gun, aberration corrector, and high counting rate EDS detector has become a powerful and robust tool to study various irradiation induced compositional changes, including irradiation induced precipitation, segregation at grain boundaries or dislocation loops, precipitate instability, etc. [1-3]. However, when it comes to investigating nano-sized features ~10 nm or smaller, conventional method of element mapping faces the challenge in balancing between pursuing higher spatial resolution (e.g., 1-3 nm) and maintaining reasonable signal-to-noise ratio in spectral imaging. The underlying reason is element mapping relies on the deconvolution and quantification of spectral information from each individual pixel. When the X-ray counts get too low, the errors in quantification become unreliably high. This is particularly problematic for nano-sized features (e.g., < 10 nm) or subtle compositional changes (e.g., < 0.1 at.%) embedded in a much thicker (i.e., > 50 nm) TEM specimen. One common “hardware” solution is the development of drift correction, enabling prolonged data collection (e.g., 1 hour) for the same area of interest. However, drift correction doesn’t always work as desired, and environment-induced vibrations sometimes exceed the drift correction capability. More importantly, prolonged exposure to electron beam (especially high-current beam) could possibly cause beam damage and carbon contamination to the specimen, shadowing the exact fine features that the prolonged data collection intends to resolve.

Concomitant to hardware developments, in the past two decades researchers have been pursuing the applications of advanced data analytics and statistical methods on improving EDS data analysis. Particularly, multivariate statistical analysis (MVSA) including principal component analysis (PCA) has been used to reduce a noisy, sparse dataset to a set of low-noise image and spectra vectors [4-7]. Until a few years ago, such unique combination of hands-on statistical analysis and microscopy expertise has been reserved to a rather small group of leading researchers, including the developers and associates of the

"AXSIA" software package at Sandia National Laboratories [4]. This has been changed as the leading vendor of microscopy hardware and software has licensed the PCA algorithm by Kotula et al. [8, 9]. Here at PNNL, the PCA analysis program COMPASS is readily available to us with a site license, namely PCA analysis can be run on each microscope user's computer.

Experimental Procedure

Ferritic PM2000 alloy (Plansee GmbH) was machined into discs of 3 mm diameter. The discs were coated with ~4 μm thickness of NiAl on one side, then irradiated in High Flux Isotope Reactor (HFIR) up to ~21 dpa at 573K, 673K, 773K, respectively. ~1230 appm of helium was injected on the NiAl coated side (i.e., ISHI side), whereas the uncoated side only experienced neutron irradiation ("neutron irradiated only", i.e., NIO side). Details regarding the ISHI technique have been reported elsewhere [2, 10, 11].

In this report, for exploring the application of PCA analysis on STEM-EDS data, we used the PM2000 samples which have a fairly simple bulk composition (at.%) 69% Fe, 19% Cr, 11% Al, 0.5% Ti, 0.2% Y_2O_3, 0.1-0.2% C. PM2000 TEM specimens for both the ISHI side and the NIO side irradiated at 400 °C were first prepared with a standard FIB procedure using an FEI (now Thermo-Fisher Scientific) Quanta 3D FIB. TEM examination of these specimens was done on a cold field-emission JEOL ARM200CF microscope operated at 200 kV, equipped with a hexapole type probe Cs-corrector (CESCOR, CEOS). To date, detailed STEM-EDS data were acquired for the ISHI side on ARM200CF microscope. We will also explore the samples on the 300 keV GrandARM, which is equipped with the Pathfinder EDS data analysis software and COMPASS program as well. For this report, detailed analysis will be focused on the ISHI specimen.

PRELIMINARY RESULTS AND FUTURE WORK

Figure 1 is the high-resolution STEM-EDS map for a representative area in PM2000 specimen that contains a grain boundary, as can be seen by the different contrast from left to right in both BF (a) and HAADF (b) images. Nano-sized features can also be seen, especially at the top-left region. Even though they are expected to be Y-Al-O nano-oxides per previous TEM studies on PM2000 [2], they cannot be clearly identified in conventional element maps in (c)-(f) for Fe, Al, Y, Cr, respectively. In contrast, some larger Cr-enriched precipitates are clearly present as shown in the Cr map. These precipitates tend to decorate the grain boundary, which is consistent with irradiation-induced grain boundary segregation of Cr [12]. Nevertheless, in Fe map, there are some "holes" where Fe is deficient. The big holes match the Cr-enriched precipitates very well, whereas the small ones match the smaller features in BF/HAADF images well. Several factors can contribute to the practical "invisibility" of suspected Y-Al-O nano-oxides in routine element maps, including specimen thickness, irradiation-induced instability, and Al being a light element.

Therefore, the COMPASS program for PCA analysis was explored, as shown in (g)-(i). The COMPASS program is fully automated and unbiased, in that it doesn't make upfront assumptions on what the main elements/phases are. In fact, it doesn't even have such an interface for users to pre-select the expected elements/phases per common practice in conventional element mapping. Instead, COMPASS starts with extracting the individual spectrum at each pixel, then it compares the spectra at each pixel and groups spectra that are statistically similar as determined by PCA. In this way, the initially sparse spectra of individual pixels will be aggregated and become more robust. Finally, the sorting and grouping of spectra reaches a steady state, resulting in a finite set of spectrum aggregates, namely the principal components. For larger scale scanning electron microscopy (SEM) based EDS-PCA analysis, these principal components often correspond to identified unique phases present in the sample [9]. This is possible because SEM "bulk" samples don't have the complication of nano-sized features being embedded in a usually thicker matrix, namely the spectrum is always the convolution of the two. Having emphasized the "unsupervised learning" process in COMPASS, users do have the option to run the process either in "Area Mode" or "Spectral Mode", leading to the same converged results thanks to the robust PCA.

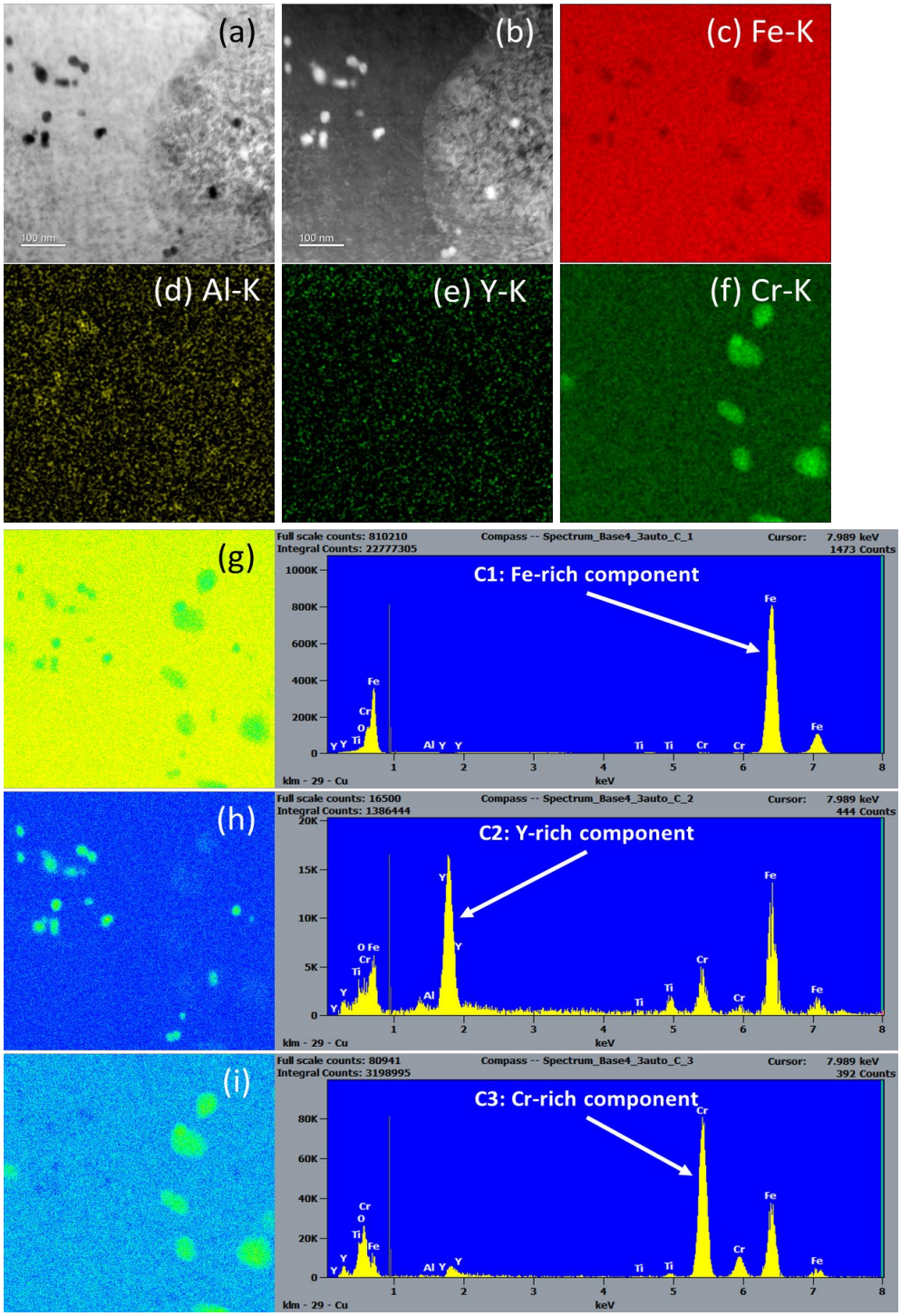

Figure 1. High-resolution STEM-EDS images for a grain boundary area in PM2000 ISHI specimen. (a) and (b), bright field (BF) and high angle annular dark field (HAADF) images. Nano-sized features visible are likely Y-Al-O nano-oxides. (b)-(f), K-line element maps for Fe, Al, Y, Cr, respectively. Note Cr-map shows Cr-enriched precipitates, whereas Al and Y maps don't clearly indicate presence of Y-Al-O nano-oxides. (g)-(i), automated PCA analysis gives 3 distinct components, rich in Fe, Y, Cr X-ray signals respectively.

In Figure 1(g)-(i), there are 3 distinct principal components, namely Fe-rich component C1, Y-rich component C2, and Cr-rich component C3. In spectral space, the summation of the 3 components is practically the spectrum of the whole EDS map. In imaging space, each component corresponds to distinct compositional features. For example, Fe-rich component C1 matches the characteristic peaks of Fe very well. In image space, the aggregate of pixels consisting of C1 matches very well with the Fe element map in Figure 1(c). Building on this "ground truth", we could next examine the Cr-rich component C3, which has a major peak corresponding to Cr, a minor peak corresponding to Fe, and other smaller peaks. The C3 pixel aggregate in Figure 1(i) again matches very well with the Cr element map in Figure 1(f). Moving to the critical Y-rich component C2, it has a major peak for Y and minor peak for Fe. The Y-enriched nano-features, clearly visualized by C2 pixel aggregate in Figure 1(h), match very well with the nano-features seen in direct BF/HAADF imaging in Figure 1(a) and (b). In contrast, the Y element map in Figure 1(e) fails to reveal any of the nano-features. In other words, EDS-PCA analysis by COMPASS successfully captures both Cr-enriched precipitates and Y-Al-O nano-oxides with one simple and robust process. In comparison, only through combining STEM images and Cr element map can the Cr-enriched precipitates be visualized, whereas STEM + element map still fails to visualize nano-oxides.

It is noted that compared to the "global" view in element mapping like those in Figure 1(c)-(f), sometimes conventional line scans of "local" areas can help visualize more detailed compositional information and help to capture the boundaries between two phases, or nano-oxide and Fe-matrix herein. Figure 3 shows one example of conventional EDS line scan analysis across a Y-Al-O nano-oxide which clearly shows up in Figure 1 (h). Indeed, the line scan clearly shows the presence of Al (~10 at.%), Cr (~7 at.% locally), even small fractions of Ti and Y with very large errors. However, two factors adversely impact the effectiveness of the line scan in resolving Y-Al-O nano-oxides:

1. The nano-oxide is embedded in the Fe-matrix, which also contains fair amounts of solid solution Al, Cr, Ti, and maybe some Y, and the "composition" of Y in the nano-oxide containing area appears very low, ~0.1 at% with errors in the same order. Consequently, it is impossible to "see" the boundaries between nano-oxide and the matrix based on Y content variation.
2. In terms of Al content, besides the fact that Al is a light element and EDS inherently has less fidelity in quantifying it (see also the large errors), the seemingly high matrix content of Al (~10 at.%) overwhelms any subtle variation the nano-oxide would cause to the spectrum in the nano-oxide containing area. So again, it is impossible to use the variations in Al content to detect the boundaries between nano-oxide and the matrix.

In a word, these two factors are both due to the underlying challenge in quantifying low content (or light) elements based on conventional deconvolution of spectrum for individual pixels.

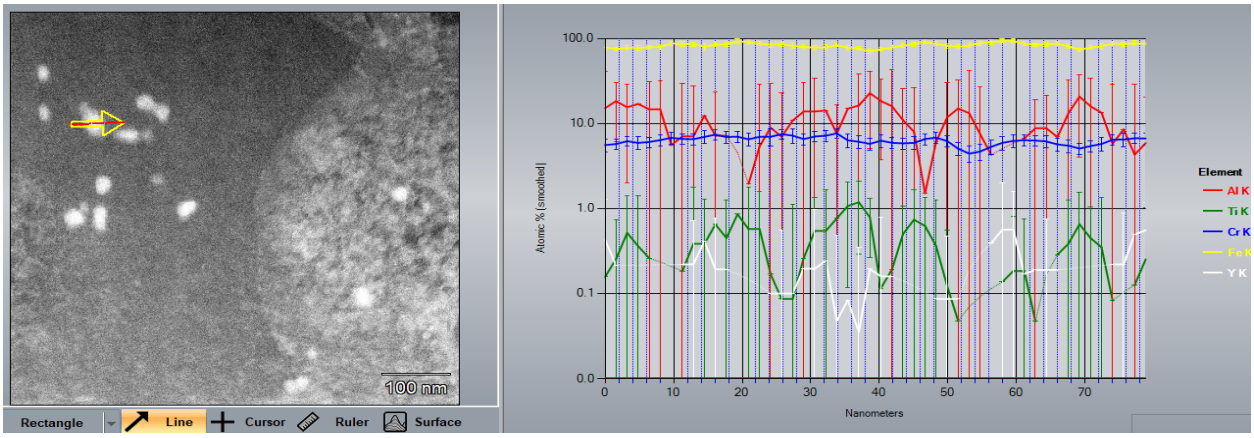

Figure 2. One example of conventional EDS line scan analysis across a Y-Al-O nano-oxide, based on the same EDS spectral imaging dataset as in Figure 1.

Figure 3 shows another high-resolution STEM-EDS dataset in the same PM2000 ISHI specimen but for an area that's at the grain interior, namely free of the influence of grain boundary segregation. Again, nano-features can be clearly seen in direct BF/HAADF imaging in Figure 3(a) and (b), although none of these features can be seen in element maps (c)-(f), for Fe, Al, Y, Cr respectively. Similarly, the "holes" in Fe element map in (c) indirectly show the presence of nano-features other than the Fe matrix. Two Cr-enriched precipitates can be seen in Cr element map in (f).

The PCA analysis in Figure 3(g)-(i) once again captures the nano-features and Cr-enriched precipitates alike. The Fe-rich component C1 looks practically identical to that in Figure 1(g). The C1 pixel aggregate obviously shows the Fe matrix similar to that in (c), but also gives a clearer view of the "holes" as compared to (c). While pixel aggregates of C2 and C3, namely Figure 3(h) and (i), visualize Y-enriched nano-oxides and Cr-enriched precipitates clearly just like that in Figure 1, there are some subtle differences. One might notice for C2, even though it's denoted "Y-rich component", the apparent major peak is in fact that of Fe. It's also the case for C3 that's "Cr-rich". This raises caution, or "double check", in interpreting PCA analysis results. One possible explanation for the smaller Y peak is that the nano-oxide in this location are generally smaller than those seen in Figure 1, possibly due to the absence of grain boundary segregation of Y/Al species. Therefore, for a given pixel at the nano-oxide, there is a larger contribution of spectrum by the Fe-matrix above/below the nano-oxide. Same reasoning can be applied to "Cr-rich" component C3. Interestingly, despite these subtle differences, COMPASS still accomplished the goal of clearly visualizing nano-oxides, along with Cr-enriched precipitates. This testifies the robustness of PCA analysis in helping with capturing nano-sized features embedded in the matrix.

This preliminary study demonstrates the application of the simple, robust PCA analysis in commercially available COMPASS program to visualize irradiation-induced compositional features. It needs to be acknowledged that in its current form with EDS spectral imaging as input, COMPASS has many limitations. The primary one is still the precise composition quantification of embedded nano-features. Correlative EDS-PCA and EELS study using a high quality, very thin specimen (< 50 nm) may improve quantification, as well as correlative TEM and atom probe tomography [7].

Future work includes EDS-PCA analysis for PM2000 NIO specimen for a more comprehensive comparative study. In addition, synergistic effects (or the lack thereof) of helium bubbles and dislocation loops on nano-oxides and precipitates will also be investigated with the assistance of PCA analysis. Moreover, such robust EDS-PCA study can be expanded to NIO and ISHI samples of 14YWT and other fusion structural materials, pushing the enhanced "resolution" for visualization to 1-5 nm.

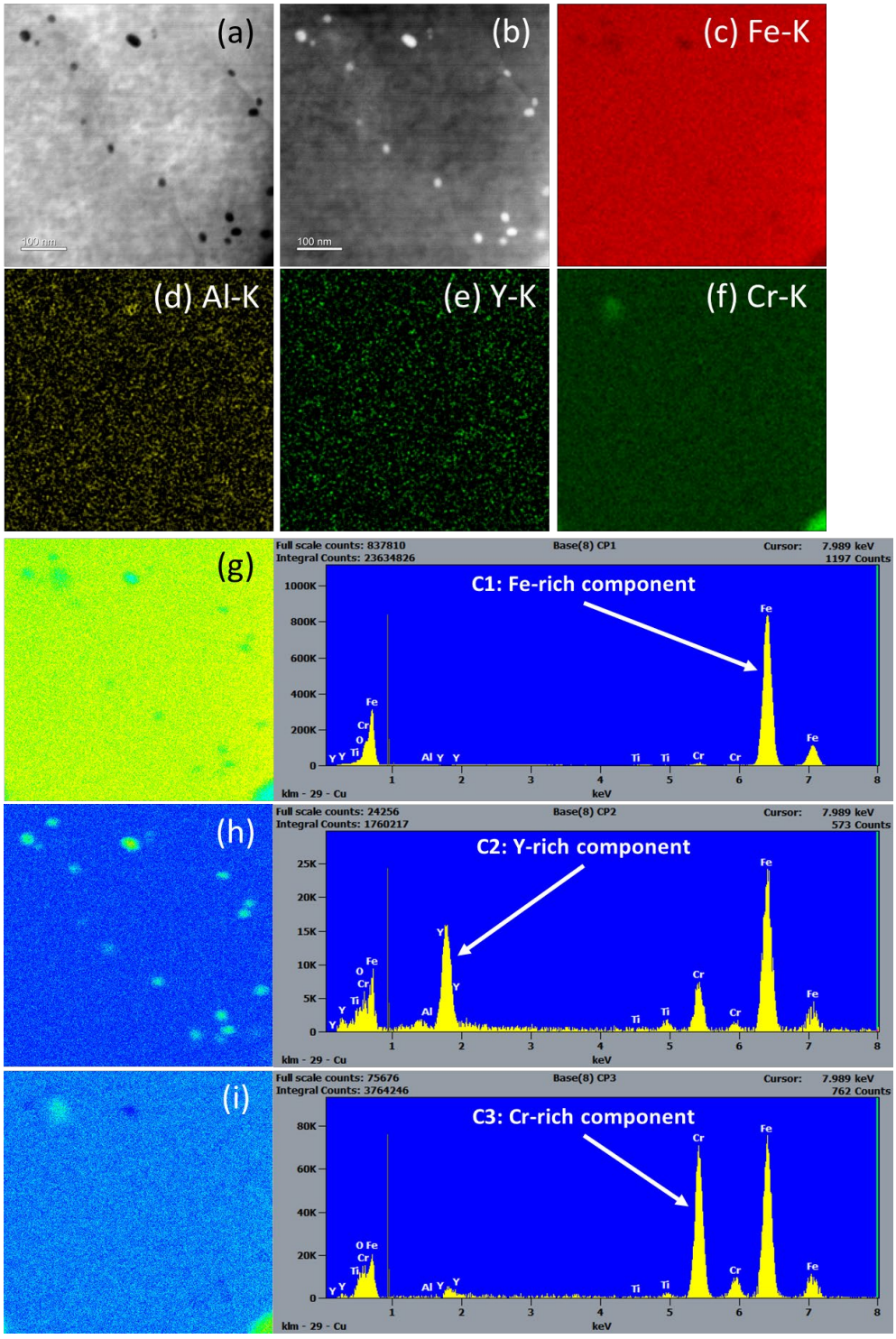

Figure 3. High-resolution STEM-EDS images for a grain-interior area in PM2000 ISHI specimen. (a) and (b), bright field (BF) and high angle annular dark field (HAADF) images. Nano-sized features visible are likely Y-Al-O nano-oxides. (b)-(f), K-line element maps for Fe, Al, Y, Cr, respectively. Note Cr-map shows Cr-enriched precipitates, whereas Al and Y maps don't clearly indicate presence of Y-Al-O nano-oxides. (g)-(f), automated PCA analysis gives 3 distinct components, rich in Fe, Y, Cr X-ray signals respectively.

ACKNOWLEDGEMENTS

This research has been supported by the U.S. Department of Energy, Office of Science, Office of Fusion Energy Sciences and performed at the Pacific Northwest National Laboratory under contract number DE-AC05-76RL01830.

References

[1] C.M. Parish, K.G. Field, A.G. Certain, J.P. Wharry, Application of STEM characterization for investigating radiation effects in BCC Fe-based alloys, Journal of Materials Research 30(9) (2015) 1275-1289.
[2] H.J. Jung, D.J. Edwards, R.J. Kurtz, T. Yamamoto, Y. Wu, G.R. Odette, Structural and chemical evolution in neutron irradiated and helium-injected ferritic ODS PM2000 alloy, Journal of Nuclear Materials 484 (2017) 68-80.
[3] Y. Zhu, C. Ophus, M.B. Toloczko, D.J. Edwards, Towards bend-contour-free dislocation imaging via diffraction contrast STEM, Ultramicroscopy 193 (2018) 12-23.
[4] P.G. Kotula, M.R. Keenan, J.R. Michael, Automated Analysis of SEM X-Ray Spectral Images: A Powerful New Microanalysis Tool, Microscopy and Microanalysis 9(1) (2003) 1-17.
[5] C.M. Parish, L.N. Brewer, Multivariate statistics applications in phase analysis of STEM-EDS spectrum images, Ultramicroscopy 110(2) (2010) 134-143.
[6] C.M. Parish, M.K. Miller, A review of advantages of high-efficiency X-ray spectrum imaging for analysis of nanostructured ferritic alloys, Journal of Nuclear Materials 462 (2015) 433-442.
[7] P.D. Edmondson, C.M. Parish, R.K. Nanstad, Using complimentary microscopy methods to examine Ni-Mn-Si-precipitates in highly-irradiated reactor pressure vessel steels, Acta Materialia 134 (2017) 31-39.
[8] D.L. West, Principal Component Analysis in EDS, Microscopy and Microanalysis 21(S3) (2015) 171-172.
[9] K.J. Spaleta, S.M. Hayes, R.J. Newberry, N.M. Piatak, Evaluating the Utility of Principal Component Analysis on EDS X-Ray Maps to Determine Bulk Mineralogy, Geostandards and Geoanalytical Research 44(4) (2020) 821-843.
[10] T. Yamamoto, G.R. Odette, P. Miao, D.T. Hoelzer, J. Bentley, N. Hashimoto, H. Tanigawa, R.J. Kurtz, The transport and fate of helium in nanostructured ferritic alloys at fusion relevant He/dpa ratios and dpa rates, Journal of Nuclear Materials 367-370 (2007) 399-410.
[11] R.J. Kurtz, G.R. Odette, T. Yamamoto, D.S. Gelles, P. Miao, B.M. Oliver, The transport and fate of helium in martensitic steels at fusion relevant He/dpa ratios and dpa rates, Journal of Nuclear Materials 367-370 (2007) 417-422.
[12] K. Wang, C.M. Parish, K.G. Field, L. Tan, Y. Katoh, Segregation behavior and phase instability of Eurofer97 after neutron irradiation to 72 dpa, Journal of Nuclear Materials 547 (2021) 152834.

2.7 A NEW CRACK HEALING MECHANISM IN AN ANNEALED 14YWT NANOSTRUCTURED FERRITIC ALLOY—M.E. Alam, S. Pal, N. J. Cunningham, G. R. Odette (University of California Santa Barbara)

OBJECTIVE

The objective of this study is to identify a new Ti-carbooxinitride redistribution driven crack healing mechanism that eventually heals the embedded microcracks of a 14YWT ODS steel for better formability.

SUMMARY

The FCRD NFA-1 is a larger best practice heat of Fe14Cr nanostructured ferritic alloy (NFA) dispersion strengthened by a large population of nano-scale $Y_2Ti_2O_7$ nano-oxides. NFA-1 was produced by ball milling FeO with argon atomized Fe-14Cr-3W-0.35Ti-0.25Y (wt.%) powders, followed by hot extrusion at 850 ºC, followed by 1 h annealing and multipass cross-rolling at 1000ºC to form an ≈ 10 mm thick plate. Cross-rolling results in a large population of {001}<110> cleavage system microcracks (MCs) running on planes parallel to the plate faces. A series of high temperature vacuum anneals were carried out from 1100 to 1300ºC for 1 and 5h to explore the possibility of self-healing, not only of the MCs, but also macroscopic fatigue cracks. Most notably, a new crack self-healing mechanism was discovered, involving the redistribution and coarsening of initially fine matrix Ti, C, O and N precipitates (TiCONs) to bridging sites on the crack faces. The relocated TiCONs grow and coarsen, thereby consuming a volume of the adjoining Fe-Cr matrix. The displaced matrix atoms diffuse to further fill the crack.

PROGRESS AND STATUS

Introduction

Nanostructured ferritic alloys (NFAs), variant of oxide dispersion strengthened (ODS) steels, are a promising candidate alloy class for the advanced nuclear fission and future fusion reactor applications, due to their high strength, unique irradiation tolerance, outstanding thermal stability and corrosion resistance [1–4]. Here we focus on a larger heat of best practice FCRD 14WYT alloy, called NFA-1, developed in a collaboration between, Oak Ridge National Laboratory (ORNL), Los Alamos National Laboratory (LANL) and the University of California Santa Barbara (UCSB); the details processing methods can be found elsewhere [5–9]. As illustrated in Figure 1, the as-processed (AP) NFA-1 plate contains a bimodal distribution of highly textured, submicron pancake-shaped grains along with a large population of preexisting microcracks (MCs) lying in planes normal to the plate thickness direction [6,7,9]. The {001}<110> cleavage MCs, form during plate cross-rolling. The MCs contribute to delamination toughening [7], but are detrimental to deformation processing of some NFA-based components, such as thin-walled fuel cladding tubes.

Cracking has been classically viewed as an irreversible phenomenon [10]. However, recent research, performed mostly on polymeric, concrete and ceramic materials report that cracks can at least be partially self-healed [11–18]. While there have been far fewer studies, self-healing of damage in metallic materials is a topic of rapidly increasing interest [19–28]. In the case of bulk metallic materials autonomous self-healing of creep cavities without any additional external stimulus has been reported [25,28]. Non-autonomous crack healing by application of external triggers, like electro pulsing [23,24], heat-treatment [19–22], diffusion and precipitation [29,30], and a bridging mechanism in shape memory alloys [26] are reported.

For example, Laha [25] and Shinya [28] reported that a modified austenitic stainless steel with added B and Ce that improved creep rupture properties by retarding cavity growth. Ce consumes S facilitating B and N segregation to, and precipitation of BN on, cavity surfaces. The BN surface film retards surface diffusion,

decreasing cavity growth rates. The authors also postulate that B and BN precipitation increased grain boundary sliding resistance and inhibit creep cavity formation. Densification and reduction of porosity in an Al-Zn-Mg-Cu alloy by heterogeneous precipitation of $MgZn_2$ on pore surfaces was reported by Lumley [29]. Lumley also showed nano-void self-healing by low service temperature precipitation in an Al-based alloy, with supersaturated Cu in the underaged condition [30]. Dislocations pile ups lead to stress concentration and formation of nano-voids/ small cracks. Cu segregates to the dislocations. When the gliding dislocations under service stresses intersect the crack, pipe diffusion transport leads to dynamic Cu precipitation, closing the cracks and enhanced fatigue resistance. Further general discussion of crack self-healing can be found in [18,31,32].

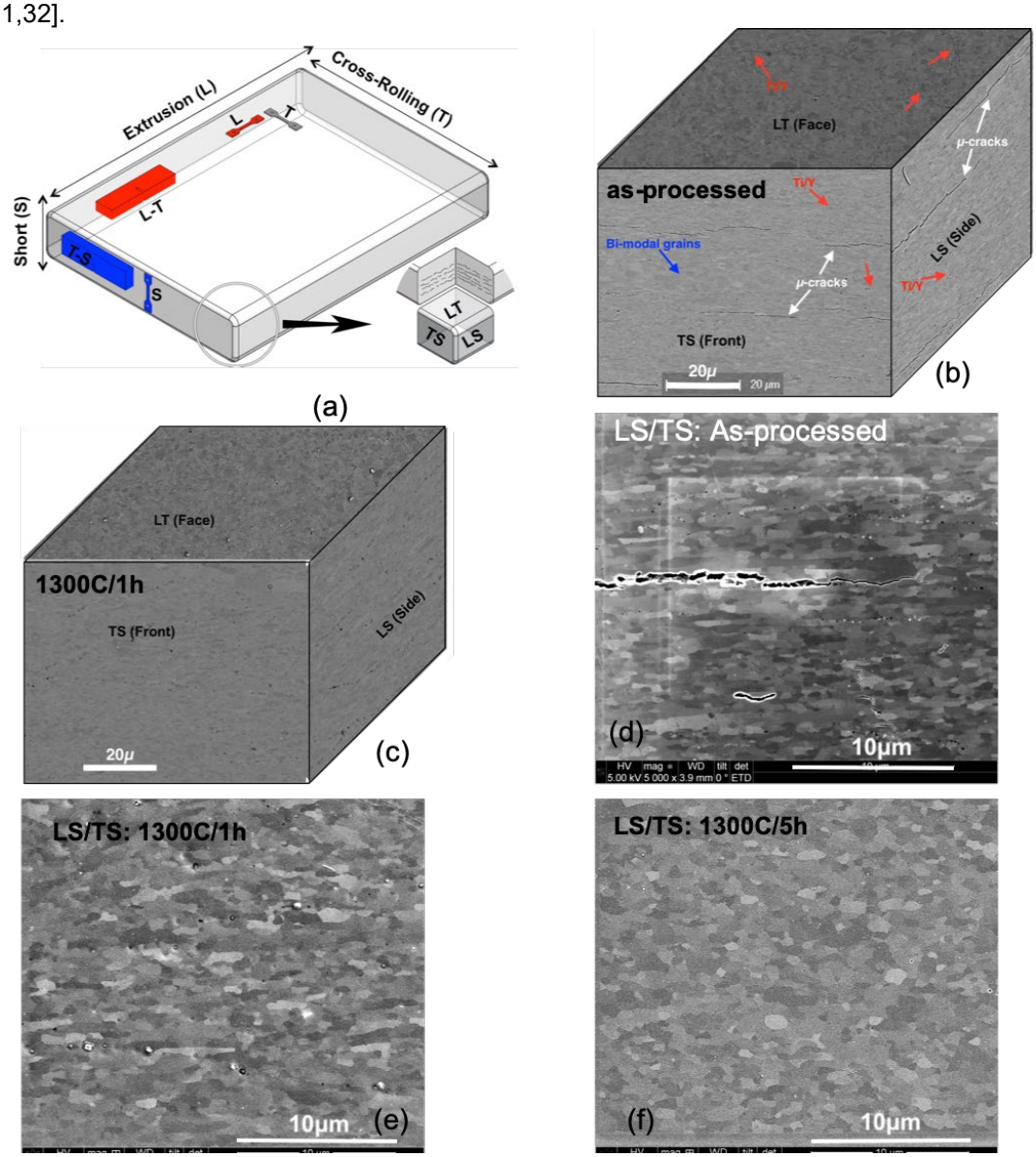

Figure 1. (a) The specimen orientations and definition of the section views with respect to the extrusion, cross-rolling and plate thickness directions; 3D view of: (b) as-processed (AP), and (c) 1300ºC/1h annealed plate section; and higher magnification SEM images showing: (d) pre-existing microcracks (MCs) with pancake-shaped grains for AP; and crack-free, rounder shaped grains for (e) 1300ºC/1h and (f) 1300ºC/5h annealed NFA-1, respectively.

Here, we investigate a newly discovered mechanism for crack self-healing in NFA-1 under high temperature annealing. This mechanism is associated with Ti-carbooxinitride (TiCON) precipitate growth and coarsening on micro and macro crack faces. The crack face TiCONs are relocated from a finer scale distribution of these precipitates in stringers initially in the matrix. The redistributed TiCONs bridge the crack faces and, as they grow into the adjoining matrix, expel (displace) Fe and Cr (mostly) atoms that help to fill the crack. This *dissolution, diffusion, reprecipitation, and displacement* mechanism is fundamentally different than those reported in previous studies. In the case of embedded microcracked NFA-1, the displaced matrix atoms join the TiCONs in very efficiently filling the cracks. Indeed, we show that this mechanism can even heal macro-scale fatigue through-thickness cracks. Based on the mechanical property trends, as confirmed by the microstructural characterization and fractographic studies, we conclude that crack self-healing starts at 1100ºC, and is essentially complete at 1300ºC.

Experimental Procedure

Details of processing of NFA-1 can be found elsewhere [4,5]. Sub sized tensile [6] and 3PB specimens [7] were electric discharge machined (EDM) from the AP NFA-1 plate. They were then wrapped in a molybdenum getter foil and annealed in vacuum at 1100, 1200 and 1300 °C for 1h and 5h. In order to image the MCs, the AP 101 and annealed condition specimens were first ground with 400 to 2000 grit SiC sand paper, to remove EDM surface oxide and then polished with 9, 3 and 1μm diamond paper to produce a good surface finish, prior to ultrasonic cleaning in acetone. The various temperature (T_a) and time (t_a) conditions are designated by a xxy nomenclature where xx is the T_a in units of 100°C and y is the t_a in units of h. The AP condition was also annealed at 1000 ºC/1h after cross-rolling, hence is labeled as the AP 101-condition. Microstructural characterization included: (i) grain size and shape (all conditions); (ii) nano-oxide size, number density and volume fractions (101 and 131-conditions); (iii) Ti-oxide locations and corresponding sizes, number densities and area fractions (101, 131 and 135-conditions); (iv) MC sizes and number densities (all conditions); (v) dislocation densities (101, 131 and 135-conditions); and, (vi) texture (101 and 131-conditions). The characterization tools included scanning electron microscopy (SEM), transmission electron microscopy (TEM), both equipped with energy dispersive spectroscopy (EDS), atom probe tomography (APT), and electron backscatter diffraction (EBSD). Comprehensive mechanical property characterization included room temperature (RT ≈ 23°C) microhardness, quasi-static uniaxial dog bone (coupon) tensile and single-edge notched three-point bend (3PB) bar toughness tests, both at RT and -150ºC, for both in- plane (L) and out-of-plane (S) loading orientations, as illustrated in Figure 1a. Some of the microstructural and mechanical properties have been reported previously [33].

RESULTS

NFA-1 grain structures and tensile property evidence of crack self-healing and metrics

Figure 1b and c shows SEM/FIB images of the grain structures and MC in the 101 and 131-conditions. Higher magnification SEM TS orientation view images are shown in Figure 1d-f. Clearly the MCs observed in the 101-condition are not seen after the 131 and 135-conditions. The grain diameter (d_g) and grain aspect ratio (GARs) are plotted in Figure 2a and b. As expected, the 101 microstructural features in the front extrusion (TS) and side cross-rolling (LS) plate section views are essentially the same [6,7], hence, they are not reported individually. In all cases, the plate face LT section view shows nearly uniform, equiaxed and predominantly ultrafine ≈ 0.5 μm grains along with a small fraction of larger grains in the range of 1-10μm. A few coarse grains larger than 10 μm are also observed [6]. The TS (and LS) GAR, slowly deceases with T_a and t_a; that is the grains become slightly less pancake shaped. Otherwise the grains are remarkably stable up to the 131-condition. It is well known that recovery heat treatments, like 101, stabilize NFA from both recrystallization and texture changes, due to lower dislocation density driving forces, coupled with grain boundary NO pinning and, in some cases, intrinsically low mobility [4]. The grains only grow modestly and become slightly more equiaxed in the 135-condition. The AP 101-condition NO's are mostly $Y_2Ti_2O_7$ pyrochlore [5], with the sizes (d_n), number densities (N_n), and volume fractions (f_n) of ≈ 2.0 nm, 6.9 x 10^{23}

m^{-3} and 0.74%, respectively. APT shows that the average diameter of NO increases from ≈ 2.0 nm for the AP 101-condition to ≈ 3.1 nm for 131-condition, while both the N_n and f_n decrease from 6.9 x 10^{23} m^{-3} to ≈ 2.2 x 10^{23} m^{-3} and 0.74% to ≈ 0.38%, respectively. TEM was used to measure the dislocation densities (ρ) in the 101, 131 and 135-conditions, under two-beam bright-field imaging conditions. The 131 anneal reduces the dislocation density a factor of ≈ 8, while the corresponding recovery factor is ≈ 220 for the 135-condition. The 135 anneal also results in more equiaxed grains, or the formation of sub grains.

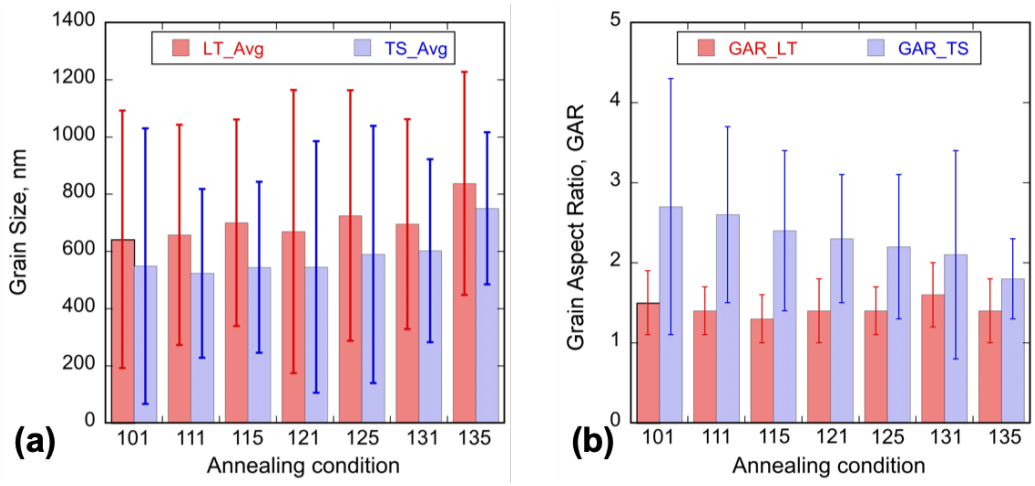

Figure 2. Bar plots showing for all annealing condition: (a) average grain sizes; and, (b) grain aspect ratio (GAR).

Visual inspections to identify MCs are useful, but not fully indicative of crack self-healing. Such observations on specimen surfaces are vulnerable to contamination (e.g., N) even in a vacuum. Further, very fine remaining MCs may be obscured by specimen preparation and Ti reaching a free surface may sublime. Perhaps, the best indirect evidence of MC self-healing is provided by changes in the out-of-plane, S orientation tensile properties and fracture surfaces for tests at RT and -150°C (see Table 1 and Figures 3 and 4). Since the basic grain structure is largely unchanged, crack self-healing can be demonstrated by difference between out-of-plane S and in-plane L orientation tensile behavior. In the former case (S), fracture in the 101-condition occurs by elastic cleavage MC propagation at both temperatures. Cleavage occurs at a fracture stress (σ_f) that is less than the 0.2% yield stress (σ_y), at a total plastic strain elongation (ε_t) of ≈ 0%. The controlling property is the critical stress for activating the {100}<01-1> cleavage oriented MCs, with fracture toughness K_{Ic} values estimated to be only ≈ 4 to 15 MPa√m [34]. The detailed mechanisms resulting in the formation of the population of cleavage oriented MCs and texture in the 101 NFA-1 cross-rolled plate are described elsewhere [9]. Figure 3 shows the engineering stress-strain $\sigma(\varepsilon)$ curves for the L and S tensile tests at RT and -150ºC in the 101 and all the annealed conditions. The L orientation tests at RT show plastic true stress-strain hardening in all the T_a-t_a conditions, with ε_t ductility's exceeding 10%. The S orientation tests also show limited plastic strain hardening, but with a much reduced ε_t, except for the 131 and 135-conditions. Notably, the S-orientation ductility, ε_t, actually exceeds that for the L orientation in the 135-condition. As expected, the σ_y and σ_u in the L orientation are higher at -150°C compared to those measured in the RT tests, while the corresponding ε_t are slightly reduced. However, the S-orientation tests at -150°C show only a very small total elongation (ε_t) ductility prior to cleavage.

Figure 4 shows high magnification SEM fractographs for the AP 101 and 131-conditions. Low magnification SEM fractographs for AP and all annealed conditions can be found in [33]. The fracture surfaces for the L orientation show less delamination and a shift to more uniform in-plane micro void coalescence, ductile-dimple fracture mode with increasing annealing T_a-t_a [33]. Crater-like features are also observed in the fracture surfaces. The size of these craters increases with T_a-t_a, since they nucleate on highly coarsened

TiCONs. The S tensile 101-condition specimen tested at RT failed in a completely brittle elastic manner, with a very flat, shiny cleavage fracture surface (see Figure 4).

Table 1. RT and -150 ºC temperature tensile test results for NFA-1 in the AP 101 and all the annealed conditions

Annealing Condition	Test Condition		s_y (MPa)	s_u (MPa)	e_u (%)	e_t (%)	RA (%)
1000 ºC/1h	23C	L	1042 ± 102	1133 ± 100	3.8 ± 3.7	12.9 ± 1.5	56 ± 8
		S	708 ± 57	730 ± 92	0.2 ± 0.3	0.2 ± 0.3	4 ± 2
	-150C	L	1384 ± 5	1509 ± 24	6 ± 6.5	13 ± 5	51 ± 3
		S	316 ± 43	316 ± 43	0	0	0
1100 ºC/1h	23C	L	1013 ± 64	1098 ± 41	6.1 ± 0.8	11.6 ± 1.3	56 ± 8
		S	792 ± 165	966 ± 86	3.8 ± 2.5	3.8 ± 2.5	12 ± 9
	-150C	L	1377 ± 38	1475 ± 43	0.9 ± 0	7 ± 4.2	42 ± 11
		S	966 ± 50	966 ± 50	0	0	0
1100 ºC/5h	23C	L	1004 ± 5	1081± 8	6.8 ± 0.2	13.4 ± 0.6	48
		S	756 ± 104	900 ± 91	3.1 ± 0.5	3.9 ± 1.6	14 ± 4
	-150C	L	1227 ± 1	1304 ± 13	5.1 ± 3	13.6 ± 3.7	47 ± 0.3
		S	966 ± 135	1027 ± 121	0.4 ± 0.1	0.4 ± 0.1	4 ± 1
1200 ºC/1h	23C	L	987 ± 15	1071 ± 8	7.1 ± 1.1	12.4 ± 1.1	51
		S	824 ± 126	914 ± 32	2.5 ± 0.6	4.5 ± 1.3	15 ± 1
	-150C	L	1223 ± 77	1322 ± 38	3.7 ± 3.8	13.5 ± 0.7	48 ± 4
		S	853 ± 116	871 ± 147	0.1 ± 0.2	0.1 ± 0.2	4
1200 ºC/5h	23C	L	914 ± 47	1016 ± 33	7.2 ± 1.1	11.4 ± 0.4	48
		S	741 ± 65	806 ± 45	3.1 ± 0.8	5.1 ± 1.9	18 ± 1
	-150C	L	1129 ± 47	1234 ± 9	8.1 ± 0.1	14.8 ± 2.5	46 ± 2
		S	833 ± 21	953 ± 15	1 ± 0.1	1 ± 0.1	7
1300 ºC/1h	23C	L	855 ± 55	953 ± 43	7.5 ± 1.5	13.6 ± 2.3	55 ± 5
		S	683 ± 24	874 ± 8	8.1 ± 1.3	15.2 ± 1.2	54 ± 1
	-150C	L	1152 ± 26	1201 ± 4	8.4 ± 0.3	14.6 ± 0.8	48 ± 0
		S	951 ± 45	1008 ± 1	0.5 ± 0.4	0.5 ± 0.4	7 ± 1
1300 ºC/5h	23C	L	770 ± 43	884 ± 19	8.1 ± 3	13.3 ± 4.5	51 ± 9
		S	655 ± 37	787 ± 14	9.6 ± 2.6	21.4 ± 1.9	60 ± 2
	-150C	L	964 ± 30	1060 ± 20	7.5 ± 3.3	10.5 ± 3.4	44 ± 9
		S	760 ± 153	826 ± 139	0.9 ± 0.5	0.9 ± 0.5	6 ± 1

Upon loading, the pre-existing MCs, which run perpendicular to the loading direction in the K_I mode, propagate by brittle cleavage. Annealing improves the S-orientation RT ductility, as marked by increasing amounts of ductile-dimple micro void fracture features. There is a transition of fracture modes from cleavage to a mix of cleavage, dimples, and shear lips (stair-like features) in the 121 and 125-conditions. Thus, the threshold T_a for extensive crack self-healing is estimated to be between 1200 and 1300ºC. The very high ductility for the 1300ºC annealed conditions is associated with fully ductile-dimple fractures, with large TiCON nucleated pockets. Additional evidence of crack self-healing can be seen on the side-surfaces of RT, S-orientation post-test shown in Figure 4 (bottom-left for the 101 and bottom-middle for the 131-conditions, respectively); in both cases, loading direction is horizontal. The red arrows show large side surface cracks normal to the loading direction in the 101-condition, while they are absent in the 131-condition.

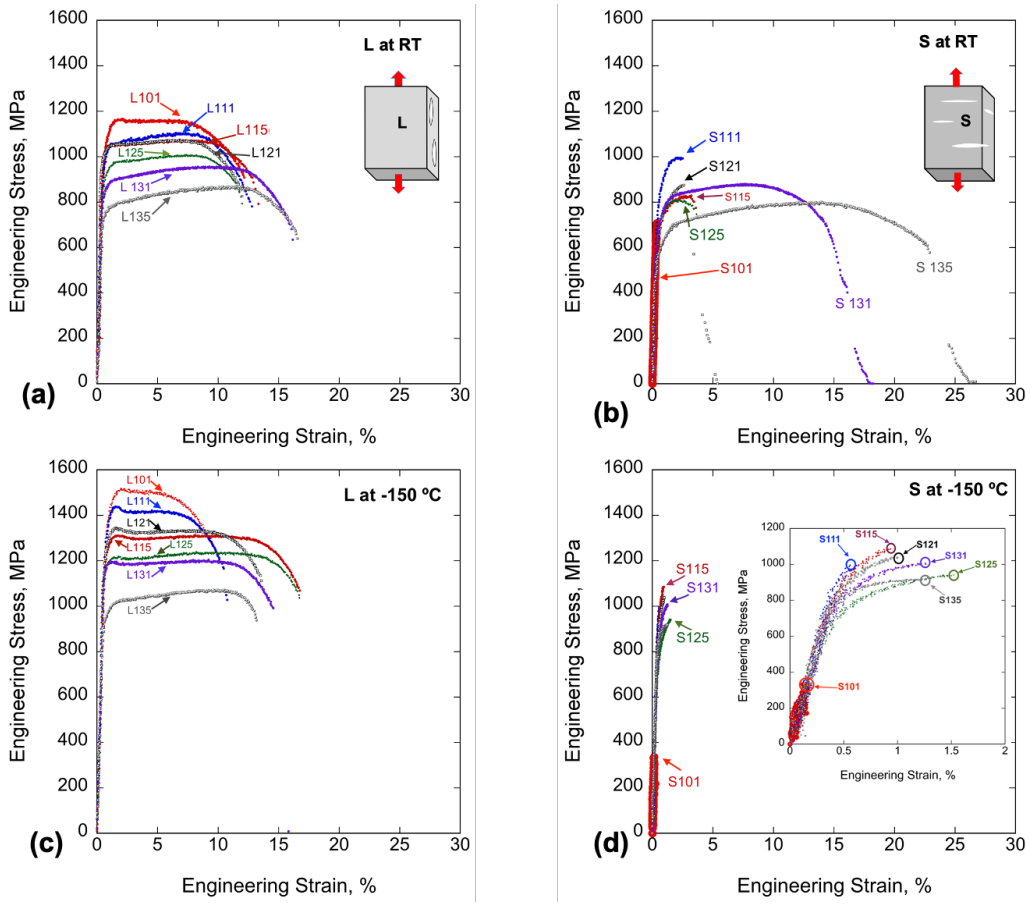

Figure 3. Engineering stress-strain curves for all the annealing conditions respectively for: (a and b) L and S-orientations at RT; and (c and d) L and S-orientations at -150 ºC.

Crack self-healing microstructures and mechanisms

The AP NFA-1 contains a large number of MCs running parallel to the cross-rolling and extrusion directions and plate surfaces. The AP 101 condition average MC size (l_c) is ≈ 10.4 μm, range up to 101 μm, and their area density (N_c) is ≈1.6 x 10^9 /m^2. The detailed micro mechanism of MC formation is reported elsewhere [6,7,9]. The N_c and l_c are summarized in Table 2. An example of a MC, marked by an indent in the 101 and 111-conditions is shown in Figure 5a and b. These micrographs show that the MC partially heal, and TiCONs begin to grow on the crack faces, during the 111 anneal. Thus, the size and number density of readily visible surface MCs quickly decreases in the 111 and 115-conditions. The larger MCs in the AP 101-

condition are divided into more numerous smaller segments by partial healing in the 111-condition, with ≈ 70% of the l_c between 1 – 5 μm (see red arrows in Figure 5a,c versus 5b,d, and 5f).

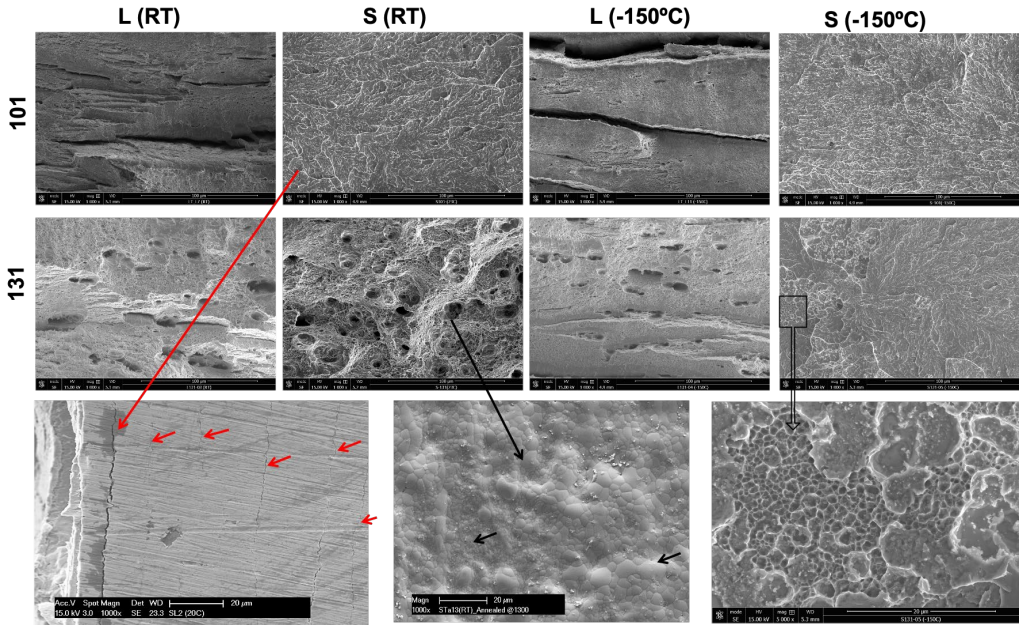

Figure 4. L and S orientations SEM fractographs for the AP (101) and 131-conditions at RT and -150ºC.

Table 2. NFA-1 MC and TiCON statistics for the AP and all the annealed conditions

Condition	Crack length, l_c (range), μm	Crack area density, N_c, /m^2	TiCON dia, d_t (range), nm	TiCON density, N_t, /m^2
101	10.4 ± 9.7 (2 - 101)	1.6 x 10^9	60 ± 33 (10 - 262)	9.8 x 10^{11}
111	4.6 ± 2.9 (1 - 18)	1.2 x 10^9	-	-
115	4.3 ± 2.3 (1 - 10)	3.7 x 10^8	-	-
121	0	0	-	-
125	0	0	-	-
131	0	0	98 ± 63 (8 - 475)	4.4 x 10^{11}
135	0	0	330 ± 121 (66 - 646)	2.5 x 10^{10}

Smaller 101-condition MCs appear to heal completely within SEM resolution limit (see red parabolas in Figure 5c, and d). Figure 5e shows the corresponding l_c distributions of a 400μm x 300μm area at 101, 111 and 115-conditions, with reduced maximum l_c size from ≈ 60 μm at AP 101 to ≈ 18μm at 111- and ≈ 10μm at 115-condition. The 111 anneal slightly reduces N_c compared to AP-101, while the 115 anneal reduces N_c by a factor of ≈ 4 (Figure 5f); however, the average residual l_c remains similar. Note, while Figure 5e shows maximum MC length for AP 101 is ≈ 60 μm for the certain 400x300 μm^2 areas; however, a total of nearly 1000 MCs in four specimens for the AP 101 condition show MC up to ≈ 100 μm (see Table 2). Notably, no surface MCs are observed by SEM at higher T_a.

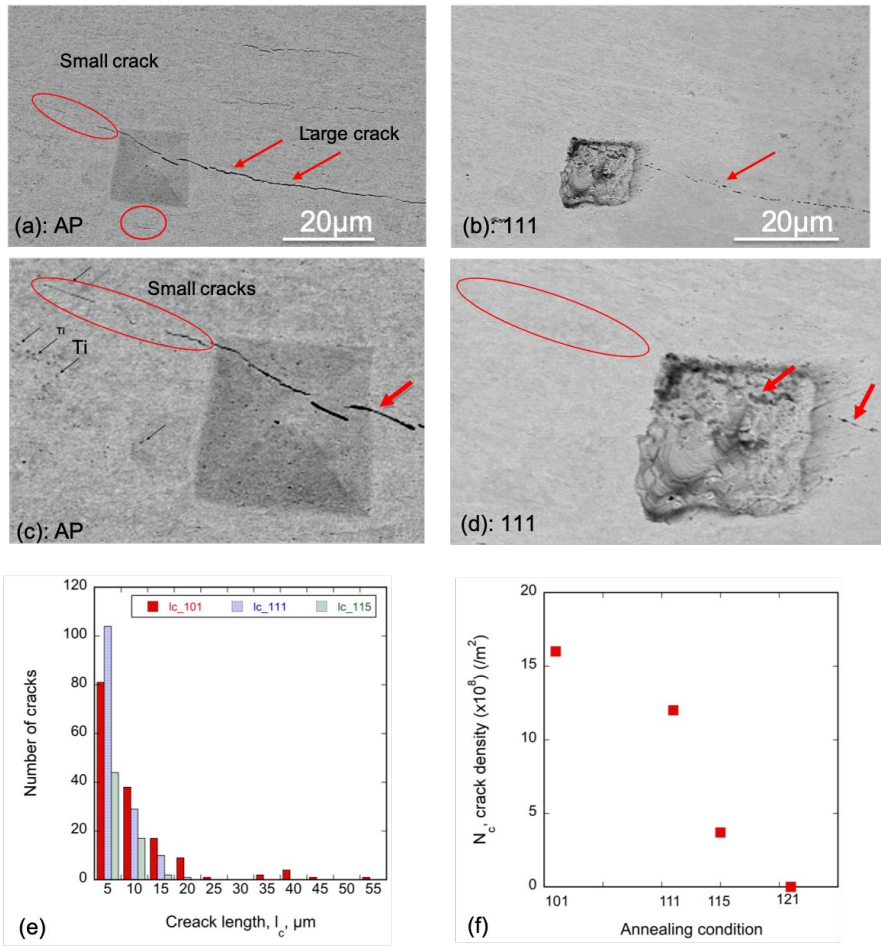

Figure 5. (a to d) SEM images for the same location in the (a,c) AP and (b,d) 111- conditions images showing some MCs and the associated TiCON redistribution; (e) the visible MC length (l_c) distributions in a 400 x 300μm area for the AP 101, 111 and 115-conditions; and, (f) the visible MC number area density (N_c) for the 101, 111, 115 and 121-conditions.

Figure 6a illustrates self-healing of a macroscopic (≈ 1mm long) through-thickness precrack. The precrack opening varies between ≈ 10 nm at the tip up to ≈ 300 nm at the notch. Figure 6b shows that the pre-crack is visibly healed after annealing at 1300ºC for 5h (the 135-condition). Large black faceted and smaller gray rounder particles are observed in the healed zone (see insert of Figure 6b, and Figure 7). Figure. 6c-e shows that when the specimen is then reloaded, the region of the precrack undergoes an unusual ductile tearing fracture to reform the crack. The in-situ images in Figure 6c, show that the ductile tearing occurs without a plastic zone and the crack faces are crenulated in association with localized plastic flow (Figure 6d and e). This behavior is likely due to the high TiCON loads. That is, the coarsened TiCONs act as micro void nucleation sites, and limit the local previously fatigue precracked region ductility. As expected, a normal

plastic zone finally forms at the end of the healed precrack. For comparison, Figure 6f and g show the flat, featureless precracked zone fracture surfaces in the 101 and 135-conditions. The coarsened TiCONs are located at the dimples of the micro voids and clearly demonstrate crack self-healing in interior regions of NFA-1, away from free surfaces (see Figure 6e). In contrast to the 135-condition behavior shown in Figure 6c-e, the 101-condition undergoes normal plastic zone formation and ductile crack tearing beginning at the fatigue precrack tip (Figure 6f). In this case, crack tearing is accompanied by extensive delamination's. The previously fatigue precracked region in the 135-condition appears featureless at lower magnification, with mushy coarse scale shear features associated with severe localized plastic flow. Delamination's are suppressed beyond the initial precrack in the corresponding ductile tearing fracture surface.

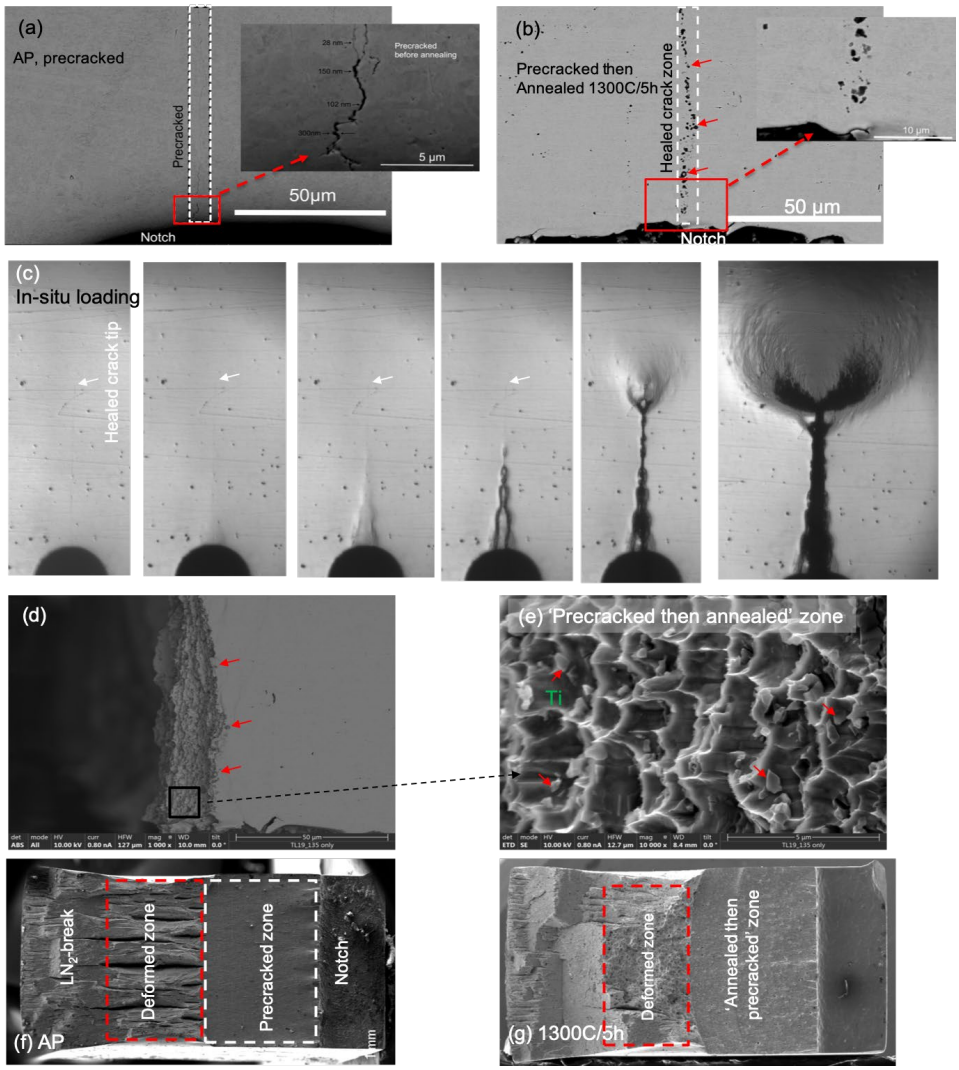

Figure 6. SEM images of the: (a) AP 101 precracked T-L specimens; (b) the 135 condition healed fatigue crack and associated coarse scale TiCONs; (c) in-situ images of the healed fatigue crack with increasing loading, showing localized plastic flow up the point of ductile tearing in the healed zone, and the formation of a normal plastic zone when the torn crack reaches its previous a/W; (d) side view of the ductile tearing surface with three red arrows marking the crack positions in Figure 6b and 6d; (e) a higher magnification image of the ductile fracture surface magnified view of the indicated by the black box in Figure 6d, showing micro voids nucleated on TiCONs (arrows) in the healed precracked zone; (f and g) low magnification view of a fractured specimen showing extensive delamination's in the AP 101 condition, versus shear dominated ductile fracture, without delamination's, in the 135 condition created by the healed then torn precrack.

Both the EDS maps and point scans in Figure 7 confirm that the particles in the healed zone are mainly composed of Ti, C, O and N-rich TiCON precipitates. The larger TiCONs that form on the crack faces, are redistributed from a population of stringers of smaller precipitates initially embedded in the matrix that were not originally associated with the MCs (see Figure 8a,b). This was also been seen in Figure 5c and d, where the TiCONs for the AP 101condition are redistributed from the matrix (small black speckles, indicated by black arrows, Figure 5c) to near the indents or crack faces for 111-conditions (Figure 5d).

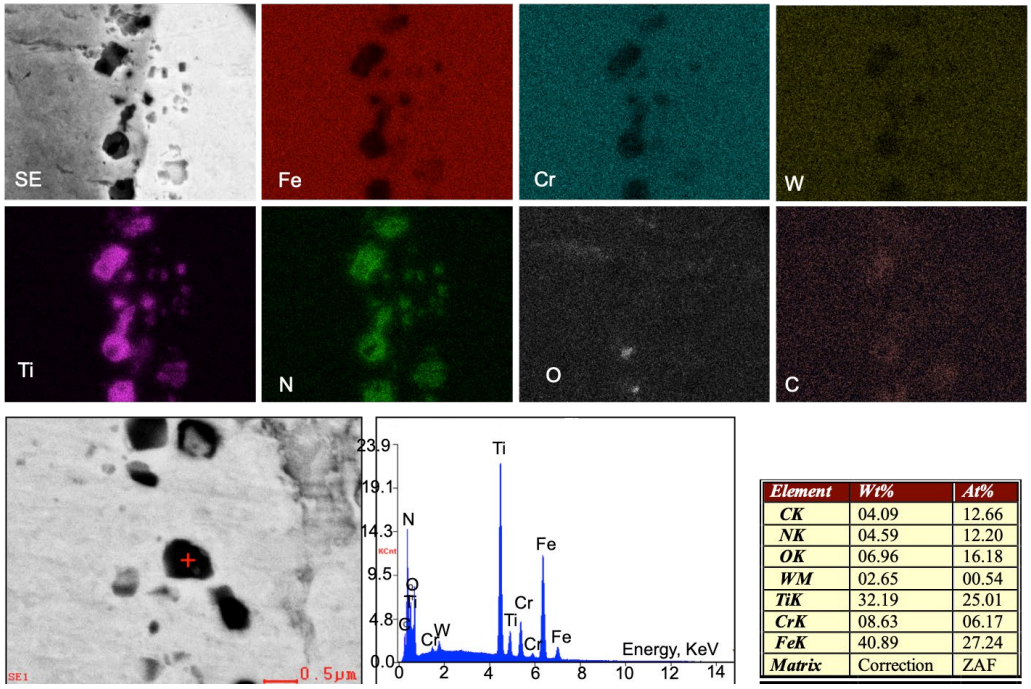

Element	Wt%	At%
CK	04.09	12.66
NK	04.59	12.20
OK	06.96	16.18
WM	02.65	00.54
TiK	32.19	25.01
CrK	08.63	06.17
FeK	40.89	27.24
Matrix	Correction	ZAF

Figure 7. SEM/EDS map and point scans along the precracked zone for the 1300ºC/5h specimen confirms Ti-C-O-N particles.

The TiCON statistics are summarized in Table 2 and the evolutions of the diameter (d_t) and area density (N_t), between the 101, 131 and 135-conditions, are plotted in Figure 8c and d, respectively. Coarsened TiCONs are observed to form along the crack faces in all the annealed conditions, (see Figures 5,6,8). The average TiCON size (d_t) of ≈ 60 nm for the AP 101-condition, grows to ≈ 100 nm in the 131condition, and to ≈ 330 nm in the 135-condition. The corresponding maximum TiCON sizes increase from ≈ 260 nm to ≈ 650 nm.

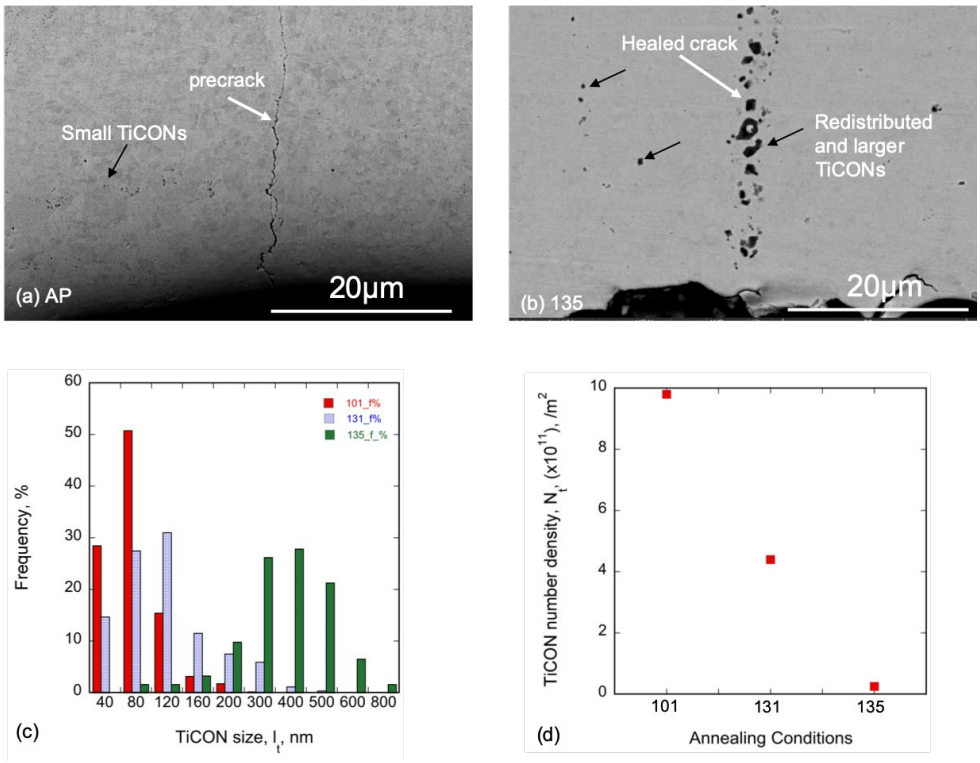

Figure 8. (a and b) SEM images showing the redistribution and coarsening of TiCONs for the AP 101 and 135 conditions; c) the TiCON size distributions for the AP 101, 131, and 135-conditions; and, (d) the corresponding N_t variations with the annealing condition.

As schematically illustrated in Figure 9, our hypothesis is that self-healing is due to mass transport in the 131 and 135-conditions associated with the finer TiCONs, initially embedded in the matrix in the AP 101-condition, dissolving and reprecipitating on the free surfaces of both MCs, and even the macro fatigue crack faces (see Figures 5c,d, 8a,b). The dissolution-reprecipitation (nucleation and growth) kinetics results in fewer, but much larger, TiCONs that bridge the crack faces. The reformed TiCONs, which are larger than the crack opening, grow into the adjoining matrix, displacing Fe and Cr (mostly) atoms, which are then deposited to faces to fill the along intervening open segments of the crack. As expected, the kinetic rates of the multiple complex processes mediating MC self-healing increase with time and temperature. Partial crack self-healing by TiCON coarsening can leave small residual micro voids, which may anneal by bulk or boundary diffusion [19–21]. Self-healing may also occur by the sintering of very small cracks by classical Gibb-Thomson driven by excess $2\gamma/r_t$ chemical potentials at their rounded tip (here, γ and r_t are the surface energy and crack tip radius, respectively). However, for larger cracks we believe that pore dissolution and crack tip sintering are secondary self-healing mechanisms (see Figure 5a and b).

Unfortunately, the data are insufficient at this time to model the precise rate controlling physics of crack self-healing, but this hypothesis can be partially tested by a mass balance applied to the fatigue crack in the 135-condition. Assuming 2D array of TiCONs, on the crack faces spaced l_t apart, adding up to a total spherical (r_s) volume equal to the filled crack. This includes the TiCON volume between the crack faces. For simplicity, assume the filled volume is a disc of radius $r_d = l_t/2$, and thickness, t. Thus

$4/3\pi r_s^3 = \pi r_d^2 t$

$1.33(r_s/t)r_s^2 = r_d^2$

$r_d = [\sqrt{(1.33r_s/t)}]r_s$

Converting a sphere to a disc provides some crack filling volume. Further, the fact that the TiCONs are larger than the crack opening, $h_c = t$, $r_s/t > 1$, further increases r_d/r_s. For example, the 135-condition average TiCON r_s = 0.24μm and the average crack width, h_c, is 0.08 μm; thus $r_d \approx 0.5$ μm and the particle spacing l ≈ 1 μm, consistent with Figure 6b.

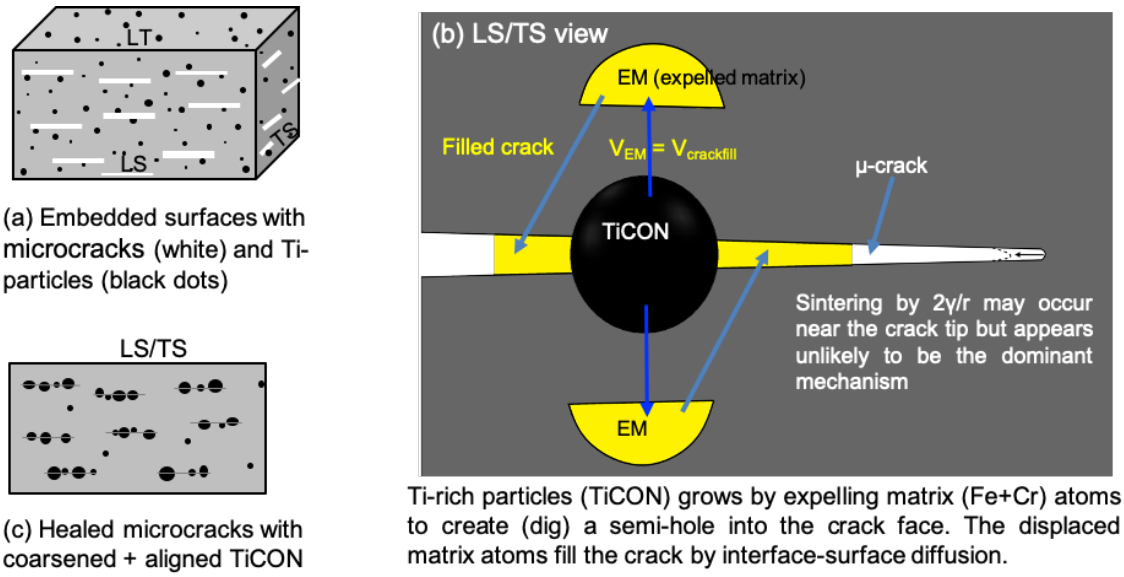

Figure 9. Schematics illustrations of the crack healing mechanism: (a) the MC and TiCON in the AP 101 condition; (b) the crack self-healing mechanism as described in the text, and, (c) healed cracks and redistributed-coarsened TiCONs after annealing.

DISCUSSION

The results of tensile tests, including fractography, at RT and -150°C clearly show that high temperature, short time anneals self-heal the pre-existing MCs in NFA-1. Self-healing begins in the 111-condition anneal (1100°C for 1h) and reaches (near) completion following the 131-condition anneal (1300°C for 1h). We hypothesize the dominant self-healing mechanism is associated with the growth of larger Ti carbooxinitride (TiCONs) precipitates on MC faces. The crack face TiCONs are relocated from stringers of smaller precipitates, initially in the matrix. The redistributed TiCONs bridge the crack faces and, as they grow into the adjoining matrix, expel Fe and Cr (mostly) atoms that fill the crack between the precipitates.

The observation of this mechanism for self-healing MCs was further demonstrated at a much larger length scale by the self-healing of macro fatigue cracks. The overall thermo-kinetics of crack self-healing are complex and detailed modeling will be explored in future. However, qualitatively, the rate-controlling step is the dissolution of matrix TiCONs and diffusion of Ti to the MCs. Dissolution establishes a local equilibrium Ti concentration at the TiCON, which in combination with the Ti diffusion coefficient and crack sink strength, establish the diffusional concentration gradients which determine the flux of reactive Ti to the crack faces. Assuming Ti diffusion is the rate-controlling step, a crude model can be based on simple rate theory. The total MC volume is $V_c \approx N_c \pi l_c^2 h_c/4$, where N_c, l_c and h_c are the MC volume metric number density, length and opening, respectively. The corresponding Ti diffusional crack filling rate is $\approx S Z_c D_{Ti} X_{Ti}$. Here, $Z_c \approx \pi l_c N_c$ is the total average MC sink strength for Ti, S ≈ 3 is the assumed Fe atoms displaced per Ti atom, as mediated by the TiCON composition and mass density, D_{Ti} is the Ti diffusion coefficient in α-Fe and X_{Ti} is the Ti concentration in the matrix far from the cracks. Thus

$$\pi l_c^2 h_c N_c/4 = [3\pi l_c D_{Ti} X_{Ti} N_c] t_h \quad (1)$$

The crack self-healing time, t_h, is

$$t_h \approx [l_c h_c]/[12 D_{Ti} X_{Ti}] \quad (2)$$

APT data shows that the Ti in NFA-1 is almost entirely tied up in the NOs and TiCONs (Table 3). APT shows that the matrix Ti increases from ≈ 6 x 10^{-4} in the AP 101 condition to ≈ 0.0014 in the 131 condition (see Table 3). For D_{Ti} = 0.21exp(-293200/RT) m^2/s [35], l_c = 50 μm, h_c = 0.1 μm and X_{Ti} = 10^{-3}, t_h = 0.079, 0.014 and 0.003 h, at 1100, 1200 and 1300°C, respectively. Thus, Ti diffusion is not expected to be rate controlling. Modeling of TiCON dissolution rates would require a much more detailed thermodynamic analysis, which is beyond the scope of this paper. Additional research will be needed to establish the detailed characteristics of the TiCONs and to quantify their dissolution (or coarsening-relocation) kinetics as a function of T_a-t_a.

Table 3. The APT bulk and matrix compositions (at. %) in the AP 101 and annealed 131 NFA-1

Materials	Fe	Cr	W	Ti	Y	O	C	Si	N
101-bulk	82.94	15.05	0.967	0.283	0.090	0.366	0.138	0.076	0.006
101-Matrix	83.57	14.97	0.969	0.056	0.016	0.125	0.127	0.073	0.005
131-bulk	87.83	10.68	1.02	0.207	0.025	0.099		0.063	
131-Matrix	88.032	10.634	1.022	0.145	0.002	0.021		0.063	

The self-healing kinetics are rapid at high temperatures > ≈ 1200°C. The performance costs and benefits of MC self-healing vary with the circumstance. However, the benefits may outweigh the costs in some cases, and the annealing mechanism that we have identified may have far broader application to other alloy systems and circumstances.

CONCLUSIONS AND FUTURE WORK

We have clearly demonstrated a high temperature (≥ 1100°C) annealing process for self-healing of micro and macro cracks in a 14YWT NFA-1, and qualitatively described the mechanism. The dissolution, diffusion, reprecipitation, and displacement mechanism has application-specific performance costs and benefits, which largely remain to be explored. Notably, however, this general type of highly efficient self-healing mechanism may be of broader interest. Thus, we hope that the exploratory work reported here will stimulate similar studies of other alloy systems.

ACKNOWLEDGEMENTS

We thank our UCSB colleagues Dr. Takuya Yamamoto, David Gragg and Kirk Fields for their important contributions to this work. We also acknowledge the support provided by U.S. Department of Energy through the Office of Fusion Energy Sciences (DE-FG02-94ER54275). The U.S. National Science Foundation supported California Nanoscience Institute provided facilities critical the success of this research. We also gratefully recognize Dr. D. T. Hoelzer at ORNL and S. A. Maloy at LANL for their key role in developing NFA-1.

References

[1] G.R. Odette, M.J. Alinger, B.D. Wirth, Recent Developments in Irradiation-Resistant Steels, Annu. Rev. Mater. Res. 38 (2008) 471–503.

[2] G.R. Odette, Recent Progress in Developing and Qualifying Nanostructured Ferritic Alloys for Advanced Fission and Fusion Applications, JOM. 66 (2014) 2427–2441.
[3] S. Ukai, Oxide Dispersion Strengthened Steels, in: R. Konings (Ed.), Compr. Nucl. Mater., 1st ed., Elsevier, Atlanta, GA, 2012: pp. 241–271.
[4] G.R. Odette, N.J. Cunningham, T. Stan, M.E. Alam, Y. De Carlan, Chapter 12 - Nano-Oxide Dispersion-Strengthened Steels, in: Struct. Alloy. Nucl. Energy Appl., Elsevier Inc., 2019: pp. 529–583.
[5] N.J. Cunningham, Y. Wu, G.R. Odette, D.T. Hoelzer, S.A. Maloy, Characterization of a larger best practice heat of 14YWT in annealed powder, HIP consolidated and extruded forms, DOE Fusion React. Mater. Progr. Semiannu. Prog. Rep. DOE0313/54 (2013) 15–26.
[6] M.E. Alam, S. Pal, K. Fields, S.A. Maloy, D.T. Hoelzer, G.R. Odette, Tensile deformation and fracture properties of a 14YWT nanostructured ferritic alloy, Mater. Sci. Eng. A. 675 (2016) 437–448.
[7] M.E. Alam, S. Pal, S.A. Maloy, G.R. Odette, On delamination toughening of a 14YWT nanostructured ferritic alloy, Acta Mater. 136 (2017) 61–73.
[8] G.R. Odette, On the status and prospects for nanostructured ferritic alloys for nuclear fission and fusion application with emphasis on the underlying science, Scr. Mater. 143 (2018) 142–148.
[9] S. Pal, M.E. Alam, S.A. Maloy, D.T. Hoelzer, G.R. Odette, Texture evolution and microcracking mechanisms in as-extruded and cross-rolled conditions of a 14YWT nanostructured ferritic alloy, Acta Mater. 152 (2018) 338–357.
[10] A. Griffith, Phenomena of rupture and flow in solids, Philos. Trans. R. Soc. Lond. Ser. A. 221 (1920) 163–198.
[11] S.R. White, N.R. Sottos, P.H. Geubelle, J.S. Moore, M.R. Kessler, S.R. Sriram, E.N. Brown, S. Viswanathan, Autonomic healing of polymer composites, Nature. 409 (2001) 794–797.
[12] J.D. Rule, N.R. Sottos, S.R. White, Effect of microcapsule size on the performance of self-healing polymers, Polymer (Guildf). 48 (2007) 3520–3529.
[13] T. Yin, M.Z. Rong, M.Q. Zhang, G.C. Yang, Self-healing epoxy composites - Preparation and effect of the healant consisting of microencapsulated epoxy and latent curing agent, Compos. Sci. Technol. 67 (2007) 201–212.
[14] R.S. Trask, I.P. Bond, Biomimetic self-healing of advanced composite structures using hollow glass fibres, Smart Mater. Struct. 15 (2006) 704–710.
[15] K.S. Toohey, N.R. Sottos, J.A. Lewis, J.S. Moore, S.R. White, Self-healing materials with microvascular networks, Nat. Mater. 6 (2007) 581–585.
[16] T.K. Gupta, Crack Healing and Strengthening of Thermally Shocked Alumina, J. Am. Ceram. Soc. 59 (1976) 259–262.
[17] G. Bandyopadhyay, J.T.A. Roberts, Crack healing and strength recovery in UO2, J. Am. Ceram. Soc. 59 (1976) 415–419.
[18] S. K. Ghosh, Self-healing materials: fundamentals, design strategies, and applications, John Wiley & Sons, Verlag GmbH & Co. KGaA, Weinheim, 2009.
[19] K.W. Gao, L.J. Qiao, W.Y. Chu, In situ TEM observation of crack healing in α-Fe, Scr. Mater. 44 (2001) 1055–1059.
[20] D. Wei, J. Han, Z.Y. Jiang, C. Lu, A.K. Tieu, A study on crack healing in 1045 steel, J. Mater. Process. Technol. 177 (2006) 233–237.
[21] J. Han, G. Zhao, Q. Cao, Internal crack recovery of 20MnMo steel, Sci. China Ser. E Technol. Sci. 40 (1997) 164–169.
[22] R.S. Xin, J. Kang, Q.X. Ma, S. Ren, H.L. An, J.T. Yao, J. Pan, L. Sun, Evolution Behaviors and Mechanisms of Internal Crack Healing in Steels at Elevated Temperatures, Metall. Mater. Trans. A. 49A (2018) 4906–4917.
[23] Y. Zhou, J. Guo, M. Gao, G. He, Crack healing in a steel by using electropulsing technique, Mater. Lett. 58 (2004) 1732–1736.
[24] H. Song, Z.J. Wang, X.D. He, J. Duan, Self-healing of damage inside metals triggered by electropulsing stimuli, Sci. Rep. 7 (2017) 1–11.

[25] K. Laha, J. Kyono, T. Sasaki, S. Kishimoto, N. Shinya, Improved creep strength and creep ductility of type 347 austenitic stainless steel through the self-healing effect of boron for creep cavitation, Metall. Mater. Trans. A. 36 (2005) 399–409.
[26] G.S. Firstov, J. Van Humbeeck, Y.N. Koval, High-temperature shape memory alloys Some recent developments, Mater. Sci. Eng. A. 378 (2004) 2–10.
[27] D. Wei, J. Han, A.K. Tieu, Z. Jiang, Simulation of crack healing in BCC Fe, Scr. Mater. 51 (2004) 583–587.
[28] N. Shinya, J. Kyono, K. Laha, C. Masuda, Self healing of creep damage through autonomous boron segregation and boron nitride precipitation during high temperature use of austenitic stainless steels, in: Proc. First Int. Conf. Self Heal. Mater., The Netherlands, 2007: pp. 1–9.
[29] R.N. Lumley, G.B. Schaffer, Precipitation induced densification in a sintered Al-Zn-Mg-Cu alloy, Scr. Mater. 55 (2006) 207–210.
[30] R.N. Lumley, R.G. O'Donnell, I.J. Polmear, J.R. Griffiths., Enhanced fatigue resistance by underageing an Al-Cu-Mg-Ag alloy, Mater. Forum. 29 (2005) 256–261.
[31] R.P. Wool, Self-healing materials: a review, Soft Matter. 4 (2008) 400.
[32] F. Tavangarian, D. Hui, G. Li, Crack-healing in ceramics, Compos. Part B Eng. 144 (2018) 56–87.
[33] M.E. Alam, S. Pal, D. Gragg, K. Fields, N.J. Cunningham, G.R. Odette, D.T. Hoelzer, S.A. Maloy, Annealing treatments to heal microcracks in 14YWT NFA-1 and their effects on microstructural and mechanical behavior, Fusion React. Mater. Progr. Semiannu. Prog. Rep. DOE0313/62 (2017) 45–60.
[34] M.L. Hribernik, G.R. Odette, M.Y. He, On the intrinsic initiation and arrest cleavage fracture toughness of ferrite, DOE Fusion React. Mater. Progr. Semiannu. Prog. Rep. DOE0313/40 (2006) 74–79.
[35] P. Klugkist, C. Herzig, Tracer diffusion of titanium in α-iron, Phys. Status Solidi. 148 (1995) 413–421.

Side note:

An elaborated and more complete version (including details microstructural and mechanical properties) of this new microcrack healing mechanism titled: "On a New Ti-carbooxinitride Redistribution Driven Microcrack Healing Mechanism in an Annealed 14YWT Nanostructured Ferritic Alloy" by M. E. Alam*, S. Pal, N. J. Cunningham, G. R. Odette has been submitted to Acta Materialia (currently under review).

3. CERAMIC COMPOSITE STRUCTURAL MATERIAL DEVELOPMENT

3.1 ADDITIVE MANUFACTURING OF SILICON CARBIDE FOR NUCLEAR FUSION APPLICATIONS—Takaaki Koyanagi, Kurt Terrani, Yutai Katoh (Oak Ridge National Laboratory), Shay Harrison (Free Form Fibers), Jian Liu (PolarOnyx, Inc.)

Abstract of a manuscript in Journal of Nuclear Materials 543 (2021) 152577

Additive manufacturing (AM) is a rapidly evolving technology being considered for nuclear applications. A special focus on AM to fabricate nuclear-grade silicon carbide (SiC) is explored in this study. Combinations of AM techniques and traditional SiC densification methods have enabled new designs of SiC components with complex shapes. The fabrication of such SiC components was explored by three different AM methods: (1) binder jet printing followed by chemical vapor infiltration, (2) laser chemical vapor deposition, and (3) selective laser sintering of SiC powders. The existing data on the effects of neutron irradiation on the properties of traditional SiC ceramics suggest the most promising additively manufactured SiC materials. A crystalline SiC system with minimal secondary phases is suggested to minimize irradiation-induced strength degradation and dimensional instability at high neutron doses. In contrast, amorphous-like SiC formed by pre-ceramic polymer pyrolysis in an AM process is likely to undergo significant dimensional instability and property changes under irradiation. AM incorporating reaction sintering of silicon and carbon, and other sintering methods using large amounts of non-SiC phases, will lead to detrimental consequences under irradiation: significant strength degradation due to spontaneous cracking attributed to the differential swelling of SiC and the secondary phases. The development of AM technology for nuclear-grade SiC materials is still immature. Further processing optimization and material characterization, including irradiation studies, are required for deployment.

4. PLASMA-FACING AND HIGH HEAT FLUX MATERIALS AND COMPONENT TESTING

4.1 INCORPORATING CRYSTALLOGRAPHIC ORIENTATION INTO THE STUDY OF TUNGSTEN HEAVY ALLOY BOUNDARIES—James V. Haag IV, Mitsu Murayama (Virginia Tech), Danny Edwards, Jing Wang, Wahyu Setyawan (Pacific Northwest National Laboratory)

OBJECTIVE

The goal of this study is to apply a combined imaging and diffraction-based approach to couple tungsten heavy alloy boundary geometry with crystallographic orientation.

SUMMARY

In this study we have prepared specimens of a tungsten heavy alloy (WHA) for transmission electron microscopy (TEM) analysis. Specimens were taken from a thermomechanically treated WHA specimen and thinned to electron transparency for the purpose of observing grain orientation and grain boundary structures. The data acquired shines light on the crystallographic matching found at both tungsten-tungsten and tungsten-ductile phase boundaries in the bi-phase composite as well as the structure at those boundaries. TEM observation is also used to aid making assertions on the nature of the deformation experienced during thermomechanical treatment. The resulting data helps in untangling the complex formation of this microstructure and aids in the characterization of non-trivial boundary structures by allowing the coupling of specimen geometry and crystallography in the description of material behavior.

PROGRESS AND STATUS

Introduction

Tungsten heavy alloys are the subject of ongoing research for their viability as plasma facing material components (PFMCs) in fusion reactors [1-5]. This is due to their increased ductility over that of polycrystalline tungsten, while retaining many of the useful properties of tungsten. Optimization of mechanical properties through the tailoring of processing conditions, composition, and microstructure have led to alloys with remarkable physical behavior [1-3]; yet in the roughly 50-year time frame in which these alloys have been discussed in literature, there is limited data available on grain and phase boundary structures as well as comparative strengths in these systems, especially in regards to crystallographic orientation. Recent work in modelling these interfaces from a lattice matching approach has revealed deeper insight about boundary strengths [5], but has thus far, there is a seeming lack of comprehensive TEM analysis of these boundaries. This is in part due to the difficulty in preparing WHAs for nanoscale characterization analysis due to their multi-phase nature and the difference in mechanical properties between the constituent BCC tungsten phase and the FCC Ni-Fe-W solid solution phase. After prior work in preparing TEM foils with minimal surface damage from ion milling; specimens can be produced with large thin regions for TEM analysis, allowing for the analysis of dozens of boundaries per specimen. As such, this study has been designed to focus in on the grain and phase boundary structures in WHAs at the TEM length scale for the purpose of determining the geometric and crystallographic contributions to observed boundary strength.

The chosen alloy is a 90W-7Ni-3Fe (wt.%) tungsten heavy alloy produced by Pacific Northwest National Laboratory (PNNL) which has been hot-rolled to achieve a brick-and-mortar microstructure [2-3]. This sample exhibits a bi-phase composite structure of a BCC tungsten-rich ‘brick’ phase and an FCC Ni-Fe-W solid solution ‘mortar’ phase. Prior in- and ex-situ characterization analyses have been conducted on this sample primarily utilizing scanning electron microscopy (SEM) and electron backscattered diffraction (EBSD) for the analysis of bulk behavior [4]. As an in-depth analysis of boundary structure necessitates a transition to the nanoscale, the focus in this report will be TEM characterization of the hot-rolled alloy specimens.

Experimental Procedure

A specimen was cut into a roughly 3 × 1 × 1 mm bar and mechanically ground and polished to thin the bar down to a foil measuring roughly 50 μm in thickness. The foil was then dimple ground with 1 μm diamond paste until perforation and Ar ion milled on a PIPS II at a series of sequentially decreasing energies ranging from 5 keV down to 250 eV. The resulting specimen exhibited a large circular electron transparent region around the rim of the hole from ion milling, allowing for much more statistically significant specimen analysis than a focused ion beam (FIB) lamellae specimen. It should however be noted that FIB milling a TEM specimen does allow for greater site specificity and specimen thickness control, albeit from a significantly smaller region and likely introduces a greater degree of surface damage. Analysis was then conducted on a JEOL-2100 at 200kV.

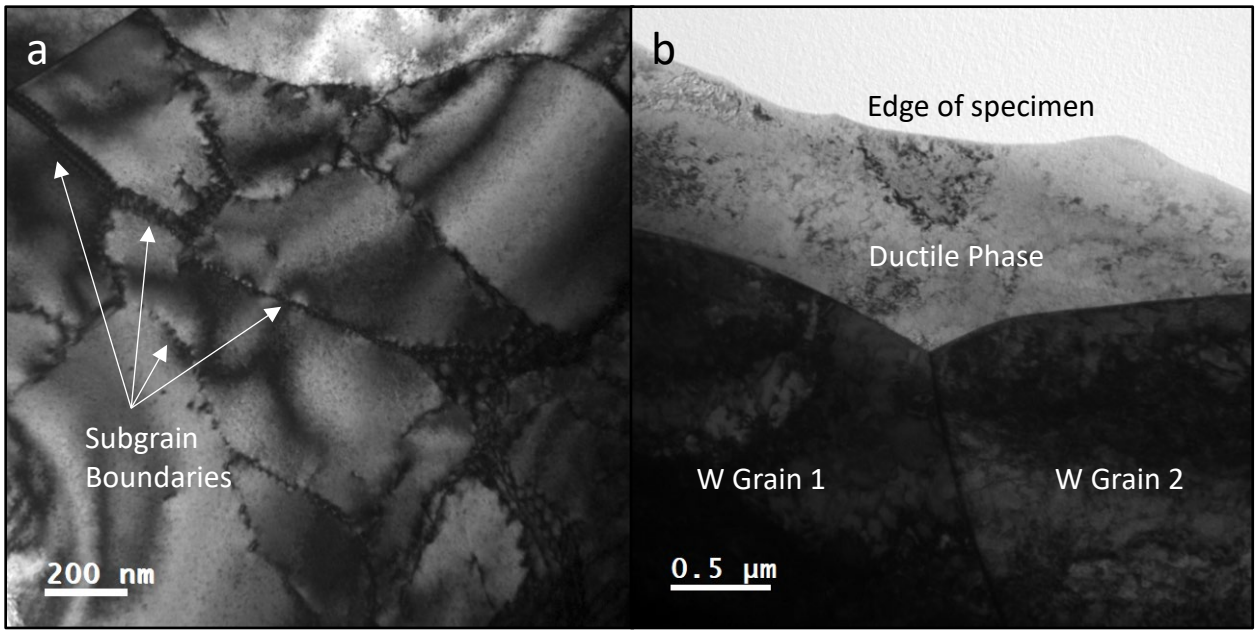

Figure 1. TEM micrographs of (a) subgrain boundaries in a tungsten phase domain and (b) heavily deformed region containing a triple junction region with the ductile phase tightening a tungsten-tungsten grain boundary.

Upon initial observation in TEM, the material appears exhibit some regions with features indicative of recovery and others retaining high dislocation densities even after hot-rolling and annealing steps. The clear presence of sharp subgrain boundary structures in the W phase with relatively low matrix dislocation densities, shown in Figure 1a, is evidence of dislocation motion and interaction; while apparent heavily deformed regions, like the one shown in Figure 1b, indicate a lack of recovery post-processing. It had previously been theorized that the material had not completely recovered post processing from acquired EBSD data, but had not been confirmed to be the case, as overly aggressive grinding and polishing conditions for EBSD sample preparation may induce surface deformation which could potentially mimic or obscure pre-existing deformation structures from processing. It should however be noted that the presence of subgrain boundary structures in the W is comparatively rare and was only noted in one single tungsten domain across the specimen. The ductile phase structure is confirmed to contain a high density of twin boundaries like the one displayed in Figure 2. This is expected to have a unique effect upon the deformation behavior of the ductile phase, and the composite structure as a whole, as materials with a high density of Σ3 (twin) type grain boundaries exhibit exemplary strength and ductility. In addition to the high density of twin boundaries, the ductile phase shows an affinity for W-W boundaries. At a majority of observed tungsten

grain boundaries, the boundary appears to have been tightened by the ductile phase. This is evident in Figure 1b as the contour of the ductile phase proceeding inward towards the tungsten grain boundary plane.

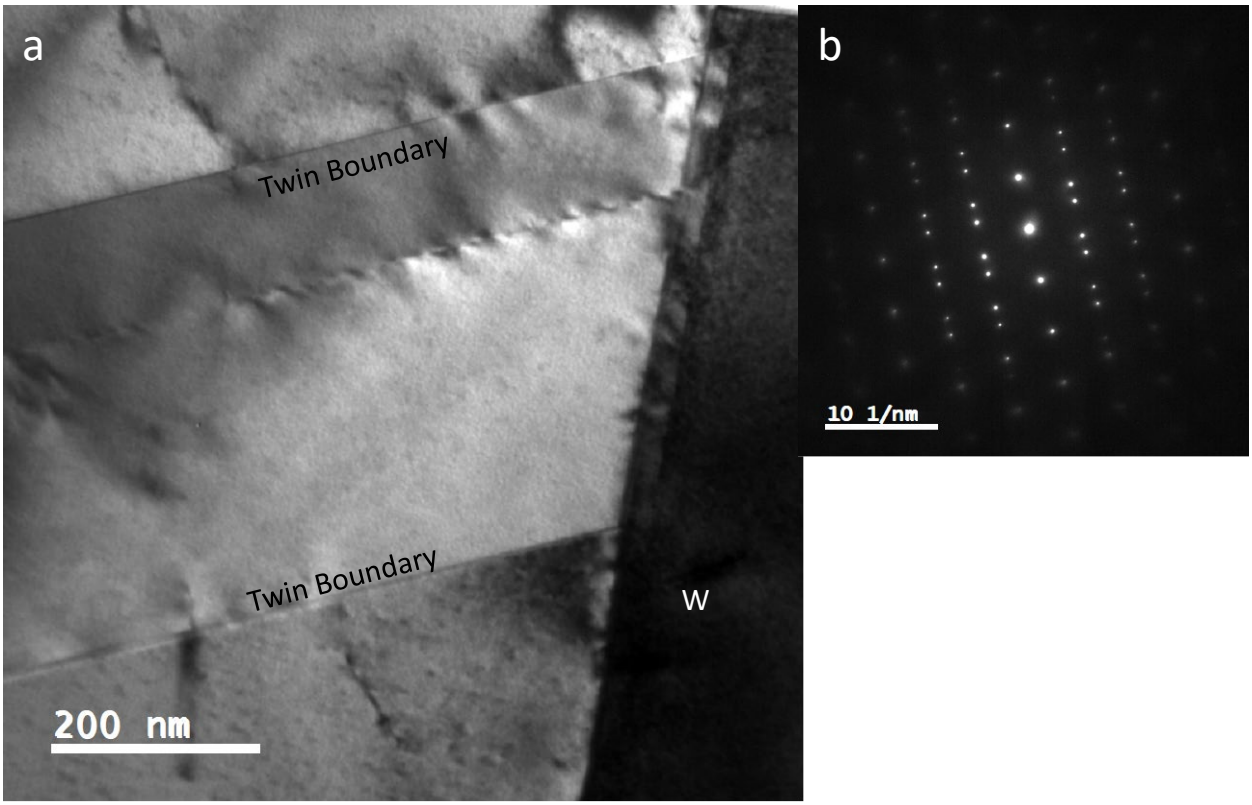

Figure 2. (a) Bright field TEM image of twin in ductile phase touching W domain. (b) [110] zone axis diffraction pattern acquired at ductile phase twin boundary showing mutual (111) plane.

The interphase boundary is of particular interest due to its apparent strength in in-situ experimental observations as well as density functional theory modelling of interphase boundary fracture energies [4-5]. Interphase boundary orientation mapping was conducted to search for any evidence of preferred orientation relationships (ORs) throughout the sample, as it is theorized that a high degree of lattice matching would lead to a correspondingly low interfacial energy, and high interfacial strength. To determine if any such predominant OR existed in the specimen, each phase at an interphase boundary of interest was tilted to multiple diffraction conditions to create a map of the crystallographic orientation. This corresponding map was then compared to the known crystallography of the specimen, BCC for W and FCC for the ductile phase, and used to determine the degree of lattice matching and catalog the OR of the observed boundary. This process is illustrated in Figure 3, and experimentally derived ORs for three different interphase boundaries have been included in Table 1.

The information collected from these boundaries seems to indicate that there is no singular preferred orientation relationship between the tungsten and ductile phases. The commonly discussed BCC-FCC ORs in literature like Bain, Kurdjumov-Sachs, Nishiyama-Wasserman, Greninger-Troiano, and Pitch are often observed in precipitation structures or phase transformation [6]; but the thermomechanical history and complex stress-state that give rise to the microstructure in this alloy introduce a level of complexity in the relative phase orientations which is difficult to predict and model. Yet there appears to be a high degree of low-index lattice plane matching present at the interphase boundaries observed. In an effort to explain this behavior, it is posited that it is more prudent to adopt the edge-to-edge matching approach in the study of

interphase boundary structure and energy discussed by Reynolds *et al*. in [7] in Ti alloy transformation structures to describe plane matching, rather than hunt for a single dominant boundary OR.

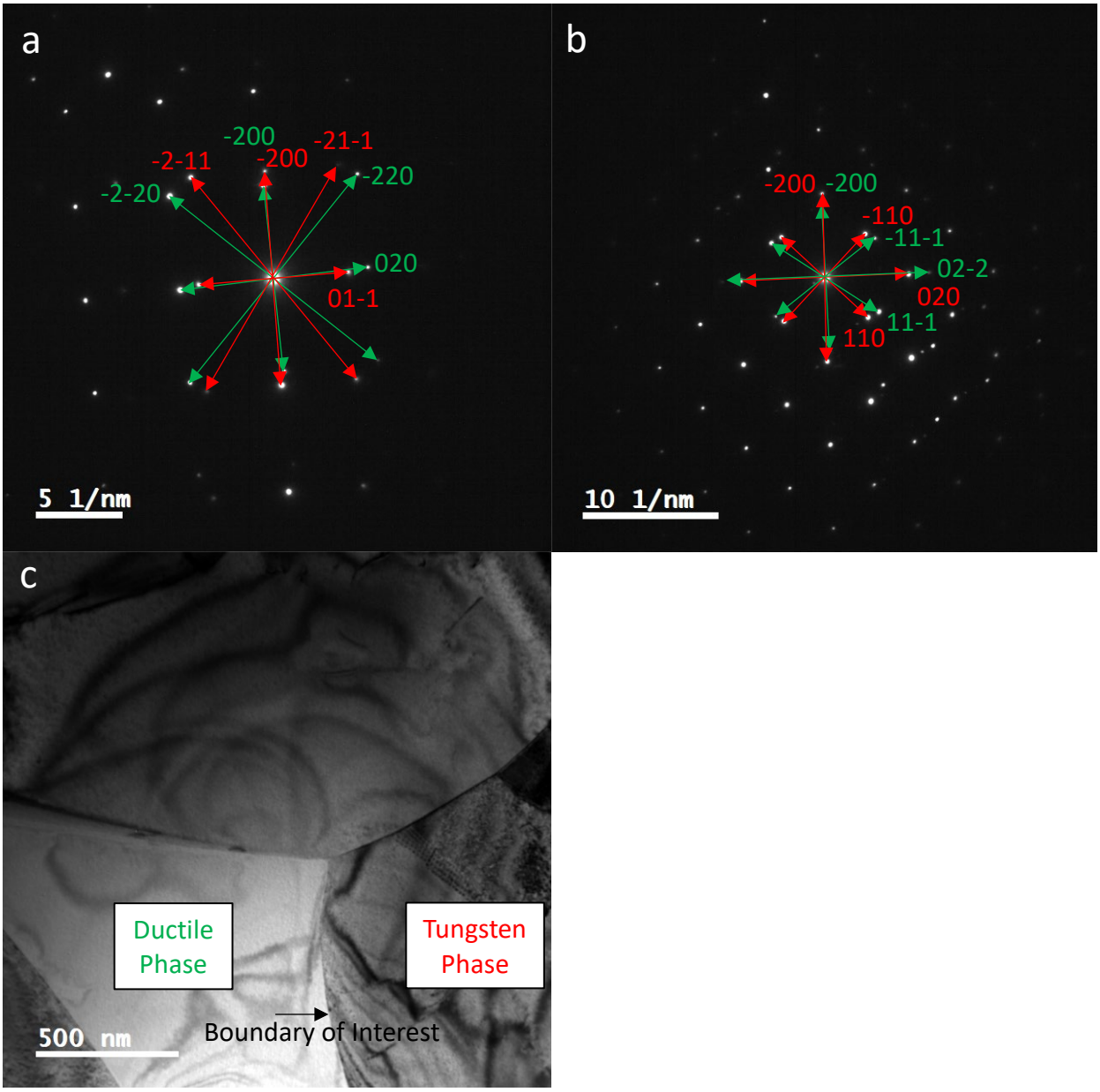

Figure 3. Crystallographic orientation mapping for interphase boundary. (a) Diffraction pattern of boundary of interest with W (in red) on a [011] zone axis and the ductile phase (in green) on a [001] zone axis. (b) Diffraction pattern of same boundary of interest at different tilt conditions with W (in red) on a [001] zone axis and the ductile phase (in green) on a [011] zone axis. (c) Bright field TEM image of region of interest.

Table 1. Experimentally determined orientation relationships (ORs) of W/ductile-phase domains. At this time, only the OR between the domains is indexed, while the planes of the boundaries will be determined in future research.

OR	Direction 1	Direction 2
1	[011]BCC // [001]FCC and [001]BCC // [011]FCC	[200]BCC // [200]FCC and [020]BCC // [02-2]FCC
2	[001]BCC // [013]FCC	[110]BCC // [1-31]FCC
3	[001]BCC // [001]FCC	[110]BCC // [200]FCC

To further characterize the nature of the interphase boundary structure, it is also necessary to describe the boundary coherency. While a more detailed characterization study of boundary coherency is in process, initial evidence suggests that the boundaries take on a partially coherent or semi-coherent structure. This is corroborated by the degree of lattice matching that has been observed as well as evidence of an array of misfit dislocations at the interphase boundary. The boundary shown in Figure 4 exhibits features indicative of a series of dislocations present at the at the interface between the tungsten and ductile phases. This would seem to show a degree of matching between the two different crystal structures and lattice constants that is accommodated by a repeating array of misfit dislocations. The highlighted boundary region in Figure 4 exhibits a short-range array spaced approximately 16.2 nm apart, and was found to have an OR very close to W [001][110] // ductile phase [001][200] (OR index 3 in Table 1), note the boundary planes will be determined in future research. The contoured nature of the boundary and selected imaging conditions make it difficult to truly observe the periodicity of the structure along the boundary and additional work is necessary to obtain a more reliable measurements of dislocation spacing and determine the nature of the dislocations along the interface.

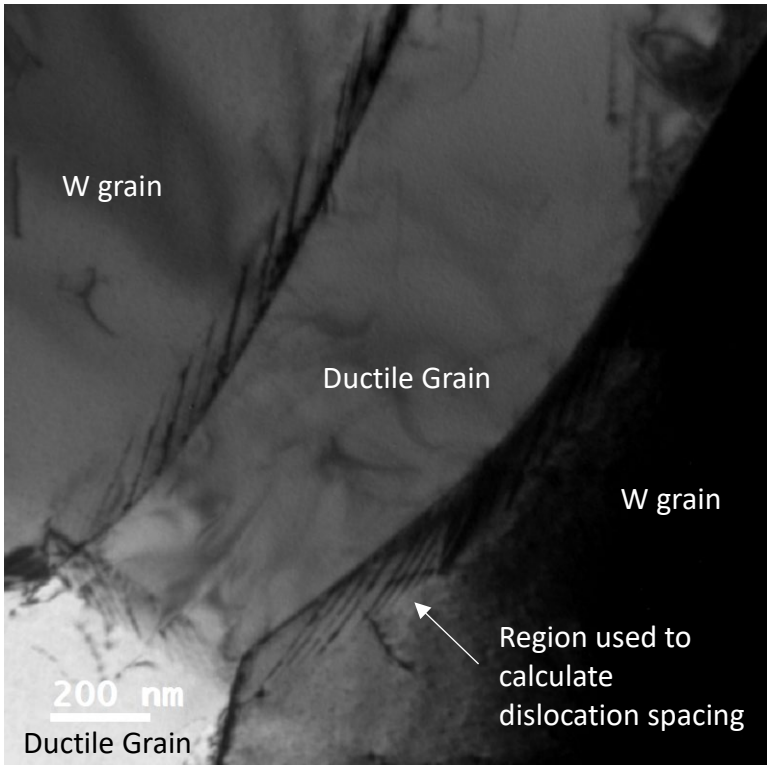

Figure 4. Bright field TEM image of apparent dislocations at the interphase boundary. Arrow points towards region in which interfacial dislocation spacing was calculated.

Although this information aids in developing a more robust framework for the description of these interfaces, it is theorized that to truly 'solve' the interface and its strength would take additional considerations over what has been described here. Namely the complex chemistry of the WHA and contoured nature of the phase boundary cause difficulties in the characterization of the interfacial region. While the BCC phase can likely be approximated as pure tungsten due to the limited solubility of Ni and Fe into the tungsten lattice, the ductile phase holds a significant fraction of tungsten in its lattice. The ductile phase has been confirmed to hold concentrations of tungsten upwards of 10 at.% in the bulk, with a diffuse interphase boundary region exhibiting a ~5-10nm wide chemical gradient transition region between the W and ductile phases. Thus, creating a complex FCC Ni-Fe-W solid solution phase that changes significantly in chemistry, and likely lattice spacing, as it approaches the interphase boundary. An effort to fully characterize the interphase boundary and its subsequent strength would require a joint experimental and modelling based approach to account for the combined effects of boundary geometry, crystallographic orientation, and chemistry on interfacial energy. Additional analysis of interphase boundary structure is in process for an un-rolled specimen of the same composition post liquid phase sintering. It is possible that a high incidence of low-index lattice matching will also be observed in this alloy as it is hypothesized that during liquid phase sintering, solid tungsten particles act as nucleation sites for liquid Ni-Fe-W growth potentially leading to solidification along defined planes based on the W domain orientation.

ACKNOWLEDGEMENTS

This research was supported by the Office of Fusion Energy Sciences, U.S. Department of Energy (DOE) under Contract DE-AC05-76RLO 1830. This work was performed at Virginia Tech and supported by Pacific Northwest National Laboratory through Subcontract 531207. The authors would also like to express their gratitude towards Chang-Yu Hung and Matthew Olszta for their assistance in electron microscopy characterization.

References

[1] M. E. Alam and G. R. Odette, "On the remarkable fracture toughness of 90 to 97W-NiFe alloys revealing powerful new ductile phase toughening mechanisms," *Acta Materialia*, vol. 186, pp. 324–340, Mar. 2020, doi: 10/ggqgkk.

[2] C. H. Henager *et al.*, "DUCTILE-PHASE TOUGHENED TUNGSTEN FOR PLASMA-FACING MATERIALS
IN FUSION REACTORS," *International Journal of Powder Metallurgy*, vol. 53, no. 2, p. 18, 2017.

[3] B. N. Nguyen, C. H. Henager, J. Wang, and W. Setyawan, "Tailoring ductile-phase toughened tungsten hierarchical microstructures for plasma-facing materials," *Journal of Nuclear Materials*, vol. 540, p. 152382, Nov. 2020, doi: 10/gg6rnz.

[4] J. V. Haag, D. J. Edwards, C. H. Henager, W. Setyawan, J. Wang, and M. Murayama, "Characterization of ductile phase toughening mechanisms in a hot-rolled tungsten heavy alloy," *Acta Materialia*, vol. 204, p. 116523, Feb. 2021, doi: 10/ghpnzr.

[5] W. Setyawan, "Density functional theory calculation of helium segregation and decohesion effect in W110/Ni111 interphase boundary," *Journal of Applied Physics,* vol. 128, 2020, doi: 10.1063/5.0011744

[6] T. J. Headley and J. A. Brooks, "A new Bcc-Fcc orientation relationship observed between ferrite and austenite in solidification structures of steels," *Metall and Mat Trans A*, vol. 33, no. 1, pp. 5–15, Jan. 2002, doi: 10/cxqjqb.

[7] W.T. Reynolds Jr. et al. "Atomic structure of high-index $\alpha_2 : \gamma_m$ boundaries in a Ti–46.54 at.%Al alloy," *Scripta Materialia,* vol. 49, pp. 405-409, May 2003, doi: 10.1016/S1359-6462(03)00307-5

4.2 TEM STUDY OF Ni^+ AND He^+ ION IRRADIATED DUCTILE-PHASE TOUGHENED TUNGSTEN—Weilin Jiang, Dalong Zhang, Alan Schemer-Kohrn, Bethany Matthews, Wahyu Setyawan (Pacific Northwest National Laboratory)

OBJECTIVE

The aim of this experimental work is to emulate ion irradiation response of a hot-rolled, ductile-phase toughened tungsten composite in a fusion power plant for the first 5 years. This study focuses on the observation and understanding of helium (He) cavity formation and distribution in the material.

SUMMARY

The response of ion irradiation in a hot-rolled, 87% thickness reduced, ductile-phase toughened tungsten composite (87R DPT W) is investigated. The composite consists of 88 wt.% W and 12 wt.% NiFeW that contains 54.68 wt.% Ni, 22.57 wt.% Fe and 22.75 wt.% W. Sequential irradiation of the composite was performed with 1.2 MeV Ni^+ ions to 2.15×10^{16} Ni^+/cm^2 and 90 keV He^+ ions to 6.5×10^{15} He^+/cm^2 at 973 K. These irradiation conditions emulate the response of 87R DPT W as the first-wall material in a conceptual fusion power plant after the first 5 years of irradiation. Preliminary TEM studies show that He cavities are formed in the irradiated 87R DPT W. Larger cavities appear in the NiFeW than W phase. There is a preferential distribution of cavities along the W/NiFeW interphase boundaries. In contrast, cavities are distributed uniformly across W/W grain boundaries. Further studies of 87R DPT W irradiated with Ni^+ ions or He^+ ions are being performed to understand the mechanisms for the He cavity distribution.

PROGRESS AND STATUS

Experimental Procedure

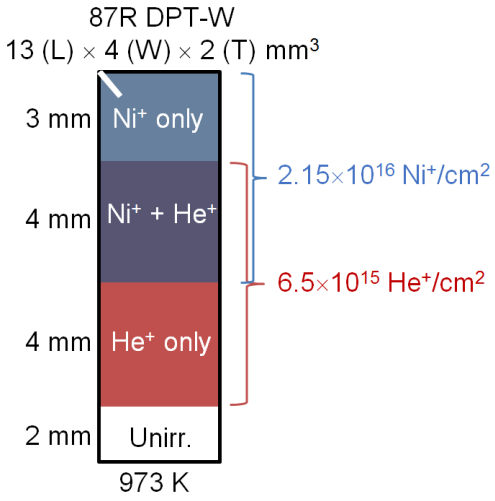

Figure 1. An illustration of an 87R DPT W composite sequentially irradiated with 1.2 MeV Ni^+ and 90 keV He^+ ions at 973 K to create 3 different irradiation regions with an unirradiated area.

The 87R DPT W (90W-7Ni-3Fe) composite used in this study was determined [1] to be 88 wt.% W and 12 wt.% NiFeW that contains 54.68 wt.% Ni, 22.57 wt.% Fe and 22.75 wt.% W. The elemental percentages in NiFeW were inadvertently reported [1,2] previously in units of at.%. As described in [2], calculations by Gilbert *et al*. [3] show that after 5-year operation of a conceptual fusion power plant at a neutron flux of 1.04×10^{15} $(n/cm^2)/s$, He concentration through elemental transmutation is 1,090 appm produced from Fe and 33.6 appm from W. He production from Ni is 2,442 appm, which is estimated based on the cross sections of Ni (99.9 mb) and Fe (44.6 mb) reactions with 14 MeV neutrons [4]. Thus, the total He

concentration in NiFeW is 1,863 appm or ~0.19 at.%. The dose in W as the first-wall material after 5-year irradiation in the conceptual fusion power plant has been estimated to be 27.4 displacements per atom (dpa) based on the data reported in [5] with a proper adjustment in the neutron flux [3].

Also as described in [2] and shown in Figure 1, sequential ion irradiation was performed in different areas of an 87R DPT W composite at 973 K, creating 3 regions of irradiation with Ni^+ ions only, Ni^++He^+ ions, and He^+ ions only. There was also an unirradiated area. 1.2 MeV Ni^+ and 90 keV He^+ ions were applied to fluences of 2.15×10^{16} Ni^+/cm^2 and 6.5×10^{15} He^+/cm^2, respectively. SIRM13 simulations [2] show that under the irradiation conditions, the peak dose is 27 dpa at 168 nm in W from Ni^+ ion irradiation and 31 dpa at 296 nm in NiFeW. For He^+ ion irradiation in NiFeW, the maximum He concentration generated is 0.39 at.% at 295 nm with the He peak well aligned with the Ni^+ ion damage peak. The He concentration is about a factor of 2 as large as that from transmutation. The irradiation condition was chosen on purpose [2] due the fact that a significant amount (assumed to be ~50%) of the implanted He atoms was released during He^+ ion irradiation at 973 K.

Preliminary Results

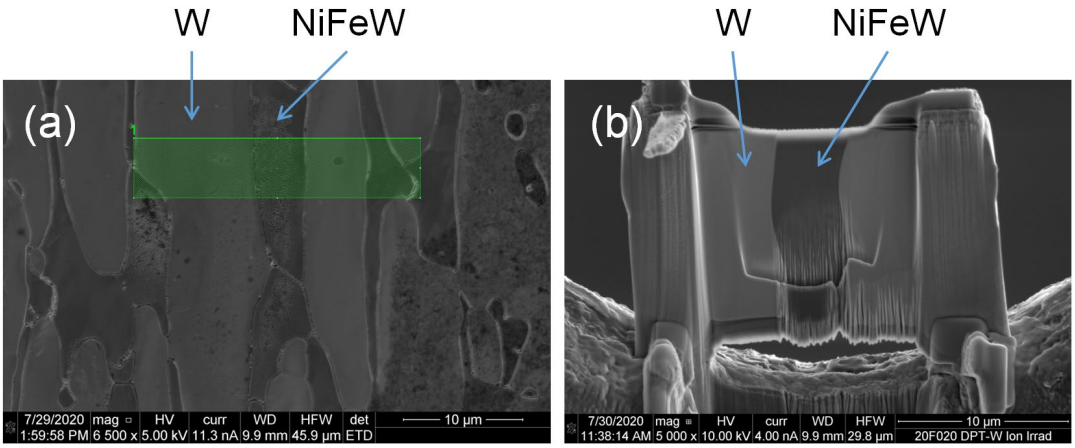

Figure 2. (a) Microstructure of an 87R DPT W composite sequentially irradiated to 2.15×10^{16} Ni^+/cm^2 and 6.5×10^{15} He^+/cm^2 at 973 K. A FIB lift-out region containing W/NiFeW grain boundaries is indicated. (b) FIB lamella from the region.

Focused ion beam (FIB) technique was used to slice a lamella in a region irradiated with both Ni^+ and He^+ ions. Figure 2(a) shows the microstructure of the composite with both W and NiFeW phases, as indicated. The lift-out is shown in Figure 2(b), where W/NiFeW interphase boundaries are clearly visible. The surface region was thinned and polished to electron transparency. As the milling rate of W is significantly lower than that of NiFeW, additional thinning of the W region was needed to obtain a more uniform thickness near the interphase boundary. The sample was examined using a Cs-aberration corrected JEOL ARM 200CF Scanning Transmission Electron Microscope (STEM) at an operating voltage of 200 kV. Figure 3 shows a general view of the surface region, where He cavities are distributed. Apparently, the cavities in NiFeW are much larger than in W. On the average, the cavity size is ~7 nm in NiFeW as compared to ~2 nm in W. There is a preferential distribution of cavities along the interphase boundary, as revealed by Figure 3. These agglomerated cavities have an average dimension of ~4 nm between the cavity sizes in the NiFeW and W. It is noticed that there are cavities in NiFeW in a much deeper region (~400 nm) than the SRIM13 prediction (296 nm). Similarly, cavities in W are also observed in a region beyond the SRIM13 predicted depth (168 nm). This behavior is attributed to the diffusion of mono-vacancies and He atoms during ion irradiation of 87R DPT W at 973K. Further quantitative analysis of the cavity size distribution in the irradiated composite is being performed using a similar procedure recently reported in [6], where the observed cavity size under defocused conditions was corrected.

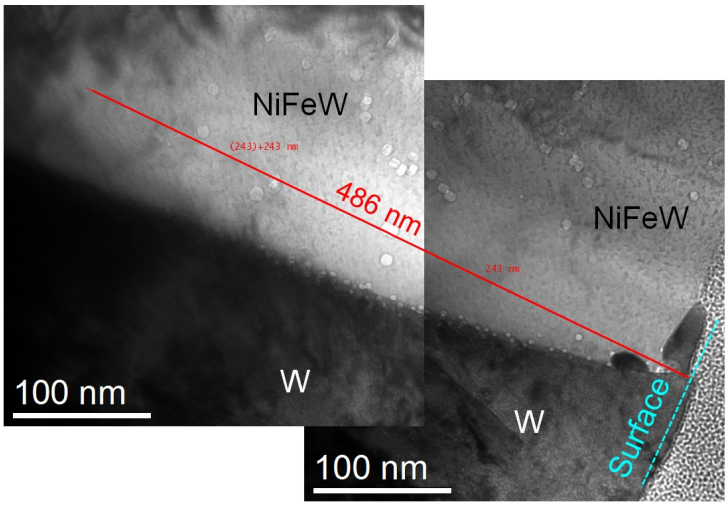

Figure 3. Bright-field TEM images showing a general view of the cavity distribution near a grain boundary in an 87R DPT W composite sequentially irradiated to 2.15×10^{16} Ni^{+}/cm^{2} and 6.5×10^{15} He^{+}/cm^{2} at 973 K.

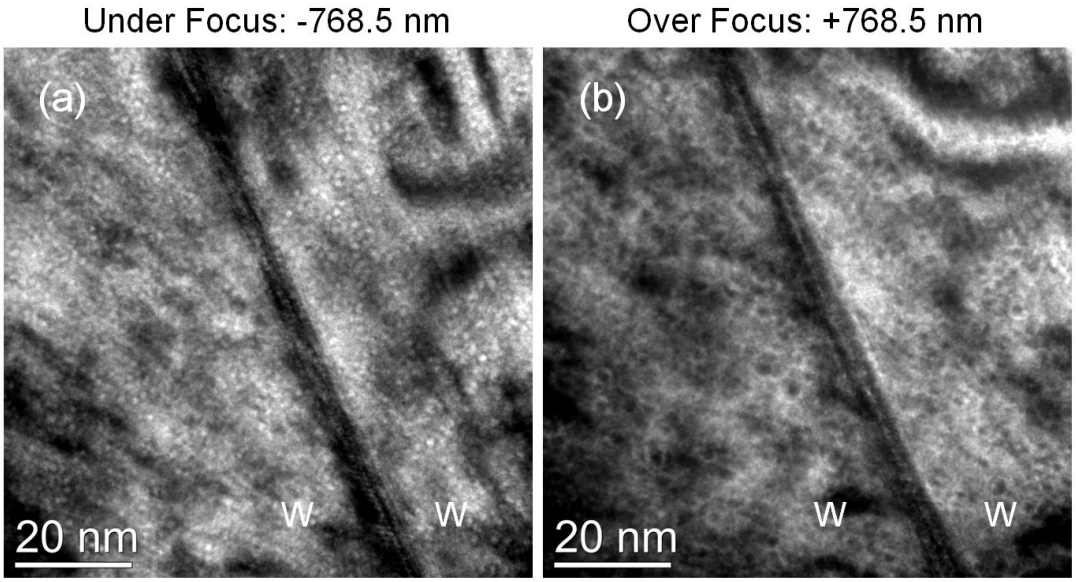

Figure 4. Bright-field TEM images in (a) under focus and (b) over focus conditions showing the cavity distribution near a W/W grain boundary of an 87R DPT W composite sequentially irradiated to 2.15×10^{16} Ni^{+}/cm^{2} and 6.5×10^{15} He^{+}/cm^{2} at 973 K. The image center is located at the depth of ~200 nm.

Figure 4 shows the cavity distribution near a W/W grain boundary at the depth of ~200 nm from the surface. The change in contrast from bright in under focus to dark in over focus images suggests that the observed features are defects of the cavity type. Additional STEM-EDS mapping (data not shown) was also performed, which provides a confirmation of the results. In contrast to the interphase boundary in Figure 3, there is no preferential distribution of cavities along the W/W grain boundary. Instead, cavities are distributed uniformly across the boundary. El-Atwani *et al*. [7] have observed a uniform distribution of He bubbles near the grain boundaries in both ultrafine-grained and nano-grained W irradiated with He^{+} ions to 1.5×10^{22} He^{+}/m^{2} at room temperature. However, the same study shows that bubbles decorating grain boundaries are formed in the materials irradiated to 3.6×10^{19} He^{+}/m^{2} and higher at 1223 K. Further investigations are planned for the cavity formation in 87R DPT W as a function of irradiation temperature.

In addition, the irradiated microstructure in W has been carefully examined by both TEM and STEM-EDS. The results do not provide any evidence for Ni precipitation in W under the irradiation conditions, where SRIM13 predicts a maximum Ni concentration of 0.98 at.% in W [2].

FUTURE WORK

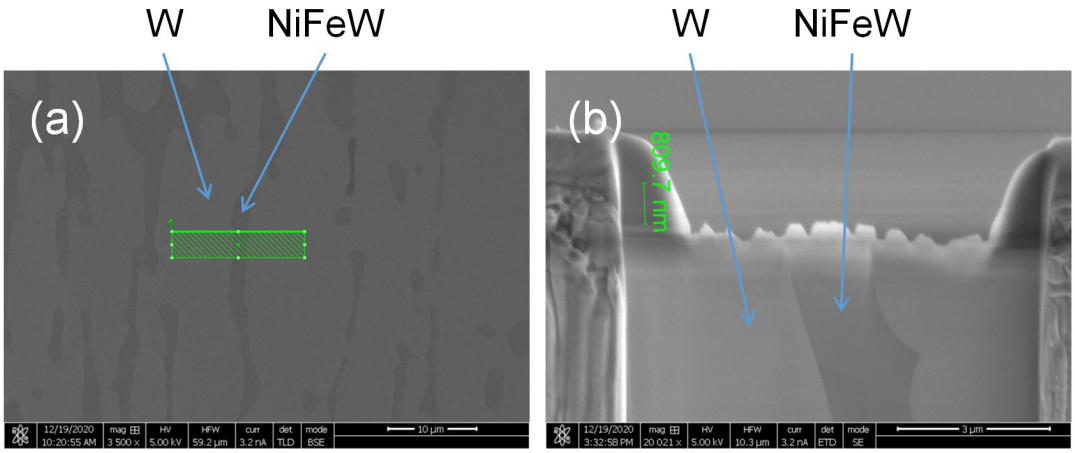

Figure 5. (a) Microstructure of an 87R DPT W composite irradiated to 2.15×10^{16} Ni^{+}/cm^{2} at 973 K. A FIB lift-out region containing W/NiFeW grain boundaries is indicated. (b) FIB lamella from the region.

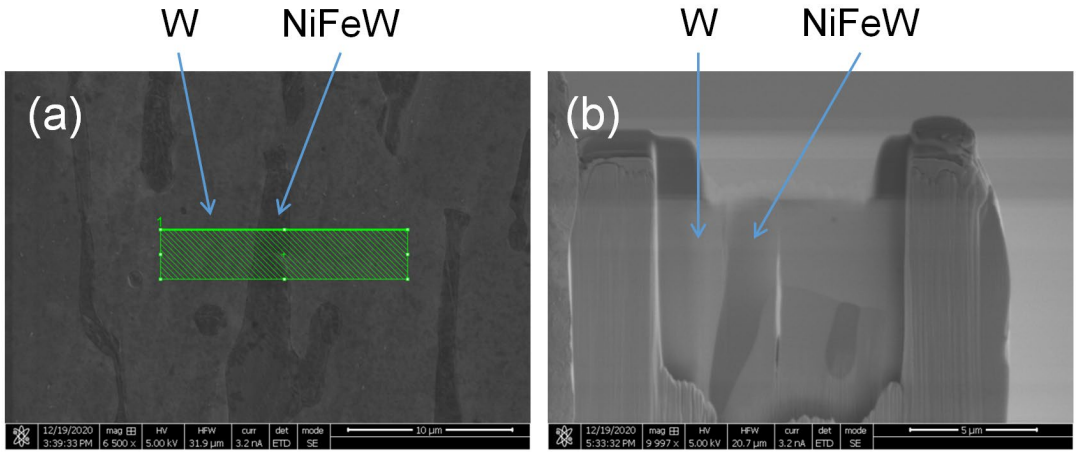

Figure 6. (a) Microstructure of an 87R DPT W composite irradiated to 6.5×10^{15} He^{+}/cm^{2} at 973 K. A FIB lift-out region containing W/NiFeW grain boundaries is indicated. (b) FIB lamella from the region.

A previous study [7] has indicated that vacancy generation and migration are needed to enhance trapping of He at W grain boundaries. Vacancies can enhance bubble growth by increasing the He mobility through the W matrix in the form of helium–vacancy complexes. Once in the boundaries, both the He and vacancies can migrate and agglomerate to form bubbles. In order to study the mechanisms responsible for the preferential formation of He cavities along the interphase boundaries in 87R DPT W, two additional FIB lift-outs from regions irradiated with only Ni^{+} and only He^{+} ions have also been prepared, as shown in Figures 5 and 6, respectively. Both contain W/NiFeW interphase boundaries. Further microscopy studies include (1) possible formation and preferential distribution of voids in Ni^{+} ion irradiated 87R DPT W, (2) possible formation of He bubbles in He^{+} ion irradiated 87R DPT W although the He ion fluence is relatively low, and (3) possible interactions between He atoms and vacancies or trapping of He atoms at voids or vacancy

clusters during ion irradiation at 973 K. The combined datasets from the single ion irradiations and the sequential ion irradiation will help better understand the mechanisms for the cavity formation and distribution in 87R DPT W composites.

ACKNOWLEDGEMENTS

This research was supported by the Office of Fusion Energy Sciences, U.S. Department of Energy and performed at PNNL under Contract DE-AC05-76RL01830. We are grateful to Charles Henager at PNNL for providing the 87R DPT W sample and to Xuemei Wang, Tianyao Wang and Zhihan Hu at Texas A&M University (TAMU) for performing the ion irradiation for this study.

References

[1] W. Jiang, N. Overman, T. Varga, W. Setyawan, C.H. Henager Jr., Fusion Materials Semiannual Progress Report for Period Ending December 31, 2019, DOE/ER-0313/67, U.S. Department of Energy, 86.
[2] W. Jiang, W. Setyawan, K. Kruska, L. Kovarik, D. Zhang, Fusion Materials Semiannual Progress Report for Period Ending June 30, 2020, DOE/ER-0313/68, U.S. Department of Energy, 96.
[3] M.R. Gilbert, J.-Ch. Sublet, Neutron-induced transmutation effects in W and W-alloys in a fusion environment, Nucl. Fusion 51 (2011) 043005.
[4] Fusion Evaluated Nuclear Data Library Ver.3.1d (FENDL-3.1d) at https://www-nds.iaea.org/fendl/.
[5] M.R. Gilbert, S.L. Dudarev, S. Zheng, L.W. Packer, J.-Ch. Sublet, An integrated model for materials in a fusion power plant: transmutation, gas production, and helium embrittlement under neutron irradiation, Nucl. Fusion 52 (2012) 083019.
[6] W. Jiang, Y.Y. Zhu, L.M. Zhang, D.J. Edwards, N.R. Overman, G. Nandipati, W. Setyawan, C.H. Henager Jr., R.J. Kurtz, Dose rate effects on disordering rate and void growth in self-ion irradiated tungsten, submitted to J. Nucl. Mater. 2020.
[7] O. El-Atwani, J.A. Hinks, G. Greaves, S.S. Harilal, A. Hassanein, Helium bubble formation in ultrafine and nanocrystalline tungsten under different extreme conditions, J. Nucl. Mater. 458 (2015) 216.

4.3 MICROSTRUCTURE-MECHANICAL PROPERTY CORRELATION IN DUCTILE PHASE TOUGHENED W-NiFe HEAVY ALLOY—Jing Wang, David Collins, Nicole R. Overman, Ramprashad Prabhakaran, Ziqing Zhai, Wahyu Setyawan, Charles H. Henager (Pacific Northwest National Laboratory)

OBJECTIVE

The objective of the project is to understand the deformation behavior of ductile phase toughened tungsten heavy alloys, such as W-NiFe, for applications in fusion reactor divertor and plasma-facing-components.

SUMMARY

This report summarizes the progress in investigating microstructure-mechanical property correlation in ductile phase toughened (DPT) W-NiFe alloys at PNNL. Preliminary microstructural characterization on the samples was performed using a scanning electron microscope (SEM) equipped with an electron back-scattering diffraction (EBSD) system. Current mechanical testing focused on tensile evaluation and assessment of stress-strain curves to facilitate Finite Element model (FEM) development. This report is focused on the preliminary results of boundaries and the fractography in W-NiFe heavy alloys. We found both W phase and NiFe phase were refined due to hot-rolling, and a significant amount of ∑3 type boundaries appeared. No dominant orientation relationships were found between FCC NiFe phase and BCC W phase and further exploration will be needed. The yield strength of DPT W was found roughly proportional to the inverse of grain sizes, however due to the refinement of both W and NiFe phases, it is difficult to deconvolute the contribution from individual phase. The ultimate tensile strength and total elongation were found correlate with contiguity on the plane perpendicular to crack path plane. More detailed analysis on the fractured surfaces and tested specimens will be needed to gain quantitative correlations between microstructure features and mechanical properties.

PROGRESS AND STATUS

Introduction

Ductile phase toughening (DPT) is a fracture toughness improvement concept being used to develop tungsten-based composites for fusion reactor divertor and plasma facing materials. Tungsten is a promising candidate material for fusion reactor component applications due to its excellent high temperature strength, low sputtering rate, and high melting temperature [1, 2]. However, the potential application of tungsten as structural material is limited due to its low ductility, which could further degrade after irradiation [3]. Introducing a ductile phase for developing W composite could serve as an alternative route to overcome its limitations.

Previously, W-Cu composite materials have been investigated, and it is found that the ductile phase could form bridges near crack tips to enhance fracture toughness of W-Cu composites [4, 5]. A finite element model was developed for understanding toughening mechanism (Dynamic Bridging Model) and for predicting load-displacement curves and crack propagation patterns (Finite Element Continuum Model) [6, 7]. Although W-Cu composites are a good starting model system for exploration, they are not suitable for fusion reactor environment due to low melting point of the ductile Cu phase. An alternative system of W-Ni-Fe composites was proposed and studied.

90W-NiFe as-received samples, in which W powders were embedded in a Ni-Fe matrix, were hot rolled at PNNL to 62%, 74% and 87% thickness reduction to attain a lamellar structure. In FY19 and FY20, efforts to collect experimental data to understand the effects of hot rolling and deformation behavior of DPT W-NiFe alloys are continued. This report summarizes the progress on mechanical testing and microstructural characterization of the as-received 90W, 95W and 97W, and hot-rolled 90W to 87% thickness reduction. The specimen matrix in this report is listed in Table 1.

Table 1. Specimen matrix in this report

Specimen ID	Details
90W-0R	90 wt% W, as received, powder purchased from MiTech, sintered at PNNL
90W-87R-Plan	90 wt% W, hot rolled to 87% thickness reduction, TD-RD orientation, along RD
90W-87R-RD	90 wt% W, hot rolled to 87% thickness reduction, ND-RD orientation, along RD

Experimental Procedure

Microstructural Characterization

The SEM and EBSD examinations on as-received samples were carried out using a JEOL 7600 field emission SEM at PNNL. Samples for characterization were polished to a 0.05 μm colloidal silica finish. A low-angle backscatter electron (BSE) detector was utilized to examine the general microstructure at various locations. EBSD was performed using the Oxford Symmetry detector to acquire W grain size distributions and orientations. The results were processed and analyzed using the AZtec software package from the Oxford Instruments. Fractography was performed in a FEI Quanta 600 SEM using both secondary and backscattered electron signals.

Mechanical Testing

The mechanical properties were characterized using tensile testing as opposed to 3- or 4-point bend testing as the former is considerably simpler and therefore more favorable for model development. Current tests are focused on acquiring strain-stress curves on un-notched tensile specimens, while notched tensile sample testing will be performed in the future to characterize fracture toughness properties. Miniature tensile specimens (SSJ3) were fabricated via EDM from the as-received bulk materials into the geometry shown in Figure 1. The samples were tested at room temperature using an Instron 5582 servo-mechanical test frame equipped with an Epsilon ONE optical extensometer.

In order to create a more accurate and comprehensive model, it is necessary to test these materials under a wide range of deformation rates. For this study, the effects of testing at three different displacement rates (0.1, 1, and 10 micron/s crosshead speed) were explored, and the corresponding strain rates are listed in the results section. The slowest rate was chosen because on a per second basis it is approximately twice the displacement resolution of the test frame (~0.06 microns), which would mitigate the “stair step” pattern that is often seen in servo-mechanical test frames at extremely low displacement rates. The fastest speed was set to two orders of magnitude higher in order to produce significantly contrasting data. To perform the tests, the samples were first preloaded up to 20N, then loaded at the prescribed displacement rate until failure. The resulting data was then smoothed, reduced to approximately 100 points, and plotted.

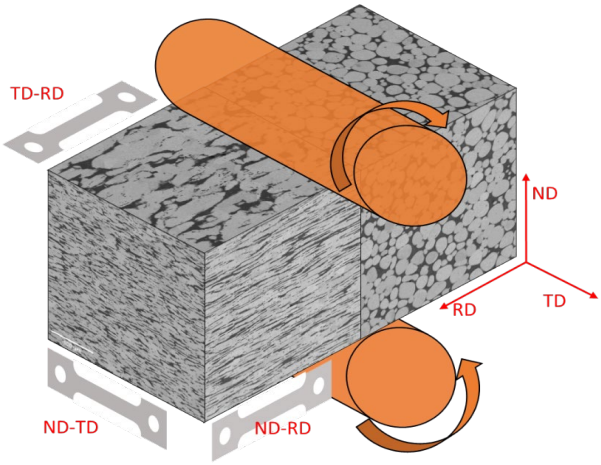

Figure 1. Tensile Specimen Orientations in 90W-87R [8]. The 90W-87R-Plan features the TD-RD orientation while 90-87R-RD features ND-RD direction. (RD = Rolling Direction, TD = Transverse Direction, ND = Normal Direction).

Preliminary Results

Microstructure

More detailed overviews of the general microstructure of W-NiFe alloy samples have been presented in previous reports [9, 10]. Figure 2 shows the microstructure of surface of as-sintered W-NiFe (90W-0R) specimens, surfaces of rolled W-NiFe (TD-RD for 90W-87R-Plan and ND-RD for 90W-87R-RD, as illustrated in Figure 1). The microstructure resembles two typical phases in this set of materials: a NiFe phase, which serves as the ductile matrix; and a W phase, which provides strength and high temperature mechanical performance. It shows that along the rolling direction, the W phase deforms significantly into a plate-like structure. In the as-sintered 90W-0R, the W-phase is mostly spherical-like and some W-W grain boundaries exists, while in the hot-rolled W-NiFe samples, the W-phase deformed into plate-like morphology. The NiFe ductile phase shows significant grain refinement in the hot-rolled samples compared to as-sintered ones.

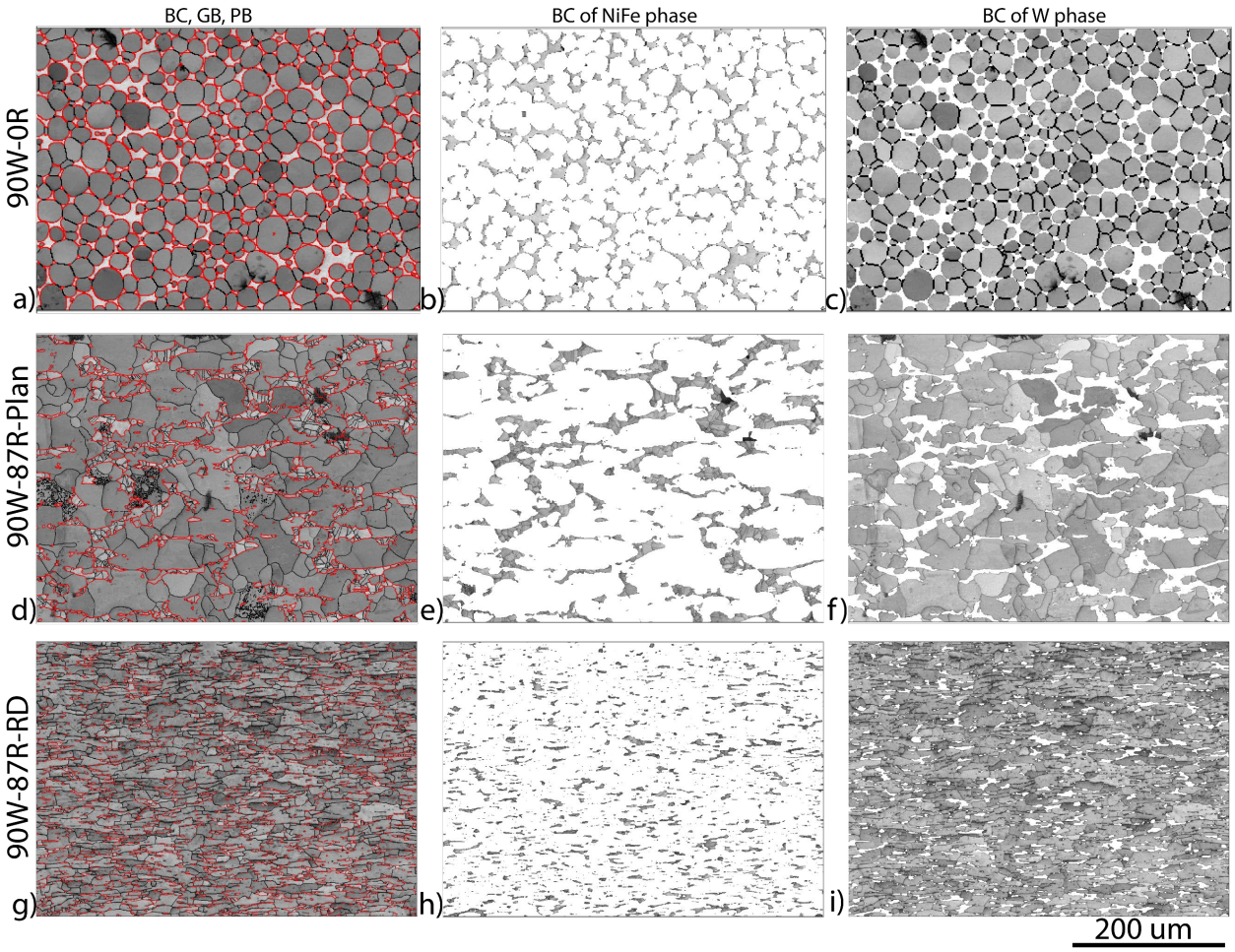

Figure 2. Band contrast (BC) images with marked grain boundary (GB, black), and phase boundary (PB, red, between W and NiFe phases) of 90W-0R, 90W-87R-Plan, and 90W-87R-RD in a), d) and g). The rest of band contrast images show W-phase and NiFe phase separately.

The grain size distributions for three examined surfaces are presented in Figure 3. In 90W-0R, the W phase grains are in the range from 5 to 50 μm with an average of 25 μm in equivalent circle diameters. The NiFe matrix in 90W-0R has a continuous network type morphology spans hundreds of micrometers [11]. In EBSD result measurement of such network can be problematic as 2D cross-section of a network type morphology can artificially break it into smaller isolated regions. In comparison, in both 90W-87R-Plan and 90W-87R-RD, the W phase shows noticeably smaller values at peak positions and the average grain sizes are around 12-18 μm. In the 90W-87R-Plan, we also saw the size distribution grow a long tail while majority of grains are below ~30μm. The size distributions for NiFe grains are similar, with range from ~2 to ~14 μm and an average size of ~3-5 μm, between 90W-87R-Plan and 90W-87R-RD samples. Note that a large amount of small grains (see Figure 5 b) inside W phase has been detected and they are likely attributed to surface artefact. These grains were excluded from size distribution calculation using a threshold filtering.

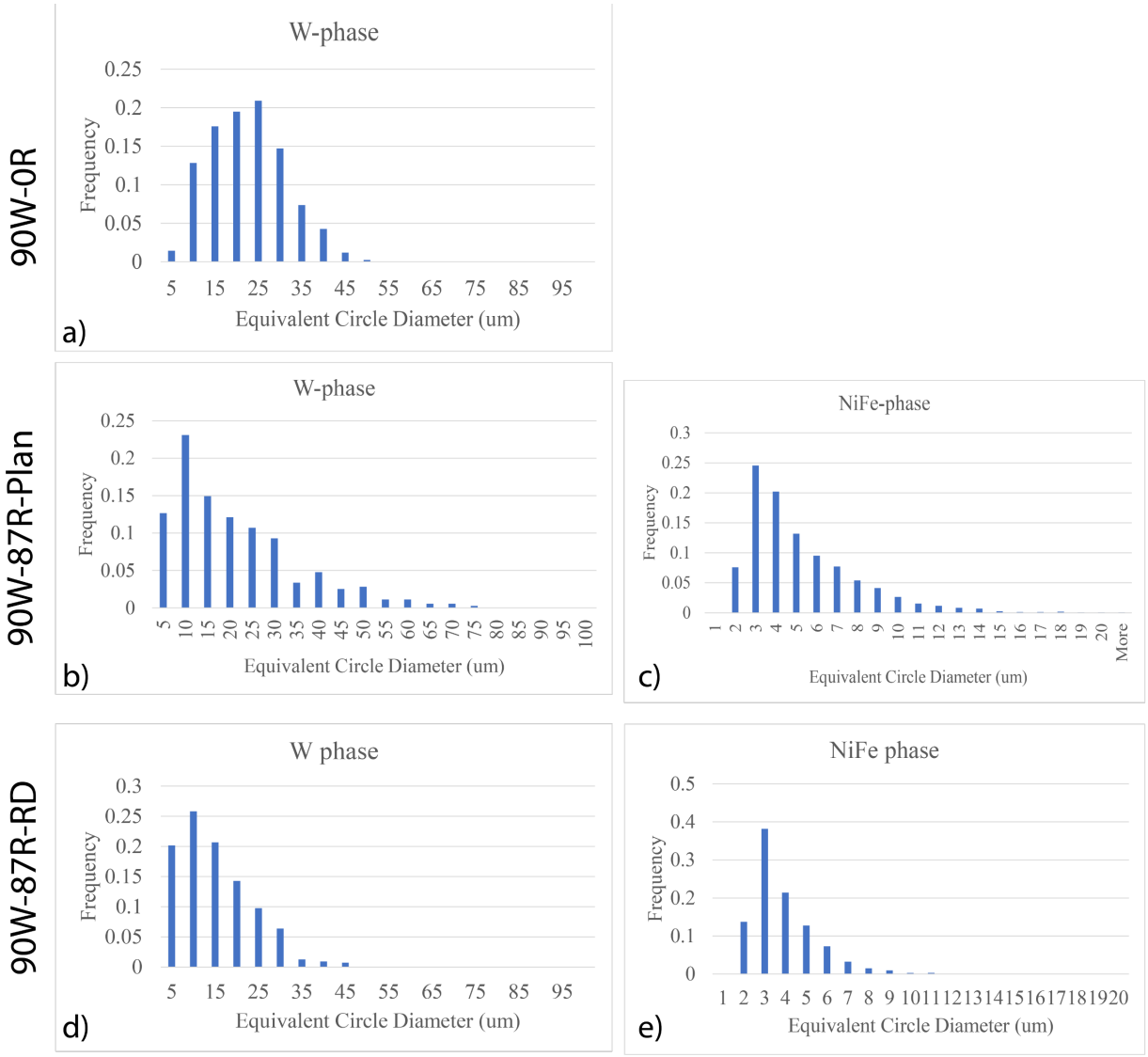

Figure 3. Grain size distributions for W phase and NiFe phase in as-sintered (90W-0R) and hot-rolled (90W-87R-Plan and 90W-87R-RD) samples. Note that the size of NiFe phase is in the range of hundreds of micrometers but due to its nature as continuous network matrix while image is in 2D, EBSD software has issue to correctly recognize NiFe grain sizes. Grain size distribution of W phase in 90W-87R-Plan was calculated after filtering out the surface artefact grains (mostly very small).

The statistics of boundaries for NiFe-NiFe, W-W, and NiFe-W are plotted in Figure 4. The total boundary lengths saw significant increases in almost all categories. This is expected in multiple ways. First, hot-rolling changes the W phase morphology to from spherical to plate-like, which effectively increased surface area to volume (SA/V) ratios since sphere has the lowest SA/V ratio in regular shapes. Secondly, with aforementioned grain refinement in both W and NiFe phase, it is reasonable to expect more boundaries in the samples.

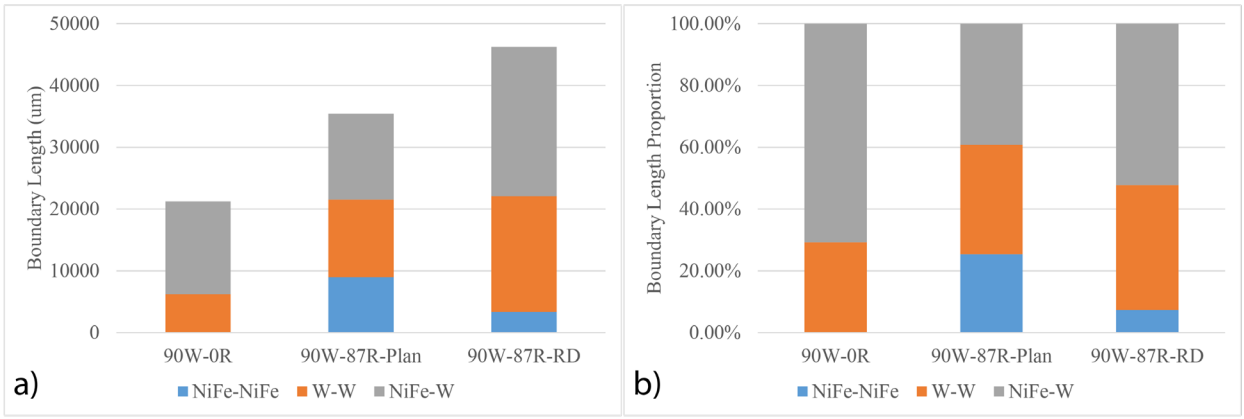

Figure 4. a) boundary lengths and b) boundary's proportion among grains in as-sintered (90W-0R) and hot-rolled (90W-87R-Plan and 90W-87R-RD) samples. Only boundaries with misorientation >10° are considered.

Previous studies have shown that the grain boundary misorientations among W-W are mostly random in as-sintered 90W-0R sample [9]. Figure 5 shows several types of special grain boundaries in both as-sintered 90W-0R and hot-rolled W-NiFe samples. For W phase, special grain boundaries are only a small fraction. Note that in 90W-87R-Plan specimen, a significant amount of ∑3 <111> 60° type boundaries have been observed within some W grains, while they are completely absent in the others. This is likely due to surface artifact due to specimen preparation. For NiFe-NiFe grain boundary, the ∑3 <111> 60° type twin boundary accounts for about 30% of total grain boundaries in the TD-RD surface sample (90W-87R-Plan) and about 12% in the ND-RD surface sample (90W-87R-RD).

The orientation relationships (OR) between BCC W phase and FCC NiFe phase, shown in Figure 6. has been briefly explored following commonly observed orientation relationships listed in Table 2. Non tested ORs are dominanting since the total lengths of boundaries following any tested OR are less than 5% of total length of phase boundary. Moreover, due to using a deviation of 5°, certain segments of boundaries can be categorized into multiple classes during the analysis. Reducing deviation angle can slightly mitigate the issue, but further reduced boundary length of a given OR, which is already insignificant.

Table 2. Common orientation relationships between ferrite and austinite in steel

Type	Orientation Relationship
Bain	BCC [101](010) // FCC [001](010)
K-S	BCC [-111](110) // FCC [-110](111)
N-W	BCC [001](110) // FCC [-101](111)
G-T	BCC [1-10](110) close to FCC [112](111)
P	BCC [-111](101) // FCC [-110](001)

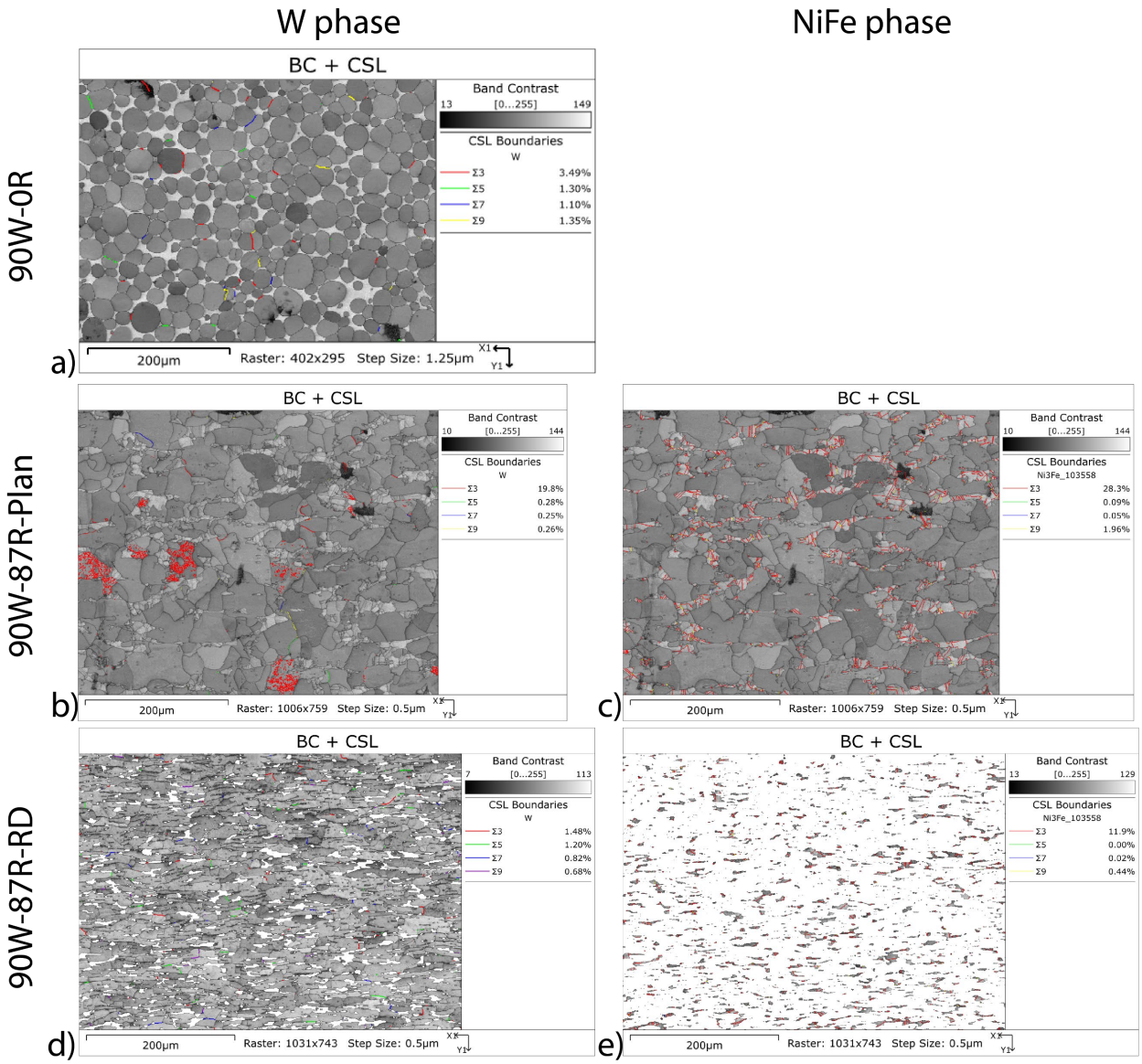

Figure 5. Special grain boundaries in as-sintered (90W-0R) and hot-rolled (90W-87R-Plan and 90W-87R-RD) samples. The special ∑3 boundaries in b) maybe caused by surface artifact. Additional specimens with better quality polishing will be examined in future.

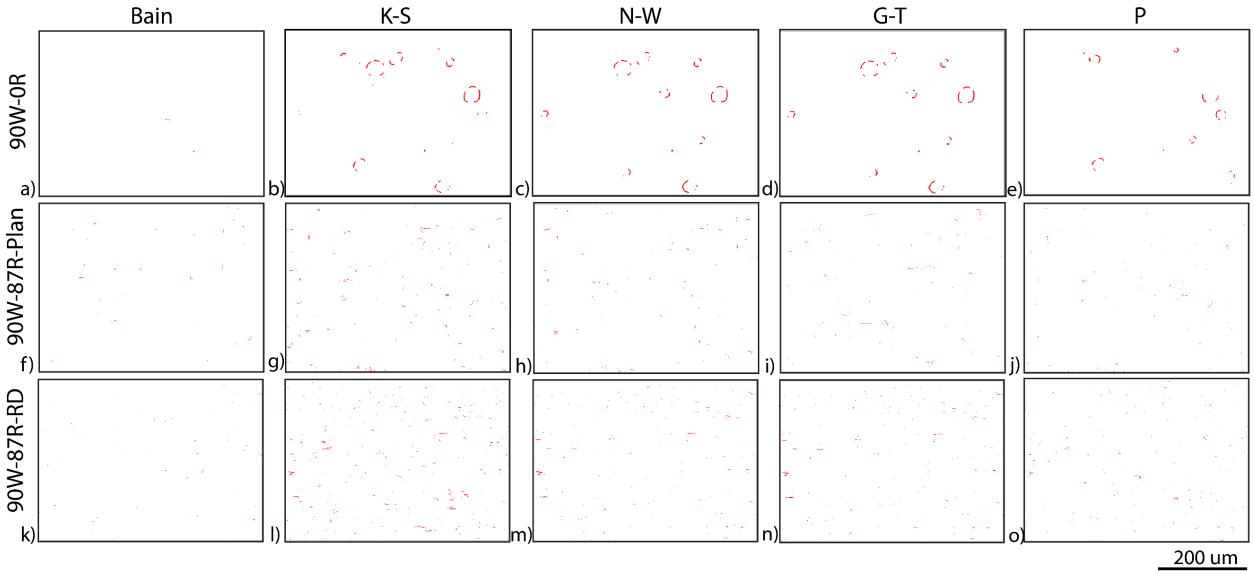

Figure 6. Orientation relationship examination in as-sintered (90W-0R) and hot-rolled (90W-87R-Plan and 90W-87R-RD) samples. A deviation of 5° is allowed. The orientation map was generated in Oxford AZtec software with manually input ORs listed in Table 2.

Figure 7 shows the Kernel Average Misorientation (KAM) for W and NiFe phase in examined samples using a 3 by 3 square kernel size and a maximum deviation angle of 5 degree, which means misorientation with. KAM calculates the average of misorientation between kernel center and its neighbors. KAM is known to be useful for visualization of deformation and small orientation changes. The average KAM is 0.13° in 90W-0R, 0.18° in 90W-87R-Plan and 0.53° in 90W-87R-RD. It's clear that some regions with higher KAM correlate with scratch marks. Since both 90W-87R-Plan and 90W-87R-RD are hot-rolled samples, it is worth investigating geometrical necessary dislocation (GND), which can be calculated based on KAM, using EBSD data. However, specimens with better surface quality will be needed for this investigation. A quick look at the hot-rolled specimen, shown in Figure 8, found a W grains occupied by many sub-grains, which indicate not fully recovered microstructure during hot rolling. Giving the grain size in TEM images, this investigation will need to be performed at a higher resolution.

Fracture surface in WHAs can typically be characterized into four possible crack propagation paths: (1) W cleavage; (2) matrix rupture; (3) W-W intergranular failure, and (4) W-matrix interfacial separation. More detailed SEM and TEM analysis of failure characteristics of these four modes including interfacial precipitation can be found in [12]. It is clearly mentioned in the work carried out by Churn and German [13] and Rabin and German [14] that W-W and W-matrix interfaces are the weaker links for crack propagation. While the weaker W-matrix interfaces can be eliminated by employing suitable heat treatments [12], W-W contacts remain weak and usually serve as the initial crack nucleation sites [14, 15]. This is attributed to segregation of interstitials in the vicinity of the interface thereby reducing the grain boundary cohesive strength [16] and this detrimental influence may not be ameliorated by heat treatment. Therefore, the only possible solution is reducing W-W contiguity and any effort to reduce such contacts will lead to improvement in properties. Alternatively, for a fixed contiguity, the ductility depends on the W matrix interfacial properties. Good cohesion between W and the matrix result in a material capable of transferring the stresses between W grains and the matrix [15]. Typical SEM tensile fractography of the WHAs are shown in Figure 10. All four failure modes have been observed in test specimens. Compared between as-sintered and hot-rolled samples, we can see that the NiFe matrix failure mode changed from ductile dimple type to more intergranular cleavage, since significant NiFe grain refinement occurred.

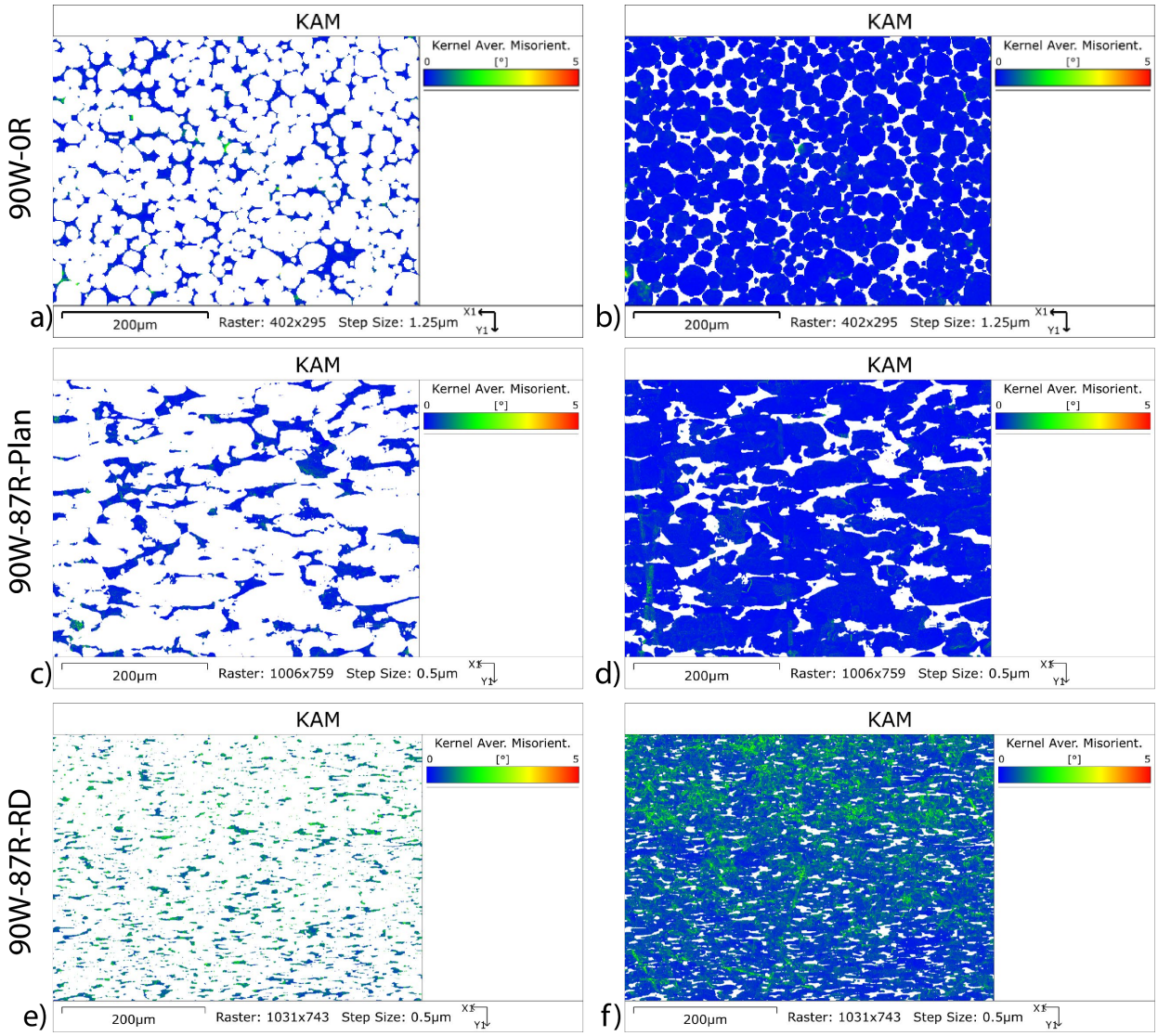

Figure 7. Kernel average misorientation (KAM) map in as-sintered (90W-0R) and hot-rolled (90W-87R-Plan and 90W-87R-RD) samples. All scales are set to 0 to 5 degree of misorientation.

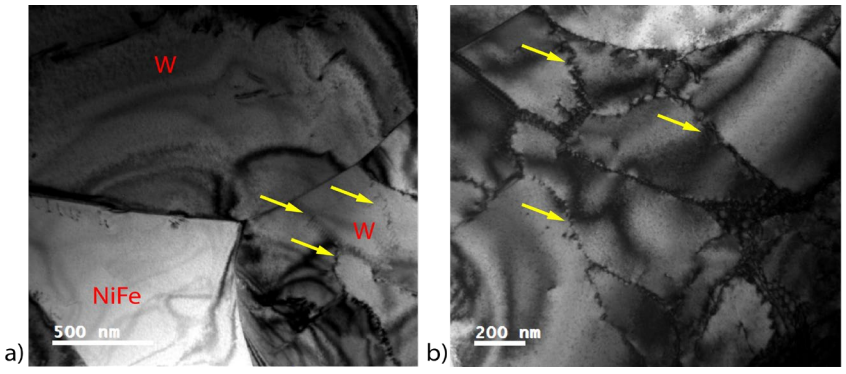

Figure 8. TEM bright field image of sub-grain boundaries/dislocation arrays (yellow) inside W grains.

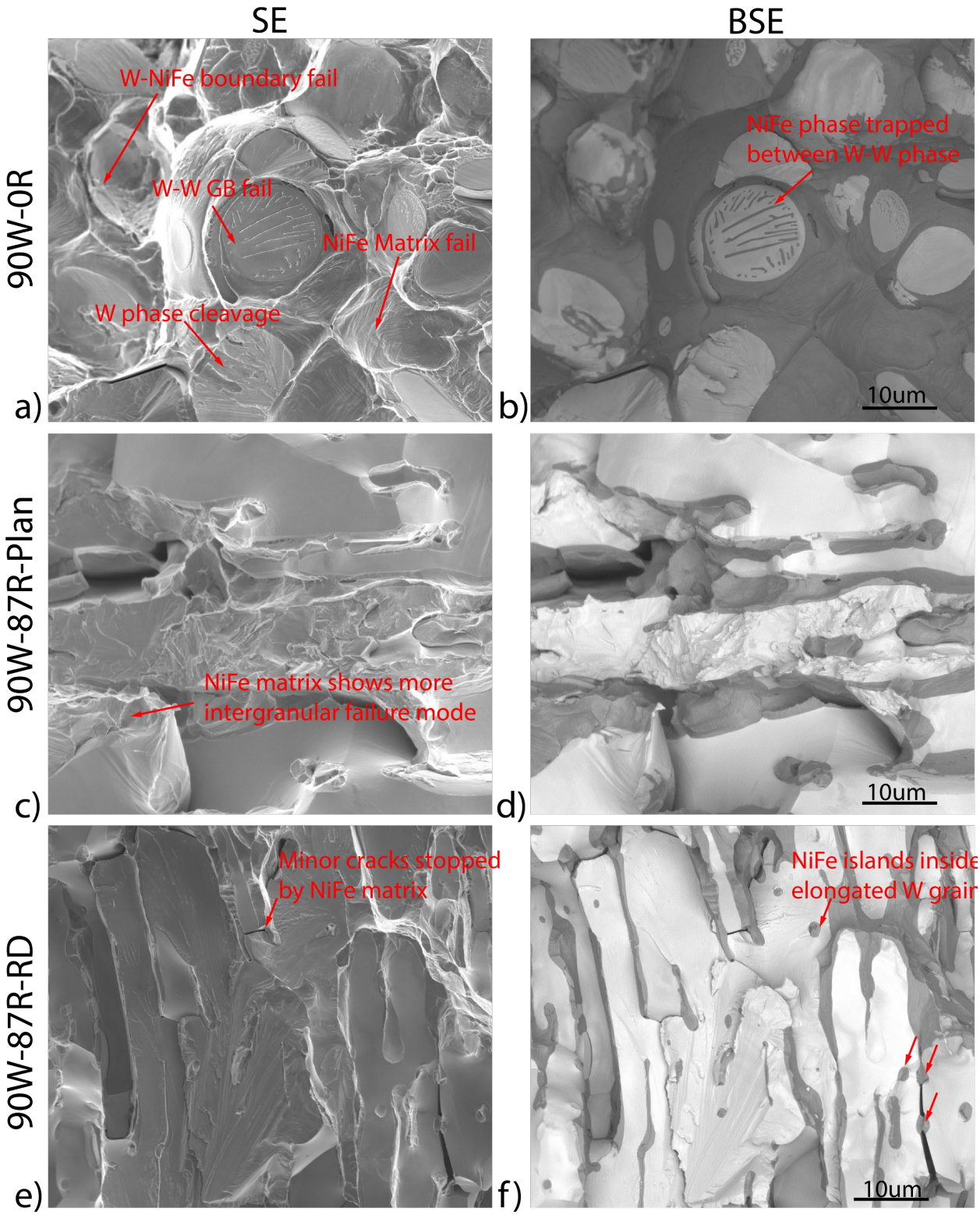

Figure 9. SEM secondary electron (SE) and back-scattered electron (BSE) images of the fractured surface of as-sintered (90W-0R) and hot-rolled (90W-87R-Plan and 90W-87R-RD) samples.

Microstructure-Mechanical Property Correlations

Mechanical properties in tungsten heavy alloys can be affected by a variety of factors, such as composition, fabrication process, heat treatment, porosity, and impurity, etc. Here we focused on the microstructural characteristics, namely grain sizes, volume fraction, and contiguity, between as-sintered and hot-rolled W-NiFe samples. The grain size was measured in terms of equivalent circle diameter, since hot-rolling resulted in anisotropic grain shape. Volume fraction was estimated using the area fraction of W-phase in SEM images. Contiguity C_{W} is the relative W-W interface area in the microstructure. It is commonly determined by placing grid lines over the two-dimensional image and counting the number of tungsten–tungsten (N_{WW}) and tungsten–matrix (N_{WM}) intercepts. It was calculated using the following equation:

$$C_{\mathrm{W}} = \frac{2N_{\mathrm{WW}}}{2N_{\mathrm{WW}} + N_{\mathrm{WM}}} \quad (1)$$

In this study, the contiguity can be estimated based on interface/boundary lengths obtained from supplementary EBSD data, instead of using intercept lines. Thus, N_{ww} is the total length of W-W boundary and N_{WM} is the total length of the boundary between W phase and NiFe phase. Table 3 listed measured microstructural factors on top surfaces of W-NiFe tensile specimens.

Table 3. Microstructure characteristics for the top surface of W-NiFe tensile specimens

Specimen	**Average Grain Size (equivalent circle length, μm)**		**Volume fraction (W)**	**Contiguity (W)**
	W phase	NiFe matrix		
90W-0R	25	>100	84.4%	0.45
90W-87R-Plan	15	5	80.7%	0.64
90W-87R-RD	13	4	89.8%	0.61

A summary of yield strength, ultimate tensile strength, and ultimate elongation is presented in Figure 10. Results with stress-strain curves and strain rates have been reported in our previous report [9]. In general, the measured yield strength and ultimate tensile strength increases as test crosshead speed increases from 0.1 um/s to 10 um/s for all materials. The ultimate elongation for the as-received 90W-0R material is ~20% at all test speeds; of all the materials tested this one shows the best ductility. The ultimate elongations of the hot-rolled 90W-87R-RD and 90W-87R-ND are on the order of 10%. Note that both 90W-87R-Plan and 90-87R-RD were fabricated along the rolling direction, which was the direction tension was applied. The only difference is the 90W-87R-Plan features the TD-RD orientation while 90-87R-RD features ND-RD orientation.

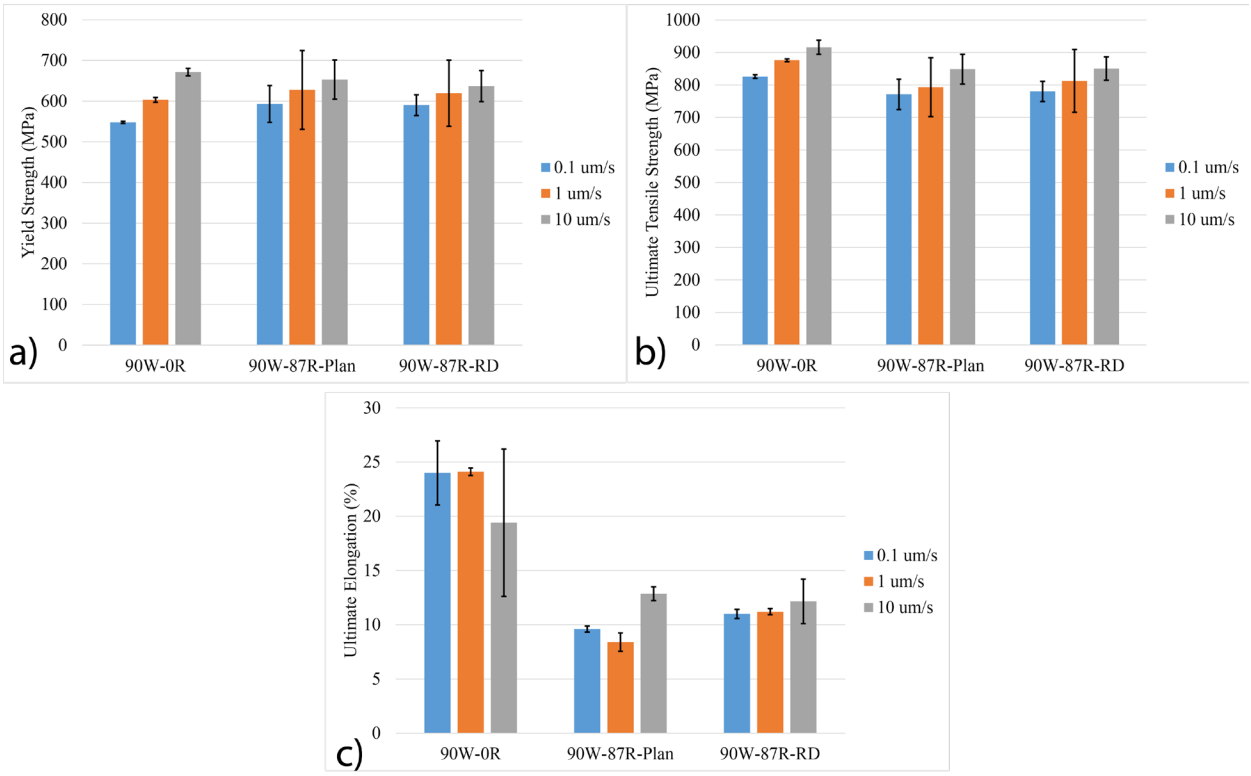

Figure 10. Yield strength (YS), ultimate tensile strength (UTS), and elongation at failure measured in as-sintered (90W-0R) and hot-rolled (90W-87R-Plan and 90W-87R-RD) W-NiFe samples. Three cross-head speeds were tested.

It is known that the yield strength of alloys has a classical Hall-Petch relationship with grain size:

$$\sigma_y = \sigma_0 + KD^{-1/2} \tag{2}$$

where σ_y is the yield stress, σ_0 is the yield strength of a single crystal, *K* is a constant, and *D* is the grain size. For dual phase alloys, this relationship can be described by incorporating the matrix volume fraction V_M [17]:

$$\sigma_y = \sigma_0 + KGb\left(\frac{1-V_{\mathrm{M}}}{DV_{\mathrm{M}}}\right)^{1/2} \tag{3}$$

where *G* is the shear modulus and *b* is the Burgers vector. The square root term is related with average thickness of the soft matrix phase. By assuming deformation of WHA began with deformation of the soft matrix phase, Lee et al. [18, 19] developed an adapted Hall-Petch relation for WHA as expressed by the following formula:

$$\sigma_y = \sigma_0 + K\left(\frac{C_{\mathrm{W}}(1-V_{\mathrm{M}})}{DV_{\mathrm{M}}}\right)^{1/2} \tag{4}$$

where the yield strength has demonstrated to be in a linear relationship with the inverse square root of the mean thickness of the matrix $DV_{\mathrm{M}}/[C_{\mathrm{W}}(1-V_{\mathrm{M}})]$.

Figure 11 shows the relationships between W phase grain size and yield strength. The reduced average size in hot-rolled W-NiFe samples agrees with the general trend in increasing yield strength. Caution needs to be taken as these grain size effect equations were proposed on as-sintered tungsten heavy alloys, they are not necessarily accurate for the highly deformed and anisotropic microstructure in hot-rolled material.

Another factor has not been considered is the sever grain refinement in the NiFe matrix. The matrix turned from continuous network spans hundreds of micrometers to become micrometer-sized grain filled between elongated W phases.

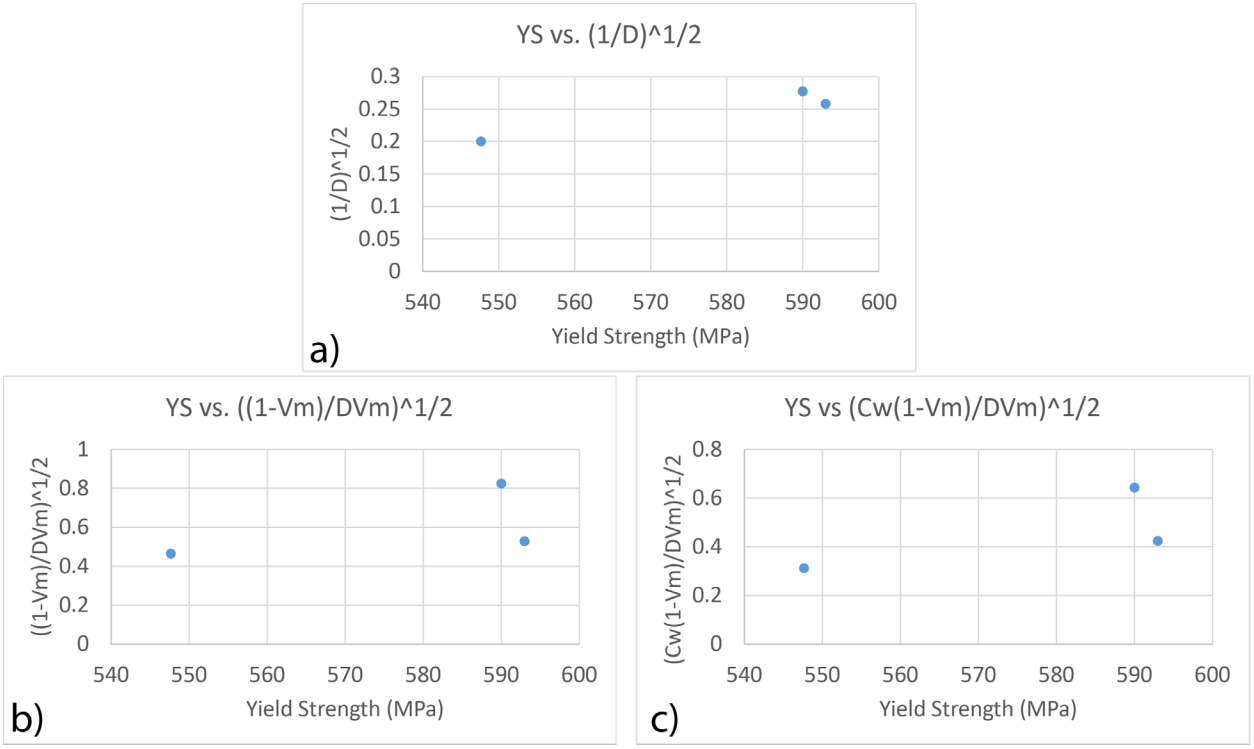

Figure 11. Yield strength (YS) plotted against square root part described in a) equation 2, b) equation 3, and c) equation 4. The yield strength measured at 0.1um/s crosshead speed is used here.

Decrease in contiguity results in improvement in mechanical properties of tungsten heavy alloys since the fraction of W-W contacts-preferred crack initiation sites are reduced. Rabin and German showed that the tensile strength and elongation of WHAs increase with decreasing contiguity [14]. Churn and German [13] have shown a linear dependence of % elongation in WNiFe heavy alloys on W-W contiguity (C_{W}) and volume fraction of matrix (V_{M}) in the form of:

$$\varepsilon = K_1 + K_2 V_{\mathrm{M}}(1 - C_{\mathrm{W}}) \quad (5)$$

where ε is elongation to failure, and K_1 and K_1 representing a collection of material constants. Figure 12 shows relationships among ultimate tensile strength (UTS), elongation, and contiguity. Both UTS and elongation correlate well with contiguity, while slightly deviate from relationships described in equation 5. This is expected as previous equations were derived in more isotropic microstructure. Hot-rolled specimens have anisotropic microstructure and characterizations only reflect one surface orientation. That is, in terms of volume fraction, 90W-87R-Plan should have the same value as 90W-87-RD, but the effective volume fraction against crack propagation may be different. As the W particles are flattened in the RD-TD direction (and are therefore more contiguous), and as cracks propagate very easily through the particles, any crack propagation through a single W particle will result in a greater effective loss of cross-sectional area for samples oriented in the RD-TD direction as opposed to the RD-ND direction, hence the strong correlation with contiguity

In the case of varying matrix volume fraction, increasing volume fraction of ductile matrix phase [23] will lead to increase in % elongation to failure and also the impact toughness. By examining a series of WNiCo WHAs with different ratio of the individual elements, Kumari et al. [20] showed that volume fraction of the

matrix increases linearly with decrease in W-W continuity. In addition, they found that microstructures with higher volume fractions of matrix and higher distances between W particles featured superior tensile strength and impact toughness, regardless the chemical composition. Therefore, optimization of tungsten heavy alloys in tensile strength and ductility while maintaining volume fraction of W requires refinement W-phase particle sizes (reduce D) and minimize W-W boundary (reduce C_w). In addition, it's evident that uniformity of the matrix can affect material properties.

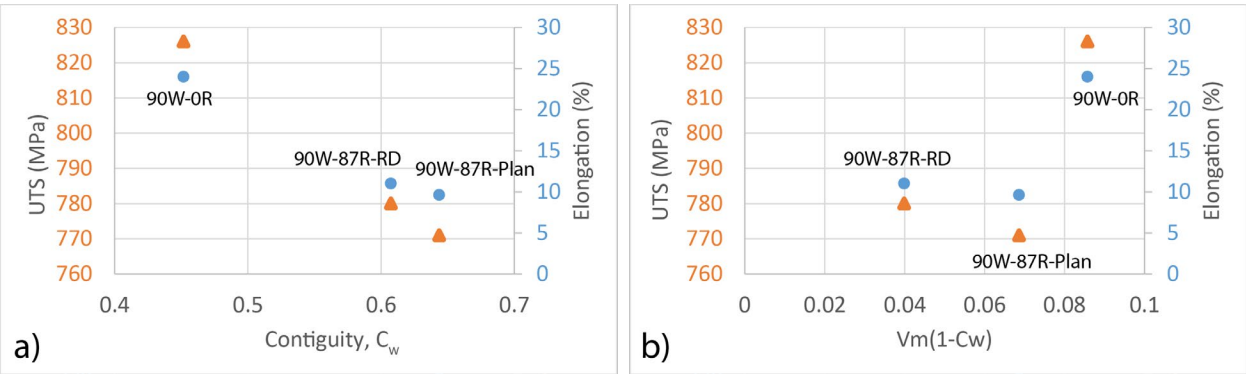

Figure 12. UTS elongation against a) contiguity and b) equation 5, in as-sintered and hot-rolled W-NiFe samples.

Other Progresses

Progresses in high temperature mechanical testing equipment:

- We obtained approval from building staff to make necessary electrical modifications.
- We received the necessary electrical components.
- Electrical modifications have been scheduled. Once an electrical outlet is ready, we will test the furnace.

Progress in applying machine learning to in-situ mechanical testing:

- Samples have been prepped and shipped for testing.
- In-situ mechanical testing data from the past have been received.
- Preliminary testing on image segmentation and tracking has been tested.

ACKNOWLEDGEMENTS

This research was supported by Office of Fusion Energy Sciences, U.S. Department of Energy (DOE) under Contract DE-AC05-76RL01830. *David Collins performed part of the work presented here while he was at Pacific Northwest National Laboratory and is currently at Oak Ridge National Laboratory.

References

[1] S. Wurster, N. Baluc, M. Battabyal, T. Crosby, J. Du, C. García-Rosales, A. Hasegawa, A. Hoffmann, A. Kimura, H. Kurishita, Recent progress in R&D on tungsten alloys for divertor structural and plasma facing materials, Journal of Nuclear Materials 442(1-3) (2013) S181-S189.

[2] D. Stork, P. Agostini, J.-L. Boutard, D. Buckthorpe, E. Diegele, S. Dudarev, C. English, G. Federici, M. Gilbert, S. Gonzalez, Developing structural, high-heat flux and plasma facing materials for a near-term DEMO fusion power plant: the EU assessment, Journal of nuclear materials 455(1-3) (2014) 277-291.

[3] A. Hasegawa, M. Fukuda, K. Yabuuchi, S. Nogami, Neutron irradiation effects on the microstructural development of tungsten and tungsten alloys, Journal of Nuclear Materials 471 (2016) 175-183.

[4] C.H. Henager, R.J. Kurtz, T.J. Roosendaal, B.A. Borlaug, W. Setyawan, K.B. Wagner, G.R. Odette, K. Cunningham, K.A. Fields, D. Gragg, Recent Progress in the Development of Ductile-Phase Toughened Tungsten for Plasma-Facing Materials, (2014).
[5] C.H. Henager, R.J. Kurtz, T.J. Roosendaal, B.A. Borlaug, E.A. Nyberg, C.A. Lavender, G.R. Odette, K. Cunningham, F.W. Zok, RECENT PROGRESS IN THE DEVELOPMENT OF DUCTILE-PHASE TOUGHENED TUNGSTEN FOR PLASMA-FACING MATERIALS: W-Ni-Fe COMPOSITES, (2015).
[6] C.H. Henager, B.N. Nguyen, R.J. Kurtz, PRELIMINARY PROGRESS IN THE DEVELOPMENT OF DUCTILE-PHASE TOUGHENED TUNGSTEN FOR PLASMA-FACING MATERIALS: DUAL-PHASE FINITE ELEMENT DAMAGE MODELS, Pacific Northwest National Lab.(PNNL), Richland, WA (United States), 2016.
[7] B.N. Nguyen, C.H. Henager, R.J. Kurtz, Modeling Ductile-Phase Toughened Tungsten for Plasma-Facing Materials: Progress in Damage Finite Element Analysis of the Tungsten-Copper Bend Bar Tests, Pacific Northwest National Lab.(PNNL), Richland, WA (United States), 2017.
[8] James V. Haag IV, Matthew Olszta, Danny Edwards, Mitsu Murayama, Charles H. Henager Jr., W. Setyawan, In-situ mechanical testing and interfacial characterization of ductile-phase toughened tungsten, Fusion Materials Semiannual Progress Report For the Period Ending December 31, 2019, 2019, pp. 78-85.
[9] J. Wang, D. Collins, N.R. Overman, W. Setyawan, TENSILE TESTING AND MICROSTRUCTURAL CHARACTERIZATION OF DUCTILE PHASE TOUGHENED W-NiFe ALLOYS, FUSION MATERIALS SEMIANNUAL PROGRESS REPORT FOR THE PERIOD ENDING June 30, 2020, 2020.
[10] J. Wang, D. Collins, N.R. Overman, C.H.H. Jr., W. Setyawan, MICROSTRUCTURAL CHARACTERIZATION AND MECHANICAL TESTING OF DUCTILE-PHASE TOUGHENED TUNGSTEN, FUSION MATERIALS SEMIANNUAL PROGRESS REPORT FOR THE PERIOD ENDING December 31, 2019, 2019.
[11] J.V. Haag, D.J. Edwards, C.H. Henager, W. Setyawan, J. Wang, M. Murayama, Characterization of ductile phase toughening mechanisms in a hot-rolled tungsten heavy alloy, Acta Materialia 204 (2021) 116523.
[12] D.V. Edmonds, Structure/property relationships in sintered heavy alloys, International Journal of Refractory Metals and Hard Materials 10(1) (1991) 15-26.
[13] K.S. Churn, R.M. German, Fracture Behavior of W-Ni-Fe Heavy Alloys, Metallurgical Transactions A 15(2) (1984) 331-338.
[14] B.H. Rabin, R.M. German, Microstructure effects on tensile properties of tungsten-Nickel-Iron composites, Metallurgical Transactions A 19(6) (1988) 1523-1532.
[15] I.S. Humail, F. Akhtar, S.J. Askari, M. Tufail, X. Qu, Tensile behavior change depending on the varying tungsten content of W–Ni–Fe alloys, International Journal of Refractory Metals and Hard Materials 25(5) (2007) 380-385.
[16] Q. Wei, H.T. Zhang, B.E. Schuster, K.T. Ramesh, R.Z. Valiev, L.J. Kecskes, R.J. Dowding, L. Magness, K. Cho, Microstructure and mechanical properties of super-strong nanocrystalline tungsten processed by high-pressure torsion, Acta Materialia 54(15) (2006) 4079-4089.
[17] M.F. Ashby, The deformation of plastically non-homogeneous materials, The Philosophical Magazine: A Journal of Theoretical Experimental and Applied Physics 21(170) (1970) 399-424.
[18] K.H. Lee, S.I. Cha, H.J. Ryu, S.H. Hong, Effect of two-stage sintering process on microstructure and mechanical properties of ODS tungsten heavy alloy, Materials Science and Engineering: A 458(1) (2007) 323-329.
[19] K.H. Lee, S.I. Cha, H.J. Ryu, S.H. Hong, Effect of oxide dispersoids addition on mechanical properties of tungsten heavy alloy fabricated by mechanical alloying process, Materials Science and Engineering: A 452-453 (2007) 55-60.
[20] A. Kumari, M. Sankaranarayana, T.K. Nandy, On structure property correlation in high strength tungsten heavy alloys, International Journal of Refractory Metals and Hard Materials 67 (2017) 18-31.

4.4 MATERIALS FOR THE US-JAPAN FRONTIER IRRADIATIONS—L. M. Garrison, J. R. Echols, N. C. Reid, Y. Katoh (Oak Ridge National Laboratory)

OBJECTIVE

The Fusion Research Oriented to Neutron Irradiation and Tritium Behavior at Material Interfaces (FRONTIER) US-Japan collaboration seeks to explore and explain the behavior of internal solid interfaces in PFCs under neutron irradiation. Advanced fusion materials, composites, and joints have been designed and are explored in this collaboration.

SUMMARY

The irradiation capsules for the FRONTIER collaboration are being prepared. Some materials were designed and fabricated at ORNL. Additional materials for the US side of the project are being supplied by other collaborators in the US and internationally. The recent focus has been in fabricating the materials and preparing samples for the irradiation. The next steps will be to dimensionally inspect the samples and then begin the non-rad sample testing of microstructure and mechanical properties.

PROGRESS AND STATUS

The FRONTIER US-Japan collaboration is focusing on understanding the behavior of advanced fusion materials for plasma-facing components (PFCs), especially internal interfaces including those present at a joint between dissimilar materials or in a composite between the constituent parts. To accomplish this, four categories of materials will be irradiated: advanced alloys, fundamental joints, composites, and baseline materials without joints. The fundamental joints consist of two or three materials that are joined one on top of the other so that the joint interface is parallel to the face of the disc sample. Because these joints must be made miniature with total thickness of both materials and the joint being 0.5 mm, in some cases, the joining methods used are different than what would be employed for engineering relevant macroscopic component development. This is appropriate because the goal of the program is the scientific investigation of the microscopic phenomena at the joints under irradiation rather than a component building program. These advanced fusion-relevant materials are being tested in the High Flux Isotope Reactor (HFIR) at Oak Ridge National Laboratory, at irradiation temperatures of 300, 500 and 800°C. Samples of each material will be irradiated for 1 cycle and 3 cycles. These materials for this part of the collaboration are being prepared as 3 mm diameter by 0.5 mm thick discs.

Table 1 lists the materials developed for the US contribution to the FRONTIER project. While ORNL is involved in the development of all the materials in Table 1 in some way (including machining samples, elemental analysis, mechanical testing, microstructure characterization, etc.), ORNL is specifically listed in the Team column where we are fabricating or procuring the material. Each material is described briefly here.

The W-ZrO_2, W-Y_2O_3, SiC-ZrO_2, and SiC-$Y2O_3$ are being fabricated at Forschungszentrum Juelich (Fz. Juelich) in Germany to test potential interlayers for W fiber and SiC fiber composites. In the complete composite, the fibers of W or SiC would be coated with ZrO_2 or Y_2O_3 before being coated in the matrix material. To study the fundamentals of the interface, these representative samples are being prepared by depositing a thin layer of the oxide on a W (or SiC) thin substrate, and then coating a layer of W (or SiC) on top of the oxide to make a three layer sandwich.

The CuCrZr is the standard fusion-relevant Cu based material that is considered for water cooled divertor applications. Recently, a research team with members from ORNL, University of Tennessee Knoxville (UTK), and Stony Brook University have used computational methods to design CuCrNbZr and CuCrTaZr alloys that will resist creep at higher temperatures. For use in a divertor these Cu-based materials would be joined with W, so that is the fundamental interface being studied here. The CuCrZr, CuCrNbZr, and

CuCrTaZr was supplied by Stony Brook University and ORNL is joining these alloys to W substrates. Both a cold press and a brazing technique are being investigated for joining.

Table 1. Materials being prepared as the US side contribution to the FRONTIER collaboration

Material Type	**Material Description**	**Team**	**Material Code**
Fundamental joint	W-ZrO_2	Fz. Juelich	ZT
	W- Y_2O_3	Fz. Juelich	YT
	SiC- ZrO_2	Fz. Juelich	ZS
	SiC- $Y2O_3$	Fz. Juelich	YS
	W/CuCrNbZr	Stony Brook U. + UTK +ORNL	CN
	W/CuCrZr	Stony Brook U. + UTK +ORNL	CZ
	W/CuCrTaZr	Stony Brook U. +UTK +ORNL	CA
	W-SiC	ORNL	SC
	W-steel laminate	ORNL	LT
Advanced alloy	Fine grain W alloy 1	Stony Brook U.	GT
	Fine grain W alloy 2	Stony Brook U.	HT
	W-Steel (50/50 SPS)	Fz. Juelich	ST
	W-1%ZrC	U. of Illinois	PT
	W-1%TiC	U. of Illinois	P2
	Ad. man. W e-beam	ORNL	AE
Composite	W-Cu sintered	ORNL	KW
	W-single fiber	IPP-Garching	F
	W/Cu ad. man. composite	ORNL	X1
	WC	Imperial College London	WC
	WC (90% WC, 10% of Fe with 8wt%Cr)	Imperial College London	FC
Reference material	Eurofer reference	ORNL	E
	Grade 92 reference	ORNL	9
	W reference	ORNL	T
	CuCrNbZr reference	Stony Brook U. + UTK	N
	CuCrZr reference	Stony Brook U. + UTK	Z
	CuCrTaZr reference	Stony Brook U. + UTK	A

The W-SiC was fabricated at ORNL using a 40 mm diameter and 2 mm thick SiC substrate and using spark plasma sintering (SPS) Model 25–10, Thermal Technology LLC to join a thin 0.025 μm W foil on one side. The SiC side was machined down so that the final sample thickness is 0.5 mm total, including the 0.025 μm W layer. The stacking inside the SPS graphite die with inner diameter 40 mm was graphite paper, W, SiC, graphite paper. The heating rate was 100°C/min, to reach a maximum goal temperature of 1300°C with a hold for 10 min. The pressure was 30 MPa during heating and the 10 min hold, and then reduced to 15 MPa during the cooling, at a rate of 50°C/ min until reaching room temperature. Actual measured temperature was 1350°C for the first run, which only had a hold of approximately 5 min. For runs 2-4 the measured maximum temperature was 1320-1325°C with a hold of 10 min. The slightly higher temperature

is often seen with the large 40 mm die. In all cases, the W appeared to make a good bond with the SiC (Figure 1). Near the edge of each SiC disc is a small zone that does not have the W foil coating because the W foil was trimmed to fit easily in the die. Samples are only machined from the regions that have the full W coating.

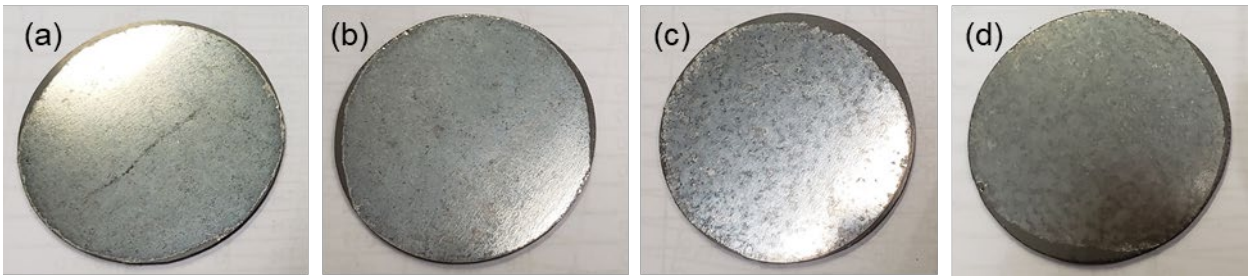

Figure 1. Thin W layer bonded to SiC substrate with SPS. (a)-(d) are runs 1-4, respectively. Each disc is 40 mm in diameter.

The W and steel have different coefficients of thermal expansion, but joints between them are needed for higher operating temperature He-cooled divertor concepts. The W-grade 92 steel laminate was fabricated at ORNL by stacking alternating layers of W and grade 92 steel foils. They were sealed in a stainless-steel box and then forged at 1000°C to varying amounts of reduction. Fz. Juelich has developed and tested several methods of making a W to steel functionally graded joint. For studying the phenomena at the interface, they prepared a material that is 50% W and 50% steel and joined with SPS.

The two fine grain W alloys were developed at Stony Brook University. The University of Illinois has developed some particle strengthened W materials, and fabricated W-1% ZrC and W-1%TiC for this project. Imperial College London is studying tungsten carbide (WC) and WC cermets for fusion applications. We will be comparing the irradiation performance of pure WC and a cermet that is 90% WC, 10% of Fe with 8wt%Cr.

The ORNL is developing additively manufactured W and W-Cu composites. W produced by electron beam additive manufacturing was developed and included for irradiation. Also, ORNL procured binder jet printed W infiltrated with Cu from the company ExOne. A second version of W-Cu composite fabricated by sintering was procured from MiTech Metals Inc.

The W fiber-W matrix composites are being developed at the Max Planck Institute for Plasma Physics in Garching, Germany (IPP-Garching). To research the fundamental interface between the W fiber and W matrix, individual W fibers, 150 μm in diameter, encased in W matrix cylinders were prepared (Figure 2). The deposition of the W onto the W fiber results in a slightly hourglass shape to the cylinders. The outer diameter of the cylinders is slightly more than 3 mm, so these cylinders have been machined into 3 mm discs.

Figure 2. W fiber runs axially through the cylinder of W matrix material.

To prepare samples for irradiation and track all of the individual materials, each material was assigned a material code (Table 1). Each sample is engraved with the material code as the first character or two characters, followed by a sequential character for each sample. For example, the ZT material is engraved as ZT01, ZT02, ZT03, etc. For the engraving to have minimal influence on any mechanical testing including 3-point bending, the engraving was done in one row for two characters (Figure 3) or two rows for four characters (Figure 4), avoiding the centerline.

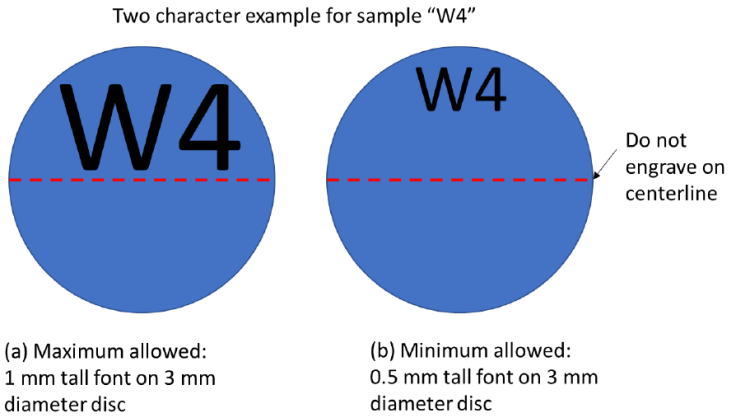

Figure 3. Engraving example for sample with material code W and unique identifier 4.

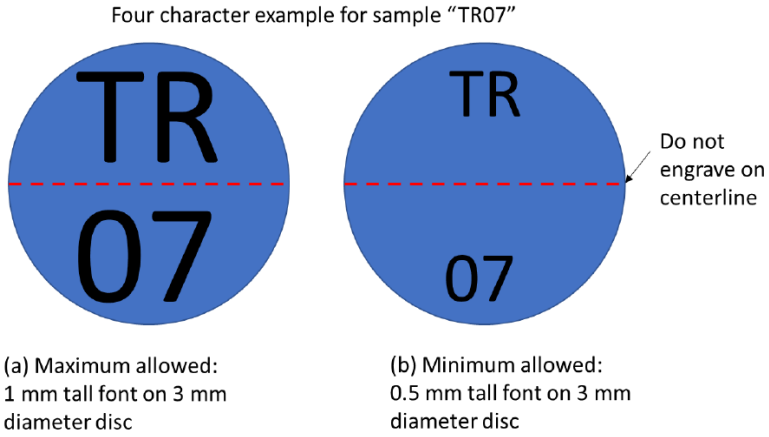

Figure 4. Engraving example for sample with material code TR and unique identifier 07.

For the fundamental joint samples, the engraving was placed strategically to identify one of the material sides, which may or may not be identifiable to the eye. For example, in the illustration in Figure 5, the W side is engraved to distinguish it from the steel side. The engraving can also be used to identify an important sample microstructure, fiber direction, or crystallographic orientation by how the engraving is done relative to that feature in the material (Figure 6).

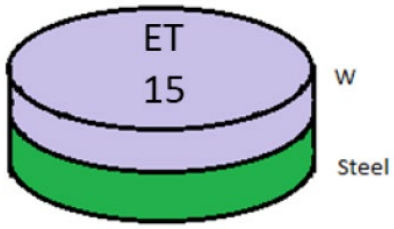

Figure 5. Illustration of an engraving for sample ET15 on the W layer of the fundamental joint.

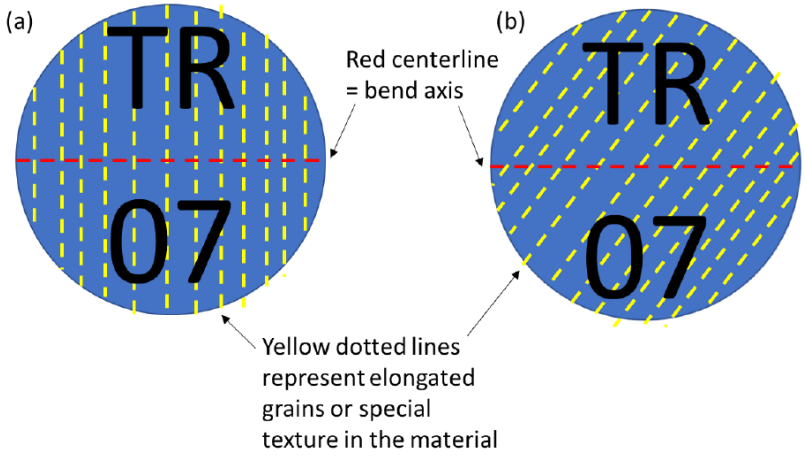

Figure 6. The engraving label placement can be used to indicate the direction of the microstructure. In this example, the "TR" material series has a rolling direction (yellow dotted lines). (a) The "TR07" label is placed so the bend axis is at the center and perpendicular to the rolling direction. (b) The "TR07" label is placed randomly compared to the rolling direction.

4.5 ELECTRICAL CONDUCTIVITY EVALUATION OF NEUTRON IRRADIATED TUNGSTEN MATERIALS FROM THE PHENIX CAMPAIGN—J. R. Echols, L. M. Garrison (Oak Ridge National Laboratory)

OBJECTIVE

The goal of the PHENIX collaboration is to expand the database on neutron irradiation effects in tungsten materials. This task evaluates the effects of irradiation at elevated temperatures on electrical resistivity.

SUMMARY

Electrical resistivity measurements conducted on single and polycrystalline tungsten samples exposed to neutron radiation between 0.2 and 0.7 displacements per atom (dpa) show increased resistivity, but do not show clear trends on the basis of dpa alone. Early results examining the effects of grain orientation in polycrystalline samples with elongated grains show measurable variation in resistivity depending on sample orientation with respect to the applied current. This effect is exaggerated at greater levels of irradiation, suggesting a relationship between grain boundary resistivity and electrical resistivity.

PROGRESS AND STATUS

The goal of the US-Japan collaboration, PHENIX, is to investigate tungsten and tungsten-based materials' responses to neutron irradiation for use in future fusion reactors. Over 1500 single crystal, polycrystalline, and W-Re alloy samples were exposed to neutron radiation in the RB*19J irradiation capsule in the High Flux Isotope Reactor (HFIR) to doses of ~0.2-0.7 dpa. The nominal irradiation temperatures for three different subcapsules were 430-670, 740-960, and 880-1080°C. A gadolinium shield was included in the capsule to reduce the thermal neutron flux, and therefore the rate of W to Re,Os transmutations, to more fusion relevant values than previous irradiations such as TITAN.

Tungsten's high thermal conductivity is critical for its use in future fusion reactors and is one of the reasons tungsten is the leading candidate material for high heat flux regions of reactors. Neutron irradiation in a reactor environment, however, degrades the thermal conductivity of tungsten. In order to separate the phonon, electron, and transmutant element contributions to tungsten thermal conductivity, electrical conductivity measurements need to be taken and compared against thermal conductivity measurements. For the purposes of this report, electrical resistivity (the inverse of conductivity) is given. Resistivity is measured by applying a current to a sample of material and determining voltage changes across a known geometry. Ideal resistivity (ρ) is defined as the resistance (R) of a uniform specimen multiplied by the cross-sectional area (A) and divided by the length (l) of the specimen, shown in **Equation 1.**

Equation 1. $$\rho = R\frac{A}{l}$$

The radioactivity levels, and HFIR capsule geometry severely limit the size of the samples which can be used. Therefore, to measure the electrical conductivity of the irradiated samples, a miniature electrical resistivity fixtures was designed and constructed for 3 mm diameter discs, which is shown in Figure 1. The measurement system utilizes a Keithley Model 182 Sensitive Digital Voltmeter to measure the voltage drop across the inner two leads. A Model 237 High Voltage Source Measure Unit provides the current source. Resistivity testing was performed at room temperature, between 20°C and 24°C. Resistivity values were then normalized to 20°C for comparison. General test procedures for electrical resistivity testing on metals are given in ASTM B 193-87, Standard Test Method for Resistivity of Electrical Conductor Materials.

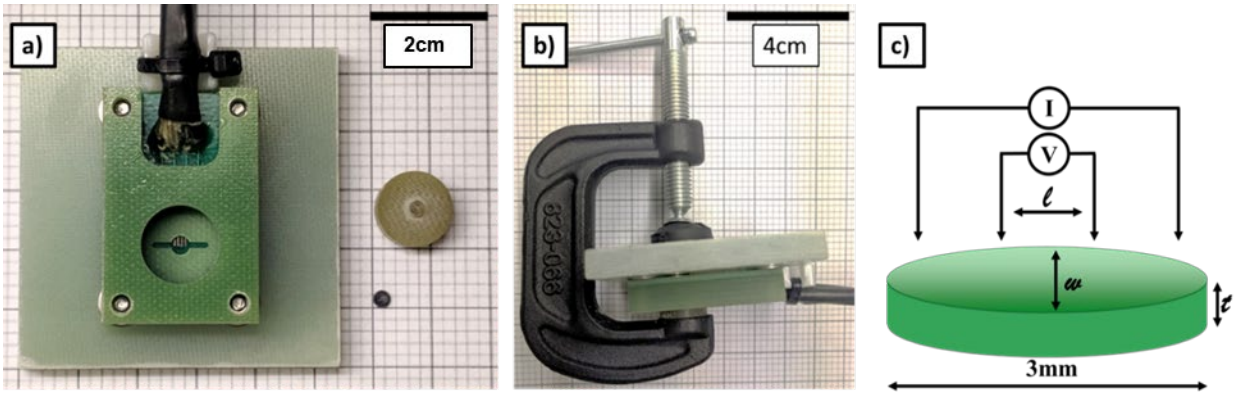

Figure 1. Electrical resistivity testing device. a) Disassembled 3 mm disk holder with the apparatus on the left and an example 3 mm disk with the plug on right. b) Assembled 3 mm disk fixture with the disc inserted and the plug clamped to the apparatus to ensure proper contact with the pins. c) Simplified schematic for the apparatus. Circuit schematic specifies length (l), width (w), and thicknesses (t) used in resistivity calculation. Major gridlines in a) and b) are 1 cm apart.

During testing, sample surfaces from the 880-1080°C irradiation subcapsule were found to be discolored by an opaque film of presumed impurities, measured to have a maximum thickness of 50 microns. This film was removed by polishing. Tests on unirradiated tungsten confirm that this amount of material removal does not have a significant effect on resistivity calculations, which are a geometric function of the measured resistance of any particular sample.

Electrical resistivity was measured for thick plate ALMT produced polycrystalline tungsten with elongated grains (material codes AT and BT) and single-crystal tungsten (material code UE). For the polycrystalline samples, samples were cut in different orientations with respect to the elongated grains. PCW materials are cut in 2 orientations: A – where grains are equiaxed in regard to the applied current, and B – where grains are not equiaxed in regard to the applied current. Resistivity results as a function of calculated dpa are shown in Figure 2. In general, there is no clear trend between resistivity and DPA. Significant grain growth has been observed in some materials from the 880-1080°C capsule, so the potential for grain growth is noted in the figure. Grain boundary effects will be discussed in more detail further in this report, however, the reduction in total GBs crossed may be a cause of the reduction in resistivity observed in the samples from the highest temperature capsule.

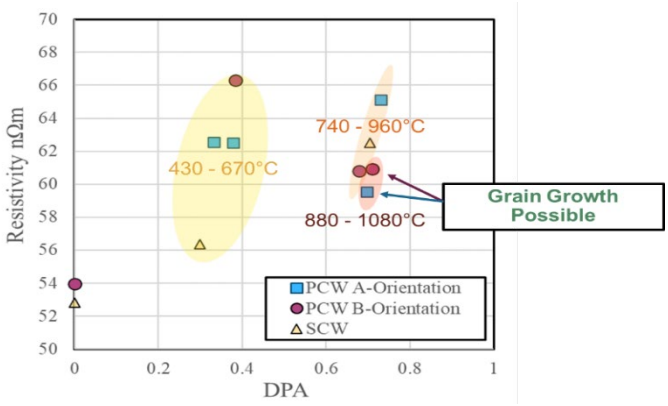

Figure 2. Electrical resistivity, as a function of DPA, for SCW and PCW materials. Irradiation temperature range for each capsule is shown by the yellow, orange, and red ovals. Measurements were taken between 20°C and 24°C and normalized for 20°C

For B-orientation samples, where grains can be elongated perpendicular or parallel to the direction of the measuring current, a methodology was developed to utilize sample orientation to quantify GB effects. As shown in **Figure 3**, the relative orientation of a sample to the measurement current will affect the average number of GBs crossed. Comparing the maximum/minimum number of GBs crossed with the maximum/minimum resistivity, in principle, allows for calculation of GB resistivity.

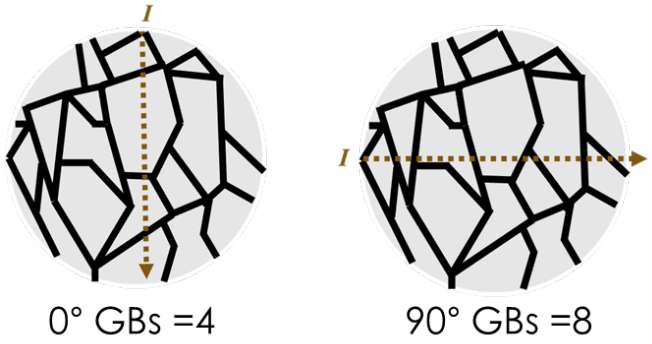

Figure 3. Illustration demonstrating how changing the orientation of the measurement current in a polycrystalline sample changes the number of GBs which the current must cross

In previous semi-annual reports, we have shown that A-orientation samples do not exhibit significant changes in resistivity due to measurement angle, while B-orientation samples do. We further observe, here, that B-orientation samples demonstrate a greater GB effect at higher irradiation doses. Figure 4 shows the angular resistivity of three samples irradiated to different doses at different temperatures. The amplitude in the sine-fits of the data is taken as the GB effect on resistivity. A plot of these three amplitudes with respect to DPA is shown in Figure 5, which fits a linear trend nicely. This trend suggests that at higher DPA, grain boundaries become stronger barriers to electron motion. Although there is not enough data to conclude that the GB effects are linear with DPA, this indicates a promising direction for future research.

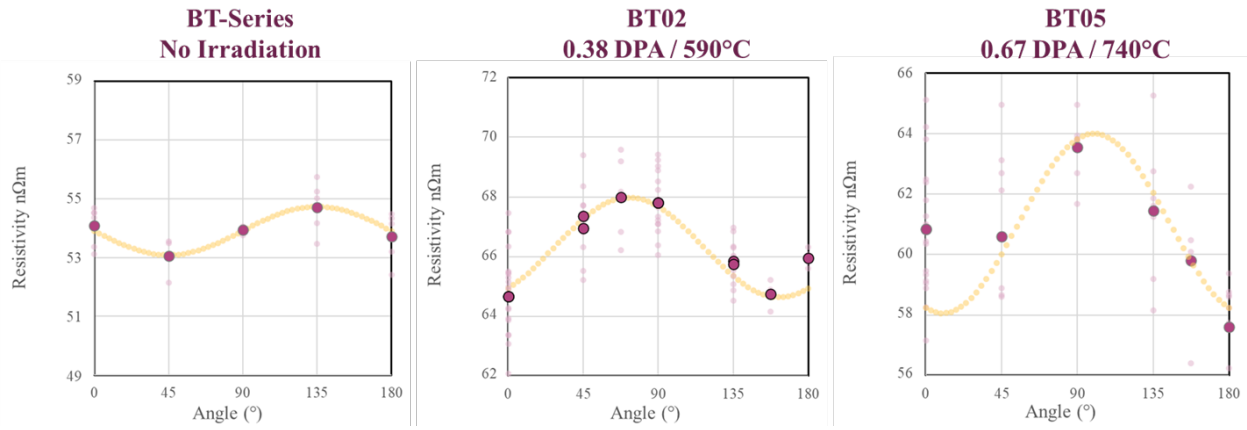

Figure 4. Resistivity of B-orientation samples as a function of arbitrary measurement angle. Note that the resistivity scale is different for all samples, but always represents a range of 10nΩm. Average values are shown in large, magenta circles, with individual measurements given with smaller, lighter circles. A sine wave fit is shown in yellow, approximating expected resistivity for any angle.

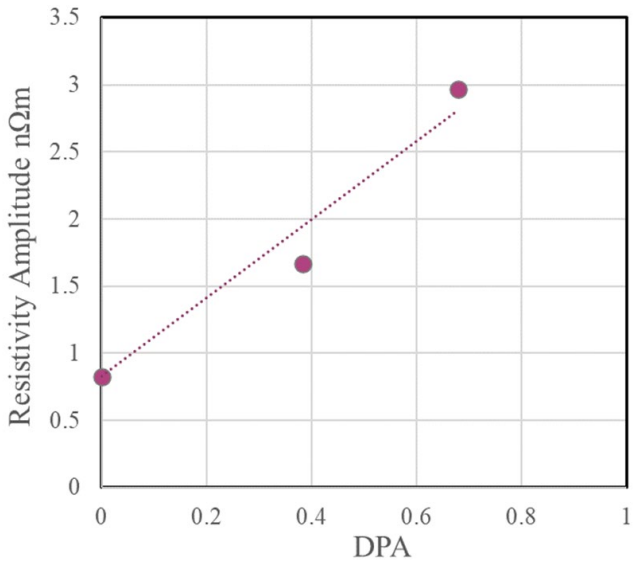

Figure 5. Resistivity amplitude plotted against DPA for three B-orientation samples. A linear fit is shown by the dashed line. Adding further data to this plot to test if a linear effect holds is an exciting avenue for further research.

FUTURE PLANS

Future work will continue quantifying GB effects on electrical resistivity. Comparisons to irradiation temperature, transmutation, microstructure, and thermal conductivity will be made in to clarify their relationship to irradiation changes in electrical resistivity.

4.6 FABRICATION OF ULTRA HIGH TEMPERATURE CERAMICS THROUGH DIRECT CURRENT SINTERING—B. Cheng, D.J. Sprouster, J. R. Trelewicz, L.L. Snead (Stony Brook University)

OBJECTIVE

In this work, we discuss our recent efforts to fabricate monolithic ultra-high temperature ceramic compacts using direct current sintering. We show that our fabrication leads to dense, uniform, crack-free microstructures. We report the thermal conductivity, density, and hardness of the compacts, and show that the sintering temperature and pressure can be lowered when sintering aids (Si or SiC) are added to the starting powder mixture. Our initial results demonstrate the utility, and ease at which controlled microstructures of UHTCs can be fabricated for fundamental and applied materials science investigations, such as irradiation performance.

SUMMARY

The development of fusion as a clean, sustainable energy source requires materials that are inherently resistant to demanding operating conditions [1]. Such extreme environments include, but are not limited to, mixed radiation fields (neutrons, plasma, electromagnetic), high stresses, high temperatures, high thermal flux, and generation of substantial gaseous (H and He) and solid transmutation products[2]. To address these harsh conditions, new engineered materials to withstand such harsh operating environments are under development. The development of next generation plasma-facing materials is one of the most challenging issues facing fusion power [3]. Novel UHTC materials, with high melting points and stable microstructures [4], offer unprecedented advancements as plasma-facing components and can potentially accelerate fusion as a sustainable commercial energy source. In this work, we report our recent efforts to fabricate UHTC materials using powder processing and direct current sintering.

Experimental Procedure

Pure, and mixed powders containing minor weight fractions of Si or SiC were initially cold pressed/loaded into a 2.5cm hardened steel dies (at ~100MPa). The pressed pellets were then transferred into a graphite sintering die and loaded into a the Sinterland DCS system (Sinterland LABOX-3010KF, Japan). The heating rate in the DCS was set to 100C/min (with the exception of the ZrB_2 specimen hat was heated at 200C/min) and specimens were heated to 1800-2000 ºC. The sintering hold time was 5 min. The combinations of pressure and temperature used to fabricate the monolithic UHTC compact specimens is given in Table 1. The final compacts dimensions are 25mm in diameter with 2-2.5mm thickness.

Results

The measured thermal conductivity, density and Vickers hardness of the pure, and Si/SiC additive specimens, as a function of sintering temperature is given in table 1. The density for all compacts is appreciably high (>95%). The addition of Si or SiC was found to effectively lower the temperature and pressure required to sinter the UHTC powder mixtures, with little change in the thermophysical, mechanical and density. The origins of the subtle differences between the pure and Si- and SiC additive specimens are currently under investigation and presumed to be due to the Si and SiC phases.

Representative optical micrographs of the fabricated monolithic NbC and NbC+4 wt% Si compacts are shown in Figure 1. The dark features in the NbC specimen are a slight surface porosity. The dark features in the NbC+4 wt% Si micrograph is due to a Si-rich particle phase. The final crystal structures of all compacts need to be investigated with X-ray diffraction (XRD). No visible cracks were seen from the optical microscopy. An additional confirmation of the uniform, defect-free microstructure is shown in the X-ray computed tomography reconstructed volume for the NbC specimen is shown in Figure 2. Again, the uniform

internal structure, with no visible cracks or defects, is seen in both (a) the cross section and (b) three-dimensional reconstruction through the monolith.

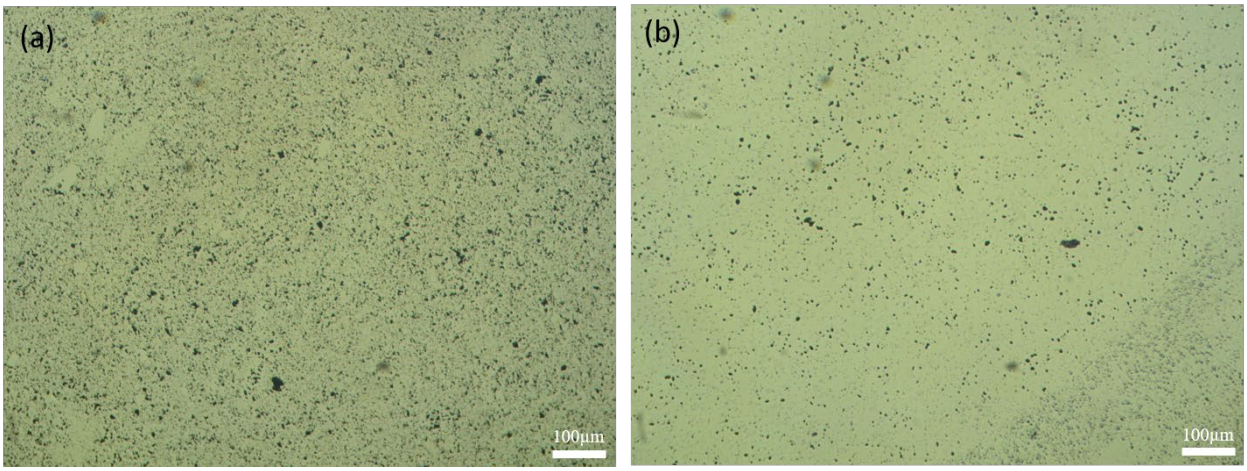

Figure 1. Optical micrographs of monolithic (a) NbC and (b) NbC+4 wt% Si UHTC compacts.

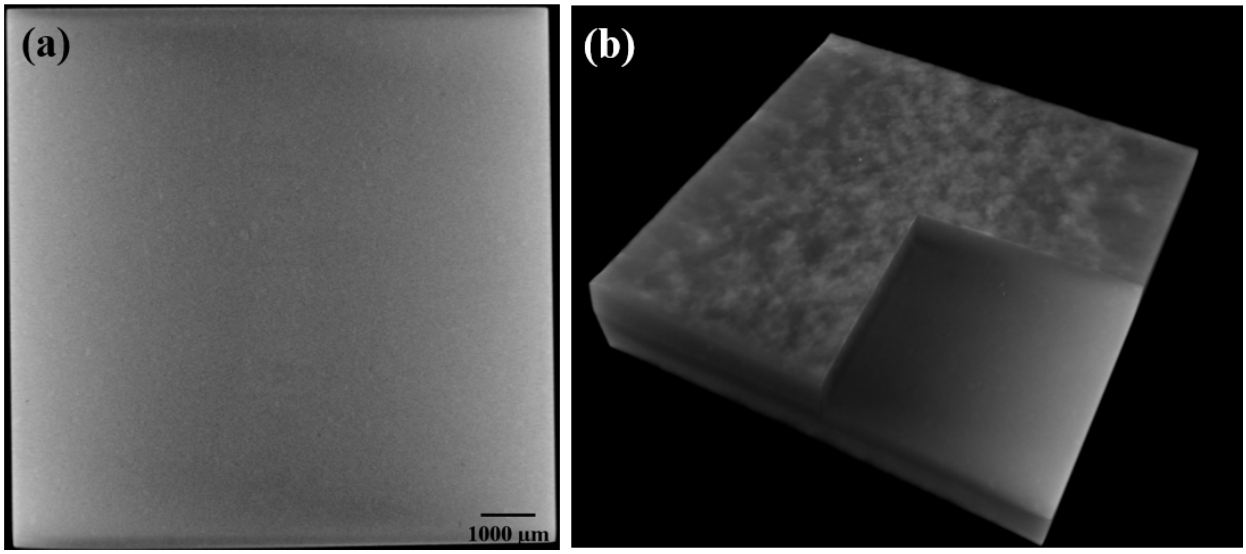

Figure 2. X-ray Computed Tomography (a) slice through thickness, and (b) 3D reconstruction with cut-away showing the uniform internal microstructure with no visible cracks or defects.

Table 1. List of UHTC materials, sintering conditions and physical properties

Composition	Sintering conditions	Thermal Conductivity at 27 ºC (W/(m*K))	True Density (g/cm^3)	Relative Density (%)	Hardness (HV@0.5Kg)
ZrC	1900 ºC, 50 MPa	29.39 ± 0.14	6.55	97.5	1869.78 ± 46.87
NbC	2000 ºC, 50 MPa	27.63 ± 0.16	7.50	96.1	1031.49 ± 59.07
Zr_2B	1900 ºC, 50 MPa	82.14 ± 1.18	6.10	99.5	1514.69 ± 81.42
ZrC+2wt%Si	1800 ºC, 10 MPa	28.12 ± 0.18	6.32	96.4	1741.19 ± 92.43
NbC+4wt%Si	1850 ºC, 10 MPa	28.67 ± 0.16	7.30	100	1785.62 ± 63.73
ZrB_2+10wt% SiC	1850 ºC, 10 MPa	100.78 ± 0.75	5.56	99.1	1821.21 ± 67.49

FUTURE WORK

Our initial results shown here indicate that simple powder processing and direct current sintering can fabricate dense UHTC compacts with relative ease. The addition of minor Si and SiC phases can effectively depress the temperatures and pressures required to sinter ZrC, ZrB_2 and NbC, with similar densities and thermophysical properties compared to their Si-free counterparts. Future work will include XRD characterization to identify the phases present, and to quantify the atomic structure with and without sintering additives. Additional thermophysical and mechanical characterization, including coefficient of thermal expansion and creep measurements are planned. These samples prepared via DCS are large enough to be machined into multiple small plate specimens ideal for neutron irradiation campaigns. Future neutron irradiation campaigns dedicated to understanding the thermophysical, mechanical and structural properties could thus be investigated to quantify the stability of UHTCs for future fusion energy applications.

ACKNOWLEDGEMENTS

These experiments and analysis were supported by the DOE Office of Fusion Energy Sciences under contract DE-SC0018322 with the Research Foundation for the State University of New York at Stony Brook

References

[1] S.J. Zinkle, L.L. Snead, Designing Radiation Resistance in Materials for Fusion Energy, in: D.R. Clarke (Ed.), Annu Rev Mater Res2014, pp. 241-267.
[2] T. Allen, J. Busby, M. Meyer, D. Petti, Materials challenges for nuclear systems, Mater Today 13(12) (2010) 14-23.
[3] C. Linsmeier, M. Rieth, J. Aktaa, T. Chikada, A. Hoffmann, J. Hoffmann, A. Houben, H. Kurishita, X. Jin, M. Li, A. Litnovsky, S. Matsuo, A. Von Müller, V. Nikolic, T. Palacios, R. Pippan, D. Qu, J. Reiser, J. Riesch, T. Shikama, R. Stieglitz, T. Weber, S. Wurster, J.H. You, Z. Zhou, Development of advanced high heat flux and plasma-facing materials, Nucl Fusion 57(9) (2017) 092007.
[4] W.G. Fahrenholtz, G.E. Hilmas, Ultra-high temperature ceramics: Materials for extreme environments, Scripta Mater 129 (2017) 94-99.

4.7 MULTIMODAL MICROSTRUCTURAL CHARACTERIZATION AND THERMAL STABILITY OF SOLUTE-STABILIZED NANOSTRUCTURED TUNGSTEN ALLOYS—N. Olynik, D.J. Sprouster, J.R. Trelewicz (Stony Brook University), C.M. Parish (Oak Ridge National Laboratory)

OBJECTIVE

Although tungsten has emerged as a promising candidate for plasma-facing components, there are several outstanding issues yet to be resolved including high temperature stability limited by recrystallization, mechanical performance, and long-term radiation tolerance. The overarching technical aim of this research is to address these limitations in tandem by precisely tailoring the volume fraction, chemistry, and structural state of grain boundaries in nanostructured tungsten alloys. We focus specifically on the W-Ti-Cr ternary system where Ti is introduced to stabilize the nanocrystalline grain boundary network while Cr is added to reduce the required sintering temperatures while simultaneously enhancing the alloy's oxidation resistance.

SUMMARY

Binary and ternary nanocrystalline tungsten alloys in the W-Ti-Cr system were synthesized via high-energy ball milling with microstructure and thermal stability characterized using a multi-modal approach involving synchrotron x-ray diffraction (XRD) and scanning transmission electron microscopy (STEM). Our results reveal stable nanocrystalline structures with grain sizes less than 20 nm at the maximum test temperature of 1400 °C, thus demonstrating targeted doping of the nanocrystalline state as an effective means for stabilizing tungsten against recrystallization and grain growth.

PROGRESS AND STATUS

Building on results from milling process development and guided by our alloy design effort, a parametric study was conducted to systematically investigate the role of Ti and Cr in the formation of heterogeneous microstructures for stabilizing tungsten against recrystallization. Using optimized milling conditions, a range of alloys were synthesized in the binary W-Ti systems with Ti varied over the range of 5-20 at.% in increments of 5 at.%. Based on the thermal stability measurements on the binary alloys, W-10 at.% Ti was selected as the base binary to explore the role of Cr additions on thermal stability with Cr varied over the range of 5-20 at.% in increments of 5 at.%. All samples were characterized using synchrotron XRD and STEM with thermal stability mapped via aging for 4 hours at 1200 and 1400 °C, which captures temperatures below and above the recrystallization temperature for pure W, respectively.

XRD results used to quantify the effect of Ti doping on thermal stability are shown in Figure 1. The as-milled powders were BCC W solid solutions across all Ti concentrations with peaks indexed accordingly, though we note the presence of two minor peaks at 2θ values of 4° and 6°. We believe these peaks are due to the formation of a complex tungsten carbide due to impurities in the feedstock powders and introduced during milling. While indexing of such minor peaks is challenging, systematic experiments are underway to facilitate identification of this minor second phase. The degree of peak broadening is consistent with a nanocrystalline state, as previously reported, and a comparable degree of peak broadening is apparent at 1200 °C with all peaks corresponding to BCC tungsten reflections. Interestingly, we note that the peaks remain broad in the pure W powders at this temperature, indicating W is stable in the nanocrystalline state up to 1200 °C. Conversely, at 1400 °C, destabilization of the nanocrystalline state was observed in the pure W and W-5 at.% Ti powders with significant sharpening of the BCC W peaks consistent with microstructural coarsening. Additionally, the W_2C phase formed with peaks indexed for the pure W spectrum. Neither of these phenomena were observed in the alloys containing ≥10 at.% Ti, indicating a threshold Ti concentration exists for stabilization of the nanocrystalline state.

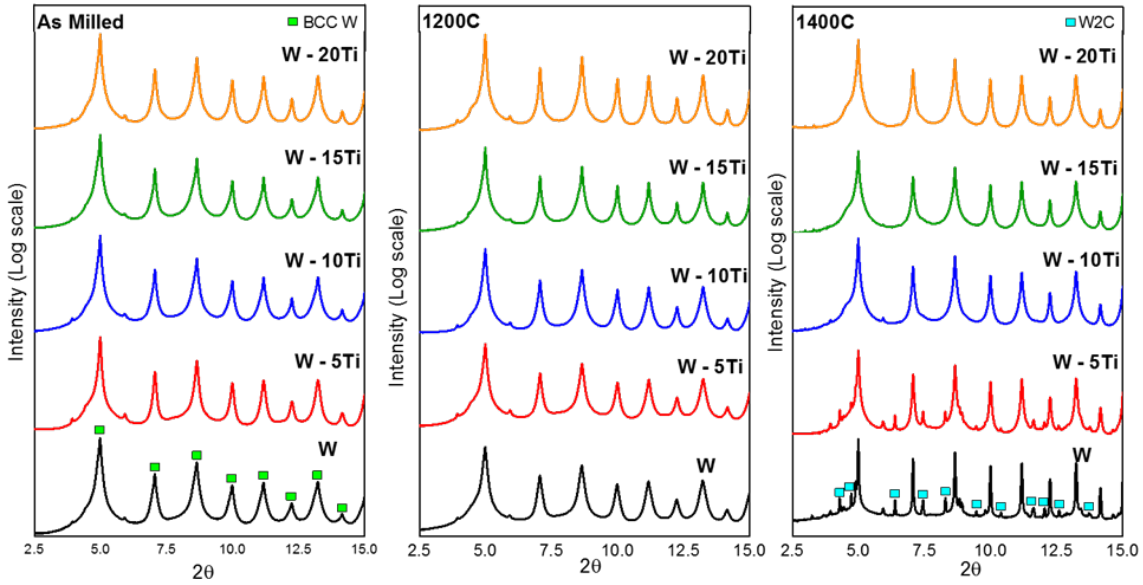

Figure 1. XRD spectra for milled W-Ti alloy powders with Ti varied from 5-20 at.% relative to commercially pure W powder milled under identical conditions to the alloys. The powder state (as milled or aging temperature) is shown in the upper left of each plot with reflections indexed for the BCC W solid solution (green squares) and tungsten carbide (blue squares).

Quantitative grain size analysis from the Rietveld refinements is summarized in Figure 2a as a function of aging temperature. Grain size stability as suggested from XRD peak broadening is confirmed up to 1200 °C in the range of 10-17 nm with variations consistent with the accuracy of XRD grain size measurements. Given that this temperature is only 35% of the melting point and below the average recrystallization temperature for pure tungsten of ~1250 °C[1, 2] (and we recognize this temperature can vary depending on the state of the material), retained stability of the nanocrystalline state is not surprising. However, if held for extended periods at this temperature, coarsening of the nanostructure is expected as previously reported in high-energy ball milled tungsten powders[3]. At 1400 °C, the grain size of pure nanocrystalline tungsten increased by an order of magnitude to approximately 230 nm while the grain size of the W-Ti alloys remained below 30 nm (Figure 2a). The grain size trend in Figure 2b demonstrates that for Ti concentrations of ≥10 at.%, the W-Ti alloys were stable at 1400 °C with only subtle increases in grain size to 15-20 nm. A doubling of the Ti concentration from 10 to 20 at.% had very little impact on stability, thus demonstrating diminishing returns at high Ti dopant concentration. These results are consistent with our previously reported modelling efforts and thus identify 10 at.% Ti as the optimal dopant concentration for stabilizing tungsten against recrystallization and grain growth.

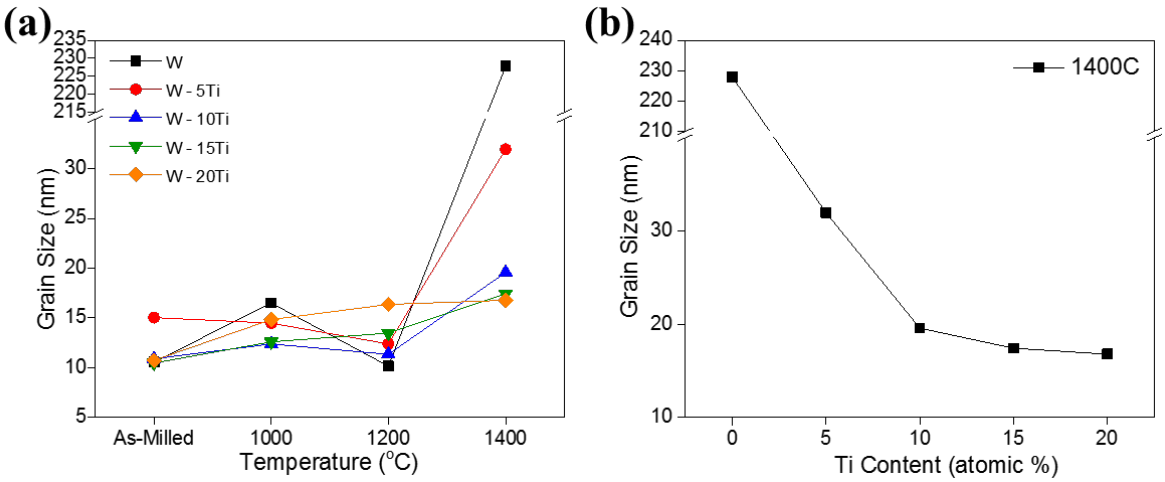

Figure 2. (a) Grain size as a function of aging temperature for the W-Ti alloy series relative to the as-milled state. (b) Grain size as a function of Ti content after aging at 1400 °C.

Using the W-10 at.% Ti alloy as a baseline, Cr was systematically added up to 20 at.% to determine the effect of Cr additions on thermal stability of the alloys. We note that Cr is of interest for reducing the sintering temperature in support of functionally graded plasma facing component architectures where lower processing temperatures are of interest. XRD results are shown in Figure 3 where all BCC W peaks exhibited broadening with Cr addition and through annealing, and as such is generally consistent with the baseline W-10 at.% Ti alloy and indicative of a stable nanostructure. At Cr concentrations of ≥15 at.%, a minor peak appeared at a 2θ value of ~5.6° in the as-milled powders, attributed to a nanocrystalline BCC Cr phase precipitating in the W solid solution. Additional reflections corresponding to the BCC Cr reflections were identified in the same composition alloys annealed at 1200 °C, while at 1400 °C these reflections only appeared in the powders containing 10 at.% Cr.

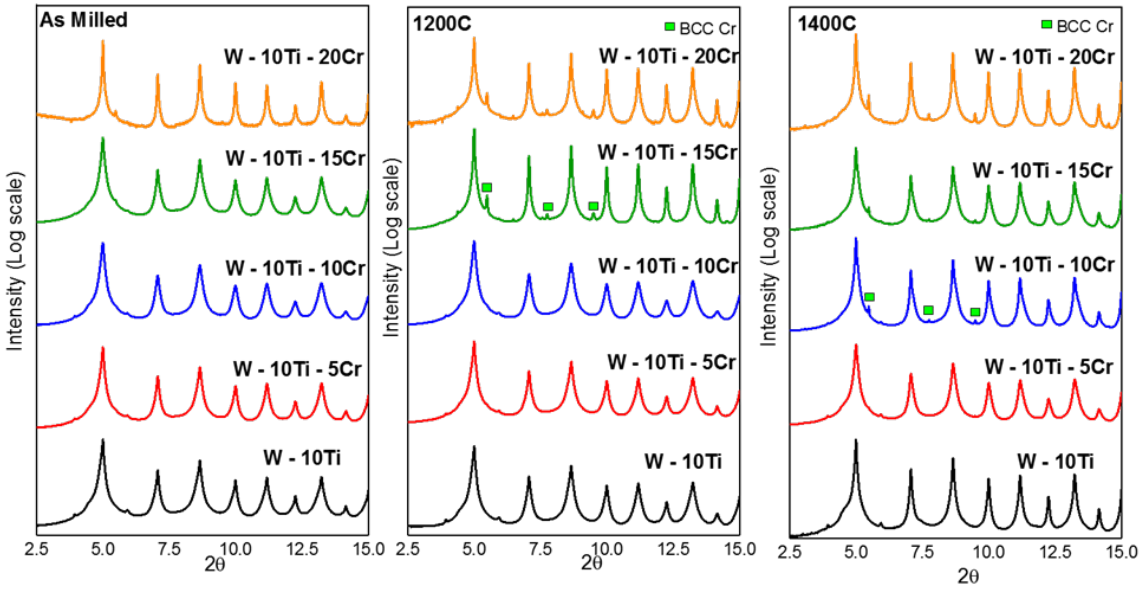

Figure 3. XRD spectra for milled W-10Ti-Cr alloy powders with Cr varied from 5-20 at.% relative to the W-10Ti alloy. Reflections are indexed for BCC Cr as green squares.

Quantitative grain size analysis from the Rietveld refinements is summarized in Figure 4a. For concentrations up to 10 at.% Cr, the grain size remained stable below 20 nm up to 1400 °C, indicating that the addition of Cr did not destabilize the binary nanocrystalline W-10 at.% Ti alloy. Furthermore, subtle improvements in stability were realized at 1400 °C. For the highest Cr concentration of 20 at.%, the grain size was largest in the as-milled state, yet remained stable up to 1400 °C. The transient increase in grain size at 1200 °C for the W-10Ti-20Cr alloy could potentially be related to the precipitation of the BCC Cr phase, as shown in Figure 4b. However, because the aging experiments were performed *ex situ* (aging followed by characterization), the mechanism cannot be directly ascertained from this data. A sample is being prepared for *in situ* XRD measurements to determine whether this anomalous grain size is truly representative of a transient state of the microstructure, or rather due to intrinsic variability in the powder samples.

With the goals of retaining thermal stability of the W-10 at.% Ti alloy while forming a small fraction of BCC Cr to serve as a sintering aid, 10-15 at.% Cr provides access to thermally stable ternary alloys with approximately 2-5 wt.% BCC Cr phase. The complex temperature dependence derives from the competition between enthalpic and entropic contributions to the free energy, consistent with our lattice Monte Carlo models. Generally, an increase in temperature above 1000 °C promotes dissolution of the BCC Cr phase, but this process also depends on the amount of Cr present in solution. Indeed, precipitation of this phase exhibits a complex dependence on both temperature and composition as discussed in the binary W-Cr system[4] and recently demonstrated through *in situ* transmission electron microscopy imaging on nanocrystalline W-Cr thin films[5]. *In situ* annealing experiments are planned to map out the formation and dissolution of the BCC Cr phase. Nonetheless, all the ternary alloys retained grain sizes below 25 nm at 1400 °C, thus demonstrating targeted doping of the nanocrystalline state for stabilizing tungsten against recrystallization and grain growth.

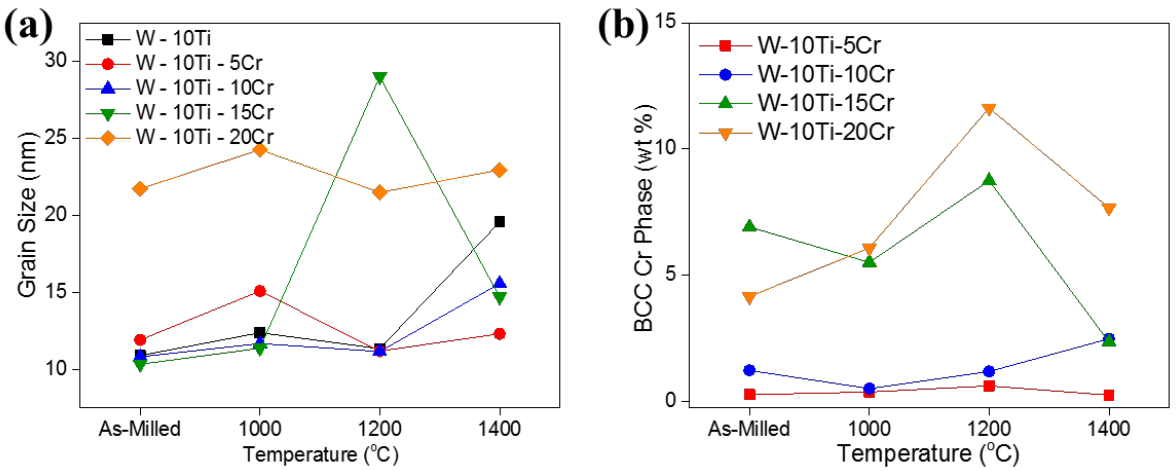

Figure 4. (a) Grain size as a function of aging temperature for the W-10Ti-Cr alloy series relative to the W-10Ti alloy milled and annealed under identical conditions as the ternary alloys. (b) Fraction of BCC Cr phase as a function of aging temperature, demonstrating a complex temperature dependency due to the interplay between the enthalpic and entropic contributions to nanostructure stability.

Grain size stability ascertained from synchrotron XRD measurements was confirmed using STEM imaging and EDS mapping. The powders were generally too thick for imaging of the nanocrystalline grain structure, even around the edges of the individual particles. Focused ion beam (FIB) milling was thus employed to extract electron transparent sections from powder particles of the W-10Ti-10Cr alloy following the 1400 °C heat treatment. Bright and dark field TEM micrographs are shown in Figure 5(a,b) with a selected area diffraction (SAD) pattern in the inset of the bright field image. The nanocrystalline grain structure is clearly visible in these micrographs and consistent with the many diffraction spots in the SAD pattern. The

nanocrystalline grain structure is also apparent in the high-angle annular dark field (HAADF) micrograph in Figure 5c, with variations in contrast suggesting the presence of compositional heterogeneities in this alloy. However, EDS mapping did not reveal clear regions of Cr and Ti segregation, which we attribute to the difficulties in adequately thinning the FIB sections extracted from the powder samples. Additional STEM experiments will be performed on the bulk alloys produced through hot consolidation of these powders.

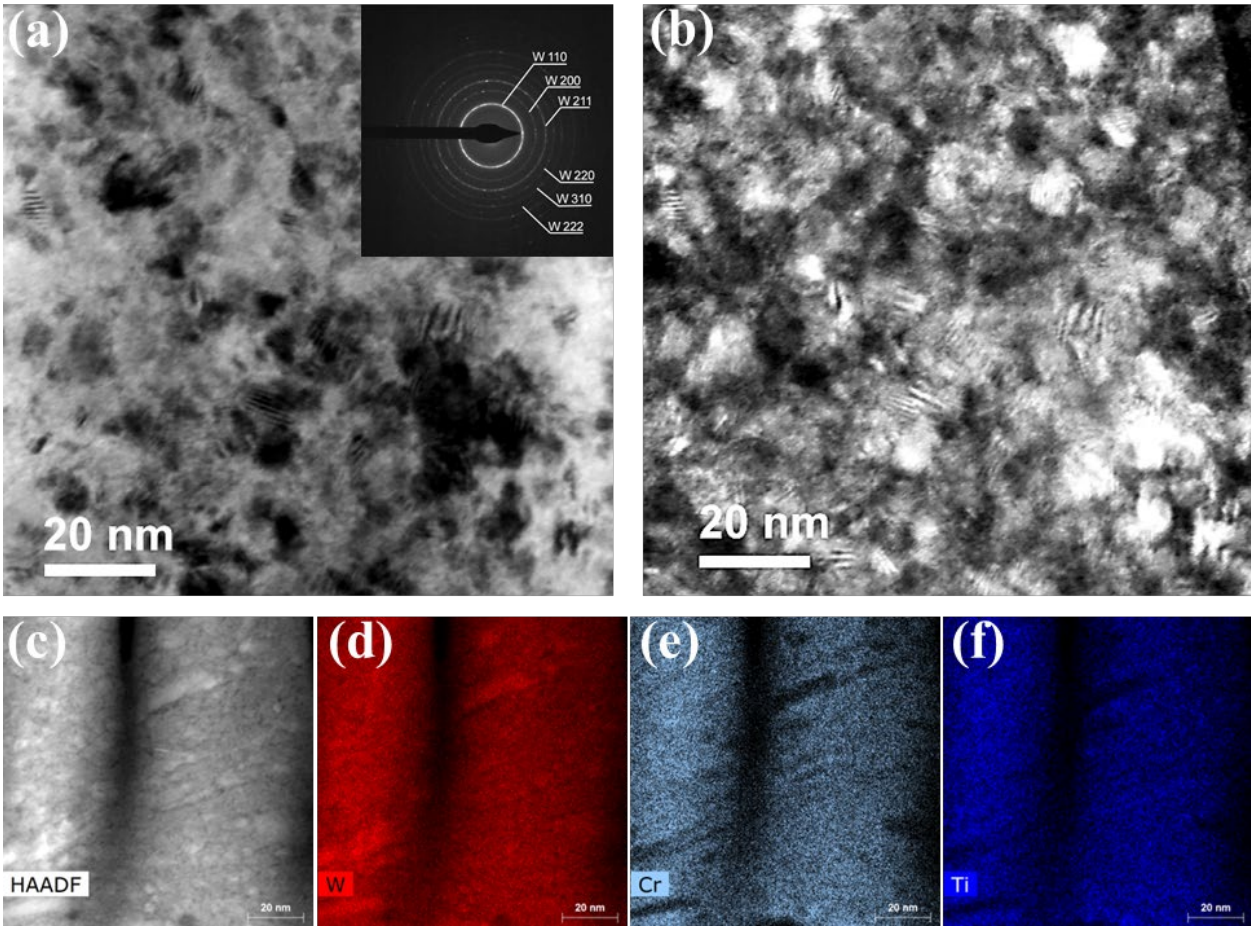

Figure 5. (a) Bright field and (b) dark field TEM micrographs of the equiaxed microstructure in the W-10Ti-10Cr alloy after aging at 1400 °C. (c) HAADF micrograph and corresponding elemental distributions for (d) W, (e) Cr, and (f) Ti demonstrating only subtle compositional heterogeneities within the resolution of the technique.

FUTURE WORK

Systematic experiments are underway to correlate structural features at the nanoscale with alloy chemistries and aging conditions. By selecting ternary configurations containing Ti at grain boundaries and a distributed Cr-rich nanophase, bulk nanostructured samples will be produced and characterized via synchrotron x-ray analysis and correlative electron microscopy experiments.

ACKNOWLEDGEMENTS

This work was supported by the Department of Energy through Grant DE-SC0017899. This research used beamline 28-ID-2 (XPD) at NSLS-II, a U.S. Department of Energy (DOE) Office of Science User Facility

operated for the DOE Office of Science by Brookhaven National Laboratory under Contract No. DE-SC0012704. ORNL research sponsored by the U.S. Department of Energy, Office of Fusion Energy Sciences under contact DE-AC05-00OR22725 with UT-Battelle LLC.

References

[1.] I. Uytdenhouwen, M. Decreton, T. Hirai, J. Linke, G. Pintsuk and G. Van Oost, *Journal of Nuclear Materials*, 2007, 363, 1099-1103.
[2.] K. Wang, D. Ren, X. Zan, L. Luo, X. Zhu and Y. Wu, *Materials Science and Engineering: A*, 2021, 806, 140828.
[3.] T. Chookajorn, H. A. Murdoch and C. A. Schuh, *Science*, 2012, 337, 951-954.
[4.] T. Chookajorn, M. Park and C. A. Schuh, *Journal of Materials Research*, 2015, **30**, 151-163.
[5.] O. K. Donaldson, K. Hattar, T. Kaub, G. B. Thompson and J. R. Trelewicz, *Journal of Materials Research*, 2018, **33**, 68-80.

5. ADVANCED MANUFACTURING

5.1 DEVELOPMENT OF NOVEL STEELS WITH NANOPRECIPITATE DISPERSIONS VIA ADDITIVE MANUFACTURING FOR HELIUM EFFECTS STUDIES—Weicheng Zhong, Ying Yang, Lizhen Tan (Oak Ridge National Laboratory), Niyanth Sridharan (Lincoln Electric), Dieter Isheim (Northwestern University), T.M. Kelsy Green, Kevin G. Field (University of Michigan)

OBJECTIVE

The goal of this project is to use newly developed nanostructured steel compositions to produce model steel samples for radiation effects testing. The samples will be used to study the role of helium on the stability of MX and $M_{23}C_6$ precipitates in steels under controlled ion beam irradiations and perform said preliminary irradiation testing.

SUMMARY

A newly designed nano-structured 9 wt.% Cr ferritic-martensitic (FM) steel, designated as ANA2 (Additive-manufactured Nanostructured Alloy, Composition #2) was fabricated via the direct energy deposition (DED) additive manufacturing (AM) method. The DED process was used to enable rapid solidification in the monolithic structures that enables an increased precipitation compared to conventional manufacturing processes. The as-printed ANA2 showed tensile properties (strength and elongation) and Charpy impact toughness (upper-shelf energy and ductile-brittle transition temperature) comparable to oxide-dispersion-strengthened (ODS) Eurofer and PM2000. Compared to wrought FM steels, the as-built ANA2 showed significantly higher yield strength but inferior Charpy impact toughness and ductility. Microstructural characterization revealed the high density of ultrafine nano-structured platelet-like precipitates in the matrix of ANA2 desired for radiation effects testing. These precipitates remained at a high density after preliminary ion irradiation testing, leading to the suppression of cavity-induced swelling.

PROGRESS AND STATUS

The as-built ANA2 has a dimension of 60 (length) × 60 (height) × 12 (thickness) mm^3, with no noticeable distortion in the build. Initial efforts focus on the mechanical properties testing and microstructure characterization on the as-built steels. Figure 1 shows the yield strength, uniform plastic elongation (UPE), total plastic elongation (TPE), and Charpy impact testing results of the ANA2, in comparison to other as-built 9-12Cr FM steels, wrought 9Cr steels and ODS steels. Compared to other as-built 9-12 wt.% Cr steels, ANA2 showed comparable yield strength, UPE and TPE in general. The ANA2 has higher yield strength but lower TPE than wrought FM steels (e.g. P91), and higher yield strength and comparable UPE and TPE than some ODS steels (ODS-Eurofer, and 20Cr PM20000). Charpy impact testing results show comparable toughness values of ANA2 with 9Cr ODS-EU and 20Cr PM2000, but a noticeable lower toughness than that of wrought G91 steels.

Microstructure characterization in Figure 2 revealed a fine grain structure with the presence of both fine laths and equiaxed grains. Detailed TEM characterization indicates a low density of large (>100 nm) V- and Mn-rich precipitates, a few $Cr_{23}C_6$ precipitates at grain boundaries, and a high density of V-rich precipitates at the boundary and in the matrix. V-rich precipitates in the matrix exhibited a platelet morphology, which have the platelet normal to the {001} planes of the matrix. The number density and average size (platelet length or diameter) of the VN platelets were quantified to be about 2.5×10^{22} m^{-3} and 5.8 ± 1.2 nm. Such a high number density of MX is approaching that of oxide particles in some ODS steels and should provide a dominant irradiation sink density for ANA2. Given the high density, it is unclear how altering the helium-to-dpa ratio under ion irradiations will contribute to the stability of precipitates at elevated temperature.

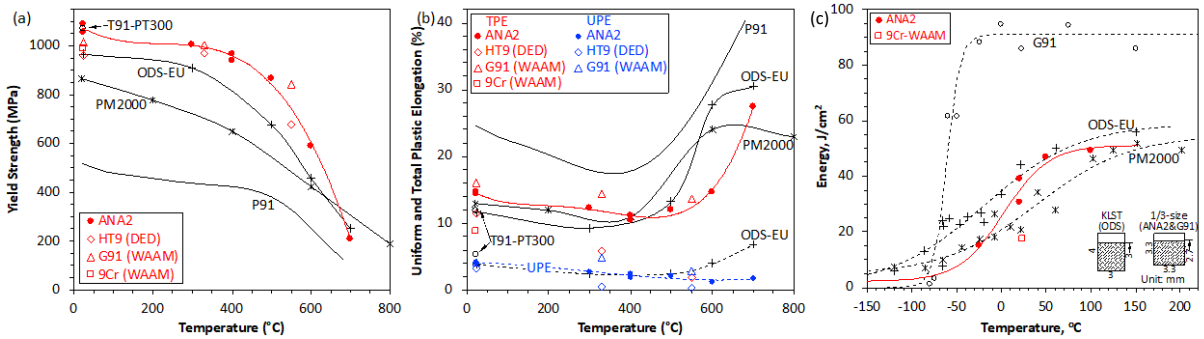

Figure 1. Temperature-dependent (a) yield strength and (b) uniform and total plastic elongation of ANA2 compared with the HT9-DED [1], G91-WAAM [2], and 9Cr-WAAM [3], as well as the wrought T91-PT300 [4], P91 [5], ODS-EU [6], and PM2000 [7]. The results of the AM as-built 9-12 wt% Cr steels are shown in red or blue. Figure reproduced from Reference [8].

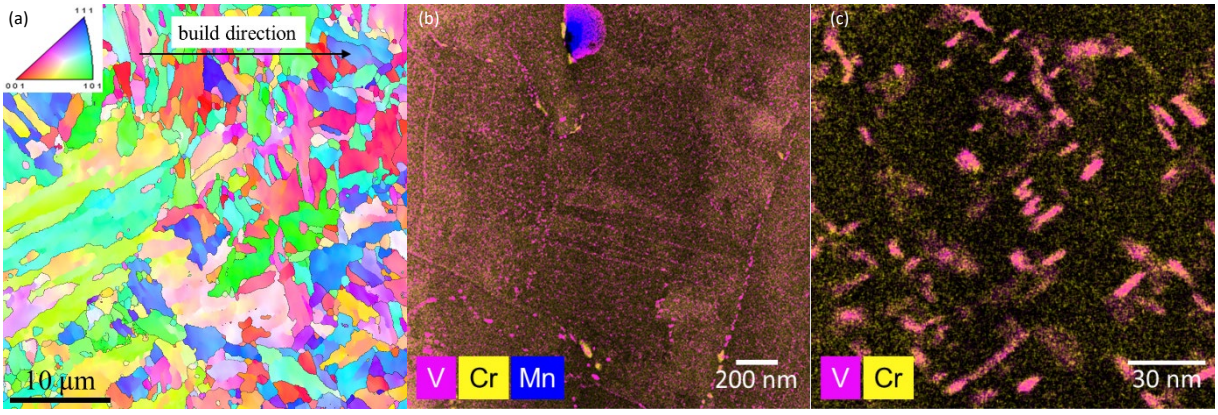

Figure 2. (a) Inverse pole figure, (b) V (pink), Cr (yellow), and Mn (blue) maps showing the precipitates distribution, and (c) V (pink) and Cr (yellow) maps showing platelets distribution in the matrix. Figure reproduced from Reference [8].

To form the basis of the irradiation response of the V-rich platelet precipitates in the ANA2 a rapid dual-beam ion irradiation was conducted. An ANA2 sample extracted from the AM build was dual ion irradiated with Fe^{++} and He^{++} ions to 16.6 dpa with a dose rate of 5.7×10^{-4} dpa/s and 4 appm He^{++}/dpa at 445°C at the Michigan Ion Beam Laboratory. Preliminary TEM analysis has shown suppression of cavity formation as compared to wrought Grade 91, a conventional and commercial FM steel, irradiated under same conditions. Traditional Grade 91 steel exhibited a number density of 5.8×10^{20} m^{-3} of cavities with an average size of 4.5 ± 0.2 nm [9]. In comparison, a number density of $(1.0\pm0.2)\times10^{21}$ m^{-3} cavities with an average size of 2.2 ± 0.4 nm was found in the ANA2 specimen. Representative images of the cavity density and structure are shown in Figure 3. The enhanced density of small cavities in ANA2 is hypothesized to be a consequence of the increased sink strength from the nanoscale precipitation and the residual stress induced from additive manufacturing. The number density of precipitates and morphology remained statistically unchanged after irradiation, exhibiting a density of $(2.0\pm0.4)\times10^{22}$ m^{-3} of platelet-like precipitates. However, after irradiation the precipitates within the matrix were mainly depleted of V while grain boundary precipitates saw no significant changes in elements present as shown in Figure 4. The average length of the irradiated platelets was 7 ± 2 nm. Ongoing studies include determining the correlation or anti-correlation of the precipitates to the cavities in the irradiated microstructure as well an expanded irradiation campaign to capture trends as a function of dose, dose rate, and temperature.

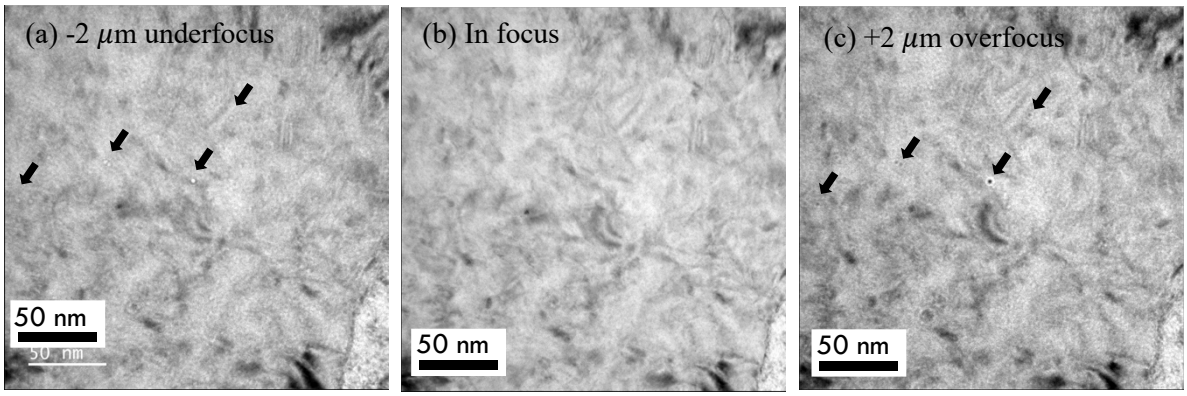

Figure 3. Conventional TEM imaging of cavities in (a) under focus, (b) in focus, and (c) overfocus conditions of the irradiated ANA2.

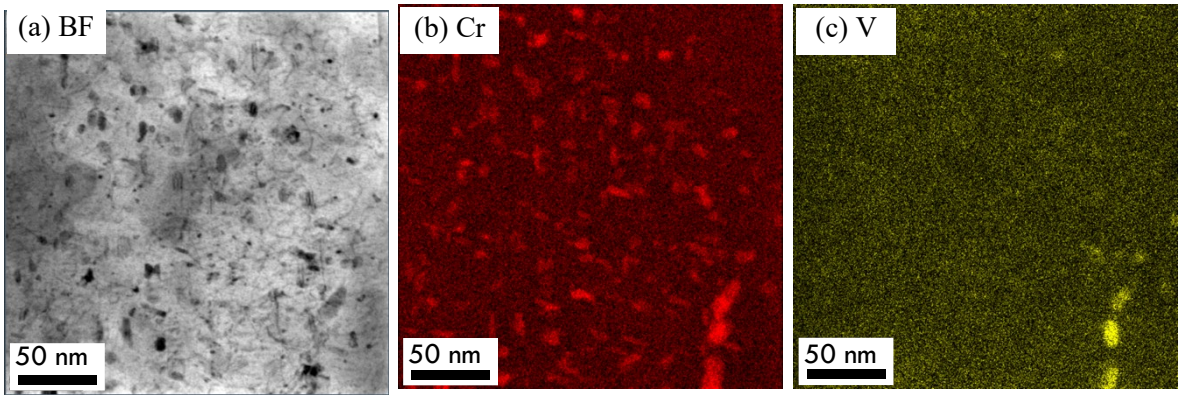

Figure 4. (a) Bright field, (b) Cr map, and (c) V map showing precipitates post-irradiation in ANA2.

CONCLUSION AND FUTURE WORK

The use of additive manufacturing to impart a high density of MX precipitates is a steel matrix has been demonstrated. Preliminary dual-beam ion irradiations have indicated a stability in the size, number density, and morphology of the precipitates but a localized change in composition. An ongoing irradiation campaign is underway to investigate the precipitate stability as a function of implanted helium as well as varying irradiation parameters such as dose, dose rate, and temperature.

ACKNOWLEDGEMENTS

Research and development efforts associated with the DED technology was supported by the Laboratory Directed Research and Development Program of Oak Ridge National Laboratory (ORNL) and the U.S. Department of Energy (DOE), Office of Nuclear Energy (NE), Advanced Fuels Campaign, under Contract no. DE-AC05-00OR22725 with UT-Battelle, LLC. Samples from these efforts were procured, irradiated, and characterized as part of an FES sponsored Early Career Award (DE-SC0021138).

References

[1] N. Sridharan, M.N. Gussev, K.G. Field, Performance of a ferritic/martensitic steel for nuclear reactor applications fabricated using additive manufacturing, J. Nucl. Mater. 521 (2019) 45-55.

[2] N. Sridharan, K.G. Field, A road map for the advanced manufacturing of ferritic-martensitic steels, Fus. Sci. Tech. 75 (2019) 264-274.
[3] C. Gao, X. Chen, X. Chen, C. Su, Microstructure and mechanical properties of as-deposited and heat-treated additive manufactured 9Cr steel, Mater. Sci. Tech. 35 (2019) 2234-2242.
[4] Z. Shang, J. Ding, C. Fan, M. Song, J. Li, Q. Li, S. Xue, K.T. Hartwig, X. Zhang, Tailoring the strength and ductility of T91 steel by partial tempering treatment, Acta Mater. 169 (2019) 209-224.
[5] NIMS Creep Data Sheet No. 43A, National Institute for Materials Science, Japan, 2014. (https://smds.nims.go.jp/creep/en/)
[6] D.A. McClintock, M.A. Sokolov, D.T. Hoelzer, R.K. Nanstad, Mechanical properties of irradiated ODS-Eurofer and nanocluster strengthened 14YWT, J. Nucl. Mater. 392 (2009) 353-359.
[7] R.L. Klueh, J.P. Shingledecker, R.W. Swindeman, D.T. Hoelzer, Oxide dispersion-strengthened steels: a comparison of some commercial and experimental alloys, J. Nucl. Mater. 341 (2005) 103-114.
[8] W. Zhong, N. Sridharan, D. Isheim, K.G. Field, Y. Yang, K. Terrani, L. Tan, Microstructures and mechanical properties of a modified 9Cr ferritic-martensitic steel in the as-built condition after additive manufacturing, J. Nucl. Mater. 545 (2021) 152742. doi:10.1016/j.jnucmat.2020.152742.
[9] S Taller et al., Emulation of fast reactor irradiated T91 using dual ion beam irradiation, Journal of Nuclear Materials (527) 2019 151831.

5.2 SYNCHROTRON ANALYSIS OF WIRE ARC ADDITIVE MANUFACTURED G-91 STEEL—I.K. Robin, S. J. Zinkle (University of Tennessee), D.J. Sprouster, L.L. Snead (Stony Brook University)

OBJECTIVE

Additive manufacturing (AM) is capable of producing highly complex geometrical shapes in a very short amount of time which may be key to fabrication of complex fusion reactor blanket structures. In this current research, AM build 9 Cr G-91 ferritic/martensitic (FM) steel is explored. Synchrotron XRD characterization was used to explore the phase composition, microstrain, and coherent grain size of the G-91 steel. The effectiveness of heat treatment was examined through XRD studies and the amount of carbon present in the martensitic structure were also determined. This work is a demonstration that a proper heat treatment of an AM build steel can be capable of producing steel as a structural material that may be employed in real-life service conditions in nuclear industry.

SUMMARY

Different variants of FM steel are being explored for the best possible mechanical properties that can be leveraged in nuclear reactors. Some well-known variants of FM steel are Grade 91 (9Cr-1Mo) and modern reduced activation derivatives such as CNA [1] in the United States, JLF1 and F82H in Japan, Eurofer91 in Europe, CLF-1, and CLAM (China Low Activation Martensite) in China, 12Cr-1.6Mo (1KH12M2S2) in Russia [2]. Traditional way of manufacturing starts with ingot production which is followed by different treatments such as hot extrusion, forging/ rolling operation, cold drawing/ pilgering, and finally heat treating the steel through normalizing and tempering to produce a feedstock material [3]. Oftentimes this requires a longer lead time. Welding and joining processes are also necessary to join FM steel for components to be uses in industrial application. These joining and weldments are the weakest link of the structure and at high temperature and high/ low stresses, fracture can occur because of Type-IV failure particularly in the fine-grained heat affected zone (HAZ) and over tempered zone often caused by thermal cycles imposed during welding. This is responsible for reducing the creep life of the steel and it becomes one major limitation for reactor engineering [4]. Moreover, producing complicated geometrical shape as a necessary requirement for advanced reactor design maybe very difficult/ impossible through conventional manufacturing means. An elegant solution for this problem is to leverage the most promising advanced manufacturing technique additive manufacturing (AM). AM not only gives us the opportunity to produce complex geometrical shape without the localized weak points common for welding joints, but also holds the possibility for us to manipulate texture, functional grading, microstructure, phase changes, nano-inclusions, dispersoids, and precipitates to come up with the most optimized mechanical property for real-life application. AM has come a long way to produce parts for nuclear application for different materials like austenitic stainless steel [5], Ni-based super alloys like Inconel 718 [6], and FM steels like G91 [7] and HT9 [8].

PROGRESS AND STATUS

Additive Manufacturing of FM G-91

Repeated thermal cycling is a common phenomenon in AM processing which may result in heterogeneous microstructures and a gradient of chemical and mechanical properties in the fabricated component [9-11]. As the solidification occurs in a typical low carbon FM steel, the first solid phase to form is δ-ferrite, which is transformed into austenite and upon further cooling a final martensite phase forms [7, 8]. Other than the primary martensite phase, some secondary phases can also form during thermal cycling which oftentimes includes $M_{23}C_6$ carbides, MX, and other carbides and carbonitrides [12-15]. As a result, prior austenite grains boundaries, lath, packets, and a complex mixture of precipitates are common characteristics of an AM build FM steel [2,3]. Often times the straightforward transformation process of Liquid → δ→ Υ during the solidification process is incomplete due to kinetics of the transformation, and residual δ-ferrite is a

common feature of AM build FM steels and associated with the loss of toughness [12]. Local segregation of alloying elements can occur during solidification and result in the retention of austenite [14, 15]. Optimizing the AM process parameters and post fabrication heat treatment are thus necessary to fabricate homogeneous microstructures of refined, tempered martensite along with a distribution of carbides. The complex kinetics during solidification in FM steel necessitates the use of characterization techniques that can uncover the phase transformations and give insight into the phases that ensue with fabrication and post build heat treatment. Here, we employ high energy synchrotron X-ray diffraction (XRD) to understand the as-built and heat treated-microstructures of AM 9 Cr G-91 FM steel.

Materials and Methods

Material Fabrication

Wire arc additive manufacturing (WAAM) was employed to produce ferritic martensitic steel at the Manufacturing Demonstration Facility (MDF) at Oak Ridge National Laboratory. Composition for both the wire composition and build material are included in the Table 1. The diameter of the electrode was chosen to be 1.2 mm. A constant gas flow rate of 200 L/min was maintained and the current was kept constant at 230 A. Scanning speed for the process was 2.22 mm/s. In order to reduce residual stress, interpass was carried out at a temperature of 300 ºC. During the manufacturing process, 5% CO_2 was intentionally bled through 95% shielding gas (Argon) in order to increase the carbon content to get more precipitation which is expected to produce better creep properties at high temperatures. A portion of the final build from AM machine is shown in Figure 1 (a).

Table 1. Nominal composition of wire-fed additively manufactured G-91 FM steel (both composition of wire and composition after build included)

Element	Fe	Co	Cr	Mn	Mo	Nb	Ni	V	Si	C	O	N
Wire Composition	Bal	-	8.62	0.41	0.92	0.08	0.15	0.24	0.31	0.08	0.008	0.04
Build ☆	89.38	0.09	8.41	0.32	0.93	0.06	0.14	0.22	NR	0.093	0.0316	0.0386

☆ Composition after post processing heat treatment

Heat Treatment

Due to very rapid heating and cooling cycle (~10^4 ºC/s) during the AM process, residual stress is common in AM build materials [16, 17]. In low carbon FM steels, the hardening from austenite to martensite is a displacive transformation and a substantial number of dislocations are produced to accommodate the volume change of the unit cell. This effectively renders the material hard but with low ductility [9]. Heat treatment is used to bring back some of the superior mechanical properties of the steel [3,18]. In this research, the heat treatment is performed in two steps. The first step is to austenitize the sample at 1100 ºC for 30 minutes. In this step, all the existing δ-ferrite and martensite will have enough time and thermodynamic driving force to form a fully austenitic phase. This heat treatment is followed by air cooling where austenite is expected to transform to a fully martensitic structure. 1100 ºC is chosen so that the austenitizing temperature is above the carbide solvus temperature where prior austenite grains coarsen in the subsequent heat treatment, but it also produces a distribution of finer carbide particles which tends to result in the most optimum microstructure. The second step of heat treatment is tempering the sample at 760 ºC for 60 minutes, followed by air cooling. During tempering, interstitial carbon atoms come out of the prior martensitic structure [3]. These carbon atoms bind with different alloying elements to produce carbides like $M_{23}C_6$ and MX (M= Cr, Ti, etc., X=C).

Experimental Methods

The XRD measurements were performed at the National Synchrotron Light Source-II (NSLS-II) using the high-energy X-rays available at The X-ray Powder Diffraction beamline (XPD). All measurements were performed in transmission mode with an amorphous Silicon-based flat panel detector (Perken-Elmer) mounted orthogonal to and centered on the beam path. The sample-to-detector distances and tilts of the detector relative to the beam were refined using a LaB_6 powder standard (NIST standard reference material 660c). The wavelength of the incident X-rays was 0.1917 Å (66.676 keV). The sample-to-detector distance was calculated to be 1387.81 mm. 300 individual patterns with detector exposures of 0.2s were collected for each specimen. All raw two-dimensional patterns were background corrected by subtracting the dark current image and the air scattering and Kapton background within IgorPro (Wavemetrics). Noticeable artefact regions of the detector (like the beam stop, dead pixels) were masked. The corrected and masked two-dimensional detector images were then radially integrated to obtain one-dimensional powder diffraction patterns.

Phase identification was performed using Match3! (Crystal Impact, Bonn, Germany). The background subtracted XRD patterns were Rietveld refined with the MAUD software package. The peak profiles were modeled by a modified pseudo-Voigt function. The instrument contribution to the broadening of the measured profiles was quantified by fitting the LaB_6 NIST powder standard, with a known coherent grain size and negligible microstrain contribution. The Gaussian and Lorentzian-based broadening parameters were subsequently fixed during the analysis of the alloys under investigation to quantify the microstructure (coherent grain size and microstrain components). The phase fraction, lattice parameter, microstrain and coherent grain size components were allowed to vary for the different crystal phases present. The microstrain components for the $M_{23}C_6$ phase (in HT-G91) was not included in the refinements. Therefore, the refined coherent grain size parameters of the $M_{23}C_6$ phase are lower limits.

RESULTS

The plate AM as-built G-91 steel is shown with in Figure 1 (a). The optical micrograph [Figure 1(b)] shows the presence of prior austenite grain boundaries, martensite packets and laths. After heat treatment, a change in microstructure and morphology is observable in the optical micrograph shown in Figure 1(c) [12]. The heat treatment leads to a homogenous and refined microstructure. The XRD results complement the results obtained from optical micrograph.

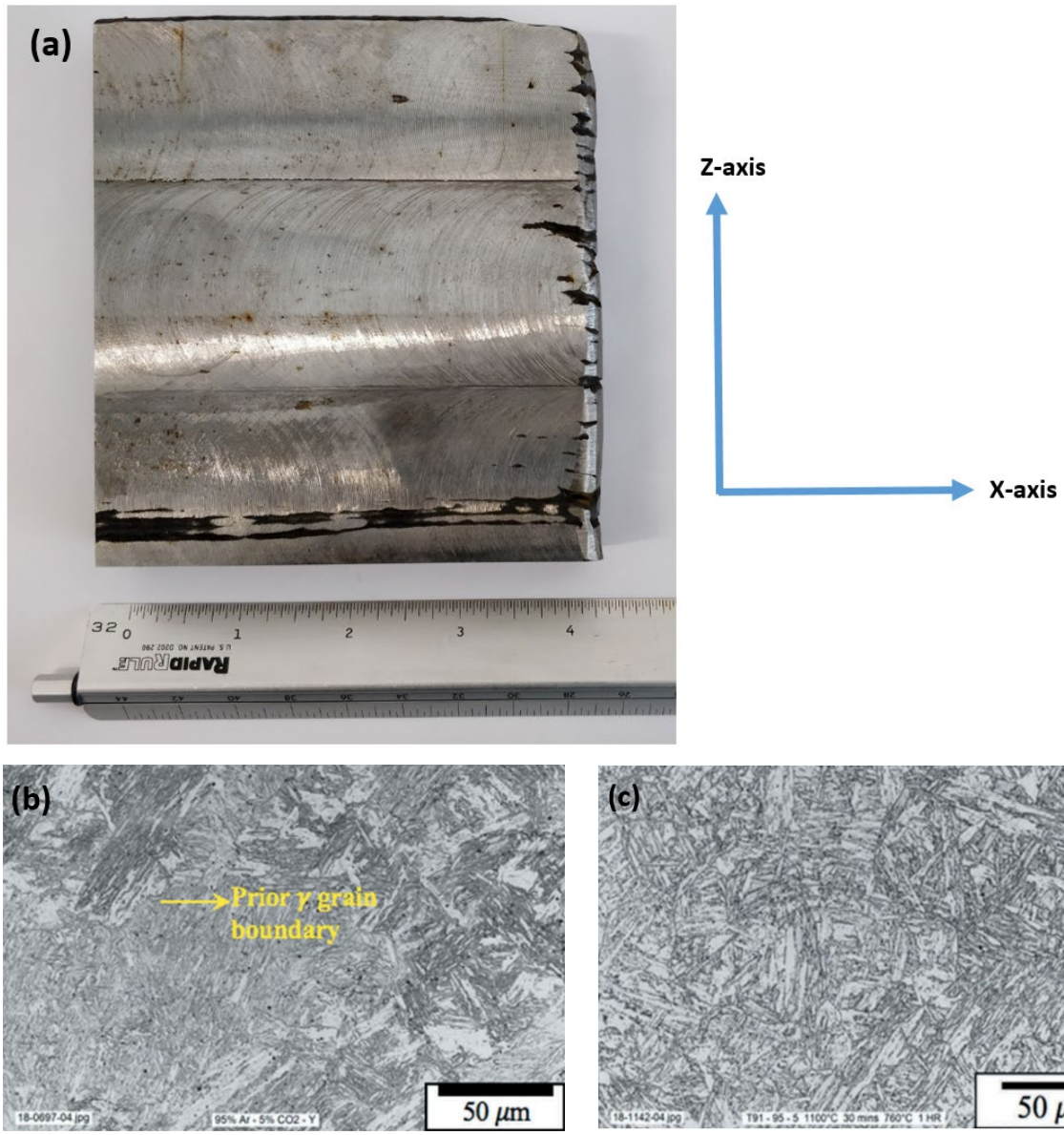

Figure 1. AM build G-91 steel is shown in (a) (length in inches). Additional Optical micrographs are shown in (b) for as built and (c) as normalized at 1100°C+760°C tempering treatment of G-91 [12].

The XRD patterns for the two specimens are shown in Figure 2. The XRD pattern for the as-deposited specimen showed reflections from BCC α-ferrite and a minor retained FCC Ɣ-austenite phase. The BCC peaks are also appreciably broad and asymmetric, indicative that a martensite phase is present (i.e. buried under the BCC peaks). The XRD pattern for the heat treated (HT) specimen shows that heating results in the removal of the retained austenite, sharper (less broad and asymmetric) BCC peaks, and the formation of a minor $M_{23}C_6$ phase.

The quantitative XRD refinement results are given in Table 2. The quantitative refinements of the measured XRD patterns are given in Figure 2 as solid lines. The individual phases identified are also included as solid lines for reference. The inset in Figure 2 (a) shows a high-angle region of the XRD pattern, highlighting the martensite contribution to the main peaks. It is to be noted that not including the body centered tetragonal

(BCT) phase resulted in large residuals and failure to effectively capture intensity under and around the BCC reflections. After heat treatment, the microstructure clearly changes, with a larger coherent grain size and lower microstrain parameter. The microstrain parameter is directly attributable to two-dimensional defects (such as dislocations). Heat treatment also removes the retained austenite and martensite phases. Previously published report on the same build [12] reported the yield strength (YS) of 1026 MPa and ultimate tensile strength (UTS) of 1288 MPa while the uniform elongation was 16.5%. After a heat treatment of normalizing at 1100 ^{o}C and tempering of 760 ^{o}C produced UTS and YS of 665 MPa and 555 MPa respectively with a uniform elongation of 20%. The heat treatment seemed successful to enhance the ductility and toughness through the recovery of dislocation and homogenization of the microstructure which was accompanied by a reduction of strength. This can be verified by both the optical micrograph and XRD results.

Quantification of Carbon Content

Understanding the carbon migration, and total fraction of carbon present in AM materials is of high importance as carbon plays a key role in determining the mechanical properties [13]. Due to very low carbon present in the as-built sample, the martensite phase has a very low tetragonality. Figure 3 shows the lattice parameter of BCT martensite [19] as function of carbon. As the tetragonality gets lower, it becomes difficult to differentiate between BCC α-ferrite and BCT martensite. High-energy synchrotron based XRD samples a significantly larger volume of material than conventional benchtop XRD and can be used to determine the structure of the martensite phase. Parameters obtained from XRD are used to find out the amount of carbon atoms. Estimated carbon weight percentage (wt%) was about 0.332 while the atomic percentage carbon in the martensite was about 1.527. This agrees with the amount of carbon expected in martensite phase as the austenite is air hardened in an AM build FM steel.

DISCUSSION

From the result shown in Figures 1 & 2 and Table 2, it is clear that the as-deposited steel has a high amount of BCT martensite in addition to the BCC α-ferrite and a small amount of retained austenite. The Martensite phase in the as built material is also responsible for the high microstrain (and large dislocation density) determined from the XRD analysis. From these results, it may be possible to conclude that the AM process is responsible for producing internal stress. The heat treatment results in a tempered martensite microstructure. The FCC and BCT phases are not apparent in the XRD results shown in Figure 2 (b), indicating that the heat treatment was successful in eliminating these phases. The BCC peaks are sharper and the quantified microstrain and coherent grain size are smaller and larger, respectively, compared to the as-built specimen. These results indicate an ideal microstructure with ferrite structure and minor carbides were produced after the heat treatment.

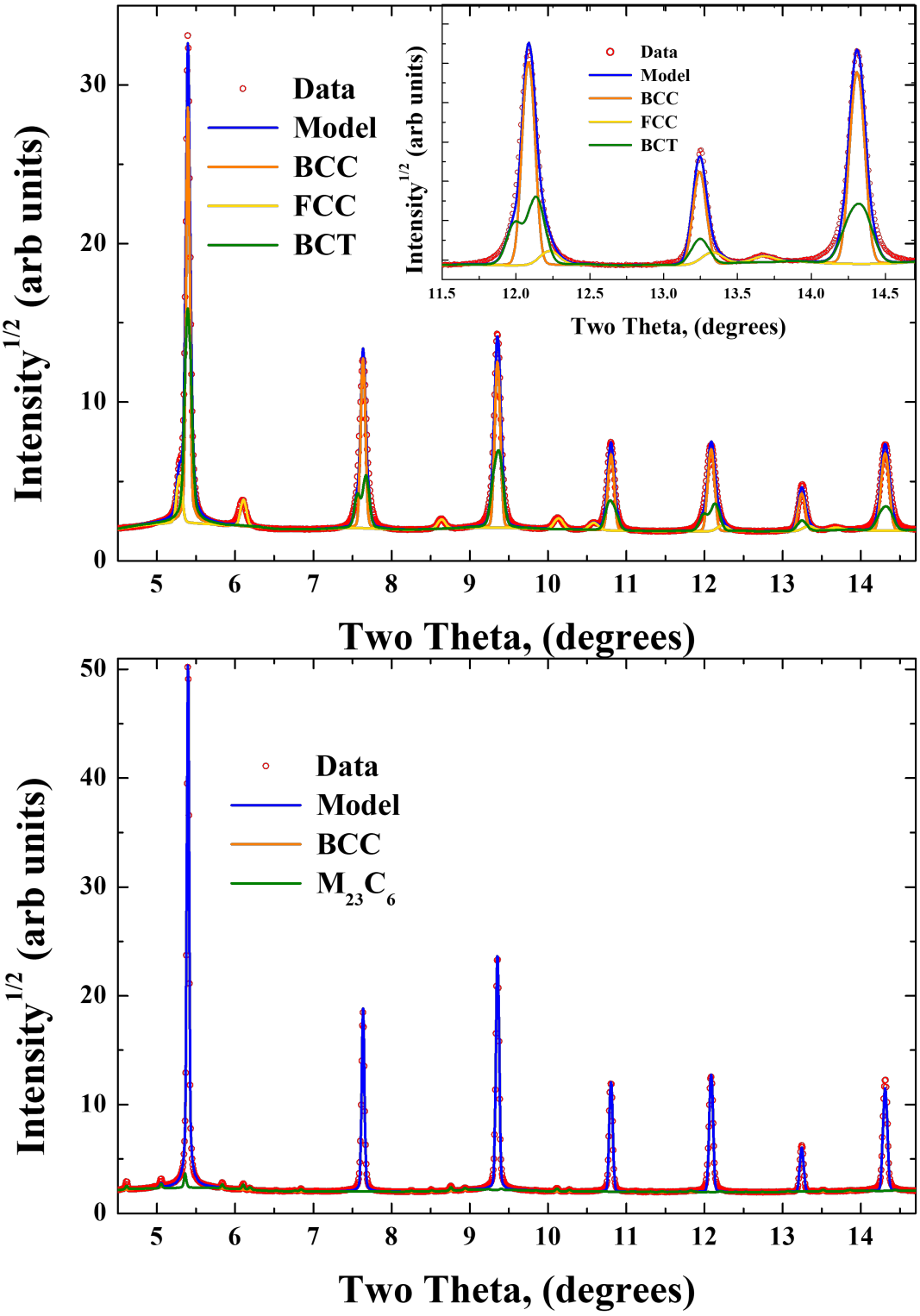

Figure 2. XRD patterns for (a) as fabricated and (b) heat treated G91. The XRD refinements and phases are overlaid for reference. The inset in (a) shows a magnified view of the high angle region, highlighting the necessity to include Martensite in the refinements.

Table 2. Quantitative XRD results for as built and heat-treated AM G-91 FM where CGS is the coherent (XRD) grain size and MS is microstrain. Yield strength, ultimate tensile strength, and elongation are also included for the same build [12].

Sample	**Phase**	***a***	**c**	**CGS**	**MS**	**wt.**	**Yield Strength**	**Ultimate Tensile Strength**	**Elongation**
		(Å)	**Å**	**nm**	**10^{-3}**	**%**	**(MPa)**	**(MPa)**	**%**
AD G91	FCC	3.5997± (0.0006)		47.4± (8.1)	4.14± (0.34)	3.9± (0.2)	1026	1288	16.5
	BCC	2.8794± (0.0001)		270.9 ± (55.2)	2.70± (0.04)	56.4 ± (1.1)			
	BCT	2.8646± (0.0005)	2.9068± (0.0009)	58.1± (4.4)	3.71± (0.11)	39.7 ± (1.5)			
HT G91	BCC	2.8793± (0.00001)		465.1 ± (16.1)	0.83± (0.01)	98.9 ± (0.3)	555	665	20
	$M_{23}C_6$	10.6515± (0.0004)		49.5± (3.9)		1.1± (0.2)			

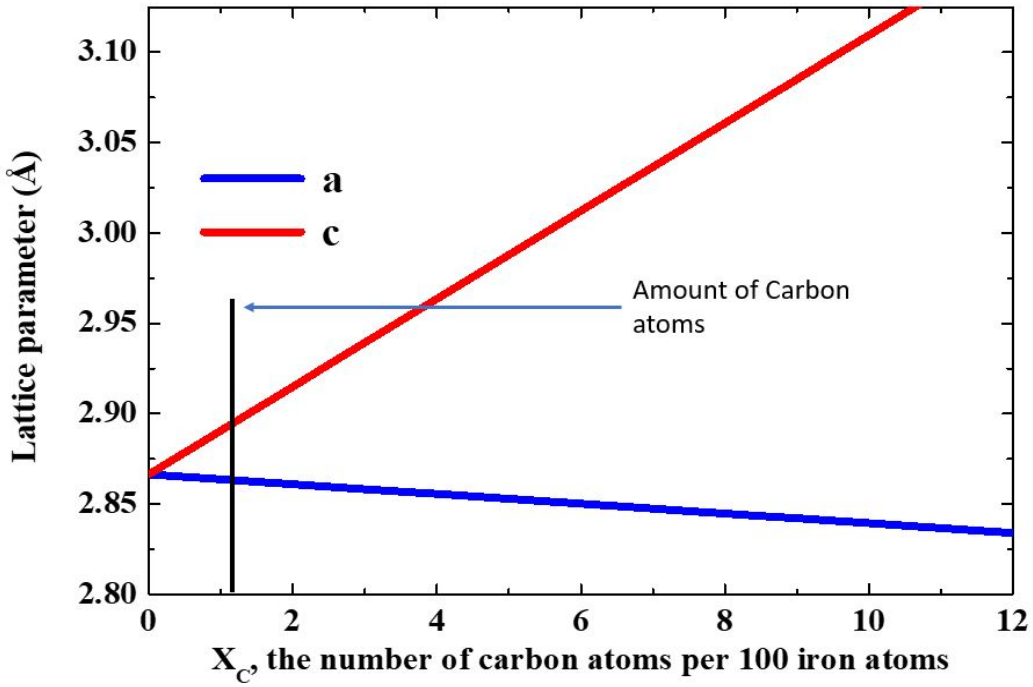

Figure 3. Lattice parameters (a and c) for martensite as a function of carbon atoms [19].

FUTURE WORK

Anisotropy is a common feature in AM steels. For this current research, only the Z-directional (build direction) was analyzed. The X-direction (transverse direction) is also important and is planned for examination in FY21. The amount of carbon within different phases, and lattice parameters for the BCC, FCC and BCT phases will aid in determining the similarity/differences in stress along the different build directions. More microstructural characterization including SEM, EDS, EBSD are needed for as built and as heat treated steels to produce a result that can complement the result obtained from the XRD.

CONCLUSION

The 9 Cr AM built G-91 FM steel was characterized through synchrotron scans. Both as-deposited and heat-treated steel were explored, and the effectiveness of heat treatment was examined. The as-built structure has ferrite, martensite and retained austenite phases present in the microstructure. The amount of microstrain was found to be higher while the coherent grain size was smaller in the as-built structure. This microstructure indicates that the AM as-built steel is going to be very hard and brittle and the substantial internal residual stress would deteriorate the mechanical properties of the steel.

Heat treatment was employed to produce a fully ferrite structure with a fine distribution of carbide (tempered martensite) which is known to produce the optimum mechanical properties. The synchrotron studies indicate that the phase fraction of heat-treated steel contains only BCC ferrite and carbide structure. No martensite or retained austenite was found and therefore, the heat treatment appeared to be successful.

The heat treatment was also effective to eliminate a large portion of microstrain. This fully ferrite structure with carbide particles and with lower microstrain should give better fatigue property and also superior creep property at higher temperature. With addition of heat treatment, AM build FM steel appears to be a promising option for fabrication of structural materials for the fusion reactor concepts.

ACKNOWLEDGEMENTS

These experiments and analysis were supported by the DOE Office of Fusion Energy Sciences under contract DE-SC0018322 with the Research Foundation for the State University of New York at Stony Brook. This research used The X-ray Powder Diffraction beamline of the National Synchrotron Light Source II, a U.S. Department of Energy (DOE) Office of Science User Facility operated for the DOE Office of Science by Brookhaven National Laboratory under Contract No. DE-SC0012704.

REFERENCES

[1.] L. Tan, T. Graening, X. Hu, W. Zhong, Y. Yang, S.J. Zinkle, Y. Katoh. Effects of carbonitrides and carbides on microstructure and properties of castable nanostructured alloys, J. Nucl. Mater. 540 (2020) 152376 pp.

[2.] Klueh, R. L., and Andrew T. Nelson. "Ferritic/martensitic steels for next-generation reactors." Journal of Nuclear Materials 371.1-3 (2007): 37-52.

[3.] Klueh, R. L. "Elevated temperature ferritic and martensitic steels and their application to future nuclear reactors." International Materials Reviews 50.5 (2005): 287-310.

[4.] David, Stan A., John A. Siefert, and Zhili Feng. "Welding and weldability of candidate ferritic alloys for future advanced ultrasupercritical fossil power plants." Science and Technology of Welding and Joining 18.8 (2013): 631-651.

[5.] Song, Miao, et al. "Radiation damage and irradiation-assisted stress corrosion cracking of additively manufactured 316L stainless steels." Journal of Nuclear Materials 513 (2019): 33-44.

[6.] Hilaire, Alexandra, Eric Andrieu, and Xinhua Wu. "High-temperature mechanical properties of alloy 718 produced by laser powder bed fusion with different processing parameters." Additive Manufacturing 26 (2019): 147-160.

[7.] Sridharan, Niyanth, and Kevin Field. "A Road Map for the Advanced Manufacturing of Ferritic-Martensitic Steels." Fusion Science and Technology 75.4 (2019): 264-274.
[8.] Sridharan, Niyanth, Maxim N. Gussev, and Kevin G. Field. "Performance of a ferritic/martensitic steel for nuclear reactor applications fabricated using additive manufacturing." Journal of Nuclear Materials 521 (2019): 45-55.
[9.] Kelly, Shawn Michael. Thermal and microstructure modeling of metal deposition processes with application to Ti-6Al-4V. Diss. Virginia Tech, 2004.
[10.] Babu, S. S., et al. "Measurement of phase transformation kinetics during repeated thermal cycling of Ti-6Al-4V using time-resolved X-ray diffraction." International Conference on Solid-Solid Phase Transformations in Inorganic Materials 2005. 2005.
[11.] Kelly, S. M., and S. L. Kampe. "Microstructural evolution in laser-deposited multilayer Ti-6Al-4V builds: Part I. Microstructural characterization." Metallurgical and Materials Transactions A 35.6 (2004): 1861-1867.
[12.] Lippold, John C., and Damian J. Kotecki. Welding metallurgy and weldability of stainless steels. 2005.
[13.] Gandy, David, et al. "Design, fabrication, and characterization of graded transition joints." Welding Journal 96.8 (2017).
[14.] Lippold, John C. "Transformation and tempering behavior of 12Cr-1Mo-0.3 V martensitic stainless steel weldments." Journal of Nuclear Materials 104 (1981): 1127-1131.
[15.] Babu, S. S., et al. Modelling and characterization of nonequilibrium weld microstructure evolution. na, 2003.
[16.] Collins, P. C., et al. "Microstructural control of additively manufactured metallic materials." Annual Review of Materials Research 46 (2016): 63-91.
[17.] Bhadeshia, H. K. D. H. "Diffusion of carbon in austenite." Metal Science 15.10 (1981): 477-480.
[18.] Francis, J. A., H. K. D. H. Bhadeshia, and P. J. Withers. "Welding residual stresses in ferritic power plant steels." Materials Science and technology 23.9 (2007): 1009-1020.
[19.] Cheng, Liu, et al. "Lattice parameters of iron-carbon and iron-nitrogen martensites and austenites." Scripta metallurgical et materialia 24.3 (1990): 509-514

5.3 ODS FeCrAl PRODUCTION USING ADDITIVE MANUFACTURING WITH IN SITU OXIDATION—Ty Austin, Steven J. Zinkle (University of Tennessee), Niyanth Sridharan (Lincoln Electric)

OBJECTIVE

The objective of this task is to explore the feasibility of producing oxide dispersion strengthened (ODS) ferritic steel alloy parts using a laser directed energy deposition (DED) additive manufacturing (AM) process in an oxygen-rich environment. This would enable fabrication of high-performance, geometrically complex ODS alloy components.

SUMMARY

Fe – 12Cr – 6Al – 2Mo – 0.18Y (wt%) alloy powder was consolidated using a DED AM process in an oxygen-rich environment using varied build parameters to explore the feasibility of producing an ODS steel without extensive mechanical alloying (MA), hot isostatic pressing (HIPing), and metalworking. In order to better evaluate the varied build parameters used to produce the specimens and better understand the effects of build parameters on oxide production, transmission electron microscopy (TEM) lamella have been prepared using conventional focused ion beam techniques. Select specimens have been examined using scanning transmission electron microscopy (STEM) and electron energy loss spectroscopy (EELS). The results thus far suggest that nanoscale precipitation is possible using *in situ* oxidation during powder consolidation. The precipitation also seems to be complex, likely stemming from the complex chemistry affiliated with Y-Al-oxides and the unique thermal conditions provided during AM.

PROGRESS AND STATUS

20mm x 20mm x 20-30mm (height) sample cubes were built using a powder-blown, DED AM system built by DM3D Technology with gas atomized metal powder (Fe – 12Cr – 6Al – 2Mo – 0.18Y wt%) provided by ATI Powder Metals. Oxygen was provided during powder consolidation by maintaining the build chamber under ambient air conditions or by adding oxygen into the welding gas streams. Some modifications to the AM system were required for the experiment. In order to directly apply the oxygen during fabrication, the welding gas system was modified to accept an external Ar-10%O_2 gas mixture. Controlled blending of the AM system's native welding gas streams of argon and helium with the external Ar-10% O_2 gas mixture allowed for precise control of the oxygen available at the surface of the melt pool for precipitate formation. Figure 1 shows a schematic of both experimental setups.

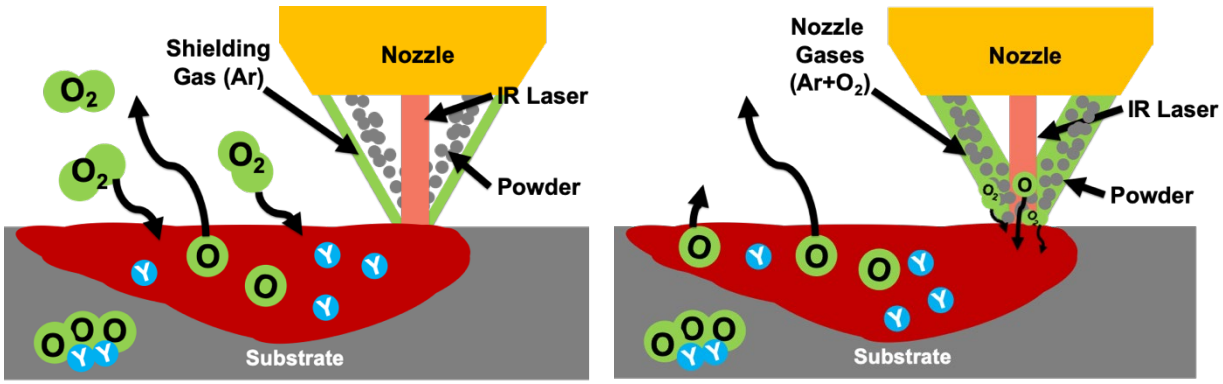

Figure 1. Schematic of DED AM process using *in situ* oxidation: consolidation under air (left), under Ar with Ar-O_2 blended gas stream (right).

The operating parameters that were varied during sample production using the above methods are shown below in Table 1. For the purposes of these experiments, a continuous raster pattern had the laser shutter remaining open for the duration of the building process. A pulsed raster pattern had the laser shutter open for eight hundredths of a second in one specific location prior to shuttering and moving to the next location during the build process. The available oxygen concentration (measured in at% or vol%) was the measure of the relative oxygen available to the sample during the building process, either in the machine atmosphere or provided welding gas per Figure 1. Additional description of processing parameters of these samples was discussed in the previous report [1].

Table 1. Sample processing parameters (NG = nozzle gas, C = continuous raster pattern, P = pulsed raster pattern)

Specimen	Laser Power (W)	Oxygen Source (Air/NG)	Raster Type (C/P)	Tool Speed (mm/min)	Available O_2 Concen. [O_2]	Pre-heat Temperature (Celsius)
400WP	400	Air	P	720	16	20
400WC	400	Air	C	720	16	20
Ar10O_2_1	400	NG	C	720	1	20
Ar10O_2_2	500	NG	C	720	1	20
Ar10O_2_3	650	NG	C	720	1	20
Ar10O_2_4	500	NG	C	600	1	20
Ar10O_2_5	500	NG	C	720	0.5	20
Ar10O_2_6	500	NG	C	720	1	350

Dirats Laboratories performed post-fabrication compositional analysis using inductively coupled plasma optical emission spectroscopy (ICP-OES) and combustion analysis using inert gas fusion (IGF) for each build condition. These results are shown in Figure 2 along with a conventionally fabricated ODS-FeCrAl alloy from literature. The oxygen content of the Ar10O_2_4 specimen approached half that of values reported for MA ODS FeCrAl alloys [2] while showing an increase of over 6x that of the as-received powder.

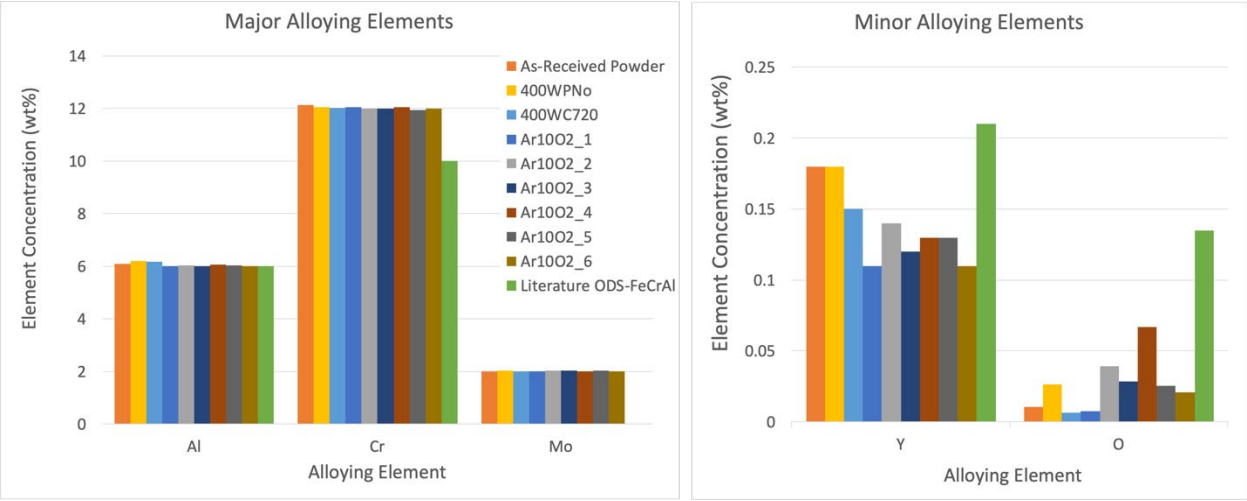

Figure 2. Compositional analysis of as-received powder, as-built specimens, and conventionally fabricated ODS FeCrAl [1].

After characterizing the above specimens using optical microscopy, Vickers hardness, and electron backscatter diffraction (EBSD), discussed in the previous report [1], samples were taken from the specimens and prepared for characterization using STEM according to conventional FIB lift-out techniques [3]. Analyzing a sample from Ar10O_2_5 using the brightfield (BF) detector of a Zeiss Libra 200 S/TEM in

STEM mode at high magnification showed contrast consistent with ODS precipitates with an average diameter of 7 nm, number density of $5x10^{21}/m^3$, and volume fraction of 0.13%. Images of these precipitates are shown in Figure 3. More detailed characterization of these nanoscale dispersoids will be performed in the next reporting period.

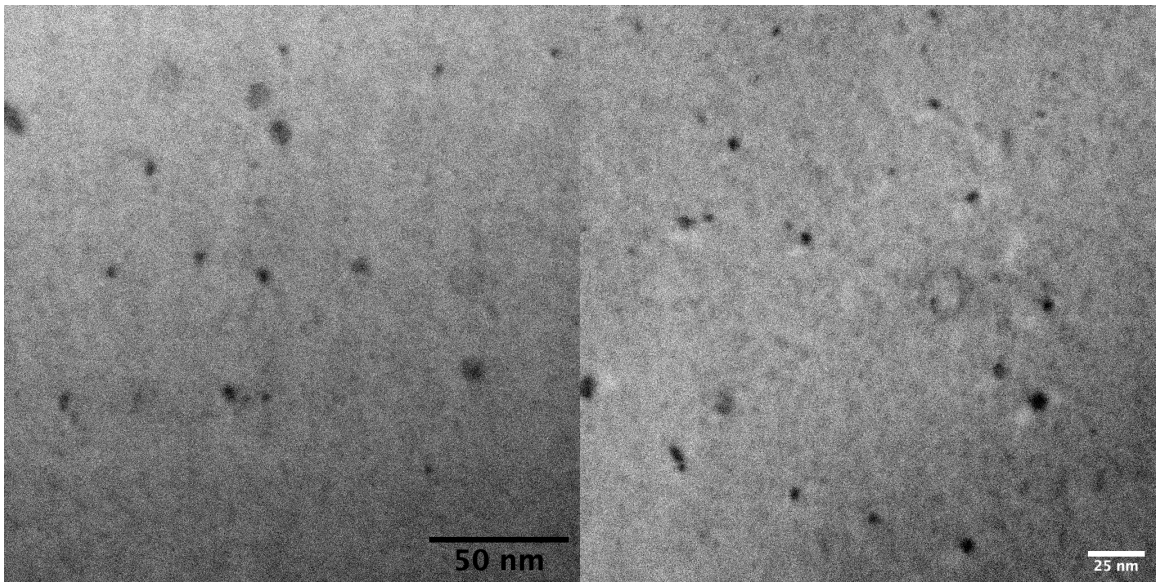

Figure 3. High magnification BF images of $Ar10O_2$_5 showing contrast that may be 5 to 10 nm ODS precipitates.

While looking for < 10 nm diameter precipitates, it was discovered that some of the larger precipitates (d > 50 nm) showed clear z-contrast under high angle annular darkfield (HAADF) imaging indicative of different phases as shown in Figure 4.

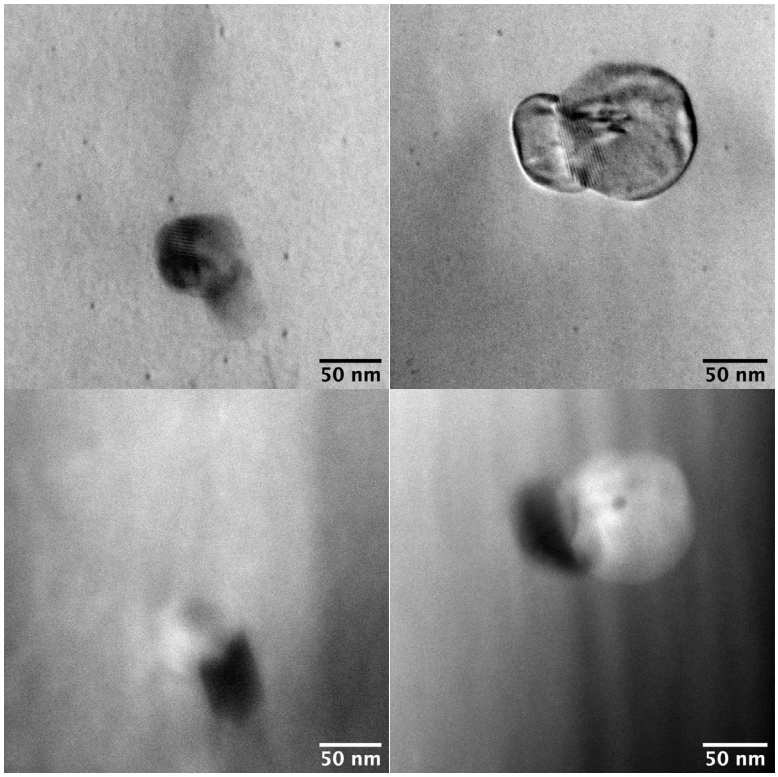

Figure 4. STEM BF (top) and HAADF (bottom) images of Ar10O_2_5 showing z-contrast suggesting co-precipitation.

Further, in a 400WP sample, a core-shell precipitation phenomenon appeared to have occurred as shown in Figure 5. To better understand how the composition was changing across the precipitate, EELS spectra was captured (also shown in Figure 5). As the EELS spectra showed, both Al K-edge (~1560 eV) and Y L-edge (~2080 eV) increased in magnitude near the center of the precipitate. Conversely, the magnitude of the Cr L-edge and Fe L-edges decreased near the center of the precipitate. However, some Fe and Cr were present at the center.

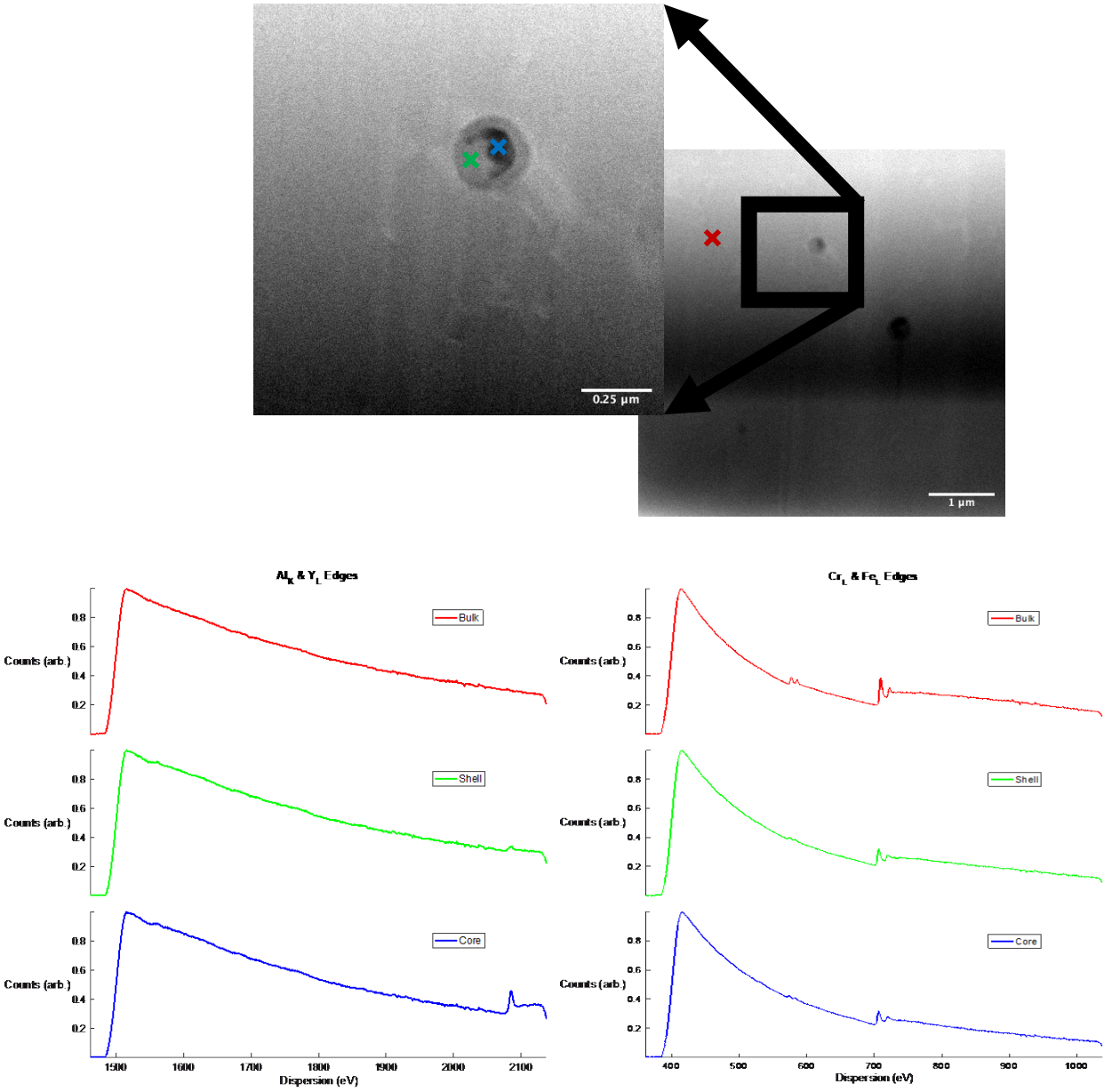

Figure 5. STEM BF images of a potential core-shell precipitation in 400WP with corresponding EELS spectra showing compositional change across the precipitate. (Red = Bulk, Green = Shell, Blue = Core).

In addition to the larger precipitates shown above, there were also some large agglomerates (d > 1µm) present within all of the samples. A lift-out containing these large particles was prepared to examine which yttrium-aluminum-oxide phase formed. Comparing the topology of the EELS spectra of the agglomerate lift-out to the literature suggested that the agglomerate was monoclinic yttrium aluminate (YAM; $Y_4Al_2O_9$) [4]. The EELS spectra also suggested that there was some Cr present in the agglomerate. Figure 6 shows the EELS spectra captured from the sample and compares it to the YAM and yttrium aluminum garnet (YAG; $Y_3Al_5O_{12}$) phases. The topology of the O and Al K-edges seem to most closely agree with the large

agglomerate being YAM. The Al K-edge does not include the leading shoulder on the first peak as the YAG phase does in addition to being much weaker in relative response to the other representative peaks of the edge. Similarly, the O K-edge does not include the leading shoulder on the first peak as the YAG phase does. It does include two peaks with a trailing shoulder as does the YAM phase.

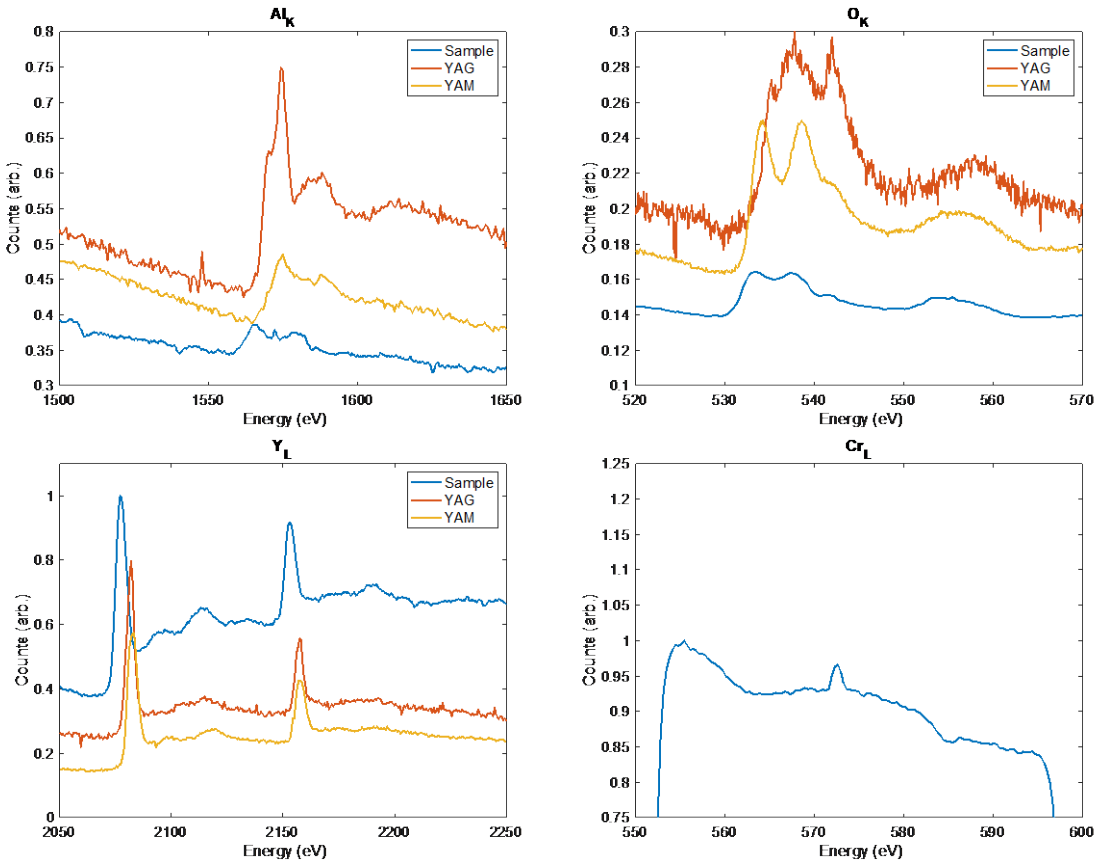

Figure 6. Compositional analysis of the large agglomerates using EELS [4].

Currently, more work is being done to characterize more samples from the specimens produced to better understand how the varied operating parameters affected the overall build quality and precipitation.

FUTURE PLANS

Characterization using S/TEM with EELS will continue to better understand how the AM process affects the formation of ODS precipitates. In the future, S/TEM samples will be characterized utilizing energy-dispersion x-ray spectroscopy (EDS) and EELS mapping to better understand the local concentration gradients that are occurring around the ODS precipitates formed as part of work done in partnership with ORNL's Center for Nanophase Materials Sciences (CNMS). Further, specimens for atom probe tomography (APT) will also be produced and analyzed at CNMS. This data should aid in determining the morphology and composition of the nanoscale oxide precipitation and how it is affected by AM. The results from these experiments will be used with the macroscale and microscale characterization results to further modify the operating parameters for producing ODS steels with AM to optimize precipitate characteristics for nuclear applications.

ACKNOWLEDGEMENTS

We thank Brian Jordan and Dennis Brown (ORNL technicians at the Manufacturing Demonstration Facility) for their assistance in planning/performing modifications to the AM system and completing production of the samples characterized above.

References

[1] T. Austin, S.J. Zinkle, N. Sridharan. “ODS FeCrAl Production Using Additive Manufacturing with *In Situ* Oxidation”, Fusion Materials Semiannual Progress Report for period ending Dec. 31, 2019, DOE-ER-0313/67 (2019), p. 109-114.

[2] C.P. Massey, S.N. Dryepondt, P.D. Edmondson, M.G. Frith, K.C. Littrell, A. Kini, B. Gault, K.A. Terrani, S.J. Zinkle, Multiscale investigations of nanoprecipitate nucleation, growth, and coarsening in annealed low-Cr oxide dispersion strengthened FeCrAl powder, Acta Materialia 166 (2019) 1-17.

[3] M.K. Miller, K.F. Russell, Atom probe specimen preparation with a dual beam SEM/FIB miller, 107(9) (2007) 761-766.

[4] Philip Ewels, Thierry Sikora, Virginie Serin, Chris P. Ewels and Luc Lajaunie. "A Complete Overhaul of the Electron Energy-Loss Spectroscopy and X-Ray Absorption Spectroscopy Database: eelsdb.eu. "Microscopy and Microanalysis, available on CJO2016. doi:10.1017/S1431927616000179.

5.4 CHEMICAL VAPOR INFILTRATION OF BINDER JETTED TUNGSTEN—J. R. Echols, L. M. Garrison, Y. Katoh (Oak Ridge National Laboratory)

OBJECTIVE

The purpose of this project is to demonstrate the densification of tungsten produced through binder jet additive manufacturing with chemical vapor infiltration.

SUMMARY

Binder-jetted tungsten preforms were produced and chemical vapor infiltration runs were conducted to begin optimizing the deposition rate for densification. Although high densification has been achieved at the preform surface, only the lowest pressure/temperature/flowrate condition shows promise in achieving bulk densification.

PROGRESS AND STATUS

There is an opportunity to leverage the advantages of additive manufacturing (AM) with plasma facing-components of fusion reactors. The design space accessed by AM allows, in principle, greater flexibility with large numbers of small/complex parts, complex internal channels, dissimilar material joins, and topological optimization. Tungsten is attractive for AM because its high melting point and brittleness at room temperature makes it difficult to fabricate through traditional machining methods.

Conventional binder jetting produces parts by selectively depositing a liquid binding agent to join powder particles. Layers of material are bonded to produce a preform. The binding agent is then baked out at high temperature and the part is either infiltrated with liquid material or subjected to hot isostatic pressing (HIPing) to achieve full density. Neither of these solutions, however, are attractive to produce a full tungsten part. Both melt infiltration (which is doubly impractical due to the extreme melting point of tungsten) and HIPing would likely generate fully recrystallized microstructures, which are potentially unattractive for fusion application. Instead, chemical vapor infiltration (CVI), where tungsten is grown on the particles from gaseous reactants, is proposed.

A diagram illustrating the proposed CVI process is shown in Figure 1. The process occurs by passing gaseous tungsten hexafluoride and hydrogen over the W preform at temperatures in excess of ~350°C as described in the following reaction:

$$3H_2 + WF_6 \rightarrow W + 6HF$$

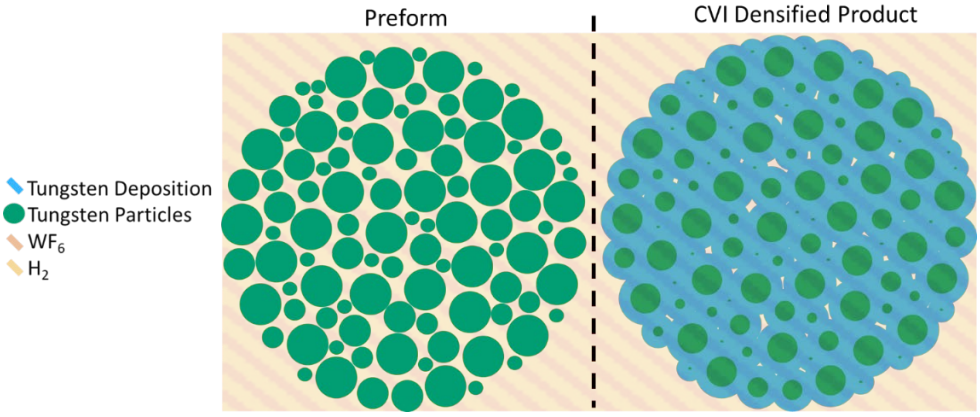

Figure 1. Principle of CVI densification of a binder jetted tungsten preform. The reaction of WF_6 and H_2 within the part deposits tungsten on exposed surfaces.

"Green" disk samples (where the binder is left in place) 4.5mm thick and 24mm in diameter were produced by the ExOne company with W-90 powder and FluidFuse binder. Debinding and CVI was performed by Archer Technicoat Limited (ATL) in the UK. Debinding was conducted within the CVI apparatus, at 5mb, 600°C, under light argon flow, for 1 hour. Immediately following this, the CVI process was started. Following infiltration, samples were analyzed for deposition rate via cross sectioning and scanning electron microscopy (SEM) at Oak Ridge National Lab. Table 1 shows infiltration parameters and deposition rates for six infiltration runs which were each carried out over 6 hours. Figure 2 shows representative SEM images during the fabrication process – from preform with binder in place, to partially densified product. An issue with vacuum stability was reported for the run ATL3, and results from this run have been omitted from this report.

Table 1. CVI parameters and measured deposition rates

Run ID	Temp (°C)	Pressure (mbarr)	WF6 flowrate (sccm)	H flowrate (sccm)	Edge dep. rate (μm/hr)	Center dep. rate (μm/hr)
ALT0*	450	470	168	3500	≥6 (sealed)	-
ATL1	375	6	100	2083	0.1	0.1
ATL2	375	42	100	2083	≥6 (sealed)	-
ATL4	375	3	130	2000	≥6 (sealed)	-
ATL5	400	3	100	2000	≥6 (sealed)	-
ATL6	400	3	130	2000	≥6 (sealed)	-

** ATL0 was produced with W-25 tekna powder (where 95% of particles have a diameter less than 25μm). All other samples were made with W-90 (diameter less than 90μm)*

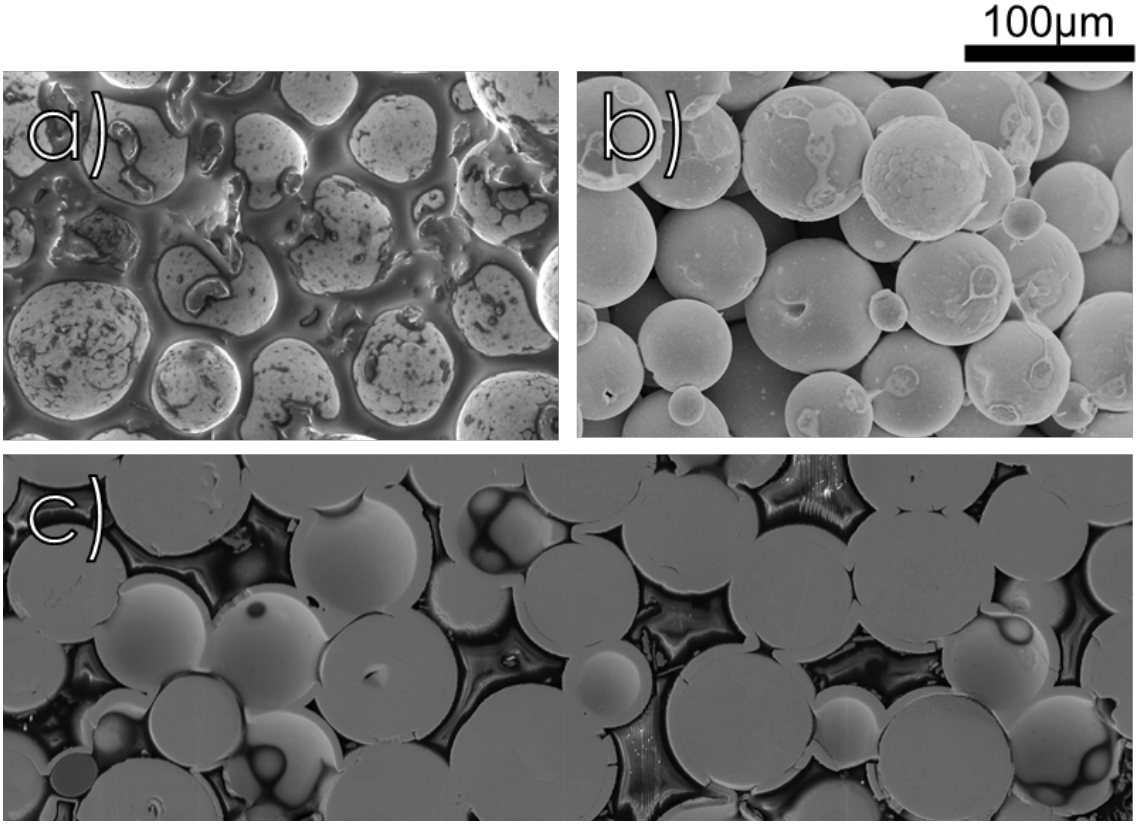

Figure 2. SEM images demonstrating stages of processing: a) Tungsten particles with binder in place b) Tungsten particles after debinding c) Polished cross-section after CVI has been performed and films have grown on the tungsten particles.

Initial SEM measurements performed on infiltrated samples highlight the difficulty in densifying samples at a uniform temperature throughout. In all but one of the samples investigated, the surface sealed off completely, blocking significant deposition to the powder in the sample bulk. The infiltration run where this has not occurred, ATL1, was run at conditions near the minimum temperature, WF_6 flowrate, and pressure which can be expected to deposit tungsten. The similar amounts of deposition observed both in the sample bulk and near the edge, however, indicate that this deposition condition may be suitable for high amounts of bulk densification. If deposition rates are linear, deposition times for such a run are expected to be on the order of hundreds of hours for W-90 powder.

For the sealed samples, the surface of the samples was closed off before bulk densification was complete. Here, increasing the powder size and decreasing the deposition temperature has increased the depth of highly dense material. The highest depths measured thus far exceed 200µm for depositions made at 375°C with W-90 powder. SEM images highlighting depths achieved for different deposition conditions are shown in Figure 3.

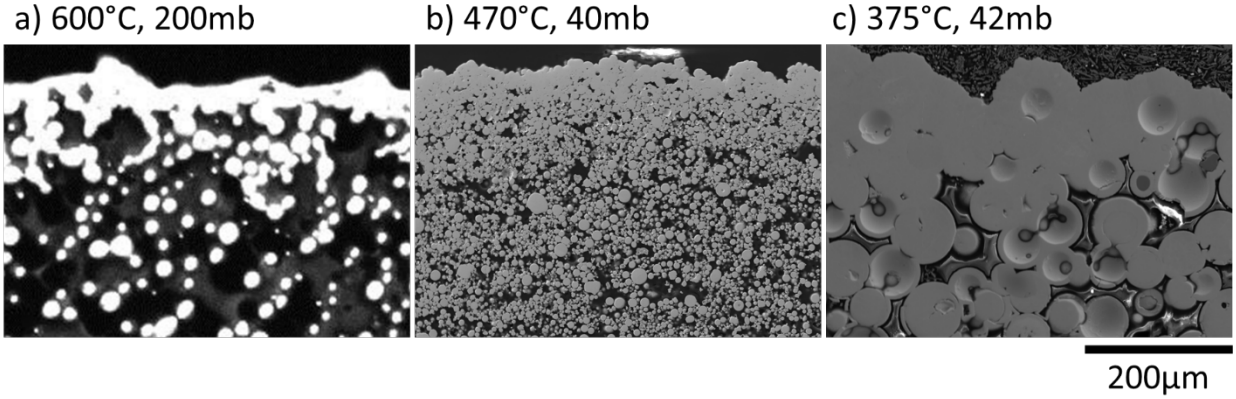

Figure 3. Cross-sectional SEM images comparing three CVI runs, showcasing improvement in depth of highly densified material from (a) ~20µm to (c) ~200µm.

FUTURE PLANS

Full densification runs at the parameters of ATL1 are planned to investigate the suitability of these parameters. Densification trials with forced flow CVI are planned for comparison with these trials. Forced flow is a modification of the CVI procedure which applies a temperature gradient with gas flow direction and has the potential to densify directionally, from one side of a part to the other, and dramatically improve deposition times and density.

5.5 AM PRODUCTION OF TUNGSTEN FOR DIVERTOR COMPONENTS—Betsy Ellis, Christopher Ledford, Lauren Garrison, Michael Kirka, Yutai Kato, Ryan Dehoff (Oak Ridge National Laboratory)

OBJECTIVE

The objective of this project is to evaluate electron beam powder bed fusion (EB-PBF) additive manufacturing (AM) techniques for manufacturing tungsten divertor components. This report covers investigations into cracking behavior in EB-PBF tungsten.

SUMMARY

Additive manufacturing has the potential to revolutionize the design of plasma-facing components (PFCs) for fusion power, but AM of refractory metals such as tungsten is still under development. In particular, AM W is highly prone to cracking. Previous work in this project has shown that it is possible to produce dense and crack-free tungsten via EB-PBF, but the mechanism by which cracks form is unclear. We seek to understand this mechanism in order to more reliably produce crack-free AM W.

PROGRESS AND STATUS

The mechanism governing cracking in additive manufacturing of refractory metals is of great importance to the successful application of AM technologies to fusion designs. To explore crack mechanisms in fusion AM including EB-PBF, a series of experiments were performed using molybdenum as a model material. Molybdenum is also a BCC refractory metal, with very similar mechanical behavior to tungsten, but with a lower melting point (2620°C vs 3422°C). Two series of single wall parts were fabricated using an Arcam Q10+, with varying wall dimensions, beam speeds, and scan strategies. The experimental setup is shown in Figure 1.

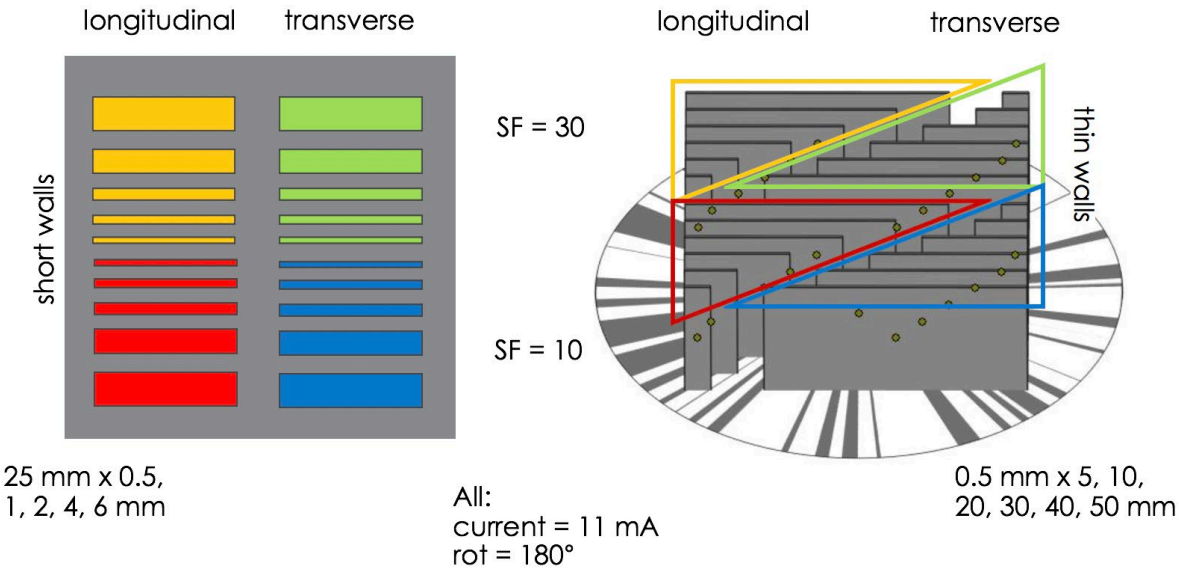

Figure 1. Build geometry and scan parameters for two wall builds. Left, short wall build, right, thin wall build. Wall dimensions, scan direction, and speed function (SF) are varied. All walls are 25 mm tall.

The build on the left (henceforth “short wall build”) comprises 20 walls 25 mm in length and 25 mm tall, with widths varying from 1 to 6 mm. The build on the right (henceforth “thin wall build”) comprises 24 walls 0.5 mm thick and 25 mm tall, with lengths varying from 5 to 50 mm. Both transverse and longitudinal scan

strategies were used, and speed function (SF, a proprietary variable controlling beam speed) was set to both 10 and 30. The completed builds, with excess powder removed, are shown in Figure 2.

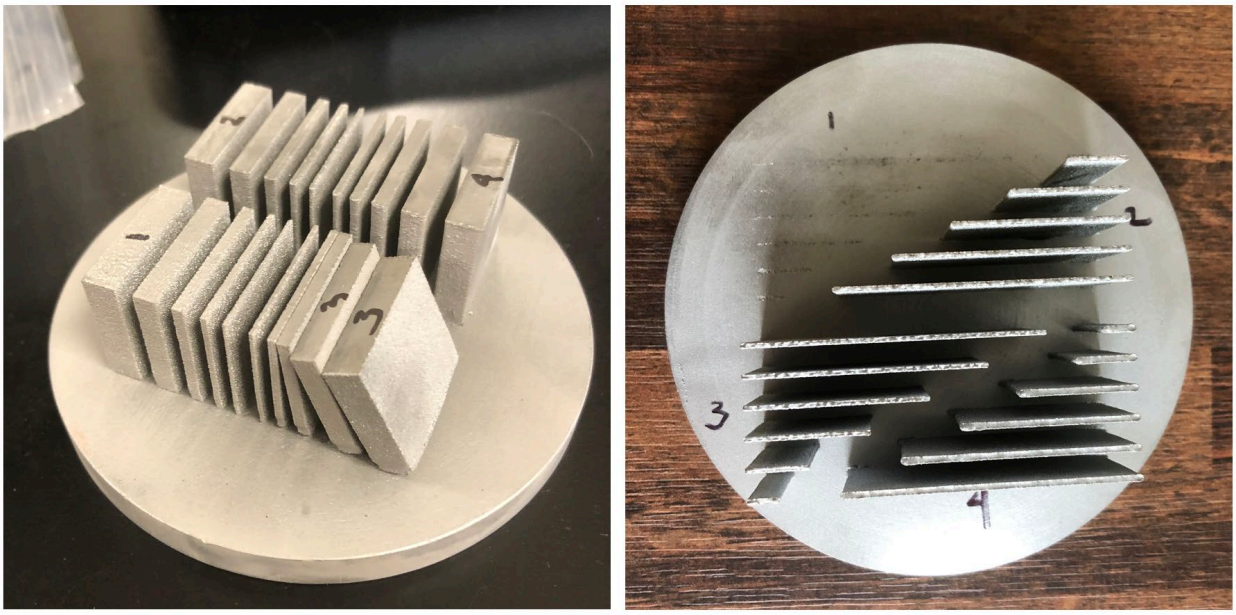

Figure 2. Completed builds. Left, short wall build; right, thin wall build.

Several walls detached immediately upon removal from the build chamber. These were sectioned immediately for metallographic analysis. The remaining walls were divided by using wire EDM to cut through the base plate between each wall, leaving a small section of the base plate attached to each wall specimen. This was done to avoid any dramatic change in residual stresses that might occur when the wall is removed from the base plate. Individual walls still attached to their base plate segments were imaged using x-ray CT.

The wall sets which detached spontaneously were the low speed, longitudinally scanned walls in the short wall build, and the high speed longitudinally scanned walls in the thin walls build. EBSD of detached thin wall specimens are shown in Figure 3.

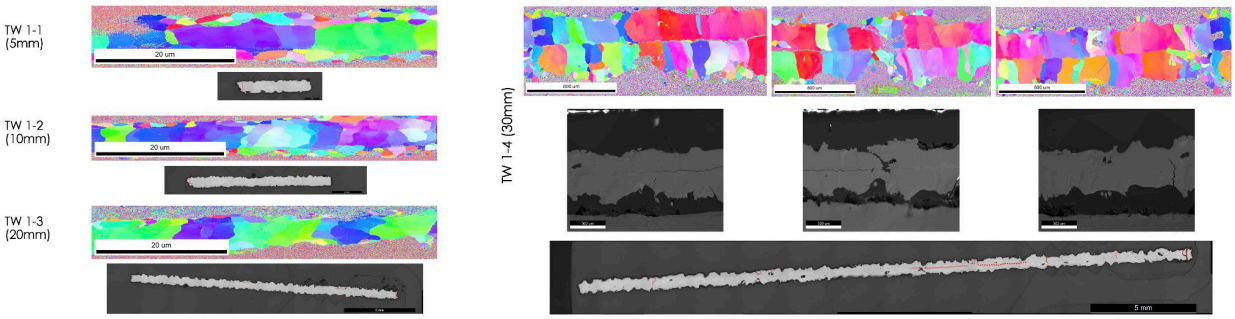

Figure 3. EBSD of four thin wall samples.

A transition in morphology is visible with respect to wall length. In TW 1-1, 5 mm in length, a small border region of small grains surrounds a large-grained interior. As wall length increases, the larger center grains reduce in size, and in TW 1-4 (30mm), there are now two rows of grains parallel to the wall length. These four samples were all fabricated using a longitudinal scan strategy, meaning that as wall length increases,

beam return time also increases. TW-1 therefore experiences a higher local temperature at time of melting than TW-4.

One detached wall was manually broken in half, then immediately imaged using SEM and EDS. Results are shown in Figure 4. Part of the fracture surface was identifiable as intergranular fracture, and examination of the grain boundary region revealed several triangular pits and a small oxygen-rich particle.

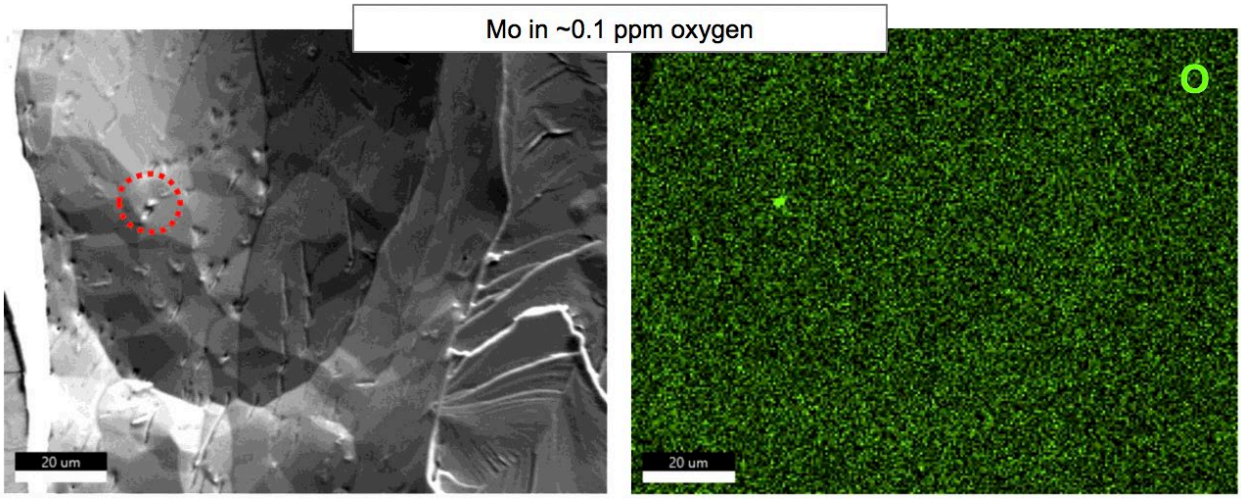

Figure 4. SEM and EDS showing a small oxygen-rich particle at a grain boundary.

X-ray CT results from three attached walls are shown in Figure 5, along with all of the attached wall samples.

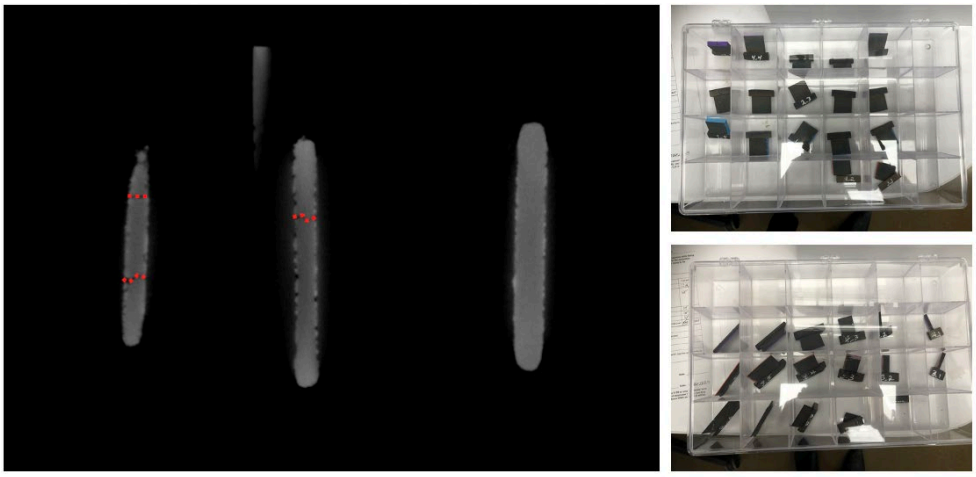

Figure 5. Left, CT image of three thin wall samples with cracks highlighted; Right, attached wall samples.

To quantify cracking behavior, CT images from each wall were examined at 0.5 mm intervals, and any identifiable cracks were tallied. Cracks that spanned several 0.5 mm intervals were counted multiple times, providing a loose estimate of crack density. The total number of cracks identified in the 25 mm of wall height is plotted versus wall aspect ratio (width divided by length) in Figure 6.

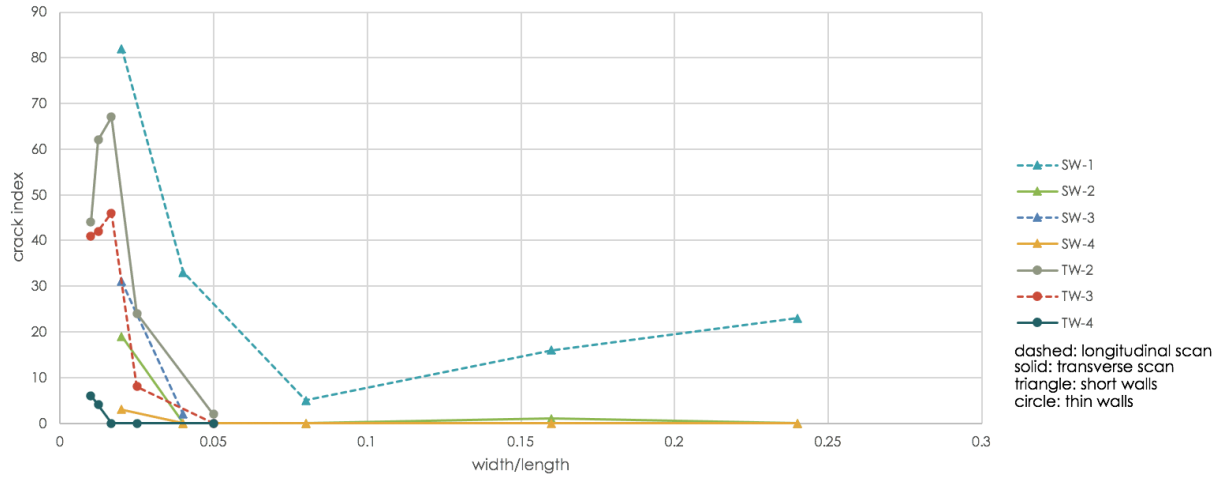

Figure 6. Crack index vs. wall aspect ratio.

Regardless of scan direction and scan speed, walls with a smaller width-to-length aspect ratio exhibited more cracks. In addition, walls fabricated using a longitudinal scan strategy exhibited more cracks than transverse-scanned walls, and walls fabricated with a higher scan speed exhibited more cracking than slower-scanned walls. All of these results point to local temperature before melting as an important parameter in crack suppression.

FUTURE PLANS

A machine learning algorithm is being developed to automatically identify cracks in the molybdenum samples.

Further tungsten EB-PBF builds in an Arcam Q10+ are scheduled for later this quarter. The work will focus on replicating the dense, crack-free builds from earlier efforts, and extending successful builds to larger and more complex geometries.

6. EFFECTS OF RADIATION

6.1 DYNAMIC OBSERVATION OF DUAL-BEAM IRRADIATED IRON AND Fe-10Cr AT 435°C—Yan-Ru Lin, Steven John Zinkle (University of Tennessee), Wei-Ying Chen, Meimei Li (Argonne National Laboratory)

Extended Abstract: Full manuscript is under peer-review in Acta Materialia

OBJECTIVE

The objective of this in-situ TEM study is to dynamically investigate the formation of dislocation loops and cavities in Fe and Fe-Cr thin foils at fusion-relevant conditions, where ferritic alloys are expected to be operated at high dose (>10 dpa) accompanied with transmutant He (~10 appm He/dpa), and at high temperature (>300 °C).

SUMMARY

The dose dependence of the irradiation-induced microstructural evolution was examined from 0 to 20 displacement per atom (dpa) in high purity Fe and Fe-10Cr during simultaneous dual-beam (1 MeV Kr + 10 appm He/dpa) irradiation at 435 °C. Using state-of-the-art transmission electron microscopy (TEM), we experimentally revealed that the mechanism for the formation of <100> loops may not follow the conventional simple dislocation reaction between two ½<111> loops. Real-time dynamic formation and evolution of defects including black dot loops, loop coarsening, loop decoration, network dislocations, and cavities were demonstrated. Several results indicated that the addition of Cr and He could impede dislocation loop motion. The evolution of the defect size/density and relative fraction of ½<111> vs <100> loops were quantitatively summarized. With increasing dose, ½<111> loops became the dominant type of loop in both materials. Notably, <100> loops were predominantly observed near grain boundaries only for pure Fe, while arrays of nanoscale black dot defects composing the <100> loop strings were frequently observed in Fe-10Cr.

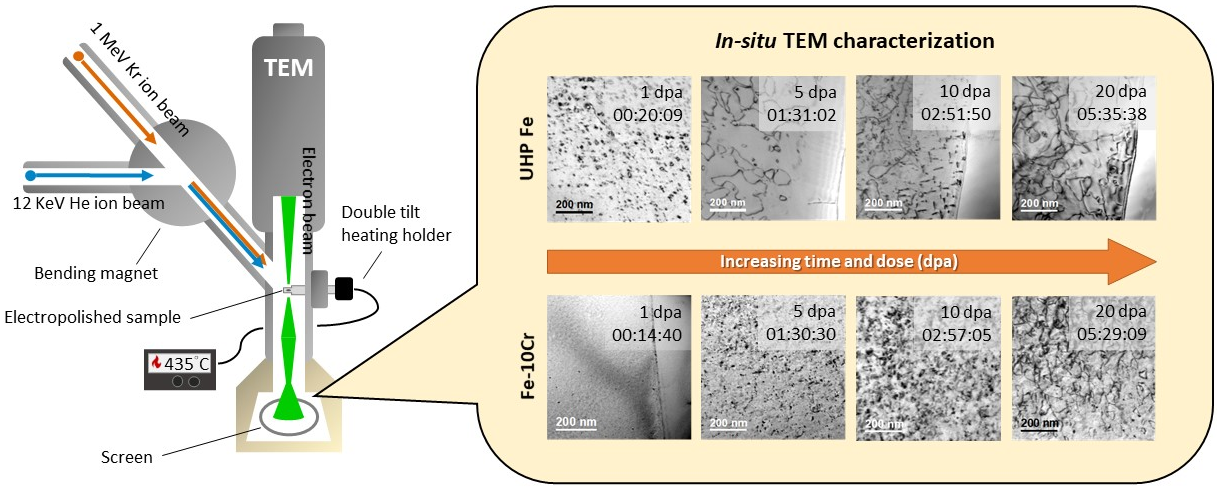

Figure 1. Schematic diagram of the in-situ irradiation experiment, and the evolution of loops in Fe and Fe-10Cr alloys.

FUTURE PLANS

The loop type of the nanoscale black dot defects composing the <100> loop strings observed in Fe-10Cr needs to be confirmed: in particular, whether or not they are ½<111> loops arrayed along <100> directions.

6.2 TEMPERATURE-DEPENDENT CAVITY SWELLING IN DUAL-ION IRRADIATED IRON AND IRON-CHROMIUM FERRITIC ALLOYS—Yan-Ru Lin, Steven John Zinkle (University of Tennessee), Arunodaya Bhattacharya (Oak Ridge National Laboratory)

Extended Abstract: Full manuscript published in Acta Materialia 207 (2021) 116660 (https://doi.org/10.1016/j.actamat.2021.116660)

OBJECTIVE

The objective of this study is to perform a comprehensive examination of the effect of irradiation temperature and Cr content on cavity swelling, as well as to investigate the microstructural and carbon-induced martensite phase effects on cavity swelling. The transferability of the results obtained for the ion-irradiated model alloys to the behavior in application-relevant (neutron-irradiated) environments are also discussed.

SUMMARY

Simultaneous dual ion irradiations (8 MeV Ni^{3+} ions and energy-degraded 3.5 MeV He^{2+} ions) were used to quantify the cavity swelling behavior in ultra-high purity Fe and Fe-Cr alloys (3-14 wt.% Cr), Fe-10 wt.% Cr-780 wt.ppm C, and Eurofer97 FM steel. The irradiations were conducted over a wide temperature range (400-550 °C) with a mid-range dose of ~30 displacements per atom (dpa), dose rate of ~10^{-3} dpa/s and 0.1 appm/dpa He implantation rate. Using state-of-the-art transmission electron microscopy (TEM), we reveal that pure Fe has a ~50 °C lower peak swelling temperature difference than Fe-Cr alloys, which is attributed to higher vacancy mobility in pure Fe. Chromium solute appears to strongly suppress cavity swelling in Fe-Cr alloys for temperatures below ~470 °C, but seems to have little effect or slightly enhances swelling above ~470°C. Cavities were observed in all the irradiated samples between 400-550 °C. This indicates that the narrow temperature range of observable cavities reported in prior ion irradiated Fe-Cr ferritic alloy studies is likely an artifact associated with the use of low ion energies (<5 MeV), which leads to pronounced near-surface and implanted ion effects that suppress cavity swelling even at midrange depths (particularly at high temperatures).

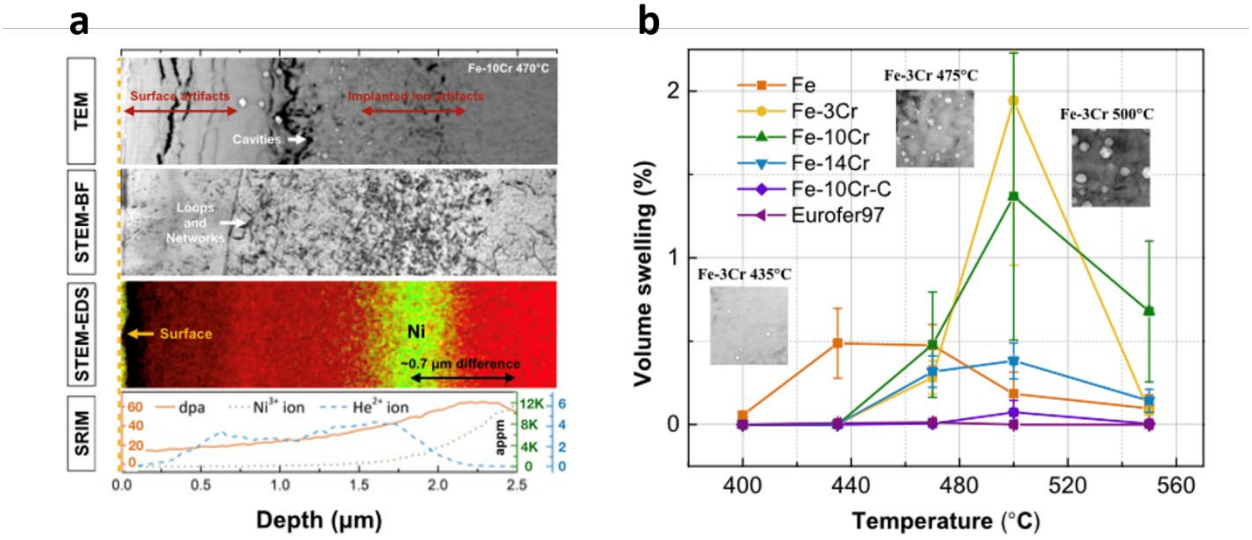

Figure 1. (a) Depth distribution of defects and STEM-EDS mapping of implanted Ni profile in irradiated Fe-10Cr at 470 °C, and SRIM simulation. (b) dependence of cavity swelling on irradiation temperature in dual beam ion irradiated Fe and Fe-Cr alloys.

FUTURE PLANS

Experiments of 10 appm He/dpa irradiations are in progress.

6.3 POST-IRRADIATION EVALUATION OF FRACTURE TOUGHNESS PROPERTIES OF F82H-Mod3 IRRADIATED IN THE RABBIT CAPSULE F13A5—X. Chen, R. Swain, J. Reed, A. Campbell, J.W. Geringer, Y. Katoh (Oak Ridge National Laboratory), T. Nozawa, H. Tanigawa (QST)

The extended abstract presents post-irradiation evaluation results of fracture toughness properties of F82H-Mod3 irradiated in the rabbit capsule F13A5. The irradiation temperature for the tested specimens was 369°C based on the SiC thermometry specimen measurements and the nominal irradiation dose was 28 displacements per atom. The measured Master Curve reference temperature (T_{0q}) was -57°C.

The F82H-Mod3 M4CVN miniature four-notch bend bar specimens were irradiated in the rabbit capsule F13A5. The initial irradiation was planned for 9 cycles in the High Flux Isotope Reactor (HFIR) at Oak Ridge National Laboratory (ORNL) and was extended to 16 total cycles with an accumulated irradiation dose of ~28 displacements per atom (dpa). The target irradiation temperature for the rabbit capsule was 300°C. Two SiC thermometry specimens (ID: HT28 and HT50) were retrieved from the rabbit capsule and cut into three equal pieces designed as left, middle, and right. Then, dilatometer measurements were performed on the middle cut piece of HT28 and all three pieces of HT50 to evaluate irradiation temperature consistency and potential irradiation temperature gradient. Figure 1 shows the dilatometer measurements of all thermometry specimens. Results indicated a very consistent irradiation temperature between the two thermometry specimens and negligible irradiation temperature gradient along the length of HT50 thermometry specimen. Based on Eq. (1), the irradiation temperature for the M4CVN specimens is calculated to be 369°C, which is higher than the target irradiation temperature of 300°C.

$$T_{irra} = (T_{left} + 2 \times T_{middle} + T_{right}) / 4 \quad (1)$$

where,
T_{irra} = M4CVN specimen irradiation temperature,
T_{left} = HT50 left cut piece irradiation temperature,
T_{middle} = average of HT28 middle cut piece and HT50 middle cut piece irradiation temperatures,
T_{right} = HT50 right cut piece irradiation temperature.

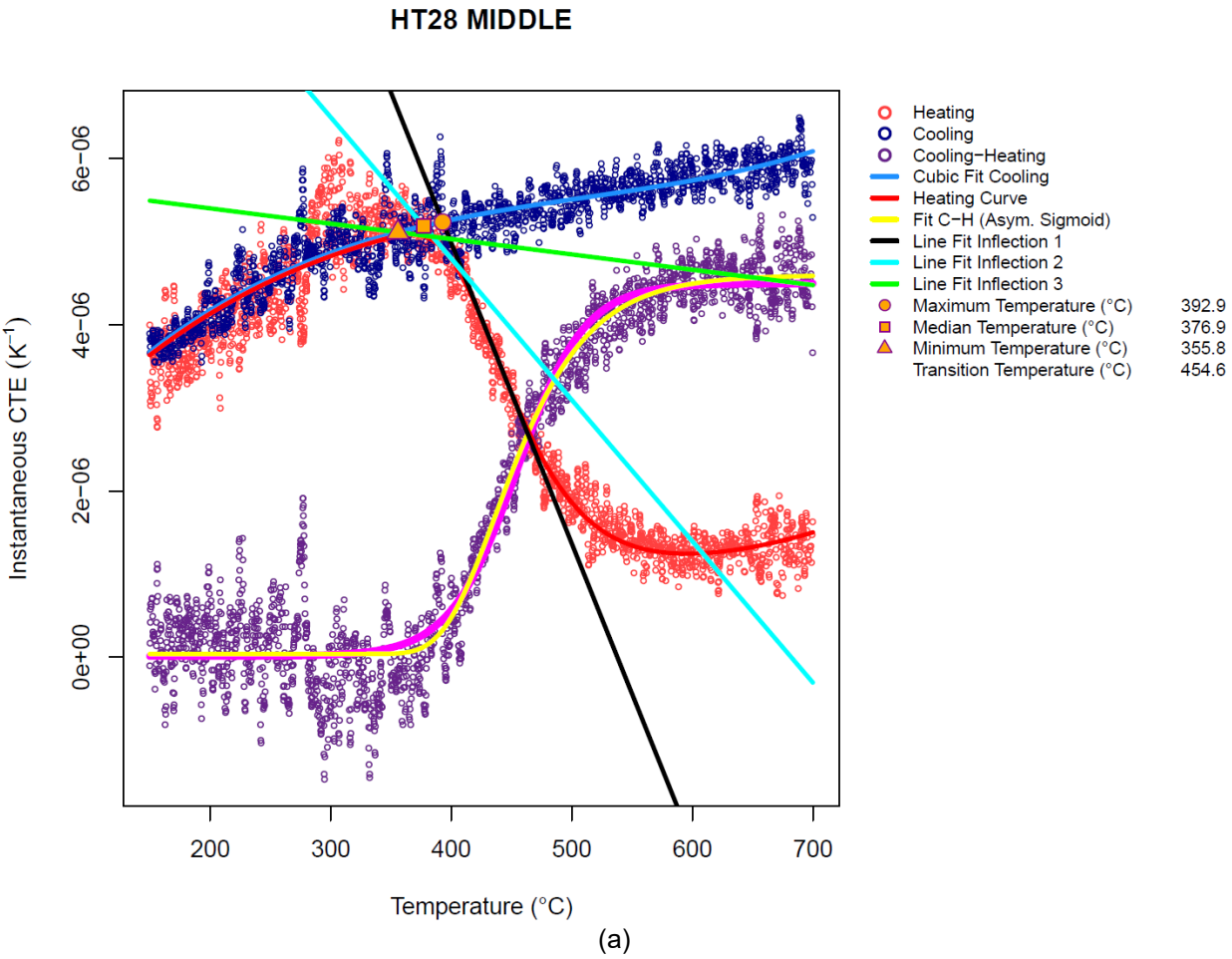
HT28 MIDDLE
Instantaneous CTE (K^{-1})
0e+00
2e−06
4e−06
6e−06
200
300
400
500
600
700
Temperature (°C)
Heating
Cooling
Cooling−Heating
Cubic Fit Cooling
Heating Curve
Fit C−H (Asym. Sigmoid)
Line Fit Inflection 1
Line Fit Inflection 2
Line Fit Inflection 3
Maximum Temperature (°C) 392.9
Median Temperature (°C) 376.9
Minimum Temperature (°C) 355.8
Transition Temperature (°C) 454.6

(a)

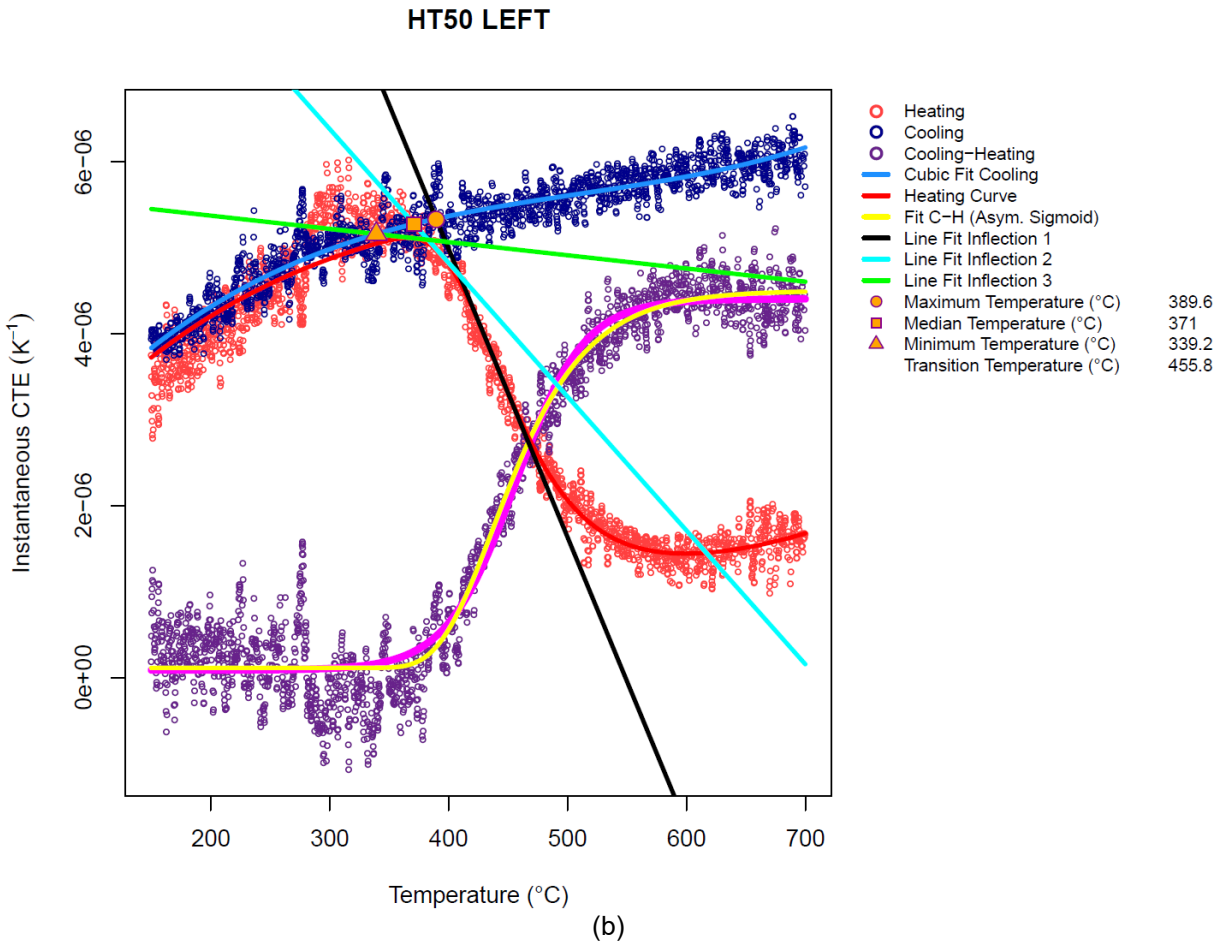
HT50 LEFT
Instantaneous CTE (K^{-1})
0e+00
2e−06
4e−06
6e−06
200
300
400
500
600
700
Temperature (°C)
Heating
Cooling
Cooling−Heating
Cubic Fit Cooling
Heating Curve
Fit C−H (Asym. Sigmoid)
Line Fit Inflection 1
Line Fit Inflection 2
Line Fit Inflection 3
Maximum Temperature (°C) 389.6
Median Temperature (°C) 371
Minimum Temperature (°C) 339.2
Transition Temperature (°C) 455.8

(b)

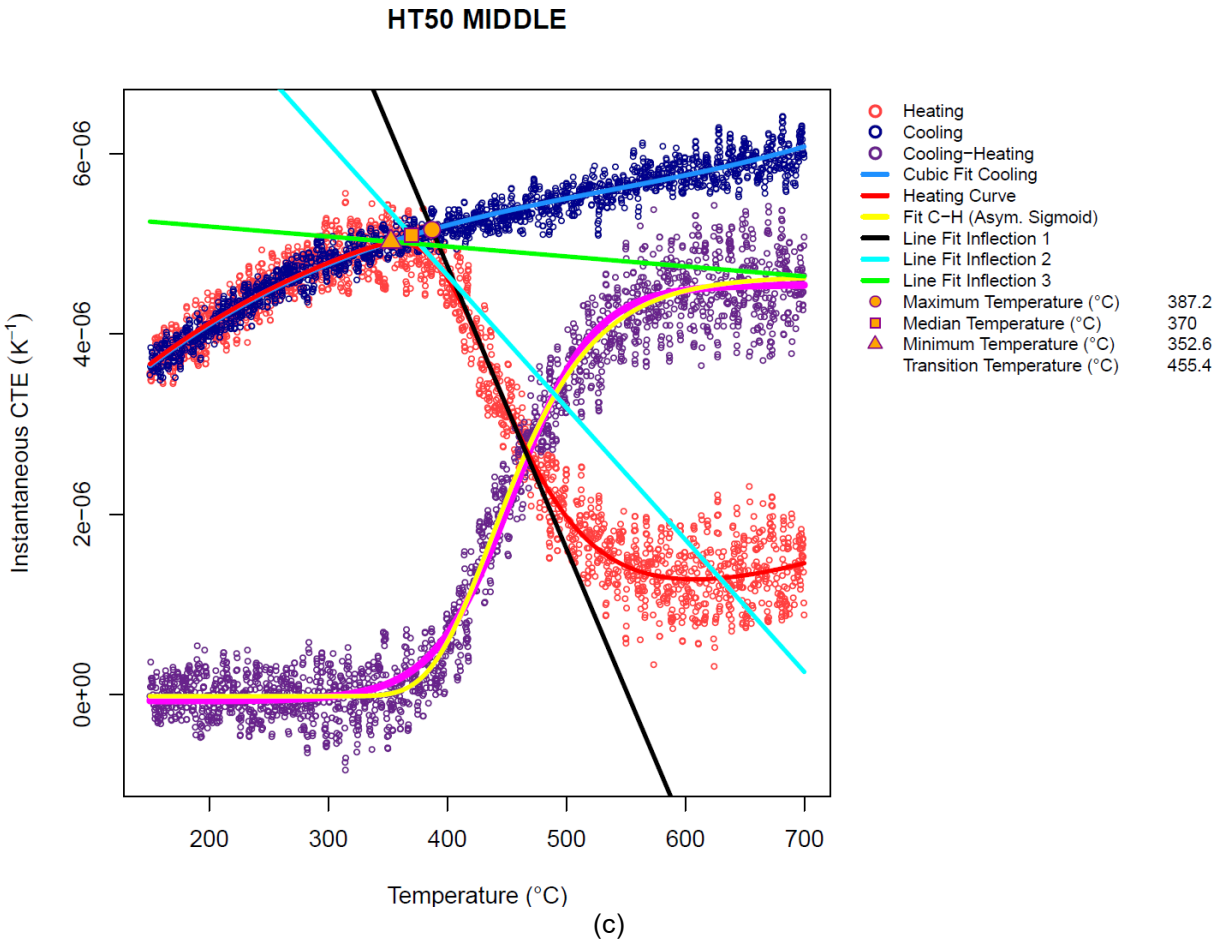
HT50 MIDDLE
Instantaneous CTE (K^{-1})
0e+00
2e−06
4e−06
6e−06
200
300
400
500
600
700
Temperature (°C)
Heating
Cooling
Cooling−Heating
Cubic Fit Cooling
Heating Curve
Fit C−H (Asym. Sigmoid)
Line Fit Inflection 1
Line Fit Inflection 2
Line Fit Inflection 3
Maximum Temperature (°C) 387.2
Median Temperature (°C) 370
Minimum Temperature (°C) 352.6
Transition Temperature (°C) 455.4

(c)

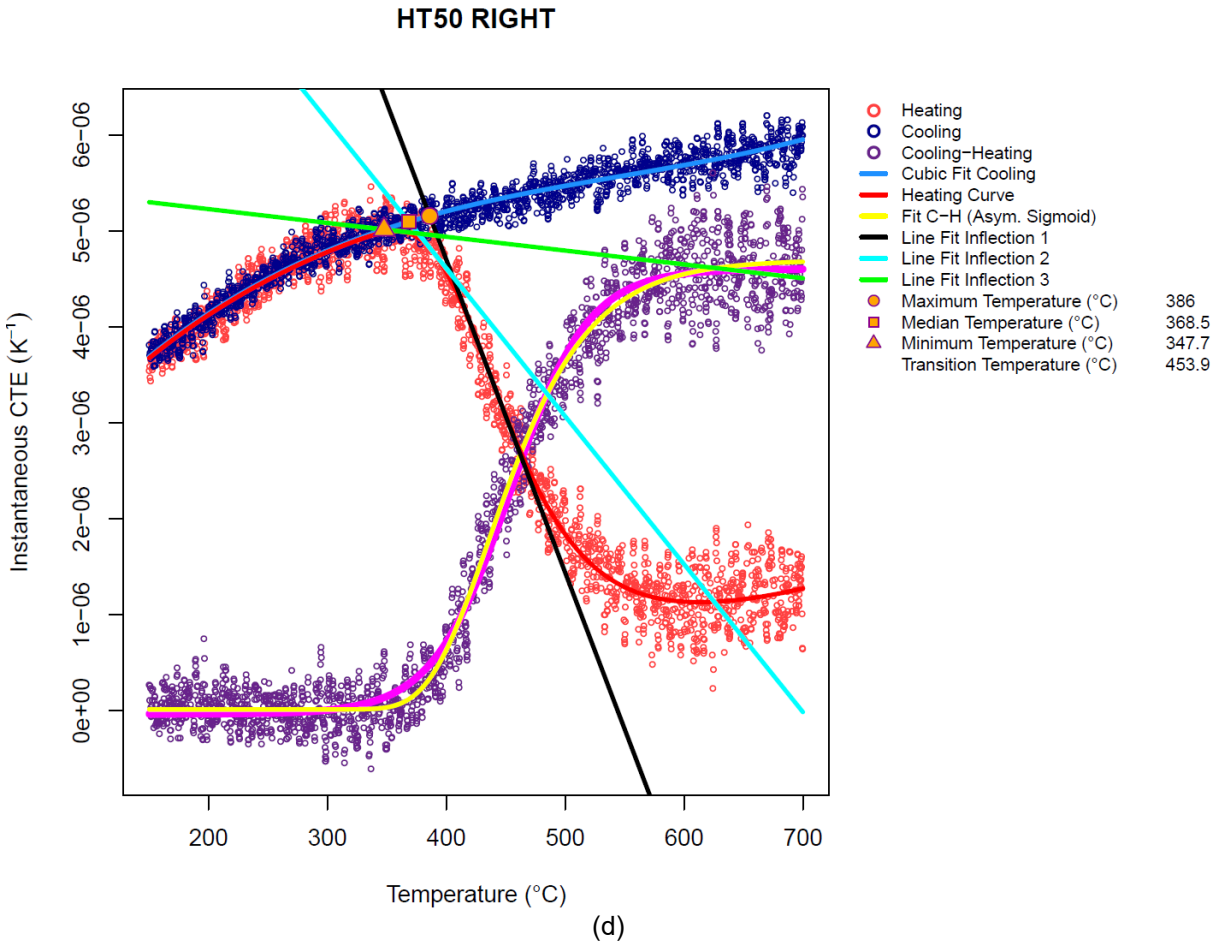

(d)

Figure 1. Dilatometer measurements for SiC thermometry specimens: (a) HT28 middle cut piece, (b) HT50 left cut piece, (c) HT50 middle cut piece, (d) HT50 right cut piece.

Before fracture toughness testing, Vickers microhardness measurements were performed near the fatigue precracking end of each notch to measure the extent of irradiation hardening. Four measurements were made for each notch with a Mitutoyo HV-120B hardness tester with 1 kg force and 15 sec dwell time. The hardness results are summarized in Table 1. Compared with the unirradiated hardness of 210-220 HV, F82H-Mod3 exhibited a very small amount of hardening after 28 dpa irradiation at 369°C.

Table 1. Vickers microhardness results for F82H-Mod3 specimens in F13A5 rabbit capsule

Specimen ID	Hardness from the notch				Avg. HV	Std. Dev.
	D	DM	UM	U		
HS3	228.3 222.4 233.7 234.5	232.4 227.5 233.7 228.3	227.1 220.5 228.3 219.7	220.1 220.8 230.0 222.8	226.9	5.06
HS4	229.5 236.6 228.3 228.3	228.7 225.5 226.3 230.4	232.4 225.9 232.4 222.0	236.2 220.1 224.0 222.0	228.0	4.69

Transition fracture toughness testing based on the Master Curve method in the ASTM E1921 standard was performed on two M4CVN specimens of F82H-Mod3. In total, eight notches were tested to calculate the Master Curve reference temperature, T_{0q}. Figure 2 shows the Master Curve testing results with T_{0q}=-57°C. Compared with the unirradiated state (T-S orientation), an upward shift of 59°C was observed in F82H-Mod3 after 28 dpa irradiation at 369°C.

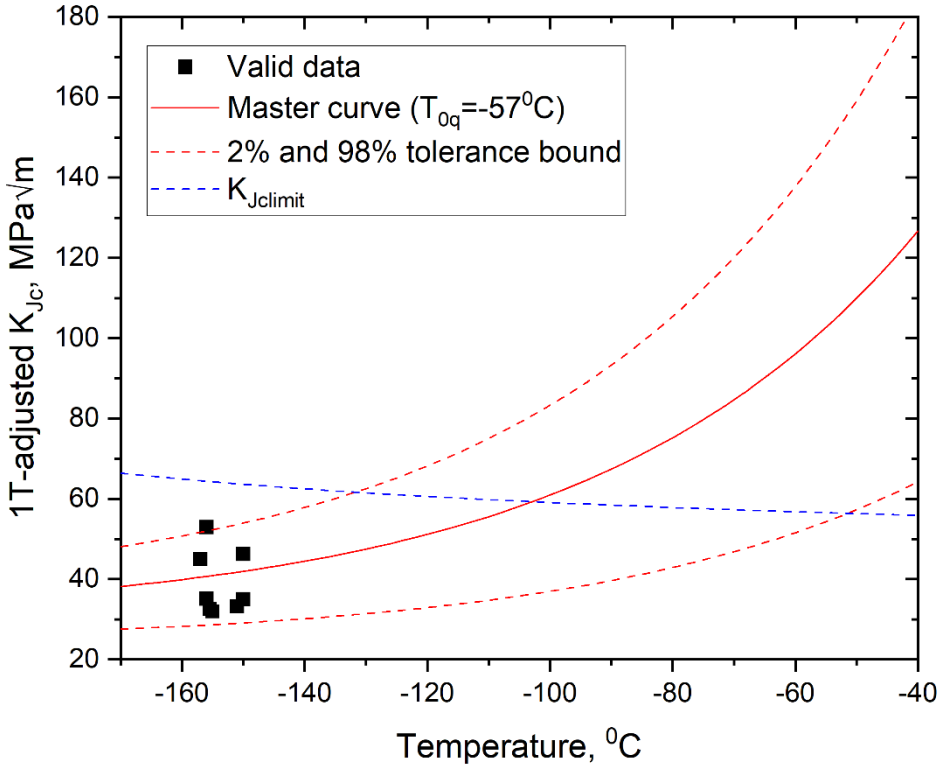

Figure 2. Master Curve testing results of F82H-Mod3 irradiated in the F13A5 rabbit capsule.

6.4 AN ELECTRON MICROSCOPE STUDY OF HEAVY ION IRRADIATED ULTRA-HIGH PURITY Fe AND Fe-Cr ALLOYS AT 350ºC—Yao Li, Steven John Zinkle (University of Tennessee), Arunodaya Bhattacharya (Oak Ridge National Lab)

OBJECTIVE

The objective of this task is to study the effect of Cr additions on dislocation loop size, density and type in high-purity Fe and Fe-Cr model alloys after heavy ion irradiation at different temperatures.

SUMMARY

Transmission electron microscopy (TEM) was used to characterize the size, density, nature, Burgers vector, and habit planes of dislocation loops after 8 MeV Fe ion irradiation to 3.5 dpa at 350℃ in high-purity Fe and Fe-Cr alloys. We are examining the effect of Cr concentration on the formation of dislocation loops. Compared with results reported previously at 0.35 dpa [1,2], the fraction of ½ <111> loops was slightly higher in samples irradiated to a higher dose of 3.5 dpa. From our preliminary analysis, the fraction of ½ <111> loops compared to <100> loops were observed to be significantly different in the near-surface, mid-range, and beyond peak damage regions, which may explain some previously reported discrepancies in the literature. Voids were only observed in pure Fe.

PROGRESS AND STATUS

This investigation is a continuation of previously reported lower-dose 8 MeV ion irradiation studies on the same materials, where the midrange damage level was 0.35 dpa and heterogenous loop formation was observed [1,2]. During this reporting period, dislocation loops were examined in ultra-high purity (UHP) iron and several Fe-Cr alloys containing 3, 5, and 8 wt% Cr after irradiation to midrange doses of 3.5 dpa at 350℃. Analysis was done in near surface region (0-300nm deep, 1.5 dpa), the midrange of irradiated region (700-1200nm deep, 3.5dpa), and beyond peak damage region (2350-2600nm deep,0 dpa). The midrange region is called “safe analysis region” in following text. In [3], Zinkle and Snead argued that the near surface sink region and the implanted ion region could modify the microstructure dramatically. A region between near-surface and implanted ion region is the best zone to emulate microstructure irradiated by neutrons, called safe analysis region. One fundamental difference of ½ <111> loops from <100> loops is that ½ <111> loops are mobile. By characterizing the beyond-peak region, it would let us understand loop evolution by migration mainly leading to loop coarsening or <100> formation proposed in [4,5]. Displacement damage and ion distribution profiles vs. depth are shown in Fig.1. In the SRIM calculations, ion distribution and quick calculation of damage method (K-P model) was applied and displacement energy was set as 40 eV. Table 1 summarizes the irradiation conditions examined in this study and table 2 lists all the diffraction vectors applied in full g·b analysis method. Inside-outside contrast method was carried out on UHP-Fe in the safe analysis region at 350℃, 0.35 dpa. Among 22 analyzed loops, 20 were interstitial type and 2 were vacancy type so it is believed that most of the loops were interstitial type for all irradiation conditions. Additional loop nature evaluations will be performed during the next reporting period.

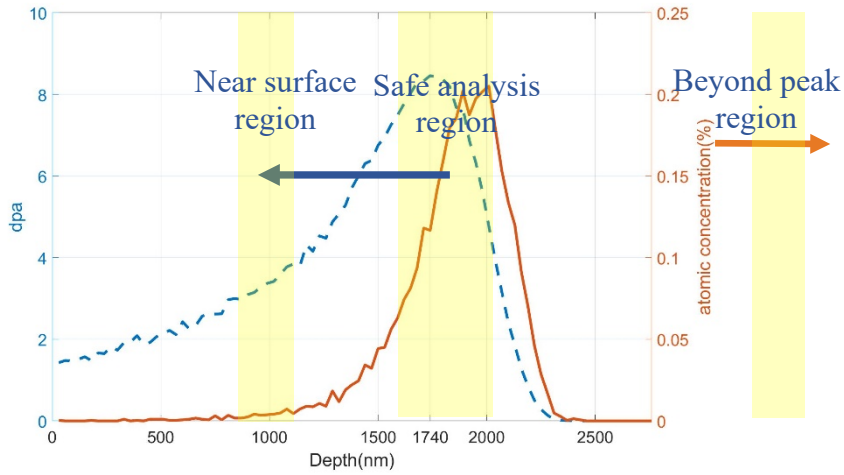

Figure 1. SRIM calculation of 8MeV Fe ions in Fe-Cr alloy (K-P model).

Table 1. Alloys and irradiation conditions examined for this report

	Fe	Fe-3Cr	Fe-5Cr	Fe-8Cr
350℃ 3.5 dpa 10^{-4} dpa/s	√	√	√	-

√: samples have been characterized and presented in this report.
-: samples have been characterized partially.

All samples discussed in this report were prepared by utilizing a final flash electropolish to remove near-surface FIB milling damage, as reported previously [2].

Table 2. Applied g vectors for loop identification in body centered cubic (BCC) Fe-Cr system. Numbers in the Table are the dot products of corresponding Burgers vector and diffraction vector. Red cells are the invisible conditions for different loops. Zero means invisible condition and non-zero means visible condition.

	diffraction vector (g)					
	[011] zone axis			[001] zone axis		
Burgers vector (b)	2 0 0	2 -1 1	0 -1 1	-1 1 0	-1-1 0	2 0 0
1 1 1	2	2	0	0	-2	2
1 1-1	2	0	-2	0	-2	2
1-1 1	2	4	2	-2	0	2
-11 1	-2	-2	0	2	0	-2
1 0 0	2	2	0	-1	-1	2
0 1 0	0	-1	-1	1	-1	0
0 0 1	0	1	1	0	0	0

UHP Fe

Loops were well distributed in the entire irradiation region of pure Fe irradiated to 3.5 dpa midrange dose. <100> loops and ½ <111> loops were identified by classical g·b analysis. Six different g vectors were

applied. They were [-200], [-1-10], and [-110] for the [001] zone axis as well as [-200], [2-11], and [0-11] for the [011] zone axis.

In the safe analysis region of the pure Fe specimen shown in Figure 2, 99 loops were randomly selected and identified. Among them, 47 loops were <100> type and 52 loops were ½ <111> type. The fraction of ½ <111> loops relative to the total number of observed loops was 52%.

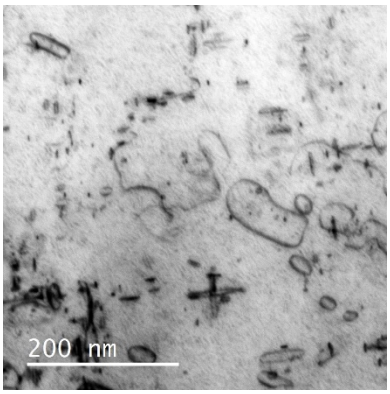

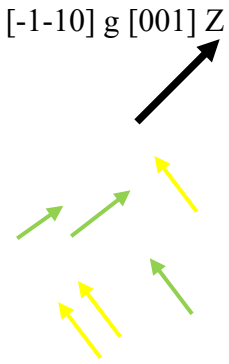

Figure 2. STEM-BF of UHP Fe safe analysis region(3.5dpa) at 350℃, 10^{-4}dpa/s safe analysis mid-range region under [-1-10] two-beam condition. Green arrays point at ½ <111> loops and yellow arrays point at <100> loops.

An overview micrograph is shown in Figure 3. In the near-surface and safe analysis region, defects were distributed homogenously in UHP Fe. Based on the prediction of SRIM, shown in Figure 1, the irradiation-induced defects were supposed to be observed in the range from the surface to 2300nm depth. However, defects were visible at depths as large as 3000nm in the UHP Fe samples. These were not FIB-induced artifacts since a clean defect-free zone was observed between the midrange safe analysis region and peak damage region. Since the surface normal was not near an ion channeling direction, the observation of dislocation loops beyond the SRIM-predicted maximum damage range may be associated with either errors in the SRIM stopping power database or evidence for long-range glide or diffusion of defect clusters beyond the irradiated region. Further analysis is needed to examine these two possibilities.

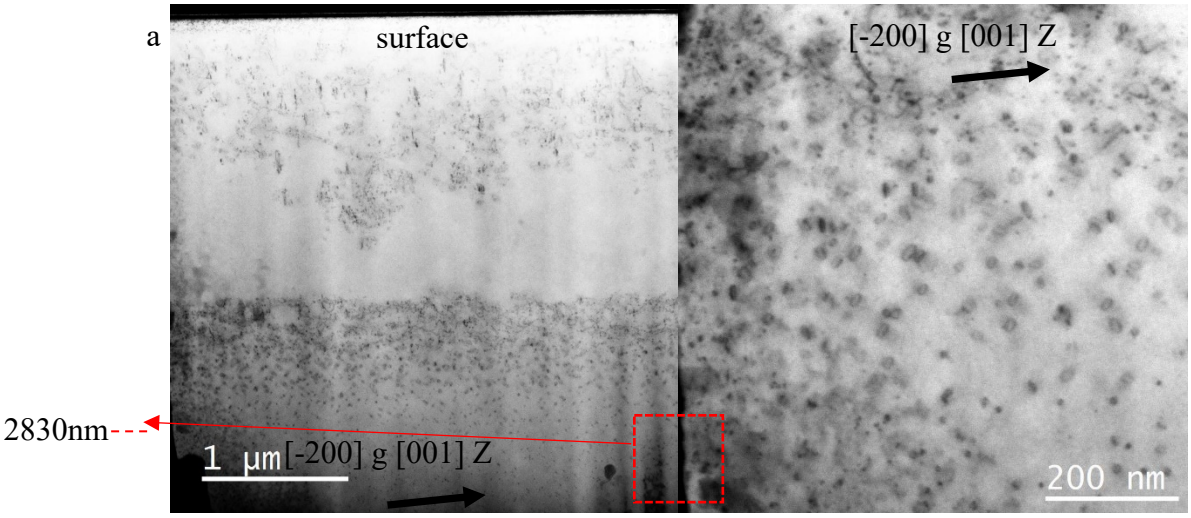

Figure 3. STEM-BF of UHP Fe irradiated at 350℃, 3.5dpa(midrange), 10^{-4} dpa/s. (a) Low magnification and (b) beyond peak damage region in high magnification. The marked region in (b) is as the depth milestone.

Well-developed loops were analyzed in the depth region from 2300nm to 2500nm in the UHP Fe samples, shown in Figure 4. It is easy to see that loops parallel or perpendicular to [-110] were totally dominant, indicating they were ½ <111> type. Among 123 identified loops in this region, 99 were randomly selected and identified to be ½ <111> loops while only 24 were <100> loops. The fraction of ½ <111> loop was 80%, significantly higher than the observed mid-range fraction of 52%.

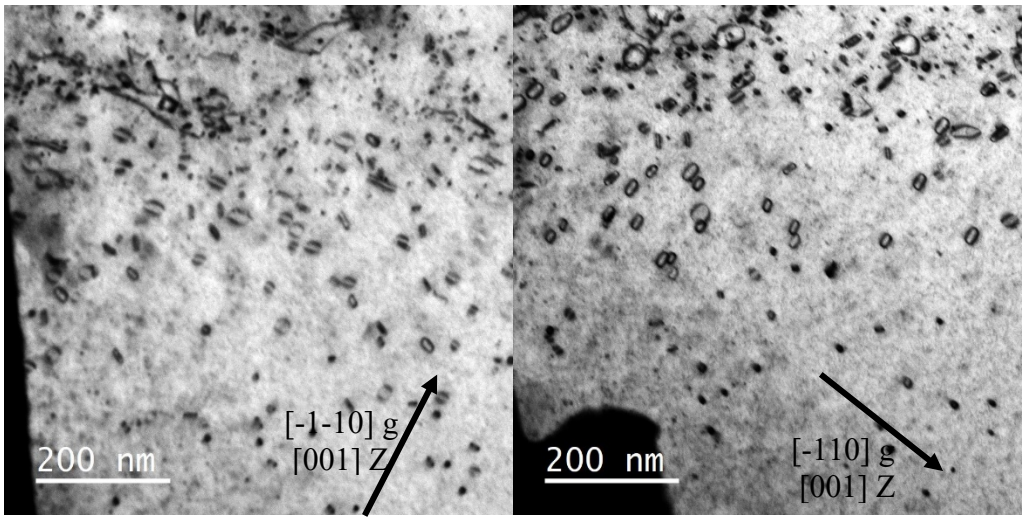

Figure 4. STEM-BF of beyond peak region(0dpa) in UHP Fe at 350℃, 10^{-4}dpa/s.

The peak damage region (~1700nm depth) was also checked (see Figure 5 for typical loop microstructure). Since the defect density was high in the peak damage region, it is not possible to perform full g·b analysis. A total of 6 diffraction vectors (3 vectors in one zone, see table 2 above) were used for partial loop analysis in the peak damage region. This was sufficient to do the loop type identification by vectors which were [-200], [-1-10], and [-110] in [001] zone axis. Among 159 loops, 72 were ½ <111> loops. The ½ <111> fraction

was 45%, comparable to the midrange (safe analysis zone) result and well below the “beyond peak damage” region result.

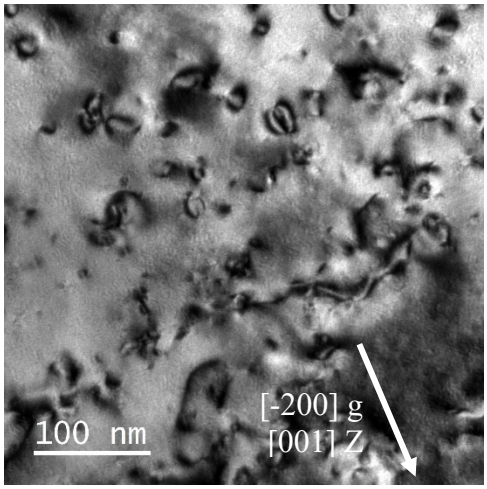

Figure 5. The peak damage region(8.5dpa) in UHP Fe at 350℃, 10^{-4}dpa/s.

Since there appears to be a significant difference between the loop habit plane distribution in the beyond-peak region and the midrange safe analysis region, this suggests the major effect of defect cluster migration on loop formation and growth in BCC Fe is loop coarsening rather than forming <100> loops, indicating models proposed in [4,5] may not be the major contributor to <100> formation. Preliminary analysis of the ½ <111> loop fraction was also performed for the near-surface region zone, which would be influenced by a large surface sink effect. Loop analysis was performed in the near-surface region (0 to 300 nm) of the irradiated UHP Fe specimen to compare with the mid-range and peak damage loop parameters. From the microstructure image in Figure 6, it is easy to see that <100> loops were dominant in the near surface region. Among 105 randomly selected loops, 90 loops were <100> loops and 15 were ½ <111> loops. The ½ <111> loop fraction was 14%, well below the analyzed mid-range value and far below the beyond peak damage value. The high fraction of ½ <111> loops in the beyond-peak-damage region is also consistent with preferential coarsening of mobile ½ <111> interstitial clusters beyond the irradiation zone.

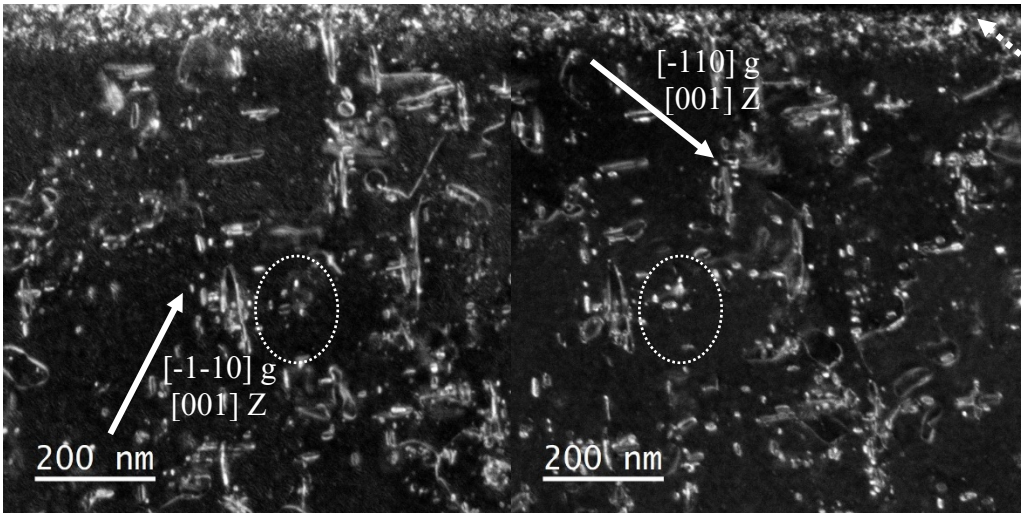

Figure 6. STEM -WBDF (2g,4g) the near surface region(1.5dpa) in UHP Fe at 350℃, 10^{-4}dpa/s. The circled loop cluster is the same loop cluster in two micrographs as a marker. Loops in the range from 0-300nm were identified.

In UHP Fe, voids were characterized by through-focus method (Figure 7(a-c). From the surface to 1500 nm depth, 207 voids were measured. The void size distribution is shown in Figure 7(d). Voids were distributed homogenously in UHP Fe and their average diameter was 4 nm. Voids were not observed in any of the Fe-Cr specimens irradiated at 350℃ in this study. This is qualitatively consistent with prior ion irradiation studies where cavity formation was observed at lower temperatures compared to Fe-Cr alloys [6].

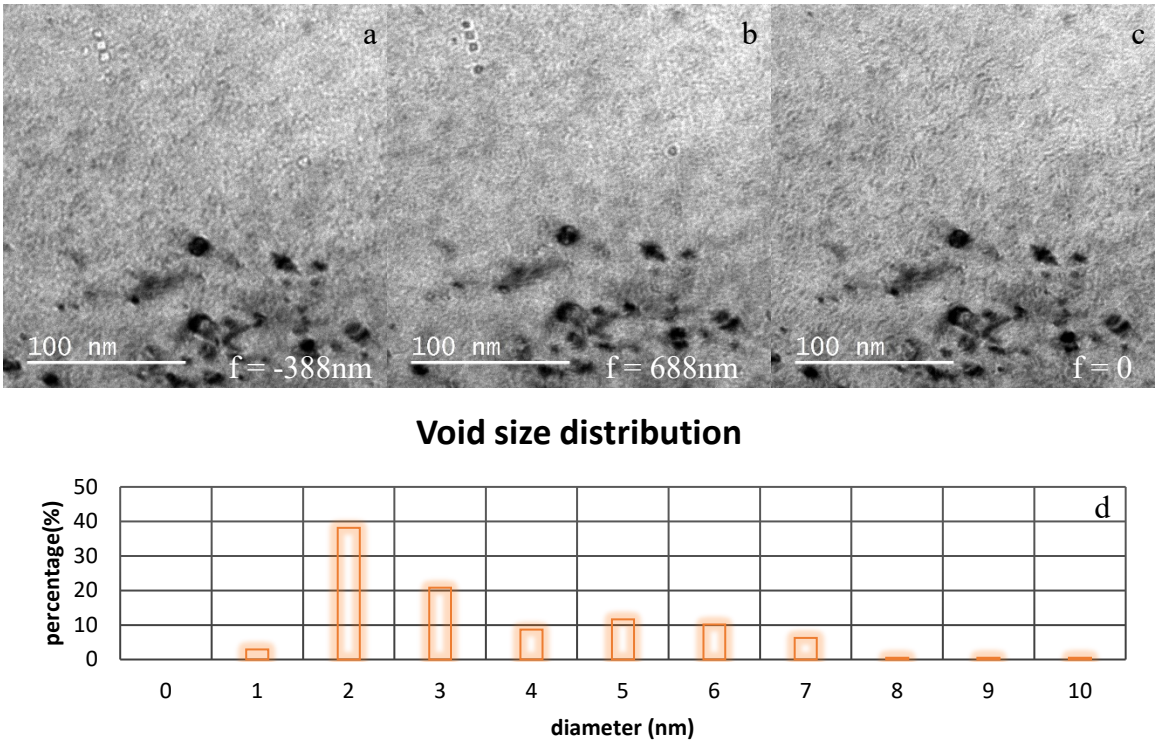

Figure 5. TEM-BF of voids in UHP Fe. (a) under-focus condition, (b) over-focus condition, (c) in-focus condition on the same region, and (d) size distribution.

Fe-3Cr

The general dislocation microstructure features in Fe-3Cr are shown in Figure 8(a). Heterogeneous loop clustering was observed in most of the irradiated region, and dense defects were observed in the near surface region that might be associated with mechanical polishing artifacts. No voids were seen in the Fe-3Cr sample by through-focus method, as shown in Figure 8(b-d).

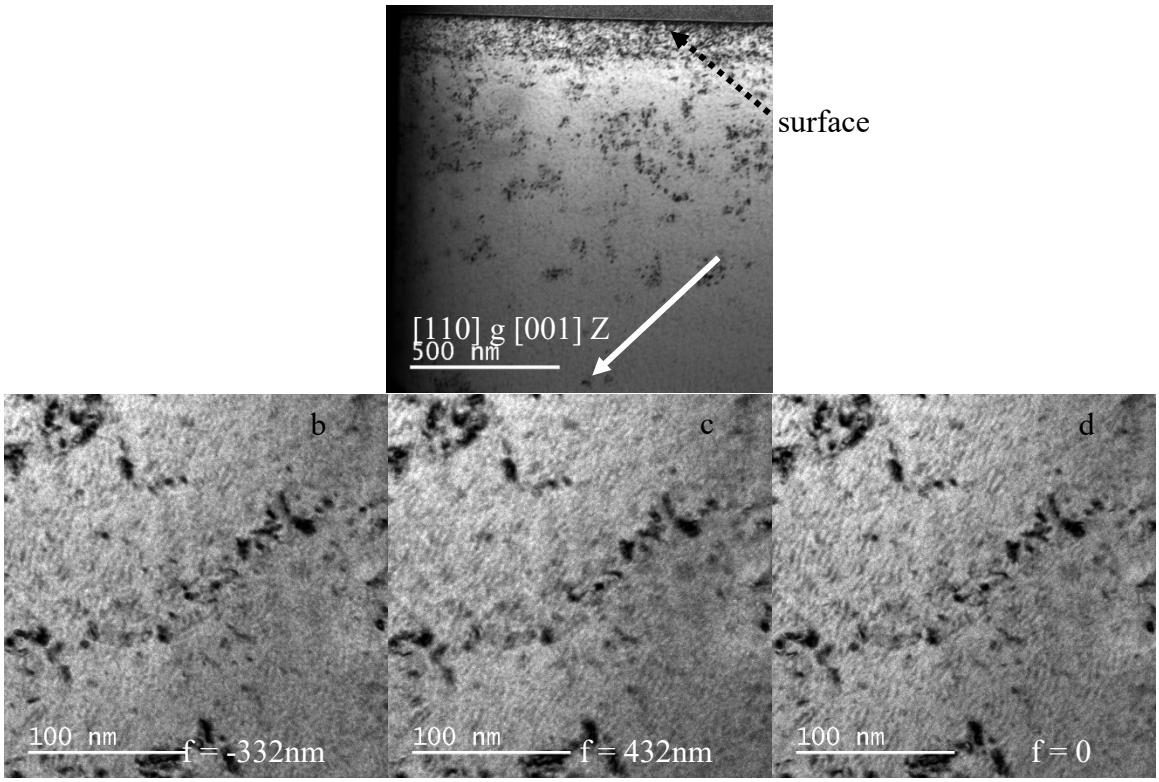

Figure 6. TEM-BF (a) overview of Fe-3Cr at 350℃, 3.5dpa(midrange), 10^{-4}dpa/s, (b) under-focus condition, (c) over-focus condition, and (d) in-focus condition. No void was seen.

Shown in Figure 9(a), in the midrange safe analysis region, 92 loops were randomly selected and characterized. Among them, 47 were identified as ½ <111> loop. The corresponding ½ <111> fraction was 51%. In the near-surface region, among 152 identified loops, 134 loops were <100> loops. The ½ <111> fraction was 11%. In the beyond-peak region, among 83 identified loops, ½ <111> loop fraction was 75%. Compared with UHP-Fe, Fe-3Cr had a similar <100> loop fraction in all three regions analyzed in this study. The variation in ½ <111> loop fraction between the midrange and beyond peak damage region was consistent with the trends observed for pure Fe.

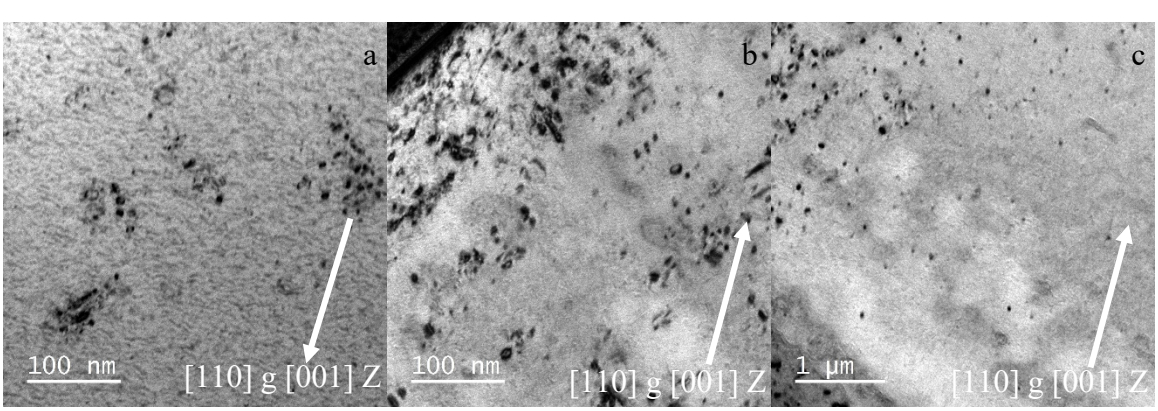

Figure 7. TEM-BF (a) safe analysis region (3.5dpa), (b) near surface region (1.5dpa), and (c) beyond peak region (0 dpa) of Fe-3Cr at 350℃, 10^{-4}dpa/s.

Fe-5Cr

Loops in Fe-5Cr showed extremely heterogenous spatial distribution, as shown in the low-magnification images in Figure 10. Two different regions from the FIB liftout foil are shown in the low-magnification images in Figure 10(a) and 10(b). In the central part of Figure 10(a), the defect density is obviously lower than any region shown in rest of Figure 10(a) and Figure 10(b). Based on the results we presented in [2], it was inferred that the vast majority of loops were distributed along pre-existing dislocation lines. The distance from the surface to the upper bound of the peak damage region is 1570 nm, shown in Figure 10(c) and the width of the peak damage region is 408 nm shown in Figure 10(d). The depth of damage zone matched the predication by SRIM in Figure 1. The beyond-peak region was not analyzed in Fe-5Cr samples since there were no observed loops in the beyond-peak region.

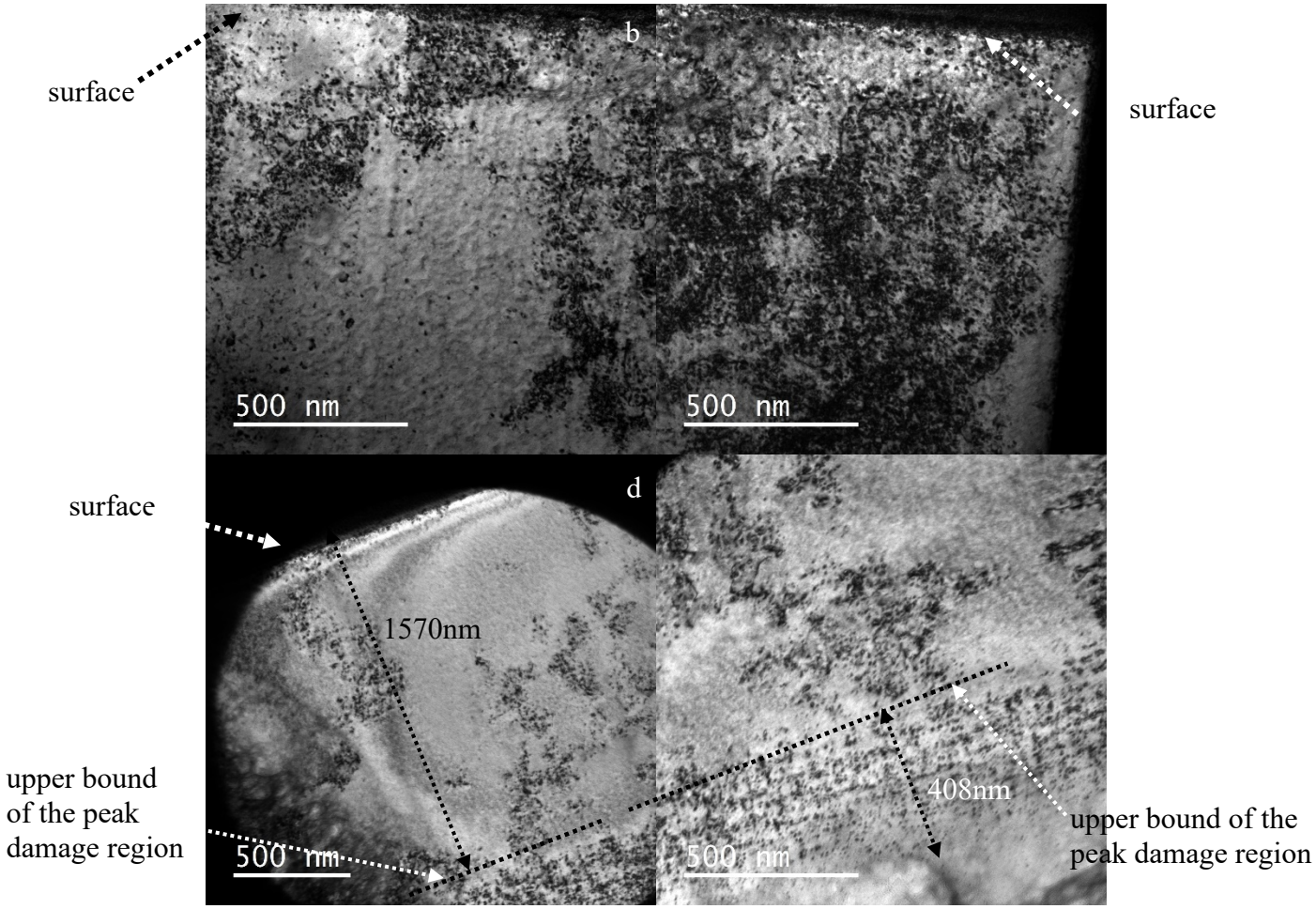

Figure 8. (a) relatively clean region vs (b) dense loop region, (c) the distance from the surface to the upper bound of the peak damage region, and (d) the distance from the upper bound to lower bound of the peak damage region in Fe-5Cr at 350℃, 3.5dpa(midrange), 10^{-4}dpa/s.

As was the situation for analyzing the peak damage region in other specimens, it is not possible to do full g·b analysis in the dense loop regions in the Fe-5Cr sample (typical microstructure shown in Figure 11), so loops were identified by the method described in [7] using a zone axis of [001] Z. In the low loop density regions, diffraction vectors of [-200], [-1-10], and [-110] were applied to identify loop type rather than perform comprehensive loop Burgers vector analysis for each individual loop. The circled loop in Figure 11 was an

example. Its long axis was perpendicular to [-1-10] direction and by the method in [7], it was identified as ½ <111> loop in Fe-5Cr.

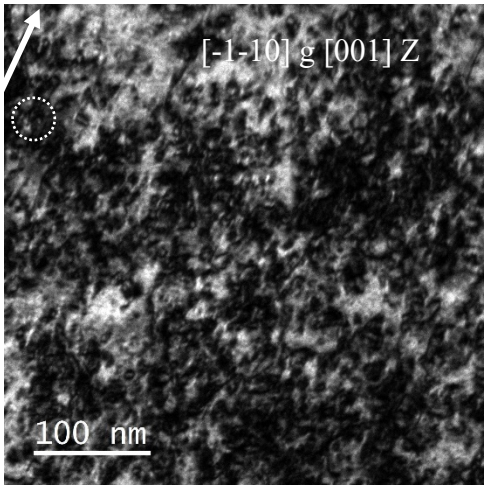

Figure 9. A TEM-BF micrograph of dense defect region in safe analysis region(3.5dpa), Fe-5Cr at 350℃, 10^{-4} dpa/s.

In the safe analysis region, among 117 randomly selected and identified loops, 57 were ½ <111> loops. The corresponding ½ <111> loop fraction is 48%. A relative clean near-surface region is shown in Figure 12. Loop type was identified by three diffraction vectors in [001]Z. In the near-surface region, among 104 identified loops, 29 were ½ <111> loops which corresponds to a ½ <111> loop fraction of 28%. Compared with the ½ <111> fraction for the near-surface regions in Fe-3Cr and UHP-Fe, the fraction of ½ <111> loop was higher in Fe-5Cr. The ½ <111> loop fraction vs. depth for Fe, Fe-3Cr and Fe-5Cr is compared in Figure 13. In all three materials, there is a consistent evolution from predominantly <100> loops in the near-surface region (attributed to preferential loss of ½ <111> loops to the nearby surface), nearly equal fractions of <100> and ½ <111> loops in the midrange safe analysis zone, and mainly ½ <111> loops in the beyond peak damage region. Yao *et al.* [8] reported that with increasing irradiation temperature the fraction of <100> loop relative to the total identified loops increased in BCC iron and the fraction of <100> surpassed 50% at 400℃ in their in-situ experiments. In contrast, ~80% of identified loops were <100> type in the near-surface region in Fe and Fe-Cr alloys reported here. Also, in another paper by Yao *et al.* [9], <100> loops were reported to be dominant in an in-situ experiment on BCC Fe at 300℃. Combining our results and the result in [9], it is inferred that mobile clusters and/or loops escaped from the matrix to free surfaces. Thus, the free surface effect appears to have a dramatic impact on the observed loop Burgers vector and habit plane.

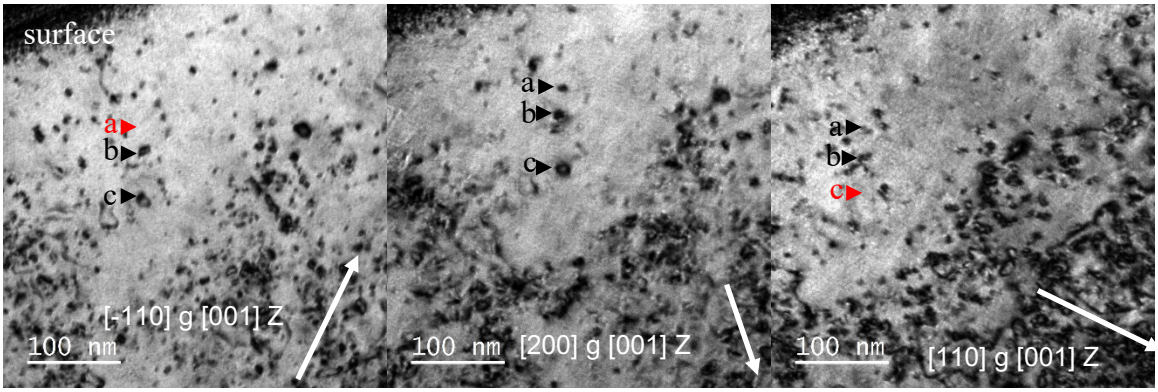

Figure 10. TEM-BF micrographs of the same area in three different diffraction vectors. Loops by black labeling scheme were visible in their micrographs and loops by red labeling scheme were invisible in their micrographs. Therefore, b was <100> type and a as well as c loops were ½ <111> type in Fe-5Cr at 350℃, 1.5dpa, 10^{-4}dpa/s.

From Figure 13, generally, Fe, Fe-3Cr, and Fe-5Cr had a similar trend with respect to fraction of ½ <111> loops at different depth regimes in the ion irradiated samples. It is also evident that Fe-5Cr sample had a slightly higher ½ <111> loop fraction in the near-surface region compared to pure Fe and Fe-3Cr. Compared with the ½ <111> fraction for safe analysis region in Fe samples, the ½ <111> fraction for peak damage region had a similar value in Fe samples so the implanted ions had no effect on the fraction of ½ <111> loops in this study.

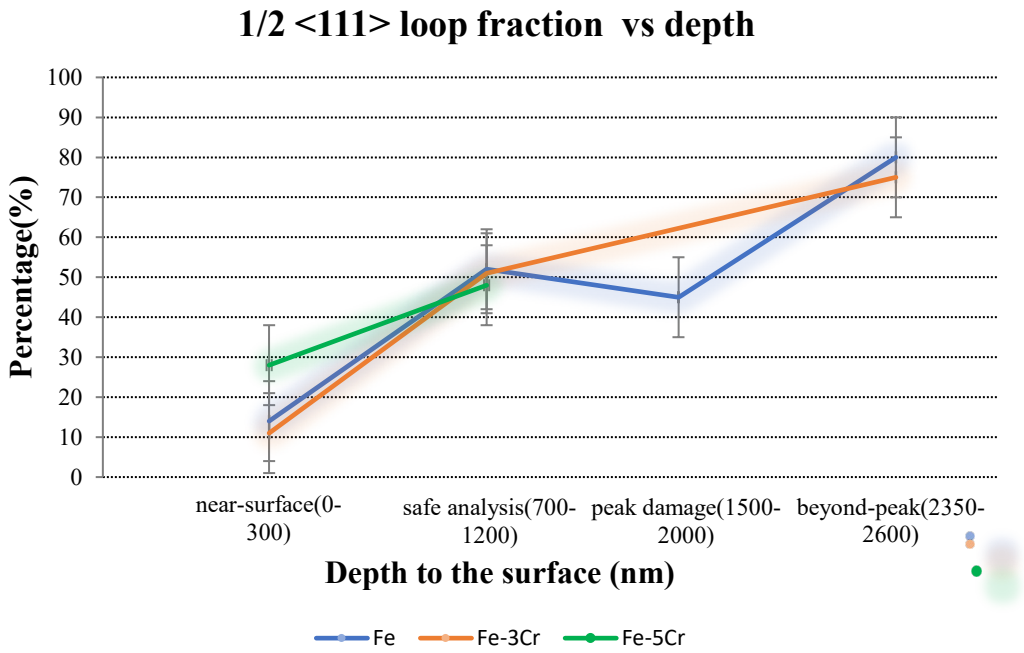

Figure 11. ½ <111> loop fraction relative to total number of identified loops in each region.

Dislocation loop rafting along <100> directions was observed in the peak damage regions(8.5dpa) of Fe-3Cr, Fe-5Cr, and Fe-8Cr following irradiation at 350℃, 10^{-4}dpa/s, as shown in Figure 14.

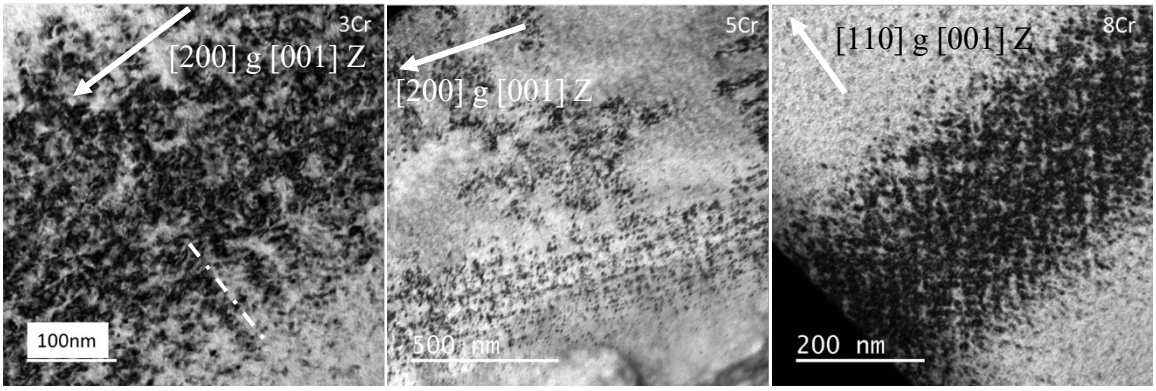

Figure 12. Loop rafting occurred in the peak damage regions(8.5dpa) in Fe-Cr alloys. (a) Fe3-Cr, (b) Fe-5Cr, and (c) Fe-8Cr at 350℃, 10^{-4}dpa/s.

FUTURE PLANS

The high fraction of <100> loops in near surface regions and the high fraction of ½ <111> loops in beyond-peak regions are considered to be important evidence associated with cluster/loop migration. Although loops in Fe at lower dose were identified as interstitial type, those analyzed loops were mainly in the safe analysis region and may not be representative of the loop nature in the near-surface regions and beyond-peak regions and/or the loop nature for Fe-Cr alloys. As a result, the nature of loops in Fe-Cr alloys and in the near-surface regions and beyond-peak regions will be quantified. Further quantitative analysis of the loop habit plane distributions will also be performed in the near-surface, midrange and beyond-peak regions. In addition to completing the full characterization on Fe-8Cr at 350℃, 3.5dpa, 10^{-4}dpa/s, pure Fe and 3-12Cr samples irradiated at 450℃, 3.5dpa, 10^{-4}dpa/s are ready to be analyzed. Based on the information we extracted from previous samples, UHP Fe, Fe-5Cr, Fe-8Cr, and Fe-12Cr are in the prioritized list. By checking those samples and comparing the data we presented in this report, we would have a better understanding of the effect of temperature as well as Cr concentration on the formation mechanism of <100> and ½ <111> loops in the BCC iron system. Also, comprehensive statistical data (e.g. size and volumetric density) will be compiled to sharpen our understanding. As shown in Figure 3(a), Figure 8(a), and Figure 10(a), there is often a low defect cluster density band between the midrange safe analysis region and the peak damage region, as previously reported by Gao et al. [10] We will examine the effect of Cr concentration and irradiation temperature on the development of this region.

REFERENCES

[1.] Y. Li, S.J. Zinkle and A. Bhattacharya, Fusion Materials Semiann. Prog. Report for period ending June 30, 2019, DOE-ER-0313/66, p. 15.

[2.] Y. Li, L. Wang, A. Bhattacharya and S.J. Zinkle, Fusion Materials Semiann. Prog. Report for period ending June 30, 2020, DOE-ER-0313/68, p. 11.

[3.] Zinkle, S.J. and L.L. Snead, *Opportunities and limitations for ion beams in radiation effects studies: Bridging critical gaps between charged particle and neutron irradiations.* Scripta Materialia, 2018. **143**: p. 154-160.

[4.] Xu, H., et al., *Solving the puzzle of <100> interstitial loop formation in bcc Iron.* Phys Rev Lett, 2013. **110**(26): p. 265503.

[5.] Marian, J., B.D. Wirth, and J.M. Perlado, *Mechanism of formation and growth of <100> interstitial loops in ferritic materials.* Phys Rev Lett, 2002. **88**(25 Pt 1): p. 255-507.

[6.] Lin, Y.-R., et al., *Temperature-dependent cavity swelling in dual-ion irradiated Fe and Fe-Cr ferritic alloys.* Acta Materialia, 2021. **207**(116660).

[7.] Yao, B., D.J. Edwards, and R.J. Kurtz, *TEM characterization of dislocation loops in irradiated bcc Fe-based steels.* Journal of Nuclear Materials, 2013. **434**(1-3): p. 402-410.

[8.] Yao, Z., et al., *The temperature dependence of heavy-ion damage in iron: A microstructural transition at elevated temperatures.* Philosophical Magazine, 2010. **90**(35-36): p. 4623-4634.

[9.] Yao, Z., et al., *Heavy-ion irradiations of Fe and Fe–Cr model alloys Part 1: Damage evolution in thin-foils at lower doses.* Philosophical Magazine, 2008. **88**(21): p. 2851-2880.
[10.] Gao, J., K. Yabuuchi, and A. Kimura, *Characterization of ordered dislocation loop raft in Fe3+ irradiated pure iron at 300 °C.* Journal of Nuclear Materials, 2018. **511**: p. 304-311.

6.5 DEVELOPMENT OF OPEN-SOURCE, HIGH-FIDELITY APT DATA ANALYSIS ALGORITHMS FOR CHARACTERIZING NUCLEAR STRUCTURAL MATERIALS—Samara Levine, Steven Zinkle (University of Tennessee), Arunodaya Bhattacharya (Oak Ridge National Laboratory), Cristelle Pareige (University of Rouen)

OBJECTIVE

The effectiveness of atom probe tomography (APT) as a technique for studying nano-scale precipitates and solute clusters in irradiated materials hinges on successful identification of clusters in a data set. The objective of this study is to develop an open-source, high-fidelity algorithm for cluster analysis, which resolved several solute cluster quantification issues associated with the mainstream APT software.

SUMMARY

The behavior of secondary phase particles and solute clusters under irradiation has significant implications for the mechanical performance of nuclear structural materials. Unlike transmission electron microscopy (TEM), APT gives chemical information with near-atomic scale spatial resolution, and therefore it is the preferred technique for examining nano-scale precipitates and solute clustering in irradiated materials. Despite advancements, correctly identifying clusters in APT data sets remains a challenge. The maximum separation method (MSM), which can be performed with the Integrated Visualization and Analysis Software (IVAS) available through CAMECA, is the most common approach to nano-scale cluster analysis. However, the MSM can produce numerous artifacts that can lead to vastly incorrect data interpretation. Some of the artifacts of MSM include the incorrect linking of two or more physically distinct clusters, the incorrect inclusion of atoms in a cluster, or, conversely, the incorrect exclusion of atoms from a cluster. To address these issues, an open-source Python program was developed. The Python program, named OSCAR (Open-Source Characterization of APT Reconstructions), uses a core-linkage method to significantly improve the flexibility and fidelity of the cluster search algorithm.

PROGRESS AND STATUS

To understand the differences between IVAS and the recently developed open-source Python method, it is essential to understand how the MSM in IVAS works. First, core solute atoms at the core of the cluster are identified by comparing the distance of the nearest solute neighbor with the characteristic clustering distance, d_{max}. If the nearest solute neighbor distance is less than d_{max}, both solute atoms are considered core atoms of the cluster. The number of solute atoms within d_{max} of a central atom, known as the order, can be modified to optimize the selection of d_{max}. Next, clusters with less than N_{min} solute atoms are excluded from the analysis. For the clusters that remain, periphery atoms are added to each cluster using an envelope distance, L. And so, if an atom is within a distance L of a core atom, it is included in the cluster. The envelope process results in a shell of excess atoms around the cluster, and therefore as a final step, the cluster is eroded. Atoms within a specified distance, $d_{erosion}$, of a matrix atom are removed from the cluster.

Although many parameters are required for cluster analysis in IVAS, results are most sensitive to the value of $d_{max.}$ The parameter d_{max} is normally selected by comparing a nearest neighbor (NN) distribution where all solute atoms have been randomized with the NN distribution of the experimental data. Incorrect selection of d_{max} can lead to several artifacts. If d_{max} is too small, solute atoms may be unnecessarily excluded from the cluster. On the other hand, if d_{max} is too large, extraneous solute atoms may be included in the cluster. However, even with reasonable values of d_{max}, physically separate clusters may be incorrectly merged, known as the single-link effect, since the MSM is very sensitive to local changes in density.

Another issue that arises from the IVAS implementation of the MSM is that a single value of $d_{erosion}$ must be selected for all clusters. In general, small clusters tend to have a thinner shell of atoms surrounding them than large clusters. When a single value of $d_{erosion}$ is selected, atoms will be unnecessarily eroded from small clusters, and the algorithm will fail to remove matrix atoms from large clusters. As a result, $d_{erosion}$ should scale with cluster size.

As an alternative to the MSM, core-linkage algorithms have been introduced [1]. The benefit of core-linkage algorithms is that the criterium for identifying core atoms is malleable. In lieu of the MSM, density-based algorithms or other methods can be used. The Python program that has been developed is based upon a core-linkage algorithm. To identify core atoms, a chemistry-based approach is currently used. For this, the solute concentration within a certain radius, r, of each atom is first calculated in 3Depict, an open-source program. The results are then imported to Python for the rest of the cluster analysis. Solute atoms with a local concentration above a threshold, c_{th}, are identified as core atoms. c_{th} is equal to where the local chemistry distribution of atoms in a randomized data set reaches 0.01% of the total counts. Because this chemistry-based algorithm is less sensitive to local density changes as r or c_{th} increases, it is less susceptible to the single-link effect. After core atoms are identified, clusters with less than N_{min} solute atoms are excluded from the analysis. Then periphery atoms are added to the cluster if they are within a distance, d_{link}, of a core atom. At this stage, a proximity histogram, such as Fig. 1, for each cluster showing composition as a function of distance from the interface is generated. The proximity histogram is fit with a four-parameter logistic function to determine an appropriate erosion distance, defined to be equal to the position of the midpoint solute concentration. For each cluster, the calculated erosion distance is then applied.

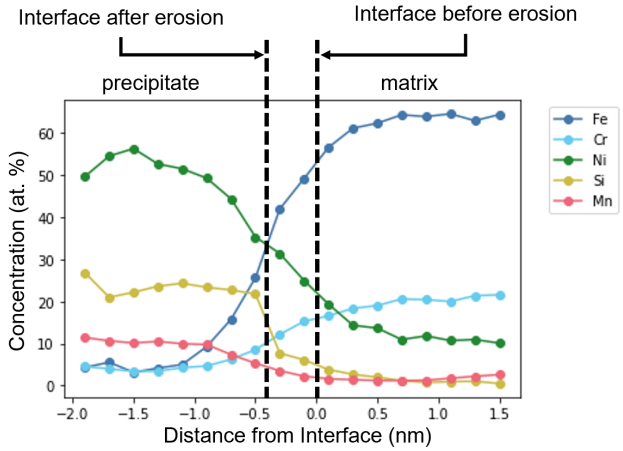

Figure 1. An example of a proximity histogram generated in Python, which shows composition near a cluster interface. The initial interface is located at 0 nm. The erosion distance for this cluster is 0.38 nm.

To test the Python algorithm, data sets from 304L stainless steel irradiated in the BOR-60 reactor were selected. This material was chosen for the study because of the vast literature available on irradiated stainless steels. Further, this 304L stainless steel, exposed to proton irradiation, was the subject of a previous interlaboratory study on APT analysis using the MSM [2]. It is known to have two families of solute clusters: Cu-based and Si-based. While the MSM does reasonably well at identifying the Cu-based clusters, it struggles with identifying the Si-based clusters. This is in part due to Si decorating dislocations in addition to forming matrix clusters. A comparison of the Si-based clusters identified by IVAS and by the Python program is given in Fig. 2. For the IVAS analysis: d_{max} = 0.82 nm, Order = 4, N_{min} = 23, L = 0.82 nm, and $d_{erosion}$ = 0.41 nm. Because d_{link} in the core-linkage algorithm is analogous to L in the MSM, d_{link} = 0.82 nm was chosen for the Python analysis. To be consistent with IVAS, N_{min} = 23 was also used. Finally, the appropriate c_{th} for this specimen was found to be 11 at. %. While the envelope/linkage parameters are similar for each program, Fig. 2 shows that the clusters identified by the Python program are more reasonable in size and visually match the Si atom map more closely. Also, physically distinct clusters that

were incorrectly merged by IVAS, indicated by the arrows, are correctly identified as separate clusters in the Python program.

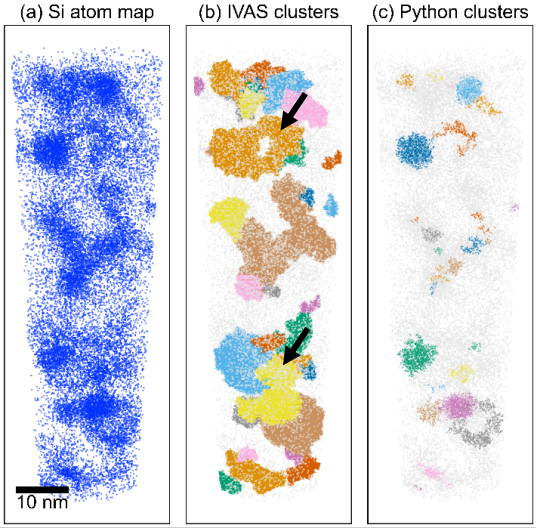

Figure 2. A comparison of clusters identified by IVAS and Python. In this example, the material is neutron irradiated 304L stainless steel and the solute of interest is silicon. (a) shows a map of silicon in the APT tip. (b) shows the Si clusters identified with IVAS using the MSM (d_{max} = 0.82 nm, Order = 4, N_{min} = 23, L = 0.82 nm, and $d_{erosion}$ = 0.41 nm). Arrows indicate examples where two or more clusters are incorrectly linked. (c) shows the Si clusters identified with Python using the core-linkage method (c_{th} = 11 at. %, N_{min} = 23, d_{link} = 0.82 nm). Analysis is ongoing to determine the optimal c_{th} for capturing Si clusters.

FUTURE WORK

The APT data has been collected from several oxide dispersion strengthened (ODS) alloys (PM2000, MA957 and 12YWT) irradiated in HFIR as a part of the JP28-29 irradiation campaign to doses greater than 60 dpa at ~300 °C. The Python program will be used to analyze the APT data for chemical variations within the irradiated ODS particles and nano-scale solute clustering in the matrix in order to better understand the stability of these alloys at high neutron irradiation doses.

ACKNOWLEDGEMENTS

The authors are thankful to Y. Zhao from the University of Tennessee, Knoxville for fruitful discussions on data analysis techniques. APT experiments were conducted at the Michigan Center for Materials Characterization and the Center for Nanophase Materials Science (CNMS), which is a US DOE user facility. The authors would also like to thank Prof. Gary Was and Dr. Zhijie Jiao from the University of Michigan for their collaboration.

References

[1] Stephenson, Leigh T., et al. "New techniques for the analysis of fine-scaled clustering phenomena within atom probe tomography (APT) data." *Microscopy and Microanalysis* 13.6 (2007): 448.

[2] Dong, Yan, et al. "Atom probe tomography interlaboratory study on clustering analysis in experimental data using the maximum separation distance approach." *Microscopy and Microanalysis* 25.2 (2019): 356-366.

7. PLASMA MATERIALS INTERACTIONS

7.1 ENHANCED THERMAL STABILITY OF HELIUM-IMPLANTED SURFACE GRAINS IN WARM-ROLLED TUNGSTEN—Cuncai Fan, Yutai Katoh, Xunxiang Hu (Oak Ridge National Laboratory)

OBJECTIVE

The objective of this work is to investigate the thermal stability of helium-implanted surface grains in warm-rolled polycrystalline tungsten. Our results suggested that recovery and recrystallization occur via subgrain coarsening and removal of low-angle grain boundaries in as-polished specimens. In the presence of implanted helium, however, such annealing phenomena can be significantly hindered. The enhanced thermal stability may arise from the pinning effect of helium bubbles on grain boundaries.

SUMMARY

We performed the thermal desorption spectroscopy (TDS) annealing experiment on as-polished polycrystalline W and the W samples implanted by 40 keV He^+ to a fluence of 1×10^{16} cm^{-2} at room temperature. It has been found that the former specimen experienced recovery and recrystallization through the removal of low angle grain boundaries and subgrain coarsening, while the latter one retained stable, He-implanted surface grains. Such enhanced thermal stability was attributed to the pinning effect of He bubbles on GBs, and the underlying mechanism was discussed based on the proposed model of cellular microstructure.

PROGRESS AND STATUS

As shown in Figure 1(a), the low-magnification SEM image of as-polished W shows grain features after TDS annealing. Enlarged views in Figure 1(b) and (c) clearly reveal polygonal grains and their grooved boundaries. By comparison, the He-implanted W after annealing in Figure 1(d)-(f) is still covered with small grains on surface. Figure 2 compiles the IPF orientation maps of annealed specimens. For as-polished W in Figure 2(a)-(c), it was found that a large fraction of surface grains lost their preferred <110> crystallographic orientations after annealing. Especially and interestingly, some of the <110>-oriented grains were poorly identified and presented as the black spots. This could be caused by the formation of surface blisters. For He-implanted W, on the other hand, no grain size and orientation change were found after TDS annealing. The annealed sample in Figure 2(d)-(i) still presents a strong <110> texture and small clustered subgrains, which seems to be identical with the as-polished specimen.

FUTURE WORK

Future work will be focused on understanding the mechanism of helium effects on the thermal stability of tungsten via simulation or high-resolution TEM experiment.

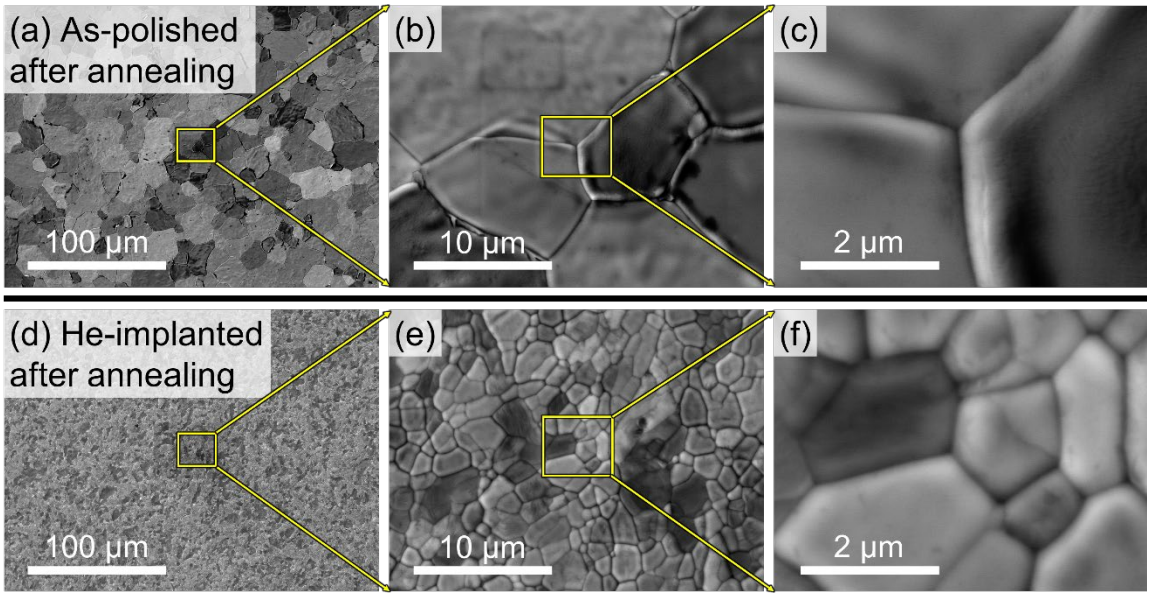

Figure 1. Comparison of surface morphology between (a)-(c) as-polished and (d)-(f) He-implanted W after annealing.

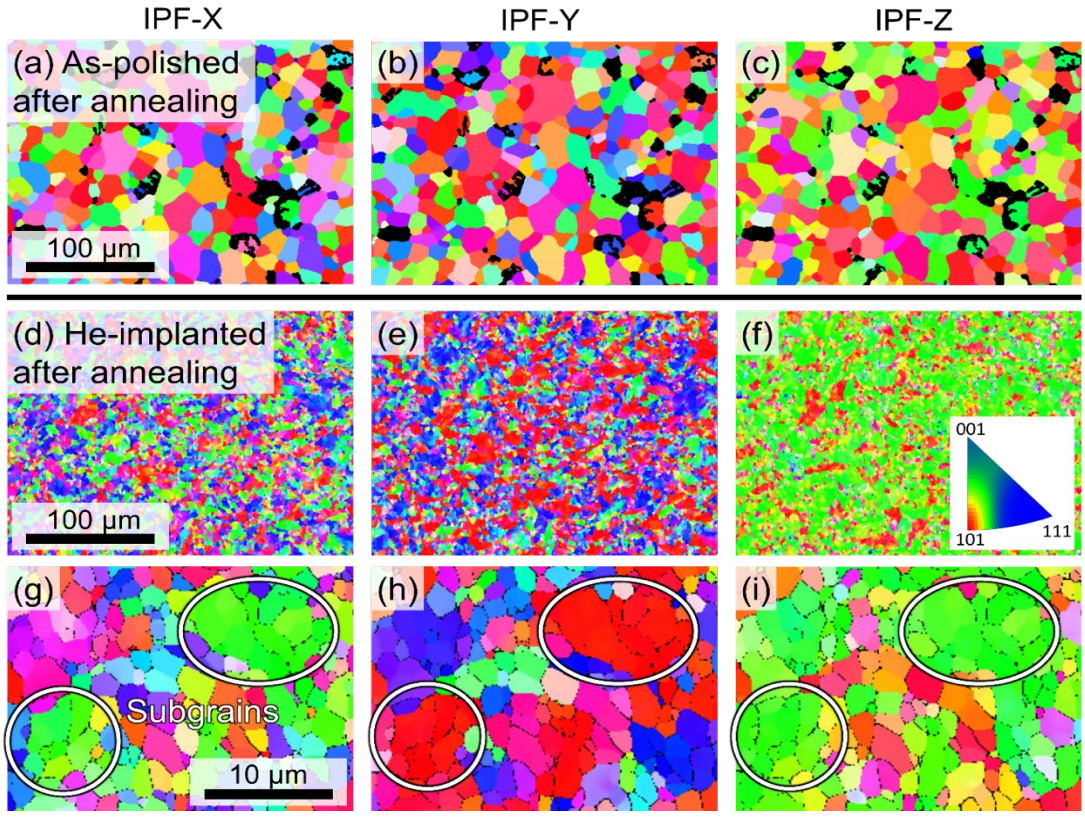

Figure 2. Orientation maps after TDS annealing for (a)-(c) as-polished and (d)-(i) He-implanted W. Inset at bottom-right in (f) shows corresponding IPF.

7.2 DAMAGE-MECHANISM INTERACTIONS AT THE PLASMA-MATERIALS INTERFACE—C. M. Parish, D. G. Morrall (Oak Ridge National Laboratory)

OBJECTIVE

The overarching objective of this work is to bridge the gap between the atomistic understanding and the phenomenological materials science underlying the design, fabrication, and service of divertors and other plasma-facing materials for magnetic confinement fusion. Specifically, the influence of intrinsic defects (dislocations, grain boundaries) and extrinsic defects (ion- and neutron-irradiation damage, impurities) interactions with He and bubbles, in terms of nucleation sites, growth, trapping, and surface degradation, will be measured.

SUMMARY

In this reporting period, the major effort was to obtain and analyze more data from monochromated, aberration-corrected scanning transmission electron microscopy (MAC-STEM) electron energy loss spectroscopy (EELS) experiments from helium bubbles in tungsten nano tendril "fuzz" grown under helium plasma exposure. Tungsten nano fuzz was grown at UC-San Diego in collaboration with R. Doerner and M. Baldwin, and MAC-STEM data was obtained at the ORNL Center for Nanophase Materials Sciences (CNMS) via a user proposal in collaboration with J.-C. Idrobo.

PROGRESS AND STATUS

Several dozen helium bubbles were interrogated using the Nion Hermes instrument at ORNL CNMS, operated at 100 keV and with an approximately 160 meV beam energy FWHM. Only a small fraction of bubbles analyzed showed data that could be clearly interpreted; the exact reason is unclear, but it is believed that the combination of tungsten fiber, oxide skin, carbonaceous contamination, and other layers can overwhelm the helium signal, and not all bubbles are anticipated to contain helium. For instance, bubbles that cut the surface of the fiber will release their helium and will simply be surface divots, but the STEM high-angle annular contrast imaging cannot differentiate a buried bubble from a surface divot.

With that low yield of experiments, it is still possible to analyze a number of helium bubbles. Multiple models were developed (using the scipy.optimize module of the Python programming language) to perform physics-informed fitting of the EELS spectra. The method that was ultimately chosen was to model the unspecified contributions as a linear background, the tungsten contributions as double gaussian constrained to the tungsten plasmon (≈24 eV) and the tungsten surface plasmon (≈18 eV), and the helium 1s→2p transition as a gaussian (≈22eV). Gaussians were found to provide a better fit than Lorentzians, particularly for the zero-loss-peak (ZLP). Curve fitting is needed because the plasmon and surface plasmon peaks are very close to the helium peak and overlap.

Once the curves are fit, the ZLP and the helium peak are integrated and the number of helium atoms can be found (from an assumption of a cross section of 9×10^{24} /m^2) and an estimate, from the HAADF image, of the bubble diameter.

Figure 1 illustrates the analysis of 12 bubbles, with measured pressures carrying from ~0.1 to ~2 GPa.

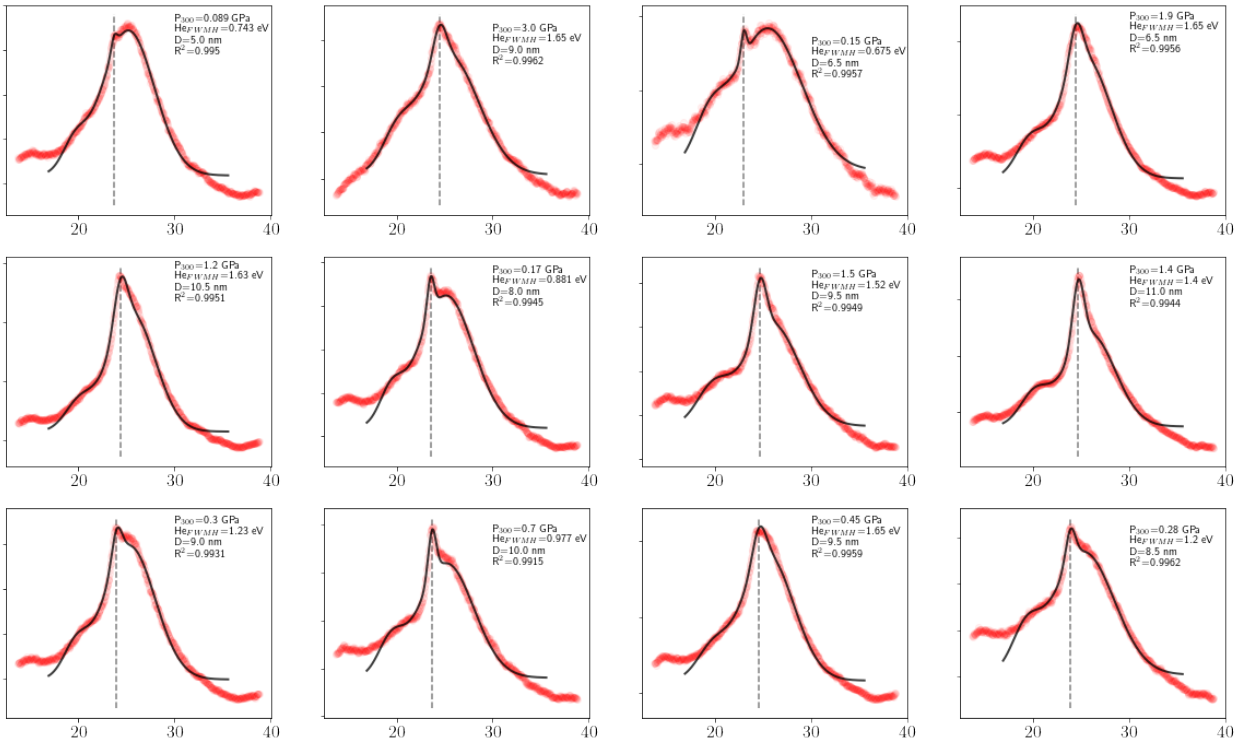

Figure 1. A montage of MAC-STEM-EELS analyses of helium bubbles in tungsten nano tendril "fuzz." The red markers are the measured data, the vertical dashed lines are the measured helium peak centroid, and the black lines are the modeled three gaussians + linear baseline.

The spread of the measured pressures are surprisingly high; whether this is an artifact of uncorrected signals or actual spread due to the highly non-equilibrium nature of the growth process is at present unknown.

FUTURE WORK

More data will be acquired at CNMS with the intention of building a larger database of bubbles for analysis.

7.3 EFFECTS OF NITROGEN ON TUNGSTEN SURFACES INVESTIGATED WITH LOW ENERGY ION SCATTERING—C. S. Wong, J. A. Whaley, R. D. Kolasinski (Sandia National Laboratories)

SUMMARY

The effect of nitrogen on the surfaces of polycrystalline ITER-grade tungsten and a tungsten single crystal were studied with low energy ion scattering (LEIS) and direct recoil spectroscopy (DRS). LEIS and DRS measurements on both tungsten surfaces were performed in an ultra-high vacuum system as various quantities of N_2 were introduced into the chamber through a variable leak valve. The obtained ion energy spectra reveal that nitrogen was readily adsorbed onto the surface, in turn limiting the amount of hydrogen that could be adsorbed onto the surface. These results not only provide insight into how the presence of nitrogen on tungsten surfaces may play a role in hydrogen adsorption and retention, but also serve to benchmark models being developed to describe the H-N-W system.

INTRODUCTION

Nitrogen seeding has been successfully used to help limit the power load at the divertor and improve energy confinement [1]. The purposeful introduction of nitrogen into the divertor, however, may lead to further complications to the already complex plasma-material interactions, due to the considerable reactivity of atomic nitrogen. Recent works have begun to unearth some of the nitrogen effects on plasma-facing materials [2,3,4], for example, finding that small quantities of nitrogen in a deuterium plasma can lead to a nearly 100-fold increase in deuterium retention in tungsten [4]. However, many of the basic mechanisms of how nitrogen affects plasma-facing surfaces remain unclear. Key mechanisms include those that may lead to material degradation of the plasma-facing materials, as well as influence tritium diffusion and retention. Addressing these issues necessitates a better understanding of the interplay between nitrogen, hydrogen, and tungsten surfaces.

As a first to step address nitrogen plasma-material interactions, we experimentally investigate how nitrogen affects the adsorption of hydrogen on tungsten surfaces. The experiments will be performed on two types of tungsten surfaces: ITER-grade polycrystalline tungsten and a tungsten single crystal W(100). The ITER-grade tungsten allows a more direct comparison to practical materials, while the tungsten single crystal is better suited to facilitate comparisons to models. Some of the key requirements for such an experimental study are surface specificity (on the order of a monolayer), ultra-high vacuum (UHV) environment to control surface impurities, direct sensitivity to surface hydrogen, and sensitivity to crystalline structure in the case of W(100). A challenge for most surface science techniques, these requirements are all met with low energy ion scattering (LEIS) and direct recoil spectroscopy (DRS). In this work, we use LEIS and DRS to show that N_2 dissociates and adsorbs on both polycrystalline W and W(100). For both W surfaces, the presence of adsorbed nitrogen causes the signal associated with hydrogen to diminish, indicating that the nitrogen may be limiting the quantity of hydrogen at the tungsten surface.

EXPERIMENTAL METHOD

In this work, LEIS and DRS are performed with an angle-resolved ion energy spectrometer (ARIES). An ion beam is directed at a glancing angle α onto the surface, as defined in Figure 1. For the W single crystal, the crystalline orientation is defined by ϕ with respect to the ion beam. Forward scattered ions, as well as recoiled ions including hydrogen, are then detected by an electrostatic analyzer (ESA) positioned at a chosen scattering angle θ. The energies of a detected scattered ion (E_S) and recoiled ion (E_R) for a given elastic collision can be computed from the following kinematic equations [5],

(1) $$\frac{E_S}{E_0} = \left(\frac{cos\,\theta \pm \sqrt{\mu^2 - sin^2\,\theta}}{1+\mu} \right)^2$$

and

(2) $$\frac{E_R}{E_0} = \frac{4\mu}{(1+\mu)^2} \cos^2\theta,$$

respectively. In these equations, μ is the ratio of the projectile ion mass to the surface atom mass, while E_0 is the initial energy of projectile ion. From Eqs. (1) and (2), the energies of detected scattered or recoiled ions can be correlated to the masses of atoms on the surface. As such, peaks in the ion energy spectra can be analyzed to extract surface compositional information.

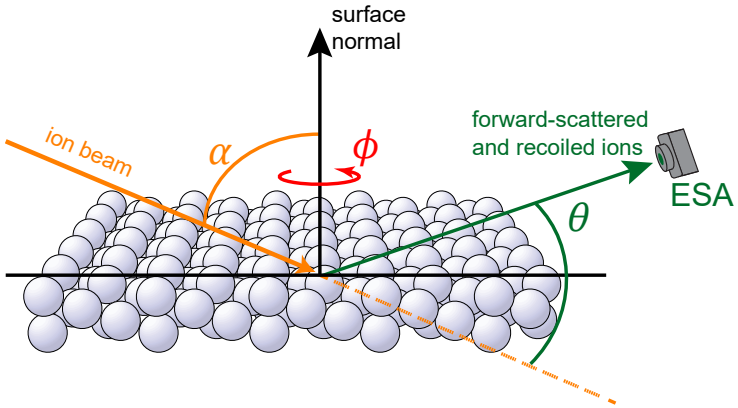

Figure 1. Illustration of low energy ion scattering geometry.

PROGRESS AND STATUS

For the polycrystalline ITER-grade tungsten, ion energy spectra were obtained with ARIES using a 3 keV Ne^+ beam incident on a polycrystalline ITER-grade W button for $\alpha = 80°$ and $\theta = 32°$. These spectra, in Figure 2, were obtained for various quantities of dosing with molecular nitrogen, with chamber N_2 partial pressures in the range of 0-125 nTorr. Peaks in the spectra are labeled X(R) for the detection a recoiled ion of species X and X(QS) for the detection of a Ne^+ that had scattered off a surface atom of species X. With no dosing, the primary peaks in the spectra correspond to W(QS) near E/E_0 = 0.96 and H(R) near E/E_0 = 0.12. Smaller peaks are associated with adsorbed oxygen and deuterium. This is consistent with a clean W surface in UHV conditions, where the residual gas is primarily hydrogen with trace quantities of oxygen.

As N_2 gas was introduced into the chamber via a variable leak valve, a peak emerged near E/E_0 = 0.58, which corresponds to N(QS). The appearance of this peak reveals that N_2 was adsorbing onto the tungsten surface and serves as evidence that LEIS can detect the presence of N adsorbates. With the appearance of the N(QS) peak, the H(R) and W(QS) peaks begin to diminish substantially, although to different extents. For the lowest quantity of N_2 dosing, a partial pressure of 2.2 nTorr, the W(QS) peak is diminished by about a factor of 2 while the H(R) peak is largely unchanged. This suggests that N is being adsorbed onto the W surface and preventing a sizeable fraction of the incident Ne^+ from scattering off the W atoms into the detector, through either shadowing or blocking. The H(R) peak remains largely unchanged, indicating that the surface coverage of N is not yet sufficient to prevent hydrogen uptake onto the surface. For the higher

quantities of N_2 dosing, the H(R) peak does begin to diminish in parallel with the W(QS) peak, suggesting that the adsorbed N was limiting the adsorption of H_2 onto the surface.

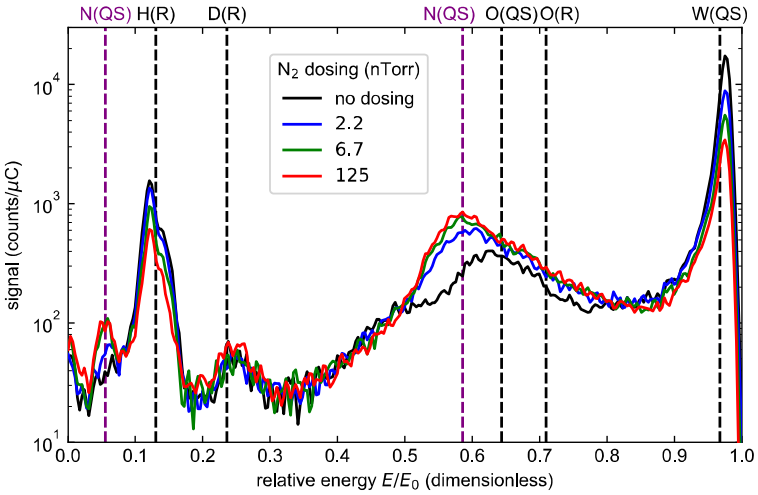

Figure 2. Ion energy spectra for various levels of N_2 dosing. The dosing was measured as the chamber N_2 partial pressure.

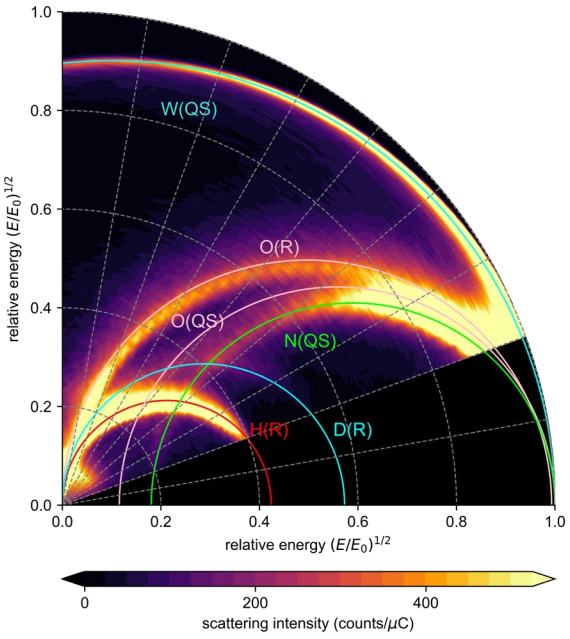

Figure 3. Collision circle plot showing the presence of N at the surface with N_2 dosing at 50 nTorr.

When analyzing these spectra, there can be ambiguity in the identification of the collisions responsible for peaks at a single scattering angle θ. To overcome this ambiguity, we obtain ion energy spectra for 36 values of θ in the range $20° \leq \theta \leq 90°$. These data are plotted in a collision circle plot [5] in Figure 3, where the θ is the polar angle and $\sqrt{E/E_0}$ is the radial coordinate. When plotted in this manner, each collision type will

trace out arcs, which can be analytically computed from Eqs. (1) and (2). The collision circle plot of Figure 3, with N_2 dosing at 50 nTorr, validates our peak assignments in Figure 2.

Next, we investigate how the tungsten surface chemical composition changed as a function of temperature as the sample was heated from 25 °C to 600 °C, with and without N_2 dosing. As can be seen in Figure 4(a), the N(QS) peak does not vary with temperature as the N_2 dosing was held constant, which is expected as N is not expected to desorb from W surfaces until well above 700 °C [6]. Changes in the spectra arose only from H desorption, as verified by Figure 4(b), for which there was no N_2 dosing. For both cases, the H(R) peak is greatly diminished at 300 °C as compared to 200 °C, indicating that hydrogen adsorbed onto the heated surface would thermally desorb rapidly. While more measurements need to be made in the 200 °C to 400 °C range, the presence of N on the surface does not appear to lead to a substantial difference in how the H(R) peak responds to increased temperatures.

Initial measurements were also made for the W(100) single crystal. Multi-angle maps were obtained for the sample with and without dosing, with a 1 keV Ne^+ beam. For these maps, the detector was located at a scattering angle $\theta = 45°$ and set to monitor an ion energy of E/E_0 = 0.090, corresponding to the H(R) peak. The magnitude of the H(R) peak was measured for $70° \leq \alpha \leq 84°$ and $0° \leq \phi \leq 360°$ to generate a 21 × 181 grid of data. These data were then plotted in Figure 5(a) for no N_2 dosing and Figure 5(b) for N_2 dosing at 500 nTorr. For these plots, the angle of incidence α was plotted as the radial coordinate, while the crystalline orientation ϕ was plotted as the polar coordinate.

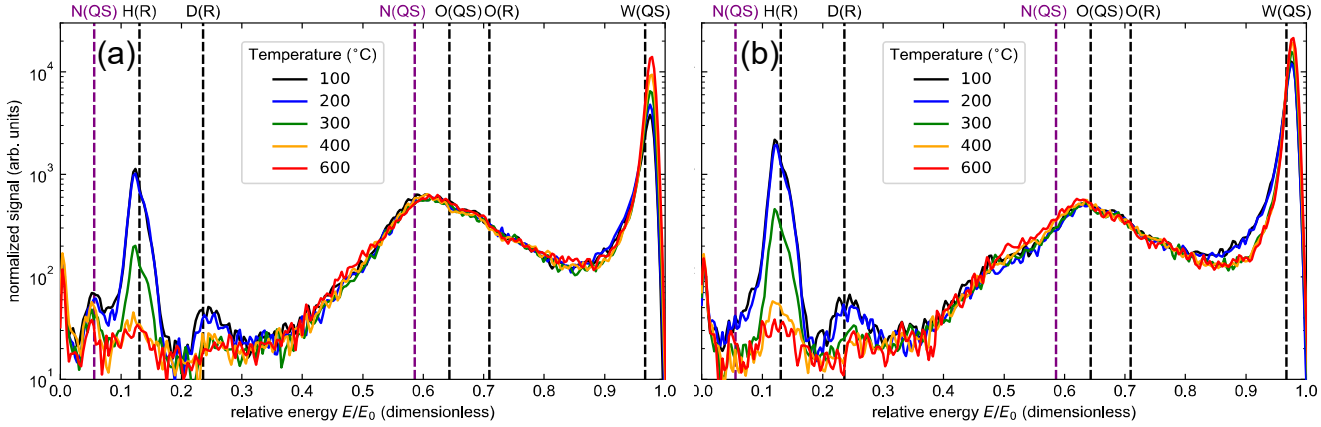

Figure 4. Ion energy spectra with the ITER-grade W sample heated to various temperatures (a) with N2 dosing at 50 nTorr partial pressure and (b) without N2 dosing.

The observed intensity profiles in the multi-angle maps provide insight into how hydrogen is adsorbed onto the W(100) surface. The map without N_2 dosing, Figure 5(a), has been analyzed and modeled in detail in Ref. [7] to show that hydrogen is bound to the hollow site. The addition of N_2 in Figure 5(b) leads to two major changes in the multi-angle map. First, the overall intensity of the H(R) peak is diminished greatly with the N present; the largest H(R) signal with N_2 dosing is more than a factor of 6 smaller than that for the no dosing case. This suggests that the N at the surface is preventing H adsorption, thereby passivating the surface. Second, there is a diminishment in the relative size of the maxima to the minima when N is on the surface. This is likely due to surface N disrupting the surface channeling of Ne^+ along prominent azimuths, which led to the distinctive patterns in Figure 5(a) as described in Ref. [7]. Further work to understand these processes and to determine the nitrogen adsorption sites are underway.

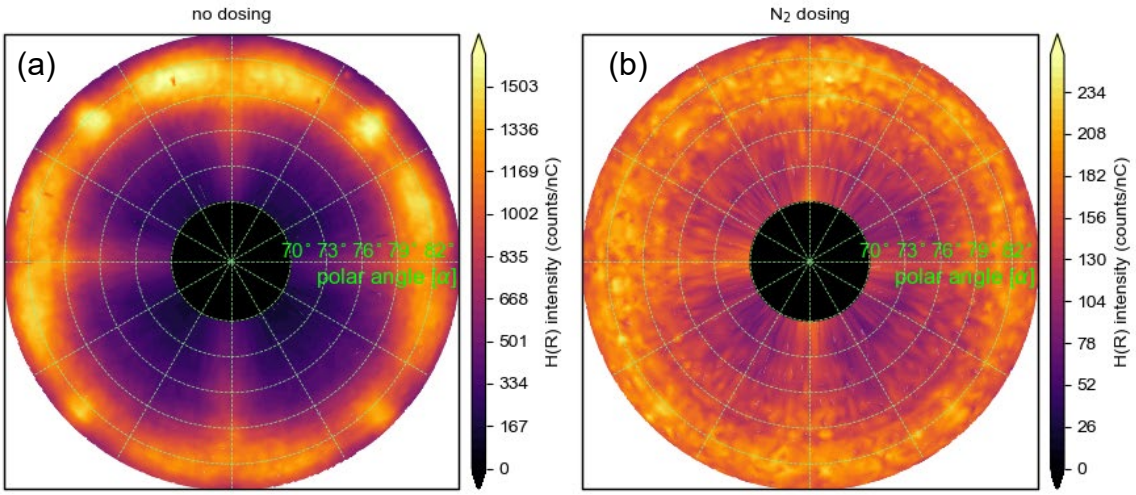

Figure 5. Multi-angle maps of the H(R) signal for the W(100) single crystal (a) without dosing and (b) with N_2 dosing at a partial pressure of 500 nTorr.

CONCLUSION

In this work, we applied low energy ion scattering and direct recoil spectroscopy to investigate how the presence of nitrogen affects hydrogen adsorption on tungsten surfaces. Our measurements showed that molecular nitrogen was capable of dissociating and adsorbing onto the surface of polycrystalline ITER-grade tungsten and a W(100) single crystal. As the surface coverage of N increased on both W surfaces, the quantity of hydrogen that could adsorb onto the surface decreased, suggesting that the adsorbed nitrogen on the W surface may be playing a role in limiting the dissociation and recombination of H_2 on the W surface. By limiting the surface recombination of H_2 and, in turn, the desorption of H from tungsten, the presence of N on W surfaces may be partially responsible for the increased retention of implanted hydrogen in tungsten when nitrogen impurities are present in hydrogen plasmas.

Future work will include more detailed studies of the W(100) surface, as well as D + N plasma exposures of polycrystalline ITER-grade W samples. Further LEIS and DRS measurements will be made of N_2 adsorption and its effect on H adsorption on the W(100) surface. With these measurements, we hope to achieve sub-angstrom determinations of hydrogen and nitrogen adsorption sites on the W(100) surface. These findings will be used to benchmark and help guide the development of interatomic potentials for the H + N + W system. Mixed D + N plasma exposures of ITER-grade W samples will also be performed in the future. Deuterium retention will be measured with thermal desorption spectroscopy, while the surface morphology will be imaged with helium ion microscopy. These material changes will be correlated to the atomic-scale findings from our LEIS and DRS measurements.

ACKNOWLEDGEMENT

Sandia National Laboratories is a multi-mission laboratory managed and operated by National Technology and Engineering Solutions of Sandia LLC, a wholly owned subsidiary of Honeywell International Inc. for the U.S. Department of Energy's National Nuclear Security Administration under contract DE-NA0003525. This paper describes objective technical results and analysis. Any subjective views or opinions that might be expressed in the paper do not necessarily represent the views of the U.S. Department of Energy or the United States Government.

References

[1] A. Kallenbach, R. Dux, J. C. Fuchs, et al., Plasma Phys. Control. Fusion 52, 055002 (2010).
[2] K. Schmid, A. Manhard, Ch. Linsmeier, et al., Nucl. Fusion 50, 025006 (2010).
[3] S. Takamura, T. Aota, Y. Uesugi, et al., Nucl. Fusion 59, 046015 (2019).
[4] A. Kreter, D. Nishijima, R.P. Doerner, et al., Nucl. Fusion 59, 086029 (2019).
[5] W. Eckstein and R. Bastasz, Nucl. Instrum. Methods Phys. Res. B 29, 603 (1988).
[6] C. Pisani, G. Rabino, and F. Ricca, Surf. Sci. 41, 277-292 (1974).
[7] R. Kolasinski, N. Bartlett, J. Whaley, and T. Felter, Phys. Rev B 85, 115422 (2012).

8. FUSION CORROSION AND COMPATABILITY SCIENCE

8.1 LIQUID METAL COMPATIBILITY OF SiC AND FeCrAl IN FLOWING Pb-Li—B. A. Pint, J. Jun, M. Romedenne (Oak Ridge National Laboratory)

OBJECTIVE

The first goal of this research was to investigate the maximum Pb-Li temperature achievable in the dual coolant lead-lithium (DCLL) blanket concept to maximize the overall system efficiency. A series of monometallic thermal convection loops (TCL) fabricated from a commercial FeCrAlMo alloy have been operated to assess the formation of a thermally-grown alumina surface layer to improve compatibility with flowing Pb-Li. New experiments are now focused on examining more fusion-relevant materials such as SiC and ODS FeCrAl in flowing Pb-Li.

SUMMARY

The fifth TCL experiment completed 1000 h with a peak temperature of 700°C and characterization is reported from the CVD SiC and ODS FeCrAl specimens exposed in Kanthal APMT tubing. The mass changes were much larger with mass gains for most SiC specimens and moderate to large mass losses for ODS FeCrAl specimens, 5-100X higher than the previous loop. The results indicate that dissolved Fe and Cr reacted with the SiC to form an Fe- and Cr-rich carbide reaction product on the surface that increased with thickness as the specimen temperature decreased in the TCL. Removing Fe and Cr from the liquid Pb-Li appeared to increase ODS FeCrAl dissolution. Such a dissimilar material interaction appears consistent with thermodynamic calculations. Significant dissolution attack at the top of the hot leg in both this experiment and the previous monometallic APMT TCL suggests that the Pb-Li compatibility of FeCrAl alloys is inadequate at 700°C in a flowing environment and the maximum PbLi temperature is < 675°C.

PROGRESS AND STATUS

Introduction

To improve liquid metal compatibility, one strategy that has been used with Pb-17at.%Li is to form a stable, adherent surface oxide such as α-Al_2O_3 on FeCrAl alloys or using an Al-rich coating on steels [1-6]. This strategy has shown very promising results for increasing blanket temperatures, but many studies were conducted in static Pb-Li. Thus, a series of four monometallic TCL experiments were conducted with flowing Pb-Li in a ~90°C temperature gradient using commercially available tubing material Kanthal alloy APMT (Advanced Power Metallurgy Tube). Each TCL used a new APMT harp-shaped loop and had an increased maximum temperature from 550°-700°C [4-6]. The fourth TCL experiment with a peak temperature of 700°C showed significant mass loss of the APMT specimens at the highest temperature, suggesting that 700°C is the highest temperature where this strategy is operable.

The fifth TCL experiment was completed in April 2000 [7,8] with nominally the same conditions as the 4th experiment but including more fusion relevant materials: chemical vapor diffusion (CVD) deposited high purity SiC and low-Cr ODS FeCrAl [9,10] to avoid issues with α' embrittlement. Previously, mass change, X-ray diffraction and plan view SEM results were presented [8]. Additional characterization of specimens from this loop is presented here [7] and the next TCL experiment is being prepared.

Experimental Procedure

The fifth TCL experiment followed similar procedures as detailed previously [4,5,7,8]. Velocity measurements varied between 0.90-0.97 cm/s during the experiment [8]. Chains of 20 specimens were exposed in the hot leg (HL) and cold leg (CL) of the TCL for 1000 h with a peak hot leg temperature of 700°C. Coupon specimens were 15 x 25 x 2 mm and the tensile specimens were 25 mm long SS-3 type. Chemical compositions of the specimens and APMT tubing are given in Table 1. Six coupon specimens of CVD SiC were added to each chain along with ODS FeCrAl coupons and tensile specimens. Four SS3 APMT specimens were included for comparison to the 4th TCL experiment. Many of the APMT and ODS Fe-10Cr-6Al specimens were pre-oxidized for 2 h at 1000°C in laboratory air [5]. The APMT loop was pre-oxidized for 8 h at 1050°C as part of the post-weld heat treatment procedure [4]. After the exposure, the PbLi was dumped into a stainless steel tank and the TCL was cleaned using the standard solution of acetic acid, ethanol and hydrogen peroxide [4,5]. Specimens were weighed before and after exposure using a Mettler Toledo X205 balance with an accuracy of ±0.04 mg. The coupons were sectioned to look at the reaction products in cross-section and analyzed using scanning electron microscopy (SEM) with energy dispersive spectroscopy (EDS).

Results

For reference, Figure 1 shows the mass change results for this 5th TCL experiment and the results from monometallic APMT TCL experiment (#4) are shown for comparison. After disassembling, it was discovered that the second and fourth specimens in the hot leg had broken due to massive mass loss and the third specimen was missing, similar to the 4th TCL, and suggesting that attack was very severe at this location. The chain break disrupted the location of the HL SiC specimens which were hung using APMT wire. The location of the six SiC specimens from the hot leg were inferred based on their recovery location. The comparison in Figure 1 indicates that many of the mass changes in the 5th TCL were much higher mass gains (e.g., SiC in cold leg) or larger mass losses (e.g., bare ODS FeCrAl in the hot and cold legs) than the previous monometallic (4th) TCL experiment [6]. Pre-oxidized ODS FeCrAl CL specimens showed relatively small mass changes, but the bare ODS FeCrAl specimen mass losses were all larger than had been observed in prior experiments.

Figure 2 shows polished cross-sections from the ODS FeCrAl coupon specimens located at the middle of the HL and CL chains. Consistent with the large mass losses for both specimens, significant section loss was observed for the HL specimens with and without pre-oxidation. Without pre-oxidation, the attack appeared more uniform around the surface. With pre-oxidation, the attack appeared more localized with the corners somewhat intact and other regions with >150μm of material removed, Figure 2b. The CL

Table 1. Alloy compositions measured using inductively coupled plasma and combustion analyses

Alloy	Fe	Cr	Al	Ni	Si	C	Other
APMT	69.0	21.6	4.9	0.12	0.53	0.03	2.8Mo,0.1Mn,0.2Hf,0.1Y,0.1Zr
APMT tube*	70.0	21.4	4.9		0.34	0.04	3.1Mo, 0.2Mn, 0.02Cu
ODS FeCrAl†	83.6	9.8	6.0			0.06	0.22Y,0.27Zr,0.10O,0.04N
CVD SiC				0.01	69.8	30.2	0.003 O

* reported by manufacturer [4] † heat 4H795C

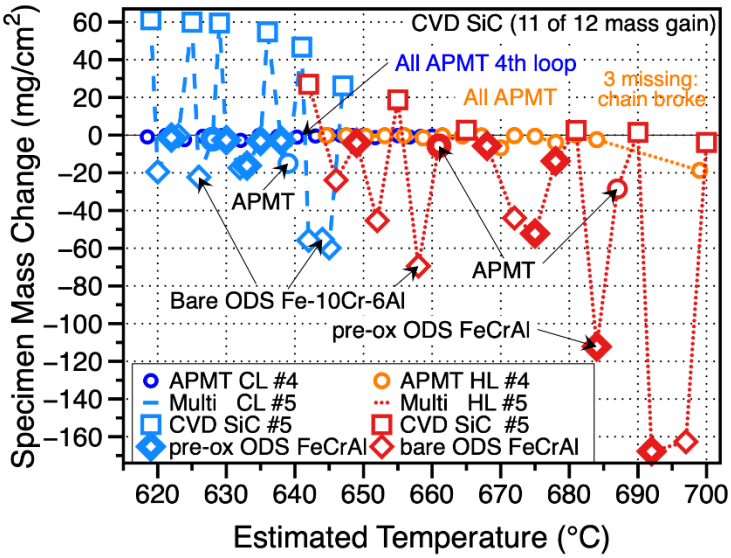

Figure 1. Specimen mass change of TCL specimens as a function of estimated temperature in the hot leg (HL) and cold leg (CL) of the 4th (APMT only) and 5th (multi-material) TCL experiments.

specimens had a similar appearance with less material removed and less mass loss, Figures 2c and 2d. Based on EDS line profiles, the surfaces of all of the specimens were Cr depleted to a depth of 30-50μm from a starting content of 9.8 wt.% (Table 1) to 4-7% at the surface. Since the exposed specimen surface was not uniform, a comprehensive study would be needed to better quantify the depletion behavior.

Figure 3 shows polished cross-sections of selected CVD SiC specimens. The bright reaction products appeared to form as nodules at the bottom of the hot leg. It is possible that cracks in the specimens occurred during specimen preparation or post-exposure handling, particularly for a brittle reaction product. In the cold leg, a continuous reaction product was observed for all of the specimens. Figure 4 shows box

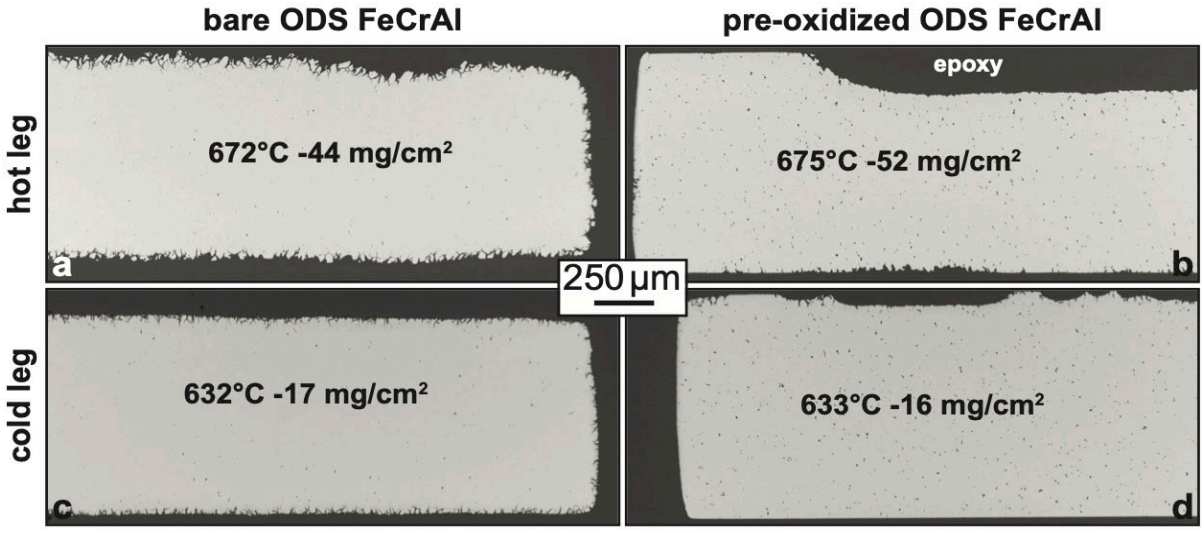

Figure 2. Light microscopy of polished sections of the ODS FeCrAl coupons. The estimated Pb-Li exposure temperature and specimen mass change values are shown.

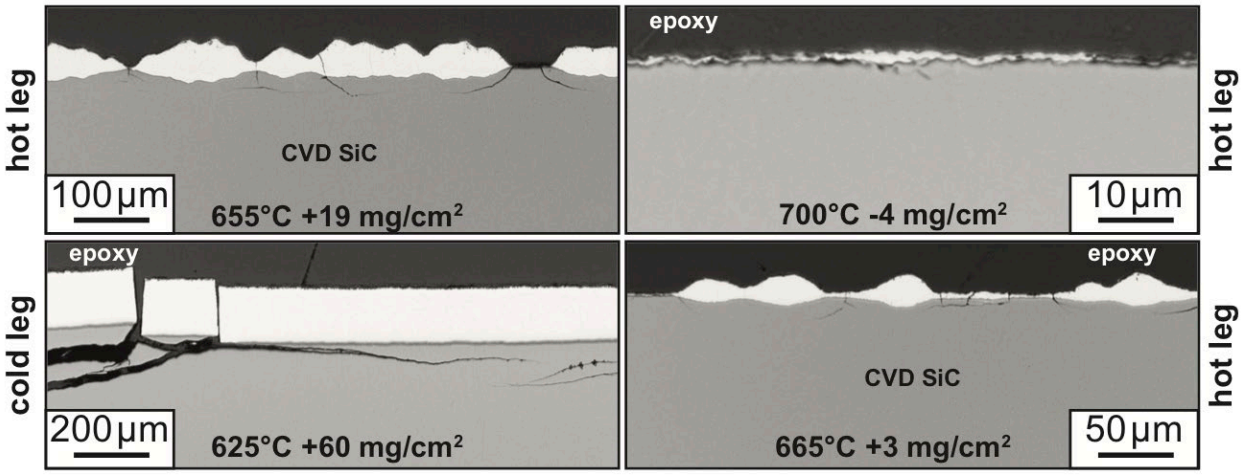

Figure 3. Light microscopy of polished sections of representative CVD SiC specimens. The estimated Pb-Li exposure temperature and specimen mass change values are shown.

and whisker plots of the reaction layer thicknesses measured that appear to be consistent with the CVD SiC mass change data in Figure 1. Figure 5 shows SEM/EDS maps from one specimen. Point EDS analyses from the reaction product indicated 30-50wt.%Fe and 30-50%Cr with 10-20%C and ~2%O detected. Carbon quantification is difficult using EDS and additional characterization is needed using wavelength dispersive spectroscopy and standards to better quantify the C content.

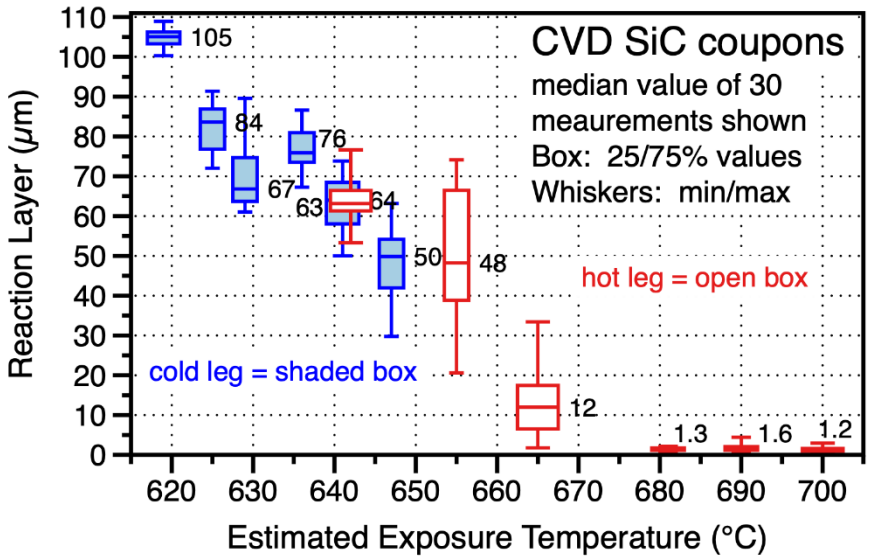

Figure 4. Box and whisker plots of the reaction layer thickness formed on each of the CVD SiC specimens in the hot leg (open box) and cold leg (shaded box) with median values shown.

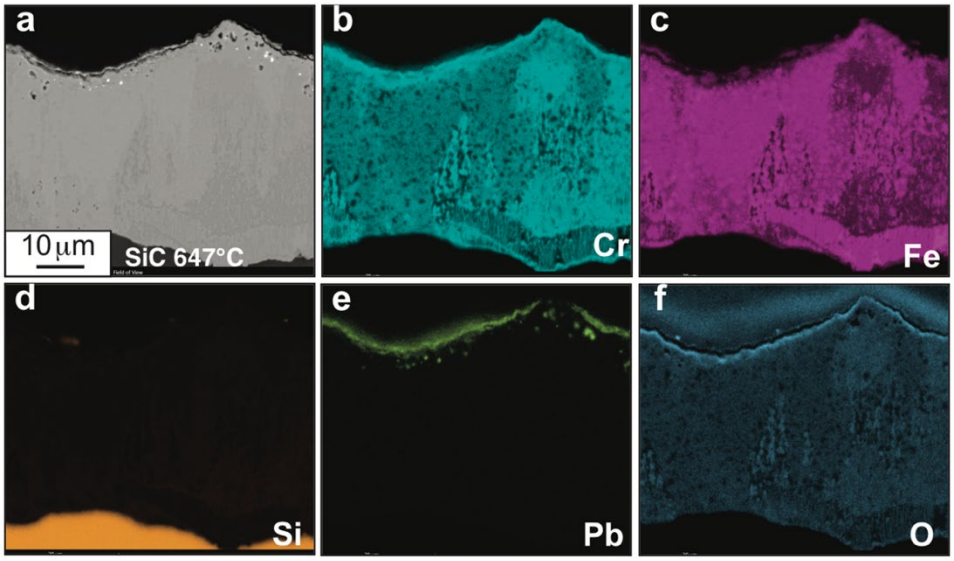

Figure 5. (a) SEM backscattered electron image of the reaction product formed on CVD SiC after 1000 h at 647°C in the cold leg. EDX maps were collected from the same region of (b) Cr, (c) Fe, (d) Si, (e) Pb and (f) O.

Figure 6 shows a pseudo-ternary phase diagram calculated between SiC and Fe-20at.%Cr at 700°C using Thermocalc software and the TCFE9 database. Two silicide intermetallics, M_3Si and M_5Si_3 (M = Fe, Cr) and two carbides, M_3C_2 and M_7C_3 (M = Fe, Cr) could be formed at equilibrium. The range of compositions measured by EDS also are shown in Figure 6 and the mixture of carbides and silicide in this region is consistent with the XRD results [7,8] that detected Fe silicide and carbides.

The results suggest that as the FeCrAl specimens (ODS and APMT) dissolved into the Pb-Li, Fe and Cr in the liquid reacted with the SiC as both Fe and Cr will form more stable carbides and silicide with SiC specimens. For the bare ODS FeCrAl specimens, a protective Al-rich oxide did not likely form. For the pre-oxidized specimens, the oxide could have been mechanically removed (i.e. spallation) but, more likely, defects or dissolution allowed liquid penetration and the subsequent localized pitting, Figures 2b and 2d. In the monometallic 4th TCL experiment, Fe and Cr may saturate in the liquid slowing any additional dissolution during the 1000 h experiment. However, if Fe and Cr were removed from the liquid to form carbide reaction products on the SiC specimens (Figure 5), that may consume Fe and Cr from the liquid and thereby accelerate dissolution of the metallic components resulting in a classic interaction of dissimilar materials. In this experiment with the relatively low Cr ODS FeCrAl specimens, the dissolution may have been accelerated because the surface was further depleted to 4-7%Cr, thereby preventing a protective Al-rich oxide from forming. The APMT specimens were not as severely affected (less mass loss compared to ODS FeCrAl shown previously [7,8]) because the higher Cr content in this alloy assisted in the formation of protective Al-rich oxide [11]. The increasing carbide reaction layer thickness on the SiC specimens with decreasing temperature (Figure 4) suggests that Fe and Cr solubility (also decreasing with temperature) may play a role in the reaction, but it does appear to be a reaction product and not deposition as there is no source of C–even in the hot leg there was no significant SiC mass loss, Figure 1. However, as this dissimilar material interaction between SiC and FeCrAl has not been previously observed, further calculations and experiments are needed to better understand these observations.

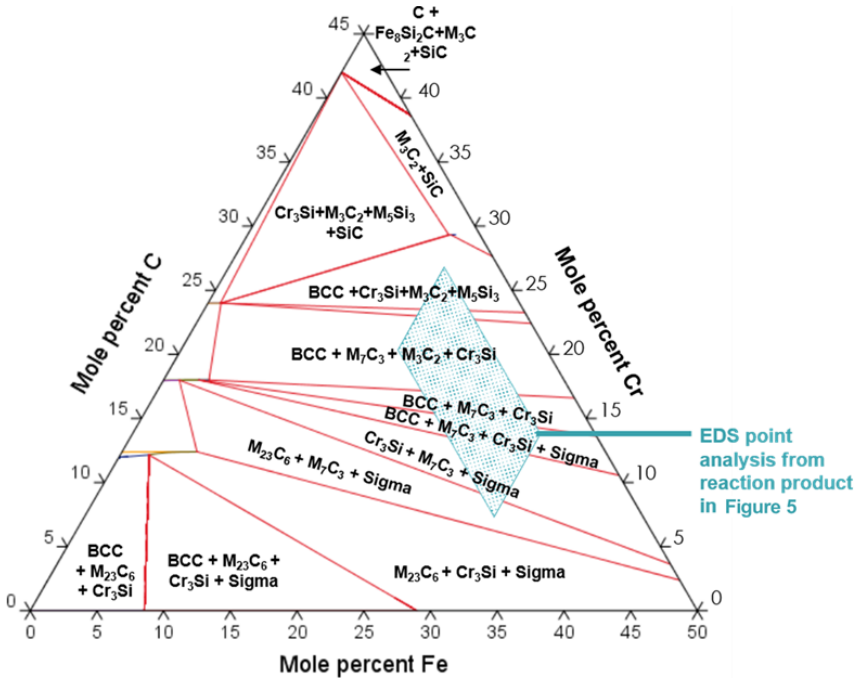

Figure 6. Calculated pseudo-phase diagram Fe-Cr-C-10at%Si at 700 ˚C using Thermocalc software and TCFE9 database. The box corresponds to the EDS point analysis of the surface reaction product in Figure 5.

The next planned TCL experiment will use a peak temperature of 650°C with CVD SiC specimens and aluminized and pre-oxidized reduced activation ferritic-martensitic F82H steel specimens from QST. Coupon and tensile specimens have been sent to Tennessee Technological University for low activity pack aluminizing to form ~50 μm thick coatings without aluminide phases, similar to previous studies [12,13].

References

[1] H. Glasbrenner, Z. Peric and H. U. Borgstedt, J. Nucl. Mater. 233-237 (1996) 1378.
[2] W. Krauss, J. Konys, N. Holstein and H. Zimmermann, J. Nucl. Mater. 417 (2011) 1233.
[3] W. Krauss, J. Konys, S.-E. Wulf, J. Nucl. Mater. 455 (2014) 522.
[4] S. J. Pawel and K. A. Unocic, J. Nucl. Mater. 492 (2017) 41.
[5] J. Jun, K. A. Unocic, M. J. Lance, H. M. Meyer and B. A. Pint, J. Nucl. Mater. 528 (2020) 151847.
[6] B. A. Pint, J. Jun, E. Cakmak, D. J. Sprouster, N. Olynik and L. L. Snead, Fus. Sci. Tech. submitted.
[7] B. A. Pint, J. Jun and M. Romedenne, Fus. Eng. Design in press.
[8] B. A. Pint and J. Jun, DOE-ER-0313/68 (2020) 134.
[9] B. A. Pint, S. Dryepondt, K. A. Unocic and D. T. Hoelzer, JOM 66 (2014) 2458.
[10] S. Dryepondt, K. A. Unocic, D. T. Hoelzer, C. P. Massey, B. A. Pint, J. Nucl. Mater. 501 (2018) 59.
[11] F. H. Stott, G. C. Wood and J. Stringer, Oxid. Met. 44 (1995) 113.
[12] Y. Zhang, B. A. Pint, K. M. Cooley and J. A. Haynes, Surf. Coat. Tech. 202 (2008) 3839.
[13] B. A. Pint and K. A. Unocic, J. Nucl. Mater. 442 (2013) 572-575.

9. MODELING AND COMPUTATIONAL STUDY

9.1 AB INITIO MODELING OF He-SOLUTE INTERACTION IN ALPHA-IRON—Huibin Ke, Wahyu Setyawan (Pacific Northwest National Laboratory)

This is an Extended Abstract of a paper "Calculation of Helium Interaction with Solutes in Nanostructured Ferritic Alloys" that will be submitted to Nuclear Materials and Energy journal

Nanostructured ferritic alloys are being research world-wide as advanced structural materials in a fusion reactor. A significant amount of helium is generated in the materials under fusion neutron irradiation. Nanostructured ferritic alloys (NFAs) contain high density Y-Ti-O oxide particles designed to trap helium atoms and manage their distribution to avoid the formation of large bubbles. Since prototypic fusion neutron source is unavailable, irradiation tests on NFAs have been performed using nuclear fission reactors. Different neutron spectra between fusion and fission produce different transmutation products as well as distribution of defect clusters generated via atomic displacement cascades. Thus, defect microstructure evolution models are needed to deduce the neutron spectrum effects. Literature data on helium interaction with solutes in NFAs is incomplete. Interaction with the solute transmutation products in addition to alloying solutes of the NFAs is needed.

In this research, first-principles density functional theory calculations are performed to study the He interaction with solutes in 14YWT alloys irradiated in HFIR. The expected solutes, including the alloying solutes, that are present after irradiation are Ti, Cr, W, Y, Mg, V, Re, Os, Al, Mn, Ni, Mo, Si. Rhenium and Os are produced from W transmutation. In fusion neutron, Ta will also be produced from W transmutation. Thus, Ta is added to the list. Figure 1 summarize the binding energy of He to these solutes, where positive value indicates attraction. Strong attraction is found for Y (0.46 eV), Mg (0.32 eV), and Ti (0.16 eV). Significant repulsion is found for Re (-0.12 eV), W (-0.10 eV), Si (-0.10 eV), Mn (-0.10 eV), Cr (-0.09 eV), Os (-0.08 eV), Mo (-0.07 eV), and V (-0.07 eV). Furthermore, binding with impurity O and C are studied. Both impurities attract He strongly with a binding energy of 0.33 eV (O) and 0.15 eV (C). Future research will be focused on developing interatomic potentials to enumerate and develop models of He interaction with defect clusters and Y-Ti-O particles.

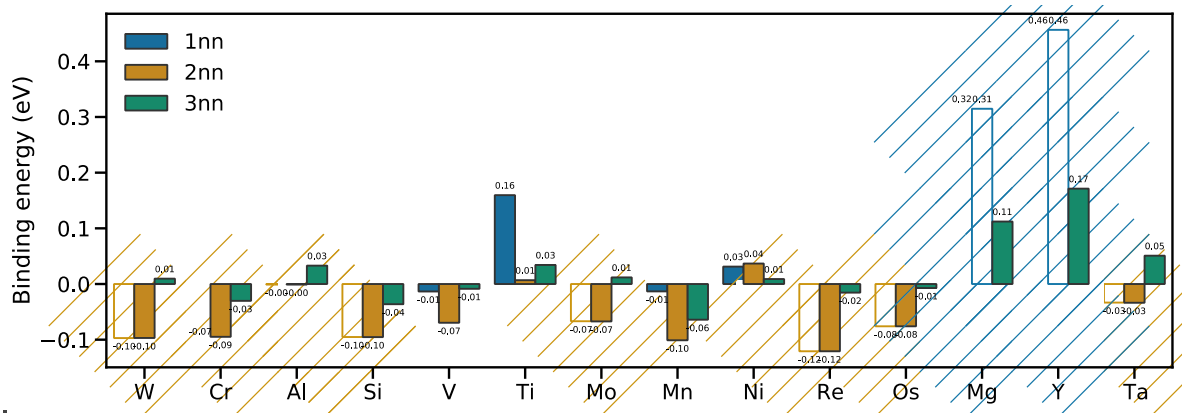

Figure 1. Binding energy between He and solute elements in bcc Fe located at first (1nn), second (2nn), and third (3nn) nearest-neighbor distance from the He. For each solute element, data for 1nn, 2nn and 3nn are ordered from left to right. Stripe bars denote that the initial structure is unstable and relaxes to the position as indicated by the color of the bar. The 1nn, 2nn and 3nn distances are $0.25a\sqrt{5}$, $0.25a\sqrt{13}$, and $0.25a\sqrt{21}$, respectively, where a is the lattice constant of bcc Fe.

ACKNOWLEDGEMENTS

This research has been supported by the U.S. Department of Energy, Office of Science, Office of Fusion Energy Sciences and performed at the Pacific Northwest National Laboratory under contract number DE-AC05-76RL01830.

9.2 CALCULATION OF DEPTH DEPENDENT ACTIVATION ENERGY BARRIERS OF TRAP MUTATION REACTIONS IN W(111) SURFACE—Giridhar Nandipati, Kenneth J. Roche, Richard J. Kurtz, Wahyu Setyawan (Pacific Northwest National Laboratory), Karl D. Hammond (University of Missouri), Dimitrios Maroudas (University of Massachusetts), Brian D. Wirth (University of Tennessee)

OBJECTIVE

This task aims to use object kinetic Monte Carlo (OKMC) simulations to study the evolution of the helium-bubble microstructure in the near-surface region of the plasma-exposed tungsten surface. KSOME (kinetic simulations of microstructural evolution) [1-3], an OKMC code, is used to simulate spatially relevant near-surface microstructures to experimentally relevant time-scales under isothermal and variable temperature conditions caused by Edge-Localized Modes (ELMs).

SUMMARY

This report documents the calculation of depth-dependent activation energy barriers and prefactors of trap-mutation processes, based on their relative occurrence probabilities reported in Refs. 3 & 4, for He clusters of size 2 to 7 in the near-surface region of W(111) surface.

PROGRESS AND STATUS

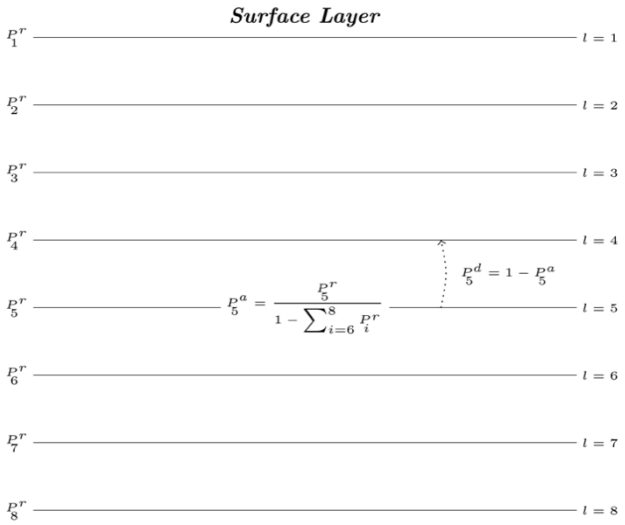

Figure. 1. P_i^r, where *i=1,⋯,8*, are the relative occurrence probabilities of TM events that occur at various depths. P_5^a is the absolute occurrence probability for a TM event that occurs at the depth of *l = 5*. P_5^d is the absolute probability for the diffusion of the He cluster from the depth of *l = 5* to *l = 4*.

In the studies reported in Refs. 4 & 5, several hundred molecular dynamics (MD) simulations of the dynamics of isolated He_n clusters (*n* = size) towards W free surfaces were performed. Individual outcomes of these simulations can be the trap mutation (TM) reactions and/or cluster dissociation reactions. Unlike W(100) (see previous report [6]), for W(111) surface, partial and complete dissociations are rare. The outcome of individual MD simulation runs for the He_n ($1 \le n \le 7$) clusters was recorded to obtain the overall occurrence probabilities of individual reactions. Accordingly, for a given cluster size, the occurrence probabilities for TM events at a particular depth reported in Refs. 4 & 5 depend on the occurrence probabilities of those that occur at lower depths. However, to calculate the activation energy barriers and prefactors for these reactions at a particular depth, probabilities of all competing processes (referred to as absolute probabilities) at that depth are required. Accordingly, the sum of these absolute probabilities

should be equal to one. Absolute occurrence probabilities for TM events at a given depth can be calculated as shown in Figure 1. More importantly, as cluster diffusion towards the surface is the primary competing process against TM events, the probability of non-occurrence of TM events is taken as the occurrence probability for the cluster to hop to an upper layer.

Expressions Used to Calculate Activation Barriers and Prefactors

When the average time scale (Δt_{avg}) or the average rate (R_T) of a process at a given temperature *T* and its activation barrier (E_a) are known, then the prefactor (D_0) is expressed using Eq. (1)

$$D_0 = \frac{1}{\Delta t_{avg}} \exp\left(\frac{E_a}{k_B T}\right) = R_T \exp\left(\frac{E_a}{k_B T}\right) \qquad (1)$$

However, if the rate R_T of a process at a given temperature *T* and its prefactor are known, then the activation barrier, E_a for this process can be calculated using Eq. (2)

$$E_a = k_B T \ln\left(\frac{D_0}{R_T}\right) \qquad (2)$$

If the rates of a process R_{T_1} and R_{T_2} at two different temperatures T_1 and T_2 are known, then the activation barrier for this process can be calculated using Eq. (3)

$$E_a = \frac{k_B T_2 T_1}{T_2 - T_1} \ln\left(\frac{R_2}{R_1}\right) \qquad (3)$$

If the ratio of the rates (R_T^{ab}) of two competing processes L_a and L_b at two different temperatures T_1 and T_2 are known, then the difference of their activation energy barriers is given by Eq. (4)

$$\Delta E_{ba} = E_b - E_a = \frac{k_B T_1 T_2}{T_2 - T_1} \ln\left(\frac{R_{T_1}^{ab}}{R_{T_2}^{ab}}\right) \qquad (4)$$

where $R_{T_i}^{ab} = \left.\frac{R_a}{R_b}\right|_{T_i}$ at a temperature T_i where *i=1,2*.

If the ratio of two different processes, R_a and R_b is known at a given temperature *T*, the difference in their activation energy barriers is given as

$$E_a - E_b = k_B T \ln\left(\frac{R_b D_0^a}{R_a D_0^b}\right) \qquad (5)$$

Activation Energy Barriers and Prefactors for Trap Mutation Reactions

He_1, He_2, He_3 Clusters

Table 1. List of reactions undergone by He_1, He_2, and He_3 clusters near W(111) surface and their relative probabilities. *I = 1* corresponds to the surface layer.

Reaction	Probability	T (K)	E (eV)	D_0 (s^{-1})
He → HeV (*I* = 4)	64.6%	1000	0.03	6.6×10^{12}
He_2 → He_2V (*I* = 9)	55.9%	1000	0.42	1.3×10^{13}
He_3 → He_3V (*I* = 12)	49.1%	1200	0.41	2.3×10^{13}

For He_1 cluster, the TM reaction occurs at *l* = *4* with 64.6% probability. Therefore, 100 − 64.6 = 35.4% is taken as the probability for the He atom to hop to the depth of *l* = *3*. The activation energy barrier for He atom to hop from *l* = *4* to *l* = *3* is 0.08 eV [6]. Note that the diffusion hop's activation energy barrier is taking into account the elastic interaction with the free surface [8, 9]. Using eq (5) and assuming that the prefactors for TM reaction and the diffusion hop are equal, TM reaction's activation barrier is 0.03 eV. Similarly, the activation energy barriers for He_2 and He_3 obtained are 0.42 and 0.41 eV, respectively. Energy barriers and the corresponding prefactors for the TM reactions are shown in the Table 1. Furthermore, for depths, *l* ≤ 3, 8, 12, for He_1, He_2, He_3, respectively, it is assumed that they will diffuse to the free surface before they can trap mutate.

He_4 He_5, and He_6 Clusters

The available information to simultaneously calculate both the activation energy barrier and the prefactor for He_n clusters for *4* ≤ *n* ≤ 6, is incomplete. Therefore, the criterion $0.2 \le E_{TM} \le 0.28$ eV on the TM activation energy barrier was used [4]. The prefactor for the TM reaction in the eq. (5) is adjusted manually such that it satisfies the criterion. Otherwise, the approach used is the same as for the He_n clusters with *1* ≤ *n* ≤ *3*. More importantly, in the MD studies [4,5], no escape of He_n clusters, for 4 ≤ *n* ≤ 6, to the free surface was observed. Hence for He_4, He_5 and He_6 clusters, TM reaction at the depths of *l* = *5*, *6* and *5*, respectively, occur with zero activation barrier. Accordingly, any He_4, He_5 and He_6 clusters that form at depths *l* ≥ *5, 6* and *5*, respectively, never escape to the free surface, while those formed at depths at *l* < *5*, *6*, and *5* always escape to the free surface.

Table 2. Probabilities for TM reactions for He_4 cluster at various depths (*l*) at 1200 K

	He_4 →								
	He_4V	He_4V	He_4V	He_4V	He_4V	He_4V_2	He_4V_2	He_4V_2	He_4V_2
Depth (l)	15	14	13	12	11	8, 11	7, 10	6, 9	5, 8
Probability (%)	0.8	9.8	0.8	48.5	11.4	12.1	12.1	3	1.5

As can be seen from table IV that a few of the occurrence probabilities for the He_4 cluster correspond to two different depths. For example, the reaction $He_4 \rightarrow He_4V_2$ can occur at the depths of *l* = *8,* and *11*. In such cases the occurrence probability is split equally between the depths. The same method is applied even for He_5 and He_6 clusters as well. Details of TM reactions, their activation energy barriers and prefactors are shown in Tables 3, 4, and 5.

Table 3. Energy barriers and prefactors for the TM reactions of the He_4 cluster.

He_4 →	*I*	$D_0(s^{-1})$	E_a (eV)
He_4V	15	1.20×10^{10}	0.231
He_4V	14	8.00×10^{12}	0.234
He_4V	13	6.50×10^{11}	0.220
He_4V	12	7.42×10^{13}	0.060
He_4V	11	3.70×10^{13}	0.241
He_4V_2	11	1.90×10^{13}	0.208
He_4V_2	10	2.60×10^{13}	0.211
He_4V_2	9	7.25×10^{10}	0.234
He_4V_2	8	6.50×10^{12}	0.210
He_4V_2	8	5.25×10^{13}	0.211
He_4V_2	7	2.00×10^{14}	0.243
He_4V_2	6	1.50×10^{14}	0.231
He_4V_2	5	10^{14}	0

Table 4. Energy barriers and prefactors for the TM reactions of the He_5 cluster.

He_5 →	*I*	$D_0(s^{-1})$	E_a (eV)
He_5V	15	1.20×10^{10}	0.213
He_5V	14	6.10×10^{10}	0.224
He_5V	13	3.10×10^{10}	0.195
He_5V	12	1.50×10^{12}	0.250
He_5V_2	12	9.00×10^{10}	0.253
He_5V_2	11	1.50×10^{11}	0.214
He_5V_2	11	4.00×10^{11}	0.245
He_5V_2	10	1.90×10^{11}	0.221
He_5V_2	8	1.75×10^{12}	0.246
He_5V_2	8	1.00×10^{10}	0.205
He_5V_2	7	5.00×10^{10}	0.201
He_5V_2	6	10^{14}	0

Table 5. Energy barriers and prefactors for the TM reactions of the He_6 cluster.

He_6 →	*I*	$D_0(s^{-1})$	E_a (eV)
He_6V	15	2.00×10^{9}	0.243
He_6V	14	3.75×10^{11}	0.229
He_6V	13	5.25×10^{11}	0.221
He_6V	12	7.50×10^{12}	0.239
He_6V_2	12	2.85×10^{12}	0.216
He_6V_2	11	2.10×10^{12}	0.239
He_6V_3	11	2.75×10^{11}	0.229
He_6V_2	9	5.50×10^{12}	0.255
He_6V_2	8	4.20×10^{13}	0.242
He_6V_3	8	5.50×10^{12}	0.232
He_6V_3	5	10^{14}	0

He_7 Clusters

In KMC simulations, He_7 cluster is considered as an immobile cluster. As there is (are) no competing process(es) for the TM reactions, it is not possible to extract energetics for He_7 cluster. Only the energetics of the TM reaction process with the highest probability can be calculated using the information in Figure 6 from Ref [4] and are shown in table VI. However, considering the low activation barrier and the depth at which the most probable TM reaction occurs and He_7 being immobile, in KMC simulations, it will be assumed that the most probable TM reaction will occur with zero barrier at depths $I \leq 9$.

Table 6. Activation energy barriers and prefactors for the TM reactions of the He_7 cluster

He_7 →	*I*	E_a (eV)	$D_0(s^{-1})$
He_7V_2	10, 11, 12, 13	0.06	10^{13}
He_7V_2	$I \leq 9$	0	10^{14}

ACKNOWLEDGEMENTS

The work described in this article was performed at Pacific Northwest National Laboratory, which is operated by Battelle for the United States Department of Energy (US DOE) under Contract DE-AC05-

76RL01830. The U.S. Department of Energy, Office of Fusion Energy Sciences (FES) and Office of Advanced Scientific Computing Research (ASCR) has supported this study through the SciDAC-4 program on Plasma-Surface Interactions [10]

References

[1] G. Nandipati, W. Setyawan, H. L. Heinisch, K. J. Roche, R. J. Kurtz, B. D. Wirth, *J. Nucl. Mater.* **462** (2015) 338
[2] G. Nandipati, W. Setyawan, H. L. Heinisch, K. J. Roche, R. J. Kurtz, B. D. Wirth, *Semiannual Progress Report* DOE/ER-0313/54 (2013) 179
[3] G. Nandipati, Kinetic Simulations of Microstructural Evolution, [Scientific Software, Ver.: 1.0] (Aug 26, 2020).
[4] L. Hu, K. D. Hammond, B. D. Wirth, and D. Maroudas, *J. Applied Physics* **118**, 163301 (2015)
[5] L. Hu, K. D. Hammond, B. D. Wirth, D. Maroudas, *Surface Science* **626** (2014) 21–25
[6] G. Nandipati, K. D. Hammond, D. Maroudas, K. J. Roche, R.J. Kurtz, B. D. Wirth, W. Setyawan, *Semiannual Progress Report* DOE/ER–0313/67 (2019) 12
[7] D. Perez, T. Vogel, B. P. Uberuga, *Phys. Rev B* **90** (2014) 014102
[8] L. Hu, K. D. Hammond, B. D. Wirth, D. Maroudas, *J. Appl. Phys.* **115** (2014) 173512
[9] D. Maroudas, S. Blondel, L. Hu, K. D. Hammond, B. D. Wirth *J. Phys.: Condens. Matter* **28** (2016) 064004
[10] Plasma Surface Interactions: Predicting the Performance and Impact of Dynamic PFC Surfaces (https://tinyurl.com/ru8mwqt)

9.3 INVESTIGATION OF THE MICROSTRUCTURAL EFFECTS ON THE MECHANICAL BEHAVIOR AND DAMAGE DEVELOPMENT IN DUCTILE-PHASE TOUGHENED TUNGSTEN COMPOSITES—

Ba Nghiep Nguyen, Jing Wang, Charles H. Henager Jr., Lay Paw, Wahyu Setyawan (Pacific Northwest National Laboratory)

OBJECTIVE

The objective of this research is to investigate the effects of the microstructure obtained from processing or forming of ductile phase toughened (DPT) tungsten (W) composites on the mechanical behavior and damage development in these materials. This investigation aims to elucidate the microstructural factors that control strength, ductility, and toughness of DPT-W composites. During the current reporting period, the multiscale microstructural approach previously developed [1-2] has been applied to simulate the tensile responses and damage development up to total failure of the as-formed 90 wt%-W/nickel-iron (Ni-Fe) composite (90W) and 87% thickness-reduction material (90W-87R) hot-rolled from the as-formed one.

SUMMARY

The developed multiscale microstructural approach to DPT-W composites [1-2] was applied to analyze the microstructural domains representative of 90W and 90W-87R composites. These domains, that cover one-half of the width of the tensile specimens made from these materials, were meshed using OOF2[1] and analyzed by Abaqus using elastic-plastic damage models to describe the behaviors of W and Ni-Fe. In addition, W-W boundaries in the 90W-87R composite were also considered to exhibit an elastic-plastic behavior. Preliminary model predictions show good agreements with the experimental results for both materials in terms of stress-strain responses, damage development, and crack patterns. Model parameters determined from the 90W composite have allowed satisfactory predictions for the 90W-87R material.

PROGRESS AND STATUS

Introduction

W-alloys and W-composites are being studied as potential materials for plasma-facing components (PFCs) of future fusion reactors due to their high melting point, strength at high temperatures, high thermal conductivity, low coefficient of thermal expansion, and low sputtering yield [3-6]. However, W and most W-alloys exhibit rather low fracture toughness and a high DBTT that would render them as brittle materials during reactor operations [4,7]. The DBTT for unirradiated W-alloys typically ranges from 573K to 1273K (300˚C to 1000˚C), and in a reactor environment radiation hardening would further elevate this range [6,8-9]. W-alloys toughened by engineered reinforcement architectures are therefore needed and are strong candidates for PFCs.

Previously, we developed a finite-element (FE) multiscale microstructural approach to investigate the deformation and fracture behavior of DPT-W materials such as W/Cu and W/Ni-Fe composites [1-2]. This approach describes the elastic-plastic deformation that is coupled to damage of individual phases in a microstructural domain. The approach effectively captures various mechanisms, including ductile-phase toughening, responsible for increased strength and ductility of the composites. In addition, the approach was employed to explore artificially designed hierarchical lamellar-like and brick-and-mortar (BAM) microstructures. We showed that strength and ductility of BAM microstructures can be tailored by adjusting the brick aspect ratio [2].

[1]Software developed at the National Institute of Standards and Technology.

During the current reporting period, we have applied this FE microstructural approach to analyze and compare the as-formed 90W to hot-rolled 90W-87R composite. The 90W composite consists of mostly spheroidal single-grained W particles while the 90W-87R material possesses a lamellar-like microstructure. Under perfect rolling conditions, where the intrinsic property of the W and ductile phase is preserved, the lamellar-like 90W-87R is expected to exhibit higher strength and fracture energy than the as-formed one, and our modeling prediction has confirmed much higher mechanical performance in terms of strength and ductility of the *perfect* 90W-87R composite than the as-formed 90W material. However, microdefects caused by processing such as weak W-W boundary regions are present in the hot-rolled composite that significantly lower its mechanical performance. The developed multiscale modeling approach helps elucidate factors that reduce the mechanical performance in this composite and will be further explored later to develop strategies to improve it.

Model Development

The central part of the W/Ni-Fe tensile specimen (made of 90W or 90W-87R composite), far from the grips and does not include the entailed portions, is 5-mm long, 1.168-mm wide and 0.25-mm thick. As the specimen was subjected to uniform tensile loading, only a representative domain (Figure 1) (0.584-mm x 0.584 mm) located on the symmetry axes and covering the half of the specimen width was modeled and discretized in 2D finite elements based on a digital image using the OOF2 software. The two-dimensional (2D) FE model containing the dual-phase microstructural domain for 90W or 90W-87R was created using the method reported in [1] that captured the constitutive behaviors of W and of the Ni-Fe alloy described by an elastic-plastic damage model. Figure. 1 shows the microstructural domains used to build the FE models for the plane-stress analyses of 90W (Figure 1a) and 90W-87R (Figures 1b and 1c) composites. For reason of visibility, the associated FE mesh is not shown for any of the whole domains given in Figure 1.

The 90W microstructure on Figure 1a shows spheroidal W phase particles well dispersed in the Ni-Fe matrix while the 90W-87R exhibits a lamellar-like microstructure with nearly parallel and elongated W phase regions (Figures 1b and 1c). The W-W boundaries observed in SEM images were modeled as separate phase (Figure 1b) using the same type of continuum FEs with the associated constitutive properties. By assigning the constitutive properties of W to these boundaries, the 90W-87R with only the W lamellae perfectly embedded in the Ni-Fe matrix was obtained (Figure 1c). Boundary conditions were applied to the microstructural FE models to simulate the tensile loading tests on 90W and 90W-87R specimens. Experimental tensile tests were performed on these specimens to obtain the material stress-strain responses and crack patterns for the model parameter identification and model validation.

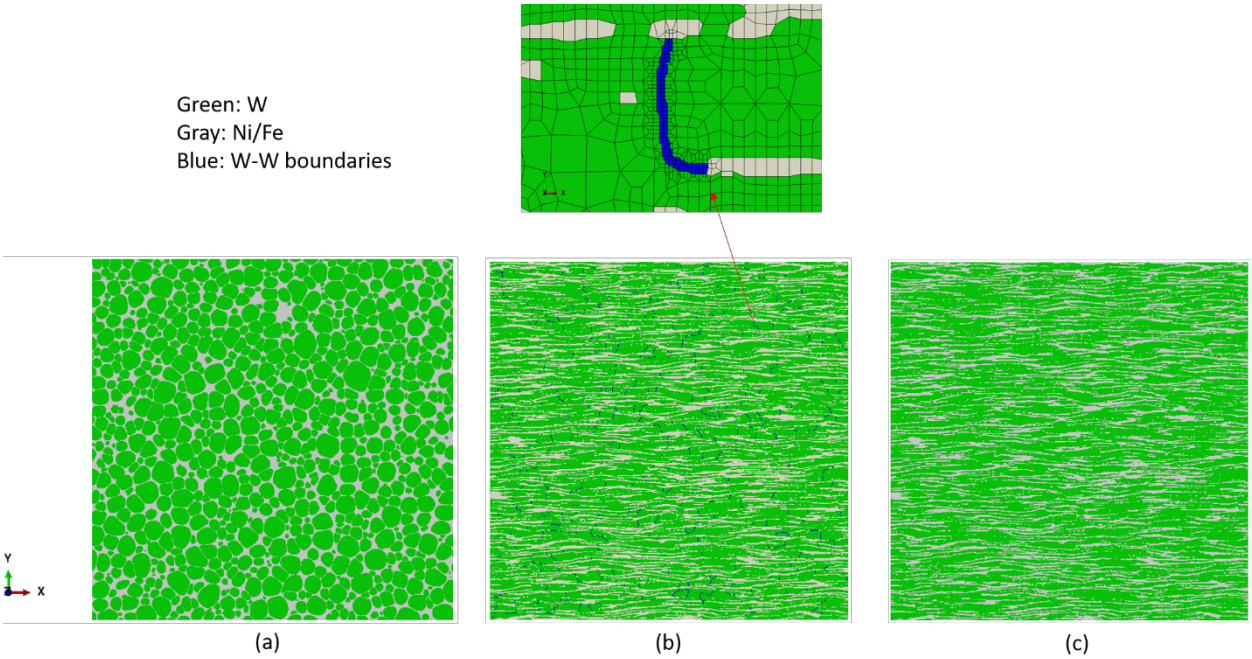

Figure 1. Microstructural domains for the analyses of (a) 90W, (b) 90W-87R containing W-W boundaries – a magnified view of a local meshed area with a W-W boundary region illustrated; and (c) perfect 90W-87R without W-W boundaries.

First, the Abaqus analysis of the 90W FE model subjected to tensile loading was performed using the microstructural approach previously developed [1-2] to correlate the predicted stress-strain response and crack pattern with the corresponding experimental results. This correlation of results allows the material parameters of the elastic-plastic damage model developed in Nguyen et al. [1] to be determined for W and Ni-Fe via this parameter identification procedure. Tables 1 and 2 provide respectively the parameters identified for the 90W composite and those for the 90W-87R material without W-W boundaries previously reported in Ref. [1]. In these tables, E and ν denote the elastic modulus and Poisson's ratio. σ_0 and n are the reference stress and power-law exponent. $\bar{\varepsilon}_{\mathrm{p}}^{\mathrm{D}}$ and $\bar{\varepsilon}_{\mathrm{p}}^{\mathrm{R}}$ are the equivalent plastic strains at damage initiation and at rupture, respectively; and D_{c} denotes the saturation (critical) value of the damage variable [1-2]. Basically, these parameters lead to a stronger Ni-Fe in the 90W composite than in the 90W-87R material previously determined. In addition, the damage model for isotropic elastic-plastic materials existing in the library of constitutive models of Abaqus was also explored for the study. The latter model requires the input data for yield stress versus equivalent plastic strain for W and Ni-Fe that could be estimated from the parameters determined for the Nguyen et al.'s model. Next, the same model parameters for these constituent phases were used in the analyses of 90W-87R FE models (Figures 1b and 1c). A series of numerical trials was conducted using the 90W-87R FE model containing W-W boundary elements to determine the constitutive parameters for these elements. At this time of the report several constitutive laws including those for elastic brittle damage and elastic-plastic damage behaviors have been examined. In the next section, we will illustrate preliminary results based on the same elastic-plastic damage model for the W-W boundaries as for W and Ni-Fe but a weaker and less ductile behavior than the Ni-Fe elements was considered for the W-W boundaries.

Table 1. Parameters of the Nguyen et al.'s model for W and Ni-Fe in 90W

Material	E (MPa)	v	σ_0 (MPa)	n	$\bar{\varepsilon}_p^D$	$\bar{\varepsilon}_p^R$	D_c
Ni-Fe	203570	0.304	400	7	0.4	0.65	0.99
W	383000	0.28	760	12.5	0.4	0.55	0.98

Table 2. Parameters of the Nguyen et al.'s model for W and Ni-Fe in 90W-87R without W-W boundaries reported in Ref. [1]

Material	E (MPa)	v	σ_0 (MPa)	n	$\bar{\varepsilon}_p^D$	$\bar{\varepsilon}_p^R$	D_c
Ni-Fe	203570	0.304	250	7	0.2	0.65	0.98
W	383000	0.28	760	12.5	0.25	0.5	0.98

Preliminary Results

Analyses for the 90W Composite

Figures 2a and 2b show the damage distributions and crack patterns predicted for the 90W material (shown in Figure 1a) by the elastic-plastic damage model from Abaqus and Nguyen et al.'s model [1-2] at 0.04 applied strain. Failure is predicted to occur if the damage initiation criterion is equal to 1 (DUCTCRT=1) according to the elastic-plastic damage model from Abaqus. Nguyen et al.'s model predicts material failure if the failure indicator defined by the damage variable D normalized by its saturation value D_{cr} is equal to 1. In both models, these indicators can vary from 0 to 1. Comparing Figure 2a to Figure 2b shows that Nguyen et al.'s model generally predicted less damage in the Ni-Fe regions although both models predicted practically the same failure locations in some Ni-Fe regions at this strain level.

The damage distributions and crack patterns predicted by these damage models for 90W at about 0.11 applied strain are given in Figures 3b and 3c. Both models predicted the occurrence of visible macrocracks formed by the linkup of microcracks in the Ni-Fe regions near the right border of the modeling domain. There are also microcracks distributed around the main macrocracks that were also observed in the 90W tensile specimens tested until rupture. Figure 4 shows illustrates a ruptured 90W specimen showing the main macrocrack and a number of microcracks on both side of the macrocrack.

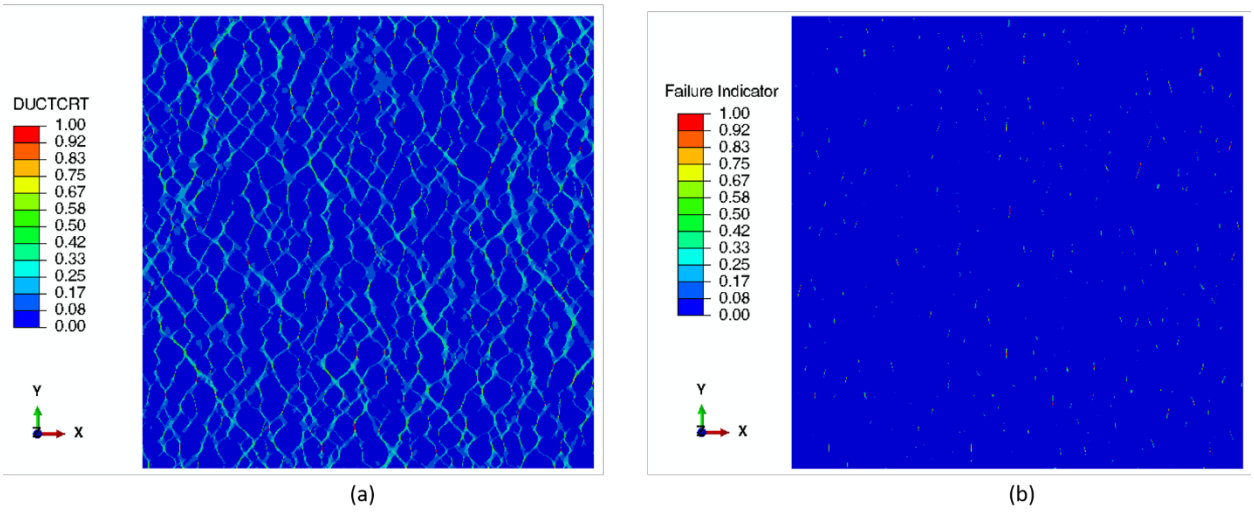

Figure 2. Prediction of damage and fracture for the 90W composite at 0.04-applied strain using (a) the elastic-plastic damage model from Abaqus, and (b) Nguyen et al.'s model [1-2].

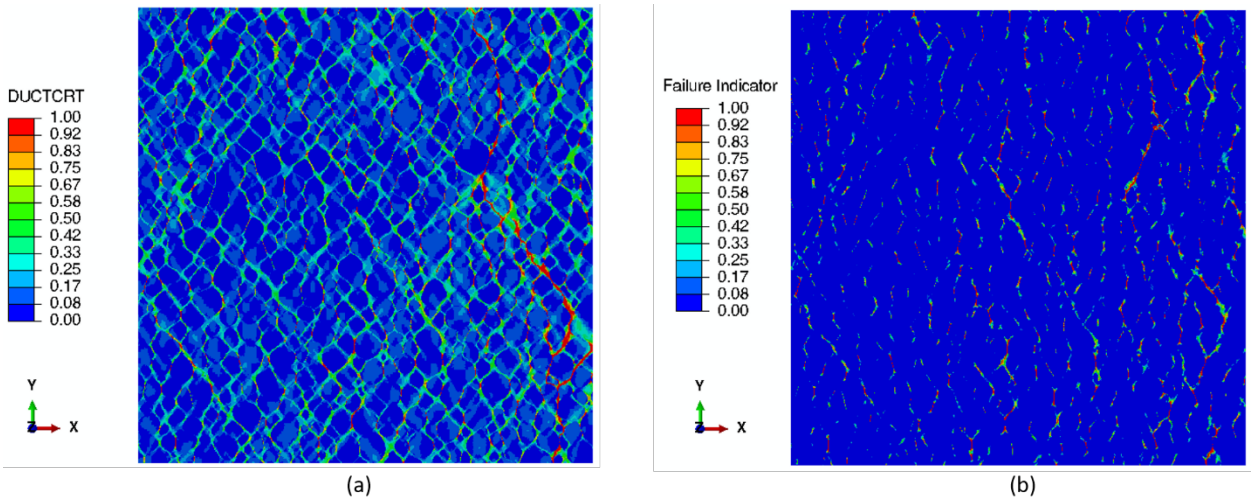

Figure 3. Prediction of damage and fracture for the 90W composite at about 0.11-applied strain using (a) the elastic-plastic damage model from Abaqus, and (b) the Nguyen et al.'s model [1-2].

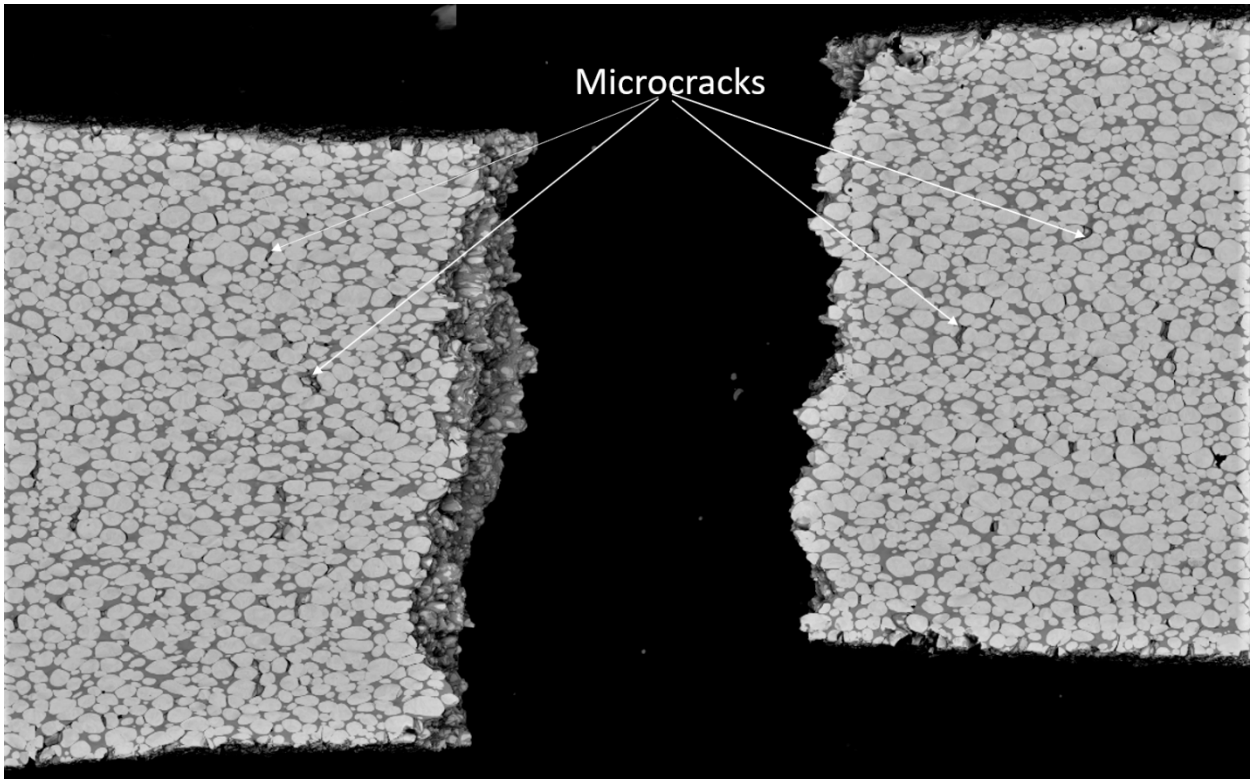

Figure 4. Picture of the fracture region of a 90W specimen tested to rupture.

The predicted stress-strain responses compared to the experimental curves obtained from two tensile tests on the 90W material are given in Figure 5. There is a good agreement between the predictions based on both models and the experimental results in terms of strength. The predicted strengths based on Nguyen et al.'s and Abaqus models are 910.8 MPa and 885.5 MPa, respectively, while the mean value of the measured strengths is about 892 MPa. The good agreement in strength for this material is expected since these stress/strain data were used to determine the parameters of these models. The difference in predicted rupture strain was due to different damage models used. In addition, the Nguyen et al.'s model [1-2] does not activate damage at a given location in the domain if that location is under a compressive stress state. Large variations in rupture strain are also expected and were experimentally observed and reported in [10] due to variations in microstructure. The microstructure varies from one tested specimen to another, and the microstructures of tested specimens were not identical to the one used to develop the FE model for damage analysis. The FE mesh for the 90W microstructural domain shown in Figure 1a was created using a region from an untested 90W specimen from the batch.

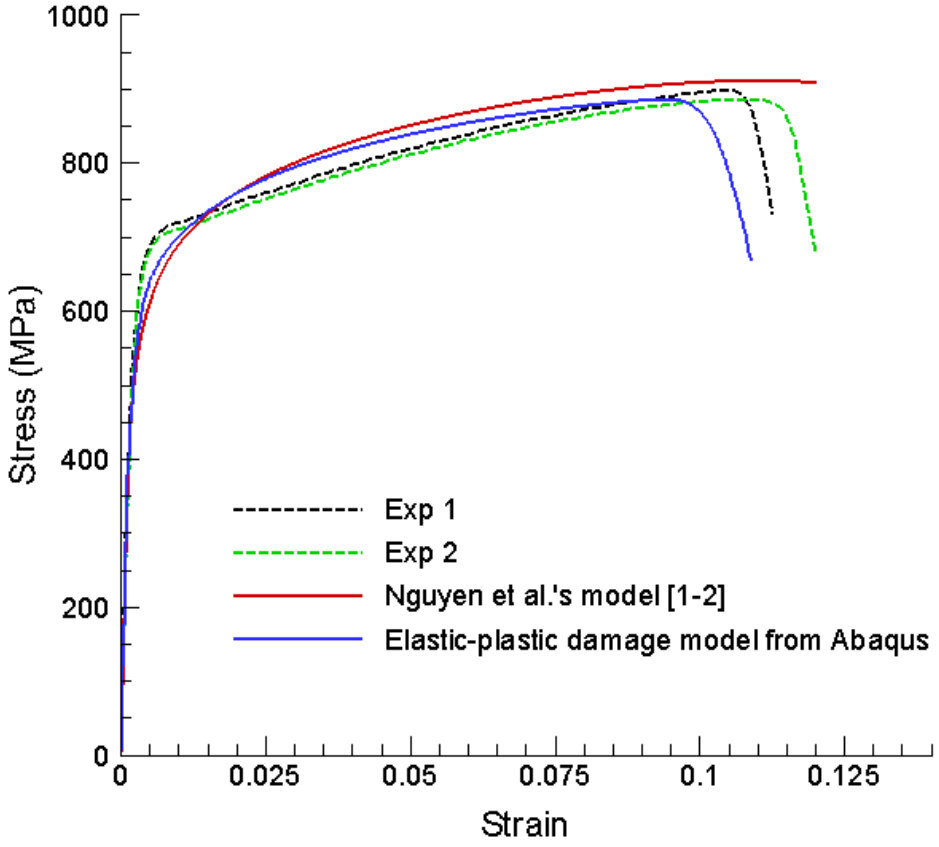

Figure 5. Predicted stress-strain responses compared to the experimental results for the 90W specimens subjected to tensile loading.

Analysis for the 90W-87R Composite

Preliminary analysis of the 90W-87R composite containing W-W boundaries was performed using the same elastic-plastic damage model from Abaqus for the W-W boundaries as for W and Ni-Fe but a weaker and less ductile behavior than the Ni-Fe elements was considered for the W-W boundaries. The model parameters determined for W and Ni-Fe in the 90W material were respectively used for these constituent phases in the 90W-87R composite. Figures 6a and 6b show the contours of damage and fracture patterns predicted at 0.04 and 0.11 applied strains. At 0.04 strain, a significant number of vertical and inclined W-W boundaries failed, and little damage occurred in the Ni-Fe phase regions, but no damage was found in the W lamellar-like regions. However, at 0.11 strain, some microcracks initiated at lower applied strains in the W-W boundaries near the center of the modeling domain could link up and propagate further through the Ni-Fe and W regions leading to the formation of a macrocrack crossing the whole domain (Figure 6b). The predicted crack pattern qualitatively agrees with the experimental one shown in Figure 7 for a 90W-87R specimen tested to fracture at about 0.12 applied strain. The predicted stress-strain response for the 90W-87R composite containing W-W boundaries given in Figure 8 also agree reasonably well with the experimental curves shown on the same figure for this material.

Finally, to determine the effects of W-W boundaries on the damage development and stress-strain response of the 90W-87R composite, a comparative analysis was conducted for a 90W-87R composite that did not

contain W-W boundaries. One way to virtually create such a material was to assign W to these boundaries to obtain the modeling domain given in Figure 1c. Figure 9 gives the stress-strain response predicted for the "perfect" 90W-87R composite compared to the response of the actual composite with W-W boundaries and the predicted response for 90W using the elastic-plastic damage model from Abaqus (also given in Figure 5). Comparison of results plotted in Figure 9 reveals important microstructural factors governing the behavior of the composite up to failure such as (1) perfect lamellar-like versus particulate-type microstructures and (2) the presence of defects such as W-W boundaries.

As expected, in the perfect lamellar-like 90W-87R that exhibits a nearly hierarchical microstructure, the elongated W lamellae are well dispersed and embedded in a Ni-Fe matrix leading to higher strength and rupture strain than the 90W particulate-type composite that contains some weak paths favoring crack propagations. The predicted strength and fracture strain for the perfect lamellar-like 90W-87R are 1039.5 MPa and 0.35, respectively, that are significantly higher than the corresponding values for the 90W (885.5 MPa and 0.095).

The predicted strength and fracture strain of the composite with W-W boundaries are 874.3 MPa and 0.084, respectively that are also substantially lower than the corresponding values for the composite without these boundaries and/or other defects. To elucidate the reason behind the important reductions of strength and fracture strain, Figure 10 compares the predicted damage distribution in the 90W-87R composite without W-W boundaries (Figure10a) to the contour of damage in the actual material containing these boundaries (Figure 10b) at the same applied strain of 0.04. At this strain level, the model predicted negligible damage in material without W-W boundaries while the actual material already suffered from cracking at many W-W boundaries that also caused damage in the neighboring W and Ni-Fe. When the loading increased, these cracks grew and could propagate through the W and Ni-Fe regions leading the actual composite to fail at substantially lower strength and fracture strain. At this time of the report, we continue our investigation on the W-W boundary effects on the stress-strain response, strength and ductility of this material, but our current findings are promising and have reinforced the soundness of the approach developed to investigate the microstructural effects on damage development and the mechanical behavior of DPT-W composites.

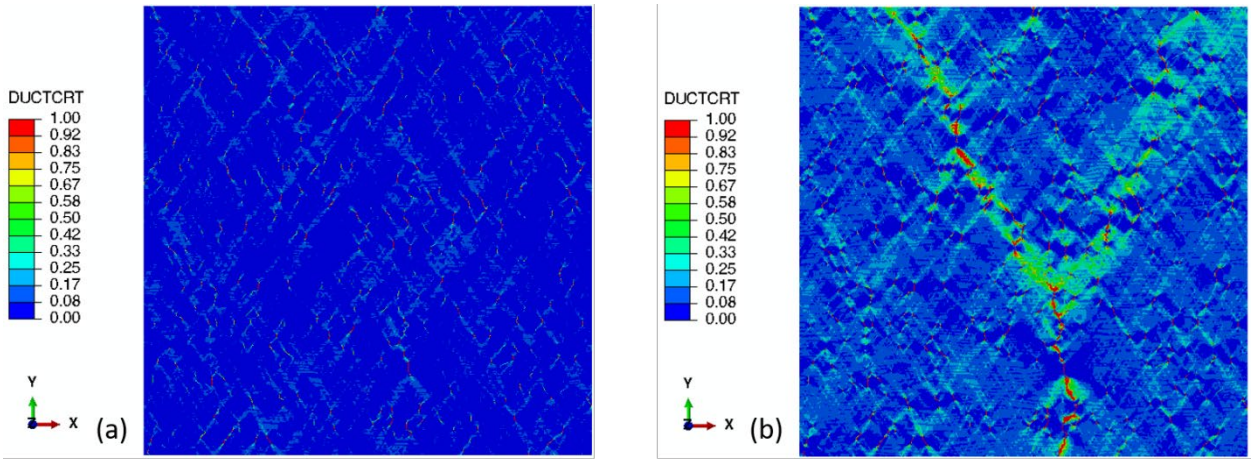

Figure 6. Predicted damage and fracture for the 90W-87R composite at (a) 0.04 and (b) 0.11 applied strains.

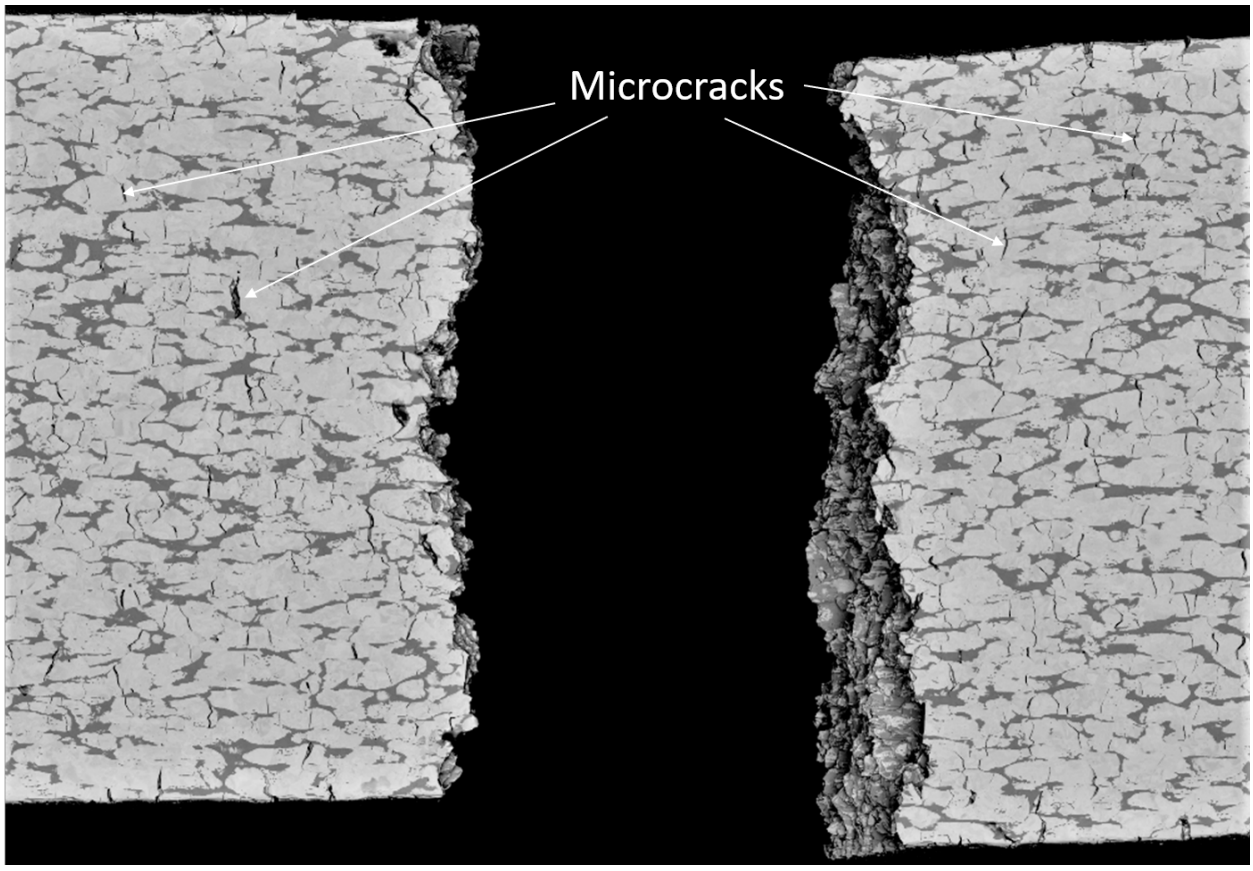

Figure 7. Experimental fracture of a 90W-87R specimen tested to ~0.12 strain.

CONCLUSIONS

We have successfully applied our microstructural modeling approach previously developed to analyze damage and fracture developments as well as the stress-strain responses of 90W and 90W-87R composites. The analyses using this approach help understand the microstructural factors that control strength, ductility, and toughness of DPT-W composites. Preliminary results reveal important effects of the defects resulted from hot rolling such as the W-W boundaries on the stress-strain response, strength and fracture strain of the as-formed composite. We continue exploring additional meshed models and investigating the material behavior for constituent phases and W-W boundaries and will present further results and findings in the next semiannual report. In particular, we will explore the change in the mechanical property of Ni-Fe and W phase due to hot-rolling and how this will improve our modeling of the 87R composites.

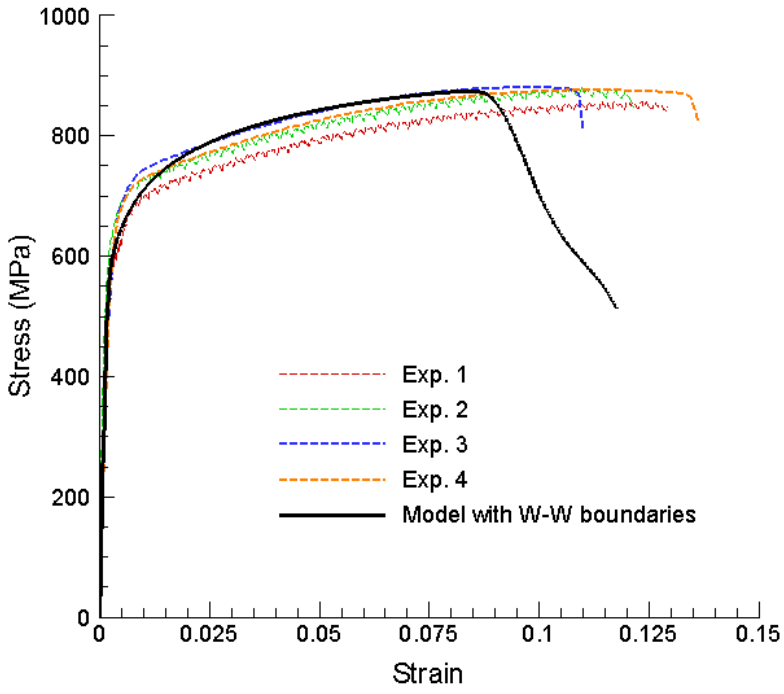

Figure 8. Predicted stress-strain responses compared to the experimental results for the 90W-87R specimens subjected to tensile loading.

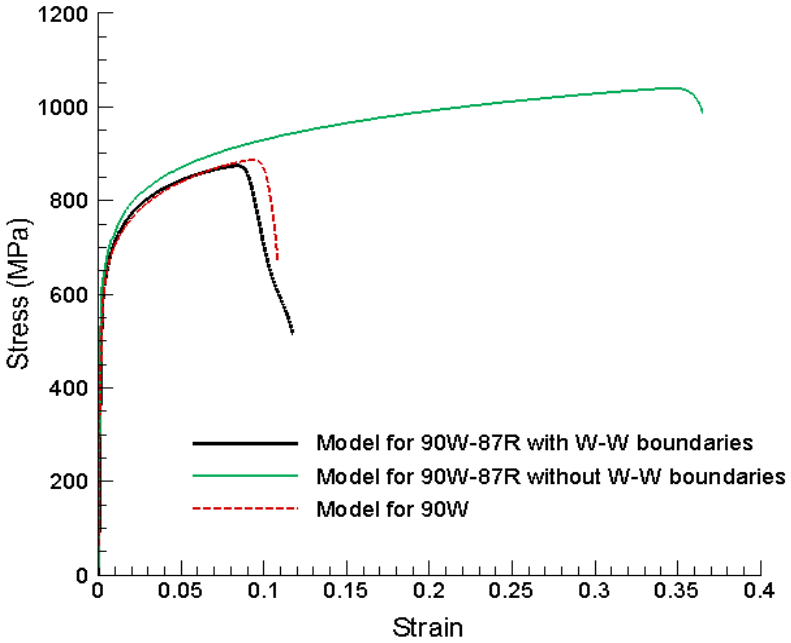

Figure 9. Predicted tensile stress-strain responses of the 90W-87R composite with and without W-W boundaries.

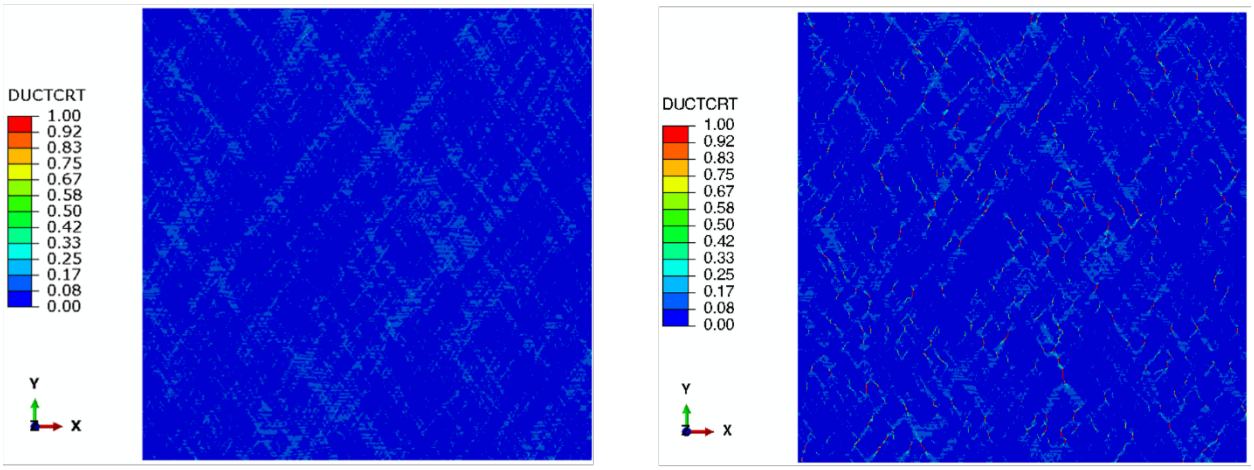

Figure 10. Predicted damage distributions at 0.04-applied strain for the 90W-87R composite (a) without W-W boundaries and (b) with W-W boundaries.

Acknowledgements

This research has been supported by U.S. Department of Energy (DOE), Office of Science, Office of Fusion Energy Sciences under Contract DE-AC05-76RL01830. PNNL is a multi-program national laboratory operated by Battelle Memorial Institute for the US DOE under DE-AC05-76RL01830.

References

[1.] Nguyen, B.N., C.H. Henager, Jr, N.R. Overman, R.J. Kurtz, J. Nucl. Mater., 508 (2018) 371-384.
[2.] Nguyen, B.N., C.H. Henager Jr., J. Wang, W. Setyawan, J. Nucl. Mater. 540 (2020) 152382.
[3.] Sigl, L.S., P.A. Mataga, B.J. Dalgleish, R.M. McMeeking, and A.G. Evans, Acta Metall., 1988. 36(4): p. 945-953.
[4.] Rieth, M. et al., J. Nucl. Mater., 417 (2011) 463-467.
[5.] Pitts, R.A., A. Kukushkin, A. Loarte, A. Martin, M. Merola, C.E. Kessel, V. Komarov, and M. Shimada, Physica Scripta Volume T, 2009 (T138), p. 014001 (10 pp.).
[6.] Mertens, P., T. Hirai, M. Knaup, O. Neubauer, V. Philipps, J. Rapp, V. Riccardo, S. Sadakov, B. Schweer, A. Terra, I. Uytdenhouwen, and U. Samm, Fusion Eng. Des., 84 (2009) 1289-1293.
[7.] Mertens, P., V. Philipps, G. Pintsuk, V. Riccardo, U. Samm, V. Thompson, and I. Uytdenhouwen, Physica Scripta Volume T, 2009 (T138), p. 014032 (5 pp.).
[8.] Gludovatz, B., S. Wurster, A. Hoffmann, and R. Pippan, Int. J. Refract. Met. Hard Mater., 28(6) (2010) 674-678.
[9.] Zinkle, S.J. and N.M. Ghoniem, Fusion Eng. Des., 51-52 (2000) 55-71.
[10.] Wang, J., D. Collins, N.R. Overman, W. Setyawan, "Tensile Testing and Microstructural Characterization of Ductile Phase Toughened W-NiFe Alloys." In Fusion Materials Semiannual Progress Report for the Period Ending June 30, 2020, FW Wiffen and S Melton, Editors, DOE/ER-0313/68, Vol. 68, pp. 102-120, Oak Ridge National Laboratory, Oak Ridge, TN.

9.4 VIRTUAL CRYSTAL APPROXIMATION CALCULATION OF LATTICE MISMATCH IN INTERPHASE BOUNDARIES IN W-NiFe ALLOYS—W. Setyawan (Pacific Northwest National Laboratory)

OBJECTIVE

The overall objective is to provide scientific understanding of the effect of fusion neutron irradiation, helium, and hydrogen isotopes on the thermo-mechanical properties of ductile-phase-toughened (DPT) W-Ni-Fe heavy alloys, as well as understanding of He and H gas retention in these DPT alloys. The specific objective in this report is to calculate lattice parameters of Ni-Fe-W fcc solid solution as a function of composition and to determine lattice mismatches in selected W/Ni-Fe-W interphase boundaries.

SUMMARY

Density functional theory (DFT) method is employed to calculate lattice parameters of Ni-Fe-W fcc solid solutions. In a previous research, pure Ni is employed as a surrogate for the Ni-Fe-W solid solution to study the cohesion of {110}⟨100⟩W//{111}⟨110⟩Ni interphase boundary. In this report, virtual crystal approximation is employed to model the solid solution as a function of composition.

PROGRESS AND STATUS

Ductile-phase-toughened (DPT) W composites derived from W-Ni-Fe heavy alloys (WHAs) are being researched as potential plasma-facing materials (PFMs). The alloys typically consist of essentially pure body-centered cubic (bcc) W particles embedded in ductile face-centered cubic Ni-Fe-W solid solution matrix phase [1-2]. Cohesion of the interphase boundary (IB) between the particle and the ductile phase is key to the excellent toughening in these materials. A previous DFT study uses pure Ni as a surrogate for the Ni-Fe-W solid solution to explore the cohesion of {110}⟨100⟩W//{111}⟨110⟩Ni interphase boundary [3]. To improve our understanding on IB cohesion, we attempt to investigate how the cohesion depends on boundary structure and local composition near the boundary. Our previous study shows that the tungsten phase near IBs is essentially pure W, while the composition of the ductile phase near the IBs gradually differs from its composition far from the IBs (denoted as bulk composition) [4, 5]. Data obtained from electron diffraction spectroscopy (EDS) show that the bulk composition of the ductile phase among the different WHAs is similar, namely approximately 66 at.% Ni, 25 at.% Fe, and 9 at.% W [6]. Our study further shows that the concentration of W in the ductile phase increases towards IBs, presumably due to considerable solubility of W in Ni and driven by interfacial energy minimization [4, 5].

In this report, density-functional-theory (DFT) method is employed to calculate lattice parameters of Ni-Fe-W fcc solid solution as a function of composition and to determine the lattice mismatch in selected W/Ni-Fe-W interphase boundaries. The DFT calculations are performed with Quantum Espresso 6.6 software. Generalized gradient approximation (GGA) with PBEsol functionals are employed for the electronic exchange and correlation energies. Ultrasoft pseudopotential formalism is employed to describe the ion-electron interactions. The pseudopotentials for Ni, Fe, and W are taken from the pslibrary.1.0.0 [7]. These pseudopotentials are Ni.pbesol-n-rrkjus_psl.1.0.0.UPF, Fe.pbesol-n-rrkjus_psl.1.0.0.UPF, and W.pbesol-spn-rrkjus_psl.1.0.0.UPF. Spin-polarized calculations are performed for all systems containing Ni and/or Fe. Electronic smearing of Methfessel-Paxton is employed with a smearing width of 0.2 eV (0.0147 Ry). Monkhorst-Pack **k**-point grids are applied with 18x18x18 grids for bcc unit cell and 16x16x16 grids for fcc unit cell. The SCF convergence tolerance is 0.1 meV*N_{atoms}. Simulation cells and atomic positions are fully relaxed. Structure relaxation is done with a force tolerance of 25 meV/Å (for slab configurations) and 10 meV/Å (for non-slab systems), a total energy tolerance of 0.5 meV*N_{atoms}, and an external pressure tolerance of 1 kbar. Energy cutoff of wave functions (Ecutwfc) of 55 Ry is employed. The energy cutoff of the charge density is set to be 10 times the cutoff of the wave functions. To model the Ni-Fe-W solid solution, virtual crystal approximation (VCA) approach introduced by Ramer and Rappe [8] is employed. The VCA

pseudopotentials are generated, based on the above elemental pseudopotentials, using the upftools/virtual_v2.x code within the Quantum Espresso software.

Initial DFT relaxations are performed to obtain an estimated lattice constant a_0*. Subsequently, DFT calculations are performed to get data of total energy E vs lattice constant a, covering a strain of 0.98, 0.99, 1.0, 1.01, and 1.02 with respect to a_0*. Then, the PW/tools/ev.x code within the Quantum Espresso software is employed to fit E vs a data to the Birch's 3rd order equation of state to determine the equilibrium lattice constant a_0 and bulk modulus B. Subsequently, special strained crystals are constructed to calculate C_{11}, C_{12}, and C_{44} elastic constants as follows. A volume-conserving orthorhombic strain:

$$\varepsilon = \begin{bmatrix} e_1 & 0 & 0 \\ 0 & -e_1 & 0 \\ 0 & 0 & \frac{e_1^2}{1-e_1^2} \end{bmatrix}$$

with e_1 = 0.01. The associated energy change, relative to the energy of an unstrained crystal, is

$$\Delta E = V(C_{11} - C_{12})e_1^2$$

where V is the volume of the crystal. A volume-conserving monoclinic strain:

$$\varepsilon = \begin{bmatrix} 0 & e_6/2 & 0 \\ e_6/2 & 0 & 0 \\ 0 & 0 & \frac{e_6^2}{4-e_6^2} \end{bmatrix}$$

with e_6 = 0.01. The associated energy change is

$$\Delta E = 0.5VC_{44}e_6^2$$

and using the following relation:

$$B = (C_{11} + 2C_{12})/3$$

Table 1 summarizes the lattice parameter and elastic constants of Ni-Fe binary solid solutions and Ni-Fe-W solid solutions, respectively. The results indicate that Fe increases the lattice parameter of fcc Ni and decreases the bulk modulus and C_{11}. The trends are observed for all Fe concentration included in this study (up to 0.5).

Table 1. Lattice parameter and elastic constants of Ni-Fe binary fcc solid solution as a function of Fe concentration xFe

Ni-Fe fcc solid solution	4-atom fcc VCA cell, Ecutwfc = 55 Ry, 16x16x16 **k**-points				
xFe	a_0 (Å)	B (GPa)	C_{11} (GPa)	C_{12} (GPa)	C_{44} (GPa)
0/32	3.46837	233	325	187	151
1/32	3.47457	231	327	183	154
2/32	3.48052	227	325	178	155
4/32	3.49194	224	323	175	152
6/32	3.50193	222	325	170	158
8/32	3.51156	219	321	168	168
10/32	3.52065	215	299	173	152
12/32	3.52924	214	287	178	156
16/32	3.54529	212	284	175	136

Subsequently, the effect of introducing W into the Ni-Fe solid solutions is explored. Tungsten is added while approximately maintaining the Ni:Fe atomic ratio of about 7:3. The results are summarized in Table 2. The results suggest that introducing W in Ni-Fe solid solution induces the opposite effects from Fe in Ni.

Table 2. Lattice parameter and elastic constants of Ni-Fe-W fcc solid solution as a function of composition. The ratio of Ni:Fe in the ternary solid solutions is approximately maintained at about 7:3.

Composition	4-atom fcc VCA cell, Ecutwfc = 55 Ry, 16x16x16 **k**-points				
	a_0 (Å)	B (GPa)	C_{11} (GPa)	C_{12} (GPa)	C_{44} (GPa)
Ni22Fe10W0	3.52065	215	299	173	152
Ni20Fe9W3	3.42892	306	458	230	213
Ni18Fe8W6	3.35487	410	590	320	171
Ni16Fe7W9	3.29986	518	593	480	-4

From Table 2, Ni16Fe7W9 exhibits a negative C_{44}, indicating that this crystal is unstable. Note the atomic concentration of W in this crystal is ~0.28. To investigate further the maximum W concentration to keep the crystal stable, we explore more compositions as presented in Table 3. In the ductile phase, the composition approximately corresponds to Ni20Fe9W3 (~9.4 at.% W). Thus, we explore the crystal stability starting from this composition by increasing the W content. It appears that the W content can be increased up to about 26 at.%.

Table 3. Lattice parameter and elastic constants of Ni-Fe-W fcc solid solution as a function of composition

	Atomic %			4-atom fcc VCA cell, Ecutwfc = 55 Ry, 16x16x16 **k**-points				
composition	Ni	Fe	W	a_0 (Å)	B (GPa)	C_{11} (GPa)	C_{12} (GPa)	C_{44} (GPa)
Ni20Fe9W3	62.5	28.1	9.4	3.42892	306	458	230	213
Ni20Fe9W6	57.2	25.7	17.1	3.36649	393	572	303	170
Ni20Fe9W9	52.6	23.7	23.7	3.32258	467	599	401	85
Ni20Fe9W12	48.7	22.0	29.3	3.29509	530	589	500	-24
Ni20Fe6W6	62.4	18.8	18.8	3.34975	410	558	336	142
Ni20Fe6W9	57.2	17.1	25.7	3.30897	489	579	445	38
Ni20Fe3W9	62.5	9.4	28.1	3.29502	504	560	475	-66

To verify the VCA results, supercell calculations are performed where the supercell contains actual Ni, Fe, and W atoms, instead of an average virtual atom. A 2x2x2 fcc supercell (32 atoms) is used. Substituting one Ni with Fe expands the lattice, consistent with the VCA data. Substituting one Ni with W expands the lattice to a more degree than Fe substitution, which seems to contradict the VCA data previously shown in Tables 2 and 3. Currently the supercell data is limited to 1/32 concentration. Future work includes supercell calculations at higher Fe and W concentrations and exploring VCA formalisms and pseudopotentials to resolve the discrepancies.

ACKNOWLEDGEMENT

This research has been supported by the U.S. Department of Energy, Office of Science, Office of Fusion Energy Sciences and performed at the Pacific Northwest National Laboratory under contract number DE-AC05-76RL01830.

References

[1] C. H. Henager Jr., et al., *International Journal of Powder Metallurgy* 53 (2017) 53.
[2] R. Neu, et al., *Journal of Nuclear Materials* 511 (2018) 567.
[3] W. Setyawan, *Journal of Applied Physics* 128 (2020) 145101.
[4] J. Haag, et al., *Fusion Materials Semiannual Progress Report*, for period ending December 31, 2019, Vol 67, page 78.

[5] J. Wang, et al., *Fusion Materials Semiannual Progress Report*, for period ending June 30, 2020, Vol 68, page 102.
[6] A. Pathak, et al., *International Journal of Refractory Metals and Hard Materials* 75 (2018) 43.
[7] A. Dal Corso, *Computational Materials Science* 95 (2014) 337, pslibrary.1.0.0. website https://dalcorso.github.io/pslibrary/.
[8] N. J. Ramer, A. M. Rappe, *Physical Review B* 62 (2000) R743.

9.5 ANALYSIS OF DISLOCATION LOOP IMPINGEMENT PROBABILITIES IN IRRADIATED MATERIALS—Peter Doyle, Steven Zinkle (University of Tennessee)

OBJECTIVE

The objective of this work is to quantify the probability of dislocation loop impingement in irradiated materials as a function of loop size and density, and correlate that impingement to observations of loop-to-network dislocation transformation as defect densities increase.

SUMMARY

A Monte Carlo simulation tool has been developed to evaluate the extent of loop impingement (overlap) as a function of dislocation loop size and density. Simulations have been performed in which loops were placed on a variety of possible planes with various probabilities using loop densities up to ρ=10^{23}/m^3 and average loop diameter of d= 4 to 100 nm. Regardless of loop size, the number of possible habit planes did not have a significant effect on the interaction probability. At low defect sizes (4nm diameter), the degree of loop impingement remained below 1% up to 10^{23}/m^3, whereas it increased to 15% interaction probability for a density of ρ=10^{22}/m^3 for 25 nm loops. Generally, the fraction of loops that stochastically interact can be predicted by $F = 1 - \exp(-5.38r^{2.88}\rho * 10^{-18})$, which is generally valid below ρ=10^{22}/m^3 where the radial standard deviation (σ_r) is $\leq 0.5r$ or up to ρ=10^{23}/m^3 for $\sigma_r \leq 0.2r$. The threshold degree of impingement that induces significant formation of network dislocations is estimated to be between 1 and 10%, regardless of material type.

PROGRESS AND STATUS

A Monte Carlo algorithm has been designed and written in Fortran and evaluated for coding errors. A variety of conditions were simulated 10^3 times. Conditions included defect diameters ranging from 4 to 100 nm with standard deviations ranging from 0 to 50% of the mean diameter. Simulations were further conducted using a variety of habit planes including 1) {111}, 2) all of the planes in {111}, {110}, and {100}, and 3) a variety of weighted fractions of each plane set. Analysis of these data has been accomplished to quantify the probability of interaction between loops up to densities of 10^{23}/m^3. Applying that analysis to previously published and forthcoming work has been used to establish a function that can be used by researchers to obtain ballpark estimates of defect diameter/density combinations where loop impingement can be expected to lead to loop unfaulting and network dislocation formation.

Simulation Algorithm and Input Parameters

The following conditions were assumed in the algorithm generation:

1. The transition from dislocation loops to network dislocations will be related to the fraction of defects interacting with each other.
2. Interactions can be estimated by creating a static “interaction volume” around each defect. Any two defects with overlapping interaction volumes can be said to have interacted.
3. Loops will form randomly on the various crystal planes, depending on the crystal structure. In BCC, loops will form on {110} and {100} planes, while in FCC, loops will inhabit {111} planes.
4. Loop motion has been ignored (all loops are sessile).
5. Loop size distribution can be described by a Gaussian distribution.

Together, the validity of these assumptions can be evaluated by comparison of the model results to experimental findings. In short, the assumptions have been designed to provide the interaction fraction due only to random packing of loops in a static volume and will thus represent the lowest bound of expected

loop impingement since some physical force and motion effects are likely to cause realistic interactions in common engineering environments.

Per these assumptions, a Monte Carlo simulation algorithm was developed using the following inputs, listed in Table 1: maximum loop density (ρ_{max}), loop average radius (r) and standard deviation, crystal structure, lattice parameter (a_0), interaction distance normal to a loop ($L_\perp$), interaction distance in the direction of the loop plane as measured from the loop center ($L_\parallel$), number of histories, and size of simulation cell (L_{cell}). Loop radii and standard deviations were varied across 2, 5, 10, 25, 50 nm with standard deviations of 0, 10, 20, and 50%. For each combination of the above, the following combination of crystals structures was used (uniform chance of each angle within the family being chosen, except where noted. For clarity, 80% {100} means that each of the three planes of the {100} family contains 27% of the populated loops.

1) {111}
2) {110}
3) {100}
4) {111}, {110}, {100}
5) 20% {100}, 80% {110}
6) 80% {100}, 20% {110}
7) 80% {100}, 20% {111}

Table 1. Input parameters for the simulations in this work. Cell simulation size and loop parameters are given in the text.

Parameter	$a_0\ (nm)$	$L_\perp$	$L_\parallel$	$\rho_{max}\ (m^{-3})$	*Histories*
Value	0.36	$2a_0$	$r + 4a_0$	10^{23}	10-10^3

The simulation algorithm is as follows. Data is read in and cubic cells with length L_{cell} are constructed and divided into sub-cells. The dual purpose of this is 1) minimize analysis time, and 2) create a periodic boundary condition to simulate the bulk impingement behavior. Each subcell is cubic with a length of $\geq 2(r_{ave} + 3\sigma_r)$, the maximum loop diameter allowed for the simulation. Because all loops are populated according to a Gaussian distribution this upper limit on loop size contains nearly all expected loop sizes.

As a consequence of the subcells structure, subcells are grouped, for data evaluation purposes, into interior and exterior cells, with separate counters for each. In the exterior region, the number of interactions will be reduced compared to the interior due to a lack of loops outside of the cell to provide additional interactions. Whereas, interior cells will be provided a “periodic boundary” by the exterior cells. Because on the bulk, and not surface-sensitive, data is of interest in this work, the exterior cell data is not presented herein.

For a single history, loops are added until the maximum density is reached. Each loop is added by first choosing a sub-cell according to a uniform distribution and then choosing a random location uniformly within that sub-cell. Random numbers for this assignment were obtained with intrinsic Fortran generator. The new loop is also given a plane to reside on, with probabilities determined at run time as given above.

The new loop’s location and orientation are compared to that of all loops in the relevant sub-cell as well as in adjacent sub-cells to determine if there is any overlap in interaction volumes. When overlap is found the number of interactions of both overlapping loops is incremented and counters updated to keep track, of how many loops have 1, 2, 3, 4, or 5+ interactions with other loops. Once all loops have been added, this process is repeated for N histories and the data is cleaned up and output.

RESULTS AND DISCUSSION

Irradiation damage leads to the formation and evolution of dislocation loops and lines. The fractional abundance of lines increases with radiation damage and the interaction probability depends chiefly on the size and density of the loops. A critical density and size is hypothesized at which dislocation lines begin to form. Across the range of histories, 10 to 10^3, no significant difference in mean or error estimates was obtained, indicating a highly reproducible system. Thus, the data for 10^3 histories are presented below for only the grouping of all internal subcells. As part of the collection, interaction data was binned into the mean and standard deviation fraction of loops having interacted at all and then specifically loops having 1, 2, 3, 4, or 5+ interactions.

Generally, this system can be viewed as analogous to a chemical system in which a fraction of loops having interacted i times reacts upon addition of another loop with the rate constant k_{i-i+1}. Or,

$$L_i \xrightarrow{k_{i\rightarrow i+1}} L_{i+1}$$

The concentration of which, C_i can be expressed mathematically as the following for loops with any interaction at all,

$$\frac{dC_{any}}{d\rho} = k_{0\rightarrow 1} C_{none}$$

Or as,

$$\frac{dC_i}{d\rho} = k_{i-1\rightarrow i} L_{i-1} - k_{i\rightarrow i+1} L_i$$

for any concentration of loops with interaction numbers between 1 and 4, and as

$$\frac{dC_5}{d\rho} = k_{4\rightarrow 5} L_4$$

Noting further that k is a measure of the probability of interaction per loop added, k will be a function of the loop size and distributions. As such, $k \approx Ar^B$ with A and B being fitted parameters and r being the loop radius (plus interaction distance). Using this model, the following figures were generated for 4, 30, and 100 nm diameter loops. In each figure, 6 curves are presented representing interactions of any, 1, 2, 3, 4, or 5+ interactions per loop. The individual points represent simulation data and the solid lines represent the fit using $A=5.38\text{x}10^{-18}$ and B=2.88 (same A and B for all loop interaction rate constants).

Figure 1 shows both data and fit for all simulated interaction fractions for 4 different orientation population conditions. A few notes are important with regard to these data. First, the fit curve for each a-d is identical. This is because the fit (solid lines) was obtained across all standard deviations and average diameters and thus represents the ideal fit to all data. Second, comparing the data across the figures and to the fit line shows that the Figure 1b) ({100} orientation data) has the least agreement with the fit, while Figure 1d fits the best. This is due to the number of planes that are available to populate loops. {100} has only 3, while {110} has 6. The more possible planes there are, the greater the chance of interacting with other loops. However, this effect is small and is not elaborated on further in this work. Third, the chemical-analog model appears to properly describe the data and is thus used in the remaining analysis.

The error between the fit and data presented in Figure 1 is better explained by Figure 2. In Figure 2, the data from the 5 nm simulations where the loops were populated on all of {100}, {110}, and {111} planes (all angles, not planes, with equal loop populations). The subplots in Figure 2 represent 0, 10, 20 and 50%

standard deviation about the mean. Comparing a)-c), the data are quite similar, whereas at 50% the data diverge substantially from the model. This effect is more pronounced with larger loops (not shown). The reason for the distortion is related to the fact that the Gaussian distribution is given a minimum point such that $r_{min} = a_0$. Thus, when the standard deviation is large enough, the actual mean is larger than the requested mean (the large radii are still allowed, but the smallest ones, which would be negative, are not. Moreover, the pseudo-rate constants are no longer the same for each interaction fraction, since the larger loops will initially interact more frequently than the smaller loops, whose size dictates a later interaction time.

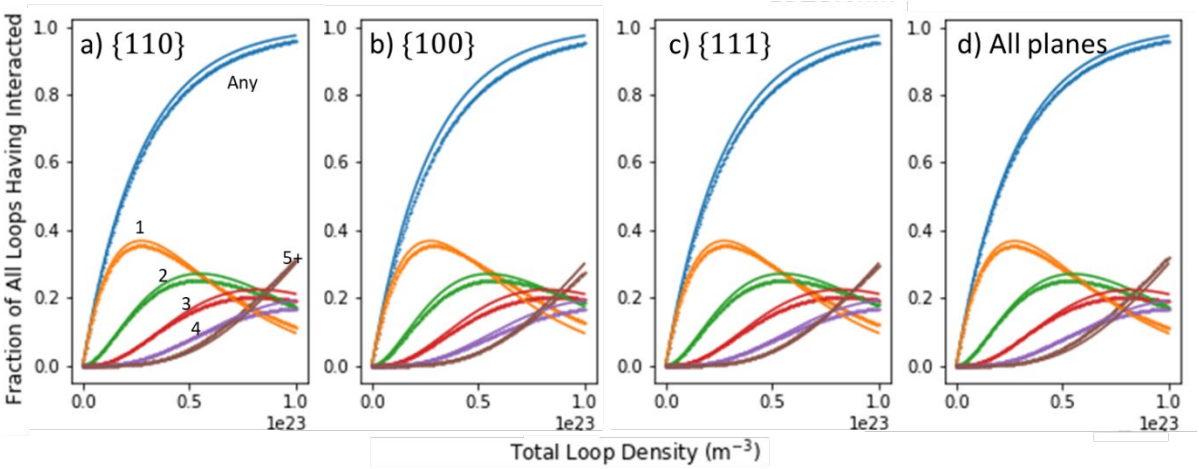

Figure 1. Fraction of 30±6nm diameter loops with any, 1, 2, 3, 4, or 5+ interactions (data points) along with data fit (solid lines) as described in the text. Loops were placed uniformly on a) {110}, b) {100}, c) {111}, or d) {111}, {100}, and {110} planes.

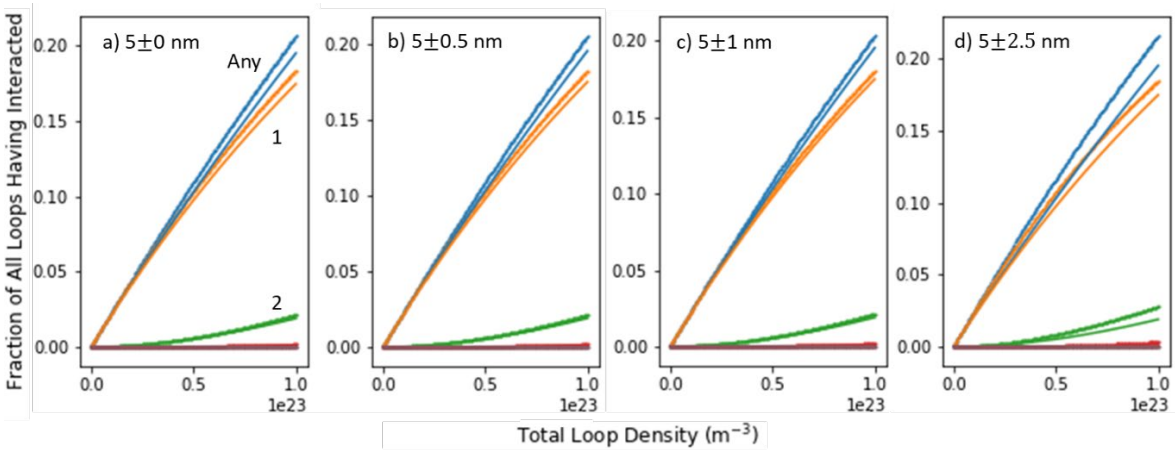

Figure 2. The fraction of interactions per loop in simulations with 10 nm average diameter loops that have a) 0, b) 1, c) 2, and d) 5 nm standard deviation. Solid lines represent data fit and data points represent simulation data.

Together, Figures 1 and 2 reveal a valuable insight. The function F = $1 - \exp(-5.38 * 10^{-18} r^{2.88})$, with r as the radius in microns, can be used to describe the fraction of loops with any interaction across a wide range of input parameters. Moreover, up to 20% standard deviation and for any combination of populated angles, the model will fit well within 10% uncertainty, especially at low loop densities. At higher standard deviations, the model overpredicts at low densities and underpredicts at high densities.

This model can be rearranged such that given a certain threshold, F, at which a transition is observed to occur from sessile loops to dislocation networks, a radius versus defect density curve can be generated. Taking the defect and dislocation data from a variety of studies, approximate overlap fractions were generated and compared to observations of networks or the lack thereof in the same studies. Corresponding empirical impingement thresholds for transition from loops to networks (based on experimental radiation effects studies) is presented in Table 2.

Table 2. Approximate transition threshold from loop-dominant to network-dominant conditions

Reference	**Transitional Fraction**
Hudson et al, 1976 [1]	0.1-0.2
Unpublished Data	0.01-0.02
Barton et al, 1977 [2]	0.1-0.2
Brager et al, 1977 [3]	<0.05
Brager et al, 1973 [4]	0.1-0.3
Chen et al, 2020 [5]	0.03-0.08
Xiu et al, 2020 [6]	>0.03
Jin et al, 2017 [7]	0.05-0.1
Yi et al, 2018 [8]	0.01
Parkin et al, 2020 [9]	0.01-0.03

While the data in Table 2 are disparate, reflective of different materials systems with disparate energetics, a reasonable threshold range between 0.01 and 0.1 is seen to approximately represent the domain in which loop-to-network transition will occur. Using the following equation (where A and B are fitting constants), Figure 3 was created for bounding values of F_{min} and F_{max}.

$$r = \left(\frac{\ln(1-F)}{A\rho}\right)^{\frac{1}{B}}$$

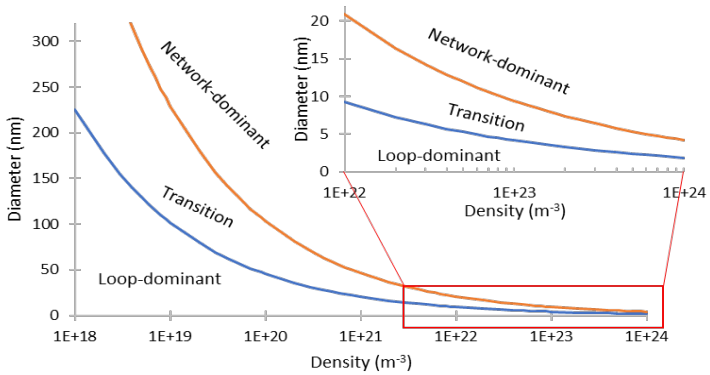

Figure 3. Predicted domains of loop-dominated, network-dominated, and transitional defect regimes using F_{min} = 0.01 and F_{max} = 0.1.

Figure 3 shows a surprisingly narrow band in which the transition is expected to occur. At low densities ($<10^{20}$ m^{-3}), extremely large loops (> 50nm) are required for any network formation by loop unfaulting. From 10^{20} to 10^{21} m^{-3} large loops are still required (>25 nm) to induce unfaulting via physical impingement. Above this density, the lower-bound transition diameter becomes quite small and by 10^{23} m^{-3} the higher-bound diameter drops as low as 10 nm. These predictions can be used to estimate how close to the transition region a particular material system is based on microstructural observations.

FUTURE WORK

Final comparisons are being made to literature data, in order to further quantify the accuracy of the model predictions presented in this work.

References

[1] J.A. Hudson, VOID FORMATION IN SOLUTION-TREATED UNDER 46.5 MeV Ni6+ IRRADIATION, J. Nucl. Mater. 60 (1976) 89–106.

[2] P.J. Barton, B.L. Eyre, D.A. Stow, The structure of fast-reactor irradiated solution-treated AISI type 316 steel, J. Nucl. Mater. 67 (1977) 181–197. https://doi.org/10.1016/0022-3115(77)90173-8.

[3] H.R. Brager, F.A. Garner, G.L. Guthrie, The effect of stress on the microstructure of neutron irradiated type 316 stainless steel, J. Nucl. Mater. 66 (1977) 301–321. https://doi.org/10.1016/0022-3115(77)90119-2.

[4] H.R. Brager, J.L. Straalsund, Defect development in neutron irradiated type 316 stainless steel, J. Nucl. Mater. 46 (1973) 134–158. https://doi.org/10.1016/0022-3115(73)90131-1.

[5] L. Chen, K. Murakami, D. Chen, H. Abe, Z. Li, N. Sekimura, In situ transmission electron microscopy study of growth of dislocation loops in Fe-Ni alloy under ion irradiation, Scr. Mater. 187 (2020) 453–457. https://doi.org/10.1016/j.scriptamat.2020.06.071.

[6] P. Xiu, Y.N. Osetsky, L. Jiang, G. Velisa, Y. Tong, H. Bei, W.J. Weber, Y. Zhang, L. Wang, Dislocation loop evolution and radiation hardening in nickel-based concentrated solid solution alloys, J. Nucl. Mater. 538 (2020) 152247. https://doi.org/10.1016/j.jnucmat.2020.152247.

[7] H.H. Jin, E. Ko, S. Lim, J. Kwon, C. Shin, Effect of irradiation temperature on microstructural changes in self-ion irradiated austenitic stainless steel, J. Nucl. Mater. 493 (2017) 239–245. https://doi.org/10.1016/j.jnucmat.2017.06.019.

[8] X. Yi, K. Arakawa, F. Ferroni, M.L. Jenkins, W. Han, P. Liu, F. Wan, High-temperature damage evolution in 10 keV He+ irradiated W and W-5Re, Mater. Charact. 145 (2018) 77–86. https://doi.org/10.1016/j.matchar.2018.08.026.

[9] C. Parkin, M. Moorehead, M. Elbakhshwan, J. Hu, W.Y. Chen, M. Li, L. He, K. Sridharan, A. Couet, In situ microstructural evolution in face-centered and body-centered cubic complex concentrated solid-solution alloys under heavy ion irradiation, Acta Mater. 198 (2020) 85–99. https://doi.org/10.1016/j.actamat.2020.07.066.

10. IRRADIATION & TESTING METHODS, EXPERIMENTS AND SCHEDULES

10.1 IRRADIATION TEMPERATURE ESTIMATION OF EUROFUSION 2.5 DPA PHASE- I IRRADIATIONS FOR SS-J3 SAMPLES USING SiC THERMOMETRY—A. Bhattacharya, J.W. Geringer, Y. Katoh (Oak Ridge National Laboratory), M. Rieth (KIT)

OBJECTIVE

Ten Eurofer97 steel variants (designated as H, I, J, K, L, M, N, O, P and reference E) were irradiated in HFIR for EUROfusion targeting 2.5 dpa, 300 °C. The irradiations were performed in rabbit capsules in conjunction with SiC passive thermometry pieces. This report details the sample temperatures, which is critical to correctly predicting the results of post-irradiation examination (PIE) testing.

SUMMARY

Using SiC thermometry and results of finite element modeling (FEM), the temperature distribution inside the EUROfusion tensile capsules were rationalized. The combined experimental and FEM input was used to estimate the temperature of test specimens inside the two EUROfusion capsules designed to target 285 and 315 C so that the target 300 °C temperature can be bracketed by acknowledging the uncertainties in FEM and temperatures inside materials test reactors. For both design temperatures, the irradiations were designed to reach 2.5 dpa. While, the estimated temperatures for SS-J3 specimens were reasonable, the tests suggest significantly higher temperatures for a stack of MPC1 coupons, that increased the overall temperature in one of the sub capsules. This report provides an estimate of the temperature of each SS-J3 sample that was irradiated in this campaign.

PROGRESS AND STATUS

Eurofer97 steels in the form of flat SS-J3 tensile test specimens were held within a specimen holder that is accommodated in a rabbit capsule housing for HFIR irradiations using the flux-trap rabbit facility targeting 2.5 dpa, 300 °C. The average temperature of the holder assembly (specimen holder and specimens) depends on the total gamma heat generation within the assembly and the gas gap between the holder and the housing. The magnitude of temperature distribution within the holder assembly depends on the volumetric heating of the specimens and components and the design of the assembly. Previously, finite element analysis (FEA) was used for the thermal design and analysis for the rabbit capsules [1]. The FEA temperature analysis is accurate typically to within ±10% of the difference between the design temperature (T_{des}) and the coolant temperature (Tc, ~60°C). Based on FEM in Ref. [1], the temperature of irradiation were expected to be stable within ±4% of (T_{des} – Tc) during the full power operation. It typically takes about a day for HFIR to ramp up to the full power upon start-up. The shutdown process is much quicker. The holder assembly temperature reaches the equilibrium within a few minutes after the reactor reaches each power step.

As a safety from the apparent temperature fluctuations inside nuclear reactors, the 300 °C target temperature was aimed to be achieved using two capsules that were designed to bracket the target temperature: first capsule designed for 285 °C (Capsule: ES21) and the second for 315 °C (Capsule: ES22). The holder diameters and fill gas for both ES21 and ES22 capsules is given in Table 1.

Table 1. Holder diameter and fill gas for the EUROfusion tensile capsules

Capsule ID	Design T (°C)	Holder Diameter (mm) at 20 °C	Fill Gas
ES21	285	9.25	Helium
ES22	315	9.20	Helium

Thermometry Measurements

SiC thermometry annealing measurements were performed at the Low Activation Materials Development and Analysis (LAMDA) lab from the ES21 and ES22 rabbit capsules containing SS-J3/MPC1 samples designed to reach 285±24 and 315±24 °C respectively. The measurements were conducted per the established test procedures at LAMDA/ORNL [2]. For ES21 and ES22 capsules, the design was such that there were 6 SS-J3 samples and 4 SiC thermometry pieces in each sub-capsule, as shown in Figure 1. There were 6 sub-capsules which gives a total of 24 SiC pieces. A total of 18 out of 24 SiC pieces were analyzed which provided a good knowledge of the temperature distribution within each capsule position.

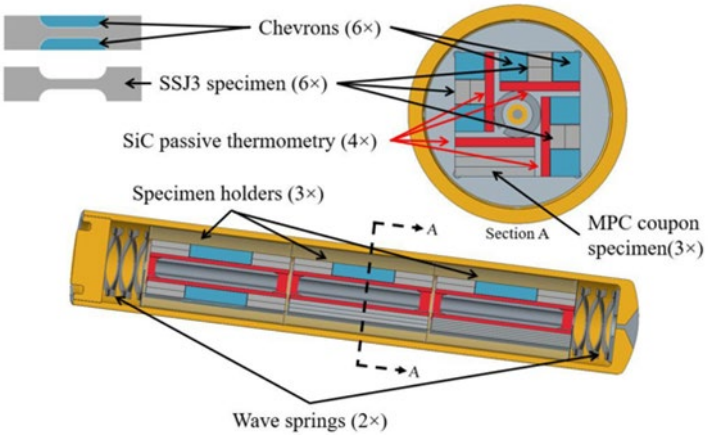

Figure 1. Capsule design for the SS-J3 samples as detailed in Ref. [2].

It is noted that because SiC thermometry pieces were located at the internal positions within the capsules, they represent the maximum temperature. The temperatures will decrease in the radially outward direction from SiC to the SS-J3 samples. This is primarily due to contact resistance heat loss at the interfaces, which was highlighted using FEM by Howard and Smith [1] and this should be considered to estimate the sample temperatures. Per this report, ~5 °C temperature difference is expected between the SiC thermometry pieces and the inner tensile sample, while ~15 °C is expected between the inner and outer tensile specimens. Therefore, if SiC temperature is A, then inner specimen is expected to be at ~A-5 °C and the outer specimen is expected to be at ~A-20 °C (pictorially represented in Figure 2). The sample temperatures were derived using this knowledge.

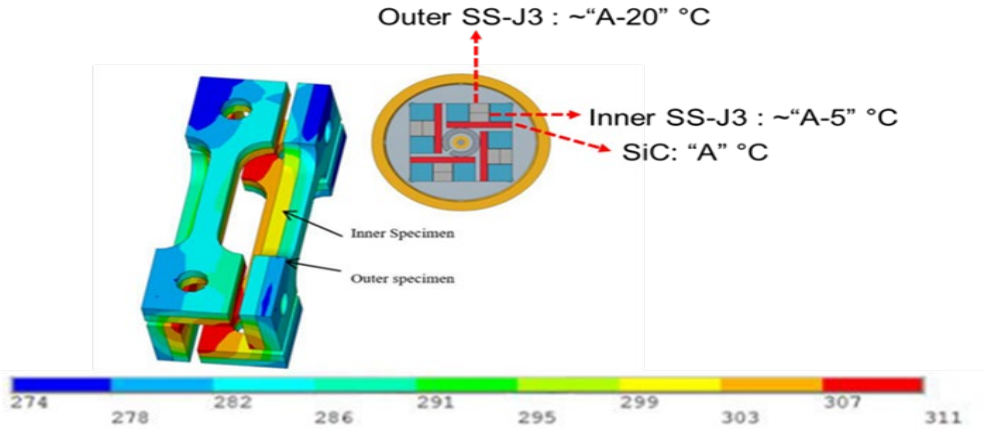

Figure 2. FEM temperature distribution and the expected sample temperatures based on SiC thermometry. Adapted from Ref. [1].

The corresponding dilatometry graphs from the 18 tested samples are provided as an Appendix to this report. To better understand the temperature distribution, the experimentally determined temperatures are overlaid with the capsule loading scheme that was followed at HFIR for the two capsules, in Figure 3. The values in red represent the experimentally determined temperatures from SiC thermometry, while those in blue are the locations from which SiC pieces were not tested. Therefore, the temperatures at these locations were estimated from the average of the experimentally determined values within the capsule.

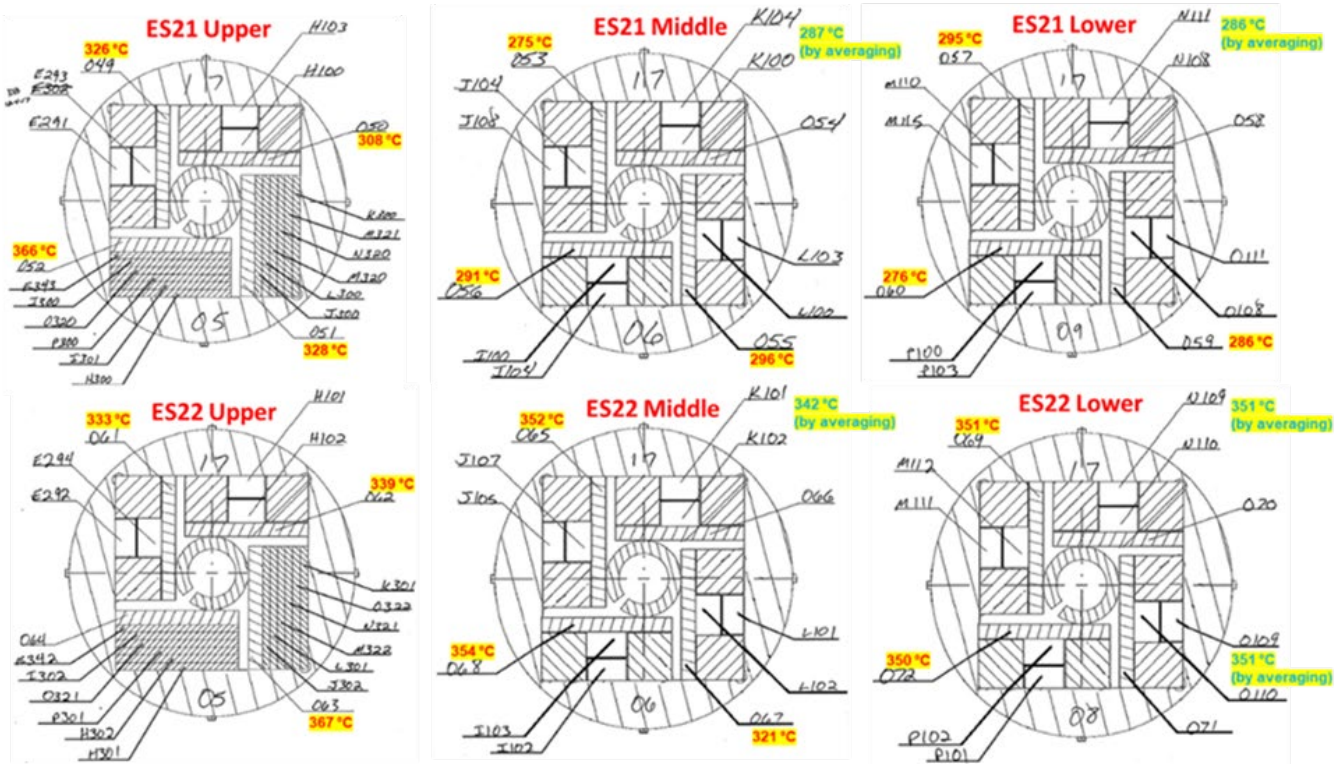

Figure 3. Temperature distribution for the ES21 and ES22 capsules. Values in red are the experimentally measured values from SiC thermometry and those in blue were obtained by average of the experimentally determined values obtained for each capsule.

From Figure 3, it is evident that the stack of MPC1 coupons in both the capsules (ES21 and ES22 Upper) were at higher temperatures (> 350 °C). We believe this is related to the high number of thermal contact resistance points (potential gap resistances) for the 6 MPC1 coupons where chances of improper contact between the samples may increase when compared with only one contact between two SS-J3 tensile specimen configuration. Nevertheless, the temperature distribution for the SS-J3 tensile specimens in ES21 is reasonably good across the upper middle and lower positions. For ES22, the SiC thermometry gives a temperature spread ranging between 321-354 °C for the SS-J3 specimens. The estimated temperatures for both the rabbit capsules, divided into upper, middle and lower positions, are additionally shown in Figure 4. This figure is just a graphical representation of the red numbers (experimentally obtained temperature values) that are shown in the previous figure.

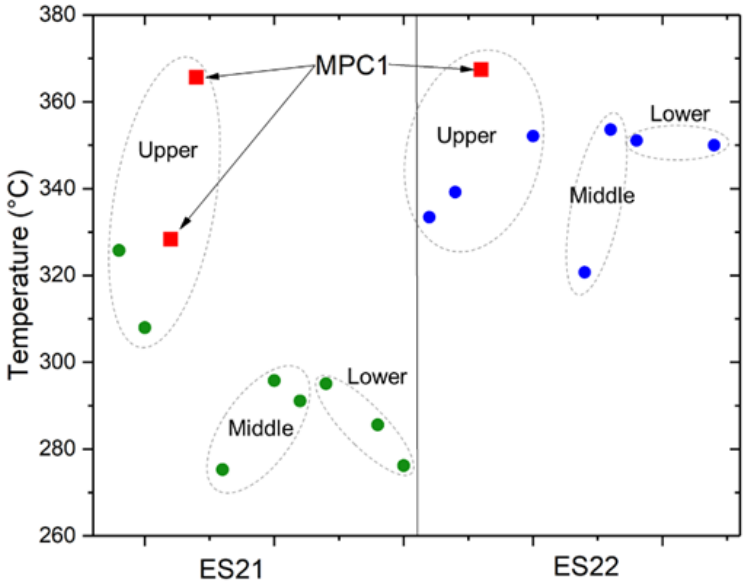

Figure 4. Temperature distribution overlaid with the HFIR loading scheme for the ES21 and ES22 capsules.

Using the thermometry data, the expected sample temperatures were estimated as detailed in the experimental details section which highlights that if SiC thermometry is A, then inner sample will be at ~A-5 °C and the outer sample at ~A-20 °C. The exact sample temperatures were derived using this knowledge and are tabulated below. In this table, the samples which are "green" represented the ones which were at acceptable condition. The acceptable condition meant T_{irr} not below ~260 °C and not above ~337-340 °C. While the lower temperature cut-off was loosely defined because RAFM steels show near-saturation hardening below 300 °C (and up to ~200 °C), the upper limit was more stringent because RAFM steels do not show significant hardening for T_{irr} ≥ 350 °C . The samples in "red" deviated significantly from the acceptable conditions.

Table 2. Estimated SS-J3 sample temperatures derived using the SiC thermometry data. Green color represents samples within acceptable temperature range while red samples are outside an acceptable range from the target designs.

Capsule	Design Temperature	Sample id	Estimated temperature (°C)	SiC thermometry (°C)
ES21	285	E293	321	
ES21	285	E291	306	326
ES21	285	H100	303	
ES21	285	H103	288	308
ES21	285	J104	270	
ES21	285	**J108**	**255**	275
ES21	285	K100	282	
ES21	285	K104	267	287
ES21	285	L100	291	
ES21	285	L103	276	296

Capsule	Design Temperature	Sample id	Estimated temperature (°C)	SiC thermometry (°C)
ES21	285	I100	286	
ES21	285	I104	271	291
ES21	285	M110	290	
ES21	285	M115	275	295
ES21	285	N108	281	
ES21	285	N111	266	286
ES21	285	O108	281	
ES21	285	O111	266	286
ES21	285	P100	271	
ES21	285	**P103**	**256**	276
ES22	315	E294	328	
ES22	315	E292	313	333
ES22	315	H102	334	
ES22	315	H101	319	339
ES22	315	**J107**	**347**	
ES22	315	J105	332	352
ES22	315	**K102**	**337**	
ES22	315	K101	322	342
ES22	315	L102	316	
ES22	315	L101	301	321
ES22	315	**I103**	**349**	
ES22	315	I102	334	354
ES22	315	**M112**	**346**	
ES22	315	M111	331	351
ES22	315	**N110**	**346**	
ES22	315	N109	331	351
ES22	315	**O110**	**346**	
ES22	315	O109	331	351
ES22	315	P101	330	
ES22	315	**P102**	**345**	350

References

[1] Howard and Smith, Development of a Flexible Design for Irradiation of Miniature Tensile and Charpy Test Specimens in the High Flux Isotope Reactor, ORNL/TM-2018/872, (2018).

[2] Campbell et. al, Method for analyzing passive silicon carbide thermometry with a continuous dilatometer to determine irradiation temperature, NIM B 370 (2016) 49–58.

APPENDIX

SiC thermometry dilatometry analysis curves for the ES21 and ES22 capsules: SS-J3 samples. The numbers on top of figures are the exact ids of SiC pieces.

51

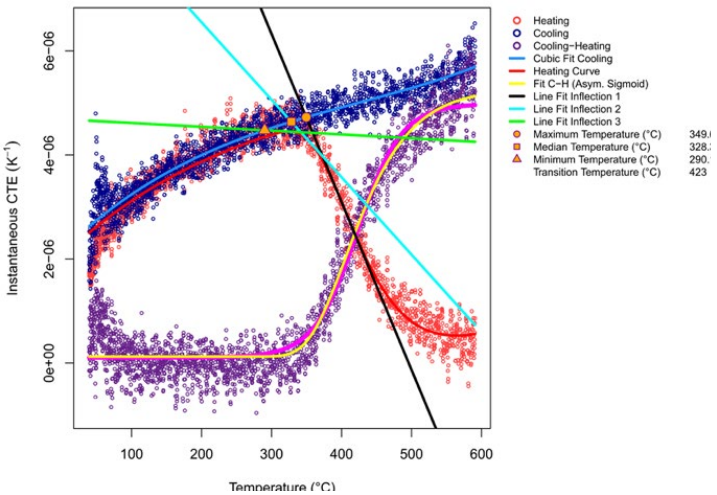

49

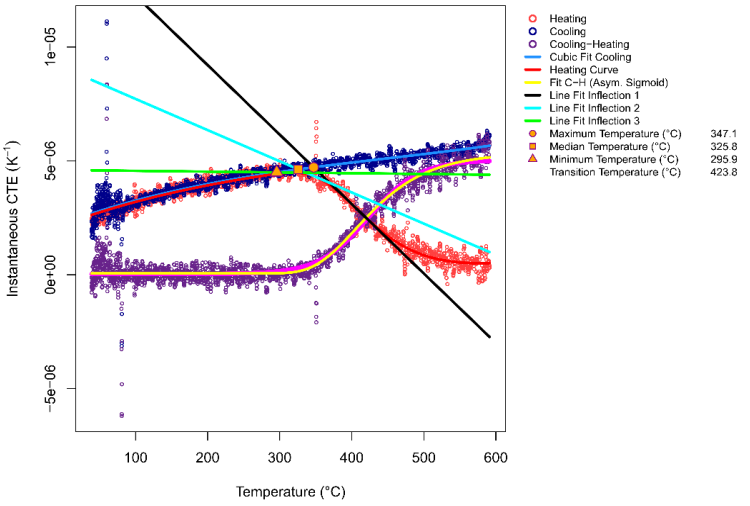

50

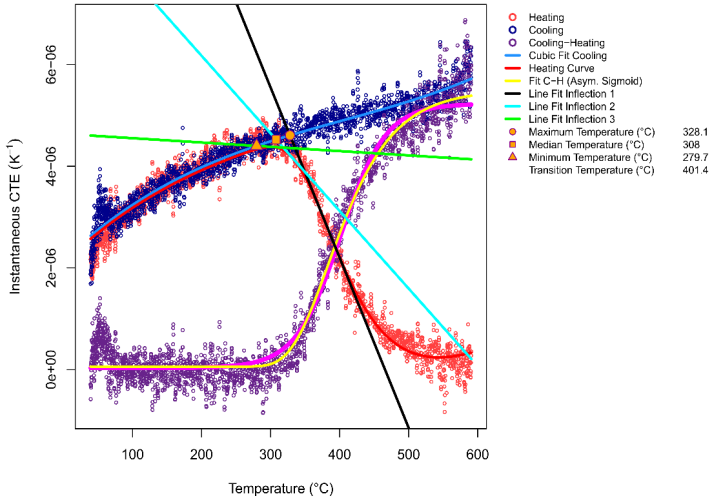

52

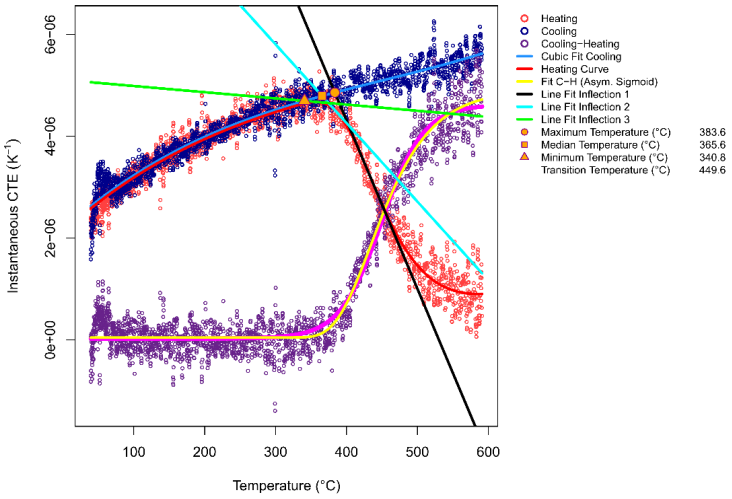

53

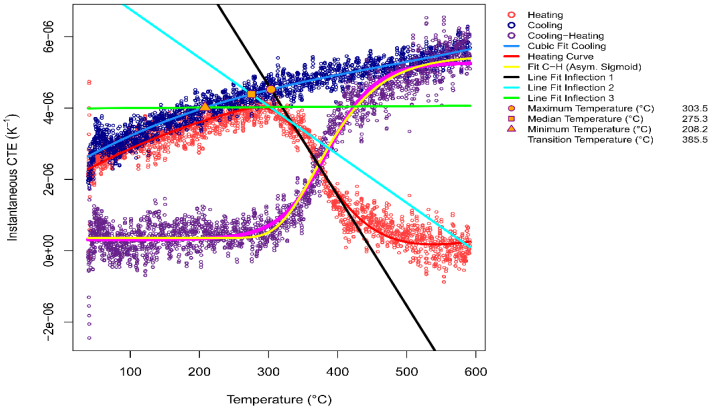

55

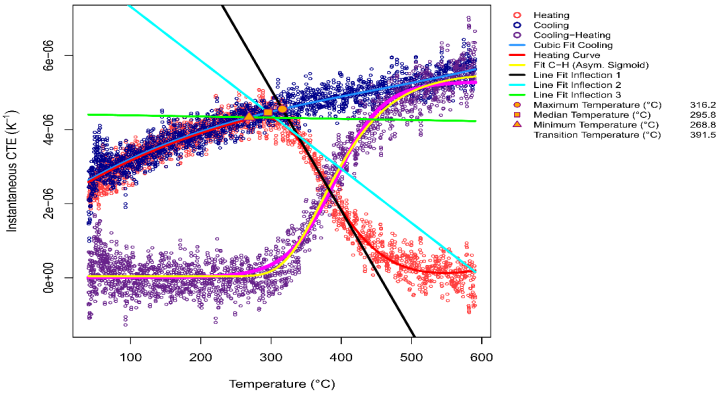

56

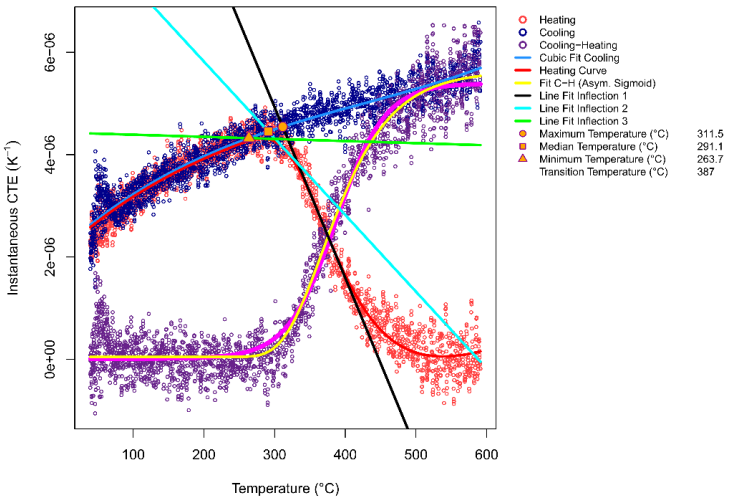

57

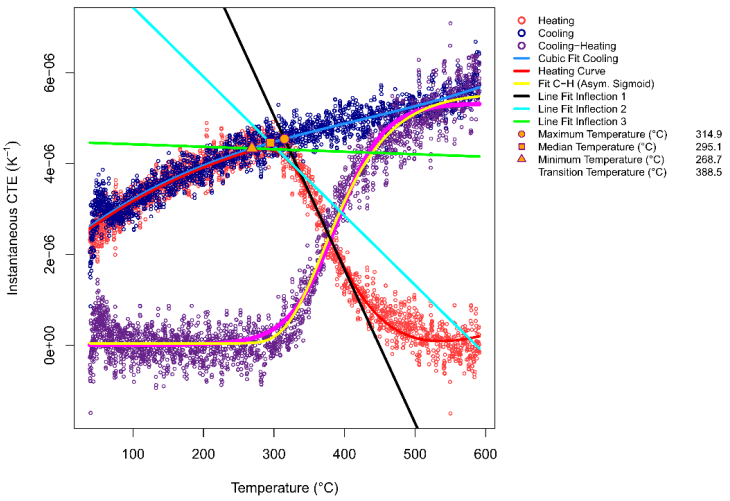

59

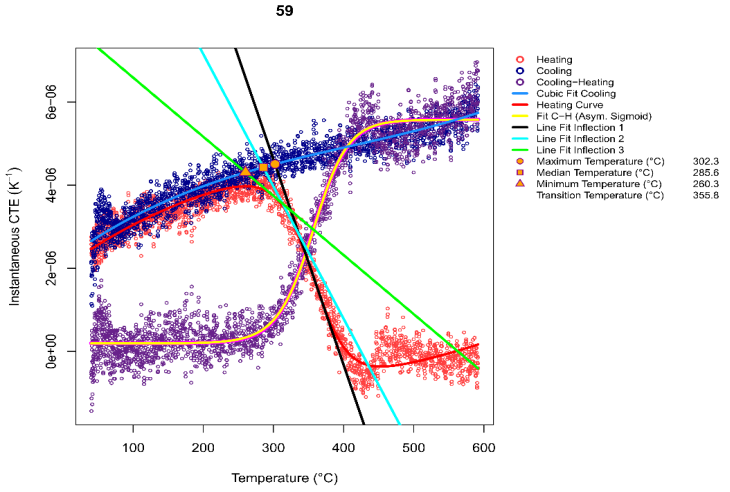

60

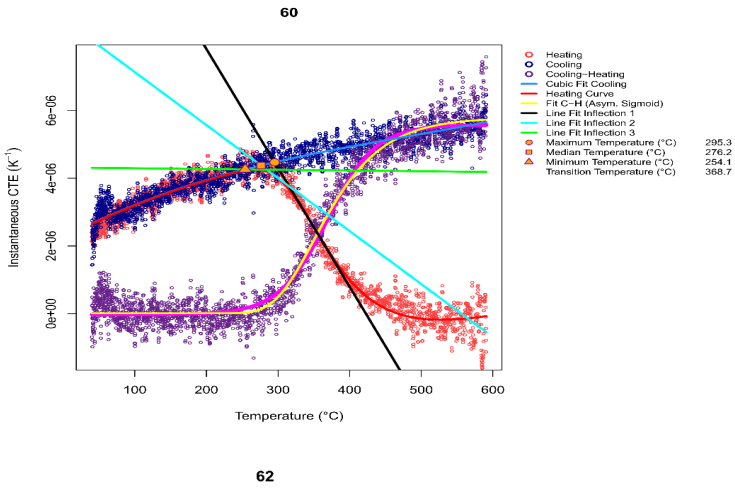

61

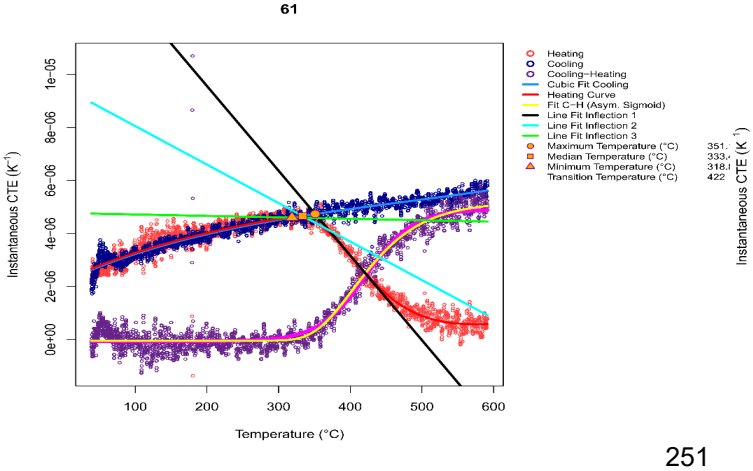

62

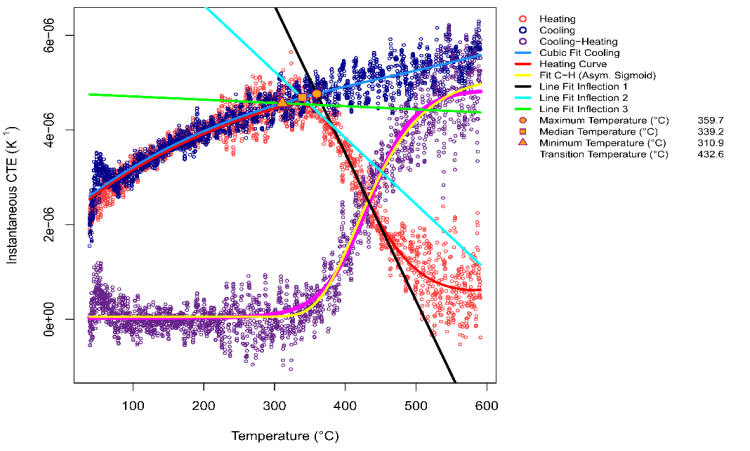

63

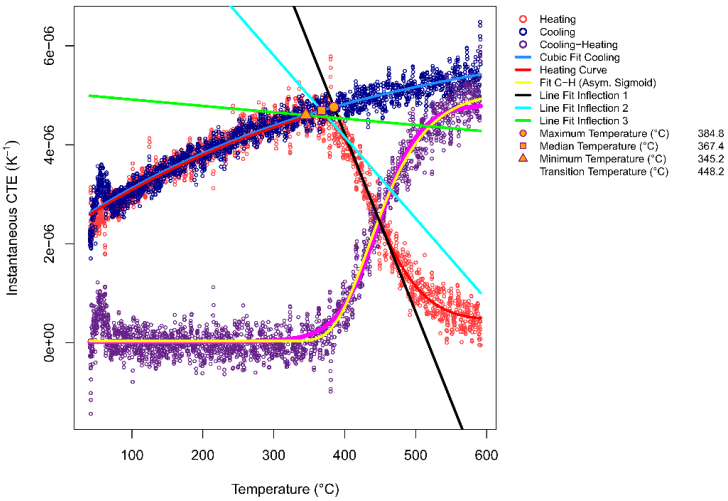

65

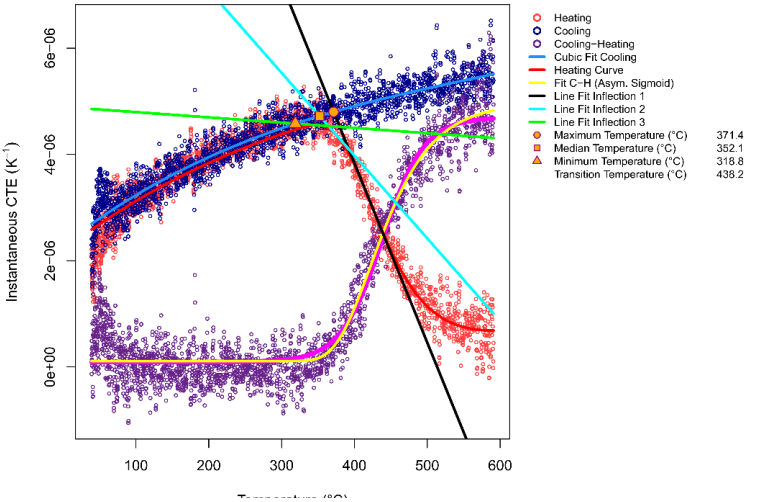

67

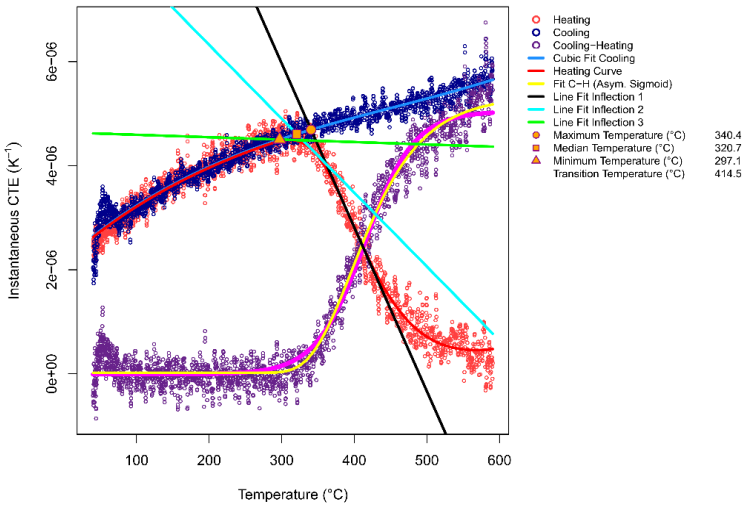

68

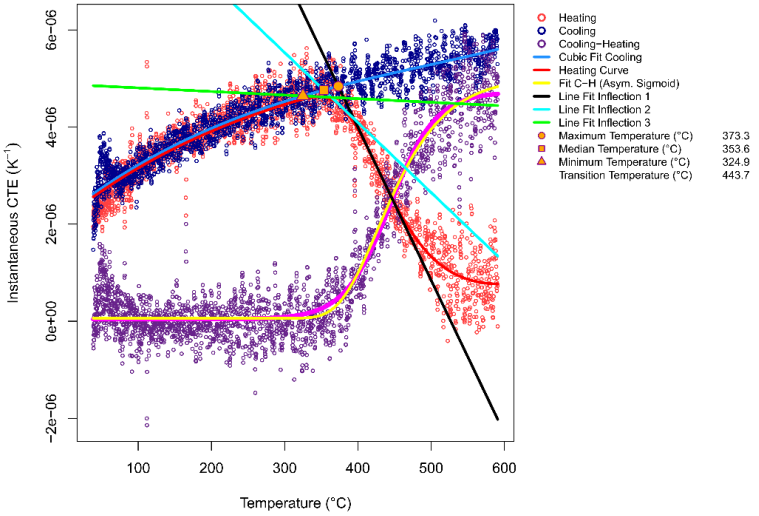

69

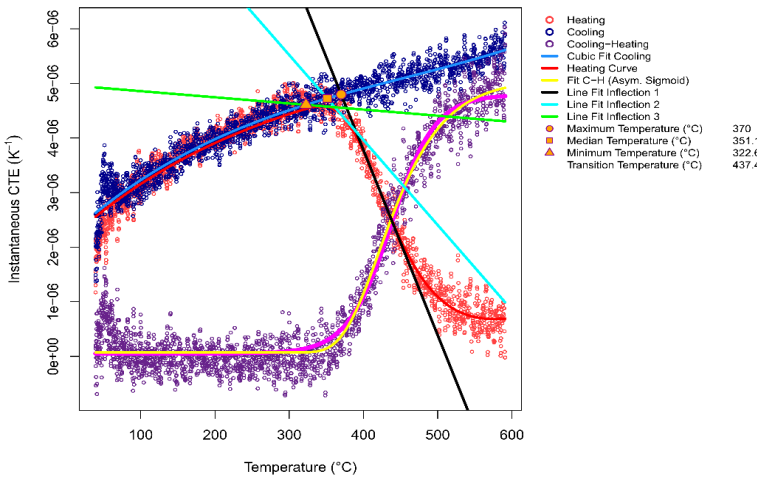

72

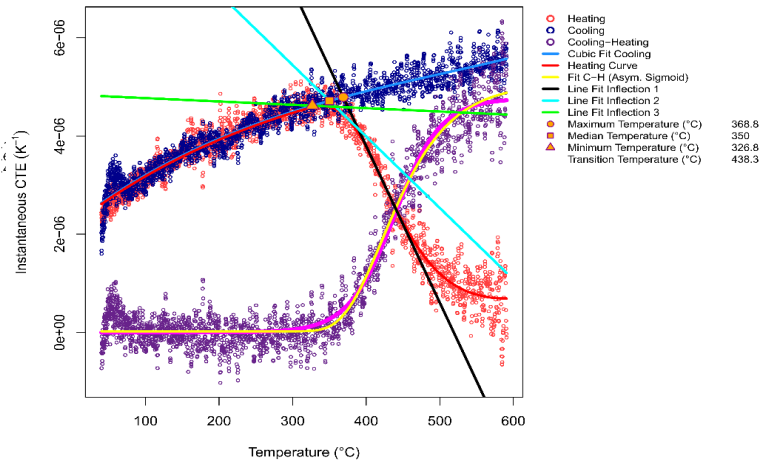

10.2 HFIR IRRADIATION EXPERIMENTS—C. On, J. W. Geringer, J. L. McDuffee (Oak Ridge National Laboratory)

OBJECTIVE

The goal of this report is to describe the progress of the neutron irradiation experiments that were performed in the High Flux Isotope Reactor (HFIR) and the operating status.

SUMMARY

During the six-month period starting from July 1st to December 31st, 2020 a total of thirty-four rabbit capsules continued their irradiation. There were no new capsules inserted or removed from HFIR during this period; however, three new capsules were assembled. These rabbit capsules shall begin irradiation in cycle 490, which will start on February 23, 2021. The cycles 488 and 489 were completed during this period, but cycle 488 was split into two (488A and 488B) due to a reactor scram.

PROGRESS AND STATUS

Neutron irradiation experiments were performed in support of the research and development of fusion reactor materials using various materials irradiation facilities in the High Flux Isotope Reactor (HFIR). The reactor operating history for the period from July 1-December 31, 2020 is detailed in Table 1.

Table 1. HFIR operating record for the semiannual FY2020

Cycle Number	Cycle End Date	Power (MWD)
488*	July 7	2164.62
489	September 12	2154.24

*Cycle was in two parts, due to reactor scrams. Cycle 488A received 14.06 MWD, while cycle 488B received 2150.56 MWD.

All the fusion materials program irradiation experiments performed during the first half of the FY2020 used the nominally two-inch rabbit capsules, with no full-length target rod nor instrumented reflector position capsules within that period. Thirty-four target zone rabbit capsules remain in the reactor to complete the scheduled irradiations. Table 2 lists the experiments to be loaded into HFIR in cycle 490. The capsules listed in Table 3 were inserted either during or before FY2020 and will continue in FY2021 and beyond. Tables 2 and 3 give condensed information on the material, specimen type, temperature, fluence, and period of irradiation.

Table 2. New irradiation capsules starting irradiation in cycle 490

Experiment Designation	Primary Materials	Specimen Types	Irradiation Temperature (°C)	Max Exposure (dpa)	Number of Reactor Cycles	HFIR Cycles Start – End
FH51	F82H-IEA, F82H-BA12	Tensile	300	5	3	490 - 492
FH61	F82H-IEA, F82H-BA12	Bend bars	300	5	4	490 - 493
FH62	F82H-IEA, F82H-BA12	Bend Bars	300	5	4	490 - 493

Table 3. The HFIR fusion materials program rabbit capsules to continue irradiation in FY2021

Experiment Designation	Primary Materials	Specimen Types	Irradiation Temperature (°C)	Max Exposure (dpa)	Number of Reactor Cycles	HFIR Cycles Start – End
FMP07	F82H	Tensile	300	20	11	487 - 497
FMP08	F82H	Tensile	300	80	45	487 - 531
FMP11	F82H	Tensile	385	20	11	488 - 498
FMP12	F82H	Tensile	385	80	45	488 - 532
FMP14	F82H	Tensile	525	20	11	484 - 494
FMP16	F82H	Tensile/MPC*	650	20	11	484 - 494
FMP17	F82H	Tensile/MPC*	650	80	45	484 - 528
FMP22	F82H	Bend Bars	300	20	11	488 - 498
FMP23	F82H	Bend Bars	300	80	45	488 - 532
F13B4	FeCrAlY Steel	Tensile	300	50	29	451 - 497
JCR11-03	SiC/SiC	Mini bend bars	950	200	100	487 - 586
JCR11-05	SiC/SiC	Mini bend bars	950	200	115	444 - 568
JCR11-07	SiC/SiC	Mini bend bars	950	100	47	444 - 492
JCR11-08	SiC/SiC	Mini bend bars	950	200	115	444 - 560
JCR11-11	SiC/SiC	Mini bend bars	950	100	55	448 - 524
SCF4	SiC/SiC	Miniature flexure bar	250	100	90	457 - 547
SCF5	SiC/SiC	Miniature flexure bar	250	200	45	457 - 511
SCF8	SiC/SiC	Miniature flexure bar	600	100	45	457 - 502
SCF9	SiC/SiC	Miniature flexure bar	600	200	90	457 - 548
SCF11	SiC/SiC	Miniature flexure bar	950	100	57	458 - 517
ES01	EUROFER 97	Tensile/MPC*	220	20	12	479 - 491
ES02	EUROFER 97	Tensile/MPC*	275	20	12	480 - 492
ES03	EUROFER 97	Tensile/MPC*	275	20	12	479 - 491
ES04	EUROFER 97	Tensile/MPC*	300	20	12	479 - 491
ES05	EUROFER 97	Tensile/MPC*	325	20	12	479 - 491
ES06	EUROFER 97	Tensile/MPC*	350	20	12	479 - 491
ES07	EUROFER 97	Tensile/MPC*	375	20	12	479 - 491
ES11	EUROFER 97	Bend bars	220	20	12	479 - 492
ES12	EUROFER 97	Bend bars	240	20	12	479 - 492
ES13	EUROFER 97	Bend bars	275	20	12	479 - 492

ES14	EUROFER 97	Bend bars	300	20	12	479 - 492
ES15**	EUROFER 97	Bend bars	325	20	12	479 - 494
ES16**	EUROFER 97	Bend bars	350	20	12	479 - 494
ES17**	EUROFER 97	Bend bars	375	20	12	479 - 494

*MPC= Multi-Purpose Coupon
**ES15, ES16, and ES17= These capsules were removed at the end of cycle 483 and put back in cycle 487. The capsules missed 3 cycles.

10.3 MINIATURE MECHANICAL TEST DEVELOPMENT FOR TUNGSTEN-BASED MATERIALS—L. M. Garrison, N. C. Reid, M. N. Gussev (Oak Ridge National Laboratory), J. P. Allain (Pennsylvania State University)

Extended abstract of manuscript submitted to Fusion Science and Technology, "Design and analysis of an advanced three-point bend test approach for miniature irradiated disk specimens"

First wall and divertor materials in a magnetic confinement fusion device must be able to withstand thermal variation that leads to internal stresses caused by the impinging heat load. In addition, the thermo-mechanical properties of these materials are degraded by irradiation-induced defect accumulation. Fission-reactor-based irradiation data is used to predict the fusion neutron damage and property change. This study investigates a custom-designed three-point bend test for neutron-irradiated disk specimens that are 3 mm in diameter, which is the typical size for transmission electron microscopy (TEM) disks. A finite element deformation analysis is performed to evaluate the mechanical stress field of disk bend specimens. A bend test fixture has been designed and fabricated (Figure 1) to enable testing of these specimens with precisely engineered tolerance and minimal machine compliance. Size and geometry effect are discussed through comparison of this test to regular three-point bend and uniaxial tensile testing.

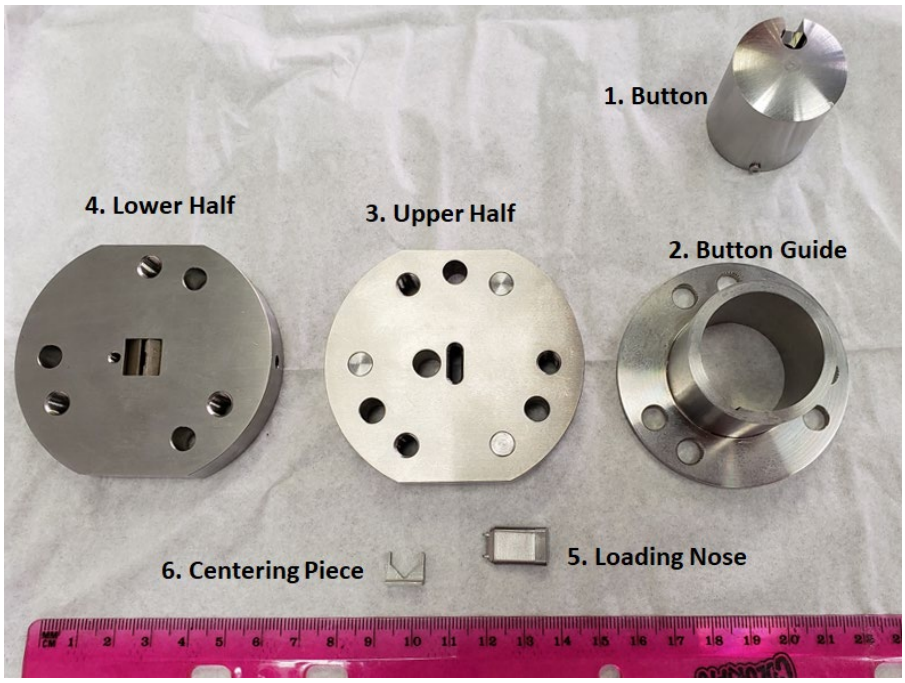

Figure 1. Picture of the three-point bend fixture for 3 mm disk samples. Load is applied via load frame to the button, which moves with restricted displacement in button guide. Loading nose is inserted into upper half, and the affixed tungsten carbide rod transfers the load to the disk, which is situated in the supports that are centered in the lower half.

ACKNOWLEDGEMENTS

This manuscript has been authored by UT-Battelle, LLC, under Contract No. DE-AC05-00OR22725 with the U.S. DOE.

10.4 AN UPDATE ON THE FRACTURE TOUGHNESS OF THE PNNL AS-SINTERED AND HOT-ROLLED W-NiFe HEAVY TUNGSTEN ALLOY: EFFECTS OF ALLOY STRENGTH, SPECIMEN ORIENTATION AND PRE-CRACK VERSUS NOTCH DEFECT GEOMETRY—M.E. Alam, G.R. Odette (University of California Santa Barbara), J. Wang, C.H. Henager, W. Setyawan (Pacific Northwest National Laboratory)

OBJECTIVE

The objective of this research is to understand the effects of alloy strength, specimen orientation and notch versus precrack defect geometry on the room temperature fracture toughness of hot-rolled 90W7Ni3Fe tungsten heavy alloys (WHA).

SUMMARY

The effects of hot rolling (HR) on the room temperature fracture toughness of PNNL's 90WNiFe WHA at different reduction percentages (i.e. 0, 62, 74 and 87%) have been characterized, at PNNL for notched bend bars, and at UCSB for precracked bend bars. The precracked K_{Jm} toughness is high (97 - 116 MPa$\sqrt{m}$) in the 0 and 87% HR alloys, which experience stable crack growth; in contrast the corresponding 62 and 74% HR WHA failed by elastic fracture, with much lower K_{Ic} (35 MPa$\sqrt{m}$). PNNL's notched specimens follow the similar trends, but, for the 0 and 87R WHA, have generally higher toughness than UCSB's precracked specimens. Tensile and microhardness data show that the precracked toughness decreases with increasing WHA strength, associated with the 62 and 74% HR conditions. The reasons for the strength versus HR pattern are not understood. However, the toughness versus strength trend is consistent with UCSB tests on as-sintered 90WFeNi (0% HR) below room temperature. Unfortunately, a strong orientation effect is observed in the precracked 87% HR condition, with a brittle LT K_{Ic} that is much lower than for the K_{Jm} for the LS tests.

PROGRESS AND STATUS

Introduction

Tungsten heavy metal alloys (WHAs), a class of bi-phase metallic composite, typically contain 78-98% W, along with a balance of lower melting point ductile phase (DP) metals like Ni, Fe, Cu and Co, are well known for their good room to high temperature tensile strength and ductility [1–4]. In addition to use in very high temperatures environments, like rocket nozzles, main applications of WHA, include use in ordnance, such as kinetic energy penetrators, counterbalances and flywheels, where high mass densities are important [1,3,5]. Recently, various WHAs have been considered as potential structural plasma facing materials for fusion reactor divertor applications [6–13]. For example, Neu et al. [8,9] reported the use of 97W-2Ni-1Fe WHAs as divertor tiles for the mid-size tokamak ASDEX Upgrade facilities that experienced cyclic plasma heat flux up to 20MW/m^2 and surface temperature up to 2200ºC, and found a lower cracking tendency for WHAs compared to pure W.

Various thermomechanical plastic deformation processing routes, like hot-rolling (HR), extrusion or swaging may increase the strength of WHA's [14–21]. Researchers at Pacific Northwest National Laboratory (PNNL) characterized the effects of the composite architecture on deep notch bend bar toughness for a 90 wt.% W-Fe-Ni WHA, with HR to different thickness reductions of 0, 62, 74 and 87% [6]. Their hypotheses was that the deformed W and DP phases, which form a 'brick-and-mortar (BAM)' like microstructure, could improve strength by HR, while enhancing ductility and toughness, by creating more distributed damage zone under deep notch bar loading [6,22]. However, our literature search found no reports on precracked fracture toughness for HR WHA. Good sharp crack fracture toughness is very important if WHA are to be used as a divertor structural material. In this study, the room temperature *precracked* elastic-plastic fracture

toughness properties of the same PNNL HR 90W7Ni3Fe (wt.%) were characterized based on ASTM Standard E1921-20 [23]. Microhardness shows an exactly opposite trends, with much higher hardness for the 62 and 74% HR alloys ($H_v \approx 400$ kg_f/mm^2), compared to the 0 and 87% WHA ($H_v \approx 315$ kg_f/mm^2). Orientation and notch versus precrack effects for 87% HR alloy have also been observed. The strength differences rationalize the toughness trends.

Experimental Procedures

Details of materials acquisition, hot-rolling, specimen fabrication, precracking and testing procedures can be found elsewhere [6,24]. Briefly, commercially available 90W7Ni3Fe (hereafter called 90W) WHA was acquired from Mi-Tech Metals, Indianapolis, In, USA as a liquid phase sintered plate, which was then hot rolled (HR), to different thinkness reductions (i.e. 0, 62, 74 and 87%) at PNNL. Here, we will refer to the hot rolling reductions as 0R, 62R, 74R and 87R. Basic microstructural characterization involves pre- and post-deformation optical, SEM, EDS and EBSD on various HR specimens, again details are reported in [6,24]. Here, we evaluate the fracture toughness of the 90WFeNi WHA as a function of the HR condition. We have also explored the specimen's orientational effect (LT vs. LS, see Figure 1) on the fracture toughness of precracked 87R alloy. Microhardness tests, including indentation at lower load, have also been conducted. We have also compared the elastic and elastic plastic toughness of notched vs. precracked specimens.

Results

Microstructure

The 3D SEM micrographs of the polished and etched HR 90WNiFe plates has been reported previously [24]. In summary, the 0R (as-received) 90W plate shows randomly oriented, roughly spheroidal ≈ 17 ± 7 μm W particles (particle aspect ratio, PAR: 1.2 ± 0.2) surrounded by an interconnected honeycomb web structure of the NiWFe ductile phase, DP (see Table 1, Figure 1c and [24,25]). Increasing the HR leads to increasingly oriented and anisotropic deformed W-particles and surrounding DP (Fig. 1d-f). For example, the W-particles are deformed along X, Y and Z directions to ≈ 44x27x10μm for 62R, 55x25x7μm for 74R and 79x27x5 μm for 87R alloys (Table 1 and Figure 1). Most notably, W phase for 87R is deformed into highly irregular, crenulated, wavy and partly interconnected layers of W blades, separated by thin NiWFe DP layers. Indeed, the multiphase 87R deformation is so large that the ductile and W phases are mechanically mixed to form roughly spherical inclusions inside the W blades (see below and [24]). The 62R HR flattens, extend and welds the initially roughly spherical W particles. Compared to the 74R to 87R HR conditions, the increment of deformation between the 62R and 74R, produces layers of discrete and more regular blade-like W particles. The EDS element maps and peaks scans both confirms that the compositions are close to 100% for the W particles and ≈ 50%Ni, 30%W and 20%Fe (by weight) for the ductile fcc phase [24].

As described in detail in [26,27], both the IPF and PF maps from EBSD on 0R plate show randomly oriented W particles embedded in the very coarse grained NiWFe DP. Most of the observed 0R DP grains exhibit {101} type texture along the in-plane direction (Y-direction), but they are insufficient in number to reach any definite conclusion [27]. The deformed W particles do not show a preferential texture, even in the 87R condition. However, HR drastically refines the DP grain size (< 10μm) and morphology with a predominance (≈ 57%) of ∑3 annealing twin boundaries [26]. These small DP grains are also randomly oriented, irrespective of scan or rolling directions. Other details can be found in [27].

Table 1. Tungsten particle size, DP%, RT Vickers microhardness and toughness for the HR 90W plates

HR, (%)	Average W particle size in X,Y,Z; (μm)	DP in top, side and front; (%)	Microhardness*, H_v, (Kgf/mm^2)	K_{IC}/K_{Jm} (MPa$\sqrt{m}$)
0R	17± 7	16.7 ± 3.6	310 ± 6	97 ± 18
62R	44 x 27 x 10	18 x 14 x 19	394 ± 8	35 ± 2
74R	55 x 25x 7	20 x 13 x 21	397 ± 12	35 ± 3
87R	29 x 27 x 5	21 x 12 x 23	327 ± 10	116 ± 20

* Vickers microhardness was averaged for 500gf and 1000gf load.

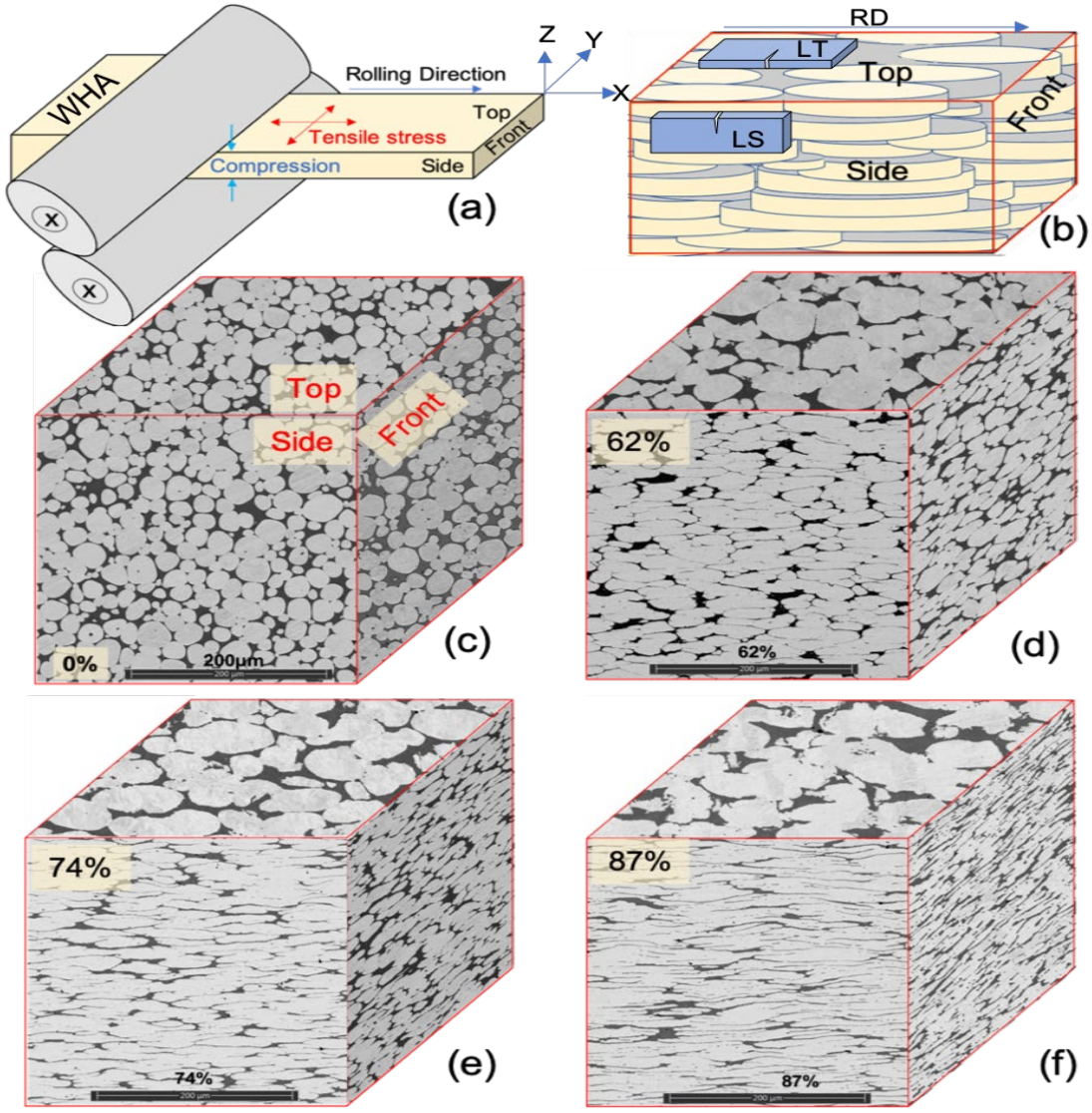

Figure 1. (a) Schematic illustration of the rolling operation and definition of plate views; (b) 3D schematic illustration of deformed W-particles, along with 3PB bend bars in LT and LS orientations. Fig.1c-f shows the 3D representation of the rolled-plate at each view for: (c): 0R; (d) 62R; (e) 74R; and, (f) 87R, respectively.

Microhardness

Room temperature Vicker's microhardness (H_v) measurements for the as-received and HR 90W alloy are shown in Table 1 and Figure 2a; further details can be found in [24]. Here the microhardness values are the average for 500g_f and 1000g_f loads. The microhardness first increases with HR from 0 to 62R (310 ± 6 kg_f/mm^2 and 394 ± 8 kg_f/mm^2, respectively), then levels of at 74R (at ≈ 397 ± 12 kg_f/mm^2), followed by a large decrease at 87R (at ≈ 327 ± 10 kg_f/mm^2). The initial increase in H_v is expected, since increasing HR increases the dislocation densities and refines W particle and DP grains [15,16,19,21].The saturation of H_v is not unexpected, if the microstructure reaches a steady state condition. However, the much lower hardness of the 87R condition, compared to the 62R and 74R, is unexpected. This may be due to a strain induced recovery/recrystallization process, but there is not enough data to reach any conclusion. We also measured H_v at lower loads at 100g_f and 200g_f for the 0R and 87R conditions [24]. The average H_v increases with decreasing indentation load. Note, indentation cracking was not observed in any of the test conditions, including for 1000g_f on 87R plate [24].

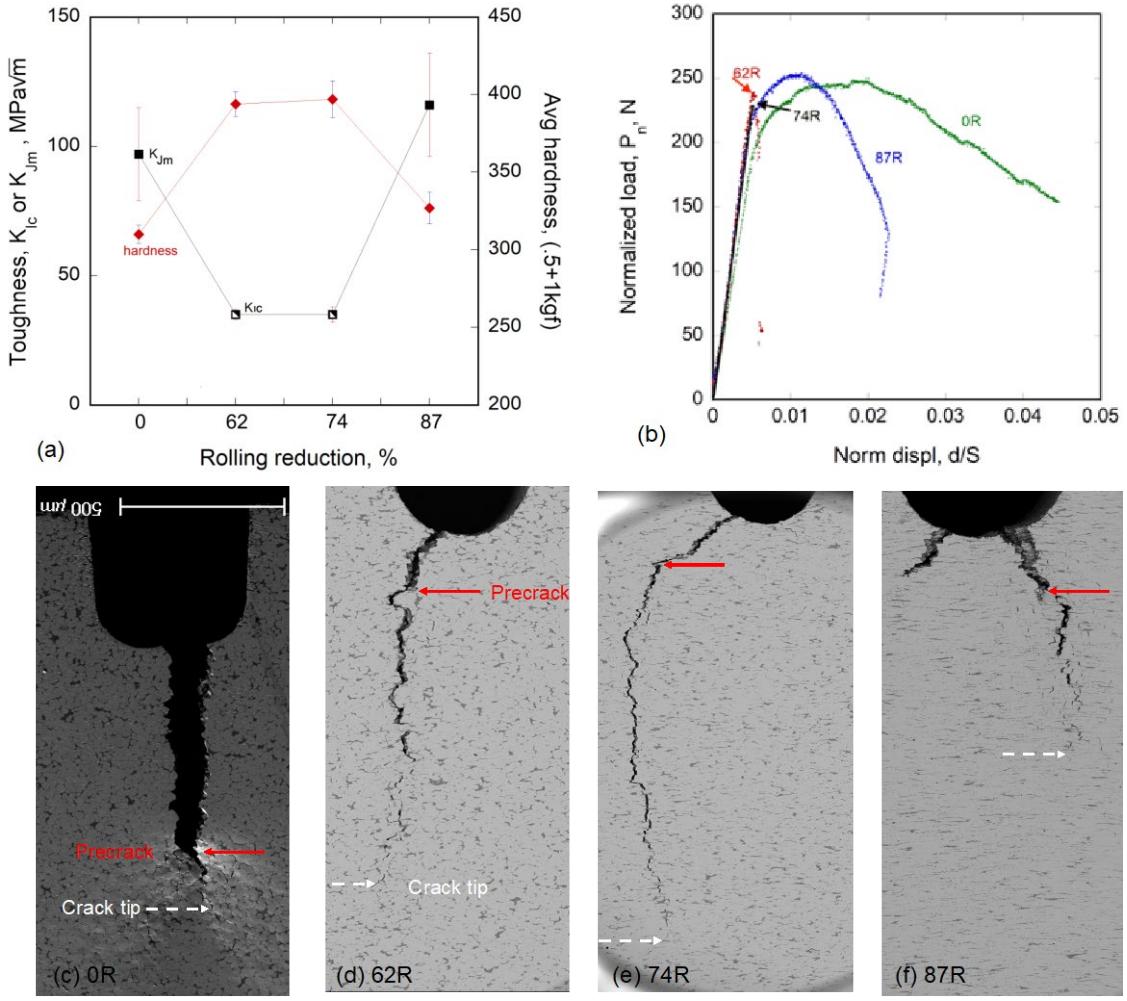

Figure 2. (a) Average microhardness values for the 500 and 1000g_f (red diamonds), and fracture toughness (black square) for HR 90W plates. Note, filled and half-filled squares represent stable and unstable crack propagation; (b) normalized RT load-displacement (P_n-d_n) curves for the rolled plates. Figure 2c-f shows the side surface crack propagation for 0, 62, 74, and 87R, respectively.

Room temperature (RT) fracture toughness

The RT fracture toughness tests on the various rolled plates were conducted on the fatigue precracked 3PB bars at UCSB. The corresponding normalized load-displacement (P_n-d_n) curves are shown in Figure 2b, and toughness data are summarized in Table 1 and plotted in Figure 2a along with the H_v data. The load-displacement normalization procedures are described in [24]. As reported previously [25], all of the 0R (as-received) 90W specimens show very stable crack growth, with a maximum load fracture toughness, $K_{Jm} \approx 97 \pm 18$ MPa$\sqrt{m}$; this is about 12 times higher than typical monolithic W toughness ($K_{Ic} \approx 8 \pm 4$ MPa$\sqrt{m}$) (Table 1 and Figure 2b). The 0R P-d curve has a linear elastic loading region, followed by a plastic yielding with increasing P due to the growth of the plastic zone and strain hardening. The large decreases in P following the maximum load (P_m) reflect stable crack growth. Note, all the 0R tests were intentionally stopped after P_m, before final specimen fracture. The high standard deviation in some K_{Jm} is due to the local microstructural inhomogeneities, especially specimen to specimen DP fraction variations [28]. In contrast, the 62R and 74R specimens experienced elastic fracture and unstable crack propagation, with a relatively low elastic fracture toughness of $K_{Ic} \approx 35 \pm 2$ MPa$\sqrt{m}$ (Table 1 and Figure 2a, b, d, e); note this is still more than 4 times higher than the typical monolithic W. In contrast, the 87R condition experienced stable crack, like the 0R condition, but with an even higher elastic plastic $K_{Jm} \approx 116 \pm 20$ MPa$\sqrt{m}$ (Table 1 and Figure 2a,b,c,f).

The process-zone microcrack arrest, blunting-plastic zone dominated toughening mechanisms for 0R 90W plate has been discussed in detail in [25]. Briefly, the W cleavage (WC) microcracks are arrested by the NiWFe DP and blunt under increased load. Many of the cleaved and unbroken W particles also deform in the principal stress direction. All these processes increase the toughness of the as-received 0R 90W plate. the same toughening mechanisms that occur in the 0R condition are observed in the 87R plate (Figure 2b, f). However, there are far fewer micro-fracture events for the 62R and 74R specimens, and minimal WC is observed near the crack propagation zone (Figure 2d-e); in this case fracture involves unstable growth of the single sharp macro-crack, or a few large microcracks quickly link up with nearby co-planar cracks, without cleaving neighboring W particles. This results in unstable crack growth (see details in [24]), similar to low temperature toughness test in the aw-sintered condition [25].

The fracture processes and lower toughness in the 62R and 74R inversely correlate with the corresponding H_v trend (see Table 1 and Figure 2a). The hypothesis that toughness correlates with strength can be tested by comparing the HR toughness-strength trends to the corresponding low temperature-higher strength fracture behavior of the as-sintered (0R) UCSB WHA plate reported in [25]. Figure 3 (see above) plots K_{Jm}/K_{Ic} versus the estimated ultimate tensile stress (σ_u), at RT, -100 and -196°C based on tensile test data. The σ_u at -196°C may be a little higher than the measured elastic fracture stress but is reasonably consistent with extrapolated trends. The σ_u data points at -50 and -150°C, are interpolated estimates. The red squares are for the PNNL's HR plate at 0/87R (lower strength) and 62/74R (higher strength). The σ_u for 0/87R are from PNNL tensile tests, while the σ_u for the 62/74R conditions are estimated from the H_v data, as $\sigma_u \approx 3.27H_v$ (≈ 1298 MPa), based on the common relation $H_v \approx 3\sigma_u$ in common units of MPa [29]. The results suggest that the lower toughness (K_{Ic}), for the 62/74R conditions, is due to the correspondingly higher strength (σ_u). Note that other comparisons suggest a lower $\sigma_u \approx 2.8H_v$(kg_f/mm^2) relation, but this does not qualitatively affect the hypothesis regarding lower toughness at higher strength. Additional tensile data for the 62/74R condition will be needed to evaluate this hypothesis further.

Orientation Effects

The LS toughness tests take maximum advantage of the HR WHA layered structure with a brick and mortar morphology. However, fracture toughness in other orientations is certainly an issue. Thus, RT toughness tests were also conducted on the 87R condition in the more standard LT orientation. The corresponding normalized P-d curves for the LT and LS oriented 87R specimens shown in Figure 4a reveal the 87R LT toughness is much lower, at $K_{Ic} \approx 38 \pm 3$ MPa$\sqrt{m}$, and is accompanied by unstable crack propagation. As

schematically illustrated in Figure 4b, toughness anisotropy is easy to understand. In the LS orientation, small WC cracks are blunted by the DP layer that cannot be avoided. Crack renucleation and deflection mechanisms may also contribute to the higher toughness in this case. However, in the LT orientation, the WC cracks are much larger (5x) and encounter far fewer DP regions. The macrocrack (or a larger process zone microcrack) is able to follow a more or less continuous WC path at tip stresses that are too low to cause microcracking in the adjoining regions (see Figure 4c). In this case only minor toughening is provided by crack wake bridging and limited plastic zone deformation. Figure 4d also shows WC dominated fracture surfaces, analogous to low temperature tests for WHAs.

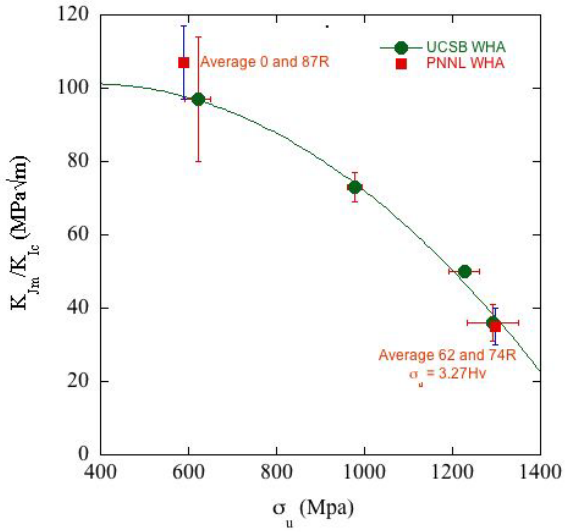

Figure 3. K_{Jm}/K_{Ic} versus the estimated WHA σ_u. The green symbols are for the as-sintered (0R) UCSB plate at various low temperatures ≤ RT. The red symbols for the HR PNNL 0R/87R and 62/74R plate averages. The PNNL 62/74R point is based on $\sigma_u(MPa) \approx 3.27H_v(kg_f/mm^2)$ [29].

Notch versus Precrack Effects

We have also compared the LS oriented RT fracture toughness of PNNL specimens that are precracked, tested at UCSB, versus the toughness of similarly fabricated notched specimens, tested at PNNL, both at RT [6]. The normalized P_n-d_n curves for the notched versus precracked specimens are shown in Figure 5a and toughness results are summarized in the Table in Figure 5b. Clearly, the PNNL notch toughness follows the similar trends to UCSB's precracked test data (Figures 2b and 5). In both cases, 0/87R specimens exhibit elastic-plastic fracture behavior, whereas 62/74R specimens show only unstable, brittle fracture with much lower toughness. However, the PNNL's notched specimen show higher toughness values than the UCSB's precracked specimens, for the 0 and 87R conditions. This is understandable as the plastic process zone for blunting the notched PNNL specimens is much larger than for the sharp, precracked UCSB specimens, accompanied by lower internal stresses ($\approx 2.2\sigma_y$ vs. $> 3\sigma_y$). From application point of view, sharp cracks are expected to develop during cyclic loading.

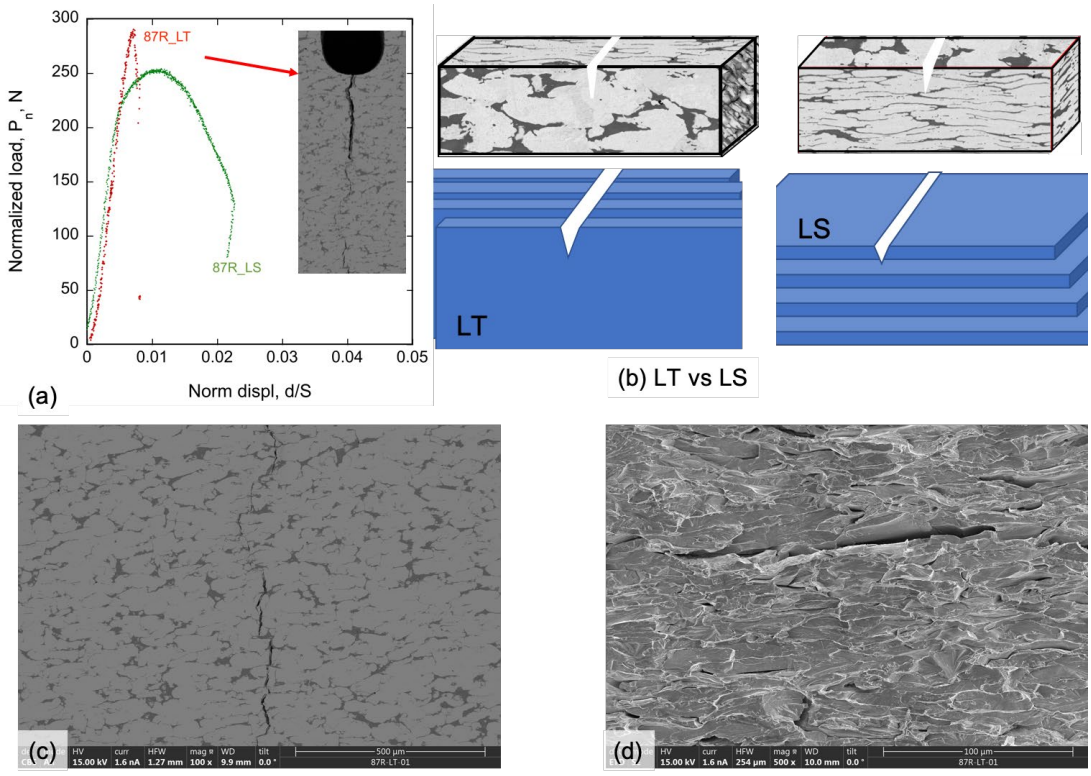

Figure 4. (a) Normalized P-d curves for 87R 90WHA for LT and LS orientations, with an inset showing unstable crack propagation in an 87R for the LT tests; (b) schematic of crack path for the LT and LS orientations; (c) sharp crack without any adjacent WC in the propagation zone for the LT orientation; and, (d) large and deep out of plane microcracks with WC in the 87R LT orientations.

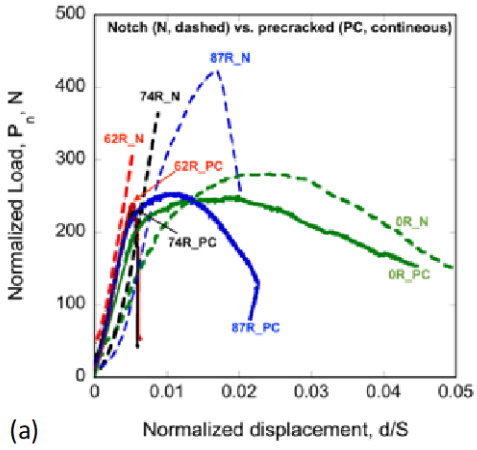

90WNiFe	UCSB_PC K_{Ic}/K_{Jm}, MPa√m	PNNL-Notch K_{Ic}/K_{Jm}, MPa√m
0%	97 ± 18	160
62%	35 ± 2	36
74%	35 ± 3	42
87%	116 ± 20	132

(b)

Figure 5. (a) Normalized P_n-d_n curves for the notched (dash lines) versus precracked (continuous lines) HR 90WHA specimens; and (b) the corresponding RT fracture toughness values.

SUMMARY

There is a strong relation between lower WHA fracture toughness and higher strength. The WHA strength varies with the amount of HR first increasing, then saturating, then decreasing for reasons that are not yet understood. HR WHA have a very large orientation dependence and are much more brittle in the LT vs.LS tests. The toughness trends are qualitatively similar for notched and precracked bend bars. However, the elastic plastic fracture K_{Jm} are somewhat lower for the precracked tests. Nevertheless, notched bend tests are useful for observing toughness trends.

FUTURE WORK

Additional characterization is needed to understand the effect of HR conditions on the WHA strength. The effect of high temperature annealing on the strength and toughness of WHA will be evaluated. High temperature tests of fracture toughness and subcritical crack growth rates will be initiated.

ACKNOWLEDGEMENTS

We like to acknowledge the support provided by U.S. Department of Energy (DOE) through the Office of Fusion Energy Sciences PNNL under contract DE-AC05-76RL01830 and UCSB DOE-Fusion 8-442520-22419-3. The U.S. National Science Foundation supported California Nanoscience Institute provided facilities critical the success of this research.

References

[1] Y. Şahin, Recent progress in processing of tungsten heavy alloys, J. Powder Technol. 2014 (2014) 1–22.

[2] K. Hu, X. Li, X. Ai, S. Qu, Y. Li, Fabrication, characterization, and mechanical properties of 93W-4.9Ni-2.1Fe/95W-2.8Ni-1.2Fe/95W-2.8Ni-1.2Fe-1Al2O3 heavy alloy composites, Mater. Sci. Eng. A. 636 (2015) 452–458.

[3] X. Gong, J. Fan, F. Ding, Tensile mechanical properties and fracture behavior of tungsten heavy alloys at 25-1100 °C, Mater. Sci. Eng. A. 646 (2015) 315–321.

[4] U.R. Kiran, A. Panchal, M. Sankaranarayana, G.V.S.N. Rao, T.K. Nandy, Effect of alloying addition and microstructural parameters on mechanical properties of 93% tungsten heavy alloys, Mater. Sci. Eng. A. 640 (2015) 82–90.

[5] W.D. Cai, Y. L, R.J. Dowding, F.A. Mohamed, E.J. Lavernia, A review of tungsten-based alloys as kinetic energy penetrator materials, Rev. Part. Mater. 3 (1995) 71–131.

[6] C. Henager Jr, W. Setyawan, T. Roosendaal, N. Overman, B. Borlaug, E. Stevens, K. Wagner, R. Kurtz, G.R. Odette, B. Nguyen, K. Cunningham, Ductile-phase toughened tungsten for plasma-facing materials in fusion reactors, Int. J. Powder Metall. 53 (2017) 53–69.

[7] M. Scapin, Mechanical characterization and modeling of the heavy tungsten alloy IT180, Int. J. Refract. Met. Hard Mater. 50 (2015) 258–268.

[8] R. Neu, H. Maier, M. Balden, S. Elgeti, H. Gietl, H. Greuner, A. Herrmann, A. Houben, V. Rohde, B. Sieglin, I. Zammuto, Investigations on tungsten heavy alloys for use as plasma facing material, Fusion Eng. Des. 124 (2017) 450–454.

[9] R. Neu, H. Maier, M. Balden, R. Dux, S. Elgeti, H. Gietl, H. Greuner, A. Herrmann, T. Höschen, M. Li, V. Rohde, D. Ruprecht, B. Sieglin, I. Zammuto, Results on the use of tungsten heavy alloys in the divertor of ASDEX Upgrade, J. Nucl. Mater. 511 (2018) 567–573.

[10] H. Sattar, S. Jielin, H. Ran, M. Imran, W. Ding, P. Das Gupta, H. Ding, Impact of microstructural properties on hardness of tungsten heavy alloy evaluated by stand-off LIBS after PSI plasma irradiation, J. Nucl. Mater. 540 (2020) 152389.

[11] Q. An, A. Elshafiey, L. Huang, D.A. Hammer, M. Hassani, Plasma and X-ray radiation-induced damage mechanisms in a tungsten heavy alloy, J. Nucl. Mater. 539 (2020) 152325.

[12] G.R. Odette, M.E. Alam, K. Cunningham, Ductile-Phase Toughened Tungsten for Plasma Facing Materials, DOE-UCSB-ER54275, United States, 2019.
[13] T. Laas, K. Laas, J. Paju, J. Priimets, S. Tõkke, B. Väli, V. Shirokova, M. Antonov, V.A. Gribkov, E. V. Demina, V.N. Pimenov, M. Paduch, R. Matulka, M. Akel, Behaviour of tungsten alloy with iron and nickel under repeated high temperature plasma pulses, Fusion Eng. Des. 151 (2020).
[14] X. Gong, J.L. Fan, F. Ding, M. Song, B.Y. Huang, Effect of tungsten content on microstructure and quasi-static tensile fracture characteristics of rapidly hot-extruded W-Ni-Fe alloys, Int. J. Refract. Met. Hard Mater. 30 (2012) 71–77.
[15] X. Gong, J.L. Fan, F. Ding, M. Song, B.Y. Huang, J.M. Tian, Microstructure and highly enhanced mechanical properties of fine-grained tungsten heavy alloy after one-pass rapid hot extrusion, Mater. Sci. Eng. A. 528 (2011) 3646–3652.
[16] Z.S. Levin, K. Ted Hartwig, Hardness and microstructure of tungsten heavy alloy subjected to severe plastic deformation and post-processing heat treatment, Mater. Sci. Eng. A. 635 (2015) 94–101.
[17] Y. Yang, H. Lianxi, W. Erde, Microstructure and mechanical properties of a hot-hydrostatically extruded 93W-4.9Ni-2.1Fe alloy, Mater. Sci. Eng. A. 435–436 (2006) 620–624.
[18] Y. Yu, H. Hu, W. Zhang, X. Xu, Microstructure evolution and recrystallization after annealing of tungsten heavy alloy subjected to severe plastic deformation, J. Alloys Compd. 685 (2016) 971–977.
[19] Y. Yu, W. Zhang, E. Wang, Effect of heat treatment on microstructure and mechanical properties of hot-hydrostatically extruded 93W-4.9Ni-2.1Fe alloy, J. Alloys Compd. 622 (2015) 880–884.
[20] Z.H. Zhang, F.C. Wang, S.K. Li, L. Wang, Deformation characteristics of the 93W-4.9Ni-2.1Fe tungsten heavy alloy deformed by hydrostatic extrusion, Mater. Sci. Eng. A. 435–436 (2006) 632–637.
[21] Z. Zhaohui, W. Fuchi, Research on the deformation strengthening mechanism of a tungsten heavy alloy by hydrostatic extrusion, Int. J. Refract. Met. Hard Mater. 19 (2001) 177–182.
[22] B.N. Nguyen, C.H. Henager, J. Wang, W. Setyawan, Tailoring ductile-phase toughened tungsten hierarchical microstructures for plasma-facing materials, J. Nucl. Mater. 540 (2020) 152382.
[23] ASTM E1921-20, Standard Test Method for Determination of Reference Temperature , To , for Ferritic Steels in the Transition Range, in: Annu. B. ASTM Stand., ASTM International, 100 Barr Harbor Drive, PO Box C700, West Conshohocken, PA 19428-2959, United States, 2020: pp. 1–25.
[24] M.E. Alam, G.R. Odette, C.H. Henager, W. Setyawan, Fracture Toughness of Rolled 90WNiFe Tungsten Heavy Metal Alloy, Fusion React. Mater. Progr. Semiannu. Prog. Rep. DOE0313/67 (2019) 52–65.
[25] M.E. Alam, G.R. Odette, On the remarkable fracture toughness of 90 to 97W-NiFe alloys revealing powerful new ductile phase toughening mechanisms, Acta Mater. 186 (2020) 324–340.
[26] J. V. Haag IV, D.J. Edwards, C.H. Henager, W. Setyawan, J. Wang, M. Murayama, Characterization of Ductile Phase Toughening Mechanisms in a Hot-Rolled Tungsten Heavy Alloy, Acta Mater. 204 (2020) 116523.
[27] J. Wang, D. Collins, N.R. Overman, W. Setyawan, Tensile Testing and Microstructural characterization of Ductile Phase Toughened W-NiFe Alloys, Fusion React. Mater. Progr. Semiannu. Prog. Rep. DOE0313/68 (2020) 102–120.
[28] M.E. Alam, G.R. Odette, On the effect of specimen size, geometry and ductile phase content on the fracture toughness of tungsten heavy metal alloys, DOE Fusion React. Mater. Progr. Semiannu. Prog. Rep. DOE0313/66 (2019) 45–52.
[29] P. Zhang, S.X. Li, Z.F. Zhang, General relationship between strength and hardness, Mater. Sci. Eng. A. 529 (2011) 62–73.

10.5 IRRADIATION OF QST F82H TENSILE AND BEND BAR SPECIMENS IN HFIR—N. Russell, C. On, X. Chen, J. Geringer (Oak Ridge National Laboratory)

OBJECTIVE

The objective of this task is the implementation of the general tensile (GENTEN) and general bend bar (GENBEN) designs for irradiation of QST F82H specimens in HFIR. There is a total of 21 irradiation capsules within this campaign consisting of three low dose (5 dpa) capsules and 18 high dose (50 and 80 dpa, 9 of each). There are three different average specimen irradiation temperatures of 300°C, 400°C, and 500°C for these capsules.

SUMMARY

The temperature performance within an irradiation capsule is controlled by optimizing the specimen holder outer diameter (OD), holder material, and fill gas to create an insulating gas gap between the hot inner holder assembly and the cold capsule housing in direct contact with HFIR coolant. Much care and consideration was taken to apply the existing GENTEN and GENBEN designs. These designs developed a surface response model that allows the user to quickly and accurately determine a combination of holder OD, holder material, and fill gas to achieve an average specimen goal temperature. These two capsule designs can be seen below in Figure 1 and Figure 2.

Existing data for high dose irradiations is sparse. It is known that some materials have different amounts of neutron induced swelling over time. As a specimen holder swells over time, the insulating gas gap shrinks, decreasing the capsule temperature. Typically, when designing capsules for low dose irradiations, the neutron induced swelling isn't accounted for due to the very low impact. However, for these high dose irradiations the swelling should be considered. These designs use Al-6061 for the 300°C case and molybdenum holders for the 400°C and 500°C cases. Al-6061 and molybdenum have different swelling rates that are also dependent on the temperatures.

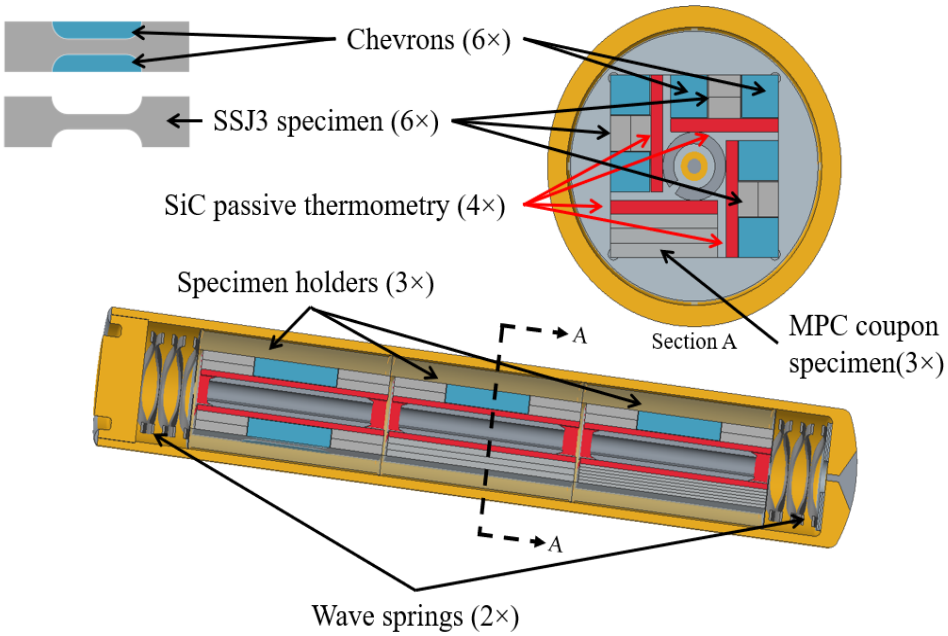

Figure 1. GENTEN irradiation capsule design.

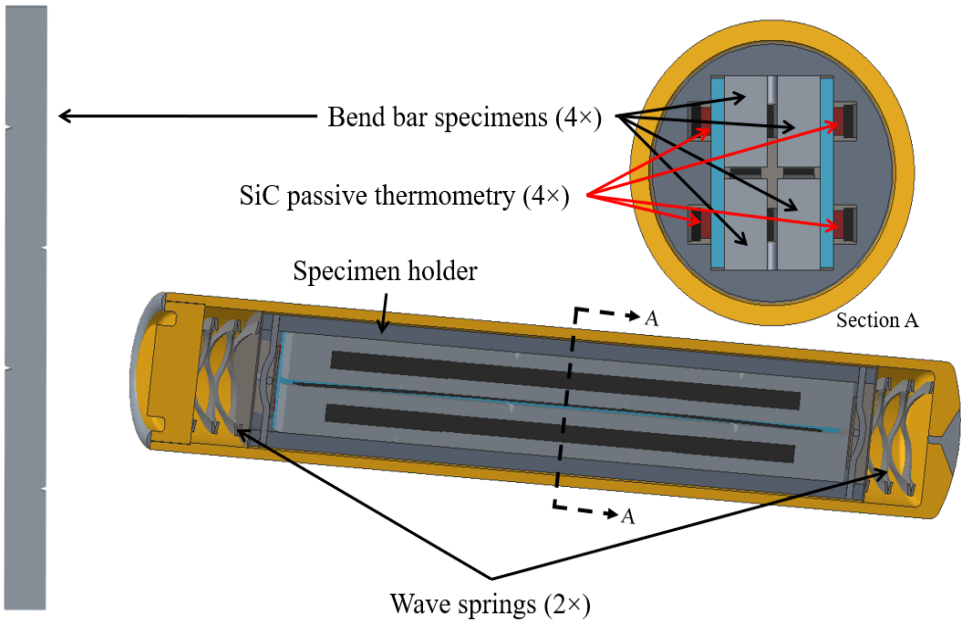

Figure 2. GENBEN irradiation capsule design.

Once the neutron induced swelling rates were determined for the different specimen holder materials and temperatures, post irradiation holder ODs were predicted. These post irradiation holder ODs could be plugged back into the surface response model to estimate final average specimen temperatures. Over the course of the irradiation the average specimen temperatures were estimated and reported to the ORNL principle investigator (PI) and the QST PI in Japan.

QST requested hold points be introduced to our standard irradiation capsule build procedure. The first hold point form was for holder design approval. This allowed the ORNL PI and QST PI to be involved in choosing appropriate holder ODs and the math behind the neutron induced swelling. All of the first hold point forms for the QST irradiation capsules have been reviewed and signed by the capsule designer, ONRL PI, and QST PI. The second hold point was introduced between assembly of the capsule parts and before welding. This hold point form for the capsules show pictures of every step in the assembly process so that QST could review the process and confirm specimen orientation. This hold form is approved for all the low dose capsules.

Based on the capsule designs shown in Figure 1 and 2, the following matrices were used to track the capsule positions and orientations during assembly. Table 1 contains the load matrix for capsule FH51, which holds the GENTEN specimens. On the other hand, Table 2 shows the load matrix for capsules FH61 and FH62, containing the GENBEN specimens.

Moving forward, all the low dose capsules have been delivered to HFIR for irradiation to begin in HFIR cycle 490. All of the hold point forms for the low dose capsules have been approved and are included with the fabrication package. The high dose capsule designs have been approved by the ORNL PI and QST PI. The high dose capsules are waiting instruction to begin building with estimated insertion into HFIR in FY21.

Table 1. GENTEN load matrix

Capsule ID	Temp (°C)	Dpa	Tier	Position	Specimen ID	Specimen Type	Material Class	Material	Mass (g)	Length (mm)	Width 2-Left (mm)	Width 2-Right (mm)	Thickness (mm)	Width 1 (mm)
FH51	300	5	Outer	Sub-holder 1 (top)	0RU	SS-J3 without notch	F82H-IEA	8Cr-2W-0.04Ta; VIM	0.2653	16.0	4.0	4.0	0.77	1.20
FH51	300	5	Inner	Sub-holder 1 (top)	0RZ	SS-J3 without notch	F82H-IEA	8Cr-2W-0.04Ta; VIM	0.2653	16.0	4.0	4.0	0.77	1.20
FH51	300	5	Outer	Sub-holder 2 (middle)	0RAa	SS-J3 without notch	F82H-IEA	8Cr-2W-0.04Ta; VIM	0.2657	16.0	4.0	4.0	0.77	1.20
FH51	300	5	Inner	Sub-holder 3 (bottom)	0RAb	SS-J3 without notch	F82H-IEA	8Cr-2W-0.04Ta; VIM	0.2658	16.0	4.0	4.0	0.77	1.20
FH51	300	5	Outer	Sub-holder 1 (top)	0RCf	SS-J3 with notch1	F82H-IEA	8Cr-2W-0.04Ta; VIM	0.2656	16.0	4.0	4.0	0.77	1.20
FH51	300	5	Outer	Sub-holder 2 (middle)	0RCg	SS-J3 with notch1	F82H-IEA	8Cr-2W-0.04Ta; VIM	0.2662	16.0	4.0	4.0	0.77	1.20
FH51	300	5	Inner	Sub-holder 2 (middle)	0RCh	SS-J3 with notch1	F82H-IEA	8Cr-2W-0.04Ta; VIM	0.267	16.0	4.0	4.0	0.77	1.20
FH51	300	5	Inner	Sub-holder 3 (bottom)	0RCk	SS-J3 with notch1	F82H-IEA	8Cr-2W-0.04Ta; VIM	0.2649	16.0	4.0	4.0	0.77	1.20
FH51	300	5	Inner	Sub-holder 1 (top)	0RDu	SS-J3 with notch2	F82H-IEA	8Cr-2W-0.04Ta; VIM	0.2655	16.0	4.0	4.0	0.77	1.20
FH51	300	5	Inner	Sub-holder 2 (middle)	0RDw	SS-J3 with notch2	F82H-IEA	8Cr-2W-0.04Ta; VIM	0.2661	16.0	4.0	4.0	0.76	1.20
FH51	300	5	Outer	Sub-holder 3 (bottom)	0RDx	SS-J3 with notch2	F82H-IEA	8Cr-2W-0.04Ta; VIM	0.2667	16.0	4.0	4.0	0.77	1.19
FH51	300	5	Outer	Sub-holder 3 (bottom)	0RDy	SS-J3 with notch2	F82H-IEA	8Cr-2W-0.04Ta; VIM	0.2641	16.0	4.0	4.0	0.77	1.20
FH51	300	5	Outer	Sub-holder 1 (top)	TR1	SS-J3 without notch	F82H-BA12	8Cr-2W-0.08Ta;EAF+ESR	0.2648	16.0	4.0	4.0	0.77	1.20
FH51	300	5	Inner	Sub-holder 1 (top)	TR2	SS-J3 without notch	F82H-BA12	8Cr-2W-0.08Ta;EAF+ESR	0.2657	16.0	4.0	4.0	0.77	1.20
FH51	300	5	Outer	Sub-holder 2 (middle)	TR3	SS-J3 without notch	F82H-BA12	8Cr-2W-0.08Ta;EAF+ESR	0.2642	16.0	4.0	4.0	0.75	1.20
FH51	300	5	Inner	Sub-holder 3 (bottom)	TR4	SS-J3 without notch	F82H-BA12	8Cr-2W-0.08Ta;EAF+ESR	0.266	16.0	4.0	4.0	0.77	1.20
FH51	300	5	Outer	Sub-holder 1 (top)	TRAm	SS-J3 with notch1	F82H-BA12	8Cr-2W-0.08Ta;EAF+ESR	0.2667	16.0	4.0	4.0	0.78	1.20
FH51	300	5	Outer	Sub-holder 2 (middle)	TRAn	SS-J3 with notch1	F82H-BA12	8Cr-2W-0.08Ta;EAF+ESR	0.2653	16.0	4.0	4.0	0.77	1.20
FH51	300	5	Inner	Sub-holder 2 (middle)	TRAo	SS-J3 with notch1	F82H-BA12	8Cr-2W-0.08Ta;EAF+ESR	0.2662	16.0	4.0	4.0	0.77	1.20
FH51	300	5	Inner	Sub-holder 3 (bottom)	TRAp	SS-J3 with notch1	F82H-BA12	8Cr-2W-0.08Ta;EAF+ESR	0.2653	16.0	4.0	4.0	0.77	1.20
FH51	300	5	Inner	Sub-holder 1 (top)	TRBr	SS-J3 with notch2	F82H-BA12	8Cr-2W-0.08Ta;EAF+ESR	0.2665	16.0	4.0	4.0	0.78	1.20
FH51	300	5	Inner	Sub-holder 2 (middle)	TRBs	SS-J3 with notch2	F82H-BA12	8Cr-2W-0.08Ta;EAF+ESR	0.2672	16.0	4.0	4.0	0.77	1.20
FH51	300	5	Outer	Sub-holder 3 (bottom)	TRBt	SS-J3 with notch2	F82H-BA12	8Cr-2W-0.08Ta;EAF+ESR	0.265	16.0	4.0	4.0	0.77	1.20
FH51	300	5	Outer	Sub-holder 3 (bottom)	TRBu	SS-J3 with notch2	F82H-BA12	8Cr-2W-0.08Ta;EAF+ESR	0.2664	16.0	4.0	4.0	0.76	1.20

Table 2. GENBEN load matrix

Capsule ID	Temp (°C)	Dpa	Tier	Position	Specimen ID	Specimen Type	Material Class	Material	Mass (g)	Length (mm)	Thickness (mm)	Width 1 (mm)
FH61	300	5	Top	Left	0RFc	M4-PCCVN(a/w=0.46)	F82H-IEA	8Cr-2W-0.04Ta; VIM	1.9406	45.1	1.66	3.32
FH61	300	5	Top	Right	0RFe	M4-PCCVN(a/w=0.46)	F82H-IEA	8Cr-2W-0.04Ta; VIM	1.9395	45.1	1.66	3.32
FH61	300	5	Bottom	Right	TRCy	M4-PCCVN(a/w=0.46)	F82H-BA12	8Cr-2W-0.08Ta;EAF+ESR	1.9325	45.1	1.66	3.31
FH61	300	5	Bottom	Left	TRCz	M4-PCCVN(a/w=0.46)	F82H-BA12	8Cr-2W-0.08Ta;EAF+ESR	1.9232	45.1	1.65	3.31
FH62	300	5	Top	Left	0RFf	M4-PCCVN(a/w=0.46)	F82H-IEA	8Cr-2W-0.04Ta; VIM	1.9336	45.1	1.66	3.31
FH62	300	5	Top	Right	0RFg	M4-PCCVN(a/w=0.46)	F82H-IEA	8Cr-2W-0.04Ta; VIM	1.9387	45.1	1.66	3.32
FH62	300	5	Bottom	Right	TRDa	M4-PCCVN(a/w=0.46)	F82H-BA12	8Cr-2W-0.08Ta;EAF+ESR	1.9357	45.1	1.66	3.31
FH62	300	5	Bottom	Left	TRDb	M4-PCCVN(a/w=0.46)	F82H-BA12	8Cr-2W-0.08Ta;EAF+ESR	1.9355	45.1	1.66	3.31